Renewed debate over risky flu studies *pp. 1101 & 1112*

Peptides from nucleotide repeats are toxic *pp. 1118, 1139 & 1192*

The coffee genome *pp. 1124 & 1181*

Science

$10
5 SEPTEMBER 2014
sciencemag.org

AAAS

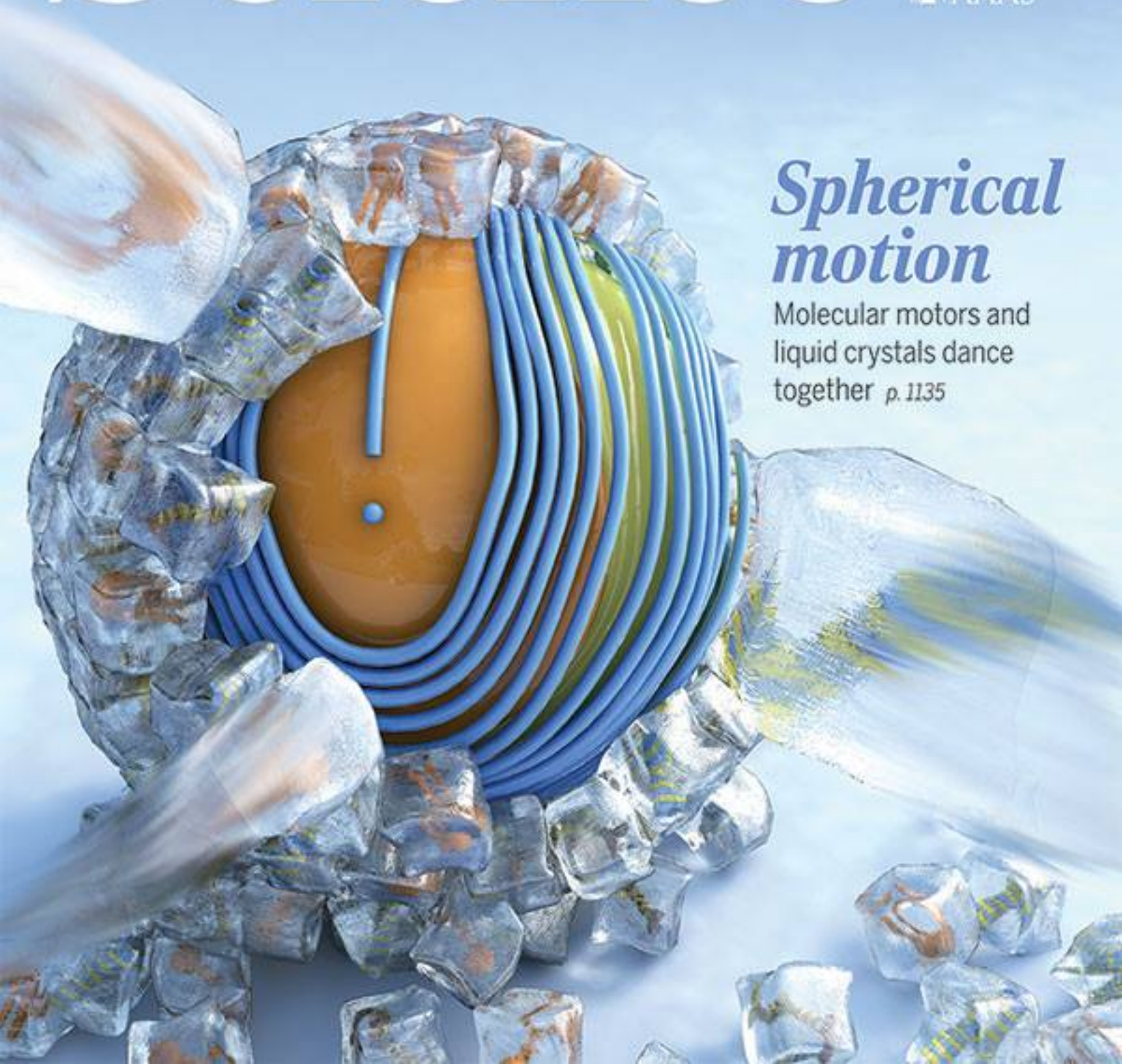

Spherical motion

Molecular motors and liquid crystals dance together *p. 1135*

CONTENTS

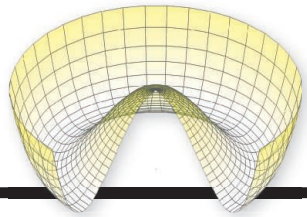

1121 & 1145
Tracking oscillations in a superconductor

5 SEPTEMBER 2014 • VOLUME 345 • ISSUE 6201

NEWS

IN BRIEF

IN DEPTH

FEATURES

INSIGHTS

PERSPECTIVES

BOOKS *ET AL.*

LETTERS

DEPARTMENTS

Published by AAAS

CONTENTS

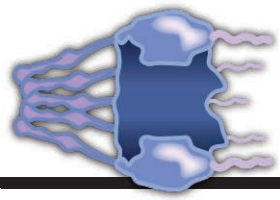

1118, 1139, & 1192
Dipeptide polymers wreak nuclear havoc

5 SEPTEMBER 2014 • VOLUME 345 • ISSUE 6201

RESEARCH

IN BRIEF

RESEARCH ARTICLES

REPORTS

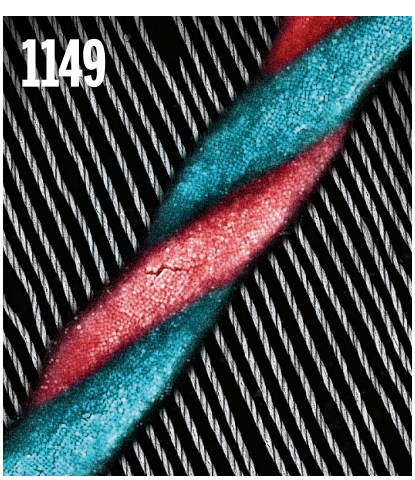

IMAGE: (LEFT) GURVINDER SINGH/RAFAL KLAJN

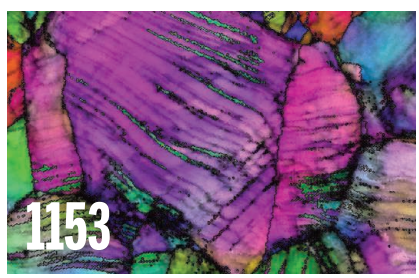

ON THE COVER

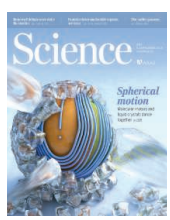

Artist's impression of how a monolayer of aligned microtubule filaments is assembled on the inner leaflet of a lipid bilayer. Powered by molecular motors, liquid crystalline microtubules generate dynamic states that include sustained oscillations of topological defects and shape-changing materials with streaming filopodia-like protrusions. See page 1135. *Image: Christoph Hohmann, Nanosystems Initiative Munich*

SCIENCE (ISSN 0036-8075) is published weekly on Friday, except the last week in December, by the American Association for the Advancement of Science, 1200 New York Avenue, NW, Washington, DC 20005. Periodicals mail postage (publication No. 484460) paid at Washington, DC, and additional mailing offices. Domestic individual membership and subscription (51 issues): $153 ($74 allocated to subscription). Domestic institutional subscription (51 issues): $1282; Foreign postage extra: Mexico, Caribbean (surface mail) $55; other countries (air assist delivery) $85. First class, airmail, student, and emeritus rates on request. Canadian rates with GST available upon request, GST #1254 88122. Publications Mail Agreement Number 1069624. **Printed in the U.S.A.**
Change of address: Allow 4 weeks, giving old and new addresses and 8-digit account number. **Postmaster:** Send change of address to AAAS, P.O. Box 96178, Washington, DC 20090–6178. **Single-copy sales:** $10.00 current issue, $15.00 back issue prepaid includes surface postage; bulk rates on request. *Science* is indexed in the *Reader's Guide to Periodical Literature* and in several specialized indexes.

Published by AAAS

EDITORIAL

Culture of responsibility

The current crisis with the Ebola virus vividly illustrates the priority that must be given to infectious diseases because of their potentially devastating consequences to individuals and to society. Few would argue against the need for more research on Ebola and the expedited development of a cure; however, recent incidents in biocontainment laboratories and the proliferation of such facilities globally raise concerns about safety and have split the scientific community. Scientists who defend research on dangerous pathogens as vital to protecting populations are opposed by those who fear the potential devastation caused by the intentional or unintentional release of pathogens from the lab. Achieving a "culture of safety," so often alluded to after recent lapses in biosafety procedures, demands adopting a "culture of responsibility" as well.

Certainly, the U.S. Centers for Disease Control and Prevention has a far broader mission today than in the 1970s, when it investigated the first outbreaks of Ebola virus in Zaire and Sudan. Nevertheless, its labs and every lab worldwide must enforce a culture of safety and responsibility. Lapses have led to illnesses and deaths in lab workers and in the community, such as in 2004, when the mishandling of the virus that causes severe acute respiratory syndrome resulted in tertiary infections and the death of an attending physician in China. The risks must be reduced, even if they cannot be eliminated. Training and safe lab operations require greater emphasis. Infrastructure, not just innovation, is critical.

"Gain-of-function" research in which pathogens are altered to increase transmissibility has raised the debate about research on dangerous pathogens to an even more contentious level. Those in public health must develop a better understanding of the real and potential benefits of such research, whereas those engaged in the research should acknowledge more fully the real and potential risks. But a far wider discussion on gain-of-function research is needed. Some have called for a meeting like the Asilomar Conference on Recombinant DNA in 1975, where biosafety guidelines were drawn up. Others have called for greater engagement by the U.S. National Academies, whose work, including the 2003 "Fink report" on research standards and practices for potentially dangerous applications of biotechnology, has been so vital. Some propose that members of the U.S. National Science Advisory Board for Biosecurity, who have already contributed greatly to the discussion, should be engaged, but report to an entity independent of funding decisions. All of these recommendations have merit, and there is no one solution. No single meeting or organization is likely to grapple successfully with the conundrum of weighing the risks and benefits of certain lines of research. Meetings held as isolated events have the potential to be more divisive than constructive.

"Why are scientists...not required to have ethical training related to the potential risks of research to the public?"

When the Human Genome Project was begun and complex ethical issues arose, an ongoing program to study the Ethical, Legal, and Societal Implications was funded as an integral part of the project. Similar dedication to scholarly work on ethical and societal issues related to the controversial study of dangerous pathogens, including gain-of-function research, should be robustly supported. The nascent (and now defunct) Policy, Ethics and Law cores of the Regional Centers for Excellence in Biodefense (funded by the U.S. National Institute of Allergy and Infectious Diseases) offer examples of contributions that can be gained from such support, including the engagement and training of scientists in ethical issues related to gain-of-function research, biosafety, and biosecurity.

Why are scientists required to understand the individual risks to participants in a clinical trial but not required to have ethical training related to the potential risks of research to the public? This is a fundamental disconnect in the ethics education of scientists and in the review process of protocols.

Scientists conduct work for the benefit of humanity. When the balance is unclear as to risks and benefits, as it currently is, should we not adhere to the principle of "first do no harm?"

– Ruth L. Berkelman and James W. Le Duc

Ruth L. Berkelman is director of the Center for Public Health Preparedness and Research at the Rollins School of Public Health, Emory University, Atlanta, GA. E-mail: rberkel@emory.edu

James W. Le Duc is a professor in the Department of Microbiology and Immunology and director of the Galveston National Laboratory at the University of Texas Medical Branch, Galveston, TX. E-mail: jwleduc@utmb.edu

PHOTOS: (TOP RIGHT) ANN BORDEN; (BOTTOM RIGHT) MICHAEL STRAVATO/STRAVATO.COM; (INSET) SCOTT SMITH/CDC

10.1126/science.1260424

> "The story follows a brilliant bioethicist who is called in at crisis moments to solve the most complicated, dynamic and confounding medical issues imaginable."
>
> *Variety*'s synopsis of a TV pilot commissioned by CBS based on well-known bioethicist Arthur Caplan.

IN BRIEF

Furry pollinator wins photo contest

The rock mouse and the pagoda lily are pollination partners.

With this picture, ecologist Petra Wester from Heinrich Heine University Düsseldorf in Germany documents for the first time that the Namaqua rock mouse (*Aethomys namaquensis*) pollinates the pagoda lily (*Whiteheadia bifolia*) in South Africa, solving a long-standing mystery. The lily's low-hanging bowl-shaped flowers, stiff stamens, easily accessible nectar, and weak nutty scent hinted that a rodent might be its pollinating partner. Wester found that as the mouse leans in to lick the nectar, the stamens transfer pollen to its nose. The image earned Wester $400 and first place in the *BMC Ecology* photo contest, a competition set up in 2012 by the journal to reward researchers who best capture ecological interactions. The journal's editorial board and a guest judge, Caspar Henderson, author of *Book of Barely Imagined Beings: A 21st Century Bestiary*, picked Wester's shot from among 313 entries. It was taken at night, after many days and nights of watching the flowers to determine how they were pollinated. In addition to a runner-up—an albatross feeding her chick—five other photographs were selected as the best in their subfields. http://scim.ag/BMCwin

AROUND THE WORLD

Japan's science-friendly budget

TOKYO | Japan's ministry of education showed strong support for research in its proposed budget for the next fiscal year, announced last week. It asked for an 18% increase, to $11.1 billion, for science and technology spending. This includes a 53% increase, to $494 million, for programs to turn lab discoveries into new products and industries. It also bolsters grants-in-aid for small groups at universities and research centers, with a 5.8% increase to $2.4 billion. Big science facilities, including the SPring-8 synchrotron and the Japan Proton Accelerator Research Complex, would also enjoy budget increases. Government-wide S&T spending won't be known until officials gather the requests from the various ministries. The budget will be finalized and submitted to the legislature in December and take effect 1 April. http://scim.ag/Jbudget

Dark matter hunters catching up

SHANGHAI, CHINA | At a 24 August press conference, physicists in China announced the latest result in the search for particles of dark matter, the mysterious stuff whose gravity binds the galaxies. Researchers with a subterranean detector called PandaX spotted no such particles floating about. That isn't surprising because the larger, more sensitive LUX detector in South Dakota hasn't seen anything either. However, PandaX is designed so

The PandaX dark matter detector.

PHOTOS: (LEFT TO RIGHT) PETRA WESTER/*BMC ECOLOGY* IMAGE COMPETITION; MENGJIAO XIAO/SHANGHAI JIAO TONG UNIVERSITY

Published by AAAS

BY THE NUMBERS

53

Cases of Ebola, including 31 deaths, confirmed in the Democratic Republic of the Congo by the World Health Organization as of 2 September, in an outbreak unrelated to the West African strain.

7.3

Distance, in light-years, from Earth of detected water clouds around a brown dwarf—the first sighting beyond our solar system.

45

Minutes during which mayfly larvae must hold their breath while molting, according to a new study in *Freshwater Science*, which suggests molting stresses may increase with rising temperatures.

that researchers can quickly quadruple its mass, giving them "a window of about a year" to try to leapfrog LUX in sensitivity before an even bigger detector called XENON1T comes on line in Italy, says PandaX spokesman Xiangdong Ji of Shanghai Jiao Tong University. Richard Gaitskell, a LUX collaborator from Brown University, calls the new result "very credible." http://scim.ag/_pandaX

U.S. begins biosafety review

WASHINGTON, D.C. | Declaring September "National Biosafety Stewardship Month," the National Institutes of Health (NIH) is conducting a "safety stand-down" to ensure that its researchers are properly tracking and handling all infectious agents. White House science officials have asked all relevant federally funded labs to do likewise, and NIH wants its grantee institutions to participate as well. The request follows three recent mishaps at federal labs involving anthrax, smallpox, and H5N1 bird flu (see p. 1112). http://scim.ag/_biosafety

What makes these stones slither?

Scientists think they have solved the mystery of the "slithering stones" in Death Valley, California. Hundreds of these boulders sporadically manage to slide across the surface of the desert lakebed Racetrack Playa, leaving behind zigzag trails. The phenomenon has never been observed, although scientists have proposed many explanations, from hurricane-force winds to floating ice sheets. In 2011, researchers installed a weather station and time-lapse cameras near the playa, and placed 15 GPS-embedded limestone rocks in the lakebed. But for 2 years the stones didn't budge an inch. Then in November 2013, rain created a shallow pond, which froze on cold desert nights. In daylight, the surface ice broke up into floating windowpane-thin sheets that, nudged by the light breezes, could push more than 60 rocks at a time. The analysis appeared on 27 August in *PLOS ONE*.

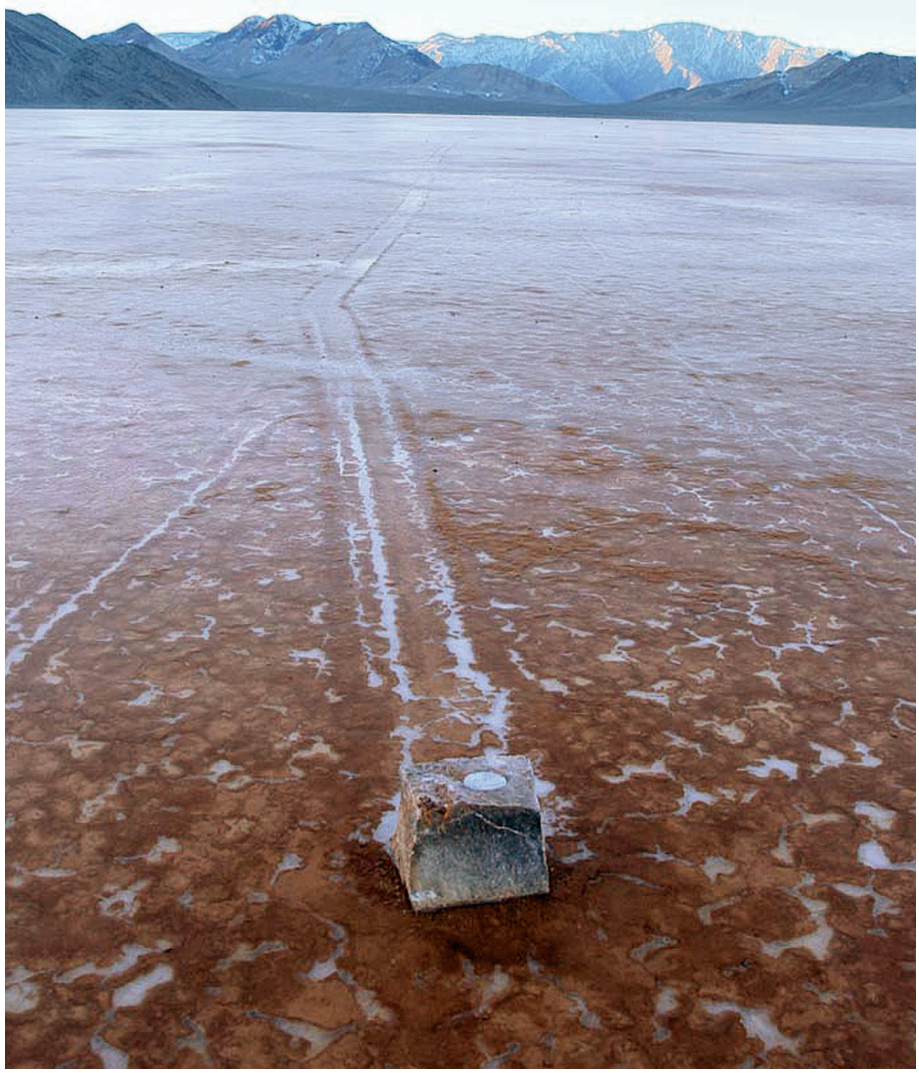

PHOTO: R. D. NORRIS *ET AL.*, *PLOS ONE* (27 AUGUST)

Ruling in skeleton dispute

SAN FRANCISCO, CALIFORNIA | Three scientists have lost their bid to prevent burial of two 9000-year-old human skeletons claimed by the Kumeyaay people of southern California. The remains, discovered beneath the University of California, San Diego (UCSD), chancellor's residence, could provide data on the origins of people in the New World. But the tribe considers the skeletons to be the remains of their ancestors rather than scientific specimens (*Science*, 8 October 2010, p. 166). The three university professors filed suit against UCSD in 2012 after it agreed to return them, arguing that the remains predate the arrival of the Kumeyaay tribe to the area. Last week, a federal circuit court upheld

Neandertal artistry?

One of the biggest debates in archaeology is whether Neandertals were capable of the kind of abstract and symbolic expression that prehistoric modern humans demonstrated in their cave wall paintings. Possible evidence for Neandertal art—a 41,000-year-old red disk on the wall of the Spanish cave of El Castillo—was reported a couple of years ago, but could have been painted by modern humans who entered Europe around that time. Now, archaeologists working at Gorham's Cave, a former Neandertal haunt on the coast of Gibraltar, have found a cross-hatched pattern etched into the hard rock floor. The deep incision lay under archaeological layers dating back at least 39,000 years—but containing stone tools that only Neandertals made, they report this week in the *Proceedings of the National Academy of Sciences*. Whether such simple patterns are good evidence for complex symbolic expression is still under debate. **http://scim.ag/_engrave**

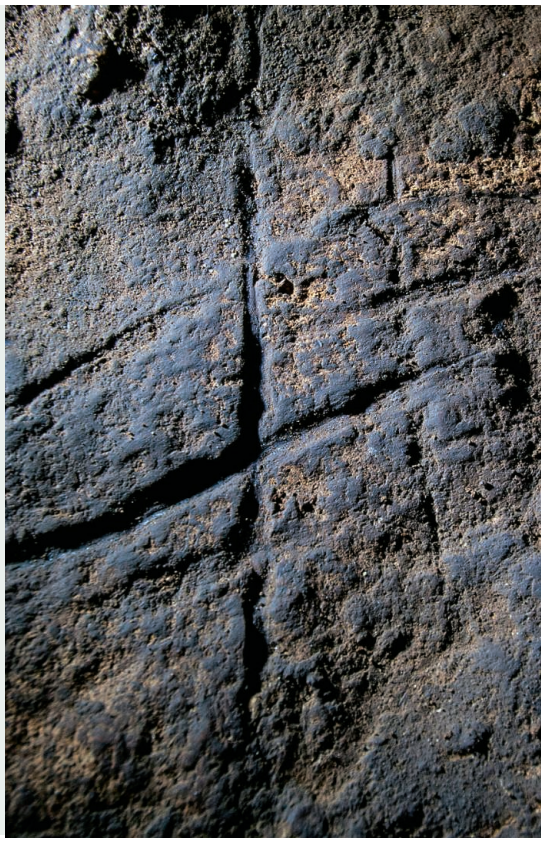

an earlier decision ruling against the professors on procedural grounds. They are now considering an appeal. **http://scim.ag/repat**

Twenty coral species protected

SILVER SPRING, MARYLAND | Ocean acidification, warming waters, and disease are stalking 20 species of Caribbean and Pacific corals, prompting the U.S. National Oceanic and Atmospheric Administration (NOAA) to seek protection for them under the Endangered Species Act (ESA). Last week, NOAA added the 20 species to two already on the list of threatened organisms. (None hold the more restrictive "endangered" status.) "I don't think we can make any decision anymore about ESA listings without taking into account the reality that the planet is warming, that the ocean is changing, and will continue to change," says the agency's Russell Brainard. NOAA's decision completes action on a 2009 request to list 83 coral species under the act. **http://scim.ag/20coral**

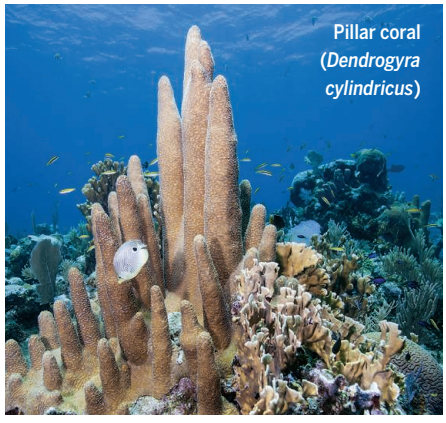

Pillar coral (*Dendrogyra cylindricus*)

Ebola vaccines fast-tracked

BETHESDA, MARYLAND | The spreading Ebola epidemic in West Africa has amplified calls for a vaccine and a treatment. Last week saw progress on both fronts. The U.S. National Institutes of Health announced on 28 August that it was fast-tracking clinical studies of an Ebola vaccine developed in collaboration with GlaxoSmithKline. Several countries will soon launch small-scale studies of the genetically engineered vaccine to assess safety and immune responses. Separately, a group led by scientists from the Public Health Agency of Canada reported that a cocktail of antibodies called ZMapp rescued 100% of 18 monkeys initially infected with high doses of Ebola and treated up to 5 days later. (See p. 1108 for more Ebola coverage.) **http://scim.ag/ebolastudies**

PHOTOS: (TOP TO BOTTOM) STUART FINLAYSON; © MICHAEL STUBBLEFIELD/ALAMY

Published by AAAS

IN DEPTH

A veterinarian inspects a goose at an Italian farm in 2006.

PHOTO: ANTONIO PARRINELLO/REUTERS

ITALY

Police claim leading flu researcher illegally sold virus

Italian probe depicts web of scandal, including illegal animal vaccines and deliberate outbreaks

By **Laura Margottini**, *in Rome*

Scientists who trafficked in potentially dangerous viruses. Company executives who produced and sold an illegal animal vaccine. Corrupt government officials turning a blind eye. A recently completed Italian police report has all the ingredients of a biothriller. It alleges that between 2000 and 2008, a "criminal organization" of more than 40 people colluded to profit financially from Italy's fight with avian influenza—and possibly even helped spread the disease.

The 400-page report, unpublished but obtained by *Science*, is the culmination of a 10-year investigation by the Italian police that involved extensive wiretapping of the key players. Among its targets are Ilaria Capua, a top avian influenza researcher at the Istituto Zooprofilattico Sperimentale delle Venezie (IZSVe) in Legnaro, along with her colleagues Stefano Marangon and Giovanni Cattoli; executives at the Italian branch of animal vaccine company Merial, which is part of Sanofi; officials within the Ministry of Health and public research agencies; and veterinarians working for the Italian poultry industry.

News about the investigation was first leaked in a story in the Italian magazine *L'Espresso* in April. But its reporters did not have access to the full report, which *Science* has reviewed, along with related government documents and transcripts of phone calls.

Capua, who was elected a member of the Italian Chamber of Deputies in 2013, dismisses the charges and says she suspects they may be politically motivated, although she declined to speculate about who might want to target her and why. Capua's lab at IZSVe is an internationally renowned reference laboratory for bird flu; her job at the institute is on hold during her government service. Cattoli says the accusations are "a huge misunderstanding that I hope will be cleared soon." Marangon declined to comment.

The report details myriad transactions over an 8-year period that included two bird flu outbreaks that devastated poultry farms in the northeast of Italy. The first one, caused by a strain called H7N1, started in 1999 and lasted until 2001; the second, with H7N3, occurred between 2002 and 2003 and sickened not only birds but also at least seven poultry farmers. (They suffered from an eye infection called conjunctivitis but recovered.)

E.U. rules forbid the use of vaccines to bring avian influenza outbreaks under control, because with most vaccines, it's impossible to tell birds that are infected but not sick from those that have been vaccinated. Instead, outbreaks are usually stamped out by culling infected flocks. The report says that Merial ignored the rules by producing an illegal vaccine against H7N1 in 2000 and selling it to Italian farmers eager to save their flocks. Police caught veterinarians administering the vaccine at a farm in Bagnolo di Sogliano al Rubicone, according to the report; the wiretaps suggested it was produced by Merial.

The report says the vaccine was produced in France, from an H7N3 bird flu strain originating in Pakistan that Capua sold to Merial for an unspecified amount, without proper government authorizations. It quotes a tapped phone conversation, years later, in which Paolo Candoli, a manager at Merial in Italy, asked a colleague "Did we buy it?" apparently referring to the virus. "Yes, we did," the colleague answered. "We bought it in Padua. We paid for it handsomely, as we did with all the strains we bought from her." Candoli did not respond to requests for comment; Merial sent *Science* a statement saying "the company has always operated in compliance with national and EU regulations."

Late in 2000, the European Commission gave Italy permission to vaccinate against H7N1 using a so-called DIVA vaccine—for "differentiating infected from vaccinated animals"—developed by the IZSVe team from the Pakistani virus and produced by Merial. At that time, Romano Marabelli, who was the government's chief veterinary officer, authorized Merial to import the Pakistani strain for vaccine production, as well as vaccine produced at Merial labs in France. In doing so, Marabelli gave Merial an unfair advantage over other animal vaccine companies, the report says, allegedly in return for money. Approving the vaccine meant that "what used to be an illegal business" became a legal one, the police say.

Marabelli, who was recently promoted to the position of general secretary of the Ministry of Health, stepped down after the story

in *L'Espresso* appeared. He did not respond to requests for comment, but in an April statement, he said he resigned "to lift the Ministry from any embarrassment due to the media attacks."

The report charges that Capua and Marangon illegally sold other virus strains to Merial as well, giving the company a head start in the production of vaccines. They also tipped Merial managers off about impending vaccination decisions, the report says, which they learned about during meetings with the Ministry of Health and the European Commission. Merial managers allegedly smuggled influenza viruses into Italy, stuffed in their carry-on luggage, or had the samples sent to them in DHL packages. The viruses were then handled illegally in makeshift labs and even stored in home fridges.

Police say that Merial rewarded the three IZSVe researchers for their services through an illegal company that they had set up, run

Ilaria Capua says the accusations against her are unfounded.

by Richard Currie, Capua's husband and a manager at Fort Dodge, another animal vaccine company. Currie, in an e-mail to *Science*, says that the allegations "come as a great surprise and … I firmly refute them."

Perhaps the most explosive charge is that Candoli and others deliberately spread bird flu viruses from 1999 on in an attempt to create a market for vaccines and pressure the government to approve them. The report uses the term "attempted epidemics," but does not specify how they might have been triggered. The evidence appears to be circumstantial. During calls with veterinarians working for poultry farms in northern Italy, Candoli told them it was time to: "Stop spreading that illness!" In 2005, he and a Merial colleague discussed whether it might be the right time for someone to find Italian ducks infected with H5; at the time, a dangerous strain called H5N1 was fanning out of Asia to Africa and Europe. Twenty days after the call, an H5N1 virus—although not of the Asian strain—was isolated from a dead duck near Modena.

Capua says many of the allegations simply don't make sense and show that police officers didn't have the scientific background to understand the conversations they were listening to. She notes, for instance, that it makes no sense to tie her to the H7N3 outbreak, as the report does, because genomic analyses have shown that the Pakistani strain she allegedly sold to Merial was different from the one that caused the outbreak. She says she is suing *L'Espresso* for defamation because of the April article.

The report does not appear to have been reviewed by scientific experts. Police repeatedly refer to the poultry outbreaks as zoonoses, for instance, a term scientists use for diseases transmitted from animals to humans. At one point, a transcript mentions a mosquito-borne disease called West Nair, when presumably West Nile was discussed.

Christianne Bruschke, chief veterinary officer of the Netherlands and a former avian influenza specialist at the World Organisation for Animal Health, says that it's "hard to believe" that an international company like Merial would deal in illegal vaccines, let alone attempt to spread disease. (Bruschke stresses that she has no specific knowledge about the case or the accusations.) The claim that Capua secretly helped a private company profit from influenza viruses is ironic, Bruschke says, because Capua became well known internationally as an advocate for openness. In 2006, she argued that avian influenza researchers should rapidly share the sequences of strains they obtained instead of hoarding such sequences so they could publish them (*Science*, 10 November 2006, p. 918).

The investigation is now in the hands of Giancarlo Capaldo, an experienced and well-respected prosecutor and mafia fighter who has handled many national and international criminal cases, including corruption in the public health system. Capaldo is expected to hear the accused in the coming weeks before deciding whether to close the case and discharge them, or recommend bringing it to trial.

As long as she is a member of the Parliament, Capua enjoys immunity from prosecution. Capua says she can return to her position at IZSVe at the end of her political career, but that she has no intention of doing so. ■

Laura Margottini is a science writer in Rome. With reporting by Martin Enserink.

ANCIENT DNA

Three-part ancestry for Europeans

Eurasian "ghost lineage" contributed to most modern European genomes

By **Ann Gibbons**, *in Basel, Switzerland*

How do you make a modern European? For years, the favored recipe was this: Start with DNA from a hunter-gatherer whose ancestors lived in Europe 45,000 years ago, then add genes from an early farmer who migrated to the continent about 9000 years ago. An extensive study of ancient DNA now points to a third ingredient for most Europeans: blood from an Asian nomad who blew into central Europe perhaps only about 4000 or 5000 years ago. This third major lineage originated somewhere in northwestern Asia, perhaps on the steppes of western Asia or in Eastern Europe.

This is a "ghost lineage," because no pure-blood member of this group survives today. But whoever these people were, their descendants successfully spread far and wide, for their genes show up not only in Europeans but also in Native Americans, according to a talk by paleogeneticist Johannes Krause of the University of Tübingen in Germany, who spoke at a biomolecular archaeology meeting here last week.

Those who heard the talk in a packed auditorium at the University of Basel were impressed by the genomic data's high resolution—it is the largest data set of ancient DNA ever presented in a single study—even though some aren't convinced about the exact details. "What's great about this is we're finally unpacking the genomic history of our species," says evolutionary biologist Greger Larson of Durham University in the United Kingdom. "But as we add more genomes, it all gets more complicated."

Ancient genome data have been coming so fast and furious lately that researchers are still adjusting to the "new" view that Europe was populated by not one, but two different types of people: hunter-gatherers, descended from the first modern humans to arrive in Europe 45,000 years ago, and

PHOTO: GETTY IMAGES

Extent of the Corded Ware culture, 3000 to 2350 B.C.E.

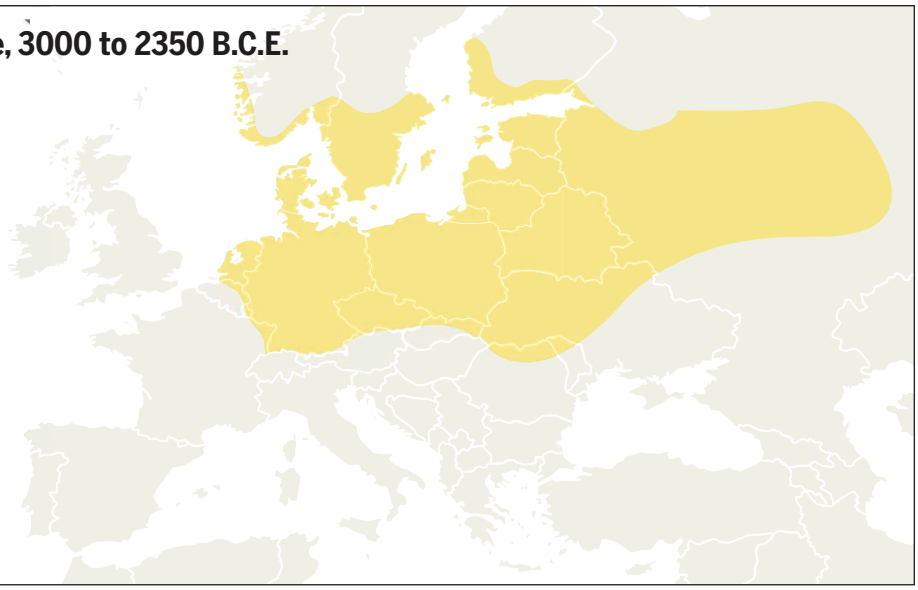

Spreading out. The Corded Ware people, known for distinctive pottery with cord impressions, began to expand their reach starting about 5000 years ago, and may have brought Eurasian genes to Europe.

farmers, who arose in the Middle East and started moving in about 9000 years ago. That picture replaced many European archaeologists' view of farming as a cultural revolution that spread through indigenous hunter-gatherers—a hypothesis that held sway until 5 years ago. It lost favor as DNA studies began to show that farming spread through the movement of people, not just ideas (*Science*, 11 October 2013, p. 181).

To sharpen the genomic picture of modern Europeans, Krause and population geneticist David Reich of Harvard University sequenced the complete genomes of a 7000-year-old farmer from Stuttgart, Germany, and eight hunter-gatherers from Luxembourg and Sweden who lived 8000 years ago. They also collaborated with 123 other researchers, who gave them access to samples from other prehistoric farmers such as Ötzi the Iceman as well as from ancient hunter-gatherers from Europe and Asia.

They compared these ancient genomes with genetic data from 2345 present-day humans from 192 populations. The resulting insights go well beyond the origin of Europeans. One discovery was that the ancestors of the first farmers to reach Europe were among the first people to split from the modern human population that swept out of Africa some 60,000 years ago and gave rise to all non-Africans, Krause said in his talk. This split might have happened in the Middle East or Arabia shortly after moderns left Africa—and long before anyone took up farming.

The study's other big discovery was the mysterious Eurasian DNA. It is missing from hunter-gatherers from Luxembourg and Spain, as well as from the early farmers sequenced so far. But it shows up in ancient hunter-gatherers in Scandinavia. And it is widespread in modern Europeans, accounting for about 20% of the genome of most Europeans, on average, reaching 29% in central and northern Europeans, such as Estonians, Lithuanians, and Scandinavians. People in southern Europe today have very little of this ghost lineage and instead inherited a high proportion of their genes—up to 90% in the case of Sardinians—from the first European farmers.

A clue to where the mystery DNA originated turned up far afield, in the genome of the 24,000-year-old Mal'ta boy from Siberia (*Science*, 25 October 2013, p. 409): It closely matches the European sequences. No living Asians still carry the boy's type of DNA. But significant portions of his genome also live on in Native Americans, suggesting that they, like Europeans, are partly derived from the same source in northern Eurasia, Krause reported. He concluded that these Eurasians lived in Siberia 24,000 years ago. Some of their descendants then crossed Beringia to the New World more than 14,000 years ago. Others reached Scandinavia—but not central or Western Europe—by 8000 years ago, explaining the presence of their DNA in Scandinavian hunter-gatherers. Then, sometime after 7000 years ago, people carrying this DNA entered central and Western Europe. In his talk, Krause noted that previous work has shown a major shift in mitochondrial DNA types in central Europe about 4000 to 5000 years ago, and speculated that this group's expansion may be the cause.

Previous studies have also found some genetic ties between Europeans and Native Americans, notes population geneticist Wolfgang Haak of the University of Adelaide in Australia, a co-author on the new study, a draft of which is available on a biology preprint server. Thanks to these ancient Eurasians, "someone with northern European ancestry is more closely related to Native Americans than southern Europeans are," says Pontus Skoglund, a postdoc at Harvard who analyzed DNA from the Swedish skeletons but was not a co-author.

In their talks, Haak and Krause each proposed that the late influx of these "ghost" Eurasians might be related to what's known archaeologically as the Corded Ware culture of nomadic herders, who imprinted twisted cord or rope onto their pottery. These nomadic pastoralists herded their cattle east from the steppes north of the Black Sea and occupied large areas of northeast and central Europe by 2500 B.C.E.

While researchers continue to track the ghost lineage, they have begun to fill in the portraits of Europeans' other ancestors. Genes from the ancient hunter-gatherers in Spain and Luxembourg suggest that they had blue or light-colored eyes, dark hair, and relatively dark skin. The early German farmer, by contrast, was a woman who had brown eyes, dark hair, and lighter skin, according to a talk by Karola Kirsanow of Johannes Gutenberg University Mainz in Germany.

As researchers talked after the presentations, several wondered if the genetic history of modern populations is likely to get even more complicated. "The more genomes you get, the more populations you find," says Robin Allaby, an evolutionary geneticist at the University of Warwick in Coventry, U.K. Some question whether three migrations are enough to explain the complex genetic history of Europeans. But if the genomicists are right, the chief components of the latest European recipe will endure. ■

PHOTO: DE AGOSTINI/GETTY IMAGES

Models of Ebola can incorporate quarantines like the one in Liberia recently lifted due to protests (*above*).

INFECTIOUS DISEASE

Estimating the Ebola epidemic

Modelers of infectious diseases strive to predict spread of the virus—and how to stop it

By **Kai Kupferschmidt**

Alessandro Vespignani hopes that his latest work will turn out to be wrong. In July, the physicist from Northeastern University in Boston started modeling how the deadly Ebola virus may spread in West Africa. Extrapolating existing trends, the number of the sick and dying mounts rapidly from the current toll—more than 3000 cases and 1500 deaths—to tens and then hundreds of thousands. "The numbers are really scary," he says.

Vespignani is not the only one trying to predict how the unprecedented outbreak will progress. Last week, the World Health Organization (WHO) estimated that the number of cases could ultimately exceed 20,000. And scientists across the world are scrambling to create computer models that accurately describe the spread of the deadly virus. Such models "are incredibly helpful" in curbing an outbreak, says infectious disease researcher Jeremy Farrar, who heads the Wellcome Trust research charity in London. They can help agencies such as WHO predict the medical supplies and personnel they will need—and can indicate which interventions will best stem the outbreak. Mathematical epidemiologist Christian Althaus of the University of Bern, who is also building Ebola models, says both WHO and Samaritan's Purse, a relief organization fighting Ebola, have contacted him to learn about his projections.

But the modelers are hampered by the paucity of data on the current outbreak and lack of knowledge about how Ebola spreads. Funerals of Ebola victims are known to spread the virus, for example—but how many people are infected that way is not known. "Before this we have never had that much Ebola, so the epidemiology was never well developed," says Ira Longini, a biostatistician at the University of Florida in Gainesville. "We are caught with our pants down."

To a mathematician, combating any outbreak is at its core a fight to reduce one number: R_e, the pathogen's effective reproductive rate, or how many people an infected person in turn infects on average. An R_e above 1 means the disease will spread. Below 1, an outbreak will stall.

Outbreak models typically track four groups of people: those who are susceptible, those who have been infected but are not contagious yet, those who are sick and can transmit the virus, and those who have recovered. A model, in essence, describes the rates at which people move from one group to the next. From those, R_e can be calculated.

If the disease keeps spreading as it has, most of the modelers *Science* talked to say WHO's estimate will turn out to be conservative. "If the epidemic in Liberia were to continue in this way until the 1st of December, the cumulative number of cases would exceed 100,000," Althaus predicts. Such long-term forecasts are error-prone, he acknowledges. But other modelers aren't much more encouraging. Caitlin Rivers of the Virginia Polytechnic Institute and State University in Blacksburg expects roughly 1000 new cases in Liberia in the next 2 weeks and a similar number in Sierra Leone.

Vespignani has analyzed the likelihood that Ebola will spread to other countries. Using data on millions of air travelers and commuters, as well as mobility patterns based on data from censuses and mobile devices, he has built a model of the world, into which he can introduce Ebola and then run hundreds of thousands of simulations. In general, the chance of further spread beyond West Africa is small, Vespignani says, but the risk grows with the scale of the epidemic. Ghana, the United Kingdom, and the United States are among the countries most likely to have an introduced case, according to the model. (Senegal, which reported its first Ebola case last week, was in his top 10 countries, too.)

The models are only as good as the data fed to them; up to three-quarters of Ebola cases may go unreported. The modelers are also assuming that key parameters, such as the virus's incubation time, are the same as in earlier outbreaks. "We might be missing the boat and we have no signal to indicate that," says Martin Meltzer of the U.S. Centers for Disease Prevention and Control in Atlanta.

The biggest uncertainty is how much doctors, nurses, and others can slow the virus. There are many ways of pushing down R_e, Farrar says—washing hands, wearing masks, or quarantining people, for example. "But given the complexity of this outbreak and the limited resources, we need to find out what are the two or three things that will most help drive down infections," Farrar says, and that's where models can help.

Rivers has evaluated interventions, such as increased use of protective equipment or campaigns to isolate infected people. In the most optimistic scenario, every contact of infected people is traced, and transmission in hospitals is reduced by 75%. Even that, while drastically reducing the number of Ebola deaths, did not push R_e below 1 in her model.

The challenge varies by country, Althaus says. "In Guinea and Sierra Leone, R_e is close to 1 and the outbreak could be stopped if interventions improve a bit." In Liberia, R_e has been near 1.5 the whole time. "That means work is only just beginning there."

People in West Africa will have to alter behaviors, Meltzer says. "We won't stop this outbreak solely by building hospitals. There will have to be a change in the way the community deals with the disease." Modeling that is easy enough, Vespignani says. "I can decrease the transmission at funerals by 40% easily in a model. That's one line of code. But in the field that is really hard." ■

PHOTO: REUTERS

ECOLOGY

Small mammals vanish in northern Australia

Scientists are struggling to rein in the culprit: feral cats, aided by fire

By **Dyani Lewis**, *in Kakadu National Park*

Just after dawn, Danielle Stokeld sets out on foot to inspect small mammal traps nestled among spindly eucalyptuses and pandanus pines in Kakadu National Park in Australia's far north. In spite of knee-high spear grass, the ecologist with the Northern Territory's Department of Land Resource Management zips through her 2.4-kilometer route, managing to check all 117 traps in less than an hour. The reason for her alacrity: Every last trap is empty.

Back at Kakadu's South Alligator ranger station later on that cool July morning, other researchers say they have fared no better. After 2 weeks of trapping, the dire reality is becoming clear. From 4000 traps at six sites, all the researchers were able to snare were a single delicate mouse and two northern quolls—spotted hedgehog-sized marsupials with long fleshy tails.

In northern Australia, mammal populations are in free fall. Over the past 2 decades, scientists have documented sharp declines in quolls, bandicoots, and other native fauna. The plight of these animals has grown so desperate that in July, the Australian government appointed the nation's first threatened species commissioner, Gregory Andrews, a Department of the Environment staffer now tasked with devising broad approaches to stem the tide of extinctions. The solutions are not obvious, but mounting evidence points to the arch villain: feral cats, aided and abetted by fire.

The European influx beginning 2 centuries ago turned the island continent into a crucible of extinction. Since then, 29 land animal species have gone extinct, including, most famously, the thylacine, or Tasmanian tiger, which winked out early last century. Other vanished fauna include species of bettongs, bandicoots, potoroos, bilbies, and wallabies. Australia's losses represent about a third of the world's mammal extinctions over the past 500 years. Many disappeared before 1950, after getting squeezed out of habitats and falling prey to invaders including cats and European red foxes. Another invader, the cane toad, has been a bane to northern quolls, which eat the toads and succumb to poison they secrete.

Other species are barely hanging on: Some 55 endemic land mammals—20% of Australia's total—are threatened with extinction. "You look at the outback and see how vast and natural it seems to be," says John Woinarski, a conservation biologist at Charles Darwin University (CDU), Casuarina. "But we've clearly fractured its ecological processes."

As losses accumulated in southern and central Australia, the sparsely populated north appeared to offer a safe haven. Bigger than Alaska, the tropical savannas that span parts of Western Australia, the Northern Territory, and Queensland have vast tracts of intact vegetation and, importantly, have proven inhospitable to the red fox. But the sanctuary was illusory. In the late 1980s, when Woinarski began his studies in the Northern Territory, 200 traps would catch 30 or 40 animals overnight. Nowadays, a typical haul is zero. "It's heartbreaking," he says. "Things that were there a decade before have just disappeared."

Northern quolls are in decline in Kakadu National Park.

PHOTO: © NT GOVERNMENT DEPARTMENT OF LAND AND RESOURCE MANAGEMENT/PHOTO BY ALARIC FISHER

Feral cats are undeniably the chief culprit. In a paper published online last month in the *Journal of Applied Ecology*, Woinarski and colleagues showed that cats unleashed in an experimental enclosure can extirpate the long-haired rat, a native of northern Australia's savannas. And after dissecting a feral cat shot by a Kakadu ranger, Stokeld found in its stomach the remains of a dusky rat, four grassland mosaic-tailed rats, and two fawn antechinuses, a carnivorous marsupial. The nonprofit Australian Wildlife Conservancy (AWC) estimates that every day in Australia, an astounding 75 million animals fall prey to roughly 15 million feral cats.

But scientists doubt that the cats, which began fanning out across Australia soon after European settlers first arrived in 1788, are acting alone. The recent declines, says Chris Johnson, an ecologist at the University of Tasmania, Hobart, beg the question, "Why now?"

The answer may be changing fire regimes. Before Europeans arrived, aboriginal Australians would burn small patches or pathways of bush to create conditions ideal for hunting or for moving more easily through the landscape. As aboriginal populations dwindled, "nastier" fires that burned hotter and left bigger fire scars became the norm, says Jeremy Russell-Smith, a fire ecologist at CDU. In recent unpublished research using GPS tracking in northwestern Australia, Sarah Legge, chief scientist at AWC, revealed that more widespread burning helps feral cats pick off critters exposed by the loss of ground cover.

To deprive the cats of their hunting grounds, AWC has implemented an intensive fire management regime at the Mornington Wildlife Sanctuary in northwestern

The dead zone

Small mammals are vanishing from tropical northern Australia.

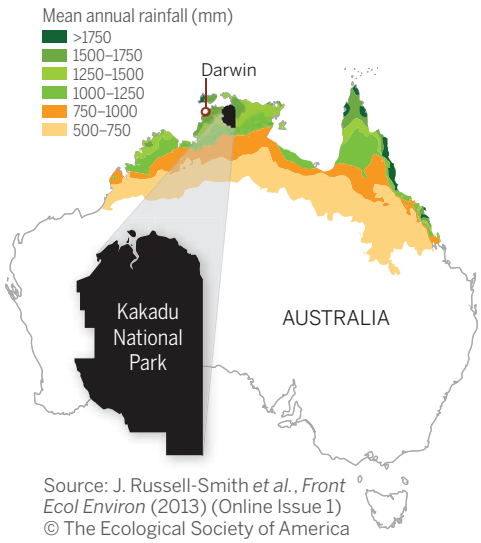

Source: J. Russell-Smith *et al.*, *Front Ecol Environ* (2013) (Online Issue 1)

Australia's Kimberley region, intended to safeguard unburned vegetation. The reserve has also assiduously culled feral herbivores such as cattle, horses, and donkeys that thin the vegetation. As a result, native rodent and marsupial numbers have shot up fourfold in some habitats over just 3 years.

Curtailing feral cat populations is a more formidable challenge. One promising approach is an experimental bait containing para-aminopropiophenone, a chemical that converts hemoglobin in the bloodstream into methemoglobin, which cannot transport oxygen. In a trial with the bait in central Australia last year, feral cat numbers fell by more than 50%. However, trials in other areas didn't go so well, perhaps due to a greater abundance of live prey, which the cats favor over bait, or heavy rainfall that dampened the bait's appeal.

Some species may end up making their last stands on islands or in mainland arks fenced off from predators. In 2003, 64 captive-bred northern quolls were released on two islands free of cane toads off Australia's northern coast. A decade on, each island has several thousand quolls, says Dion Wedd, a curator at the Territory Wildlife Park in Berry Springs who was involved in the breeding program. Still, most scientists see such refuges as a last resort. Says Alaric Fisher, an ecologist at the Department of Land Resource Management: "We need [approaches] that work outside of fences." ■

Dyani Lewis is a writer in Melbourne, Australia.

JAPAN

RIKEN shrinks troubled center

Japan's developmental biology powerhouse brought to knees by misconduct revelations

By **Dennis Normile**, *in Tokyo*

Two discredited papers have subjected a leading Japanese research center to an extraordinary form of collective punishment. On 27 August, chemist Ryoji Noyori, president of RIKEN, Japan's biggest research institution, announced that its Center for Developmental Biology (CDB) in Kobe will be stripped of half of its 500-plus staff, renamed, and put under new management.

The hammer blow to the 14-year-old CDB is coming under heavy fire. Some outsiders see it as an overreaction to the research fiasco, in which CDB's Haruko Obokata and colleagues announced what would have been a revolutionary new way to produce stem cells. They say RIKEN is needlessly sacrificing a research powerhouse that has produced groundbreaking results. RIKEN officials say they have received more than 170 letters from scientists worldwide lobbying to keep the CDB intact. "I worry the downsizing will lead to a deterioration of research activity," says CDB director Masatoshi Takeichi. "But I hope that the reform will give it a fresh start as a new, more dynamic research institute," he says.

Critics are calling for Ryoji Noyori to step down.

The papers at fault, published online in *Nature* on 29 January, reported that exposing mature mouse cells to a mild acid solution produced stem cells capable of developing into all tissue types. This stimulus-triggered acquisition of pluripotency (STAP) method was far simpler than other ways of creating stem cells. But the claims quickly unraveled (*Science*, 21 March, p. 1299). On 1 April, a RIKEN committee pronounced Obokata guilty of misconduct for falsifications and fabrications in the papers. The authors retracted the papers on 2 July. Then in a tragic turn, Yoshiki Sasai, one of the senior co-authors, committed suicide on 5 August. A RIKEN team trying to replicate the STAP method reported last week that it has so far failed to do so.

Meanwhile, a RIKEN-appointed outside committee on 12 June recommended dismantling CDB in order to head off a recurrence of such misconduct. The committee laid most of the blame on Obokata's shoulders, but it also found that lax oversight and a push for breakthrough results by top management set the stage for disaster.

Norio Nakatsuji, a stem cell scientist at Kyoto University, blames CDB management for what he calls "hyperpromotion" of the STAP findings, which turned Obokata into a media sensation. Nakatsuji believes CDB orchestrated the hype to build a case for more funding. Critics also fault RIKEN's initial response when questions arose about the STAP papers. The first investigating committee never asked why senior co-authors endorsed such a sloppy paper, says Robert Geller, a geophysicist at the University of Tokyo. Others say management shortcomings stretch to the top. "RIKEN's leaders, including Professor Noyori, must resign," says Masahiro Kami, a medical doctor at the University of Tokyo who follows ethical issues.

Asked about this at the 27 August press conference, Noyori replied that "it is the responsibility of the president to lead the charge in executing" the reform. Many of the reform's details are still hazy, but Noyori said that RIKEN will form a new institute around 250 CDB researchers, with the remaining staff moved to other RIKEN facilities. RIKEN will recruit a new director.

For those at the lab bench, "Downsizing and renaming the center in such a negative way is discouraging," says Shigeo Hayashi, a developmental biologist and CDB principal investigator. While waiting for the new institute to take shape, he says that he and his colleagues are "making every effort" to keep their research going. And Hayashi doesn't want others to share their fate. "I really hope that this will not set a precedent of making the penalty for fraudulent papers organizational upheaval." ■

PHOTO: ASSOCIATED PRESS

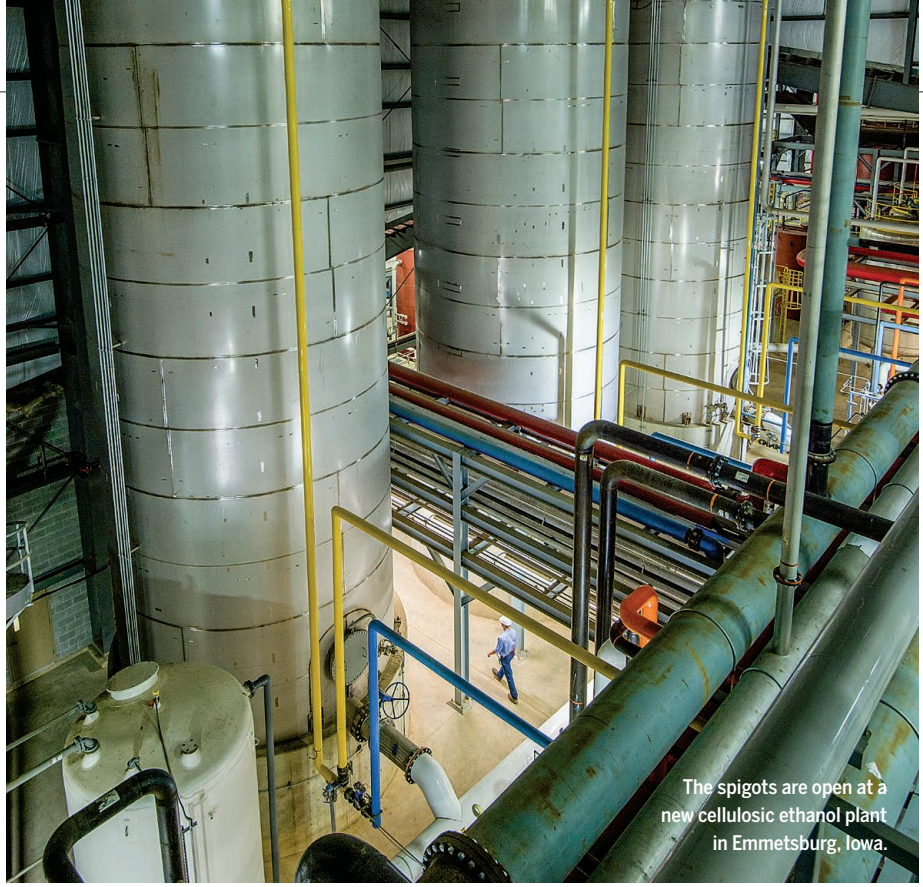

The spigots are open at a new cellulosic ethanol plant in Emmetsburg, Iowa.

PHOTO: © GREG LATZA/POET-DSM ADVANCED BIOFUELS

RENEWABLE ENERGY

Cellulosic ethanol at last?

Large volumes of fuel from crop wastes will soon start flowing in the U.S.—unless policymakers balk

By **Robert F. Service**

What could possibly lure Willem-Alexander, king of the Netherlands, to a sleepy farm town in the northwest corner of Iowa? Cellulosic ethanol, in quantities that have never flowed before. This week, with the king in attendance, officials were scheduled to turn on the spigots at a new plant in Emmetsburg—a joint venture between POET, an American biofuels company, and the Dutch firm Royal DSM. It is the first facility capable of producing ethanol from plant waste on a commercial scale.

"It's finally a start," says Wallace Tyner, an agricultural economist at Purdue University in West Lafayette, Indiana, who tracks biofuels. Similar plants in Kansas and elsewhere in Iowa are set to open within the next few months. They and a few smaller plants could ultimately produce some 340 million liters (90 million gallons) of cellulosic ethanol a year. But cellulosic ethanol producers still face another daunting hurdle: politics.

In the United States, ethanol made mostly from corn kernels has long been mixed with gasoline to reduce smog. Cellulosic ethanol comes instead from the nonedible parts of crops—so-called corn stover, for instance. Boosters of the new technology say using agricultural waste instead of food crops offers farmers a new source of revenue, generates far less greenhouse gases, requires no new cropland, and displaces additional imported oil.

But commercializing cellulosic ethanol has been a heavy lift. To convert plant matter to fuel, producers have to add costly chemical treatments to unzip the plants' biopolymers, called cellulose and hemicellulose, into simple sugars that can be fermented with yeast. According to the U.S. Department of Energy, the cost of making small volumes of ethanol this way has dropped from about $2.38 per liter ($9 per gallon) in 2001 to about $0.53 per liter ($2 per gallon) today. Even so, Tyner and others say it remains to be shown whether they can do so in large volumes to match the $2.80 cost of wholesale gasoline today.

In 2005, Congress set out to ensure demand by passing the Renewable Fuel Standard, which requires oil refiners and importers to sell rising volumes of renewable fuels. This year, they were supposed to sell 6.6 billion liters of cellulosic ethanol. But technical challenges and the 2008 recession hit the industry hard. Last year, cellulosic ethanol producers turned out just 1.1 million liters of fuel from a handful of small facilities. In response, the U.S. Environmental Protection Agency (EPA) waived most of its blending requirements and imposed a system of credits that gasoline refiners and importers must now purchase for each gallon of mandated cellulosic ethanol that they fail to blend. Lately, those incentives have added about $0.23 per liter ($1 per gallon). So if current commercial cellulosic ethanol producers can manufacture fuel below $1 per liter ($3.80 per gallon), market forces should push refiners and importers to buy it.

Even that price target will be a stretch for the new commercial plants, Tyner believes. And if producers achieve it, the industry will still face the problem of inadequate demand. As Tyner puts it: "Where is all that ethanol going to go?" EPA now requires gasoline blenders to add 10% ethanol to their fuel, a mix known as E10. Fulfilling that mandate requires about 51.1 billion liters of ethanol a year. But corn ethanol companies already produce more than 53 billion liters of ethanol and sell the excess overseas, leaving no market for still more ethanol from the new cellulosic plants.

Producers want EPA to take up the slack by raising the blend requirements. But oil companies and gas station owners have balked at the cost of changing their pumps and other infrastructure to support higher ethanol fuels. After weighing their arguments against those of ethanol supporters, EPA last November sided with the oil companies and proposed lowering the total ethanol volume (corn plus cellulosic) requirement for 2014 to 49.2 billion liters.

That would be misguided, says Bruce Babcock, an economist with Iowa State University in Ames. In the September 2014 issue of *Energy Economics*, he and Iowa State colleague Sébastien Pouliot suggest that even a modest increase in the cost of cellulosic ethanol credits probably would encourage the fuel industry to make major changes in infrastructure—enough to boost new investment in cellulosic ethanol plants.

For that to happen, however, EPA would have to reverse course and increase the volume of ethanol it mandates. Is the Obama administration willing to risk provoking the ire of deep-pocketed oil interests with tight midterm elections looming? The answer may come soon: EPA is scheduled to release its final rules for ethanol volumes in 2014 later this month and unveil its proposed volumes for 2015 shortly thereafter. ■

By **Jocelyn Kaiser**

The catalyst

This past July, Harvard University epidemiologist Marc Lipsitch sat down with a group of other experts worried about controversial flu experiments. The studies create potentially dangerous new viruses that critics fear could escape from laboratories and cause a pandemic or be used as bioweapons; Lipsitch and his colleagues hoped to find ways to persuade governments to rein them in. But the agenda took an unexpected turn. Phones began ringing: Journalists wanted reaction to several recent lab accidents involving dangerous pathogens—and to news that four of the 18 scientists participating in the meeting had just been abruptly dismissed from a high-profile panel that advises the U.S. government on biosecurity. "It quickly became clear to us that this was an opportunity," Lipsitch says.

His group seized it. They came up with a name—the Cambridge Working Group (CWG)—and crafted a statement that they distributed widely. "Experiments involving the creation of potential pandemic pathogens should be curtailed" until risks and benefits could be thoroughly weighed publicly, it argued. The 14 July statement drew extensive media attention, and nearly 300 researchers eventually signed on. Then came an online response a few days later from Scientists for Science—an opposing alliance of researchers who support the controversial flu experiments, arguing that they are adequately regulated and potentially valuable. Still, to Lipsitch's surprise, they gave a little ground: They agreed that researchers needed to publicly air the issues. Soon, plans were being firmed up for a symposium later this year at the National Academy of Sciences in Washington, D.C., and perhaps a broader discussion organized by the U.S. government.

The turn of events highlights Lipsitch's rapid rise as a prominent voice in the debate over risky research, which has roared back to life after a lull lasting nearly 2 years. The one-time philosophy major turned biologist has recently shown a knack for being in the right place at the right time, with a message and data that have helped shape the conversation.

Earlier this year, for instance, Lipsitch published a critical analysis that argued for safer alternatives to the controversial flu studies—just as other scientists reported new experiments that rekindled concern. He and colleagues highlighted the accident risks facing the growing number of labs working with dangerous pathogens—just before a spate of biosafety and biosecurity incidents at government labs. And despite Lipsitch's relatively extreme views—he'd like to essentially end most of the contested research—even some opponents say his persistence has helped force the opposing camps to try to reach consensus.

"I appreciate the concern" that Lipsitch and others have helped articulate, says virologist Ron Fouchier of Erasmus MC in Rotterdam, the Netherlands, who published one of the most controversial of the flu studies. "Hopefully, the meetings … will address the facts properly, and as a consequence be more constructive."

Lipsitch is "an incredibly thoughtful guy who's able to step back a bit and take an unbiased, dispassionate position," says David Relman, a CWG member and a microbiologist at Stanford University in Palo Alto, California. "He bends over backward to hear both sides and find common ground."

Lipsitch, 44, is a relative latecomer to the debate over how to balance science and safety in studies of dangerous pathogens. In the United States, the September 2001 anthrax attacks (see timeline, p. 1113) led to a vast expansion of federal funding and labs for biodefense research—and a slew of new safety and security rules for U.S.-funded scientists working with "select agents." Journal editors pledged to think twice before publishing "dual use" results that could be used for good or evil.

The most recent chapter in the debate began 3 years ago this month, after Fouchier presented a startling study at a meeting in Malta. His lab had altered the H5N1 avian flu virus, which can kill humans who catch it from birds, so that it could spread more easily among mammals (*Science*, 2 December 2011, p. 1192). A short time later, it became known that another researcher—Yoshihiro Kawaoka of the University of Wisconsin, Madison—had conducted similar experiments. The researchers—who had submitted their papers to *Science* and *Nature*, respectively—argued the work would help

PHOTO: KENT DAYTON/HARVARD SCHOOL OF PUBLIC HEALTH

Marc Lipsitch is worried about accidents at high-containment laboratories, such as the U.S. Army Medical Research Institute in Maryland.

PHOTO: AP PHOTO/PATRICK SEMANSKY

Marc Lipsitch wants to turn the bitter debate over risky virus research into a search for solutions

the world better prepare for a flu pandemic.

Critics were appalled: Some said the work amounted to a recipe for bioterrorists; others raised the specter of a catastrophic lab escape. A U.S. government advisory panel—the National Science Advisory Board for Biosecurity (NSABB)—recommended that journals publish the studies only if editors cut key details. That idea proved unworkable, however, and 2 years ago the studies were published in full. But the uproar led flu researchers to voluntarily declare a yearlong moratorium on "gain-of-function" studies that enhance dangerous pathogens. It also prompted the U.S. government to develop new rules aimed at strengthening funding reviews for so-called DURC, or dual use research of concern (see sidebar, p. 1115).

The controversy fascinated Lipsitch, who is not an influenza virologist. He's a mathematical modeler and experimental bacteriologist who studies the spread of pathogens including influenza, and he has always been interested in the world beyond science. He studied philosophy at Yale University, and before going abroad to earn his doctorate in zoology at the University of Oxford, he spent a summer working at a newspaper, *The Jewish Daily Forward*, where he says he learned to write fast. In his hometown of Atlanta for a postdoc at Emory University in the late 1990s, he persuaded about 50 scientists to sign a letter protesting a state plan to put a disclaimer in biology textbooks that cast doubt on the evidence for evolution. "I do think scientists have a responsibility to use what we know to be socially useful," says Lipsitch, who comes across as resolute yet soft-spoken.

That outlook drew him into the H5N1 controversy soon after Fouchier gave his Malta talk. Lipsitch was intrigued by the challenge of weighing the potential risks and benefits of the studies. On the benefit side, the H5N1 researchers had argued that their genetic tinkering, which enabled the virus to gain the ability to move more easily between ferrets, would help identify mutations useful to vaccine developers and public health officials on the lookout for dangerous new flu strains. The risk was that if strains like those created by Kawaoka or Fouchier ever

A risky research timeline

Debate over biosafety and biosecurity has deep roots

September 2001
Anthrax mail attacks kill 5, infect 17 in U.S.

February 2003
U.S. tightens regulation of labs studying dangerous "select agents"

October 2003
U.S. National Academies identifies 7 types of risky research, recommends government advisory board on biosecurity

June 2005
First meeting of U.S. National Science Advisory Board for Biosecurity (NSABB)

October 2005
Science publishes sequence of 1918 flu virus (after NSABB consultation)

December 2011
NSABB recommends against publishing H5N1 papers

January 2012
Flu researchers impose voluntary moratorium on gain-of-function studies

March 2012
NSABB, in split vote, recommends publishing H5N1 papers

New U.S. policy for oversight of biomedical dual use research of concern (DURC)

January 2013
Flu research moratorium ends

February 2013
New U.S. rules for reviewing H5N1 studies

August 2013
U.S. drafts rules for university oversight of DURC; new rules for H7N9 flu studies

June 2014
Anthrax accident at Centers for Disease Control and Prevention (CDC)

July 2014
Live smallpox found in storage at National Institutes of Health

CDC reveals H5N1 accident; suspends some lab work and shipments

August 2014
White House announces new biosafety reviews, asks labs to inventory pathogens

escaped—by design or accident—they might sicken or kill large numbers of people.

Lipsitch and others were skeptical of the alleged benefits of lab studies. Such studies in the early 2000s had suggested that a mutation making the H1N1 flu strain resistant to the antiviral drug Tamiflu would never emerge in nature because it lowered the virus's fitness. But in fact, the resistance mutation did appear and spread widely in 2007 and 2008. Such results, Lipsitch says, suggested that the arguments for the H5N1 studies "make sense only if you think that there's a high chance that what you see in the limited number of strains you can study in a lab is strongly predictive of what will happen in nature."

When Lipsitch examined the safety of laboratories working with H5N1 and other dangerous viruses, he began to think the risks of such work had been downplayed. It is typically restricted to the most secure laboratories—so-called biosafety level 3 (BSL-3) and BSL-4 laboratories, which have contained workspaces and can require employees to wear respirators or head-to-toe "moon suits." But he found that government data show U.S. biosafety labs have plenty of accidents: between 100 and 275 potential releases of pathogens each year in labs that handle select agents, or two to four per week, between 2008 and 2012. (Lipsitch's critics point out that the reports include mundane things like spills and record-keeping errors; rarely has a lab worker become infected.) And many researchers suspect that a 1977 H1N1 flu outbreak resulted from a lab escape.

"I had always found biosafety a pretty dry topic, to be honest," says Lipsitch, who runs his own small BSL-2 lab. "But when you start to think of it in terms of a contagious disease and the risk of a new pandemic, it suddenly becomes something that's more connected to what I am interested in."

The accident data helped persuade Lipsitch that gain-of-function experiments that create potential pandemic pathogens—what he and others call PPPs—simply aren't warranted. An inadvertent humanmade pandemic would be inflicted by scientists on people who had no say in whether the risks were justified, he argues. And in June 2012, he and three co-authors summed up their views in an opinion piece for *Science* (22 June 2012, p. 1529), arguing that proposed PPP studies posed an "exceptional level of risk" and calling for a new U.S. government body to conduct risk-benefit analyses.

Not long after the *Science* paper appeared, the controversy faded and the H5N1 studies ultimately resumed. But beneath the surface, the debate continued to simmer. And earlier this year, it boiled over once more after Fouchier, Kawaoka, and other researchers published a new series of virus studies (see box, p. 1114). Although some had been reviewed by U.S. officials under the new rules, they again raised questions about risky research—and who should decide whether a study gets funded or published.

Just as those papers were drawing attention, Lipsitch and Yale epidemiologist Alison Galvani argued that such studies are not only risky, but also unnecessary. Their 20 May *PLOS Medicine* paper laid out detailed alternatives to gain-of-function studies, including using computers and lab work with benign strains to identify important mutations. The paper also marshaled recent data on lab accidents, finding that if just 10 BSL-3 laboratories operated for 10 years, the chances of lab-acquired infection would be nearly 20%. About 1100 U.S. BSL-3 labs are now registered to work with select agents (some are clustered in one facility); that's nearly triple the number that existed in 2001.

The paper drew media attention and, in the scientific world, stirred strident reactions. Fouchier said it overstated the risks, pointing out that there had been only 11 nonfatal infections in U.S. labs over 7 years, and none involved viruses. Kawaoka argued that studying only benign flu strains could produce misleading results. Columbia University's Vincent Racaniello, who has dismissed Lipsitch's efforts as a "crusade," bashed the paper's ethical, scientific, and safety arguments on his popular podcast, *This Week in Virology*, along with several guests. "I'm disturbed. … [A]ll of its points are really unfounded," Racaniello said. In reaction, one Lipsitch defender, bioethicist Nicholas Evans of the University of Pennsylvania, wrote a blog post calling the podcast "a platter of incorrect statements, bad reasoning, and some all-out personal attacks."

Tensions rose in mid-June, after the U.S. Centers for Disease Control and Prevention (CDC) disclosed that a high-security biodefense lab had mishandled live anthrax cultures, potentially exposing dozens of workers. Within days, Lipsitch had submitted a commentary to *The New York Times,* which it published with the headline: "Anthrax? That's Not the Real Worry." Experiments creating PPPs were a "[m]uch more troubling" threat, he wrote.

Lipsitch's uncanny timing continued in the following weeks. First came news that scientists had discovered forgotten vials of smallpox dated to 1954 in a refrigerator on the National Institutes of Health (NIH) campus, ramping up worries about lab safety. Then came the Cambridge meeting. Its organizers, Lipsitch and Peter Hale of the Foundation for Vaccine Research in Washington, D.C., had told invitees that the plan was to discuss "strategies and tactics" for influencing the debate on PPP experiments.

But 3 days before the Monday gathering, CDC chief Thomas Frieden held an unusual press conference to discuss the anthrax and smallpox incidents—and unveil a new revelation that made Lipsitch and Galvani look remarkably prescient. A CDC lab, Frieden announced, had shipped out a relatively benign poultry flu sample that workers had accidentally contaminated with the more dangerous H5N1 virus. Frieden halted some research and shipments and launched a broad biosafety review. The message was unmistakable: Even the best, most regulated labs in the world make errors.

Lipsitch's skeptical message got yet another coincidental boost that weekend. News surfaced that the Department of Health and Human Services was completely remaking the membership of its NSABB biosafety advisory group, excusing all the remaining members who had helped found the panel in 2005 and served through the H5N1 controversy. Though NIH officials said it was a routine turnover, some observers saw it as another sign that government biosafety efforts were in worrying disarray.

By that Monday in July, it was an obvious step for the CWG to piggyback on such news with its statement, Lipsitch says. But reaching consensus wasn't easy: Some group members resisted calling for a complete moratorium on PPP studies. For instance, microbiologist Arturo Casadevall of Albert Einstein College of Medicine in New York City and Michael Imperiale of the University of Michigan disagree with Lipsitch and Galvani's argument

Controversial papers

Three papers this year have helped renew debate over efforts to create or enhance dangerous pathogens:

2 April, *Journal of Virology*
H7N1 is not on the U.S. government's list of flu strains requiring special review, but Daniel Perez's lab at the University of Maryland, College Park, makes it transmissible in ferrets while remaining highly pathogenic.

10 April, *Cell*
Ron Fouchier's lab at Erasmus MC in the Netherlands identifies specific set of mutations that make H5N1—a bird flu that does not spread readily in mammals—transmissible in ferrets.

11 June, *Cell Host & Microbe*
Yoshihiro Kawaoka's group at the University of Wisconsin, Madison, creates a virus similar to 1918 flu using genes from current bird strains.

that the flu experiments aren't justified because they are of limited scientific value. Such work may not be able to pinpoint mutations that could emerge in nature, but it can be "of huge value" in answering broader questions, such as whether a particular bird strain could ever become transmissible in mammals, Casadevall says. He says he finally agreed to the word "curtail" because under U.S. rules the gain-of-function flu experiments "are already curtailed."

Still, Lipsitch's impact on the public conversation was clear when Scientists for Science weighed in a few days later with its response, which was partly organized by Racaniello and has attracted more than 170 signers. "[O]nly by engaging in open constructive debate can we learn from one another's experience," the Scientists for Science statement says. And, in a sign of how eager some are to reach detente, a few researchers, including Imperiale and Columbia University virologist Ian Lipkin, signed both statements. "There has to be a coming together of what should be done," Lipkin says. "It doesn't help for people to be pissing on one another."

Lipsitch is clearly pleased by the more polite turn. "The good thing is that I think the temperature of the rhetoric is much cooler now." And he's willing to accept some credit for helping establish a middle ground "that has been suddenly occupied from both sides," he says. "Whatever the outcome, I think there's reason to expect that it will lead to less risk of accidents than allowing the status quo to continue. And luckily everybody seems to think [the issue is] worth discussing."

It's not easy to see how the two sides might strike a truce. Kawaoka and Fouchier both hope that if their critics better understand the safety and security measures in their labs, they will agree that the flu studies should continue. Some researchers, such as Casadevall, have suggested technological solutions, such as engineering a gene sequence into experimental viruses that could prevent them from replicating in humans. Others believe more inclusive and powerful government review bodies are needed to oversee proposed experiments.

Whatever the outcome this time, the current drama has helped place the spotlight on a new player. Lipsitch "is one of the bravest scientists I know," says epidemiologist Lone Simonsen, a CWG member and longtime friend and collaborator now at George Washington University in Washington, D.C. "If he feels strongly about an issue he will pursue and talk about it, even though it is a point of view most of his sympathetic colleagues share but would not discuss aloud." ■

A policy morass

By **David Malakoff**

Even as scientists and government officials struggle anew with the question of how to regulate risky biological research, the United States and other nations are still working to fully implement the rules and policies that emerged from the last big debate, over the 2011 studies that made H5N1 more transmissible.

Some of the biggest changes have occurred in the United States, by far the single largest funder of potentially risky research. Under rules adopted in 2012, the National Institutes of Health (NIH) and other funding agencies now screen proposals for "dual use research of concern" (DURC)—work that could be used for good or bad ends. At NIH, proposals deemed DURC get a special review and, if funded, special requirements, including that researchers submit manuscripts for prior review before sending them to a journal. As of this past June, NIH tells *Science*, it had reviewed about 30 DURC papers from extramural researchers and six from intramural researchers. In addition, it was monitoring eight DURC projects and had requested changes to some experiments.

A second U.S. government policy, which calls on universities and other institutions to play a bigger role in identifying DURC and mitigating risks, has been in limbo since a draft was released in April 2013. It has drawn criticism from both academic officials, who fear it could be too onerous, and biosafety advocates, who fear it is too lax. The issue got new attention this past June, when Yoshihiro Kawaoka of the University of Wisconsin, Madison, published a study on a flu virus similar to the deadly 1918 strain. University reviewers had judged the study was not DURC, *Nature* reported, but federal officials disagreed. (They nonetheless agreed to fund it.)

Other new rules require NIH to give special reviews to projects aimed at giving new capabilites to two dangerous flu viruses—H5N1 and H7N9. As of June, one grant and one contract had received those reviews, NIH says.

Critics argue that the new reviews are still not preventing NIH from funding questionable studies—but there is wide disagreement on whether or how the process should be altered. In the meantime, some researchers are also calling for clearer rules for journal editors, who often must decide whether to publish findings that could be misused. Others see the need for new government oversight bodies to decide which results should see the light of day. ■

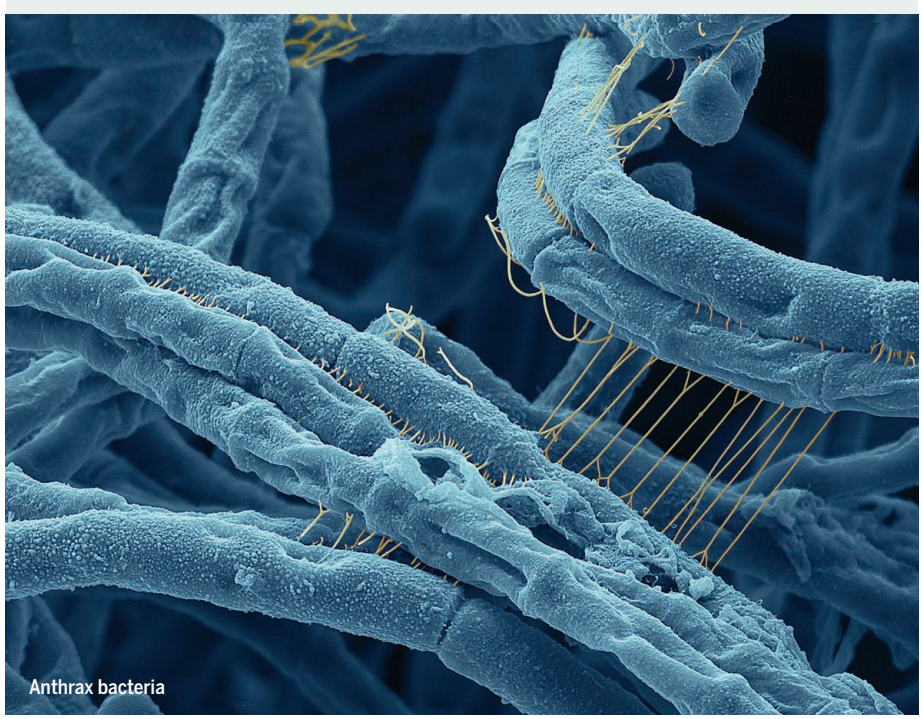

Anthrax bacteria

PHOTO: EYE OF SCIENCE/SCIENCE SOURCE

INSIGHTS

Dipeptide repeat proteins block RNA biogenesis *p. 1118*

Microbial responses to nutrient stress *p. 1120*

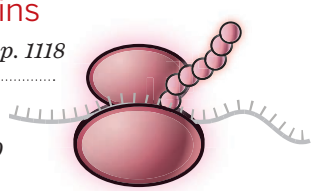

PERSPECTIVES

Summer melt water on glacial ice, George VI Sound, Antarctica.

PHOTO: BRITISH ANTARCTIC SURVEY

CLIMATE

Greenland deglaciation puzzles

Nitrogen isotope data help to resolve puzzling observations during the last deglaciation

By **Louise Claire Sime**

About 23,000 years ago, the southern margins of the great Northern Hemisphere ice sheets across Europe and North America began to melt. The melt rate accelerated ~20,000 years ago, and global sea level eventually rose by ~130 m as meltwater flowed into the oceans. Ice cores from the Greenland and Antarctic ice sheets show the rise in atmospheric CO_2 concentrations that accompanied this shift in global ice volume and climate. However, discrepancies in the temperature reconstructions from these cores have raised questions about the long-term relationship between atmospheric CO_2 concentrations and Arctic temperature. On page 1177 of this issue, Buizert *et al.* (*1*) report temperature reconstructions from three locations on the Greenland ice sheet that directly address these problems.

The relative amount of heavy to light water isotopes in snow mostly depends on how cold it is when the snow falls. For this reason, ratios of light to heavy water isotopes from ice cores (see the figure) have long been used to reconstruct past temperatures in Antarctica and Greenland (*2*). These temperature reconstructions, alongside ice core CO_2 records, have been crucial for advancing understanding of past climate, but they also have puzzling features.

The first puzzle is the timing of Northern Hemisphere warming. Once a certain mass of Northern Hemisphere ice has accumulated, changes in Northern Hemisphere summer insolation—that is, the amount of solar irradiation received at Earth's surface

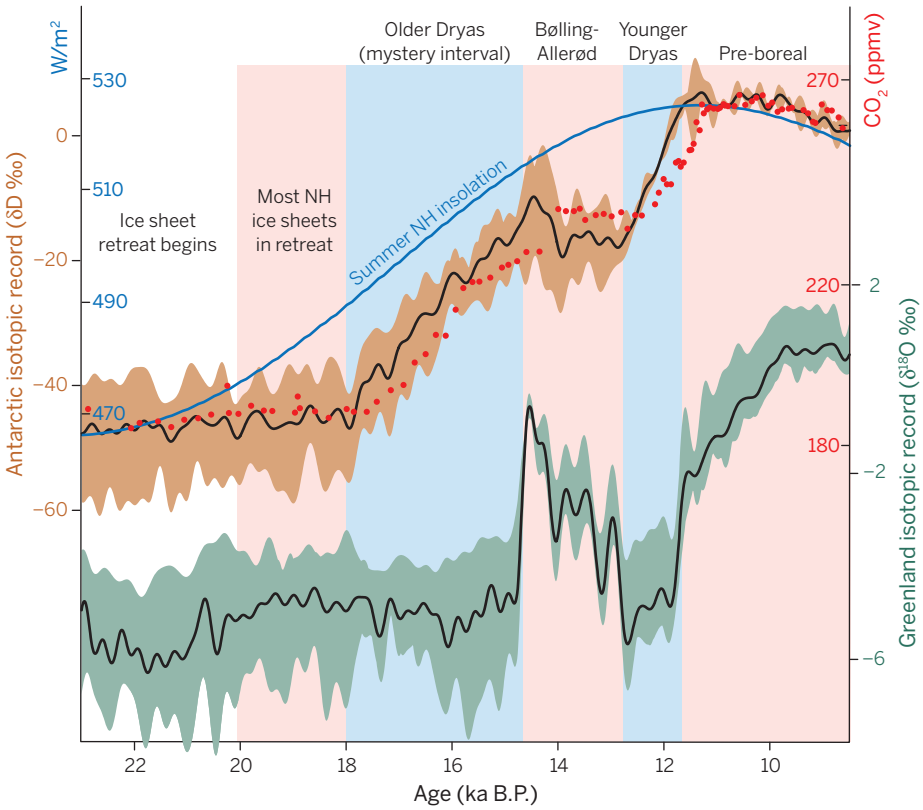

Glacial termination puzzles. Ice core water isotope records suggest that Greenland warmed suddenly and much later than Antarctica, even though summer Northern Hemisphere insolation and atmospheric CO_2 levels rose in step with Antarctic warming. Buizert *et al*. report temperature reconstructions that help to resolve this puzzling observation. Envelopes show the maximum and minimum values for each set of ice cores. See (*13*) for more details.

during summer—are expected to initiate melting. Northern Hemisphere warming would thus be expected to precede or accompany Southern Hemisphere warming. Yet, although most Northern Hemisphere ice sheets were in retreat by ~19,000 years ago (*3*), the Greenland isotopic record does not begin to rise until ~14,700 years ago (see the figure). Denton *et al*. (*4*) used the term "mystery interval" to describe the Oldest Dryas period (~18 thousand to 15 thousand years ago), when Northern Hemisphere summer insolation, Northern Hemisphere ice melt, atmospheric CO_2 concentrations, and Southern Hemisphere temperatures rose, yet Greenland water isotope ratios do not record a similar rise in Northern Hemisphere temperatures.

Using a general circulation model (GCM), He *et al*. (*5*) have shown that allowing Northern Hemisphere ice sheet meltwater to flow into the ocean generates a bipolar seesaw effect, with the Southern Hemisphere warming at the expense of the Northern Hemisphere. This effect is large enough to explain most of the north-south onset discrepancy. In the North Atlantic, surface freshwater from ice melt inhibits the formation of dense salty deep water, leading to extensive winter sea ice in the Northern Hemisphere.

Buizert *et al*. further this analysis by exploiting the fact that water isotopes are not the only way to track temperature in ice cores. When snow becomes denser after it has been deposited, the nitrogen isotope ratio, $\delta^{15}N$, changes as a function of temperature, thus providing information that does not depend on water isotope data. The authors use $\delta^{15}N$ to reconstruct temperatures from three locations in Greenland. They show that previous temperature reconstructions based on water isotopes masked a small temperature rise during the mystery interval. Furthermore, the geographical pattern of their results supports the idea that the timing of the deglacial warming onset strongly depended on heat transported by the Atlantic Ocean (*6*). Thus, variations in meltwater flowing into the North Atlantic, via ocean circulation, largely controlled both the timing and magnitude of the onset of the Greenland deglacial warming (*5*, *6*).

A second puzzle lies in the temperature relationship between the Oldest Dryas and the Younger Dryas (~12.8 thousand to 11.5 thousand years ago). Atmospheric CO_2 concentrations rose by about 50 parts per million (ppm) between these intervals. The ocean likely delivered a similar amount of heat to Greenland during each interval. Yet, Greenland ice core temperature reconstructions based on water isotopes imply that the Younger Dryas was colder than the Oldest Dryas (*7*). Scientists have suggested that the Younger Dryas was an outlier, triggered either by a single catastrophic flood discharge or a comet impact, but these ideas have lost traction due to a lack of evidence (*8*). Climate models predict that rising CO_2 will cause a rise in Greenland temperature. The colder temperatures of the Younger Dryas thus represent the second puzzle.

Liu *et al*. (*9*) performed GCM simulations of the whole period and also modeled water isotope behavior during selected intervals. Despite a simulated ~5°C Greenland warming, their modeled water isotope results match the observed isotopic drop in the Younger Dryas. Buizert *et al*.'s temperature reconstructions confirm this warming. The misleading water isotope results may have come about because reduction in the Northern Hemisphere ice sheet height by 2 km between the Oldest and the Younger Dryas modified atmospheric circulation, causing a relative increase in moisture advected from the North Pacific region (*9*, *10*) that reduced water isotope ratios.

Buizert *et al*.'s successful Greenland temperature reconstructions based on $\delta^{15}N$ imply that similar Antarctic core reconstructions may be possible. Alongside GCM-based paleoclimate modeling tools (*5*, *9*), new Antarctic temperature information could help to clarify the relationship between Antarctic climate and ice sheet changes. ■

British Antarctic Survey, High Cross, Cambridge, CB23 7PP, UK. E-mail: lsim@bas.ac.uk

REFERENCES AND NOTES

1. C. Buizert *et al*., *Science* **345**, 1177 (2014).
2. W. Dansgaard, *Tellus* **16**, 436 (1964).
3. A. E. Carlson, K. Winsor, *Nat. Geosci.* **5**, 607 (2012).
4. G. Denton, W. Broecker, R. Alley, *PAGES News* **14**, 14 (2006).
5. F. He *et al*., *Nature* **494**, 81 (2013).
6. J. D. Shakun, A. E. Carlson, *Quat. Sci. Rev.* **29**, 1801 (2010).
7. K. M. Cuffey *et al*., *Science* **270**, 455 (1995).
8. W. Broecker *et al*., *Quat. Sci. Rev.* **29**, 1078 (2010).
9. Z. Liu *et al*., *Proc. Natl. Acad. Sci. U.S.A.* 10.1073/pnas.1202183109 (2012).
10. P. Kindler *et al*., *Climate Past Discuss.* **9**, 4099 (2013).
11. B. Lemieux-Dudon *et al*., *Quat. Sci. Rev.* **29**, 8 (2010).
12. D. Lüthi *et al*., *Nature* **453**, 379 (2008).
13. The Antarctic ice core record is an average of the Dome C, EPICA (European Project for Ice Coring in Antarctica) Dronning Maud Land, and Vostock water isotopes. The Greenland record is an average of the North Greenland Ice Core Project (NGRIP), GRIP, Greenland Ice Sheet Project 2, and Renland ice cores. Envelopes show the maximum and minimum values from each set of cores. Each ice core record is shown as an anomaly relative to the past 3000 years. All cores are on the Lemieux-Dudon *et al*. (*11*) time scale and are low-pass filtered at 3000 years for clarity. The summer Northern Hemisphere insolation record is solstice insolation at 60°N (W m^{-1}). The CO_2 (ppmv) record is from Lüthi *et al*. (*12*).

10.1126/science.1257842

CELL BIOLOGY

Clogging information flow in ALS

Dipeptide repeat proteins produced in certain neurodegenerative diseases exert toxicity by blocking RNA biogenesis

By **Joseph Paul West III**[1,2] *and* **Aaron D. Gitler**[1]

Amyotrophic lateral sclerosis (ALS), also known as Lou Gehrig's disease, is a devastating neurodegenerative disorder that causes a progressive loss of motor neurons, leading to paralysis and death typically within 2 to 5 years of onset. There are no cures and few treatments. ALS shares some genetic and pathological overlap with another neurodegenerative disease, frontotemporal dementia (FTD), which causes changes to personality and language. Mutations in the gene called *chromosome 9 open reading frame 72* (*C9orf72*) are the most common genetic cause of both ALS and FTD. On pages 1139 and 1192 of this issue, Kwon *et al.* (*1*) and Mizielinska *et al.* (*2*), respectively, describe how *C9orf72* mutations might cause neurodegeneration.

Mutations in the *C9orf72* gene were identified as the most common cause of ALS and FTD (*3*, *4*). This discovery completely revolutionized research on both conditions, with intense efforts now focused on understanding the mechanisms by which C9orf72 mutations cause disease and developing therapeutic strategies to treat patients harboring these mutations. The mutational mechanism is a massive expansion of a hexanucleotide repeat, GGGGCC (G is guanine and C is cytosine) located in a noncoding region of the *C9orf72* gene. Normally, the number of repeat copies ranges from 2 to 23, whereas hundreds or even thousands of copies constitute the disease-causing range. How do these extra GGGGCC repeats cause disease? There are three main hypotheses. One proposal is that expanse of repeats may interfere with the expression of *C9orf72,* thereby resulting in a loss of gene function that is detrimental (*5*). Another possibility is that the GGGGCC repeat transcript (as well as the antisense CCCCGG repeat transcript) may accumulate in RNA foci (*6*) and sequester RNA binding proteins, which could disrupt RNA metabolism. There is also the idea based on the perplexing finding that the long repeat is translated into protein in all six reading frames of the RNA (sense and antisense directions) in a manner that does not depend on the presence of the start codon ATG (A, adenine; T, thymine; G, guanine). This repeat-associated non-ATG translation (RAN translation) thus produces the dipeptide repeat proteins glycine-alanine (GA), glycine-proline (GP), proline-alanine (PA), glycine-arginine (GR), and proline-arginine (PR). These dipeptide repeat proteins are themselves aggregation-prone and accumulate in affected brain regions (*7*). Of course, these three mechanisms are not mutually exclusive, but determining the contribution of each aberration will be critical for the development of effective therapeutic interventions.

To dissect potential contributions from the repeat RNA and those of the dipeptide translation products to disease, Mizielinska *et al.* generated repeat RNA constructs harboring interruptions that preclude their translation. The authors engineered a series of stop codons in both the sense and antisense RNAs every 12 GGGGCC repeats. This way, the RNA could be expressed but the dipeptide translation products would not. They validated that the pure repeats and interrupted repeats formed the G-quadruplex structures characteristic of GGGGCC repeats (*5*), indicating that the interruption strategy did not grossly affect the repeat structure. Both pure and interrupted constructs also formed RNA foci when expressed in cultured neuronal cells. The authors then generated transgenic fruit flies expressing either the pure or interrupted GGGGCC repeats. Remarkably, expression of pure

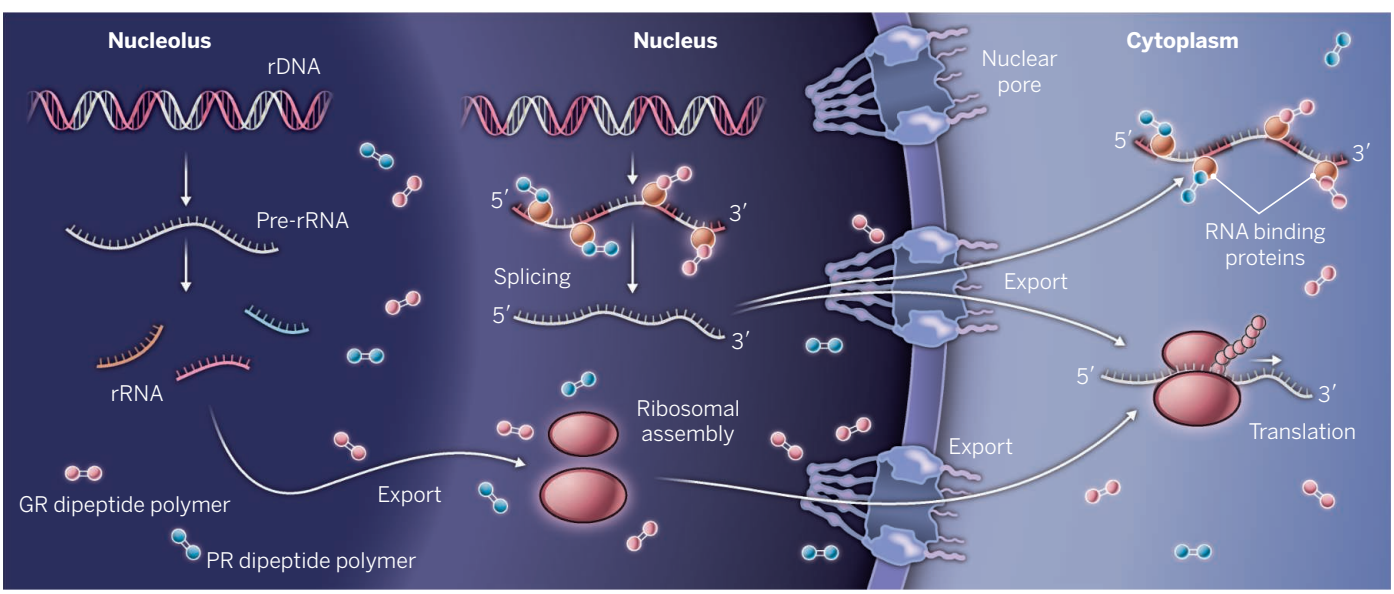

ILLUSTRATION: C. BICKEL/*SCIENCE*

Nuclear havoc. Polymers of arginine-rich dipeptides (GR and PR) derived from the *C9orf72* GGGGCC repeat expansion can enter cells, transport to the nucleus, and accumulate in the nucleolus. These dipeptides can interfere with the splicing of precursor mRNA and rRNA biogenesis. The dipeptides might disrupt mRNA export and import from the nucleus, localization, and translation in the cell.

repeats (able to form dipeptides) in the fly eye caused degeneration, whereas the interrupted constructs (producing RNA only) did not. Likewise, expressing pure repeats in the nervous system of adult flies led to toxicity and early lethality, whereas the interrupted repeats had no effect. Blocking translation by cycloheximide treatment of flies partially suppressed the phenotype, indicating that toxicity was attributable to translation. Thus, Mizielinska *et al.* demonstrate that the GGGGCC repeats can cause toxicity through the production of aberrant translation products and not from the RNA alone.

But which of the five possible dipeptides (GA, GP, PA, GR, PR) translated from the C9orf72 repeat drives neurodegeneration? Mizielinska *et al.* generated transgenic flies expressing each dipeptide independently, but not in the context of a repeat sequence—that is, rather than using GGGGCC to produce the dipeptides, because the genetic code is degenerate (more than one codon codes for the same amino acid), the authors could use different codons to make the dipeptides of interest (e.g., GR) without having a repetitive sequence. Expression of two of the dipeptides, GR and PR, was sufficient to cause toxicity and early lethality when directed to the eye or nervous system. The others were less toxic, but the GA dipeptide did show some toxicity later in life. These results focus attention on the arginine-containing dipeptides (GR and PR), and, to a lesser extent, GA, on driving neurodegeneration caused by C9orf72 mutations in FTD and ALS.

Kwon *et al.* also identify the arginine-containing C9orf72 dipeptides GR and PR as drivers of toxicity, but present a new hypothesis to explain how they might contribute to FTD and ALS pathogenesis. In a broader sense, their study connects two of probably the most exciting new concepts in ALS and FTD research: *C9orf72* nucleotide repeat expansion and the remarkable property of some RNA binding proteins (e.g., FUS, EWSR1, TAF15, hnRNPA2) harboring low-complexity sequences (also known as prion-like domains) to form polymeric assemblies, which incorporate into hydrogels in vitro (*8*). Such assemblies are akin to RNA granules (e.g., P-bodies and stress granules) that play key regulatory roles in gene expression (*9*). Many of the RNA binding proteins that can associate with hydrogels have serine-arginine (SR) repeat domains. These SR domain–containing proteins are regulated by phosphorylation (on the serine residues of the SR domains) by kinases. Kwon *et al.* show that this phosphorylation can control the association of SR proteins with hydrogels made up of RNA binding proteins such as hnRNPA2. Phosphorylation releases the SR domain protein from the gel. Mutating most of the serines in the SR domain protein to glycine (e.g., to convert these domains to GR instead of SR) blocks the effects of the kinases, and the mutant SR domain proteins are no longer able to be released from the hydrogel.

Kwon *et al.* recognized that some of the dipeptide RAN translation products produced from the C9orf72 repeat transcripts resembled the mutated SR domains (e.g., GR and PR). The authors thus proposed an intriguing hypothesis: These RAN translation products associate with hydrogels (or similar types of assemblies in vivo, such as RNA-containing granules) but are impervious to the regulatory action of kinases, and consequently, might clog up the trafficking of SR domain–containing RNA binding proteins that are moving in and out of these granules to transfer information throughout the cell. This block in information flow (e.g., alterations in RNA processing) could lead to cellular dysfunction and might underpin neurodegeneration in ALS and FTD. Indeed, recombinant RAN translation products comprising either polymers of GR or PR bound hnRNPA2 hydrogels and were resistant to kinase treatment (just like the mutated SR domains). When Kwon *et al.* added these recombinant GR and PR proteins to cultured cells, they entered the cells, got into the nucleus, and then localized to the nucleolus, where they caused cell death (see the figure).

"The derangements in RNA processing pathways, perhaps initially mild but accumulating over decades, may eventually lead to neurodegenerative disease pathogenesis."

To determine why GR and PR proteins are toxic and to define the potential consequences of their accumulation in nucleoli, Kwon *et al.* added one of the dipeptides (PR) to cultured astrocytes (a key cell type relevant for ALS) and performed RNA sequencing to assess potential RNA processing alterations. They identified a number of splicing changes as well as changes in the amounts of different mRNAs and major impairments in synthesis of ribosomal RNA (rRNA). These results suggest that by binding to nucleoli and clogging multiple steps along the pathway of RNA biogenesis, dipeptide products of the C9orf72 repeat expansion could cause disease. Kwon *et al.* hypothesize that the arginine-rich stretches of the GR and PR peptides make them rogue mimics of nuclear localization signals, which may facilitate their entering the nucleus and wreaking havoc on multiple steps of RNA biogenesis. The derangements in RNA processing pathways, perhaps initially mild but accumulating over decades, may eventually lead to neurodegenerative disease pathogenesis.

The studies of Mizielinska *et al.* and Kwon *et al.* strongly implicate dipeptide toxicity as a central component of neurodegeneration. A major challenge is to decipher the mechanism by which RAN translation products contribute to neurotoxicity, and to reexamine dipeptide pathology in human disease with a focus on distinguishing GR and PR from the other ones (e.g., GP, GA, PA). Another recent study by Su *et al.* (*10*) presents a potentially game-changing biomarker assay to detect and quantify one of the RAN translation products from patient cerebrospinal fluid. Assays for the abundance of the disease-associated dipeptides could be used in a clinical trial setting to monitor the efficacy of potential disease-modifying therapies that target the repeat RNA expansion. These approaches could include small molecules, as shown by Su *et al.* (*10*), and antisense oligonucleotides (*6*, *11*, *12*). More focus on understanding the molecular mechanisms of RAN translation could reveal new and unexpected therapeutic strategies. Perhaps there are ways to specifically prevent the production of the more toxic dipeptides in exchange for expressing more of some of the benign ones. Unbiased screens using model organisms (yeast, flies, worms, etc.) to identify suppressors of dipeptide toxicity, combined with validation in human patient samples and cell lines, may also reveal mechanisms underpinning dipeptide toxicity and may suggest approaches to mitigate this toxicity. ■

[1]Department of Genetics, Stanford University School of Medicine, Stanford, CA 94305, USA. [2]East Carolina University, Greenville, NC 27834, USA. E-mail: agitler@stanford.edu

REFERENCES

1. I. Kwon *et al.*, *Science* **345**, 1139 (2014).
2. S. Mizielinska *et al.*, *Science* **345**, 1192 (2014).
3. M. DeJesus-Hernandez *et al.*, *Neuron* **72**, 245 (2011).
4. A. E. Renton *et al.*, *Neuron* **72**, 257 (2011).
5. A. R. Haeusler *et al.*, *Nature* **507**, 195 (2014).
6. C. J. Donnelly *et al.*, *Neuron* **80**, 415 (2013).
7. K. Mori *et al.*, *Science* **339**, 1335 (2013).
8. M. Kato *et al.*, *Cell* **149**, 753 (2012).
9. Y. R. Li, O. D. King, J. Shorter, A. D. Gitler, *J. Cell Biol.* **201**, 361 (2013).
10. Z. Su *et al.*, *Neuron* 10.1016/j.neuron.2014.07.041 (2014).
11. C. Lagier-Tourenne *et al.*, *Proc. Natl. Acad. Sci. U.S.A.* **110**, E4530 (2013).
12. D. Sareen *et al.*, *Sci. Transl. Med.* **5**, 208ra149 (2013).

10.1126/science.1259461

OCEAN SCIENCE

Microbial proteins and oceanic nutrient cycles

Ocean microbes respond to limited nutrients by tuning the abundance of specific proteins

By **C. Mark Moore**

Marine microbes play a central role in the biogeochemical cycles of carbon and nutrients such as nitrogen, phosphorus, and iron. The processes that control these complex cycles range from subcellular metabolism to the properties and dynamics of whole oceanic regions. Two studies in this issue provide further insight into how fundamental biological processes affect biogeochemical cycles in the oceans. On page 1173, Saito *et al.* (*1*) show how nutrient availability drives large-scale patterns in the abundances of nutrient-related proteins. The catalytic site in one such protein, reported on page 1170 by Yong *et al.* (*2*), suggests a potential biochemical linkage between two key nutrient cycles.

Phytoplankton—the tiny single-celled photosynthetic organisms that form the base of the marine food web—are responsible for roughly half of global oxygen production. The sinking and breakdown of the organic material produced by these organisms lowers atmospheric carbon dioxide concentrations and removes essential nutrients from the surface ocean (*3*). Limited availability of some of these nutrients, particularly nitrogen (N) and iron (Fe), can be a key constraint on the productivity of surface ocean regions (*3*).

The coupling between carbon and nutrient cycles depends on the activity, composition, and abundance of the macromolecules that make up most biological material (*3*). Over the past two decades, oceanographers have therefore increasingly turned to molecular biology techniques to interrogate the abundance, activity, and diversity of marine microbes and the biomolecules they contain. For example, changes in lipid composition have been linked to nutrient availability (*4*).

Proteins are also useful biomarkers of nutrient stress (*5*). Surveys of oceanic microbial populations have revealed many diverse nutrient transport proteins in low-nutrient systems (*6*). Saito *et al.* now use quantitative proteomic mass spectrometry to determine changes in the absolute abundance of multiple proteins over oceanic scales spanning thousands of kilometers. Sampling across a transition between mainly N-limited and mainly Fe-limited regions, the authors focus on proteins associated with the abundant open-ocean phytoplankton *Prochlorococcus* (*7*). They observe coherent changes in the abundances of multiple-nutrient stress-related proteins, demonstrating in situ microbial responses to varying nutrient limitation regimes (see the figure, panels A and B).

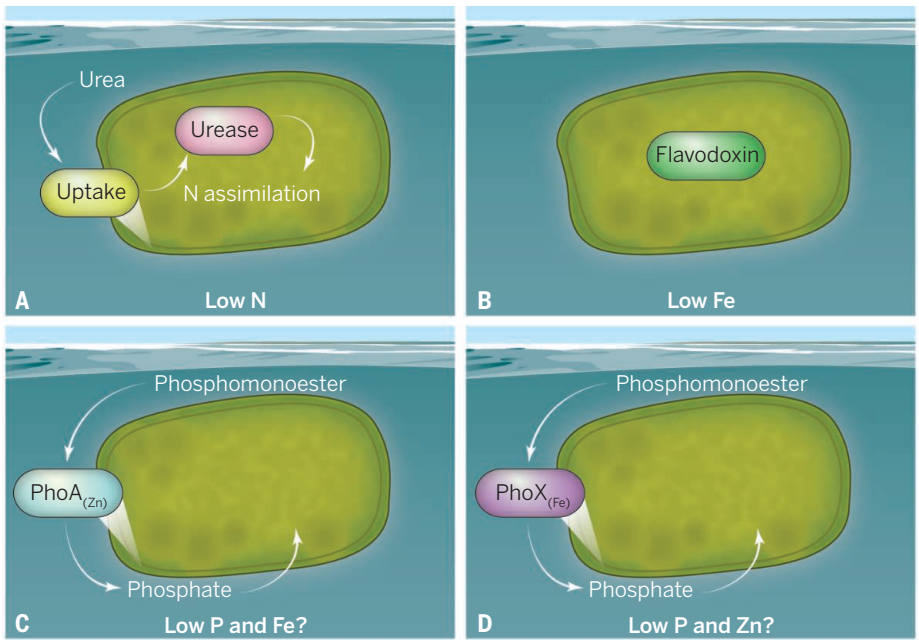

How proteins respond to nutrient limitations. The availability of limiting nutrients varies throughout the oceans. Saito *et al.* (*1*) show that urease proteins associated with uptake and assimilation of urea, an organic N source, are abundant in low-N regions (**A**); in contrast, the flavodoxin protein, which can replace an Fe binding equivalent, is abundant in a low-Fe region (**B**). In low-P regions, uptake of P from phosphomonoesters can be facilitated by alkaline phosphatase enzymes such as PhoA and PhoX. Yong *et al.* (*2*) show that a member of the PhoX family (*11*) binds Fe, in contrast to the Zn-binding PhoA. Selection between these enzymes, or the organisms containing them, might thus be expected in low-P environments depending on the relative availability of Zn (**C**) or Fe (**D**).

"Over the past two decades, oceanographers have therefore increasingly turned to molecular biology techniques to interrogate the abundance, activity, and diversity of marine microbes and the biomolecules they contain."

They are able to detect these large-scale patterns of multiple nutrient limitations without the need for complex time-consuming incubation experiments (*3*).

Understanding of protein abundance and function is particularly important because these macromolecules catalyze and mediate the reactions that drive biogeochemical cycles (*8*). Proteins can also be a large sink for cellular nutrients, including N and trace metals (*3*). Saito *et al.* show that in the boundary region sampled between the low-N and low-Fe regions, essential cellular N resources are simultaneously allocated to different proteins related to N and Fe stress, at least at the community level. These results argue against a simple interpretation where only one nutrient becomes limiting at a time, instead suggesting a degree of colimitation (*3*, *9*).

Many catalytic proteins require transition metals, including Fe, Mn, Co, Ni, and Zn (*10*). Requirements for such proteins are a key driver of the potential for these nutrients to become (co)limiting in the oceans (*9*). A new example of this potential

Ocean and Earth Science, National Oceanography Centre Southampton, University of Southampton, Southampton, SO14 3ZH, UK. E-mail: c.moore@noc.soton.ac.uk

ILLUSTRATION: P. HUEY/*SCIENCE*

is provided by Yong *et al.* Under conditions of low phosphorus (P) availability, marine microbes extract inorganic phosphate from organic phosphomonoester substrates using alkaline phosphatase enzymes (*11*). The best-studied of these enzymes, PhoA, binds Zn, leading to suggestions that P and Zn may be colimiting in certain environments (*9*, *11*). However, the alternative PhoX family of phosphomonoesterases does not require Zn and appears to be more widely distributed in marine systems (*11*).

Yong *et al.* show that a member of the PhoX family binds 2 Fe and 3 Ca atoms in a catalytic cofactor that has several distinctive characteristics. From the biogeochemical perspective, the presence of Fe in the PhoX active site suggests a direct biochemical linkage between the Fe and P cycles, which could lead to these elements becoming colimiting. The relative availability of Zn or Fe in low P environments might thus drive selection between PhoA and PhoX or between the organisms capable of producing these enzymes (*11*) (see the figure, panels C and D). Techniques of the type used by Saito *et al.* could be used to determine whether distributions of PhoA and PhoX correspond to patterns of P, Zn, and Fe availability in the oceans.

The two studies (*1*, *2*) substantially advance our understanding of some of the microbial proteins that influence global nutrient cycles. Wider application of the techniques used by the authors holds great promise for further discoveries. Many metal-binding proteins remain largely uncharacterized (*10*, *12*). Proteomic identification and quantification techniques (*1*, *6*) could also be combined with biogeochemical rate measurements to decipher how microbial proteins operate to maintain elemental cycles (*8*). Given the dual role of proteins as biogeochemical catalysts and as a major sink for nutrients, fuller characterization (*2*), alongside quantification of abundance (*1*) and activity, could provide a fundamental mechanistic underpinning of the coupled nutrient cycles. ■

REFERENCES

1. M. A. Saito, *Science* **345**, 1173 (2014).
2. S. C. Yong, *Science* **345**, 1170 (2014).
3. C. M. Moore *et al.*, *Nat. Geosci.* **6**, 701 (2013).
4. B. A. S. Van Mooy *et al.*, *Nature* **458**, 69 (2009).
5. J. La Roche, R. J. Geider, L. M. Graziano, H. Murray, K. Lewis, *J. Phycol.* **29**, 767 (1993).
6. S. M. Sowell *et al.*, *ISME J.* **3**, 93 (2009).
7. F. Partensky, L. Garczarek, *Annu. Rev. Mar. Sci.* **2**, 305 (2010).
8. P. G. Falkowski, T. Fenchel, E. F. Delong, *Science* **320**, 1034 (2008).
9. M. A. Saito, T. J. Goepfert, J. T. Ritt, *Limnol. Oceanogr.* **53**, 276 (2008).
10. K. J. Waldron, J. C. Rutherford, D. Ford, N. J. Robinson, *Nature* **460**, 823 (2009).
11. M. Sebastian, J. W. Ammerman, *ISME J.* **3**, 563 (2009).
12. A. Cvetkovic *et al.*, *Nature* **466**, 779 (2010).

10.1126/science.1258133

PHYSICS

Particle physics in a superconductor

A superconducting condensate can display analogous behavior to the Higgs field

By **Alexej Pashkin** *and* **Alfred Leitenstorfer**

The recent discovery of the Higgs boson has created a lot of excitement among scientists. Celebrated as one of the most fundamental results in experimental physics (*1*), the observation of this particle confirms the existence of the associated Higgs field that plays a pivotal role in the Standard Model of particle physics. Because of the Higgs boson's large mass (about 125 GeV), it could be detected only in the world's largest and most powerful accelerator—the Large Hadron Collider at CERN, Geneva. Although it sounds strange, the theoretical proposal of the Higgs mechanism was actually inspired by ideas from condensed matter physics, which typically works at much lower energies (a few electron volts or less). In 1958, Anderson discussed the appearance of a coherent excited state in superconducting condensates with spontaneously broken symmetry (*2*). Later, this approach was advanced by Nambu (*3*). The existence of superconducting condensates has been firmly established. In contrast, unambiguous experimental evidence for the coherent excited state (called the Higgs mode) had been missing. On page 1145 of this issue, Matsunaga *et al.* (*4*) report direct observation of the Higgs mode in the conventional superconductor niobium nitride (NbN) excited by intense electric field transients.

Conventional superconductivity appears in metals when the phases of electronic wave functions lock to each other, forming a macroscopic quantum state that conducts current without energy dissipation. It can be described by a complex order parameter $\Phi(\mathbf{k}) = |\Phi(k)|\exp(i\phi)$, which acquires a nonzero value only in the superconducting state. A result of this description is that a superconducting phase transition must lead to a spontaneous breaking of symmetry. Consequently, the energy of the system shows a minimum at a certain value of the radial amplitude $|\Phi(k)|$, which is, how-

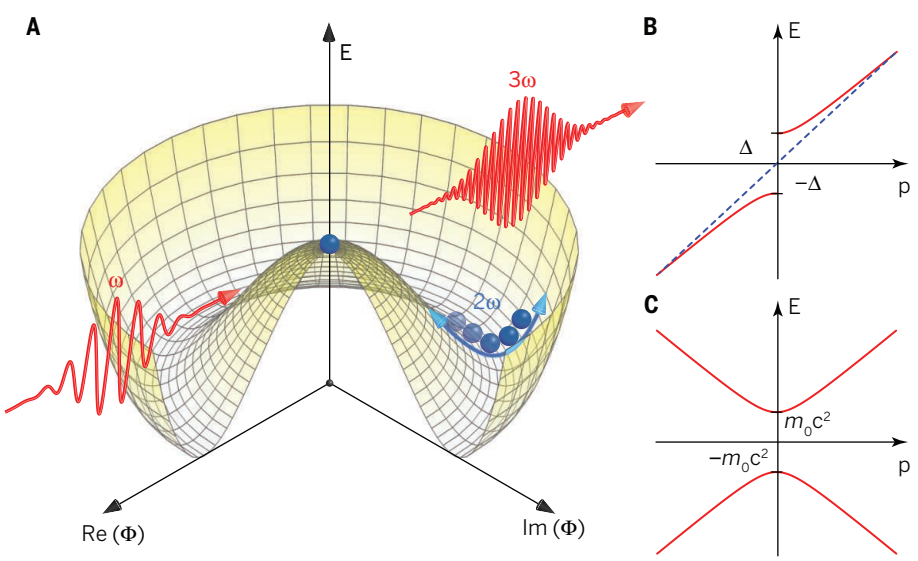

The Higgs amplitude mode. (**A**) Energy of a system as a function of the complex order parameter Φ in a state with spontaneously broken symmetry. The Higgs mode corresponds to the amplitude oscillations of Φ shown by the blue arrow. The excitation by a light pulse at half the resonance frequency starts a coherent oscillation of the order parameter. The induced superconducting current is nonlinear and leads to emission of the third harmonic of the excitation wave. (**B**) Energy of quasi-particles as a function of their momentum near the Fermi energy of a normal metal (dashed blue line) and a superconductor with energy gap 2Δ (solid red line). (**C**) Energy of a relativistic particle-antiparticle system with rest mass m_0 as a function of its momentum.

ever, independent of the phase ϕ (see the figure, panel A). Thus, only a displacement of $|\Phi(k)|$ comes with a restoring force that establishes the Higgs mode at a finite frequency of $2\omega_\Delta$.

The collective Higgs mode appears only in a Lorentz-invariant relativistic theory (*5*), which is usually associated with high-energy particle physics. Obviously, the energy scale in superconductors is far below the level where relativistic effects play a noticeable role. Why, then, does the Higgs mode appear in this case? The reason is that the superconducting energy gap opens up in the spectrum of quasi-particles at the Fermi energy. Electrons with properties modified by their environment are termed quasi-particles in condensed matter physics, and the Fermi level denotes the energy limit up to the point that their quantum states are occupied at zero temperature. Whereas the energy of quasi-particles in a normal metal depends linearly on their momentum in this region, it acquires a form analogous to the relativistic case in the superconducting state. The gap energy $2\Delta = 2\hbar\omega_\Delta$ plays the role of the rest mass of a particle-antiparticle pair (see the figure, panels B and C). Mathematically, this situation results in a formal identity of the Dirac Hamiltonian of Lorentz-invariant quantum theory and the BCS Hamiltonian used in the microscopic description of superconductivity developed by Bardeen, Cooper, and Schrieffer.

"...the goal is to gain insight into strongly coupled low-energy excitations of complex matter by investigating their nonlinear dynamics..."

The Higgs amplitude mode in superconductors does not come with a dipole moment. Therefore, it cannot couple to electromagnetic radiation directly. Nonetheless, using the formalism of Anderson's pseudospins, Matsunaga *et al.* demonstrate that there exists a quadratic coupling between light and the Higgs mode that should result in resonant excitation at half the resonance frequency ω_Δ. To prove this prediction, Matsunaga *et al.* irradiated a superconducting NbN sample with intense light pulses with central frequencies from 0.3 to 0.8 THz (1.2 meV to 3.3 meV). Such energies correspond to the low superconducting transition temperature of 15 K in NbN. They fall into the terahertz spectral region, where both microwave and optical sources were once rather limited in amplitude. This problem has been solved recently with the development of tabletop terahertz sources based on femtosecond laser amplifiers. Optimized nonlinear conversion schemes now deliver unprecedented peak electric fields of terahertz light beyond 1 MV/cm (*6*) or even 100 MV/cm in the multi-terahertz region (*7*).

Matsunaga *et al.* have observed two manifestations of the Higgs mode. First, they used a delayed broadband probe terahertz pulse to trace the dynamics of the order parameter (the superconducting energy gap). By careful measurements at different excitation frequencies and gap energies tuned by temperature, they convincingly demonstrate that the order parameter oscillates at twice the terahertz driving frequency, confirming their initial report (*8*). Second, in accordance with the theoretical prediction by the authors, the superconducting current induced in the sample should oscillate at the third harmonic of the excitation. The experiment clearly detects the terahertz field emitted by this current and its resonant character with respect to the superconducting gap energy.

The results reported by Matsunaga *et al.* show that superconductors exhibit a strong "quantum" nonlinearity that originates from spontaneous breaking of symmetry and the resulting Higgs mode. Novel high-field terahertz technology is now actively used to study such quantum nonlinearities in solids (*9*–*12*). Quite generally, the goal is to gain insight into strongly coupled low-energy excitations of complex matter by investigating their nonlinear dynamics with subcycle temporal resolution. This powerful new approach will continue to provide information that is inaccessible to conventional techniques based on linear analysis in the spectral domain. ■

Department of Physics, University of Konstanz, 78457 Konstanz, Germany. E-mail: alfred.leitenstorfer@uni-konstanz.de

REFERENCES

1. A. Cho, *Science* **337**, 141 (2012).
2. P. W. Anderson, *Phys. Rev.* **110**, 827 (1958).
3. Y. Nambu, *Phys. Rev.* **117**, 648 (1960).
4. R. Matsunaga *et al.*, *Science* **345**, 1145 (2014).
5. M. Varma, *J. Low Temp. Phys.* **126**, 901 (2002).
6. J. Hebling, K.-L. Yeh, M. C. Hoffmann, B. Bartal, K. A. Nelson, *J. Opt. Soc. Am. B* **25**, B6 (2008).
7. A. Sell, A. Leitenstorfer, R. Huber, *Opt. Lett.* **33**, 2767 (2008).
8. R. Matsunaga *et al.*, *Phys. Rev. Lett.* **111**, 057002 (2013).
9. S. Leinß *et al.*, *Phys. Rev. Lett.* **101**, 246401 (2008).
10. B. Zaks, R. B. Liu, M. S. Sherwin, *Nature* **483**, 580 (2012).
11. F. Junginger *et al.*, *Phys. Rev. Lett.* **109**, 147403 (2012).
12. O. Schubert *et al.*, *Nat. Photonics* **8**, 119 (2014).

10.1126/science.1257302

PHYSIOLOGY

Partitioning the circadian clock

Sirtuin proteins divide control of the circadian gene expression and metabolism

By **Yannan Xi** *and* **Danica Chen**

Many physiological and behavioral events exhibit circadian rhythms, which are driven by internal circadian "clocks" that coordinate biological functions through the cyclic expression of at least 10 to 20% of the genes in any given tissue (*1*). The robustness of circadian rhythms deteriorates with age, and circadian perturbation results in the development of disorders such as diabetes, obesity, and brain dysfunction. Central to the mammalian clock is the complex of transcriptional regulatory proteins CLOCK and BMAL1 (*2*). A recent study by Masri *et al.* (*3*) proposes that SIRT1 and SIRT6, two sirtuin family members with nicotinamide adenine dinucleotide (NAD^+)–dependent deacetylase activity, regulate different facets of the CLOCK-BMAL1 network, and more surprisingly, control distinct classes of hepatic circadian genes. Partitioning circadian transcription by sirtuins suggests that in response to internal and external stimuli, circadian clocks selectively control sirtuin-dependent functions that are broadly associated with metabolism, stress resistance, inflammation, aging, and tissue regeneration, to provide organisms with plasticity to adapt to changing environments.

The molecular basis of circadian rhythms is a transcriptional-translational feedback loop (*2*). The CLOCK-BMAL1 complex induces the expression of a number of genes, including the negative regulators of CLOCK-BMAL1. CLOCK has acetyltransferase activity toward BMAL1 and histones (*4*), implicating chromatin remodeling in regulating circadian transcription. Acetylated BMAL1 appears more stable, and histone acetylation is associated with a relaxed chromatin state that is more permissive to gene transcription in eukaryotic cells. Masri *et al.* show that SIRT6, a histone deacetylase (*5*), associates with CLOCK-BMAL1 and reduces their chromatin binding. This finding provides a critical piece in the circadian clock

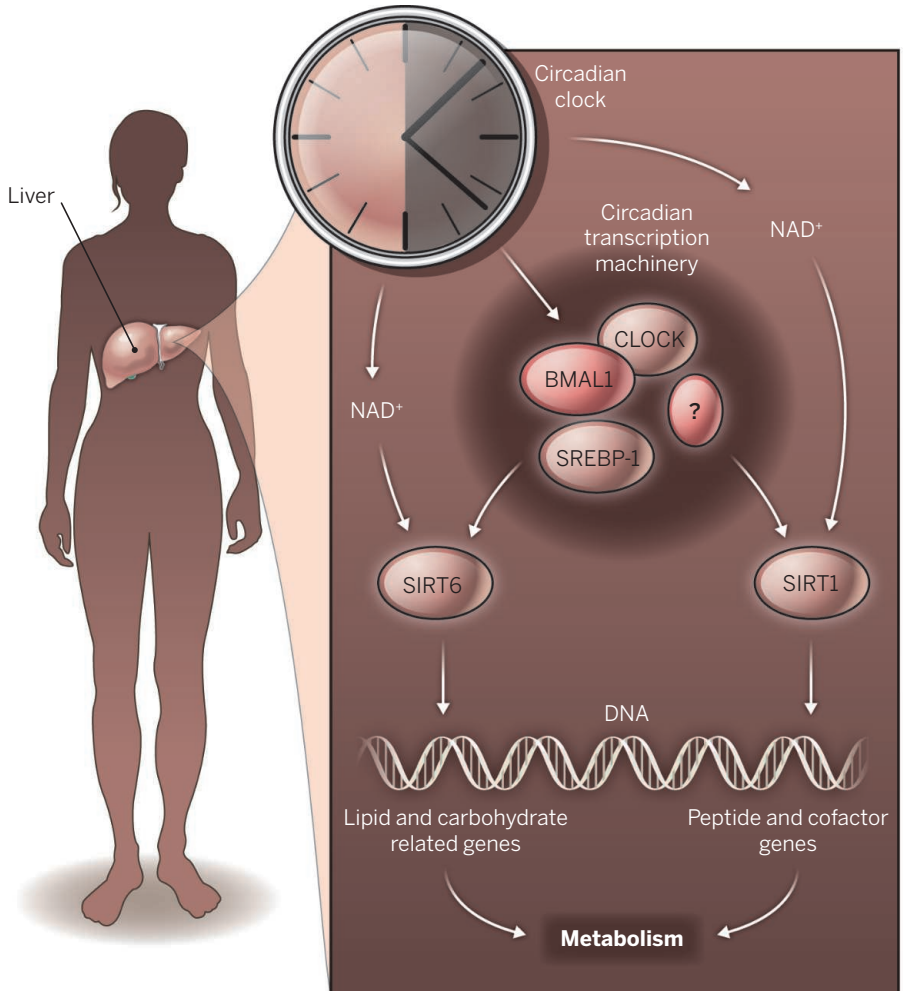

Clock control. SIRT1 and SIRT6 regulate CLOCK-BMAL1 activity through different mechanisms and control distinct classes of hepatic circadian transcription and metabolic outputs.

puzzle. CLOCK-BMAL1 induces the expression of the gene *Nampt*, which encodes an enzyme that catalyzes a rate-limiting step in NAD^+ biosynthesis (*6*, *7*). The resulting increase in the cellular NAD^+ concentrations activates SIRT1 and SIRT6. The deacetylase activity of SIRT1 counteracts CLOCK to drive the cyclic acetylation/deacetylation of BMAL1 and histones and orchestrate their function along the circadian cycle (*8*, *9*). By contrast, SIRT6 activation reduces chromatin binding of CLOCK-BMAL1, tipping the balance toward the establishment of a repressive chromatin state.

Masri *et al*. further took a systems biology approach to study hepatic circadian transcription regulated by SIRT1 and SIRT6. Ablation of the genes encoding SIRT1 or SIRT6 specifically in the mouse liver disrupted the expression of a large number of genes whose expression normally oscillates over a 24-hour period. This supports an essential role for these sirtuins in regulating CLOCK-BMAL1 activity. Surprisingly, the absence of hepatic SIRT1 or SIRT6 also caused a widespread oscillatory transcription of genes that was not observed in the livers of wild-type mice. Such large-scale de novo oscillating transcripts can also be triggered by nutritional challenge (*10*). These findings highlight the existence of numerous molecular pathways that influence circadian clocks, which may serve to systematically reprogram biological functions in a cell in response to changing environments.

A key discovery of Masri *et al*. is that SIRT1 and SIRT6 regulate distinct classes of circadian genes (see the figure). Comparison of SIRT1- and SIRT6-dependent oscillating transcripts revealed remarkably little overlap. Genomic partitioning by sirtuins has physiological consequences. By integrating high-throughput circadian transcriptomics with circadian metabolomics data, Masri *et al*. found that SIRT1 and SIRT6 control different classes of circadian metabolites, reflecting their differential regulation of circadian transcription. Whereas SIRT1 preferentially controls peptide and cofactor metabolism, SIRT6 preferentially regulates fatty acid and carbohydrate metabolism.

How does a deficiency in SIRT6 result in de novo rhythmic expression of a large number of transcripts and their related metabolites? Sterol regulatory element–binding protein 1 (SREBP-1), a transcription factor that controls fatty acid metabolism, may play an essential role. Masri *et al*. found that SREBP-1 binding sites are highly enriched at the promoters of circadian genes that respond to SIRT6. Circadian recruitment of SREBP-1 to the promoter of its target gene increased in the absence of SIRT6. The livers of SREBP-1–deficient mice displayed disrupted circadian expression of SREBP-1 target genes. How SIRT6 specifically influences the circadian chromatin recruitment of SREBP-1 remains an open question.

The findings by Masri *et al*. have many important implications. The high-resolution systems approach used in their study, integrating circadian transcriptome and circadian metabolome, contrasts with current metabolic and physiological studies that sample gene expression and metabolites at one nonspecified time point, which may inevitably miss important information and generate inconsistency. The systems approach provides a new framework for future physiological studies. The discovery that circadian genes can be differentially controlled by sirtuins will also initiate further studies into signals that differentially activate sirtuins. This may yield new insights about the reorganization of circadian rhythms by environmental stimuli.

A closer connection between sirtuins and circadian clocks is likely to enrich the understanding of both sirtuin biology and circadian regulation. Elucidating the circadian regulation by SIRT2 and SIRT7, two other sirtuin family members with nuclear localization and important physiological functions (*11*, *12*), may provide insights into the etiology of metabolic diseases and aging. ■

Program in Metabolic Biology, Nutritional Sciences and Toxicology, University of California, Berkeley, CA 94720, USA. E-mail: danicac@berkeley.edu

ILLUSTRATION: C. BICKEL/*SCIENCE*

REFERENCES AND NOTES

1. S. Masri, P. Sassone-Corsi, *Nat. Neurosci.* **13**, 1324 (2010).
2. C. Dibner, U. Schibler, U. Albrecht, *Annu. Rev. Physiol.* **72**, 517 (2010).
3. S. Masri *et al*., *Cell* **158**, 659 (2014).
4. M. Doi, J. Hirayama, P. Sassone-Corsi, *Cell* **125**, 497 (2006).
5. E. Michishita *et al*., *Nature* **452**, 492 (2008).
6. Y. Nakahata, S. Sahar, G. Astarita, M. Kaluzova, P. Sassone-Corsi, *Science* **324**, 654 (2009).
7. K. M. Ramsey *et al*., *Science* **324**, 651 (2009).
8. G. Asher *et al*., *Cell* **134**, 317 (2008).
9. Y. Nakahata *et al*., *Cell* **134**, 329 (2008).
10. K. L. Eckel-Mahan *et al*., *Cell* **155**, 1464 (2013).
11. H. S. Kim *et al*., *Cancer Cell* **20**, 487 (2011).
12. J. Shin *et al*., *Cell Reports* **5**, 654 (2013).

ACKNOWLEDGMENTS

This work was supported by NIH (AG040990), Ellison Medical Foundation, and American Heart Association.

10.1126/science.1259601

BOTANY

A wake-up call with coffee

Recording and archiving crop phenotype diversity needs to catch up with genomic data

By **Dani Zamir**

Smell the coffee. *Coffea canephora* joins many other crop species and varieties with a draft genome sequence.

The captain of the starship Voyager from one of the latter-day *Star Trek* television series expressed the sentiments of many by stating: "Coffee, the finest organic suspension ever devised." On page 1181, Denoeud *et al.* present a draft genome of the diploid *Coffea canephora* (*1*), one of the two founder species of the tetraploid crop *Coffea arabica*. Coffee, the plant bearing the irresistible bean that delivers the most widely consumed psychoactive drug in the world—caffeine—joins a long list of crop species that have been sequenced using ever-improving genomic hardware and assembly software (*2*). High-quality genome assemblies facilitate the resequencing of many cultivated varieties, landraces (local ecotypes), and sometimes wild, crop-related species. The challenge now is to translate these decoded genomes into new and improved tools for plant breeding; there is a need for a better balance of research priorities, with greater emphasis on crop phenotypes.

Linking genotypes to phenotypes is currently a game with few rules, particularly when traits are challenging to describe or measure because of their continuous distribution in populations—for example, mean yield or yield stability. One reason for the slower progress in the arena of crop productivity phenotyping is that scientists in academic institutions are less inclined to be passionate about observable or simply measured traits than about results from sophisticated high-throughput machines that profile many molecular or growth-related traits. In addition, phenotyping of such integrative quantitative traits is much more challenging to archive than the digital cracking of four-base nucleic acid codes or 20 amino acid–based proteins. Unlike the well-established, publicly available repositories for DNA and proteins, there exists no equivalent consensus on the structuring of repositories for data generated from the many phenotypic studies that are being conducted on sequenced plant varieties (*3*).

What's worse is that in most cases following publication of crop biology papers, molecular data are released without the corresponding potentially commercially valuable phenotypic data. For example, in rice (*Oryza sativa*), which feeds roughly half the world population, 3000 variants from 89 countries were sequenced revealing 18.9 million single-nucleotide polymorphisms (SNPs) (*4*). But what good are 3000 genomes if the associated phenotypic data, and sometimes seed stocks, are kept proprietary? A wake-up call is needed for scientists, granting agencies, journal editors, and referees: What we eat are phenotypes, and seriously addressing global food security demands that, at least in the domain of crop plants, phenotypic data should be shared between scientists in the same manner as for sequences (*3*).

Coffee, which is admired for its aroma, flavor, and the alkaloid stimulant caffeine, has a number of attributes that make it particularly suitable for linking genomes and phenotypes for the purpose of sustaining an industry that is struggling with climate change and pests (*5*). The center of coffee diversity is in Africa. From there the beverage spread throughout the world beginning as early as 500 years ago. Nowadays, the top coffee-growing countries are Brazil, Vietnam, Indonesia, Colombia, and Ethiopia—this last being the birthplace of the crop plant and where more than 1 million households are engaged in growing coffee. The worldwide production of Arabica coffee relies on a small number of cultivars with very little genomic and phenotypic diversity between them, relative to those available in Africa, the center of origin. The key for ensuring that coffee can survive as an affordable crop lies in the genetic variation found in African species. This variation will help to mitigate the effects of unstable climate and plant diseases, as well as modify the wealth of health-related chemicals present in the coffee seeds (*6*) (e.g., naturally decaffeinated Arabica coffee) (*7*).

A recent survey of coffee genetic resources in Ethiopia found an alarming rate of genetic erosion of the gene pool due to deforestation coupled with inadequate conservation efforts. According to the Biological Diversity Convention (*8*), the benefits derived from discoveries made on the basis of biodiversity must be equitably shared with the country of origin. The complexity of monitoring beneficial traits introduced from endemic species often leads to situations where countries refuse to make their genetic resources accessible. Perhaps the draft coffee genome presented by Denoeud *et al.* can be used to provide an unequivocal means to monitor, via SNP diversity, the utilization of genetic resources after they leave their country of origin. The substantial value of the coffee production chain is accrued by highly profitable companies that transport, roast, blend, and sell the coffee; these are typically located in rich, coffee-importing countries. The danger to the coffee crop (*5*) should provide an incentive for all stakeholders to initiate international collaborations in genomic-assisted breeding projects and germ plasm conservation with poor, coffee-exporting countries. This proposal is compatible with the fact that coffee is the most popular plant associated with genomics, because every genome meeting has coffee breaks that are needed to reinvigorate the audiences and to promote communication, conversation, and the sharing of knowledge. ■

Institute of Plant Sciences and Genetics, Faculty of Agriculture, Hebrew University of Jerusalem, Rehovot 76100, Israel. E-mail: dani.zamir@mail.huji.ac.il

REFERENCES

1. F. Denoeud *et al.*, *Science* **345**, 1181 (2014).
2. R. K. Varshney, R. Terauchi, S. R. McCouch, *PLOS Biol.* **12**, e1001883 (2014).
3. D. Zamir, *PLOS Biol.* **11**, e1001595 (2013).
4. 3,000 Rice Genomes Project, *GigaScience* **3**, 7 (2014).
5. M. Gross, *Curr. Biol.* **24**, R503 (2014).
6. J. P. Labouisse, B. Bellachew, S. Kotecha, B. Bertrand, *Genet. Resour. Crop Evol.* **55**, 1079 (2008).
7. M. B. Silvarolla, P. Mazzafera, L. C. Fazuoli, *Nature* **429**, 826 (2004).
8. S. McCouch *et al.*, *Nature* **499**, 23 (2013).

10.1126/science.1258941

PHOTO: JOHN M. SCOTT/ISTOCKPHOTO

Applying scientific principles in international law on whaling

The approach might address disputes beyond whaling and the courtroom

By **William de la Mare**[1†] *and* **Nick Gales**[1], **Marc Mangel**[2*]

In March 2014, the International Court of Justice (ICJ), the principal judicial organ of the United Nations, ruled that a Japanese whaling program in the Antarctic, ostensibly for scientific purposes, was not sufficiently research-oriented and thus was illegal (*1*). The ICJ's critical assessment represents the first time that scientific whaling has been reviewed by an authoritative body outside the International Whaling Commission (IWC). With Japan considering a replacement program, and the IWC meeting later this month, we discuss minimum realistic actions the IWC should take in response to the ICJ judgment. More broadly, we believe the approach used by the ICJ in reaching its judgment provides a precedent for how arbitrators might assess scientific principles when resolving complex technical disputes.

POLICY

Commercial whaling is currently prohibited under the International Convention on the Regulation of Whaling (ICRW). Japan argued that its Japanese Whale Research Program under Special Permit in the Antarctic (JARPA II) program satisfied Article VIII of ICRW, which allows special permits authorizing killing, taking, and treating of whales "for purposes of scientific research" (*2*). The stated objectives of JARPA II, which also had no stated time limit, were (i) monitoring the Antarctic ecosystem, (ii) modeling competition among whale species and developing future management objectives, (iii) elucidation of temporal and spatial changes in stock structure, and (iv) improving the management procedure for minke whales. Under JARPA II, Japan issued permits to take up to 935 minke whales (850 ± 10%) per year and 50 each of humpback and fin whales. The number of minke whales taken was substantially less than 850 in all but one year; more than 3500 were taken from 2005 to 2013 (see the photo). No humpback and fewer than 20 fin whales were taken.

[1]*Australian Antarctic Division, Kingston, Tasmania 6050, Australia.* [2]*University of California, Santa Cruz, CA 95064, USA.* **Corresponding author. msmangel@ucsc.edu.* *†The opinions expressed herein are those of the authors. They do not necessarily reflect the position of the Australian government on any of the issues raised.*

The ICJ decided in favor of Australia, which had argued that JARPA II was not "for purposes of scientific research" as required by Article VIII (*3*). The ICJ ordered Japan to revoke permits granted to JARPA II. This ended Japan's program of Southern Ocean whaling, which had polarized and disenfranchised scientists (*4*, *5*) and galvanized environmentalists.

States that appear before the ICJ understand that its judgments are binding and without appeal. Whereas Japan indicated that it would abide by the judgment and terminated JARPA II, it appears that Japan hopes to devise a replacement program to commence in 2015. Although the judgment does not preclude whaling under Article VIII, the reasoning of the ICJ has clear implications that any future special permit program must meet higher scientific standards than JARPA II did.

LOGIC OF SCIENCE, NOT DETAILS. At the heart of the judgment was whether Japan's program is "for purposes of scientific research." Japan argued that its activities involved science and, therefore, Article VIII rendered JARPA II wholly outside any other provisions of the ICRW. In essence, Japan argued that if an activity involves scientific research it is also "for the purposes of scientific research," which fulfills obligations under Article VIII. Japan argued that this decision is self-determined by the state issuing the permit.

Australia argued that "scientific research" is subject to internationally accepted norms not unique at the level of the nation-state. Australia argued that scientific research in the context of Article VIII should be characterized by features that include (i) defined and achievable objectives; (ii) use of appropriate methods, including use of lethal methods only where objectives cannot be answered through alternate methods; and (iii) proper assessment and response through the community of scientists. Japan offered no alternative model but argued that Australia's interpretation was overly restrictive.

The ICJ was not persuaded that activities must satisfy Australia's normative criteria in order to constitute "scientific research" in the context of Article VIII, although many elements of those criteria were taken into account by the ICJ (*3*). Rather than offering its own definition of science, the ICJ proceeded by first asking whether, and ultimately concluding that, the activities associated with

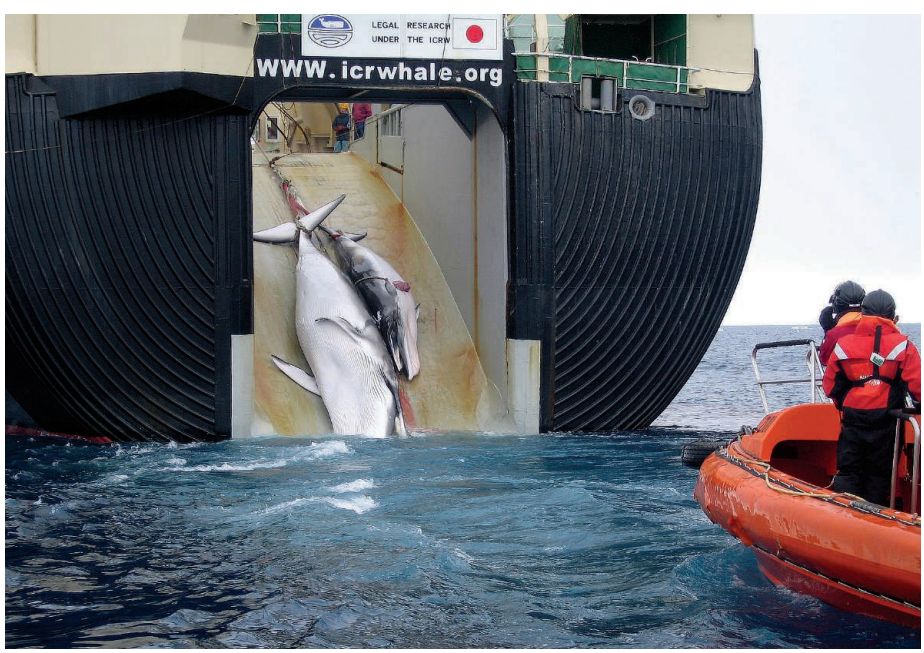

PHOTO: AUSTRALIAN CUSTOMS SERVICE

An adult and subadult Minke whale are dragged aboard the Nisshin Maru, a Japanese whaling vessel.

the lethal take in JARPA II could in principle be characterized as scientific research.

The ICJ then considered whether the whaling itself was "for purposes of scientific research," as required by the ICRW, by examining whether the elements of the program's design and implementation were reasonable in relation to achieving its stated scientific objectives. The ICJ relied heavily on presentations by Australia and Japan, using commonalities of expert testimony (authors N.G. and M.M. called by Australia and L. Walløe called by Japan) when examining relevant elements of the program's design and implementation. These elements included (i) use and scale of lethal research, (ii) methods used to select sample sizes, (iii) comparisons of target sample sizes and actual take, (iv) program time frame, (v) scientific output of the program, and (vi) degree to which the program coordinates its activities with related research projects.

The ICJ paid particular attention to inconsistencies between the methods of determining sample sizes for the different species (*6*). Rather than trying to decide whether sample sizes were scientifically correct or necessary, the ICJ looked at the logic: If the sample sizes were purported to be necessary for achieving the objectives, then failing to collect the specified numbers must mean either that the objectives would not be attained or that the specified sample sizes were unnecessarily large. In either case, program design and implementation are not logically consistent, that is, not reasonable.

> ***"[Were] elements of the program's design and implementation ... reasonable in relation to achieving its stated scientific objectives[?]"***

The ICJ noted that no adjustments were made to JARPA II objectives when specified sample sizes were not achieved. The ICJ found that the statements and practices of Japan supported the argument by Australia that sample sizes were determined using criteria other than science. The ICJ found that JARPA II failed against the measure of reasonableness for the other criteria as well (*6*). The ICJ found that if a state issues a permit, it cannot fund the activities by using more lethal sampling than consistent with the objectives of the research.

Because the practice of JARPA II was not reasonable in relation to achieving its scientific objectives, the ICJ concluded that it was not "for purposes of scientific research." Even if a program involved some "scientific research," the taking of whales in such a program does not fall within Article VIII unless the activities are pursued "for the purposes of scientific research," the ICJ having concluded that the two elements were cumulative (*7*).

In addition, the ICJ concluded that determination of whether whaling under Article VIII was for the "purposes of scientific research" is not open to self-judgment and cannot simply depend on a state's perception.

POLITICIZED REVIEW. The ruling is a challenge both to Japan's determination to continue whaling in Antarctica and to the IWC's ability to respond credibly to serious external judgment. Although not explicitly noted by the ICJ, the judgment highlights weaknesses of the review process within the IWC. Logical and scientific inconsistencies in JARPA II were pointed out in the IWC scientific committee's mandatory review of the original proposal (*8*). Cogent scientific criticisms were dismissed by Japan as politically motivated, a label that makes many scientists reluctant to engage in the review process. Consequently, even though logical inconsistencies noted by the ICJ as flaws had been identified by many members of the scientific committee, these did not stand out in the committee's reviews as being so serious that they required attention. The salience of the committee reports was further degraded because proponents of the program were involved in writing and editing the reviews.

It is fair to say that the scientific committee is politicized, as it involves scientists from both whaling and nonwhaling countries, most of whom are appointed by their governments. However, in a scientific review, the motivations of critics should be irrelevant. Either criticisms are scientifically valid or they are not. If they are valid, they should not be ignored because of political differences. Weak reviews of the JARPA II proposal by the scientific committee enabled commissioners to dismiss divergent views as reflecting political opinions rather than being serious scientific flaws.

Regardless of Japan's future actions, its approach in self-determining scientific validity has been found to be incorrect. The reasoning of the ICJ indicates that a state proposing a scientific take should provide sufficient information on program design and implementation and on how the sample sizes are necessary for achieving the objectives. Objectives cannot be stated in such vague terms that scientific judgment of their achievability is reduced to a contest of scientific opinions based on differing interpretations of what the objectives mean. Objectives, methods, and sample sizes must be sufficiently detailed so as to be capable of quantitative evaluation using normal scientific procedures. Long-term proposed research should specify intermediate objectives so research can be adjusted or abandoned if they are not achieved.

The IWC review processes need to be improved so that clear advice on the scientific achievability of a program's objectives can be provided by its scientific committee despite the variety of political views therein. This is why measurable objectives and prospective quantitative evaluations are needed. The burden of proof on the validity of a scientific proposal properly resides with the proponent, who should sit outside the review process. The IWC should transmit the advice of the scientific committee to the proposing state along with any other observations it may have. A state proposing a special permit should adjust its proposal to take full account of scientific criticisms and the advice from the commission and scientific committee.

BEYOND THE COURTROOM. By using the test of reasonableness, the ICJ provided a clear, well-constructed judgment focused on the logic, rather than details, of science. Such an approach could serve as a useful model in resolving other disputes over complex technical issues. Beyond the courtroom, the misrepresentation of science to advance nonscience agendas is a common feature in disputes involving economic, social, or political values (*9*–*11*). The ICJ's approach represents a model for separating scientific matters and the nonscientific agenda in other complicated disputes involving science, society, and law. The ICJ demonstrated that it is possible to sit above the detailed technicalities of scientific research and still determine whether practices were for purposes of science or nonscience. We hope the IWC can learn from their example. ■

REFERENCES AND NOTES

1. The judgment of the ICJ, the written material submitted by Australia, Japan, and New Zealand, and transcripts of the oral proceedings can be accessed at www.icj-cij.org/docket/index.php?p1=3&p2=1&code=&case=148&k=64.
2. International Convention for the Regulation of Whaling, signed 2 December 1946, (ICRW, Washington, DC, 1946). http://iwc.int/private/downloads/1r2jdhu5xtuswws0ocw04wgcw/convention.pdf.
3. Paragraph 227 of the judgment in (*1*).
4. V. Morrell, *Science* **316**, 533 (2007).
5. N. J. Gales, T. Kasuya, P. J. Clapham, R. L. Brownell Jr., *Nature* **435**, 883 (2005).
6. Paragraphs 224–226 of the judgment in (*1*).
7. Paragraph 71 of the judgment in (*1*).
8. S. Childerhouse *et al*., *J. Cetacean Res. Manag.* **8** (suppl.), 260 (2006).
9. N. Oreskes, E. M. Conway, *Merchants of Doubt* (Bloomsbury Books, New York, 2010).
10. G. Taubes, *Good Calories, Bad Calories* (Knopf, New York, 2007).
11. M. Mangel, *Trends Ecol. Evol.* **16**, 110 (2001).

10.1126/science.1254616

BOOKS *et al.*

PERCEPTION

Pay attention!

By **Adrienne Wang**

As infants entering the world, we are bombarded with a cacophony of bright lights, loud noises, and our first encounters with hard edges and visual stimuli. A baby will stare at a seemingly empty corner, transfixed at the contrast in the line formed where two walls meet. Everything is novel and demands scrutiny, but eventually we are able to ignore extraneous and repetitive information as we learn to direct our attention.

In *On Looking: A Walker's Guide to the Art of Observation*, Alexandra Horowitz aims to reverse normal human development by opening our eyes to unseen worlds that surround us but often go unnoticed. Accompanied by a progression of "experts," including a typographer, a naturalist, an animal behaviorist, an urban planner, and a sound engineer, Horowitz weaves through city blocks, focusing on elements that are ordinarily tuned out or missed entirely. She does this conversationally, interspersing conversation with nuggets of information on the science behind why we see, hear, smell, and feel things a certain way—or why we don't.

On Looking
A Walker's Guide to the Art of Observation
Alexandra Horowitz
Scribner, 2013. 319 pp

From an entire universe of insect life contained in a single tree to the emergent properties of herd behavior governing the unstated rules of navigating a busy sidewalk, each chapter is intended to shift the reader's perspective. The walls of skyscrapers become man-made habitats providing ecological niches for rodents, pigeons, raptors, and plants that evolved cliff-side. Faded lettering on a building becomes the individual biography of the structure—"ghost signs" layered over or removed by years of paint or changing facades—that offer a glimpse backward in time.

Even when nothing appears to be there at all, there is something to perceive. Horowitz repeatedly illustrates how the absence of signs can be just as telling as a sign itself. The muting of sound can give information about one's surroundings or climate through reflection or absorption of sound waves. Layers of warm and cool air can usher sound waves farther by creating a sound corridor, a phenomenon that assists songbirds that sing at twilight. The absence of insect markers like galls, excrement, or the leftovers from a meal can indicate the presence of a non-native tree, which local insects have not had a chance to develop a taste for.

Horowitz is so successful at igniting one's curiosity, she leaves us wanting just a bit more from her book. Much like the walks from which it is composed, some chapters in *On Looking* can seem like a meandering ramble through discrete neighborhoods, creating a desire in the reader for a more additive experience and connection between chapters. Additionally, some theories posited make one wonder about the evidence that may support or argue against the presented perspective and the qualifications of her experts. This, however, is just a testament to how well *On Looking* challenges the reader's perception and encourages the reader to look at seemingly small or insignificant pieces of an experience from all perspectives, allowing one to find interest in almost anything should one simply look.

The reviewer is at the Kaeberlein Lab, Department of Pathology, University of Washington, Seattle, WA 98195, USA. E-mail: amwang@uw.edu

10.1126/science.1255876

How much do you see?

PHOTO: JOHN ANDERSON/ISTOCKPHOTO

SCIENCE COMMUNICATION

Whimsical math

By **Rachael Skyner**

Math Bytes: Google Bombs, Chocolate-Covered Pi, and Other Cool Bits in Computing manages to fulfill its aim of providing a "tasty byte of math and computing" while following a clear, concise, and to-the-point format. It achieves this without losing the reader in an off-putting ramble, which can often be the case with books relating to math and computing that are intended for the general public.

The fonts that we see in everyday digital text are actually represented in computers as functions. Because of this, we can, with the touch of a button, make the letters appear at various sizes without losing any resolution. The "font can be stored with

Math Bytes
Google Bombs, Chocolate-Covered Pi, and Other Cool Bits in Computing
Tim Chartier
Princeton University Press, 2014. 150 pp.

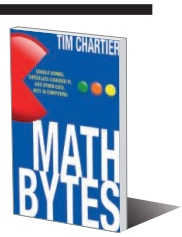

only a few points even though thousands of pixels will make up the complete curve." Tim Chartier's book talks through and explains many examples such as this, which we often take for granted in our everyday computing activities. The book also considers some more abstract ideas, such as using milk and white chocolate chips to visualize an estimation of the value of pi (hence the slightly bizarre book title). Chartier also describes a way to use matrix operations to see which celebrities you physically resemble. The variation in complexity of the material covered within the book makes it an extremely satisfying read. Ideas such as "chocolate-covered pi" may be used as a fun and educational activity with children, whereas understanding Google's page-rank algorithm may be more suited to those with a solid grounding in post–high school mathematics. For those who are struggling with certain materials, the author offers additional online resources and a rich list of references. This book is not suitable for a quick read on the beach; it requires a willingness to be challenged intellectually.

"Let's start with a simple chocolatey problem that will open a door to ideas of calculus."

Chartier's format for this rather unique book involves using an assortment of examples to extract the theoretical knowledge required to understand the underlying mathematical theory, often offering a "challenge" for readers to work through themselves. This kind of hands-on or learn-by-example approach is something that the general reader may not have come across since high school. I feel this book bridges the gap between a traditional popular science format and the higher level of understanding that academic texts often provide. Overall, this book delivers on its intentions and provides interesting insights to some of the complex, highly sophisticated algorithms that lie behind some of our most widely used technological resources. This book gives the general public a sense of the world of computer science, without them having to enroll in an undergraduate computer science course.

10.1126/science.1255950

The reviewer is at the School of Chemistry, University of St. Andrews, North Haugh, St. Andrews, Fife KY16 9ST, UK. E-mail: res3@st-andrews.ac.uk

ECOLOGY AND CLIMATE

Desert wisdom and agriculture

By **Kay Watt**

A miller's daughter spun gold thread from hay. Stone soup fed an entire town. A farmer grew tons of juicy melons in one of the harshest desert climates in the Americas. In each story, something is created from nothing.

Of the three, only the story of the Chihuahuan melon farmer is neither fairy tale nor parable. Centuries-old technology known as olla irrigation breathes life into acres of melon vines, enabling them to thrive in an otherwise inhospitable environment. The paltry 9 inches of annual rainfall is harnessed to support a robust agricultural business. Judicious water use and resource conservation are the main tenets of desert farming worldwide, transforming arid scrubland and desert margins into flourishing and resilient farmsteads.

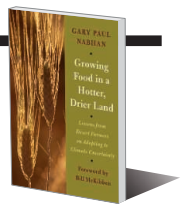

Growing Food in a Hotter, Drier Land
Lessons from Desert Farmers on Adapting to Climate Uncertainty
Gary Paul Nabhan
Chelsea Green Publishing, 2013. 268 pp.


Olla irrigation.

Gary Nabhan is a conservation scientist, ecologist, and farmer; he is intimately familiar with the challenges faced by traditional desert agricultural communities. He visits with farmers in Saharan oases and the margins of the Gobi Desert, as well as other desert regions, learning the techniques and adaptations that have sustained life in extreme environments for thousands of years. A full third of the land on our planet is desert or semi-desert, receiving on average less than 20 inches of rainfall per year (*1*). Over the tens of thousands of years of human migration and agricultural evolution, societies have found elegant and simple solutions to living in water-compromised environments.

These solutions are increasingly relevant as countries experience progressively hotter average temperatures and face dwindling water resources. Dramatic changes are already being witnessed by ecologists and experienced by farmers. Pests such as bark beetles have been able to spread without a cold-weather check, damaging and killing thousands of trees in U.S. and European forests. Severe drought conditions in the United States this year have left 385,000 acres of farmland fallow in California alone (*2*). Desert vegetation has adapted to its environment over millennia. Each native species contains a wealth of evolutionarily derived resiliencies in form and function. Scientists and traditional farmers have drawn on these botanical success stories to shape physical farmland, advance water harvesting, and create hardy agricultural ecosystems. Biomimicry of living desert systems in particular has been a noted success, especially the use of nurse trees to create microenvironments in which crops can blossom.

Each chapter contains a Planning and Practice section with practical step-by-step advice on how to create desert-adapted and ecoconscious garden and agricultural landscapes. Lessons range from reducing summer heat loads on houses to creating effective rain irrigation, inspired by traditional farming on the floodplains of the Sonoran Desert. These solutions are both ingenious and effective, drawing on our global heritage to solve today's problems as well as prepare for those of the future.

By learning from agricultural desert experiences, farmers, scientists, and ecologically conscious citizens will be prepared for the challenges created by future climate change.

The reviewer is at the Department of Plant Sciences, University of California, Davis, CA 95616, USA. E-mail: kaywatt@ucdavis.edu

REFERENCES AND NOTES

1. www.idrc.ca/EN/Documents/CARIAA_COP18_Policy_Semi-arid.pdf.
2. www.reuters.com/article/2014/02/05/us-usa-drought-california-idUSBREA141VS20140205.

10.1126/science.1256005

PHOTO: NMSU AGRICULTURAL COMMUNICATIONS/PHOTO BY J. VICTOR ESPINOZA

LETTERS

Edited by **Jennifer Sills**

Fauna in decline: Meek shall inherit

ALTHOUGH LARGE ANIMALS capture our attention and directly or indirectly play essential ecological and ecosystem functions (*1*), it is the sheer diversity and abundance of invertebrates that make them "run the world" (*2*). A recent Review presented evidence of human-induced pervasive defaunation in terrestrial ecosystems ("Defaunation in the Anthropocene," R. Dirzo *et al.*, special section on Vanishing Fauna, 25 July, p. 401). Given that larger animals are more likely to go extinct [Dirzo *et al.* and (*3*)], invertebrates may soon play even more important roles in the dynamics of ecosystems than they already do (*1, 4*).

Many of the vertebrate species that have been locally extirpated or are in decline are herbivores, seed dispersers, or granivores

[Dirzo *et al.* and (*1, 3*)]. Therefore, as the Anthropocene progresses, invertebrates—and notably ants—will be the prospective heirs of these plant-animal interactions.

Although human disturbances affect ants, the effect is frequently much less pronounced than on vertebrates or on other insects such as Lepidoptera and bees (*3, 5*). Ants are remarkably abundant across most terrestrial ecosystems, interacting with many other species of insects, plants, and vertebrates. There is increasing evidence that ants benefit fleshy-fruited plants adapted for vertebrate seed-dispersal; indeed, they can be quantitatively as important as birds as seed removers (*6*). The dominant herbivore in the Neotropics—leaf-cutter ants (*Atta spp.*)—actually increases in abundance after ecosystem disturbance, which could profoundly alter plant regeneration and ecosystem processes (*7*). As invasive ant species continue to change the composition of local biota across the globe, there could be further cascading effects on plant and animal communities (*8*). With continued Anthropocene extinctions, it will become increasingly critical to elucidate the myriad ways through which this dominant group of invertebrates influences ecosystem functions across continents and biomes.

Alexander V. Christianini,[1]* Paulo S. Oliveira,[2] Emilio M. Bruna,[3,4] Heraldo L. Vasconcelos[5]

[1]Departamento de Ciências Ambientais, Universidade Federal de São Carlos, Sorocaba SP, 18052-780, Brazil. [2]Departmento de Biologia Animal, Universidade Estadual de Campinas, CP 6109, Campinas SP, 13083-970, Brazil. [3]Department of Wildlife Ecology and Conservation, University of Florida, Gainesville, FL 32611-0430, USA. [4]Center for Latin American Studies, University of Florida, Gainesville, FL 32611-5530, USA. [5]Instituto de Biologia, Universidade Federal de Uberlândia, Uberlândia MG, 38400-902, Brazil.

*Corresponding author. E-mail: avchrist@ufscar.br

REFERENCES

1. J. A. Estes *et al.*, *Science* **333**, 301 (2011).
2. E. O. Wilson, *Conserv. Biol.* **1**, 344 (1987).
3. IUCN, The IUCN Red List of Threatened Species (2014); www.iucnredlist.org.
4. F. Keesing, T. P. Young, *Bioscience* **64**, 487 (2014).
5. S. G. Potts *et al.*, *Trends Ecol. Evol.* **25**, 345 (2010).
6. A. V. Christianini, P. S. Oliveira, *J. Ecol.* **98**, 573 (2010).
7. I. R. Leal, R. Wirth, M. Tabarelli, *Biotropica* 10.1111/btp.12126 (2014).
8. C. E. Christian, *Nature* **413**, 65 (2000).

Fauna in decline: Extinct pigeon's tale

E. STOKSTAD'S NEWS article about the ecological consequences of elimination of megafauna resulting from overhunting ("The empty forest," special section on Vanishing Fauna, 25 July, p. 397) is especially poignant, given that 2014 marks 100 years since the extinction of the passenger pigeon (*Ectopistes migratorius*), once the most abundant bird of eastern North American forests. In the 19th century, new railroads across the eastern United States expanded the market for wild meat, just as new roads through the tropical forests are affecting hunting in Borneo and elsewhere in the developing world today. The passenger pigeon was unable to withstand the onslaught of unregulated commercial hunting, and the story is being repeated in the forests of Borneo and elsewhere.

The passenger pigeon population crashed from billions in the mid–19th century, to extinction of the wild population in less than half a century, to extinction with the loss of the last captive bird in 1914. Stokstad describes alarmingly similar trajectories for hunted mammals and birds of Borneo, even in an area that is nominally protected as a national park.

There were a number of ecological consequences of the extinction of the passenger pigeon. The pigeons damaged forest canopies and deposited nutrient-rich excrement, which may have been important for the maintenance of now-rare canebrakes in the southeastern United States (*1*). Because of their dietary preferences, their extinction changed the balance

between white oaks and red oaks (*2*). The extinction of the passenger pigeon may even have led to an increase in the incidence of Lyme disease (*3, 4*). The pigeons were effective seed predators. In years with a bumper crop of acorns and beechnuts, the pigeons ate so much that competitors for the food, such as white-footed mice (*Peromyscus*), could not eat enough to increase in number. Now, in the pigeons' absence, the mice increase during these years (*5*). Because mice are the reservoir for the tick-transmitted Lyme disease bacterium (*Borrelia*), when they increase in number, the *Borrelia* do as well, and increased cases of Lyme disease result (*6*). These impacts are still being felt a century after the last passenger pigeon died.

David E. Blockstein[1]* and Stanley A. Temple[2,3]

[1]National Council for Science and the Environment, Washington, DC 20036, USA. [2]Department of Forest and Wildlife Ecology, University of Wisconsin-Madison, Madison, WI 53706, USA. [3]Aldo Leopold Foundation, Baraboo, WI 53913, USA.

*Corresponding author. E-mail: david@NCSEonline.org

REFERENCES

1. R. Noss, *Forgotten Grasslands of the South* (Island Press, Washington, DC, 2012).
2. A. W. Schorger, *The Passenger Pigeon: Its Natural History and Extinction* (Univ. of Wisconsin Press, Madison, WI, 1955).
3. D. E. Blockstein, *Science* **279**, 1831 (1998).
4. D. E. Blockstein, *Birding* **33**, 302 (2001).
5. R. Ostfeld, *Lyme Disease: The Ecology of a Complex System* (Oxford Univ. Press, New York, 2011).
6. J. Bunikis *et al.*, *J. Infect. Dis.* **189**, 1515 (2004).

IMAGES (LEFT TO RIGHT): ALEXANDER V. CHRISTIANINI/UNIVERSIDADE FEDERAL DE SÃO CARLOS; JOHN JAMES AUDUBON/WIKIMEDIA COMMONS

Carbon: No silver bullet

ON BEHALF OF the European Academies Science Advisory Council (EASAC)—established by the national science academies in Europe to advise EU policy-makers on the science underpinning key decisions—we would like to respond to S. M. Benson's Editorial, "Negative-emissions insurance" (27 June, p. 1431). EASAC has recently completed two studies on carbon capture and storage (CCS) (*1*) and on biofuels in Europe (*2*). The studies broadly support Benson's view that bioenergy with CCS might make a useful contribution to climate change mitigation in Europe, but their overall conclusion is that it is likely to be modest.

As Benson recognizes, CCS is expensive. Costs are likely to be higher for biomass CCS than for CCS associated with large fossil-fuel–based plants, as the biomass CCS will be smaller scale and often remote from CO_2 transport and storage facilities. The EASAC study concluded that there is rather limited scope to bring costs down.

Confidence in the long-term integrity of CO_2 storage will build slowly, given the need to monitor geological processes over long periods of time. This will slow the rate of the rollout of CCS in Europe. Furthermore, only limited indigenous biomass resources in Europe can sustainably be harvested for energy uses without deleterious impacts on the environment and food production.

The research, development, and demonstration of relevant technologies to promote biomass-based CCS should be actively pursued, but it is no silver bullet.

Jos W. M. van der Meer,[1] Herbert Huppert,[2] John Holmes[3]*

[1]President of EASAC; German National Academy of Sciences, Halle Saale, 06019, Germany. [2]Chair of the EASAC working group on CCS; Institute of Theoretical Physics, University of Cambridge, Cambridge, CB3 0WA, UK. [3]Secretary to the EASAC Energy Programme; Department of Earth Sciences, University of Oxford, Oxford, OX1 3AN UK.

*Corresponding author. E-mail: john.holmes@earth.ox.ac.uk

REFERENCES

1. Carbon capture and storage in Europe, EASAC Policy Report 20 (May 2013); www.easac.eu/fileadmin/Reports/Easac_13_CCS_Web_Complete.pdf.
2. The current status of biofuels in the European Union, their environmental impacts and future prospects, EASAC Policy Report 19 (December 2012); www.easac.eu/fileadmin/PDF_s/reports_statements/Easac_12_Biofuels_Complete.pdf.

TECHNICAL COMMENT ABSTRACTS

Comment on "Local impermeant anions establish the neuronal chloride concentration"

Juha Voipio, Walter F. Boron, Stephen W. Jones, Ulrich Hopfer, John A. Payne, Kai Kaila

■ Glykys *et al.* (Reports, 7 February 2014, p. 670) conclude that, rather than ion transporters, "local impermeant anions establish the neuronal chloride concentration" and thereby determine "the magnitude and direction of $GABA_A$R currents at individual synapses." If this were possible, perpetual ion-motion machines could be constructed. The authors' conclusions conflict with basic thermodynamic principles.

Full text at http://dx.doi.org/10.1126/science.1252978

Comment on "Local impermeant anions establish the neuronal chloride concentration"

Heiko J. Luhmann, Sergei Kirischuk, Werner Kilb

■ Glykys *et al.* (Reports, 7 February 2014, p. 670) proposed that cytoplasmic impermeant anions and polyanionic extracellular matrix glycoproteins establish the local neuronal intracellular chloride concentration, $[Cl^-]_i$, and thereby the polarity of γ-aminobutyric acid type A ($GABA_A$) receptor signaling. The experimental procedures and results in this study are insufficient to support these conclusions. Contradictory results previously published by these authors and other laboratories are not referred to.

Full text at http://dx.doi.org/10.1126/science.1255337

Response to Comments on "Local impermeant anions establish the neuronal chloride concentration"

J. Glykys, V. Dzhala, K. Egawa, T. Balena, Y. Saponjian, K. V. Kuchibhotla, B. J. Bacskai, K. T. Kahle, T. Zeuthen, K. J. Staley

■ We appreciate the interest in our paper and the opportunity to clarify theoretical and technical aspects describing the influence of Donnan equilibria on neuronal chloride ion (Cl^-) distributions.

Full text at http://dx.doi.org/10.1126/science.1253146

TECHNICAL RESPONSE

NEUROSCIENCE

Response to Comments on "Local impermeant anions establish the neuronal chloride concentration"

J. Glykys,[1] V. Dzhala,[1] K. Egawa,[1] T. Balena,[1] Y. Saponjian,[1] K. V. Kuchibhotla,[2] B. J. Bacskai,[1] K. T. Kahle,[3] T. Zeuthen,[4] K. J. Staley[1]*

We appreciate the interest in our paper and the opportunity to clarify theoretical and technical aspects describing the influence of Donnan equilibria on neuronal chloride ion (Cl^-) distributions.

We first address the concerns of Voipio *et al.* (*1*) about Donnan equilibria and then the concerns of Luhmann *et al.* (*2*) on technical aspects of our study (*3*). Regarding Donnan energetics, Voipio *et al.* state: "If Cl^- were initially in equilibrium across a membrane, then the mere introduction of immobile negative charges (a passive element) at one side of the membrane would, according to their line of thinking, cause a permanent change in the local electrochemical potential of Cl^-, thereby leading to a persistent driving force for Cl^- fluxes…". The first section of the quote is a concise description of Donnan effects on the Cl^- distribution, and the resultant electrochemical potential is the Donnan potential (*4*). The last part of the quote—"thereby leading to a persistent driving force for Cl^- fluxes"—is the point of confusion.

The Donnan potential is the membrane voltage at which the system is at equilibrium— i.e., at which there is no free energy available to do work such as moving Cl^- across the membrane. The free energy to drive membrane Cl^- currents is supplied by the process that shifts the membrane potential away from the Donnan potential and thereby shifts the system away from equilibrium. The driving force for electrogenic Cl^- flux across the membrane depends on the difference between the shifted membrane potential and the Donnan potential, not the Donnan potential itself. Without the addition of energy to the system to shift the membrane potential, there will be no net ion flux across the membrane in a system at equilibrium.

Regarding the distribution of impermeant charges, Voipio *et al.* express two concerns. First, they cite charge screening studies to support their argument that impermeant anion distributions do not alter either the bulk $[Cl^-]$ or the free energy of Cl^- flux across the membrane. For sufficiently thin anion layers, we agree. Charge screening studies concern the effects of the charged polar heads of phospholipids comprising lipid bilayers. These are not the distributions that we describe.

Intracellularly, most intracellular anions cannot permeate γ-aminobutyric acid type A ($GABA_A$) receptor–operated channels, and these impermeant anions are not confined to a thin layer along the membrane. Nevertheless, Voipio *et al.* are concerned that "[a] consequence of the logic of Glykys *et al.* is that local charges could even reverse 'the polarity of local $GABA_AR$ signaling.'" Since the classic studies of Coombs, Eccles, and Fatt (*5*), it has been routine to manipulate the Cl^- equilibrium potential in intracellular recordings by replacing various amounts of Cl^- in the recording electrode solution with less permeant anions. Thus, it is widely accepted that (exogenous) intracellular impermeant local charges can displace $[Cl^-]_i$ and thereby change the polarity of $GABA_AR$ signaling.

Extracellularly, bulk cerebrospinal fluid has a high $[Cl^-]$ and few impermeant charges. However, neurons are not apples bobbing in a sea of cerebrospinal fluid. Rather, they are embedded in a gelatinous extracellular matrix composed of polyanionic biopolymers that are sufficiently dense to impart the matrix with a tortuosity that far exceeds that of cerebrospinal fluid (*6*). Although the exceptionally high charge density of these anionic biopolymers is well established (*7*), the actual spatial distribution of fixed anionic charges in the brain's extracellular matrix has only rarely been considered (*8*) and merits more study.

Voipio *et al.* express a second concern regarding the distribution of intracellular impermeant anions: "…a gradient in cytosolic impermeant charge density would create opposing $[Cl^-]$ and electrical potential gradients within the cell. However, under these conditions, the electrochemical potential of Cl^- would be uniform within the cell." This was our point also. If the electrochemical potential for $[Cl^-]_i$ is uniform within the neuron, then oppositely directed Cl^- cotransport is not required to maintain differences in subcellular $[Cl^-]_i$ (*9*). Although the electrochemical potential of Cl^- would be uniform within the cell, the electrochemical potential of Cl^- across the cell membrane would not be uniform at subcellular locations containing differing concentrations of impermeant anions, as has been repeatedly observed (*10*, *11*).

Luhmann *et al.* raise several technical questions for which we provide the following clarifications. Regarding the sensitivity of Clomeleon, with a dissociation constant (K_d) of ~100 mM, the change in the fluorescence ratio is 1% Δ ratio per 1- to 2-mM change in Cl_i for Cl_i between 1 and 20 mM [figure 3C in (*12*); figure 3C in (*11*); and supplemental figure 7B in (*13*)]. This sensitivity is sufficient to test our hypotheses. $[Cl^-]_i$ and volume stability experiments can be found in figure S4 in (*3*).

Regarding the variance in $[Cl^-]_i$, including immature preparations: A key finding driving the current study is the substantial variance in neuronal $[Cl^-]_i$, which has also been reported by other groups using Clomeleon (*11*, *14*), as well as perforated patch (*15*) and dual cell–attached recordings (*16*). Intraneuronal $[Cl^-]_i$ is also variable (*10*, *11*). Rather than being an experimental deficiency, we propose that the variability of $[Cl^-]_i$ is a fundamental feature of the brain's composition.

Regarding the effects of NKCC1 inhibition, our data are consistent with the cited studies. Data in figure 3, H and I, in (*3*) are from two different populations of neurons and are well within the range of values shown in figure 1, B and C, in (*3*). NKCC1 inhibition reduces $[Cl^-]_i$ in neurons with high initial $[Cl^-]_i$ and increases $[Cl^-]_i$ in neurons with low initial $[Cl^-]_i$ [figures S1B, S2B, and S3 in (*3*)] (*17*, *18*). Fluorometric techniques sample dozens to hundreds of neurons. Electrophysiological studies, including our earlier studies, report a handful of recorded cells selected based on the experimenter's preferences for cell turgor. In light of our findings regarding the relation between neuronal volume and $[Cl^-]_i$, such selection could readily bias small samples of neurons.

Regarding knockout studies of transporters, as stated in the concluding sentence of the summary of our study, cation-chloride transporters are critically important for restoring $[Cl^-]_i$ and volume after signaling transients. The sequelae of chronic cation-chloride cotransport inhibition [e.g., (*19*)] do not invalidate our hypotheses.

Regarding Na/K/ATPase (adenosine triphosphatase), the suggested experiment was not included because we had previously reported that perforated patch measurement of $[Cl^-]_i$ during Na/K/ATPase inhibition showed only very modest changes in $[Cl^-]_i$ that were well within the range we would predict (*20*).

Regarding the permeability of gluconate, this anion permeates a variety of Cl^- channels with permeabilities ranging from 10 to 40% of Cl^- (*21*–*23*), which is ample for the experiment we performed. The interesting hypotheses put

[1]Department of Neurology, Massachusetts General Hospital, Harvard Medical School, Boston, MA, USA. [2]New York University School of Medicine, Skirball Institute for Biomolecular Medicine, New York, NY, USA. [3]Department of Neurosurgery, Massachusetts General Hospital, Harvard Medical School, Boston, MA, USA. [4]Department of Cellular and Molecular Medicine, University of Copenhagen, Denmark.
*Corresponding author: E-mail: staley.kevin@mgh.harvard.edu

forward as to why the experiment using weak organic acids might not work would only be valid if proton buffering were purely passive—i.e., only in the absence of proton pumps and exchangers. We and others, including Luhmann's group [e.g., (*24*)], have also altered the cytoplasmic concentration of relatively impermeant anions by introducing gluconate directly from the recording pipette solution. This approach of altering $[A]_i$ eliminates the dependence on membrane transport or permeation. Much larger reductions in $[Cl^-]_i$ can be demonstrated with this technique, and the data robustly support the idea that $[A]_i$ and $[Cl^-]_i$ are inversely related.

Regarding the seizure experiments, our confirmation of the predicted correlation between neuronal volume and $[Cl^-]_i$ changes during seizures has not been previously reported. As indicated in our publication, cation-chloride cotransporters are important elements in $[Cl^-]_i$ homeostasis, but, based on our experiments, what they do not do is determine the $[Cl^-]$ set point.

We accept that this is a complex topic to introduce in a short communication, and we appreciate the opportunity to provide clarifications based on the theoretical and technical questions raised here. These questions do not affect the validity of our conclusions. Cl^- homeostasis and GABA signaling are more complex than we initially envisioned. Our hypothesis and data have provided an explanation for the inter- and intraneuronal variance of $[Cl^-]_i$ observed in different preparations and experimental approaches and create broad opportunities for further research.

REFERENCES

1. J. Voipio *et al*., *Science* **345**, 1130 (2014).
2. H. J. Luhmann, S. Kirischuk, W. Kilb, *Science* **345**, 1130 (2014).
3. J. Glykys *et al*., *Science* **343**, 670–675 (2014).
4. F. G. Donnan, *J. Membr. Sci.* **100**, 45–55 (1995).
5. J. S. Coombs, J. C. Eccles, P. Fatt, *J. Physiol.* **130**, 326–374 (1955).
6. E. Syková, C. Nicholson, *Physiol. Rev.* **88**, 1277–1340 (2008).
7. N. S. Gandhi, R. L. Mancera, *Chem. Biol. Drug Des.* **72**, 455–482 (2008).
8. W. Härtig *et al*., *Brain Res.* **842**, 15–29 (1999).
9. S. Khirug *et al*., *J. Neurosci.* **28**, 4635–4639 (2008).
10. J. Szabadics *et al*., *Science* **311**, 233–235 (2006).
11. J. Duebel *et al*., *Neuron* **49**, 81–94 (2006).
12. T. Kuner, G. J. Augustine, *Neuron* **27**, 447–459 (2000).
13. J. Glykys *et al*., *Neuron* **63**, 657–672 (2009).
14. K. Berglund *et al*., *Brain Cell Biol.* **35**, 207–228 (2006).
15. S. Ebihara, K. Shirato, N. Harata, N. Akaike, *J. Physiol.* **484**, 77–86 (1995).
16. R. Tyzio *et al*., *Eur. J. Neurosci.* **27**, 2515–2528 (2008).
17. V. I. Dzhala *et al*., *J. Neurosci.* **30**, 11745–11761 (2010).
18. V. Dzhala, G. Valeeva, J. Glykys, R. Khazipov, K. Staley, *J. Neurosci.* **32**, 4017–4031 (2012).
19. D. D. Wang, A. R. Kriegstein, *Cereb. Cortex* **21**, 574–587 (2011).
20. A. C. Brumback, K. J. Staley, *J. Neurosci.* **28**, 1301–1312 (2008).
21. K. Fatima-Shad, P. H. Barry, *Proc. Biol. Sci.* **253**, 69–75 (1993).
22. R. Enz, B. J. Ross, G. R. Cutting, *J. Neurosci.* **19**, 9841–9847 (1999).
23. T. A. Gilbertson, *Chem. Senses* **27**, 383–394 (2002).
24. S. N. Kolbaev, K. Achilles, H. J. Luhmann, W. Kilb, *J. Neurophysiol.* **106**, 2034–2044 (2011).

25 March 2014; accepted 31 July 2014
10.1126/science.1253146

TECHNICAL COMMENT

NEUROSCIENCE

Comment on "Local impermeant anions establish the neuronal chloride concentration"

Heiko J. Luhmann,* Sergei Kirischuk, Werner Kilb

Glykys *et al*. (Reports, 7 February 2014, p. 670) proposed that cytoplasmic impermeant anions and polyanionic extracellular matrix glycoproteins establish the local neuronal intracellular chloride concentration, $[Cl^-]_i$, and thereby the polarity of γ-aminobutyric acid type A ($GABA_A$) receptor signaling. The experimental procedures and results in this study are insufficient to support these conclusions. Contradictory results previously published by these authors and other laboratories are not referred to.

Glykys *et al*. (*1*) performed experiments with the Cl^- indicator Clomeleon, which has a K_d of ~90 mM (*2*, *3*). Therefore, most of the data points (the ones with low $[Cl^-]_i$) were obtained in a range, in which it is difficult to reliably calculate $[Cl^-]_i$ from the yellow fluorescent protein/cyan fluorescent protein (YFP/CFP) ratio. The low Cl^- sensitivity of Clomeleon at low $[Cl^-]_i$ and the potential temporal instability of fluorescent signals (CFP, YFP, background, and the like) require thorough control measurements, which are not provided in this publication. Moreover, despite the broad distributions of $[Cl^-]_i$ in the present study (from almost 0 mM to >50 mM), in many cases the distributions presented for individual experiments are much narrower [figures 3, B and I, and S6B in (*1*)].

The authors report nearly identical $[Cl^-]_i$ values for immature and adult hippocampal neurons, which is in contradiction to numerous previous reports using electrophysiological measurements of γ-aminobutyric acid (GABA) reversal potentials [e.g., (*4*, *5*)] or fluorimetric $[Cl^-]_i$ measurements with Clomeleon [e.g., (*2*, *3*)]. The authors also report that inhibition of the cation-Cl^- transporter NKCC1 with bumetanide does not significantly influence $[Cl^-]_i$, which is in disagreement with previous studies in comparable age groups demonstrating that inhibition of NKCC1 reduces $[Cl^-]_i$ [e.g., (*3*, *6*)] and attenuates the depolarizing effect of GABA (*7*–*10*). Even in the current study, bumetanide caused a substantial reduction in basal $[Cl^-]_i$ (from 16.6 ± 14.6 to 7.1 ± 10 mM) [figure 3, H and I, in (*1*)], but this effect is not discussed appropriately. Furthermore, a variety of studies demonstrated that overexpression, knockdown, or knockout of the Cl^- transporters KCC2 and NKCC1 affects $[Cl^-]_i$ homeostasis [e.g., (*11*–*13*)]. We postulate that the discrepancies between the data obtained in this present study and previously published results must be discussed in this paper.

We also wonder why the ouabain effect on the cellular volume was determined with the Na^+-sensitive dye sodium-binding benzofuran isophthalate (SBFI) and not by Clomeleon fluorescence, although the latter was used by the authors to measure volume changes induced by hyperosmotic solution and epileptiform activity [figures 3, F and G, and 4 in (*1*)], as well as in previous papers by these authors (*3*, *14*). Measurements of $[Cl^-]_i$ during ouabain application would be an ideal test for the main hypothesis of the authors. In addition, to verify "that extracellular Na^+ does not exert a significant Donnan effect," it must be demonstrated that ouabain affects the intracellular Na^+ concentration, which is not shown in the manuscript. Finally, blocking Na^+/K^+ adenosine triphosphatase (ATPase) massively interferes with the driving forces for many secondary active transporters, which is not adequately discussed in the current Report.

To test prediction 2, the authors use weak organic acids to increase the intracellular concentration of anions. However, D-lactate and pyruvate permeate the membrane in the uncharged form and dissociate inside the cell, with the vast majority of the protons being buffered intracellularly (*15*). The resulting decrease in the concentration of intracellular buffer anions will thus roughly balance the additional amount of organic anions introduced by the weak acids, leaving the total intracellular charges mostly unchanged. In contrast, and unlike what was stated by Glykys *et al*., gluconate is a membrane-impermeable weak acid. Thus, the observation that this weak acid induces the same effect as the membrane-permeable weak acids D-lactate and pyruvate further disproves that this effect can be attributed to an accumulation of intracellular anionic charges.

The $[Cl^-]_i$ increase induced by epileptiform activity in organotypic slice cultures [figure 4 in (*1*)] has already previously been reported by the authors and has been linked to seizure-induced elevations of $[K^+]_e$, shifting the driving force on NKCC1 (*14*). Thus, this finding is not new and nicely supports the conventional hypothesis of $[Cl^-]_i$ homeostasis.

In our opinion, the experiments shown by Glykys *et al*. (*1*) do not provide convincing data to support the hypothesis that fixed anionic charges establish the transmembrane Cl^- distribution. Astonishingly, Glykys *et al*. fully ignore the majority of previous observations on the role of KCC2 and NKCC1 in neuronal Cl^- regulation (including their own previous papers), which are in contradiction with their current hypothesis. Therefore, we are afraid that the authors' major hypothesis is in disagreement with the newly provided experimental evidence, as well as with previously published data.

Institute of Physiology, University Medical Center, University of Mainz, Duesbergweg 6, D-55128 Mainz, Germany.
*Corresponding author: E-mail: luhmann@uni-mainz.de

REFERENCES

1. J. Glykys *et al*., *Science* **343**, 670–675 (2014).
2. T. Kuner, G. J. Augustine, *Neuron* **27**, 447–459 (2000).
3. V. Dzhala, G. Valeeva, J. Glykys, R. Khazipov, K. Staley, *J. Neurosci.* **32**, 4017–4031 (2012).
4. Y. Ben-Ari, E. Cherubini, R. Corradetti, J.-L. Gaiarsa, *J. Physiol.* **416**, 303–325 (1989).
5. H. J. Luhmann, D. A. Prince, *J. Neurophysiol.* **65**, 247–263 (1991).
6. K. Achilles *et al*., *J. Neurosci.* **27**, 8616–8627 (2007).
7. J. Yamada *et al*., *J. Physiol.* **557**, 829–841 (2004).
8. V. I. Dzhala *et al*., *Nat. Med.* **11**, 1205–1213 (2005).
9. A. C. Brumback, K. J. Staley, *J. Neurosci.* **28**, 1301–1312 (2008).
10. M. Minlebaev, G. Valeeva, V. Tcheremiskine, G. Coustillier, R. Khazipov, *Front. Cell. Neurosci.* **7**, 1–10 (2013).
11. C. Rivera *et al*., *Nature* **397**, 251–255 (1999).
12. C. A. Hübner *et al*., *Neuron* **30**, 515–524 (2001).
13. I. Chudotvorova *et al*., *J. Physiol.* **566**, 671–679 (2005).
14. V. I. Dzhala *et al*., *J. Neurosci.* **30**, 11745–11761 (2010).
15. M. S. Szatkowski, R. C. Thomas, *J. Physiol.* **409**, 89–101 (1989).

28 April 2014; accepted 21 July 2014
10.1126/science.1255337

TECHNICAL COMMENT

NEUROSCIENCE

Comment on "Local impermeant anions establish the neuronal chloride concentration"

Juha Voipio,[1]* Walter F. Boron,[2] Stephen W. Jones,[2] Ulrich Hopfer,[2] John A. Payne,[3] Kai Kaila[1,4]

Glykys *et al*. (Reports, 7 February 2014, p. 670) conclude that, rather than ion transporters, "local impermeant anions establish the neuronal chloride concentration" and thereby determine "the magnitude and direction of $GABA_AR$ currents at individual synapses." If this were possible, perpetual ion-motion machines could be constructed. The authors' conclusions conflict with basic thermodynamic principles.

The magnitude and polarity of chloride (Cl^-) currents mediated by γ-aminobutyric acid type A receptor ($GABA_AR$) channels depend on the transmembrane Cl^- electrochemical gradient. It is generally thought that cation-chloride cotransporters (CCCs) (*1*)—and, to a lesser extent, bicarbonate-coupled chloride transporters (*2*, *3*)—are the primary mechanisms that generate and maintain nonequilibrium transmembrane distributions of Cl^- and thereby generate the driving force for Cl^- currents.

In their recent Report, Glykys *et al*. (*4*) conclude that immobile negative charges near the extracellular surface of the cell membrane and impermeant negative charges in the cytosol play a central role in generating the driving force for Cl^- currents through $GABA_ARs$. Notably, however, any hypothetical mechanism based on immobile or impermeant charges that, without consuming energy, would maintain a driving force for channel-mediated Cl^- currents or for transporter-mediated Cl^- fluxes would conflict with basic thermodynamics.

The driving force of a channel-mediated Cl^- flux depends on the difference in electrochemical potential (free energy) of Cl^- ions between the intracellular and extracellular solutions. If immobile negative charges are present near the membrane, they cause a negative shift in local electrical potential that repels Cl^- ions (*5*–*7*). Although the resulting fall in local Cl^- concentration (or, more precisely, in local Cl^- activity) decreases the chemical component of the electrochemical potential of Cl^- ions, the change in local electrical potential has exactly the opposite effect on the electrical component (*5*–*7*). In more general terms, mobile ions such as Cl^- affected by electrostatic effects will move until they attain an equilibrium distribution. Consequently, the electrochemical potential gradient of Cl^- ions between the intracellular and extracellular solutions is not sensitive to local immobile charges. Consider the consequences if Glykys and co-workers were correct. If Cl^- were initially in equilibrium across a membrane, then the mere introduction of immobile negative charges (a passive element) at one side of the membrane would, according to their line of thinking, cause a permanent change in the local electrochemical potential of Cl^-, thereby leading to a persistent driving force for Cl^- fluxes with no input of energy.

A comparable argument, based on Donnan theory, can be made for impermeant negative charges distributed throughout the cytosol. A change in the concentration of impermeant cytosolic negative charge would—in the absence of further energy input—cause both a change in intracellular $[Cl^-]$ and an opposing change in membrane potential (V_m), so that the electrochemical potential for Cl^- is unchanged. Similarly, a gradient in cytosolic impermeant charge density would create opposing $[Cl^-]$ and electrical potential gradients within the cell. However, under these conditions, the electrochemical potential of Cl^- would be uniform within the cell. It is possible that a change in impermeant cytosolic negative charge could lead to a secondary change in V_m that would alter transmembrane driving forces of ion species. However, producing and maintaining such a shift in V_m would require the input of energy. Moreover, in the absence of active ion transport, a persistent change in V_m would lead to the dissipation of electrochemical gradients for ions across a membrane with a finite leak. Therefore, we focus next on Cl^- transporters.

The free energy of Cl^- transport mediated by CCCs and other secondary active Cl^- transporters depends on the product of the activities of the transported ion species on each side of the membrane (*8*). Immobile charges influence the local activities of these ion species, as well as the local electrical potential. The net effect is no change in the product of local ion activities (a_i). Taking as an example the K^+-Cl^- cotransporter 2 (KCC2), the product $a_K \cdot a_{Cl}$ remains constant, as can be readily shown using the free energy function electrochemical potential or the Boltzmann equation (*7*, *8*). Qualitatively, this lack of effect is a consequence of the attracting and repelling action of immobile charges on cations and anions. Therefore, transmembrane driving forces calculated for CCCs using bulk ion activities are not affected by immobile charges present in the vicinity of membranes, and these driving forces correctly predict the direction in which CCCs transport Cl^-, which is important in setting the transmembrane electrochemical gradient of Cl^- ions. The same considerations apply to mobile impermeant cytosolic charges, which have no effect on electrochemical potentials of cytosolic ions. If the above arguments were not true, perpetual ion-motion machines could be constructed along the lines outlined above for Cl^- channels.

In summary, a fundamental misconception in the paper by Glykys *et al*. is their central assumption that local immobile or impermeant charges could, by altering local Cl^- concentrations, affect the driving forces for channel-mediated Cl^- currents or transporter-mediated Cl^- fluxes and thereby (in their words) "determine the homeostatic set point for $[Cl^-]$" in neurons. However, by themselves, changes in the density of immobile or impermeant charges cannot cause maintained changes in the energy of any mobile ion species, including HCO_3^-, to which Glykys *et al*. ascribed special properties ("$[HCO_3^-]$ is fixed by pH requirements"). A consequence of the logic of Glykys *et al*. is that local charges could even reverse "the polarity of local $GABA_AR$ signaling." This is energetically impossible.

Given these theoretical objections to their interpretations, we choose not to comment here on the experimental results of Glykys *et al*.

[1]Department of Biosciences, University of Helsinki, Helsinki, Finland. [2]Department of Physiology and Biophysics, Case Western Reserve University School of Medicine, Cleveland, OH, USA. [3]Department of Physiology and Membrane Biology, School of Medicine, University of California, Davis, CA 95616, USA. [4]Neuroscience Center, University of Helsinki, Helsinki, Finland.
*Corresponding author. E-mail: juha.voipio@helsinki.fi

REFERENCES

1. P. Blaesse, M. S. Airaksinen, C. Rivera, K. Kaila, *Neuron* **61**, 820–838 (2009).
2. M. F. Romero, A. P. Chen, M. D. Parker, W. F. Boron, *Mol. Aspects Med.* **34**, 159–182 (2013).
3. M. D. Parker, W. F. Boron, *Physiol. Rev.* **93**, 803–959 (2013).
4. J. Glykys *et al*., *Science* **343**, 670–675 (2014).
5. S. G. McLaughlin, G. Szabo, G. Eisenman, *J. Gen. Physiol.* **58**, 667–687 (1971).
6. B. Hille, A. M. Woodhull, B. I. Shapiro, *Philos. Trans. R. Soc. London B Biol. Sci.* **270**, 301–318 (1975).
7. B. Hille, *Ion Channels of Excitable Membranes* (Sinauer, Sunderland, MA, ed. 3, 2001), pp. 340–342, 545–548, 649–656.
8. P. S. Aronson, W. F. Boron, E. L. Boulpaep, in *Medical Physiology. A Cellular and Molecular Approach, Updated 2nd Edition* (Elsevier, Philadelphia, 2012), pp. 106–146.

5 March 2014; accepted 28 July 2014
10.1126/science.1252978

RESEARCH

Marine microbes get creative amid scarcity
Yong et al., *p. 1170*

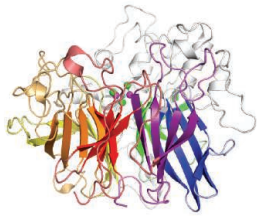

IN *SCIENCE* JOURNALS

Edited by **Melissa McCartney** *and* **Margaret Moerchen**

NANOMATERIALS

Tuning the twisting in helical nanowires

Assembly of inorganic nanoparticles into complex structures often requires a template. Researchers can now assemble helical nanowires out of cubic magnetite nanocrystals by tuning interactions that bind or separate them. Singh *et al.* floated the nanocrystals on a liquid and aligned them with a magnetic field. After the liquid evaporated, different twisted nanowires remained. The helices varied according to the concentration of nanocrystals, their shape, and the strength of the magnetic field. Competition between weak forces drives this self-assembly and can lead to arrays with the same twist direction. — PDS

Science, this issue p. 1149

METAL ALLOYS

A metal alloy that is stronger when cold

Metal alloys normally consist of one dominant element, with others in small amounts to improve specific properties. For example, stainless steel is primarily iron with nickel and chromium but may contain trace amounts of other elements. Gludovatz *et al.* explored the properties of a high-entropy alloy made from equal amounts of chromium, manganese, iron, cobalt, and nickel. Not only does this alloy show excellent strength, ductility, and toughness, but these properties improve at cryogenic temperatures where most alloys change from ductile to brittle. — MSL

Science, this issue p. 1153

DEVELOPMENT

Bringing up baby

Diet influences microbes in the intestine, and for the immune system to develop normally, microbes must colonize the gut. It remains unclear how profoundly diet shapes the primate immune system or how durable the influence is. Ardeshir *et al.* demonstrate that breast-fed and bottle-fed infant macaques develop dramatically different immune systems, which remain different for at least six months after they begin receiving identical diets. These findings may explain the variation in people's susceptibility to conditions involving the immune system, as well as the variation in how well the immune system protects people against certain infectious diseases. — OS

Sci. Transl. Med. **6**, 252ra121 (2014).

Feeding methods matter to macaques

NEURODEGENERATION

Dipeptide repeat peptides on the attack

Certain neurodegenerative diseases, including amyotrophic lateral sclerosis (ALS), are associated with expanded dipeptides translated from RNA transcripts of disease-associated genes (see the Perspective by West and Gitler). Kwon *et al.* show that the peptides encoded by the expanded repeats in the C9orf72 gene interfere with the way cells make RNA and kill cells. These effects may account for how this genetic form of ALS causes disease. Working in *Drosophila*, Mizielinska *et al.* aimed to distinguish between the effects of repeat-containing RNAs and the dipeptide repeat peptides that they encode. The findings provide evidence that dipeptide repeat proteins can cause toxicity directly. — SMH

Science, this issue p. 1139 and p. 1192; see also p. 1118

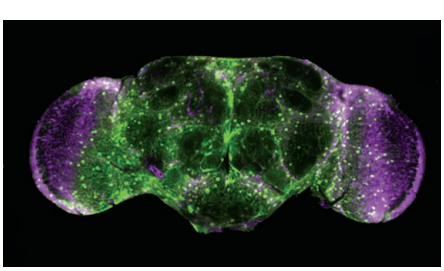

Studying neurodegeneration in *Drosophila*

PHYSIOLOGY

Connecting DNA damage to fibrosis

In the autoimmune disease systemic sclerosis (SSc), high collagen production by fibroblasts causes "scarring" of the skin and internal organs. During this process, called fibrosis, the Wnt signaling pathway is frequently activated. Svegliati *et al.* found that antibodies in the

serum from SSc patients stimulated a pathway that suppressed the expression of *WIF-1*, which encodes a Wnt inhibitor, and triggered collagen production in fibroblasts from normal individuals. Effects were similar when cells were treated with DNA-damaging agents. In fibroblasts from SSc patients, inhibiting this pathway caused the cells to express *WIF-1* and produce less collagen. In a mouse model of fibrosis, inhibiting this pathway prevented fibrotic skin thickening. – LKF

Sci. Signal. **7**, ra84 (2014).

PLANT GENOMICS

Coffee, tea, and chocolate converge

Caffeine has evolved multiple times among plant species, but no one knows whether these events involved similar genes. Denoeud *et al*. sequenced the *Coffea canephora* (coffee) genome and identified a conserved gene order (see the Perspective by Zamir). Although this species underwent fewer genome duplications than related species, the relevant caffeine genes experienced tandem duplications that expanded their numbers within this species. Scientists have seen similar but independent expansions in distantly related species of tea and cacao, suggesting that caffeine might have played an adaptive role in coffee evolution. — LMZ

Science, this issue p. 1181; see also p. 1124

PALEOCLIMATE

Old and older, cold and colder

Greenland surface air temperatures changed dramatically during the last deglaciation. The exact amount is unknown, which makes it difficult to understand what caused those changes. Buizert *et al.* report temperature reconstructions for the period from 19,000 to 10,000 years before the present from three different locations in Greenland and interpret them with a climate model (see the Perspective by Sime). They provide the broad geographic pattern of temperature variability and infer the mechanisms of the changes and their seasonality, which differ in important ways from the traditional view. — HJS

Science, this issue p. 1177; see also p. 1116

GENOME EDITING

Genome editing corrects a muscle disease

Patients with Duchenne muscular dystrophy find their muscles growing progressively weaker. Studies identified *dystrophin* as the culprit gene, which galvanized research into gene-targeted therapies. Long *et al*. apply genome editing to "correct" the disease-causing mutation in mice genetically destined to develop the disease. This germline editing strategy kept muscles from degenerating, even in mice harboring only a small percentage of corrected cells. Although not feasible for humans, this proof of concept sets the stage for applying genome editing to specific cell types involved in the disease. — PAK

Science, this issue p. 1184

THE RIBOSOME

Caught in the act of making protein

The ribosome is a large RNA-protein complex that converts the genetic code stored in messenger RNA (mRNA) into proteins. Zhou *et al*. have determined the structure of a bacterial ribosome caught in the act of decoding an mRNA. Transfer RNAs (tRNAs) decipher the genetic code in the mRNA to ensure that the ribosome uses the correct amino acids. The structure shows tRNAs in the process of being moved between successive protein-building binding pockets as the ribosome reads the mRNA like a piece of old-fashion computer tape. — GR

Science, this issue p. 1188

IN OTHER JOURNALS

Edited by **Kristen Mueller** *and* **Jesse Smith**

CELL BIOLOGY

A long noncoding RNA helps cells divide

When cells divide, they distribute chromosomes to the daughter cells. Centromeres—specialized regions of chromosomes—ensure that the chromosomes segregate properly during the process. Quénet and Dalal find that an RNA transcribed from human centromeric DNA recruits proteins that form this specialized region. Unlike many RNAs, the centromeric RNA does not encode a protein, but instead binds to two proteins, CENP-A and HJURP, that help "package" DNA and proteins together so that the centromere can function properly. — GR

eLife 10.7554/eLife.03254 (2014).

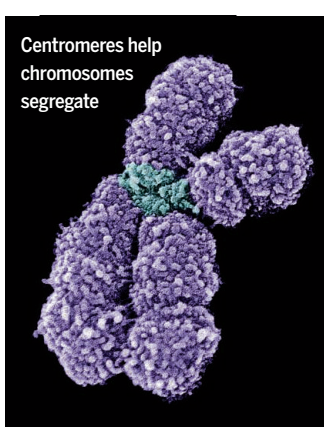

Centromeres help chromosomes segregate

SIGNAL TRANSDUCTION

A drug's two-part way to block dopamine

The dopamine receptor DR2 is a potential target for antipsychotic drugs. A new study reports an unusual mechanism of action for a small molecule that targets DR2. The core structure of the molecule, called SB26952, suggests it would bind to the same place as dopamine (the orthosteric site). Instead, however, it acts like an allosteric inhibitor—that is, an inhibitor that binds to a secondary (allosteric) site on DR2, preventing dopamine from binding to the orthosteric site. Campbell *et al*. now report that SB26952 binds to both the orthosteric and allosteric sites in one DR2 molecule, which is part of a pair. This inhibits dopamine binding to the orthosteric site of the second DR2 molecule. — VV

Nat. Chem. Biol. 10.1038/nchembio.1593 (2014).

CLIMATE CHANGE

Anthropogenic de-icing on a grand scale

The Greenland ice sheet has been losing mass at increasingly rapid rates over the past several decades, as expected due to climate warming, but it is

PHOTOS: (TOP TO BOTTOM) GETTY IMAGES/UNIVERSAL IMAGES GROUP; SPL/SCIENCE SOURCE

PLANT SCIENCE

Tolerating aluminum

Sorghum bicolor can tolerate hot and dry conditions, which makes it an important grain in West Africa. But low phosphorus and high aluminum concentrations in soil there impede its growth. Leiser *et al.* studied sorghum varieties in West Africa and discovered a region in the sorghum genome that allowed plants to tolerate both aluminum toxicity and low amounts of phosphorus. The authors hypothesized that aluminum toxicity activates a key gene that may have the felicitous side effect of helping the plant use phosphorus more efficiently. — PJH

BMC Plant Biol. **14**, 206 (2014).

Harvesting sorghum in West Africa

PHOTO: GABRIELA BARRETO LEMOS/AUSTRIAN ACADEMY OF SCIENCES

difficult to tell whether that loss is a result of human forcing. Fyke *et al.* examine how that can be done, using a coupled ice sheet/climate model. They find that anthropogenic warming should produce a bimodal pattern of melting between the interior and the coast and suggest that such a pattern is already emerging. They also suggest that a well-studied location, the Greenland Ice Sheet summit region, may be an ideal place to monitor the pace of climate change. — HJS

Geophys. Res. Lett. 10.1002/2014GL060735 (2014).

DRUG DELIVERY

Layers of ways to control drug release

When people overuse antibiotics, microbes can develop resistance. In a setting such as a hospital, where bacteria may accumulate on the surfaces of medical devices, it is important to be able to administer antibiotics on demand, without overusing them. Zhuk *et al.* show how films made from tannic acid and one of three antibiotics can decrease antibiotic use. They created a film that does not release any antibiotic at a pH of 7.4, but which does release it when it is exposed to *Staphylococcus epidermidis* or *Escherichia coli*, which acidify their local environments. The release depends on the antibiotic used, the film fabrication method, and the overall thickness of the film, providing multiple ways to control antibiotic delivery. — MSL

ACS Nano 10.1021/nn500674g (2014).

QUANTUM MECHANICS

Quantum imaging of Schrödinger's cat

These images of a cardboard cutout of a cat were made with light that never touched it. Barreto Lemos *et al*. began with two identical photons, one shining through the object and the other going by it, and made them overlap and interfere. Each photon is also created with a photon of shorter wavelength; they share a quantum connection called entanglement which allows the researchers to make the shorter-wavelength photons also interfere. The pair can then go one way or the other when they hit a beam splitter. Thus, by scanning the longer-wavelength photon pairs over the object, the team can construct two images—one for each direction out of a beam splitter—using the shorter-wavelength photons that never actually touched the object. The technique makes it possible to image an object using a color of light that would normally pass through it. — AC

Nature 10.1038/nature13586 (2014).

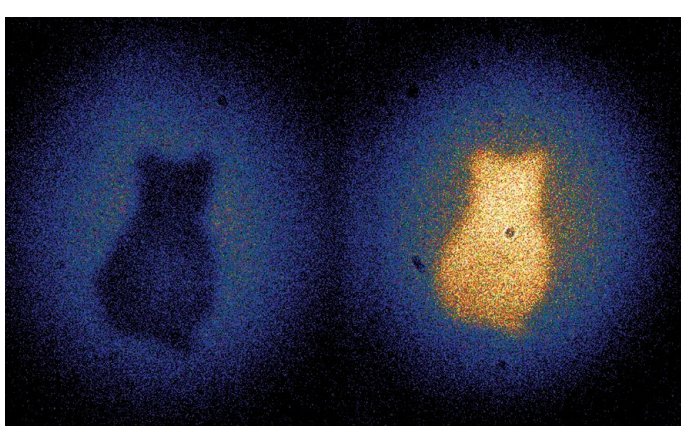

CO_2 REDUCTION

An edgy way to transform carbon dioxide

Plants are adept at turning CO_2 into organic material. Unfortunately, humans have outpaced them in the other direction, releasing substantially more CO_2 into the atmosphere than natural photosynthesis can concurrently consume. Although chemists are late entrants to the CO_2 conversion game, they're now redoubling their effort in the face of climate change. Asadi *et al.* present a cost-effective catalyst for electrochemical reduction of CO_2 to CO, an important feedstock for a wide range of commodity chemicals. The catalyst, molybdenum disulfide, is highly active at its edges and ultimately less expensive than the gold and silver previously investigated for this purpose. — JSY

Nat. Commun. 10.1038/ncomms5470 (2014).

HUMAN GENETICS

When genetic diversity hurts the kids

Although we think of the genome as fixed, errors in DNA replication and recombination can cause changes. As the organism develops, individual nucleotides may mutate, or genetic material may duplicate or be deleted. Such "somatic mosaicism" means that different cells and tissues in the body may have different genomes. To determine whether this affects human disease, Campbell *et al*. took blood samples from 100 families with children who have genetic disorders. They found that approximately 4% of the parents (who were all healthy) exhibited somatic mosaicism, which suggests that the affected children inherited the mutation from a mosaic parent. These results suggest that somatic mosaicism is probably more common than previously thought and affects human health. — LMZ

Am. J. of Hum. Genet. 10.1016/j.ajhg.2014.07.003 (2014).

ALSO IN *SCIENCE* JOURNALS

Edited by **Melissa McCartney** *and* **Margaret Moerchen**

SUPERNOVAE

Surprise found by γ-ray metal detector

Astronomers commonly use type-Ia supernovae as standard distance measurement tools, though the physics of these bright sources are not fully understood. One product of the thermonuclear explosion is ^{56}Ni, which probably lies at the heart of the supernova cloud. Diehl *et al.* detected the gamma-ray emission from ^{56}Ni in SN2014J much earlier than expected, only about 20 days after the initial explosion. This early exposure suggests both an asymmetric event and the production of ^{56}Ni farther out in the ejecta than predicted. These sources will help astronomers measure distances far beyond where supernovae have been studied. — MMM

Science, this issue p. 1162

EARTHQUAKE DYNAMICS

The earthquake that rocked northern Chile

Subduction zones often produce the largest earthquakes on Earth. A magnitude 8.2 earthquake (Iquique) occurred in one such zone off the coast of northern Chile on 1 April 2014, in a seismic gap that had not experienced a large earthquake since the 9.0 one in 1877. Ruiz *et al.* analyzed continuous GPS data to monitor the movement of plates over time in this region, including before and after major earthquakes. The most recent large quake was preceded by an extended series of smaller earthquakes and creeping westward movement of the coastline. — NW

Science, this issue p. 1165

SUPERCONDUCTIVITY

Optically manipulating superconductors

In superconductors, electrons of opposite momenta pair to form a highly correlated state that manages to flow without encountering any resistance. Matsunaga *et al.* manipulated the wavefunction of these pairs in the superconductor NbN with an electromagnetic pulse that they transmitted through a thin layer of the material (see the Perspective by Pashkin and Leitenstorfer). The superconducting gap, which is the energy needed to break the pairs apart, oscillated at twice the frequency

ILLUSTRION: ESO

Published by AAAS

of the pulse's electric field. When they matched this frequency to half the gap, the authors excited a collective mode in the superconductor called the Higgs mode, a relative of the Higgs boson in particle physics. — JS

Science, this issue p. 1145; see also p. 1121

METALLOPROTEINS

Cofactors linked to nutrient limitation

Microbes require inventive ways to acquire scarce nutrients from the environment. Enzymes that catalyze the acquisition of phosphorus from dissolved organic matter, for example, rely on complex metal cofactors in the active site. Yong *et al.* determined the crystal structure of the PhoX alkaline phosphatase from *Pseudomonas fluorescens* (see the Perspective by Moore). The metal centers arrange themselves in a triangular structure of two iron atoms and one calcium atom, bridged together by an oxide ion. The presence of iron, which itself is a trace nutrient in most environments, suggests that it limits phosphorus acquisition. – NW

Science, this issue p. 1170; see also p. 1120

CRYSTAL NUCLEATION

Watching nucleation pathways in calcite

The initial stage of crystallization, the formation of nuclei, is a critical process, but because of the length and time scales involved, is hard to observe. Nielsen *et al.* explored the crystallization of calcium carbonate, a well-studied material but one with multiple nucleation theories. Different calcium and carbonate solutions were mixed inside a fluid cell and imaged using a liquid cell inside a transmission electron microscope. Competing pathways operated during nucleation, with both the direct association of ions into nuclei from solution and the transformation of amorphous calcium carbonate into and between different crystalline polymorphs. — MSL

Science, this issue p. 1158

INNATE IMMUNITY

Bringing in the agent of your own destruction

Cells need mechanisms to detect and disable pathogens that infect them. Tam *et al.* now show that complement C3, a protein that binds to pathogens in the blood, can enter target cells together with the pathogen. Once inside the cell, the presence of C3 triggers both immune signaling and degradation of the internalized pathogen. The discovery of this pathway reveals that cells possess an early warning system of invasion that works against a diverse array of pathogens and does not require recognition of any specific pathogen molecules. — SMH

Science, this issue p. 1134

DYNAMIC ORDERING

Liquid crystals on a deformable substrate

The orientation of the molecules in a liquid crystalline material will change in response to either changes in the substrate or an external field. This is the basis for liquid crystalline devices. Vesicles, which are fluid pockets surrounded by lipid bilayers, will change size or shape in response to solvent conditions or pressure. Keber *et al.* report on the rich interactions between nematic liquid crystals placed on the surface of a vesicle. Changes to the vesicle size, for example, can "tune" the liquid crystal molecules. But conversely, the shape of the vesicles can also change in response to the activity of the nematic molecules. — MSL

Science, this issue p. 1135

MARINE MICROBES

Protein markers of cyanobacterial stress

Nutrients including iron, nitrogen, and phosphorus limit primary productivity in the oceans. Determining how abundant cyanobacteria such as *Prochlorococcus* adapt to nutrient stress across marine settings requires accurate molecular assays. Saito *et al.* developed a proteomic and metaproteomic approach capable of targeting specific metabolic biomarkers from mixed communities in seawater (see the Perspective by Moore). *Prochlorococcus* proteins are indicative of a major limiting nutrient across a wide transect in the Pacific Ocean; however, they also show that the limitation of multiple nutrients at overlapping biomes is an additional source of stress. — NW

Science, this issue p. 1173; see also p. 1120

RESEARCH ARTICLE SUMMARY

INNATE IMMUNITY

Intracellular sensing of complement C3 activates cell autonomous immunity

Jerry C. H. Tam, Susanna R. Bidgood, William A. McEwan, Leo C. James*

INTRODUCTION: Intracellular pathogens, which include viruses and some bacteria, typically disseminate through extracellular fluids before entering their target cells and beginning replication. While in the extracellular environment, pathogens can be intercepted by humoral immunity or by professional immune cells. However, immune surveillance is not always sufficient to prevent infection, and all cells need innate mechanisms to detect and disable pathogens.

RATIONALE: We hypothesized that one method of pathogen detection may be to take advantage of the pathogen's transition between extracellular and intracellular environments. Complement is a system of immune serum proteins with the ability to attach covalently to pathogens. We investigated whether this irreversible tagging of pathogens results in complement component C3 being carried into the cytosol during infection. Given that C3 should not otherwise be present inside the cell, we tested whether this could act as an invasion signal.

RESULTS: Antibodies and complement components C3 and C4, but not other serum proteins, were found to associate with adenovirus. During adenoviral infection, deposited C3 was carried into cells, resulting in potent nuclear factor–κB (NF-κB) activation. Activation of NF-κB by C3 required viral entry into the cytosol, and no activity was observed when C3-coated adenovirus was trapped in endosomes. In addition to NF-κB, C3 also activated the activating protein 1 (AP-1) and interferon regulatory factor 3 (IRF3)/IRF5/IRF7 transcription pathways. Induction of these signaling pathways resulted in robust cytokine secretion, including interferon-β. Cytosolic C3 sensing was dependent on a number of signaling hubs known to be involved in innate immunity. In addition to activating immune signaling, C3 targeted cytosolic adenovirus for rapid degradation via the AAA–adenosine triphosphatase (ATPase) valosin-containing protein (VCP) and the proteasome. This degradation pathway potently restricted viral infection.

C3-dependent intracellular sensing was widely conserved in mammals. Moreover, C3 activated NF-κB upon infection of diverse cell lines and primary cells including human lung cells, a physiologically relevant adenovirus target. Intracellular C3 also activated NF-κB in response to infection by diverse nonenveloped viruses—including papillomavirus, astrovirus, calicivirus, rhinovirus, poliovirus, coxsackievirus, enterovirus, and the facultative cytosolic bacteria *Salmonella*—but not enveloped respiratory syncytial virus. Picornaviruses were much less susceptible to complement sensing as a result of antagonism by their 3C protease, which cleaved C3 and prevented NF-κB activation and proteasome-mediated restriction. However, treatment with the 3C antagonist rupintrovir prevented 3C cleavage and restored full complement sensing of rhinovirus and poliovirus.

ON OUR WEB SITE

Read the full article at http://dx.doi.org/10.1126/science.1256070

CONCLUSION: Complement mediates a potent intracellular immune response to nonenveloped viruses and cytosolic bacteria. The deposition and covalent attachment of C3 onto pathogens results in its translocation into cells during infection, in which it simultaneously induces an antiviral state and directs the degradation of viral particles. Intracellular complement immunity is highly effective against a range of pathogens, occurs in a variety of cell types, is independent of professional immune cells, and is highly conserved in mammals. ■

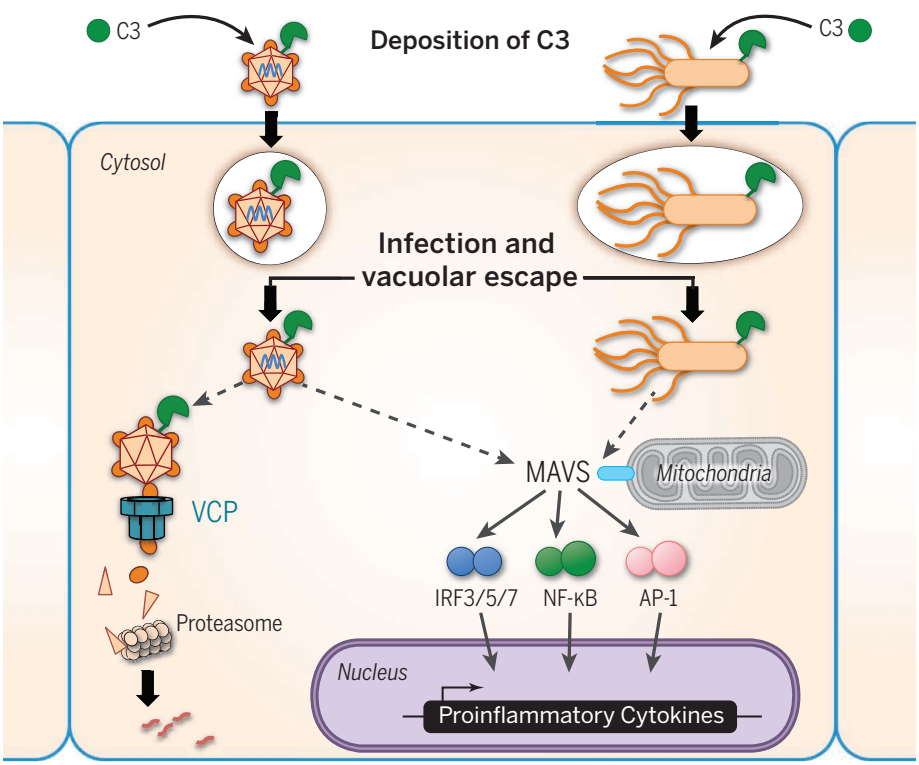

Intracellular complement C3 activates innate immunity. Complement component C3 covalently attaches to pathogens in the extracellular space. Upon pathogen entry into the cytosol, the cell senses attached C3. Sensing of C3 triggers a dual sensor and effector response, involving mitochondrial antiviral signaling (MAVS)–dependent immune signaling and proteasome-mediated viral degradation.

Medical Research Council Laboratory of Molecular Biology, Division of Protein and Nucleic Acid Chemistry, Francis Crick Avenue, Cambridge Biomedical Campus, Cambridge, CB2 0QH, UK.
*Corresponding author. E-mail: lcj@mrc-lmb.cam.ac.uk
Cite this article as: J. C. H. Tam *et al.*, *Science* 345, 1256070 (2014). DOI: 10.1126/science.1256070

RESEARCH ARTICLE

INNATE IMMUNITY

Intracellular sensing of complement C3 activates cell autonomous immunity

Jerry C. H. Tam, Susanna R. Bidgood, William A. McEwan, Leo C. James*

Pathogens traverse multiple barriers during infection, including cell membranes. We found that during this transition, pathogens carried covalently attached complement C3 into the cell, triggering immediate signaling and effector responses. Sensing of C3 in the cytosol activated mitochondrial antiviral signaling (MAVS)–dependent signaling cascades and induced proinflammatory cytokine secretion. C3 also flagged viruses for rapid proteasomal degradation, preventing their replication. This system could detect both viral and bacterial pathogens but was antagonized by enteroviruses, such as rhinovirus and poliovirus, which cleave C3 using their 3C protease. The antiviral rupintrivir inhibited 3C protease and prevented C3 cleavage, rendering enteroviruses susceptible to intracellular complement sensing. Thus, complement C3 allows cells to detect and disable pathogens that have invaded the cytosol.

Host colonization by intracellular pathogens typically involves the penetration of mucosal layers and dissemination through extracellular fluids. Humoral immunity has two major components—the heat-labile complement system and the heat-stable immunoglobulin system—and provides robust protection against invading pathogens. Such protection has been extensively studied, but insights into its function have recently emerged. Antibodies have been shown to be carried into cells by nonenveloped viruses during infection, where they act as danger-associated molecular patterns (DAMPs) to activate innate immunity (*1*, *2*) and inhibit viral replication both in vitro (*2*–*5*) and in vivo (*6*). We hypothesized that this phenomenon may not be specific to antibodies and that mislocalization of serum proteins as a result of pathogen movement from extracellular to intracellular compartments might be a strategy widely exploited by host immunity.

The complement system is composed of more than 30 proteins (*7*), with three activation methods—classical (antibody-directed), lectin (mannan-binding lectin or ficolin-directed), and alternative (spontaneous) pathways—leading to covalent deposition of C3 on the pathogen surface. Effector functions of complement stem from this deposition: C3 prevents receptor engagement, acts as an opsonin, and activates the terminal complement components to form a membrane attack complex, whereas cleaved components are anaphylatoxins. Most antiviral complement studies have used enveloped viruses (*8*). However, nonenveloped viruses and adenoviral gene therapy vectors are also susceptible to complement deposition (*9*), whereas some possess specific complement-evasion strategies (*10*, *11*). Owing to the lack of a lipid bilayer, the membrane attack complex cannot form on nonenveloped viruses, so aside from blocking receptor engagement, it is not clear how complement inhibits nonenveloped virus infection.

Medical Research Council Laboratory of Molecular Biology, Division of Protein and Nucleic Acid Chemistry, Francis Crick Avenue, Cambridge Biomedical Campus, Cambridge CB2 0QH, UK.
*Corresponding author. E-mail: lcj@mrc-lmb.cam.ac.uk

Results

Complement component C3 elicits NF-κB activation

Antibody in the cytosol has been shown to activate innate immune signaling cascades, establishing an antiviral state via receptor, TRIM21 (*1*, *2*). We tested whether other serum components are able to elicit similar responses by attaching to incoming pathogens. Infection of human embryonic kidney (HEK) 293T cells carrying a nuclear factor κB (NF-κB)–driven luciferase reporter, with an adenovirus type 5 vector (AdV), did not activate NF-κB (Fig. 1A). In contrast, incubation of AdV with normal human serum (Serum) led to robust NF-κB activation. Treatment of this serum by means of heat-inactivation at 56°C [heat-inactivated serum (HI Serum)] or addition of EGTA (Serum+EGTA) to chelate calcium each reduced NF-κB induction. Plasmin is a host serine protease that is pathogenically activated by *Staphylococci* to cleave protein components from their capsule for immune evasion (*12*). Serum was treated with plasmin for 30 min before quenching with α-2-antiplasmin (Serum+Plasmin) and then incubated with AdV (Fig. 1A). Plasmin treatment abolished NF-κB induction but did not alter AdV infection. We then determined the antibody component of signaling, with the use of antibody-depleted serum (Serum-Ig) and a heat-inactivated form (HI Serum-Ig). Incubation of AdV with either Serum-Ig or HI Serum-Ig confirmed that antibody is responsible for part of this NF-κB activation (*1*). However, a heat-labile component functioned independently of antibody (Fig. 1B). This signaling component within serum consisted of a heat-labile, calcium-dependent protein (Fig. 1, A and B) that appears to function alongside and independently of antibody, which is consistent with known properties of the complement system (*7*).

To categorize which serum components can attach to nonenveloped virus particles and thereby activate signaling, serum was incubated with AdV and spun through 30% sucrose to remove unbound proteins, with attached proteins detected by means of enzyme-linked immunosorbent assay (ELISA) (Fig. 1C). Antibodies of immunoglobulin M (IgM), IgA, and IgG isotypes bound to AdV, but IgD and IgE did not. Complement component C3 was strongly detected, showing that it deposited on AdV. C4 was also detected, indicating that classical activation had occurred. Mannan-binding lectin (MBL) and C-reactive protein (CRP) were not detected, suggesting that the lectin pathway was not required for complement deposition on AdV. Pentaxin 3 (PTX3) has antiviral activity against influenza (*13*) but was not detected bound to AdV (Fig. 1C). These data are supportive of complement activating NF-κB upon AdV infection. Infection experiments were carried out in the presence of serum lacking specific complement components (Fig. 1D). Although there was reduced NF-κB activation in C1- and C2-deficient serum (Serum-C1 and Serum-C2, respectively), only C3-deficient serum (Serum-C3) diminished induction comparably with heat inactivation. Serum deficient in components after C3—Serum-C5 and Serum-C6—did not have any impact compared with AdV+Serum. C4-deficient serum (Serum-C4) also gave similar responses to that observed from Serum-C1 and Serum-C2 (Fig. 1E). To further confirm the importance of C3, Serum was treated with *Naja naja kaouthia* cobra venom, which is known to cleave and inactivate C3 (*14*), and this resulted in a similar reduction in NF-κB induction by serum as heat-inactivation (Fig. 1F). NF-κB activation in C3-deficient serum was restored by the addition of recombinant C3 protein (Fig. 1G). Serum deficient in factor B or factor D, which are components of the alternate pathway (*7*), gave similarly diminished NF-κB activation to serum lacking C1 or C2, suggesting that both the alternate and classical pathways are important for C3 deposition (Fig. 1, D and H). We reconstituted the alternate deposition pathway using purified proteins (AdV+C3fBfD). Activated purified C3 potently induced NF-κB in the presence but not the absence of AdV (Fig. 1H). To test whether signaling was mediated by C3 attached to virus or by cleaved anaphylatoxins, AdV+C3fBfD was pelleted through 30% sucrose. Pelleted AdV+C3fBfD stimulated NF-κB comparably with unpelleted material, showing that it was C3-bound AdV that

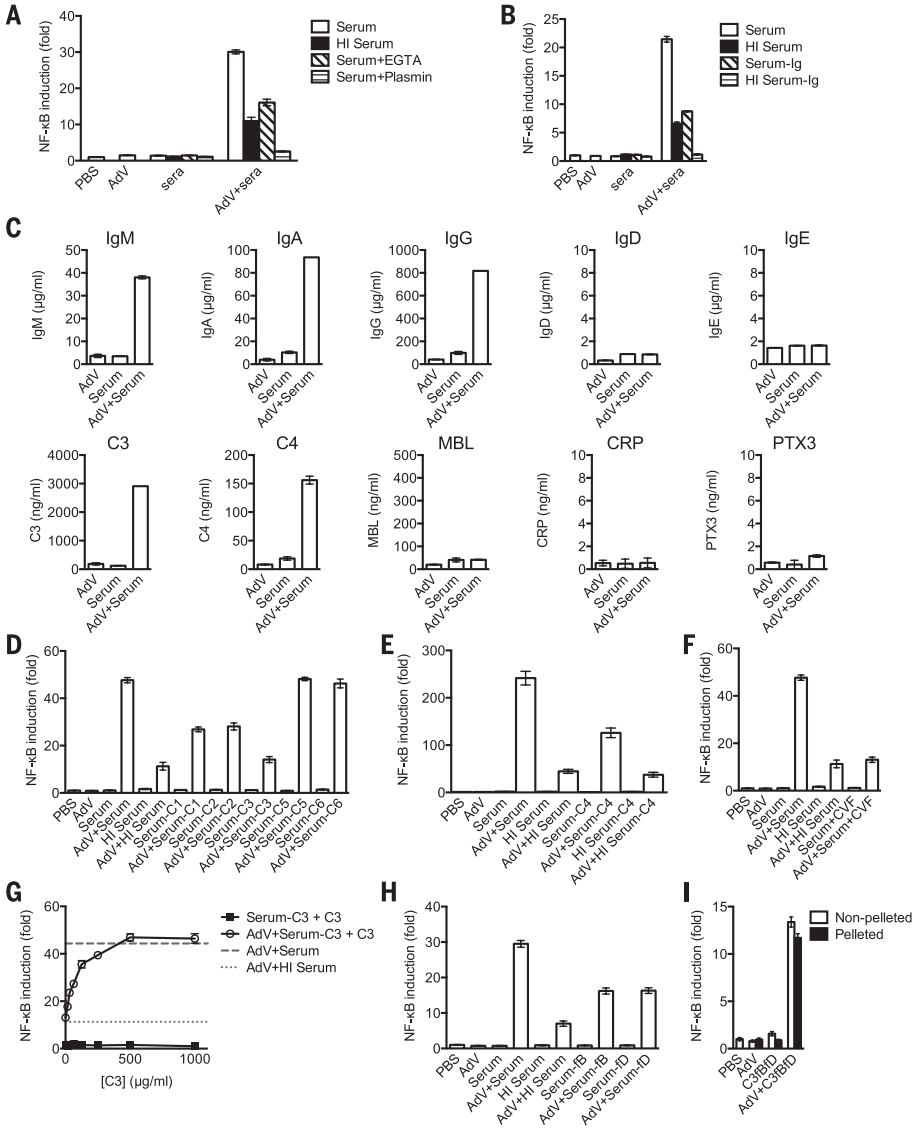

Fig. 1. Complement C3-bound virus induces NF-κB signaling in nonimmune cells. (**A**) NF-κB activity of HEK293T cells challenged with PBS, AdV, serum, HI Serum, EGTA-treated serum (Serum+EGTA), Plasmin-treated serum (Serum+Plasmin), or AdV incubated with the previous sera. (**B**) HEK293T cells treated with AdV incubated with Serum, HI Serum, antibody-depleted Serum (Serum-Ig), or HI Antibody–depleted Serum (HI Serum-Ig). (**C**) Concentration of serum components IgM, IgA, IgG, IgD, IgE, C3, C4, Mannan-Binding Lectin (MBL), C-Reactive Protein (CRP), and Pentaxin 3 (PTX3) bound to AdV after incubation of AdV+Serum as measured with ELISA. (**D** to **F**) NF-κB activity of HEK293T cells treated with AdV incubated with (D) serum deficient in complement components (Serum-C1 to -C6), (E) serum deficient in complement C4 (AdV+Serum-C4) or heat-inactivated Serum-C4 (AdV+HI Serum-C4), or (F) CVF-treated serum (AdV+Serum+CVF). (**G**) NF-κB activity of HEK293T cells after challenge with AdV+Serum, AdV+HI Serum, or Serum-C3 reconstituted with purified C3 (Serum-C3 + C3). (**H**) HEK293T treated with AdV incubated with serum deficient in factor B (AdV+Serum-fB) or factor D (AdV+Serum-fD). (**I**) NF-κB activity of HEK293T cells treated with AdV incubated with C3-Factor B-Factor D (AdV+C3fBfD) with and without subsequent virus pelleting. Data are representative of three experiments; results in (A), (B), and (D) to (I) are as fold change over PBS-treated controls; mean ± SEM; data in (C), mean ± SEM.

initiated signaling (Fig. 1I). Thus, C3 attached to the pathogen surface activates NF-κB upon infection.

Nonimmune cells have an intracellular C3 receptor

Most cells express inhibitory complement receptors CD46 (also known as complement regulatory protein) and CD55 (decay accelerating factor), whereas professional immune cells express a number of activating complement receptors (*15*). Consistent with this, HEK293T, HeLa, and Caco-2 cells and primary normal human lung fibroblasts (NHLFs) all expressed CD46 and CD55 (Fig. 2A), whereas only THP-1 monocytes expressed the activating receptors, complement receptor 1 (CR1, also known as CD35), CR3 (made up of CD11b and CD18), and CR4 (CD11c and CD18). Depletion of CD46 or CD55 (fig. S1A) had no impact on signaling detected in HEK293T cells (Fig. 2B), suggesting that C3-mediated NF-κB activation is not due to detection by these cell-surface receptors.

Antibodies activate immune signaling in nonprofessional cells when carried into the cytosol by an infecting virus (*1*). We investigated whether C3 similarly activates signaling when carried into the cell during virus infection. Because AdV infection is dependent on receptor-mediated endocytosis (*16*), we tested whether endocytosis inhibitors prevent C3 activation of NF-κB. Inhibition of endosomal acidification by bafilomycin A1 (BafA1), or the endocytic pathway by Ras superfamily inhibitor CID1067700 (CID) (*17*), abolished AdV+C3fBfD–mediated NF-κB signaling in HEK293T, whereas induction by tumor necrosis factor (TNF) remained unaffected (Fig. 2C). The same effect was seen in NHLFs (Fig. 2D). However, signaling in THP-1 cells, which have activatory cell-surface receptors for C3, was not affected by endocytosis inhibitors (Fig. 2E). To confirm that C3 induced signaling in nonprofessional cells was a result of intracellular sensing, we used an endosomal disruption assay, in which we measured cytosolic delivery of a constitutively expressing nano-luciferase plasmid. Incubation of cells with C3fBfD had little impact on AdV escape from endosomes, whereas BafA1 and CID abolished it (Fig. 2F), verifying that AdV did not reach the cytosol in the presence of these inhibitors. To test whether C3 remained attached to AdV during entry of the virus, cells were examined by means of confocal microscopy. AdV particles could be detected within the cell and colocalized with AlexaFluor-488–labeled C3 that was deposited before infection (Fig. 2G). Moreover, no C3 was detected in the absence of virus, suggesting that C3 was deposited onto virus and transported into the cell. Last, to show that signaling by intracellular C3 is independent of corecognition of viral pathogen–associated molecular patterns (PAMPs), beads were incubated with the C3fBfD mix and transfected into cells (Fig. 2H). Only Beads+C3fBfD that had been transfected into cells were capable of signaling. Thus, nonimmune cells possess a signaling pathway that allows them to sense intracellular complement C3.

C3 signaling leads to pro-inflammatory cytokine production by activating NF-κB, IRF, and AP-1 transcription factors

Next, we investigated which signaling pathways are activated by intracellular C3 sensing. Canonical NF-κB signal transduction involves the transforming growth factor β (TGFβ)–activated kinase (TAK)–binding protein (TAB)–TAK complex, which activates the inhibitor of NF-κB (IκB) kinase (IKK) complex to phosphorylate IκB, promoting IκB degradation and releasing NF-κB to translocate into the nucleus. Inhibitors of the TAB-TAK complex (5Z-7-oxozaeanol), the IKK complex (IKK

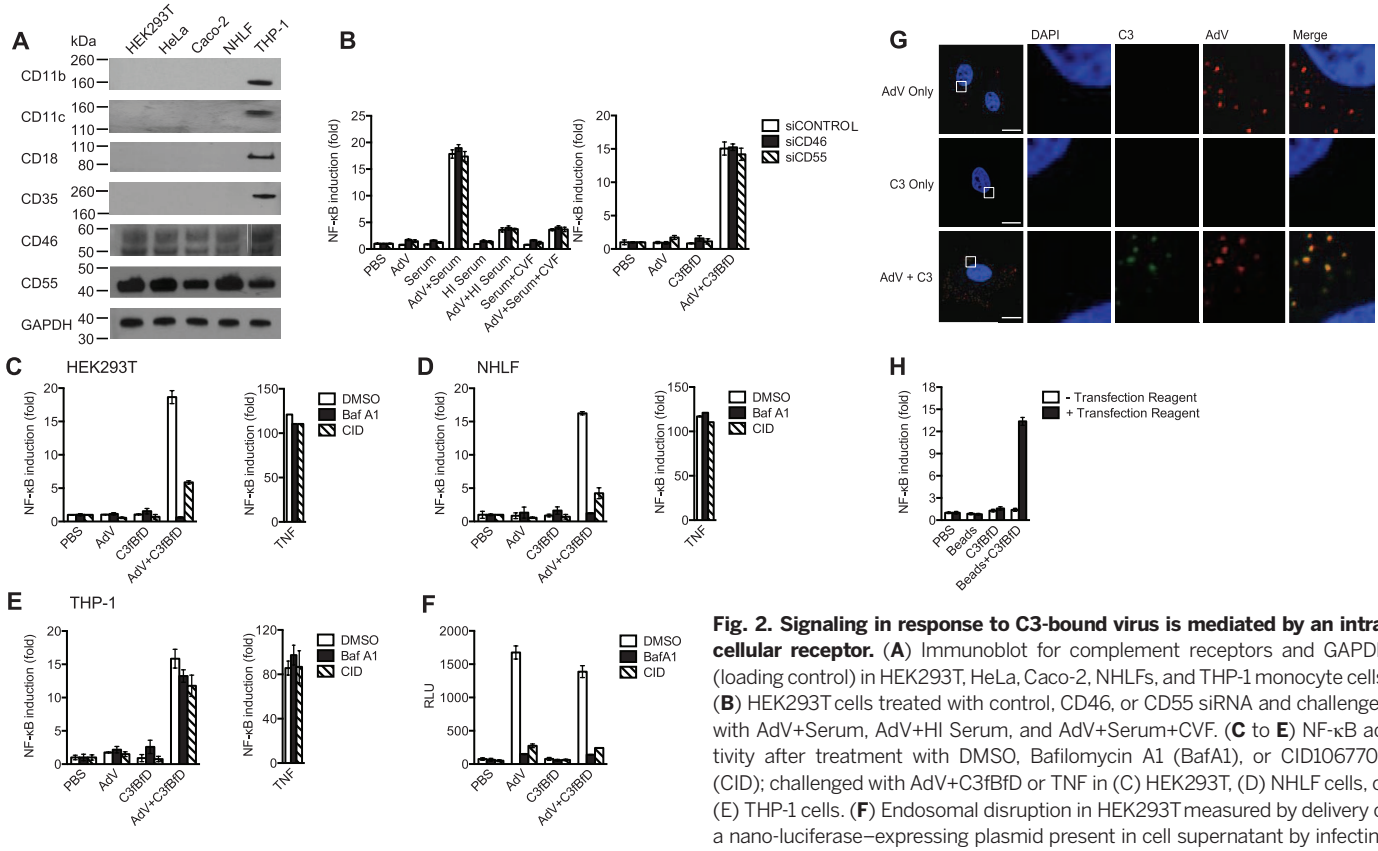

Fig. 2. Signaling in response to C3-bound virus is mediated by an intracellular receptor. (**A**) Immunoblot for complement receptors and GAPDH (loading control) in HEK293T, HeLa, Caco-2, NHLFs, and THP-1 monocyte cells. (**B**) HEK293T cells treated with control, CD46, or CD55 siRNA and challenged with AdV+Serum, AdV+HI Serum, and AdV+Serum+CVF. (**C** to **E**) NF-κB activity after treatment with DMSO, Bafilomycin A1 (BafA1), or CID1067700 (CID); challenged with AdV+C3fBfD or TNF in (C) HEK293T, (D) NHLF cells, or (E) THP-1 cells. (**F**) Endosomal disruption in HEK293T measured by delivery of a nano-luciferase–expressing plasmid present in cell supernatant by infecting AdV, after treatment with DMSO, BafA1, or Rab7, as relative luminescence units (RLUs). (**G**) Confocal microscopy of HeLa cells 30 min after treatment with AdV with AlexaFluor-488–labeled C3, stained with DAPI and antibody to AdV. Scale bars, 20 μm. (**H**) HEK293T cells treated with Beads incubated with C3fBfD (Beads +C3fBfD), with or without transfection reagent. Data are representative of three experiments; results in (B) to (E) and (H) are as fold change over PBS-treated controls; mean ± SEM; data in (F), mean ± SEM.

VII), and NF-κB release (panepoxydone) each inhibited signaling (Fig. 3A). Furthermore, increased phosphorylation of these components was detected upon infection with virus carrying deposited C3 (Fig. 3B). NF-κB components p65, p50, and p52 were activated by AdV+C3fBfD (Fig. 3C) as well as interferon regulatory factor 3 (IRF3), IRF5, and IRF7 (Fig. 3D) and the activating protein 1 (AP-1) family, c-Jun, JunB, JunD, and FosB (Fig. 3E). c-Fos was activated by virus regardless of C3, suggesting that other mechanisms are involved in its activation. Thus, C3 is sensed by a pattern recognition receptor (PRR) that activates classical immune transduction pathways. Immune activation by complement-coated virus, but not virus alone, induced secretion of pro-inflammatory cytokines, as demonstrated by the detection of interleukin-6 (IL-6), TNF, CCL4, IL-1β, and interferon-β (IFN-β) by means of ELISA after challenge with AdV+Serum and AdV+HI Serum (Fig. 3F), as well as the reconstituted alternate pathway of AdV+C3fBfD (Fig. 3G).

C3 enables proteasome-dependent restriction of virus infection

The above data suggest that C3 can act as a DAMP to activate innate immunity. Next, we investigated whether C3 also mediates a direct effector response to inhibit viral infection. We used an adenovirus vector that expresses green fluorescent protein (GFP) after productive infection. AdV incubated with Serum, HI Serum, Serum +EGTA, or Serum+Plasmin and AdV alone was added to HeLa cells, with infected cells enumerated by means of flow cytometry (Fig. 4A). As with signaling, restriction by a heat-labile, calcium-dependent protein component capable of functioning independently of antibody was observed (Fig. 4B). This restriction was C3-dependent, as shown by the loss of heat-labile neutralization after CVF treatment (Fig. 4C). Moreover, restriction could be reconstituted in the absence of serum by using C3fBfD (Fig. 4D). Depletion of CD46 or CD55 had no effect on restriction, showing that capture via these membrane complement receptors was not responsible for this phenotype (Fig. 4E and fig. S1A). Binding to complement receptor CD46 has been suggested to stimulate autophagy (*18*); however, the autophagy inhibitor 3-methyladenine (3-MA), and phosphatidylionsitol-3-kinase inhibitors KU55933 and Gö6976 (*19*) had no effect on restriction (Fig. 4F) but induced p62 retention (fig. S1B). TRIM21 is required for intracellular neutralization of antibody-coated pathogens (*4*, *5*). Depletion of TRIM21 removed the heat-stable component of restriction but did not affect the heat-labile component (Fig. 4G and fig. S1C), confirming that TRIM21 has a role in antibody-mediated neutralization but not complement-mediated restriction.

A characteristic of antiviral immunity is IFN regulation, and most antiviral genes are IFN-stimulated (*20*). *TRIM21* is an IFN-stimulated gene (*4*, *5*), and the efficiency of antibody-dependent intracellular neutralization is dependent on the amount of TRIM21 in the cell. To determine whether C3-mediated restriction was also IFN-inducible, cells were stimulated before infection (Fig. 4H). IFN increased the ability of the cell to restrict viral infection via complement C3, suggesting that complement recognition occurs through an IFN-stimulated gene.

Antibodies mediate intracellular neutralization by targeting viruses for degradation by the AAA–adenosine triphosphatase (ATPase) valosin-containing protein (VCP) (also known as p97) (*3*) and the proteasome (*4*). To determine whether C3 also mediates restriction by recruiting these enzymes, we tested the effect of DBeQ (a VCP inhibitor) and epoxomicin (a proteasome inhibitor). Each inhibitor perturbed restriction of AdV by C3, suggesting that C3 activates an intracellular, VCP, and proteasome-dependent pathway (Fig. 4I). To test directly whether the block to infection was the result of targeted degradation of incoming virions, we performed a fate-of-capsid experiment

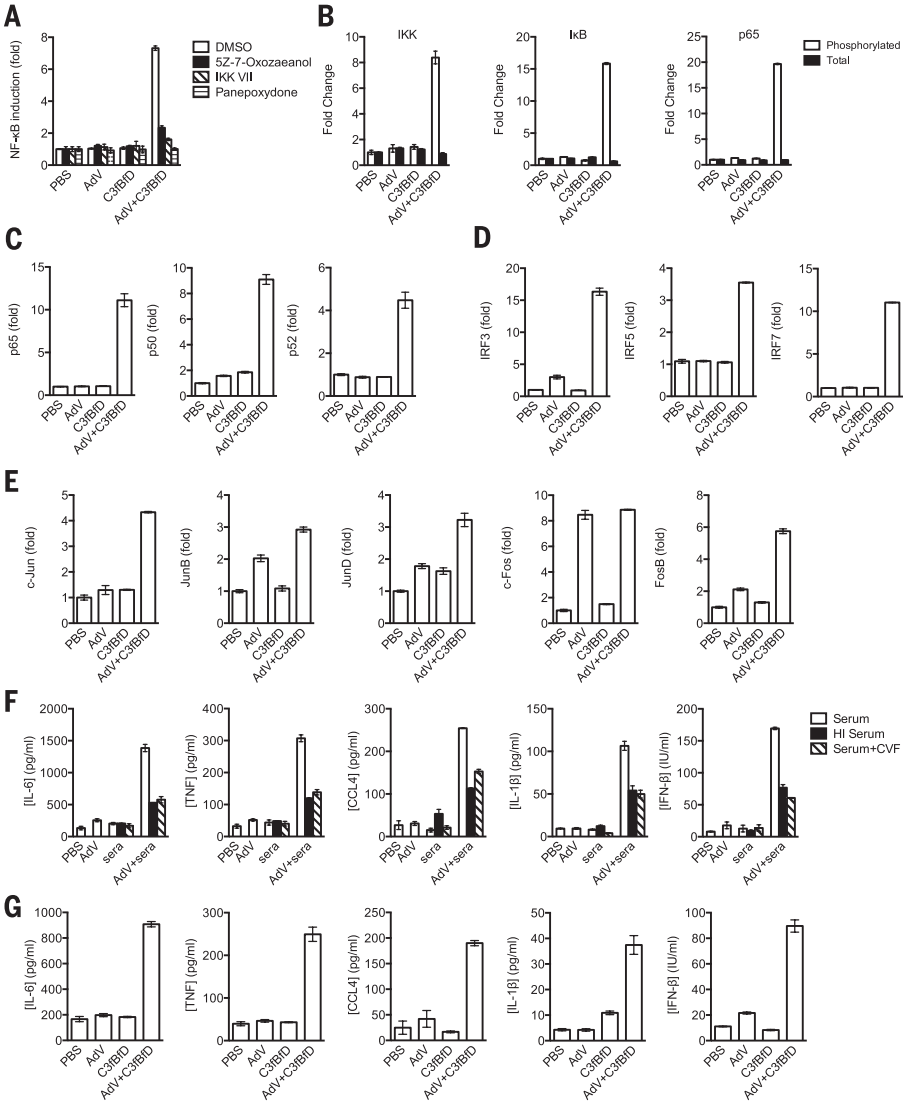

Fig. 3. C3-mediated signaling initiates proinflammatory cytokine production. (**A**) NF-κB luciferase activity in NHLF cells treated with DMSO, 5Z-7-oxozaeanol, IKK VII, or panepoxydone. (**B**) Levels of total and phosphorylated IKKα, IκB, or p65 in HEK293T cells treated with AdV+C3fBfD 4 hours after infection as measured with ELISA. (**C** to **E**) Levels of (C) NF-κB components (D) IRF family proteins, and (E) AP-1 components measured with DNA-binding ELISA from NHLFs 4 hours after challenge with AdV+C3fBfD. (**F** and **G**) Levels of cytokines 24 hours after challenge by AdV incubated with (F) Serum, HI Serum, or Serum+CVF or (G) AdV+C3fBfD. Data are representative of three experiments; results in (A) to (E) as fold change over PBS-treated controls, mean ± SEM; data in (F) and (G), mean ± SEM.

in which levels of the AdV major capsid protein, hexon, were measured at different time points. Hexon was rapidly degraded in a proteasome-dependent manner, but only when complement was present (Fig. 4J). These restriction phenotypes did not just occur in HeLa cells but could also be replicated in primary NHLF cells (Fig. 4K). Thus, in addition to activating innate immunity, the attachment of C3 to invading virions labels them for degradation by VCP and the proteasome, restricting virus infection.

Intracellular complement immunity conserved in mammals

Complement protein/receptor interactions are thought to be species-specific (*21*), although recent observations have disagreed with this view (*22*). We investigated whether intracellular complement immunity is conserved among mammals. Serum from different mammalian species was incubated with AdV, pelleted to remove unattached complement components, and then added onto HEK293T cells. Human, mouse, cat, rabbit, and guinea pig serum all elicited complement-mediated signaling (Fig. 5A). We then tested whether this signaling was present in cell lines derived from different mammals. Human (HEK293T), African green monkey (Vero), mouse [mouse embryonic fibroblasts (MEFs)], cat [feline embryonic airway (FEA)], and dog [Madin-Darby canine kidney (MDCK)] cells all signaled in response to complement-coated AdV (Fig. 5B). Thus, a system of intracellular complement immunity is conserved within mammals.

Intracellular complement immunity effective against diverse pathogens

Because complement-sensing was independent of viral PAMPs (Fig. 2H), we hypothesized that it may be an effective way of activating immunity during infection by diverse pathogens. Complement-sensing allowed detection of infection by replication-competent wild-type adenovirus 5 (WT AdV), confirming previous experiments that were carried out with replication-deficient virus lacking the *E1* and *E3* genes (Fig. 5C). In addition, infection by human papillomavirus virus (HPV)–like particles, human astrovirus 1 (hAstV), feline calicivirus (FCV), human rhinovirus 14 (HRV), poliovirus 2 (PV), and coxsackievirus B3 (CVB) also elicited NF-κB induction in a complement-dependent manner (Fig. 5C). These viruses use different strategies for cell entry. Adenovirus (*23*) and rhinovirus 14 (*24*) lyse the endosome during infection, whereas poliovirus (*25*) and coxsackievirus (*26*) form a pore in the endosome membrane. Accordingly, endosomal disruption assays revealed an association between endosomal disruption, and the potency of complement mediated signaling for these viruses (fig. S1K).

Complement deposition on an enveloped virus occurs on the lipid membrane and not its internal capsid. Consequently, during infection by an enveloped virus, complement should be left behind on the outside of the plasma membrane or inside endosomes. To test this, we infected cells with respiratory syncytial virus (RSV), an enveloped virus that enters through membrane fusion (*27*) in the presence of serum. As expected, no complement signaling was observed during RSV infection (Fig. 5D).

Nonenveloped viruses are not the only intracellular pathogen capable of being targeted by complement deposition. *Salmonella enterica enterica* serovar Typhimurium can escape from their salmonella-containing vesicles and replicate in the cytosol (*28*). Antibody deposited on bacterial surfaces has previously been shown to be detected by TRIM21 (*1*). In HeLa, Caco-2, and MEF cells, signaling in response to C3-coated wild-type bacteria was detected (Fig. 5E). Signaling was substantially more pronounced in the ΔSifA mutant, which has a reduced vesicular integrity and a greater propensity to enter the cytosol (Fig. 5F) (*29*). Thus, a variety of different pathogens can be detected by the presence of intracellular C3.

Viral antagonism to intracellular complement immunity

The hallmark of an antiviral response is that it should exert selection pressure on pathogens so as to evolve and escape it (*30*). To investigate the possibility of viral antagonism, we compared the activation of immunity by complement between different viruses. We observed that although there was complement-mediated NF-κB activation upon infection with viral particles such as AdV and

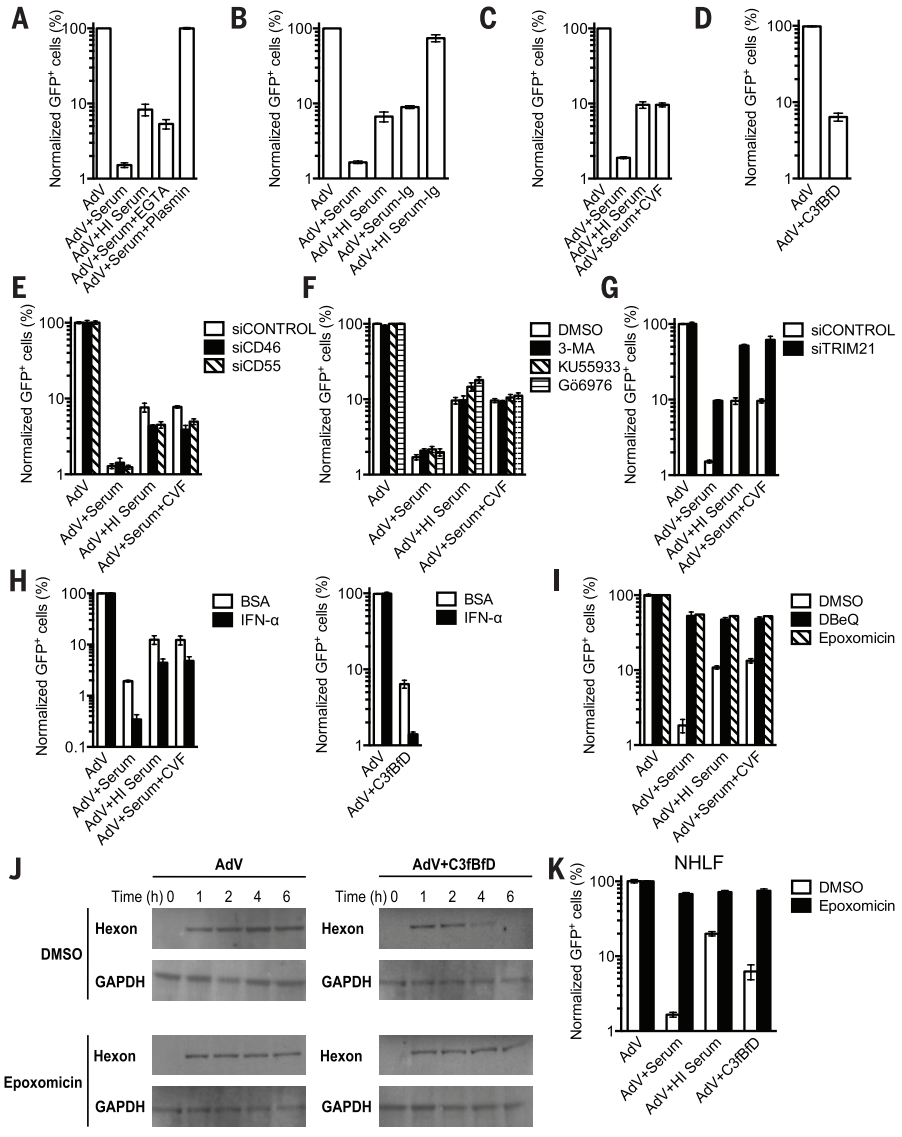

Fig. 4. C3 promotes intracellular restriction of virus. (**A** to **D**) Levels of infection in HeLa cells after challenge with GFP-encoding adenovirus AdV, pretreated as indicated. (**E**) Levels of infection in HEK293T cells treated with control, CD46, or CD55 siRNA. (F and G) Levels of infection in HeLa cells treated with (F) DMSO, 3-MA, KU55933, or Gö6976 or (G) control or TRIM21-directed siRNA. (**H** and **I**) HeLa cells after stimulation with (H) BSA, or IFN-α or (I) treated with DMSO, VCP inhibitor DBeQ, or proteasome inhibitor epoxomicin. (**J**) Immunoblot for AdV capsid component hexon and GAPDH in HeLa cells treated with DMSO or epoxomicin at indicated times after challenge with AdV+C3fBfD. (**K**) Levels of infection in NHLF cells treated with DMSO or epoxomicin. Data are representative of three experiments; results in (A) to (I) and (K) are percentage infected cells normalized to AdV only controls, mean ± SEM.

HPV (Fig. 6A), this was substantially weaker during infection with viruses such as hAstV, PV, and HRV. This suggests that these viruses have strategies that allow them to evade detection by C3. hAstV is known to inactivate complement component C1, limiting the amount of complement deposition (*10*). Ultraviolet (UV)–inactivation of HRV restored complement-mediated NF-κB activation to the levels of replication-deficient vectors, AdV and HPV, suggesting that an encoded component was antagonizing C3-mediated signaling (Fig. 6A).

HRV expresses a cytosolic 3C protease (HRV 3C Pro) that we hypothesized to mediate antagonism, given previous observations of 3C-mediated cleavage of RIG-I (*31*). Using in silico analysis of potential 3C cleavage sites (*32*), both HRV 3C Pro and PV 3C protease (PV 3C Pro) were predicted to cleave complement C3. To test whether expression of 3C proteases enables viruses to inhibit intracellular C3 signaling, we incubated AdV+C3fBfD with albumin or with recombinant HRV 3C Pro (Ext HRV 3C) and observed cleavage of C3 by means of immunoblot (Fig. 6B). HRV 3C Pro did not cleave the viral proteins but removed the larger complement-bound band (Fig. 6C). Next, we expressed HRV 3C Pro or PV 3C Pro in HEK293T cells before infection with AdV+Serum. Expression of either 3C protease reduced NF-κB induction to levels observed with AdV+HI Serum and AdV+Serum+CVF, suggesting that complement signaling had been prevented (Fig. 6D). Indeed, expression of either protease was sufficient to cause AdV to behave similarly to HRV (AdV+HRV 3C Pro, AdV+PV 3C Pro) (Fig. 6D). To confirm that the observed effect of 3C protease was due to cleavage of complement and not a factor inside the cell, AdV incubated with different sera was treated with recombinant 3C protease before pelleting the virus to remove the protease, before addition to HEK293T cells (Fig. 6E). Preinfection treatment with recombinant 3C proteases (Ext HRV 3C and Ext PV 3C) perturbed NF-κB induction similarly to expression inside target cells. In addition to antagonizing sensing, HRV 3C Pro or PV 3C Pro were also effective in preventing complement-mediated restriction (Fig. 6F). In order to permit escape from intracellular complement immunity, 3C protease must be synthesized and act rapidly after infection. When we blotted for C3 after infection, full cleavage was noted for HRV+C3fBfD within 45 min (Fig. 6G). However, no changes for AdV+C3fBfD were observed after 2 hours. Overexpression of HRV 3C Pro was sufficient to confer C3 cleavage during AdV infection. Thus, cleavage of C3 is a fast and effective method of evading intracellular complement immunity.

We further hypothesized that if 3C protease allows viruses such as PV or HRV to evade intracellular complement immunity, then inhibition of 3C protease should make these viruses susceptible. To test this, we used rupintrivir, a specific, nonreversible inhibitor of the HRV 3C protease (*33*). Its addition to cells infected with HRV increased the levels of complement-mediated signaling so that HRV+Rupintrivir behaved similar to viruses lacking complement antagonism (Fig. 6H). Rupintrivir treatment was also sufficient to make PV visible to complement sensing. When cells were treated with rupintrivir, this lead to a loss of C3 cleavage by HRV (Fig. 6I). To investigate the kinetics of antagonism, rupintrivir was added at various times after infection with AdV, HRV, or PV, and its effect on signaling was determined. Rupintrivir inhibited a process that antagonized complement-mediated sensing within the first hour of infection (Fig. 6J). This time scale matches the kinetics of C3 cleavage by 3C. By 1.5 hours after infection, addition of rupintrivir was unable to restore heat-labile signaling, which is consistent with C3 cleavage being completed by this time. Rupintrivir had no impact on complement-mediated AdV sensing. These rapid kinetics are similar to those previously reported for PV 2A protease (*34*), formed from the same polypeptide as 3C protease. Complement also activates cell-surface signaling in professional cells. Virally encoded 3C antagonism did not prevent this response. Rupintrivir had no effect on signaling in THP-1 cells infected with HRV+Serum, a finding

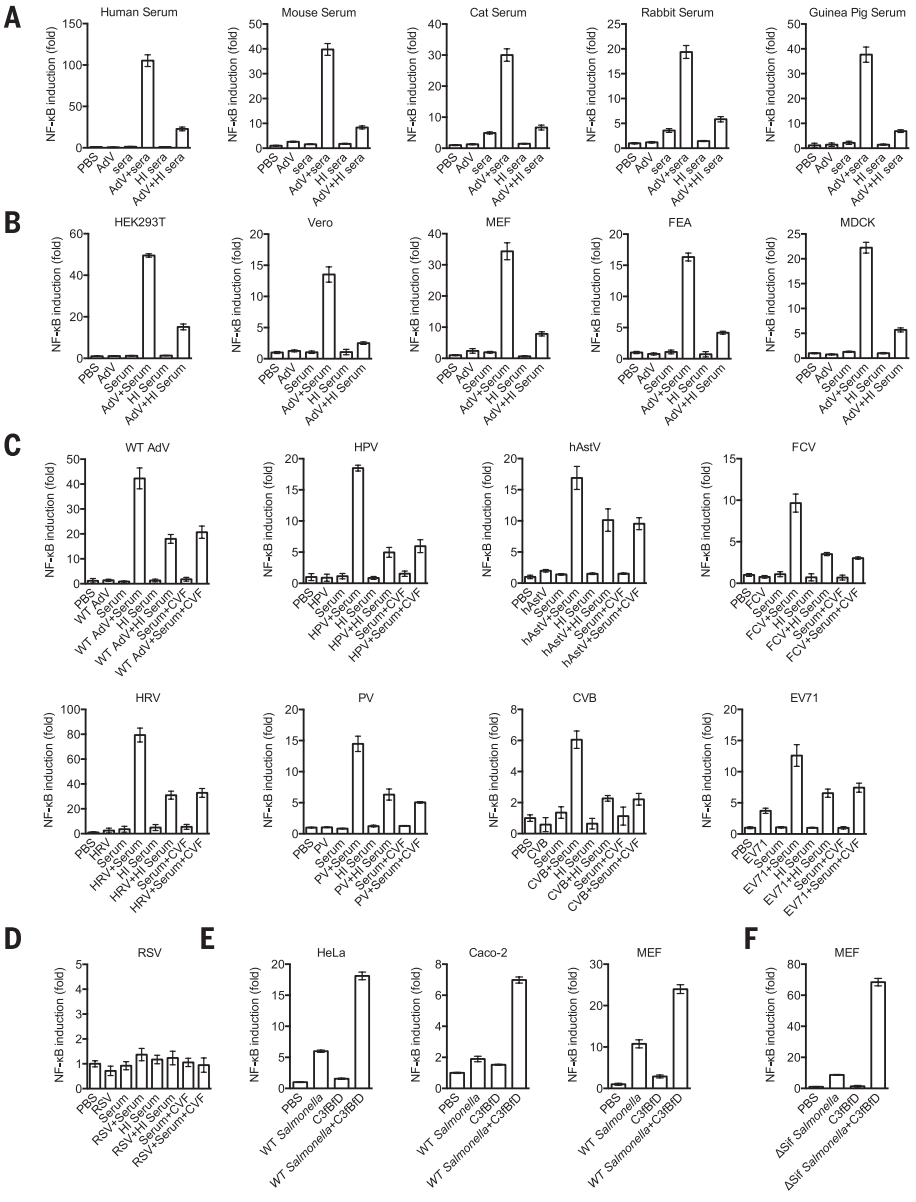

Fig. 5. C3 detection is conserved in mammals and is active against RNA and DNA nonenveloped viruses and bacteria. (**A**) HEK293T cells challenged with AdV incubated with human, mouse, cat, rabbit, and guinea pig serum. (**B**) HEK293T (human), Vero (African green monkey), MEF (mouse), FEA (cat), and MDCK II (dog) cells challenged with AdV+Serum or AdV+HI Serum. (**C**) NF-κB activity after challenge with WT AdV, HPV, hAstV, FCV, HRV, PV, and CVB. WT AdV and HRV were carried out on HEK293T; HPV, PV, and CVB were carried out on HeLa; hAstV was carried out on Caco-2; and FCV was carried out on FEA cells. (**D**) NF-κB activity in HeLa after challenge with RSV incubated with sera. (**E**) NF-κB activity in HeLa, Caco-2, and MEF cells after challenge with WT *Salmonella*+C3fBfD. (**F**) MEF cells challenged with ΔSif *Salmonella*+C3fBfD. Results are representative of three experiments, as fold change over PBS-treated controls; data in (A) to (D), mean ± SEM; data in (E) and (F), mean ± SEM.

that is consistent with their extracellular detection of the C3-coated virus (Fig. 6K). Our data suggest that rupintrivir could be used therapeutically to enhance host detection of 3C-expressing viruses. We found that NF-κB induction by complement, facilitated by rupintrivir treatment, was sufficient to induce IFN-β secretion upon HRV infection (Fig. 6L). Thus, viral expression of 3C protease cleaves complement C3 inside the cell to disable signaling and restriction. Inhibition of 3C protease counteracts this effect.

Complement-mediated signaling independent of known PRRs, but requires MAVS

The ability of complement C3 to enable sensing of a wide variety of different pathogens suggests that a particular PAMP is not required for detection. To test this, we blocked Toll-like receptor activity by inhibiting MyD88 and TRIF (Fig. 7A), as well as knockdown of RIG-I and MDA5 (Fig. 7B and fig. S1D). In addition, we inhibited Syk (Fig. 7C), which blocks signaling through Fc receptors and type II C-type lectin receptors, and depleted cells of STING, the endoplasmic reticulum–associated adaptor involved in cytosolic DNA detection (Fig. 7D and fig. S1E). All of these perturbations to known signaling pathways had no effect on complement-mediated signaling.

However, depletion of mitochondrial antiviral signaling (MAVS) abolished the heat-labile component of signaling, suggesting that MAVS is required for C3-mediated immune activation (Fig. 7D and fig. S1E). Sendai virus has been reported to activate MAVS activation by inducing aggregation (*35*), as detected with microscopy and semidenaturing gel electrophoresis. We carried out microscopy for MAVS and mitochondrial marker TOM20 in cells treated with phosphate-buffered saline (PBS), AdV, C3fBfD, or AdV+C3fBfD 6 hours after infection (fig. S2A) and noted no apparent aggregation at this time point. This is consistent with published literature, in which aggregation of MAVS only occurs after 9 hours of infection (*35*). Overexpression of MAVS lead to increased protein levels, but the same localization was observed (fig. S2B). We carried out semidenaturing gel electrophoresis but were not able to detect aggregation, except when MAVS was overexpressed (fig. S2C). Thus, we observed rapid MAVS-dependent signaling that was independent of aggregation, with similar kinetics to that observed during MAVS-induced IRF3 dimerization (*36*) and IκBa phosphorylation (*37*).

Owing to the involvement of MAVS in C3 sensing, we investigated whether TNF receptor–associated factor (TRAF) proteins are required for signal transduction. Depletion of TRAF6 reduced complement-mediated NF-κB signaling (Fig. 7E and fig. S1F), although simultaneous knockdown of TRAF2, -3, -5, and -6 (siT2,3,5,6) was required to abolish signaling, similar to published data (*38*). Given the importance of TRAF6, we also investigated the adaptor p62 (*39*). Depletion of p62 (Fig. 7F) lead to a similar loss of NF-κB induction, as did knockdown of TRAF6. Individual depletion of TRAF proteins had a partial effect on IRF activation (Fig. 7G), whereas siT2,3,5,6 depletion was completely inhibitory, demonstrating redundancy. In addition, knockdown of TBK1 or inhibition with BX795 (*40*) prevented IRF activation (Fig. 7H), demonstrating that TBK1 is important in C3-mediated signaling. Thus, intracellular C3 activates MAVS with downstream signaling proceeding via the TRAF proteins in a partially redundant manner.

Intracellular antibody and complement cooperate to activate signaling

TRIM21 has previously been identified as a PRR for cytosolic antibody (*1*, *4*), and depletion of TRIM21 (fig. S1C) resulted in decreased signaling from AdV+Serum (Fig. 8A). However, TRIM21 depletion only decreased the heat-stable component of signaling because only AdV+IgG, and not AdV

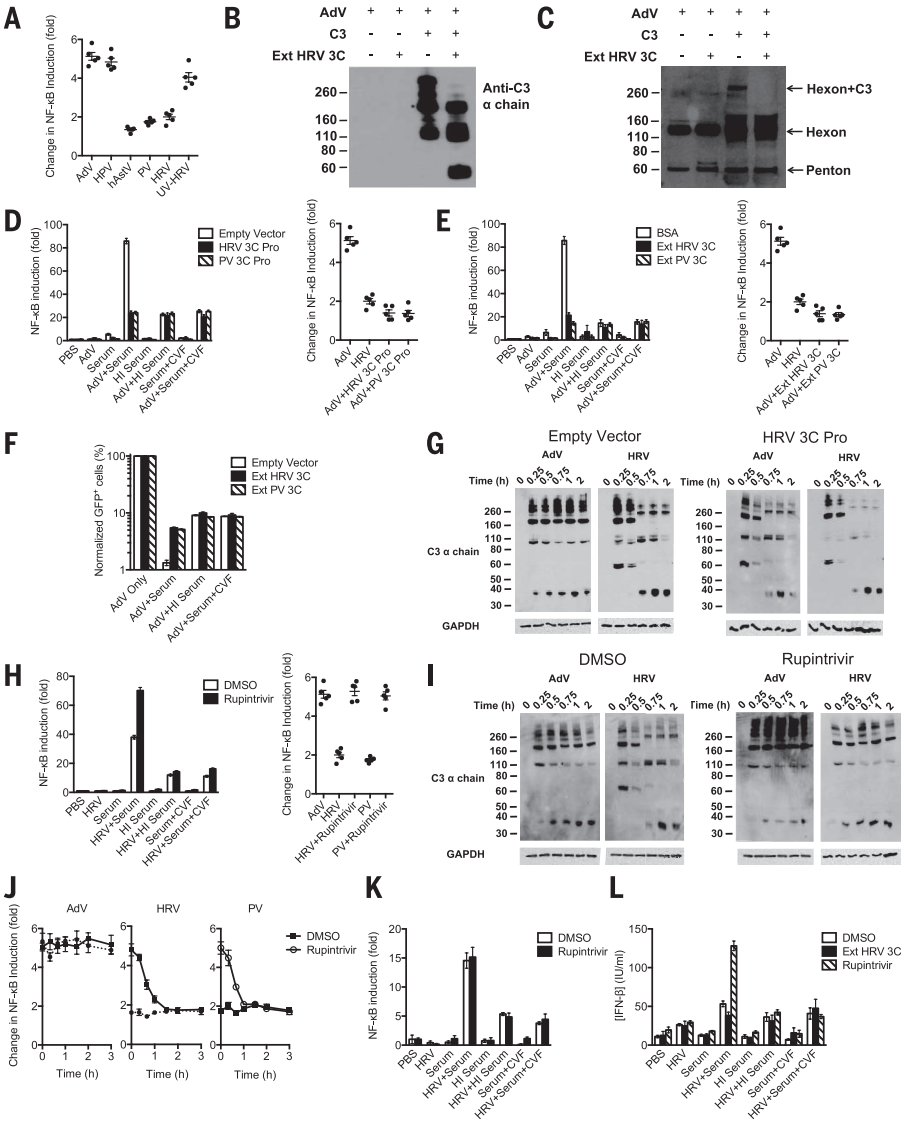

Fig. 6. Viral antagonism of C3-mediated signaling. (**A**) NF-κB induction by the heat-labile component of serum activity after infection of HEK293T cells by AdV, HPV, hAstV, PV, HRV, and UV-inactivated HRV (UV-HRV), shown as fold change of Virus+Serum over Virus+HI Serum signaling levels. (**B** and **C**) Immunoblot for C3 (B) and AdV (C) in samples comprising C3 deposited on AdV incubated with recombinant HRV 3C Protease (Ext HRV 3C) or components thereof. (**D**) NF-κB activity in HEK293T expressing HRV 3C Protease (HRV 3C Pro) or PV 3C Protease (PV 3C Pro). (**E**) NF-κB activity in HEK293T treated with BSA, Ext HRV 3C, or recombinant PV 3C Protease (Ext PV 3C), with AdV complexes pelleted. (**F**) Levels of infection of HeLa cells challenged with AdV, AdV+Serum, AdV+HI Serum, and AdV+Serum+CVF treated with Ext HRV 3C, or Ext PV 3C, followed by pelleting. (**G**) Immunoblot for C3 after infection of HeLa cells expressing empty vector or HRV 3C Pro by AdV+C3fBfD or HRV+C3fBfD. (**H**) NF-κB activity in HEK293T cells treated with DMSO or 3C antagonist rupintrivir, challenged with HRV incubated with sera. (**I**) Immunoblot for C3 after infection of HeLa with AdV+C3fBfD or HRV+C3fBfD treated with DMSO or rupintrivir. (**J**) NF-κB activity induced by the heat-labile component of serum upon AdV, HRV, or PV infection of HEK293T cells treated with DMSO or rupintrivir at indicated times after infection. (**K**) NF-κB activity in THP-1 cells treated with DMSO or rupintrivir and challenged with sera-incubated HRV. (**L**) IFN-β ELISA from NHLF cells infected with HRV under different conditions after treatment with DMSO, Ext HRV 3C, or rupintrivir. Data from dot plots are from five experiments (dots are mean of 6 replicate samples), bar graphs are representative of three experiments, data in (D), (E), (H), and (K) are as mean ± SEM; data in (L) are mean ± SEM; data in (J) are mean ± SEM.

+C3fBfD, signaling was affected. This confirms that although TRIM21 is a receptor for antibody, it is not a receptor for complement C3. Codepletion of TRIM21 and MAVS abolished signaling from AdV+IgG, AdV+C3fBfD, or AdV+Serum, suggesting that the ability of intracellular serum proteins to induce signaling (Fig. 1A) is entirely dependent on these two pathways.

We noted that knockdown of MAVS did not have any effect on AdV infection in the presence of serum, whereas knockdown of TRIM21 increased infection (Fig. 8B), which is consistent with loss of antibody-dependent intracellular neutralization. However, neither MAVS nor TRIM21 depletion had any effect on the restriction of AdV+C3fBfD (Fig. 8C). This suggests that C3 mediates an effector response that is independent of MAVS and TRIM21.

C3 signaling and restriction contribute independently to reduce viral infection

Next, we investigated the relationship between C3-mediated signaling and restriction. Transfection of complement C3–coated beads was sufficient for NF-κB induction, and this activity was dependent on MAVS and TRAF6 (Fig. 8D), demonstrating that PAMPs are not required for C3 detection. Moreover, there was strong induction of IRF3, -5, and -7 in cells in which restriction was prevented by using a proteasome inhibitor (Fig. 8E). Thus, C3-mediated detection is not dependent on viral components liberated during restriction. Last, restriction of AdV was not affected by addition of the IκB inhibitor panepoxydone (Fig. 8F), which previously inhibited signaling (Fig. 3A), suggesting that restriction is also independent of cell signaling. Thus, C3 mediates independent signaling and restriction pathways, as has been shown previously for antibody (*1*, *2*, *4*).

Although the above data show that C3 mediates an effector response that is independent of signaling, we investigated whether signaling leads to an antiviral state that also contributes toward reducing viral infection. Supernatant was collected from HEK293T cells 3 days after challenge with PBS, AdV, C3fBfD, or Adv+C3fBfD and transferred to fresh uninfected HeLa cells. These uninfected cells were then challenged with an IFN-sensitive reporter virus (Sindbis with a GFP transgene). Supernatant from AdV+C3fBfD–infected cells was sufficient to protect cells from Sindbis infection (Fig. 8G) in a MAVS-dependent manner. Adenovirus is relatively resistant to IFN treatment (*41*), but rhinovirus is IFN-sensitive (*42*). To investigate the relative contributions of C3-mediated signaling and restriction on a spreading infection, we added epoxomicin or panepoxydone during HRV infection of HeLa cells treated with control or MAVS-targeted small interfering RNA (siRNA) (Fig. 8H). Epoxomicin reversed the ability of complement to restrict HRV, which is in line with the finding for AdV. However, panepoxydone and MAVS depletion also partially reversed restriction, suggesting that signaling in response to C3 contributes to the antiviral state. Thus, C3 elicits a direct antiviral restriction mechanism and promotes signaling, which induces an antiviral state.

Discussion

We investigated whether extracellular serum proteins mediate intracellular immune responses inside nonimmune cells upon pathogen infection. We found evidence for intracellular pathogen detection via the sensing of attached complement.

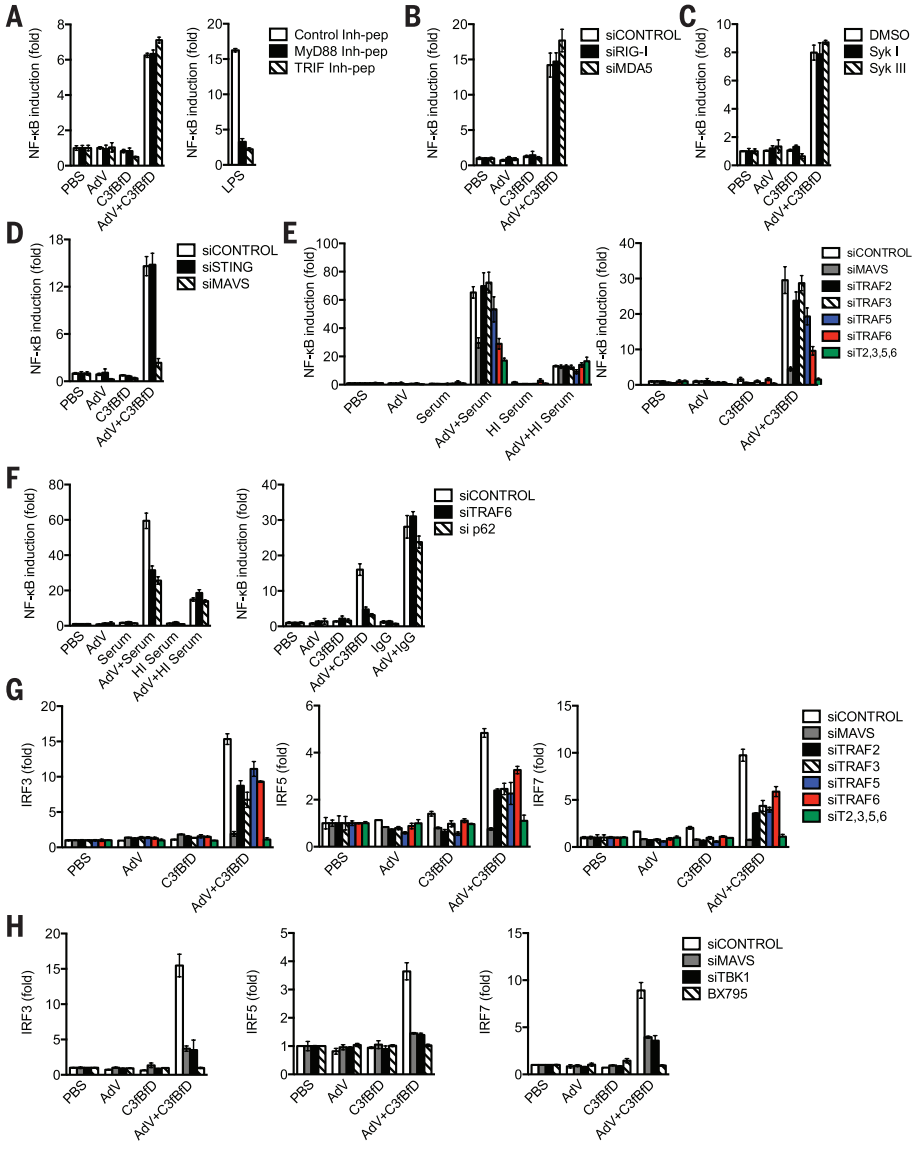

Fig. 7. C3-mediated signaling is MAVS dependent. (**A**) NF-κB activity in HEK293T cells treated with control peptides, or inhibitors of MyD88 or TRIF after challenged with AdV+C3fBfD or LPS. (**B** to **F**) NF-κB activity after challenge by AdV incubated as indicated on HEK293T cells treated with (B) control, RIG-I, or MDA5 siRNA; (C) DMSO or inhibitors Syk I and Syk III; (D) control, MAVS, or STING-directed siRNA; (E) control, TRAF2, TRAF3, TRAF5, TRAF6, or pooled TRAF2,3,5,6 (siT2,3,5,6) siRNA; and (F) control, TRAF6, or p62 siRNA. (**G**) IRF3, -5, and -7 binding to consensus DNA response elements in HEK293T cells treated with siRNA as in (E). (**H**) IRF3, -5, and -7 binding to DNA response elements in HEK293T cells treated with control, MAVS, or TBK1 specific siRNAs, or with inhibitor, BX795. Data are representative of three experiments; results in (A) to (H) are as fold change over PBS-treated controls, mean ± SEM.

Complement C3 is covalently deposited onto pathogens in the extracellular space. During infection, pathogens carry C3 inside the cell, activating innate immunity and mediating a restriction pathway that degrades virus. Key features of this intracellular complement immune response are that it is cell-type–independent and requires translocation of C3 into the cytosol. This allows pathogens to be sensed during their natural infection pathway rather than relying on the capture of immune complexes by professional cells. The importance of this system is suggested by the evolution of countermeasures that allow certain viruses to antagonize it. Both rhinovirus and poliovirus have evolved a mechanism to evade C3 detection by cleaving C3 using an encoded 3C protease.

C3 signaling was independent of known PRRs, such as Toll-like receptors and RIG-like receptors, and occurred for DNA and RNA nonenveloped viruses and intracellular bacteria, suggesting that exposure of PAMPs is not directly responsible. Detection was dependent on MAVS, activating transcription factors, and proinflammatory cytokine secretion. The minimum requirement for NF-κB activation was found, comprising reconstituted alternate pathway components (C3, factor B, and factor D) bound to beads and transfected into cells. C3-coated AdV only initiated signaling when intracellular and post-endosomal, suggesting that the initial receptor is cytosolic.

Sensing of complement-coated virus results in a restriction response that leads to degradation of virus and inhibition of infection. This process involves the proteasome, which is similar to the restriction phenotypes after recognition of retroviral capsid by TRIM5α (*43*) and antibody by TRIM21 (*1*, *4*). As with antibody, complement-mediated degradation also requires the AAA-ATPase VCP (*3*).

Taken together with our previous work on intracellular antibodies (*1*–*6*), the data here suggest that serum proteins may have an important role in detecting breaches in the physiological barrier of cell membranes. C3 has recently been described as mediating immunity to *Chlamydia psittaci*, which is an obligate intracellular bacterium in mice (*44*). In addition, C1q has been implicated as providing an intracellular signaling role by interacting with RIG-I and MDA5 (*45*). Whether these effects are related to the signaling described in this study is still to be investigated. Ultimately, there may be a number of host proteins and corresponding set of receptors that stimulate immunity based on a system of topological displacement.

The discovery that picornaviruses such as HRV and PV encode a 3C protease capable of cleaving C3 and inactivating its intracellular function has implications for treatment strategies. HRV is particularly sensitive to IFN (*42*), and treatments that prevent the virus from suppressing IFN induction could be highly effective. Rupintrivir is used to control viremia and has been reported to decrease cytokine production (*46*). However, cytokines such as IL-6 and IL-8 were measured 3 days after infection, by which time rupintrivir may have reduced viremia, resulting in a complex phenotype. In our study, rupintrivir was removed 3 hours after infection, resulting in the measurement of responses from a single round of infection and unbiased by differing levels of replication. We propose that in vivo, rupintrivir may have dual functions, increasing the complement-mediated detection of virus and hence production of IFN-β as well as inhibiting the production of progeny virions by interference with polypeptide cleavage.

Last, this system illustrates how a single DAMP can lead to the simultaneous detection and restriction of a pathogen. Signaling in response to C3-coated pathogens is independent of PAMPs and does not require proteasome-dependent restriction to reveal molecular determinants. Restriction of the pathogen occurs immediately upon infection and is not dependent on the simultaneous activation of cell signaling. However, these two responses cooperate to enable the efficient reduction of spreading infection. Although this is a relatively new concept in immunology, it is exemplified by the receptors TRIM5α (*43*, *47*),

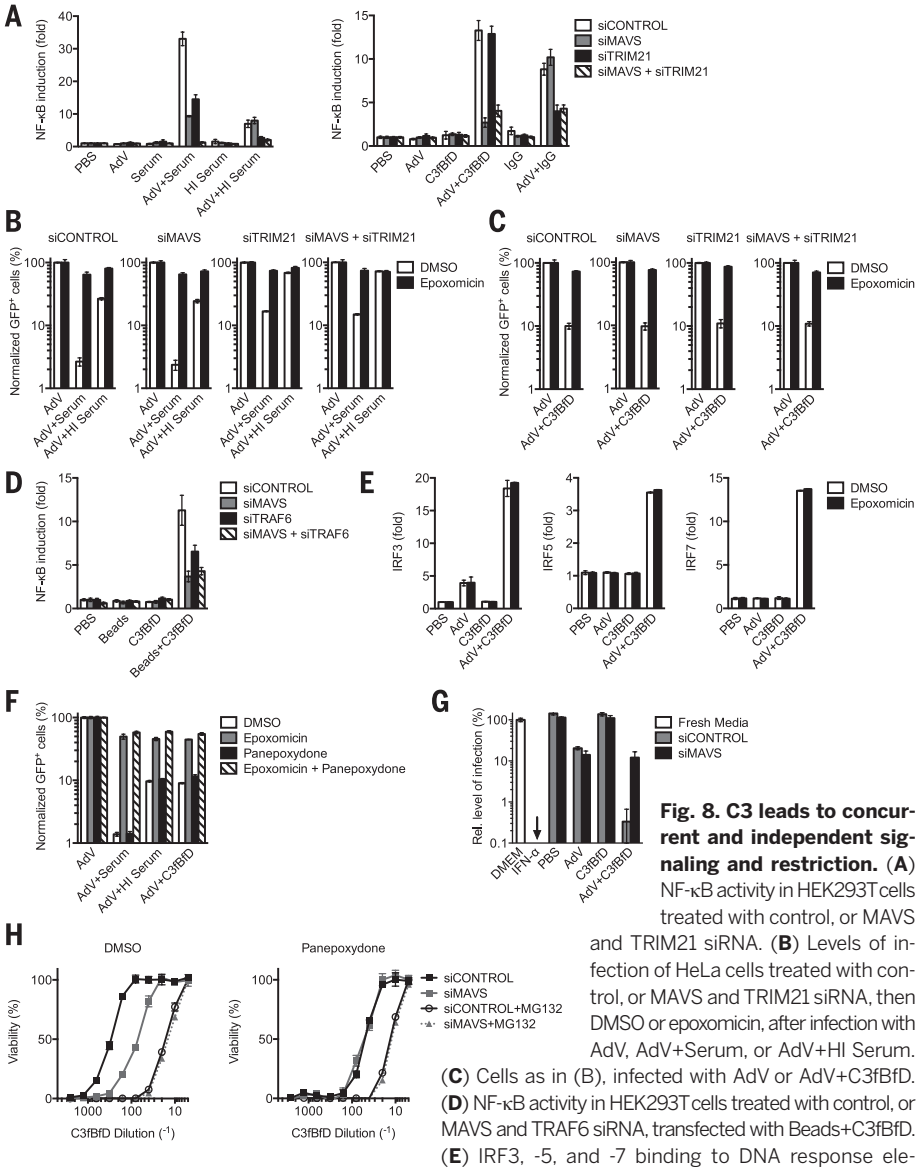

Fig. 8. C3 leads to concurrent and independent signaling and restriction. (**A**) NF-κB activity in HEK293T cells treated with control, or MAVS and TRIM21 siRNA. (**B**) Levels of infection of HeLa cells treated with control, or MAVS and TRIM21 siRNA, then DMSO or epoxomicin, after infection with AdV, AdV+Serum, or AdV+HI Serum. (**C**) Cells as in (B), infected with AdV or AdV+C3fBfD. (**D**) NF-κB activity in HEK293T cells treated with control, or MAVS and TRAF6 siRNA, transfected with Beads+C3fBfD. (**E**) IRF3, -5, and -7 binding to DNA response elements in HEK293T cells treated with DMSO or epoxomicin. (**F**) Levels of infection of HeLa cells treated with DMSO or epoxomicin and panepoxydone after challenge with AdV, treated as indicated. (**G**) Relative level of Sindbis infection of HeLa cells in the presence of fresh medium (DMEM), medium with IFN-α, or supernatant from cells treated with control or MAVS siRNA, challenged with PBS or AdV and C3fBfD. (**H**) Viability of HeLa cells challenged with dilutions of C3fBfD in a spreading HRV infection assay. Cells were treated with control or MAVS siRNA, then with DMSO, MG132, or panepoxydone. Data are representative of three experiments; results in (A) to (G) are mean ± SEM; data in (H) are mean ± SEM.

TRIM21 (*1*, *4*), and tetherin (*48*, *49*). These systems allow the cell to capitalize on a single sensing event to elicit multiple immune responses.

Materials and methods

Cells

HEK293T, HeLa, Vero, Caco-2, FEA, MDCK II, and MEF cell lines were maintained in Dulbecco's Modified Eagle Medium (DMEM) supplemented with 10% fetal calf serum, 100 U/ml penicillin, and 100 μg/ml streptomycin. MEF cells were obtained from C57BL/6 mice as in (*5*). THP-1 cells were maintained in RPMI-FCS with penicillin/streptomycin as above and 20 nM 12-*O*-tetradecanoylphorbol-13-acetate (TPA). NHLFs from Lonza (Basel, Switzerland) were maintained in Fibroblast Growth Medium 2 (Lonza), supplemented with 10% fetal calf serum, 0.1% insulin, 0.1% amphotericin-B, and 0.1% gentamicin according to the manufacturer's instructions.

Viruses and bacteria

E1- and E3-deleted adenovirus vector bearing a GFP transgene (AdV) was from Viraquest (North Liberty, Iowa). WT AdV, HRV, PV, and enterovirus 71 (EV71) were all from ATCC (Manassas, Virginia) and grown in HeLa cells, and cell-free supernatant was harvested and frozen 8 days after infection. HPV 16 L1/L2 virus-like particles were produced with plasmids from M. Müller, German Cancer Research Center, following the protocol of Buck and Thompson (*50*). Human Astrovirus 1 molecular clone pAVIC (hAstV) (*51*) was provided by I. Goodfellow, University of Cambridge, and recovered following the method of Fuentes *et al.* (*52*). Respiratory syncytial virus GFP-expressing molecular clone rgRSV(224) (RSV) (*53*) was provided by M. Peeples, Ohio State University. RSV was expanded in HeLa cells and harvested 2 days after infection. Feline calicivirus strain F9 (FCV) was provided by D. Brown, University of Cambridge. FCV was expanded in FEA cells and harvested 24 hours after infection. Coxsackie virus B3 molecular clone expressing a GFP transgene (CVB), eGFP-CVB3 (*54*), was obtained from J. L. Whitton, Scripps Institute. Sindbis virus–GFP (Sindbis) vector was produced by means of in vitro transcription of linearized plasmids DH-BB and pSin-eGFP with mMessage mMachine SP6 kit (Life Technologies, Carlsbad, California) and transfection of RNA into HEK293T cells with Lipofectamine 2000. WT AdV, HRV, and CVB were prepared by means of CsCl banding (*4*), and HPV was prepared by means of banding in OptiPrep (Sigma-Aldrich, St Louis, Missouri). PV, EV71, hAstV, RSV, and Sindbis were used directly from cell-free supernatant, with FCV by pelleting cell-free supernatant through 30% sucrose. Viruses were quantified by the median tissue culture infectious dose ($TCID_{50}$) method, or GFP where possible. Wild-type (strain 12023) or ΔsifA *Salmonella enterica enterica* serovar Typhimurium were prepared as in (*1*).

Serum and serum treatments

Normal human serum (Serum) as well as the complement series–depleted serum (Serum-C1, -C2, -C3, -C5, and -C6) were obtained from Sigma. Rabbit serum was also obtained from Sigma. Antibody-depleted serum (Serum-Ig), with the control serum were from SCIPAC (Kent, UK). Serum depleted of C4 (Serum-C4), factor B (Serum-fB), and factor D (Serum-fD), along with matching control serum, was from Quidel (San Diego, California). Mouse and cat serum were from Equitech Bio (Kerrville, Texas). Heat inactivation was carried out at 52°C for 45 min. EGTA treatment was performed by adding 0.2 M EGTA in 0.2 M $MgCl_2$. Purified complement C3, factor B, and factor D were from Millipore (Billerica, Massachusetts). Cobra venom factor (CVF) was purified from *Naja naja kaouthia* venom (MP Biomedicals, Santa Ana, California) by using the method of Vogel and Muller-Eberhard (*55*). Recombinant human rhinovirus 3C protease was from Expedeon (Cambridgeshire, UK), and recombinant poliovirus 3C protease was prepared by I. Goodfellow, University of Cambridge. Serum was used at the maximum concentration that had no impact on entry, as found by the endosomal disruption assay (typically 1/5 to 1/10 dilutions in PBS), with depleted serum verified by using sheep red blood cell hemolysis assays (*56*).

Antibodies

Serum components binding to AdV ELISAs—goat anti-human IgM HRP, goat anti-human IgA HRP, goat anti-human IgG HRP, mouse anti-human IgD HRP, and mouse anti-human IgE HRP—were obtained from Abcam (Cambridge, UK). Detection of human C3b, C4b, Mannan-binding lectin, and C-reactive protein were modified from ELISA detection kits from Abcam. Pentraxin 3 detection was by means of modified ELISA kits from Hycult Biotech (Uden, Netherlands). Immunoblot of CD11b, CD11c, CD18, CD35, CD46, CD55, p62, and complement C3 was by antibodies from Abcam. Immunoblot of RIG-I, MDA5, phosphorylated IKK, total IKK, phosphorylated IκB, total IκB, phospshorylated NF-κB p65, total p65, TRAF2, TRAF3, TRAF5, TRAF6, and glyceraldehyde-3-phosphate dehydrogenase (GAPDH) (loading control) used antibodies from Cell Signaling Technologies (Beverly, Massachusetts). Immunoblot for STING and MAVS used antibodies from Santa Cruz Biotechnology (Dallas, Texas). Immunoblot and immunofluorescence for AdV hexon used polyclonal goat anti-adenovirus 5 antibody from Millipore. Immunofluoresence was performed by using MAVS and TOM20 antibodies from Santa Cruz Biotechnology.

siRNA knockdown

TRIM21 siRNA was carried out as in (*4*). siRNA against RIG-I, MDA-5, STING, MAVS, TBK1, TRAF2, TRAF3, TRAF5, and TRAF6 were from Santa Cruz Biotechnology. siRNA against CD46 and CD55 were from Origene (Rockville, Maryland). p62 siRNA was from Life Technologies. siRNA was transfected by using RNAiMAX from Life Technologies.

Inhibitors

Pepinh-MyD and Pepinh-TRIF (Invivogen, Toulouse, France) were used alongside the supplied control peptide at 50 μM. One μM 5Z-7-Oxozaeanol (Sigma), 2 μg/ml panepoxydone (Enzo Life Sciences, Exeter, UK), 200 nM IKK Inhibitor VII (Millipore), 1 μM Bafilomycin A1 (Santa Cruz Biotechnology), 20 nM CID1067700 (Millipore), and Epoxomicin (Millipore) was added at 2 μM. KU55933 (Millipore) was used at 10 μM, Gö6976 (Millipore) was used at 5 μM, DBeQ (BioVision, Milpitas, California) was used at 8 μM, and rupintrivir (Santa Cruz Biotechnology) was used at 2 μM. All were added 1 hour before infection.

Plasmids and reporter constructs

Luciferase reporter cell lines were produced by transfection of pGL4.32 NF-κB (Promega, Fitchburg, Wisconsin). NHLFs were transduced with Cignal Lenti NF-κB (Qiagen, Hilden, Germany). Minimal-CMV promoter–driven nano-luciferase plasmid, pNL1.1CMV, was from Promega. Expression constructs for HRV 3C Protease and PV 3C Protease were from Origene. Flag-MAVS was cloned into pcDNA3.1(+) by using NotI and XhoI primers: forward 5′- ACGTGCGGCCGCCACCATGGACTACAAAGACGATGACGACAAGATGCCGTTTGCTGAAGACAAGAC-3′ and reverse 5′-GGCGTCTGCACTAGTGACTCGAGTCTA-3′. Plasmids were transfected by using Lipofectamine 2000 (Life Technologies).

Luciferase reporter assay

Cells were plated at 1×10^4 per well in 96 well plates. The day after plating, virus and serum were incubated 1:1 for 1 hour before addition to cells. Viruses were added at the following titers: AdV, 1.5×10^6 IU per well; WT AdV, 4.22×10^6 IU per well; HPV, L1/L2 protein at 1.92 μg per well; hAstV, 7.5×10^5 IU per well; FCV, 2.8×10^5 IU per well; HRV, 3.16×10^6 IU per well; PV, 2.0×10^6 IU per well; CVB, 2.0×10^6 IU per well; EV71, 2.0×10^5 IU per well; and RSV, 2.0×10^5 IU per well. For positive controls, 10 pg/ml recombinant TNF or 50 pg/ml LPS was used. Cells were incubated for 6 hours (18 hours for HPV) at 37°C before addition of Steadylite Plus luciferase reagent (Perkin Elmer, Waltham, Massachusetts) and reading on a BMG Pherastar FS platereader. For assays involving pelleting, AdV and PBS or serum were mixed before layering onto 30% sucrose and spinning for 4 hours at 28,000 x g at 4°C, resuspending pellet in PBS. For transfection of beads, 0.25 μm biotin-coated latex beads (Sigma) were incubated with 500 μg/ml C3, factor B, and factor D (Sigma) or PBS for 1 hour. Beads were transfected by using Lipofectamine 2000 (Life Technologies). For infections with *S. Typhimurium*, overnight stationary phase cultures were diluted 1/33 into 5 ml of fresh LB medium and grown at 37°C, 400 rpm for 3.5 hours. A 1/500 dilution of these cultures was incubated with 250 μg/ml C3, factor B, and factor D for 15 min before addition of a 10 μl mix onto cells. Luciferase was read 7 hours after infection.

ELISAs

Serum-binding ELISAs carried out incubating AdV+Serum for 1 hour before ultracentrifugation at 28,000 x g for 4 hours at 4°C through 30% sucrose. The pellet was resuspended in PBS before binding to polystyrene high-binding Microlon plates (Greiner-Bio-One, Frickenhausen, Germany) overnight, blocking for 2 hours with Marvel, before addition of serum. Quantification was carried out by using kits listed in antibodies section, with subtraction of signal from Marvel-blocked wells. NHLF cells were plated and infected in the same manner as for luciferase reporter assays. Cells were fixed with 4% paraformaldehyde and permeabilized with 0.1% Triton-X100 in the plate 4 hours after infection, and abundance of phosphorylated proteins was measured by using the NF-κB signaling kit (Cell Signaling Technologies). For analysis of cytokine production, supernatant was harvested 24 hours after infection and analyzed by means of ELISA kits: IL-6 (Life Technologies), TNF (Life Technologies), CCL4 (Abnova, Taipei City, Taiwan), and IFN-β (Life Technologies). Plates were read by using a SpectraMAX 340PC (Molecular Devices, Sunnyvale, California) at 450 and 650 nm.

Endosomal disruption assay

Endosomal disruption assay was modified from Seth *et al.* (*57*). Cells were plated at 1×10^4 per well in 96 well plates, in DMEM containing 12 μg/ml pNL1.1CMV (Promega). Virus mixes were added as for the NF-κB reporter. Cells were left for 18 hours after infection at 37°C, before addition of NanoLuc reagent (Promega) and reading on a BMG Pherastar FS platereader.

Confocal microscopy

For intracellular C3 visualization, HeLa cells were plated on glass coverslips and permitted to adhere overnight. Purified C3 was labeled with Alexa-Fluor488-SDP Ester (Life Technologies) at 4°C for 2 hours, before storage at –80°C. AdV was incubated with 250 μg/ml labeled C3, factor B, and factor D for 15 min before infection for 30 min. For MAVS activation visualization, HEK293T cells were transfected with pcDNA3.1-EV or pcDNA3.1-FLAG-MAVS 48 hours before infection by using Fugene 6. Cells were plated on glass coverslips pretreated with CellTak (Becton Dickinson, Franklin Lakes, New Jersey) and permitted to adhere overnight. AdV was incubated with 250 μg/ml of C3, factor B, and factor D; or AdV was incubated with PBS; or C3, factor B, and factor D were incubated alone for 1 hour before addition to cells for 6 hours. Cells were washed and fixed with 4% paraformaldehyde, before permeabilization with 0.1% Triton X-100 and blocking with 5% bovine serum albumin (BSA). Immunostaining for AdV was by anti-adenovirus 5 goat polyclonal antibody (Millipore), MAVS was by mouse monoclonal (Santa Cruz Biotechnology), and TOM20 was by a rabbit polyclonal (Santa Cruz Biotechnology). Coverslips were mounted on medium containing 4' 6-diamidino-2-phenylindole (DAPI) and imaged by using a Zeiss 63X objective on a Jena LSM 710 microscope (Carl Zeiss MicroImaging, Oberkochen, Germany).

Neutralization assay

HeLa cells were plated at 1×10^5 per well in 6 well plates. The day after plating, AdV and sera were incubated 1:1 for 1 hour before addition to cells. AdV was infected with 3.75×10^4 IU per well. Eighteen hours after infection, cells were harvested and GFP positive cells enumerated by means of flow cytometry by using a BD FACS Calibur 2. IFN treatment was with addition of 1000 U/ml Interferon-α (Sigma) 24 hours before infection.

Fate-of-capsid experiment

HeLa cells were plated at 1×10^5 per well in 6 well plates. The day after plating, AdV and sera were incubated 1:1 for 1 hour before addition to cells. AdV was infected with 7.5×10^4 IU per well. Cells were harvested by scraping at 0, 1, 2, 4, and 6 hours after infection, followed by immunoblot for AdV.

MAVS aggregation

MAVS aggregation was carried out as previously described by Hou *et al.* (*35*). Briefly, HEK293T cells were challenged with PBS, AdV, C3fBfD, or AdV+C3fBfD for 6 hours, after which they were harvested, and mitochondrial extracts were produced by douncing and ultracentrifugation. HEK293T cells expressing Flag-MAVS was harvested 3 days after transfection. Samples were

controlled for total protein and ran in Tris-Acetate gels as semidenaturing gel electrophoresis, with immunoblot carried out for MAVS.

Transfer of media experiment

Sindbis experiment was carried out as previously described (*1*). Briefly, HeLa cells were infected with PBS, AdV, C3fBfD, or AdV+C3fBfD. Cell supernatant was collected 3 days after challenge and used to treat fresh "reporter" HeLa cells. Other reporter HeLa cells were provided fresh media (DMEM) or were stimulated with 1000 U/ml Interferon-α (Sigma). The following day, cells were infected with Sindbis virus at multiplicity of infection = 0.3, before enumeration of GFP-positive cells 1 day after infection.

Restricting titer experiment

Cells were plated at 5×10^3 per well in 96 well plates. Serial dilutions of 250 μg/ml C3, factor B, and factor D were incubated with 20× $TCID_{50}$ units HRV for 1 hour before addition to cells. DMSO, MG132, or panepoxydone were added 1 hour before infection, and cells were washed 16 hours after infection into DMEM supplemented with 2% fetal calf serum. Seven days after infection, a MTT [3-(4,5-dimethylthiazol-2-yl)-2,5-diphenyltetrazolium bromide] assay (Sigma) was performed, permeabilizing cells by DMSO, measuring absorbance with a SpectraMAX 340PC (Molecular Devices) at 540 nm.

REFERENCES AND NOTES

1. W. A. McEwan *et al*., Intracellular antibody-bound pathogens stimulate immune signaling via the Fc receptor TRIM21. *Nat. Immunol.* **14**, 327–336 (2013). doi: 10.1038/ni.2548; pmid: 23455675
2. R. E. Watkinson, J. C. H. Tam, M. J. Vaysburd, L. C. James, Simultaneous neutralization and innate immune detection of a replicating virus by TRIM21. *J. Virol.* **87**, 7309–7313 (2013). doi: 10.1128/JVI.00647-13; pmid: 23596308
3. F. Hauler, D. L. Mallery, W. A. McEwan, S. R. Bidgood, L. C. James, AAA ATPase p97/VCP is essential for TRIM21-mediated virus neutralization. *Proc. Natl. Acad. Sci. U.S.A.* **109**, 19733–19738 (2012). doi: 10.1073/pnas.1210659109; pmid: 23091005
4. D. L. Mallery *et al*., Antibodies mediate intracellular immunity through tripartite motif-containing 21 (TRIM21). *Proc. Natl. Acad. Sci. U.S.A.* **107**, 19985–19990 (2010). doi: 10.1073/pnas.1014074107; pmid: 21045130
5. W. A. McEwan *et al*., Regulation of virus neutralization and the persistent fraction by TRIM21. *J. Virol.* **86**, 8482–8491 (2012). doi: 10.1128/JVI.00728-12; pmid: 22647693
6. M. Vaysburd *et al*., Intracellular antibody receptor TRIM21 prevents fatal viral infection. *Proc. Natl. Acad. Sci. U.S.A.* **110**, 12397–12401 (2013). doi: 10.1073/pnas.1301918110; pmid: 23840060
7. M. J. Walport, Complement. First of two parts. *N. Engl. J. Med.* **344**, 1058–1066 (2001). pmid: 11287977
8. H. W. Favoreel, G. R. Van de Walle, H. J. Nauwynck, M. B. Pensaert, Virus complement evasion strategies. *J. Gen. Virol.* **84**, 1–15 (2003). doi: 10.1099/vir.0.18709-0; pmid: 12533696
9. D. M. Appledorn *et al*., Complex interactions with several arms of the complement system dictate innate and humoral immunity to adenoviral vectors. *Gene Ther.* **15**, 1606–1617 (2008). doi: 10.1038/gt.2008.114; pmid: 18615115
10. R. S. Bonaparte *et al*., Human astrovirus coat protein inhibits serum complement activation via C1, the first component of the classical pathway. *J. Virol.* **82**, 817–827 (2008). doi: 10.1128/JVI.01847-07; pmid: 17959658
11. Z. Xu *et al*., Coagulation factor X shields adenovirus type 5 from attack by natural antibodies and complement. *Nat. Med.* **19**, 452–457 (2013). doi: 10.1038/nm.3107; pmid: 23524342
12. S. H. Rooijakkers, W. J. van Wamel, M. Ruyken, K. P. van Kessel, J. A. van Strijp, Anti-opsonic properties of staphylokinase. *Microbes Infect.* **7**, 476–484 (2005). doi: 10.1016/j.micinf.2004.12.014; pmid: 15792635
13. P. C. Reading *et al*., Antiviral activity of the long chain pentraxin PTX3 against influenza viruses. *J. Immunol.* **180**, 3391–3398 (2008). doi: 10.4049/jimmunol.180.5.3391; pmid: 18292565
14. D. C. Fritzinger, R. Bredehorst, C. W. Vogel, Molecular cloning and derived primary structure of cobra venom factor. *Proc. Natl. Acad. Sci. U.S.A.* **91**, 12775–12779 (1994). doi: 10.1073/pnas.91.26.12775; pmid: 7809120
15. P. F. Zipfel, C. Skerka, Complement regulators and inhibitory proteins. *Nat. Rev. Immunol.* **9**, 729–740 (2009). pmid: 19730437
16. O. Meier, U. F. Greber, Adenovirus endocytosis. *J. Gene Med.* **6** (suppl. 1), S152–S163 (2004). doi: 10.1002/jgm.553; pmid: 14978758
17. J. O. Agola *et al*., A competitive nucleotide binding inhibitor: In vitro characterization of Rab7 GTPase inhibition. *ACS Chem. Biol.* **7**, 1095–1108 (2012). doi: 10.1021/cb3001099; pmid: 22486388
18. G. Meiffren *et al*., Pathogen recognition by the cell surface receptor CD46 induces autophagy. *Autophagy* **6**, 299–300 (2010). doi: 10.4161/auto.6.2.11132; pmid: 20087059
19. T. Farkas, M. Daugaard, M. Jäättelä, Identification of small molecule inhibitors of phosphatidylinositol 3-kinase and autophagy. *J. Biol. Chem.* **286**, 38904–38912 (2011). doi: 10.1074/jbc.M111.269134; pmid: 21930714
20. D. B. Stetson, R. Medzhitov, Type I interferons in host defense. *Immunity* **25**, 373–381 (2006). doi: 10.1016/j.immuni.2006.08.007; pmid: 16979569
21. J. J. Houle, E. M. Hoffmann, Evidence for restriction of the ability of complement to lyse homologous erythrocytes. *J. Immunol.* **133**, 1444–1452 (1984).pmid: 6430999
22. C. L. Harris, O. B. Spiller, B. P. Morgan, Human and rodent decay-accelerating factors (CD55) are not species restricted in their complement-inhibiting activities. *Immunology* **100**, 462–470 (2000). doi: 10.1046/j.1365-2567.2000.00066.x; pmid: 10929073
23. P. Seth, Mechanism of adenovirus-mediated endosome lysis: Role of the intact adenovirus capsid structure. *Biochem. Biophys. Res. Commun.* **205**, 1318–1324 (1994). doi: 10.1006/bbrc.1994.2809; pmid: 7802664
24. D. Schober, P. Kronenberger, E. Prchla, D. Blaas, R. Fuchs, Major and minor receptor group human rhinoviruses penetrate from endosomes by different mechanisms. *J. Virol.* **72**, 1354–1364 (1998). pmid: 9445036
25. B. Brandenburg *et al*., Imaging poliovirus entry in live cells. *PLOS Biol.* **5**, e183 (2007). doi: 10.1371/journal.pbio.0050183; pmid: 17622193
26. J. J. Seitsonen *et al*., Structural analysis of coxsackievirus A7 reveals conformational changes associated with uncoating. *J. Virol.* **86**, 7207–7215 (2012). doi: 10.1128/JVI.06425-11; pmid: 22514349
27. E. C. Smith, A. Popa, A. Chang, C. Masante, R. E. Dutch, Viral entry mechanisms: The increasing diversity of paramyxovirus entry. *FEBS J.* **276**, 7217–7227 (2009). doi: 10.1111/j.1742-4658.2009.07401.x; pmid: 19878307
28. C. L. Birmingham, J. H. Brumell, Autophagy recognizes intracellular *Salmonella enterica* serovar Typhimurium in damaged vacuoles. *Autophagy* **2**, 156–158 (2006). doi: 10.4161/auto.2825; pmid: 16874057
29. C. R. Beuzón, S. P. Salcedo, D. W. Holden, Growth and killing of a *Salmonella enterica* serovar Typhimurium sifA mutant strain in the cytosol of different host cell lines. *Microbiology* **148**, 2705–2715 (2002). pmid: 12213917
30. R. S. Harris, J. F. Hultquist, D. T. Evans, The restriction factors of human immunodeficiency virus. *J. Biol. Chem.* **287**, 40875–40883 (2012). doi: 10.1074/jbc.R112.416925; pmid: 23043100
31. P. M. Barral, D. Sarkar, P. B. Fisher, V. R. Racaniello, RIG-I is cleaved during picornavirus infection. *Virology* **391**, 171–176 (2009). doi: 10.1016/j.virol.2009.06.045; pmid: 19628239
32. N. Blom, J. Hansen, S. Brunak, D. Blaas, Cleavage site analysis in picornaviral polyproteins: Discovering cellular targets by neural networks. *Protein Sci.* **5**, 2203–2216 (1996). doi: 10.1002/pro.5560051107; pmid: 8931139
33. A. K. Patick *et al*., In vitro antiviral activity of AG7088, a potent inhibitor of human rhinovirus 3C protease. *Antimicrob. Agents Chemother.* **43**, 2444–2450 (1999). pmid: 10508022
34. A. Gradi, Y. V. Svitkin, H. Imataka, N. Sonenberg, Proteolysis of human eukaryotic translation initiation factor eIF4GII, but not eIF4GI, coincides with the shutoff of host protein synthesis after poliovirus infection. *Proc. Natl. Acad. Sci. U.S.A.* **95**, 11089–11094 (1998). doi: 10.1073/pnas.95.19.11089; pmid: 9736694
35. F. Hou *et al*., MAVS forms functional prion-like aggregates to activate and propagate antiviral innate immune response. *Cell* **146**, 448–461 (2011). doi: 10.1016/j.cell.2011.06.041; pmid: 21782231
36. S. Paz *et al*., Ubiquitin-regulated recruitment of IκB kinase epsilon to the MAVS interferon signaling adapter. *Mol. Cell. Biol.* **29**, 3401–3412 (2009). doi: 10.1128/MCB.00880-08; pmid: 19380491
37. R. B. Seth, L. Sun, C. K. Ea, Z. J. Chen, Identification and characterization of MAVS, a mitochondrial antiviral signaling protein that activates NF-κB and IRF 3. *Cell* **122**, 669–682 (2005). doi: 10.1016/j.cell.2005.08.012 pmid: 16125763
38. S. Liu *et al*., MAVS recruits multiple ubiquitin E3 ligases to activate antiviral signaling cascades. *eLife* **2**, e00785 (2013). doi: 10.7554/eLife.00785; pmid: 23951545
39. L. Sanz, M. T. Diaz-Meco, H. Nakano, J. Moscat, The atypical PKC-interacting protein p62 channels NF-κB activation by the IL-1-TRAF6 pathway. *EMBO J.* **19**, 1576–1586 (2000). doi: 10.1093/emboj/19.7.1576; pmid: 10747026
40. K. Clark, L. Plater, M. Peggie, P. Cohen, Use of the pharmacological inhibitor BX795 to study the regulation and physiological roles of TBK1 and IκB kinase epsilon: A distinct upstream kinase mediates Ser-172 phosphorylation and activation. *J. Biol. Chem.* **284**, 14136–14146 (2009). doi: 10.1074/jbc.M109.000414; pmid: 19307177
41. J. G. Gallagher, N. Khoobyarian, Adenovirus susceptibility to human interferon during one-step replication. *Infect. Immun.* **5**, 905–908 (1972).pmid: 4344095
42. P. E. Came, T. W. Schafer, G. H. Silver, Sensitivity of rhinoviruses to human leukocyte and fibroblast interferons. *J. Infect. Dis.* **133** A136–A139 (1976). doi: 10.1093/infdis/133.Supplement_2.A136; pmid: 180194
43. T. Pertel *et al*., TRIM5 is an innate immune sensor for the retrovirus capsid lattice. *Nature* **472**, 361–365 (2011). doi: 10.1038/nature09976; pmid: 21512573
44. J. Bode *et al*., A new role of the complement system: C3 provides protection in a mouse model of lung infection with intracellular *Chlamydia psittaci*. *PLOS One* **7**, e50327 (2012). doi: 10.1371/journal.pone.0050327; pmid: 23189195
45. Y. Wang, X. Tong, J. Zhang, X. Ye, The complement C1qA enhances retinoic acid-inducible gene-I-mediated immune signalling. *Immunology* **136**, 78–85 (2012). doi: 10.1111/j.1365-2567.2012.03561.x; pmid: 22260551
46. L. S. Zalman *et al*., Inhibition of human rhinovirus-induced cytokine production by AG7088, a human rhinovirus 3C protease inhibitor. *Antimicrob. Agents Chemother.* **44**, 1236–1241 (2000). doi: 10.1128/AAC.44.5.1236-1241.2000; pmid: 10770757
47. M. Stremlau *et al*., The cytoplasmic body component TRIM5alpha restricts HIV-1 infection in Old World monkeys. *Nature* **427**, 848–853 (2004). doi: 10.1038/nature02343; pmid: 14985764
48. R. P. Galão, A. Le Tortorec, S. Pickering, T. Kueck, S. J. Neil, Innate sensing of HIV-1 assembly by Tetherin induces NFκB-dependent proinflammatory responses. *Cell Host Microbe* **12**, 633–644 (2012). doi: 10.1016/j.chom.2012.10.007; pmid: 23159053
49. S. J. Neil, T. Zang, P. D. Bieniasz, Tetherin inhibits retrovirus release and is antagonized by HIV-1 Vpu. *Nature* **451**, 425–430 (2008). doi: 10.1038/nature06553; pmid: 18200009
50. C. B. Buck, C. D. Thompson, Production of papillomavirus-based gene transfer vectors. *Curr. Protoc. Cell Biol.* **26**, 26.1 (2007).
51. U. Geigenmüller, N. H. Ginzton, S. M. Matsui, Construction of a genome-length cDNA clone for human astrovirus serotype 1 and synthesis of infectious RNA transcripts. *J. Virol.* **71**, 1713–1717 (1997).pmid: 8995706
52. C. Fuentes, A. Bosch, R. M. Pintó, S. Guix, Identification of human astrovirus genome-linked protein (VPg) essential for virus infectivity. *J. Virol.* **86**, 10070–10078 (2012). doi: 10.1128/JVI.00797-12; pmid: 22787221
53. L. K. Hallak, D. Spillmann, P. L. Collins, M. E. Peeples, Glycosaminoglycan sulfation requirements for respiratory syncytial virus infection. *J. Virol.* **74**, 10508–10513 (2000). doi: 10.1128/JVI.74.22.10508-10513.2000 pmid: 11044095
54. R. Feuer, I. Mena, R. Pagarigan, M. K. Slifka, J. L. Whitton, Cell cycle status affects coxsackievirus replication, persistence,

and reactivation in vitro. *J. Virol.* **76**, 4430–4440 (2002). doi: 10.1128/JVI.76.9.4430-4440.2002 pmid: 11932410
55. C. W. Vogel, H. J. Müller-Eberhand, Cobra venom factor: Improved method for purification and biochemical characterization. *J. Immunol. Methods* **73**, 203–220 (1984). doi: 10.1016/0022-1759(84)90045-0 pmid: 6491300
56. M. Costabile, Measuring the 50% haemolytic complement (CH50) activity of serum. *J. Vis. Exp.* **37**, 1923 (2010). pmid: 20351687
57. P. Seth, M. Rosenfeld, J. Higginbotham, R. G. Crystal, Mechanism of enhancement of DNA expression consequent to cointernalization of a replication-deficient adenovirus and unmodified plasmid DNA. *J. Virol.* **68**, 933–940 (1994). pmid: 7507187

ACKNOWLEDGMENTS

We thank I. Goodfellow for the kind gift of reagents, including the Caco-2 cell line, human Astrovirus-1 infectious clone pAVIC, and PV 3C protease. This work was funded by the Medical Research Council (UK; U105181010), the European Research Council (281627IAI), and the Frank Edward Elmore Fund of the University of Cambridge School of Clinical Medicine (J.C.H.T.). The data are presented in the main manuscript and the supplementary materials.

SUPPLEMENTARY MATERIALS

www.sciencemag.org/content/345/6201/1256070/suppl/DC1
Figs. S1 and S2

14 May 2014; accepted 8 July 2014
10.1126/science.1256070

RESEARCH ARTICLES

DYNAMIC ORDERING

Topology and dynamics of active nematic vesicles

Felix C. Keber,[1,2]* Etienne Loiseau,[1]* Tim Sanchez,[3]* Stephen J. DeCamp,[3] Luca Giomi,[4,5] Mark J. Bowick,[6] M. Cristina Marchetti,[6] Zvonimir Dogic,[2,3] Andreas R. Bausch[1]†

Engineering synthetic materials that mimic the remarkable complexity of living organisms is a fundamental challenge in science and technology. We studied the spatiotemporal patterns that emerge when an active nematic film of microtubules and molecular motors is encapsulated within a shape-changing lipid vesicle. Unlike in equilibrium systems, where defects are largely static structures, in active nematics defects move spontaneously and can be described as self-propelled particles. The combination of activity, topological constraints, and vesicle deformability produces a myriad of dynamical states. We highlight two dynamical modes: a tunable periodic state that oscillates between two defect configurations, and shape-changing vesicles with streaming filopodia-like protrusions. These results demonstrate how biomimetic materials can be obtained when topological constraints are used to control the non-equilibrium dynamics of active matter.

Fundamental topological laws prove that it is not possible to wrap a curved surface with lines without encountering at least one singular point where the line is ill defined. This mathematical result is familiar from everyday experience. Common examples are decorating Earth's surface with lines of longitude or latitude or covering a human hand with parallel papillary ridges (fingerprints). Both require the formation of singular points known as topological defects (*1*). The same mathematical considerations apply when assembling materials on microscopic length scales. Nematic liquid crystals are materials whose constituent rod-like molecules align spontaneously along a preferred orientation that is locally described by the director (line) field. Covering a sphere with a nematic leads to the formation of topological defects called disclinations. Mathematics dictates that the net topological charge of all defects on a spherical nematic must add up to +2, where a charge of s denotes a defect that rotates the director field by $2\pi s$. The basic nematic defects have charge +½ or −½, corresponding to a π rotation of the director field in the same sense or the opposite sense, respectively, as that of any closed path encircling the defect (*2*–*6*). Defects on topologically constrained geometries can acquire highly complex and tunable spatial arrangements, which can drive assembly of intriguing higher-order hierarchical materials (*7*, *8*). For this reason, combining conventional soft materials with topological constraints has emerged as a promising platform for organizing matter on micrometer length scales. So far, most studies in this area have focused on investigating equilibrium materials confined on rigid nondeformable surfaces of varying topology (*9*–*17*). Equilibrium statistical mechanics imposes tight constraints on the properties of such topological soft materials, which can acquire remarkable spatial complexity but cannot sustain persistent temporal dynamics.

Recent advances have enabled the assembly of active nematic liquid crystals in which the constituent rod-like building blocks continuously convert chemical energy into mechanical motion (*18*–*20*). Such materials are no longer constrained by the laws of equilibrium statistical mechanics. Consequently, unconfined active nematics exhibit highly sought-after properties such as spontaneous chaotic flows that are tightly coupled to continuously generating and annihilating motile defects (*21*–*23*). We have merged active nematics with soft topological constraints to create topological active matter. Microtubule-based active nematics were confined onto a deformable spherical surface provided by a lipid vesicle. Similar to well-studied equilibrium nematics confined on a sphere, topology requires the formation of defects with a net topological charge of +2. In stark contrast to the equilibrium case, however, activity generated by energy-consuming kinesin motors endows the active nematic defects with motility. As a result, the complex spatial defect structure becomes dynamic and the active nematic vesicles are turned into robust colloidal clocks with tunable frequency. By controlling the vesicle tension, we coupled the oscillatory dynamics of the active nematic cortex to vesicle deformations, creating biomimetic shape-changing materials. Our experiments suggest a route for designing soft materials with controlled oscillatory dynamics. They further raise intriguing questions about how the dynamics of topological active matter can be enriched by increasing the complexity of the constraining surface, by controlling the nature of the synchronization transitions that occur in arrays of colloidal oscillators, and through the use of active crystals and other far-from-equilibrium materials (*24*).

Assembly of active nematic vesicles

We built on recent work by encapsulating active nematics into deformable vesicles. Active nematic vesicles encapsulating microtubules, kinesin motor clusters, and the nonadsorbing polymer polyethylene glycol (PEG) within a lipid vesicle were produced using an emulsion transfer technique (*25*). PEG induces adsorption of microtubule filaments onto the inner leaflet of the vesicle by the depletion mechanism (*26*). At high microtubule concentration, the entire vesicle surface is coated with a dense monolayer of extensile microtubule bundles, effectively creating a two-dimensional (2D) nematic cortex. Individual kinesin motors, fueled by energy from adenosine triphosphate (ATP) hydrolysis, processively move along a microtubule backbone at velocities up to 0.8 μm/s (*27*). When bound into multimotor clusters through a biotin-streptavidin linkage, kinesin clusters form cross-links with adjacent microtubules, inducing them to slide relative to each other and generating active extensile stresses (*19*, *28*, *29*). We image active nematic vesicles by confocal microscopy (*30*).

In equilibrium there are multiple defect arrangements that minimize the free energy of a 2D spherical nematic, with the exact configuration depending on the strength of the elastic constants. Under the assumption that the bend and splay elastic moduli are equal, the free energy is minimized when four +½ defects are located at the corners of a tetrahedron inscribed within the sphere (*2*, *3*, *5*). This configuration is favored because defects of the same charge repel each other. Placing them at the corners of a tetrahedron maximizes their separation, thus minimizing liquid crystal distortions. The 3D reconstruction of the surface-bound active nematic reveals the presence of four +½ disclination defects (Fig. 1), in agreement with theoretical predictions for equilibrium systems and previous experimental observations of spherical nematic shells of finite thickness (*4*).

Oscillating defect dynamics in active nematic vesicles

At finite ATP concentrations, active energy input provided by kinesin clusters drives the microtubule nematic far from equilibrium, yielding surprising dynamics. In planar nematics active stresses destabilize the homogeneous state (*31*–*33*) and generate self-sustained streaming flows, with the continuous creation and annihilation of motile defects that interact through elastic and hydrodynamic forces (*19*, *21*–*23*). When the nematic film is confined to the surface of a sphere, active

[1]Department of Physics, Technische Universität München, 85748 Garching, Germany. [2]Institute for Advanced Study, Technische Universität München, 85748 Garching, Germany. [3]Department of Physics, Brandeis University, Waltham, MA 02474, USA. [4]SISSA International School for Advanced Studies, Via Bonomea 265, 34136 Trieste, Italy. [5]Instituut-Lorentz for Theoretical Physics, Leiden University, 2333 CA Leiden, Netherlands. [6]Physics Department and Syracuse Biomaterials Institute, Syracuse University, Syracuse, NY 13244, USA.
*These authors contributed equally to this work. †Corresponding author. E-mail: abausch@mytum.de

unbalanced stresses drive motility of the four +½ surface-bound disclinations, which leads to streaming flows of the entire vesicle (Fig. 1 and movie S1). The dynamics of spherical active nematics is simpler than that of their planar counterpart, as the four +½ defects on spherical nematics never disappear and their lifetime is limited only by the vesicle stability. Furthermore, the spatial confinement used in our experiments suppresses the production of additional defect pairs, thus providing a unique opportunity to study the dynamics of a few isolated interacting defects in a controlled way. We speculate that the defect proliferation seen in planar nematics does not occur in our vesicles because they are too small. In all cases, the vesicles' diameter is well below the length scale ℓ_a at which the homogeneously ordered system is unstable to bend deformations. For microtubule-based planar active nematics, ℓ_a is estimated to be ~100 μm (*19*).

Similar to the equilibrium case, the repulsive elastic interactions between four +½ disclinations in an active spherical nematic normally favor a tetrahedral defect configuration (*2*, *3*, *5*). In active systems, however, the asymmetric shape of comet-like +½ disclinations also generates active stresses and associated flows that in turn drive defect motion. For extensile systems, defects are propelled at constant speed toward the head of the comet (Fig. 1C) (*21*). It is not possible for the four defects to simultaneously minimize elastic repulsive interactions and move with a prescribed velocity determined by the ATP concentration while keeping their relative distance constant. As a result, defects move along complex spatiotemporal trajectories. To elucidate this emergent dynamics, we imaged the time evolution of active vesicles by confocal microscopy and traced the 3D position of the individual defects (Fig. 1 and movie S1). At any given time, the positions of the four defects are described by the variables α_{ij}, which denote the angle between radii from the vesicle center to each of the six defect pairs ij (Fig. 2A). For a tetrahedral configuration, all six angles are $\alpha_{ij} = 109.5°$, while for a planar configuration $\alpha_{12} = \alpha_{23} = \alpha_{34} = \alpha_{41} = 90°$ and $\alpha_{13} = \alpha_{24} = 180°$ (and permutations), resulting in an average angle of $\langle\alpha\rangle_{\text{planar}} = \frac{1}{6}\sum_{i<j=1}^{4}\alpha_{ij} = 120°$ (Fig. 2A). The temporal evolution of all six angles reveals a clear pattern of defect motion (Fig. 2B). For example, at time $t = 602$ s, two angles assume a large value near 180° while the other four are ~90°, indicating a planar configuration. Forty-three seconds later, this configuration switches to a tetrahedral configuration in which all angles are equal (Fig. 2D). Observations on longer time scales demonstrate that the defects repeatedly oscillate between the tetrahedral and planar configurations, with a well-defined characteristic frequency of 12 mHz (Fig. 2C). The frequency is set by the motor speed and the size of the sphere, and can be tuned by the ATP concentration, which determines the kinesin velocity (fig. S1) (*27*).

Particle-based theoretical model describes oscillatory dynamics of active nematic vesicles

The oscillatory dynamics of spherical nematics can be described by a coarse-grained theoretical model. As shown recently, +½ defects in extensile nematics behave as self-propelled particles with velocity v_0 proportional to activity and directed along the axis of symmetry $\mathbf{u}$ (Fig. 3A and fig. S2) (*10*). Each defect is then characterized by a position vector on the sphere $\mathbf{r}_i = \mathbf{r}_i(\theta, \varphi)$, where θ and φ are the spherical coordinates, and a unit vector $\mathbf{u}_i = (\cos\psi_i, \sin\psi_i)$ describing the orientation of the comet axis and directed from the tail to the head. In local coordinates $\mathbf{u}_i = \cos\psi_i\,\mathbf{e}_{\theta i} + \sin\psi_i\,\mathbf{e}_{\varphi i}$, where $\mathbf{e}_{\theta i}$ and $\mathbf{e}_{\varphi i}$ are unit vectors in the latitudinal and longitudinal directions, respectively, and ψ_i is the local orientation (fig. S3). Adapting the planar translational dynamics to the curved surface of the sphere, and augmenting it with the dynamics of orientation, the equations of motion of each defect are given by the overdamped Newton-Euler equations for a rigid body

$$\zeta_t\left(\frac{d\mathbf{r}_i}{dt} - v_0\mathbf{u}_i\right) = \mathbf{f}_i \qquad (1)$$

$$\zeta_r\frac{d\psi_i}{dt} = M_i \qquad (2)$$

where $\mathbf{f}_i = -dE/d\mathbf{r}_i$ and $M_i = -dE/d\psi_i$ are the force and torque on the ith defect due to the

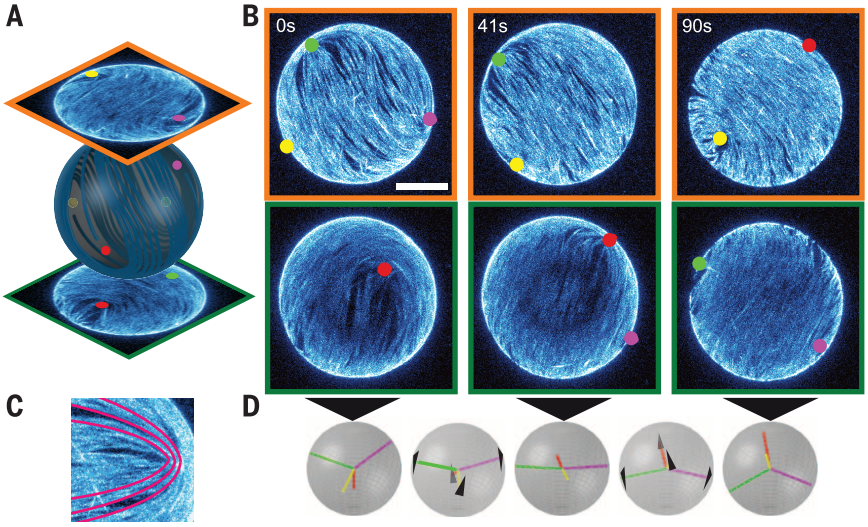

Fig. 1. Defect dynamics of an active nematic film on the surface of a spherical vesicle. (**A**) Hemisphere projection of a 3D confocal stack of a nematic vesicle. The positions of four +½ disclination defects are identified. (**B**) Time series of hemisphere projections over a single period of oscillation in which the four defects switch from tetrahedral ($t = 0$ s) through planar ($t = 41$ s) and back to tetrahedral ($t = 90$ s) configurations. Scale bar, 20 μm. (**C**) Comet-like +½ disclination defect with schematic of the orientation of the nematic director (red lines). (**D**) Schematic of the defect configurations at the time points of (B) and intermediate times ($t = 24$ s, $t = 65$ s). The black arrowheads indicate the direction of defect motion.

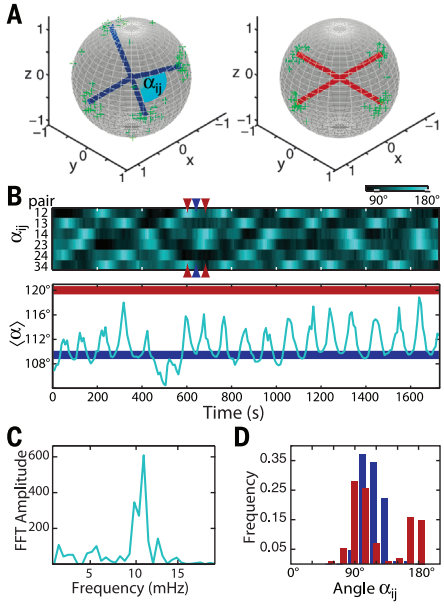

Fig. 2. Oscillatory dynamics of topological defects. (**A**) Tetrahedral (blue) and planar (red) defect configurations. The green scatterplots show the measured positions of the defects on the unit sphere at the extremal configurations. (**B**) Top: Kymograph showing the time evolution of angular distances α_{ij} of all six defect pairs [as indicated in (A)]. Bottom: The average angle oscillates between the tetrahedral configuration ($\langle\alpha\rangle = 109.5°$, blue line) and the planar configuration ($\langle\alpha\rangle = 120°$, red line). An exemplary transition between the two configurations is indicated by the colored arrowheads ($t = 602$ s, $t = 643$ s, $t = 684$ s). (**C**) Power spectrum of $\langle\alpha\rangle$. The peak at 12 mHz is associated with tetrahedral-planar oscillations. FFT, fast Fourier transform. (**D**) Distributions of angles α_{ij}. Gaussian fits return angles of 109° ± 13° for the tetrahedral configuration (blue) and 90° ± 12° and 163° ± 9° for the planar configuration (red).

repulsive interactions with the other three, with E the elastic energy of the defects, and ζ_t and ζ_r are translational and rotational frictions, respectively (*30*). The dynamical equations are solved numerically on the sphere, with defects initially randomly spaced along the equator and with random orientations. In equilibrium $v_0 = 0$ and the defects relax toward the minimum of their potential energy, with the four defects sitting at the vertices of a regular tetrahedron (Fig. 3B and fig. S4).

In the presence of activity, a finite v_0 allows the defects to escape from their minimal-energy configuration. This leads to an oscillatory dynamics characterized by a periodic motion of the defects between two symmetric tetrahedral configurations (Fig. 3, C and E), passing through an intermediate planar one (Fig. 3D). The oscillations arise from the competition between the active force $\zeta_t v_0 \mathbf{u}_i$ and the elastic force $\mathbf{f}_i$. The period is determined by the sum of the time scales for the defect to move uphill and downhill in the energy landscape (Fig. 3F, fig. S5, and movie S2). The period of the oscillations is equal to the time required for a defect to perform a full revolution around the sphere axis; thus, $T \approx 2\pi R/v_0$ and the frequency increases linearly with activity (fig. S6). Oscillations occur if the rotational dynamics is fast relative to the translational dynamics. For the defects to overshoot when they approach the minimum in the energy landscape, they need to quickly reorient before being attracted back into the energy minimum (fig. S7). The dynamics of the average angle $\langle\alpha\rangle$ (Fig. 3F) reproduces very closely our experimental findings (Fig. 2B).

Thus, the perpetual oscillatory dynamics of active nematic vesicles results from the interplay of topology, liquid crystalline order, and activity. The spherical topology of the vesicles imposes the existence of exactly four +½ defects with particle-like features. The entropic elasticity originating from the local nematic order shapes the energy landscape through which the defects move. Finally, activity powered by ATP hydrolysis fuels the defect motion. The outlined mechanism leads to robust oscillatory dynamics that survives the presence of noise, which is inevitable in the experimental system.

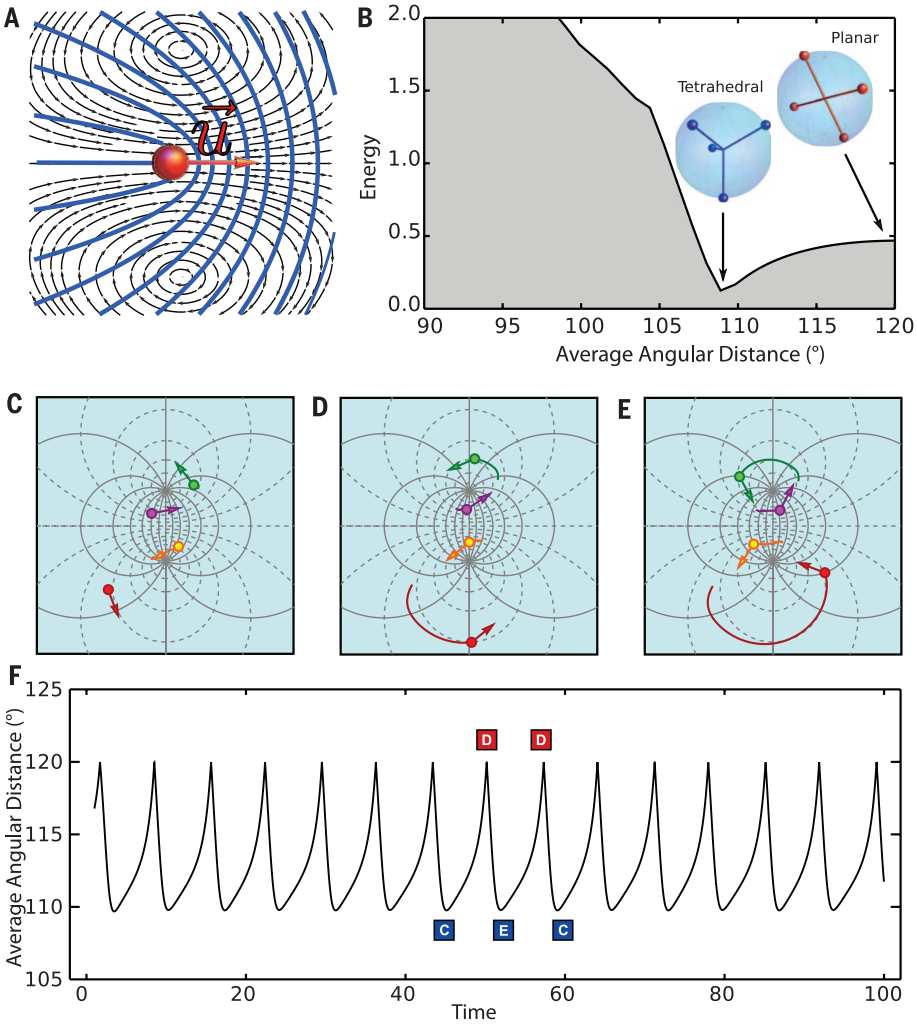

Fig. 3. A theoretical model that describes nematic defects as self-propelled particles predicts oscillatory dynamics. (**A**) Active +½ disclinations with an axis of symmetry **u** behave as self-propelled particles by generating a local flow (black lines) that convects the defect core toward the head of the comet-like structure described by the director field (blue lines). (**B**) In the absence of activity, four +½ sphere-bound disclinations relax toward the minimum of their potential energy, with the four defects sitting at the vertices of a regular tetrahedron. (**C** to **E**) For active nematics, the defects undergo a self-organized periodic motion: Starting from a passive equilibrium tetrahedral configuration (C), they pass through a planar configuration (D) on the way to another tetrahedral configuration (E) and then back again periodically. (**F**) The average angular distance $\langle\alpha\rangle$ as a function of time with asymmetric oscillations between a tetrahedral state [i.e., $\langle\alpha\rangle = 109.5°$, shown in (C) and (E)] and a planar state [i.e., $\langle\alpha\rangle = 120°$, shown in (D)]. The energy landscape reveals a minimum for the tetrahedral configuration and a maximum for the planar one. The average angle $\langle\alpha\rangle$ does not distinguish between the two equivalent alternating tetrahedra shown in (C) and (E). When described in terms of this coordinate, the dynamics oscillates from the minimum of the plot in (B) to the maximum, then back to the same minimum.

Active nematic cortex drives large-scale vesicle shape changes

The flexibility of the encapsulating vesicle allows us to study the uncharted regime in which the dynamics of an active nematic cortex couples to a deformable constraining surface (movie S3). To explore the dynamics of this entire regime, we apply a hypertonic stress inducing a water efflux that deflates the vesicle (Fig. 4 and movie S4). The shape of slightly deflated vesicles continuously fluctuates around a mean spherical shape and is characterized by the continuous growth and shrinkage of the major and minor axis of an ellipse, with a periodicity set by the defect transport speed. In addition, these vesicles exhibit four motile protrusions that are tightly coupled to the dynamics of the underlying disclination defects. Deflating the vesicles further causes a marked change in shape: The overall vesicle becomes anisotropic and motile, with filopodia-like protrusions growing in size and reaching lengths of tens of micrometers. The 3D reconstruction of shape-changing flaccid vesicles demonstrates the existence of only four protrusions (Fig. 4B), this number being determined by the fundamental topological constraints. Reswelling the vesicle causes the amplitude of the shape deformations to continuously decrease, the protrusions to vanish, and the vesicle to recover its initial spherical shape.

The other parameter that critically affects the emergent behavior of spherical nematics is the vesicle diameter (*34*, *35*) (Fig. 5). Decreasing the diameter increases the curvature of surface-bound microtubules and the energetic cost of confining active nematics to a spherical surface. For vesicles with radii larger than 18 μm, we only observe oscillations of four motile +½ defects (Fig. 5H). For smaller radii, the population of vesicles and the emergent dynamics becomes heterogeneous (Fig. 5I). For example, we observe a dynamical mode in which microtubules form a

rotating ring around the equator of a spherical vesicle (Fig. 5A). The diameter of the microtubule ring increases because of extensile forces driven by molecular motors. To satisfy the spherical confinement the ring eventually buckles out of the equatorial plane, forming a saddle shape configuration which initiates the formation of the four +½ defects. The defects collide pairwise and fuse, such that a new ring is formed (Fig. 5, C and D, and movies S5 and S6). By this mechanism, the vesicle switches between the ring structure and the structure characterized by four +½ defects (Fig. 5B). For the same parameters we also find that stiff microtubules can deform the vesicle, forming a spindle-like structure with two +1 defects at the spindle poles. Structurally, spindle-like vesicles resemble the isotropic-nematic tactoids found in equilibrium liquid crystals (Fig.

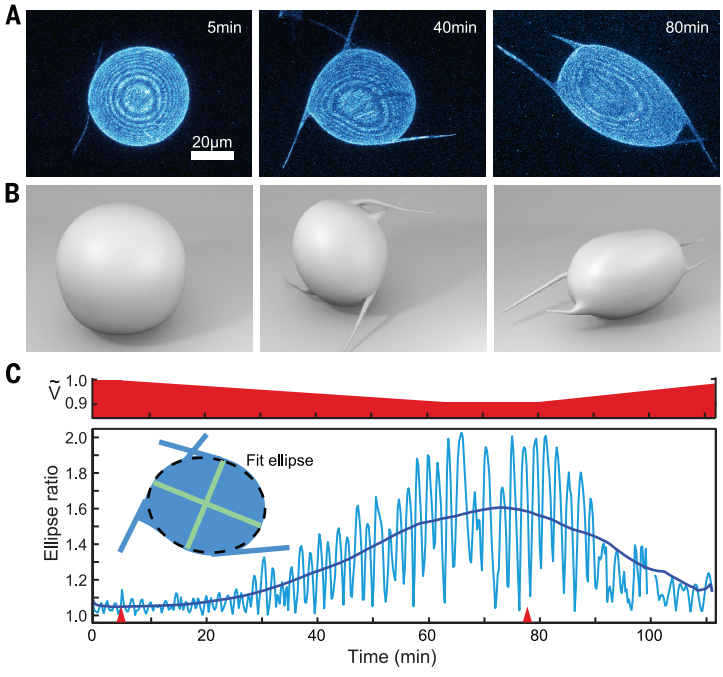

Fig. 4. Vesicle shape changes driven by defect dynamics. A 10% hypertonic stress is applied at t = 5.2 min to provide an excess membrane area. (**A**) Confocal images showing the z-projection of the vesicle shape, with corresponding 3D schematics shown in (**B**). Starting from a spherical nematic vesicle with four +½ defects (t = 5 min), four dynamic protrusions grow from the defect sites while the vesicle slowly deswells. At t = 78 min, the vesicle reswells and the protrusions decrease in size and eventually disappear. (**C**) Bottom: The amplitude of shape deformations increases over time, as shown by the plot of the vesicle aspect ratio (ratio of major to minor ellipse axis), reaching a maximum value of 1.6 at t = 75 min. Restoring vesicle volume $\tilde{V}$ by applying a hypotonic stress at t = 78 min inverts the effect, suppressing shape fluctuations. Red arrowheads denote when osmotic stresses are applied. Top: Estimate of the time evolution of $\tilde{V}$.

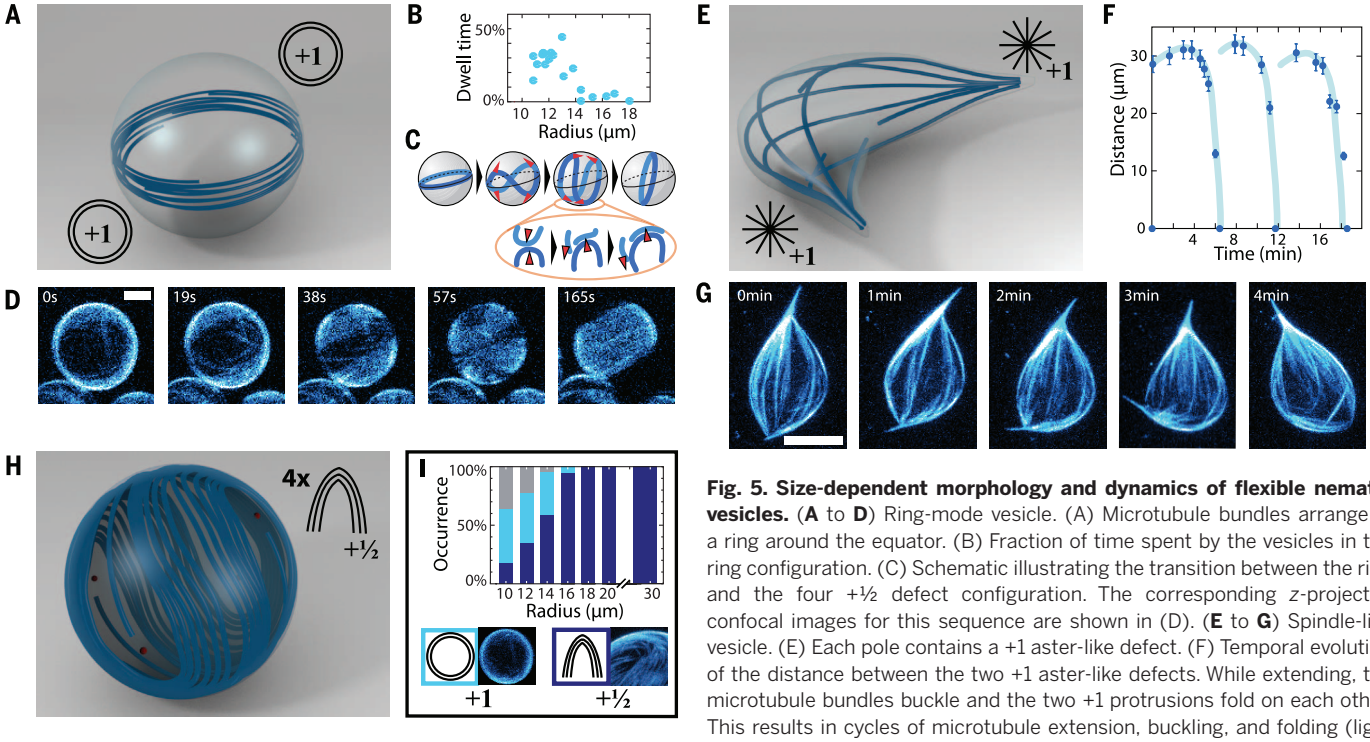

Fig. 5. Size-dependent morphology and dynamics of flexible nematic vesicles. (**A** to **D**) Ring-mode vesicle. (A) Microtubule bundles arrange in a ring around the equator. (B) Fraction of time spent by the vesicles in the ring configuration. (C) Schematic illustrating the transition between the ring and the four +½ defect configuration. The corresponding z-projected confocal images for this sequence are shown in (D). (**E** to **G**) Spindle-like vesicle. (E) Each pole contains a +1 aster-like defect. (F) Temporal evolution of the distance between the two +1 aster-like defects. While extending, the microtubule bundles buckle and the two +1 protrusions fold on each other. This results in cycles of microtubule extension, buckling, and folding (light blue lines are guides to the eye). A sequence of confocal images illustrating this dynamics is shown in (G). (**H**) Schematic of a large spherical vesicle exhibiting four +½ defects. (**I**) Types of dynamics. The histogram shows the percentage of vesicles displaying a defect configuration as a function of the radius (total count = 168). For radii above 18 μm, all the vesicles exhibit the four +½ defect configuration shown in (H). For radii in the range 10 to 18 μm, vesicles that undergo continuous transitions between four +½ defect (blue) and ring (cyan) configurations [shown in (A)] are found. The color code for the defect topology is shown in the pictograms; some cases remain uncharacterized because of resolution limitations. Scale bars, 8 μm.

5E) (*36*). Active spindle-like vesicles also exhibit interesting dynamics. Taking advantage of the excess membrane area stored in the membrane tension, the constituent extensile microtubule bundles push outwardly to extend the spindle poles. At a critical bundle length, the connectivity of the constituent microtubule bundles in the central spindle region decreases and the spindle becomes unstable, buckles, and folds into a more compact shape. At this point, the microtubules start extending again, and the cycle of vesicle extension, buckling, folding, and reextension repeats multiple times (Fig. 5, F and G, and movie S7). It is also possible to observe vesicles that transition between spindle and ring structures (fig. S8 and movie S8).

Our results demonstrate how combining active matter with topological constraints yields structures and dynamics that cannot be observed in conventional equilibrium systems (*37*–*40*). Specifically, we have shown that confining active nematic films onto the surface of a sphere suppresses defect generation and yields a robust and tunable oscillatory dynamics that is well described by a coarse-grained theoretical model. Furthermore, confinement and the constraints imposed by topology simplify the complex dynamics of planar active nematics that exhibit complex chaotic spatiotemporal behavior.

REFERENCES AND NOTES

1. L. S. Penrose, *Nature* **205**, 544–546 (1965).
2. T. C. Lubensky, J. Prost, *J. Phys.* **2**, 371–382 (1992).
3. D. R. Nelson, *Nano Lett.* **2**, 1125–1129 (2002).
4. T. Lopez-Leon, V. Koning, K. B. S. Devaiah, V. Vitelli, A. Fernandez-Nieves, *Nat. Phys.* **7**, 391–394 (2011).
5. H. Shin, M. J. Bowick, X. Xing, *Phys. Rev. Lett.* **101**, 037802 (2008).
6. V. Vitelli, D. R. Nelson, *Phys. Rev. E* **74**, 021711 (2006).
7. P. Poulin, H. Stark, T. C. Lubensky, D. A. Weitz, *Science* **275**, 1770–1773 (1997).
8. I. Musevic, M. Skarabot, U. Tkalec, M. Ravnik, S. Zumer, *Science* **313**, 954–958 (2006).
9. A. R. Bausch *et al*., *Science* **299**, 1716–1718 (2003).
10. W. T. M. Irvine, V. Vitelli, P. M. Chaikin, *Nature* **468**, 947–951 (2010).
11. C. P. Lapointe, T. G. Mason, I. I. Smalyukh, *Science* **326**, 1083–1086 (2009).
12. B. Senyuk *et al*., *Nature* **493**, 200–205 (2013).
13. I. H. Lin *et al*., *Science* **332**, 1297–1300 (2011).
14. J. A. Moreno-Razo, E. J. Sambriski, N. L. Abbott, J. P. Hernández-Ortiz, J. J. de Pablo, *Nature* **485**, 86–89 (2012).
15. P. Lipowsky, M. J. Bowick, J. H. Meinke, D. R. Nelson, A. R. Bausch, *Nat. Mater.* **4**, 407–411 (2005).
16. G. Meng, J. Paulose, D. R. Nelson, V. N. Manoharan, *Science* **343**, 634–637 (2014).
17. U. Tkalec, M. Ravnik, S. Čopar, S. Žumer, I. Muševič, *Science* **333**, 62–65 (2011).
18. S. Zhou, A. Sokolov, O. D. Lavrentovich, I. S. Aranson, *Proc. Natl. Acad. Sci. U.S.A.* **111**, 1265–1270 (2014).
19. T. Sanchez, D. T. N. Chen, S. J. DeCamp, M. Heymann, Z. Dogic, *Nature* **491**, 431–434 (2012).
20. G. Duclos, S. Garcia, H. G. Yevick, P. Silberzan, *Soft Matter* **10**, 2346–2353 (2014).
21. L. Giomi, M. J. Bowick, X. Ma, M. C. Marchetti, *Phys. Rev. Lett.* **110**, 228101 (2013).
22. S. P. Thampi, R. Golestanian, J. M. Yeomans, *Phys. Rev. Lett.* **111**, 118101 (2013).
23. T. Gao, R. Blackwell, M. A. Glaser, M. D. Betterton, M. J. Shelley, http://arxiv.org/abs/1401.8059 (2014).
24. J. Palacci, S. Sacanna, A. P. Steinberg, D. J. Pine, P. M. Chaikin, *Science* **339**, 936–940 (2013).
25. M. Abkarian, E. Loiseau, G. Massiera, *Soft Matter* **7**, 4610–4614 (2011).
26. S. Asakura, F. Oosawa, *J. Chem. Phys.* **22**, 1255–1256 (1954).
27. M. J. Schnitzer, S. M. Block, *Nature* **388**, 386–390 (1997).
28. C. Hentrich, T. Surrey, *J. Cell Biol.* **189**, 465–480 (2010).
29. T. Surrey, F. Nedelec, S. Leibler, E. Karsenti, *Science* **292**, 1167–1171 (2001).
30. See supplementary materials on *Science* Online.
31. R. Voituriez, J. F. Joanny, J. Prost, *Europhys. Lett.* **70**, 404–410 (2005).
32. D. Marenduzzo, E. Orlandini, M. E. Cates, J. M. Yeomans, *Phys. Rev. E* **76**, 031921 (2007).
33. R. Aditi Simha, S. Ramaswamy, *Phys. Rev. Lett.* **89**, 058101 (2002).
34. T. S. Nguyen, J. Geng, R. L. B. Selinger, J. V. Selinger, *Soft Matter* **9**, 8314–8326 (2013).
35. M. Elbaum, D. Kuchnir Fygenson, A. Libchaber, *Phys. Rev. Lett.* **76**, 4078–4081 (1996).
36. P. Prinsen, P. van der Schoot, *Phys. Rev. E* **68**, 021701 (2003).
37. E. Abu Shah, K. Keren, *eLife* **3**, e01433 (2014).
38. H. Baumann, T. Surrey, *J. Biol. Chem.* **289**, 22524–22535 (2014).
39. M. Pinot *et al*., *Curr. Biol.* **19**, 954–960 (2009).
40. E. Tjhung, D. Marenduzzo, M. E. Cates, *Proc. Natl. Acad. Sci. U.S.A.* **109**, 12381–12386 (2012).

ACKNOWLEDGMENTS

Research was supported by ERC-SelfOrg (F.C.K., E.L., A.R.B.), partly by the SFB863 and the Nanosystems Initiative Munich (F.C.K., E.L., A.R.B.), the Institute of Advanced Study-Technical University Munich (Z.D., F.C.K.), NSF grants DMR-1305184 and DGE-1068780 (M.C.M.), and the Soft Matter Program at Syracuse University (M.J.B., M.C.M.). The primary support for work at Brandeis was provided by the W. M. Keck Foundation and NSF-MRSEC-0820492 (T.S., Z.D.). Acquisition of ATP dependence data was supported by the U.S. Department of Energy, Office of Basic Energy Sciences, grant DE-SC0010432TDD (S.J.D., Z.D.). We also acknowledge use of the Brandeis MRSEC optical microscopy facility.

SUPPLEMENTARY MATERIALS

www.sciencemag.org/content/345/6201/1135/suppl/DC1
Materials and Methods
Supplementary Text
Movies S1 to S8

14 April 2014; accepted 30 July 2014
10.1126/science.1254784

NEURODEGENERATION

Poly-dipeptides encoded by the *C9orf72* repeats bind nucleoli, impede RNA biogenesis, and kill cells

Ilmin Kwon,[1] Siheng Xiang,[1] Masato Kato,[1] Leeju Wu,[1] Pano Theodoropoulos,[1] Tao Wang,[2] Jiwoong Kim,[2] Jonghyun Yun,[2] Yang Xie,[2] Steven L. McKnight[1]*

Many RNA regulatory proteins controlling pre–messenger RNA splicing contain serine:arginine (SR) repeats. Here, we found that these SR domains bound hydrogel droplets composed of fibrous polymers of the low-complexity domain of heterogeneous ribonucleoprotein A2 (hnRNPA2). Hydrogel binding was reversed upon phosphorylation of the SR domain by CDC2-like kinases 1 and 2 (CLK1/2). Mutated variants of the SR domains changing serine to glycine (SR-to-GR variants) also bound to hnRNPA2 hydrogels but were not affected by CLK1/2. When expressed in mammalian cells, these variants bound nucleoli. The translation products of the sense and antisense transcripts of the expansion repeats associated with the *C9orf72* gene altered in neurodegenerative disease encode GR_n and PR_n repeat polypeptides. Both peptides bound to hnRNPA2 hydrogels independent of CLK1/2 activity. When applied to cultured cells, both peptides entered cells, migrated to the nucleus, bound nucleoli, and poisoned RNA biogenesis, which caused cell death.

Among familial causes of amyotrophic lateral sclerosis (ALS) and/or frontotemporal dementia (FTD), between 25 and 40% of cases are attributed to a repeat expansion in a gene designated *C9orf72*, with an open reading frame (ORF). The hexanucleotide repeat sequence GGGGCC normally present in 2 to 23 copies is expanded in affected patients to 700 to 1600 copies (*1*, *2*). The pattern of genetic inheritance of the *C9orf72* repeat expansion is dominant, and multiple lines of evidence suggest that the repeat expansion causes disease. Two theories have been advanced to explain repeat-generated toxicity. First, in situ hybridization assays have identified nuclear dots containing either sense or antisense repeat transcripts (*3*–*5*), which leads to the idea that the nuclear-retained RNAs might themselves be toxic. More recently, equally clear evidence has been generated that both the sense and antisense transcripts of the GGGGCC repeats associated with *C9orf72* can be translated in an ATG-independent manner (without an ATG start codon) known as repeat-associated non-ATG (RAN) translation (*6*). Depending on reading frame, the sense transcript of the repeats can be translated into glycine:alanine (GA_n), glycine:proline (GP_n), or glycine:arginine (GR_n) polymers. RAN translation of the antisense transcript of the GGGGCC repeats of *C9orf72* lead to the production of proline:alanine (PA_n), proline:glycine (PG_n), or proline:arginine (PR_n) polymers.

[1]Department of Biochemistry, UT Southwestern Medical Center, 5323 Harry Hines Boulevard, Dallas, TX 75390-9152, USA. [2]Quantitative Biomedical Research Center, Department of Clinical Sciences, UT Southwestern Medical Center, 5323 Harry Hines Boulevard, Dallas, TX 75390-9152, USA.
***Corresponding author. E-mail: steven.mcknight@utsouthwestern.edu**

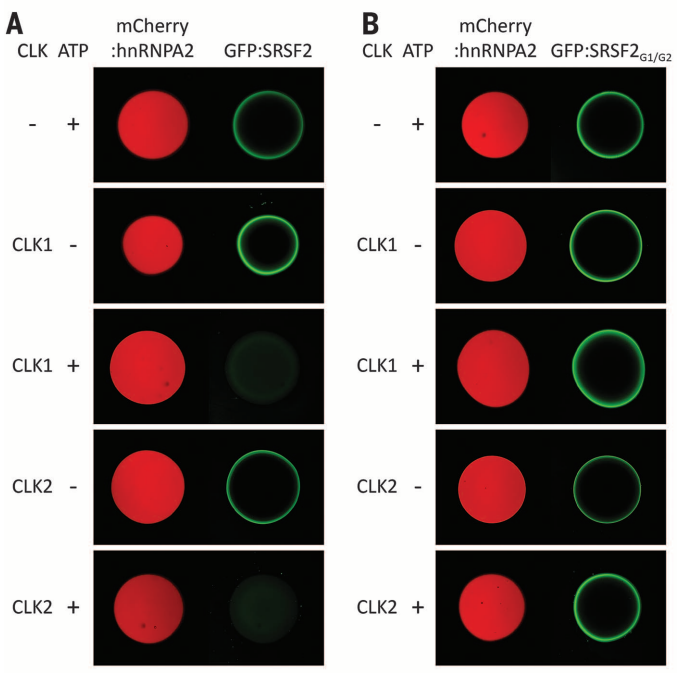

Fig. 1. CLK1/2-mediated release of GFP-fused SR domain from mCherry:hnRNPA2 hydrogel droplets. Hydrogel droplets composed of mCherry fused to the LC domain of hnRNPA2 were incubated with protein solution of GFP-fused to SR domains from either SRSF2 (**A**) or $SRSF2_{G1/G2}$ (**B**). Both GFP proteins bound well to the mCherry:hnRNPA2 hydrogels as revealed by GFP signal trapped at the periphery of hydrogel droplets (*22*). After overnight incubation with either CLK1 or CLK2, prebound GFP-fused SR domain of SRSF2 was released from the mCherry:hnRNPA2 hydrogels in the presence of ATP [third and fifth panels of (A)]. The GFP-fused to the SR domain of $SRSF2_{G1/G2}$ was resistant to CLK1/2-mediated release from hydrogels [third and fifth panels of (B)].

These repeat-encoded polymers are expressed in disease tissue (*5*, *7*–*9*). The disordered and hydrophobic nature of these polymers, at least the GA_n, GP_n, and PA_n versions, properly predicted that they would aggregate into distinct foci within affected cells (*5*, *9*). Another plausible explanation for repeat-generated toxicity is the idea that the polymeric aggregates resulting from RAN translation of either the sense or antisense repeats are themselves toxic.

Here, we investigated a third and distinct interpretation as to the underlying pathophysiology associated with repeat expansion of the hexanucleotide repeats associated with the *C9orf72* gene. We suggest that two of the six RAN translation products, GR_n encoded by the sense transcript and PR_n encoded by the antisense transcript, act to alter information flow from DNA to mRNA to protein in a manner that poisons both pre-mRNA splicing and the biogenesis of ribosomal RNA.

Serine:arginine domains of pre-mRNA splicing factors bind hnRNPA2 hydrogels in a phosphorylation-regulated manner

Our standard method of retrieving proteins enriched in unfolded, low-complexity (LC) sequences involves the incubation of cellular lysates with a biotinylated isoxazole (b-isox) chemical (*10*). When incubated on ice in aqueous buffers, the b-isox chemical crystallizes. X-ray diffraction analyses of the b-isox crystals revealed the surface undulation of peaks and valleys separated by 4.7 Å. It is hypothesized that, when exposed to cell lysates, disordered, random-coil sequences can bind to the surface troughs of b-isox crystals and, thereby, be converted to an extended β-strand conformation. When the crystals are retrieved by centrifugation, they selectively precipitate DNA and RNA regulatory proteins endowed with LC sequences. When these methods were used to query the distribution of nuclear proteins precipitated by b-isox microcrystals, scores of proteins annotated as being involved in the control of pre-mRNA splicing were retrieved (*11*).

Many splicing factors contain long repeats of the dipeptide sequence serine:arginine (SR). Given the LC nature of SR domains, we hypothesized that it was this determinant that facilitated b-isox precipitation. Focusing on a member of the SR protein family that has been studied extensively, serine:arginine splicing factor 2 (SRSF2), we appended its SR domain to green fluorescent protein (GFP) to ask whether the SR domain might be sufficient to mediate b-isox precipitation. GFP is a well-folded protein that, alone, is not precipitated by b-isox crystals (*10*). When fused to the SR domain of SRSF2, GFP was precipitated efficiently by b-isox crystals (fig. S1, A and B).

When incubated at high concentrations, the LC domains of certain RNA regulatory proteins, including FUS, EWS, TAF15, and hnRNPA2, polymerize into amyloid-like fibers. In a time- and concentration-dependent manner, these fibers adopt a hydrogel-like state (*10*). No evidence of polymerization or hydrogel formation was observed upon incubation of the GFP fusion protein containing the SR domain of SRSF2 (designated GFP:SRSF2). We then asked whether the fusion protein might be bound and retained by hydrogel droplets formed from polymers of the LC domain of hnRNPA2 (*10*). Indeed, GFP:SRSF2 bound avidly to hydrogel droplets formed from the LC domain of hnRNPA2 (Fig. 1A).

The SR domains of splicing factors can be phosphorylated (*12*–*14*). Two related protein kinase enzymes, CDC2-like kinase 1 (CLK1) and CDC2-like kinase 2 (CLK2), phosphorylate serine residues within SR domains (fig. S1C) (*15*–*18*). In order to ask whether phosphorylation of SR domains might affect their binding to hydrogel droplets formed from the LC domain of hnRNPA2, we prebound the GFP:SRSF2 fusion protein and then exposed the droplets to ATP alone, CLK1/2 enzymes alone, or a mix of ATP and enzymes. Release of the GFP:SRSF2 test protein was observed in a time-, enzyme-, and ATP-dependent manner (Fig. 1A).

The CLK1/2 protein kinases themselves contain SR domains, presumably to help guide these enzymes to the proper subnuclear locations where they serve to regulate the activities of SR domain–containing splicing factors (*17*). Hydrogel droplets were coexposed to GFP:SRSF2 along with a derivative of CLK2 containing an SR domain. In this case, exposure to ATP alone facilitated release of GFP:SRSF2, presumably because of activation of the CLK2 enzyme held by its SR domain in proximity to the GFP:SRSF2 test protein (fig. S1D).

The SRSF2 splicing factor contains two SR domains, one located between residues 117 and 169 of the polypeptide and another located between residues 177 and 221 (fig. S2). Out of 21 serine residues within the former SR domain, 16 were mutated to glycine, which led to a variant designated $SRSF2_{G1}$. Likewise, 14 out of 17 serine residues within the latter SR domain were mutated to glycine, which led to the $SRSF2_{G2}$ variant. These two mutants were recombined to produce the $SRSF2_{G1/G2}$ variant (fig. S2). The altered SR domain of the $SRSF2_{G1/G2}$ variant was fused to GFP ($GFP:SRSF2_{G1/G2}$), expressed in bacteria, purified, and exposed to hnRNPA2 hydrogel droplets. Like the native SR domain, the $GFP:SRSF2_{G1/G2}$ variant bound to the hydrogel droplets. By contrast, when the bound hydrogel droplets were exposed to ATP and either of the CLK1/2 enzymes, no GFP was released (Fig. 1B).

Binding of native and serine-to-glycine variants of SRSF2 to nuclear puncta

SR domain–containing pre-mRNA splicing factors localize to various puncta in the nucleus of eukaryotic cells (*19*). In interphase nuclei, SR-containing proteins are found in puncta variously termed "interchromatin granule clusters" or nuclear speckles. These puncta are roughly 1 to 3 μm in diameter and are composed of smaller granules connected by a thin fibril (*20*). Hypophosphorylated SR domains associate with the periphery of nucleoli in a region termed nucleolar organizing region (NOR)–associated patches (NAPs) (*21*). Knowing that the SR domain of the $SRSF2_{G1/G2}$ mutant binds to hnRNPA2 hydrogels in a manner immune to CLK1/2-mediated release, we transfected cultured cells with GFP-tagged versions of the four SRSF2 variants (the native protein and the three mutants: $SRSF2_{G1}$, $SRSF2_{G2}$, and $SRSF2_{G1/G2}$). Unlike the native SRSF2 protein,

which distributed to nuclear speckles, the other three proteins associated with nucleoli (Fig. 2A). When cotransfected with an expression vector encoding CLK1 enzyme, partial release from nucleoli was observed for the $SRSF2_{G1}$ and $SRSF2_{G2}$ mutants, yet no release was observed for the $SRSF2_{G1/G2}$ mutant (Fig. 2B). Thus, it appears that, by changing serine residues to glycine in the three mutants of SRSF2, we created mimics of the hypophosphorylated state of SR proteins. Because the $SRSF2_{G1}$ and $SRSF2_{G2}$ proteins can only be partially phosphorylated by CLK1, and because the $SRSF2_{G1/G2}$ variant cannot be phosphorylated, we reason that these proteins become trapped in nucleoli at an early stage of the pathway of nuclear speckle formation and pre-mRNA splicing.

The GR_n and PR_n RAN translation products of *C9orf72* bind hnRNPA2 hydrogels

The sense and antisense transcripts of the GGGGCC repeat expansions associated with familial forms of ALS and FTD can be translated in an ATG-independent manner (*5*, *7*, *9*). Depending on reading frame, the sense repeat transcript encodes GA_n, GP_n, or GR_n polymers. Likewise, the antisense transcripts of the repeats encode PA_n, PG_n, and PR_n polymers. We focused on the GR_n translation product of the sense repeat transcript and the PR_n translation product of the antisense repeat transcript for three reasons. First, these polymers are considerably more hydrophilic than the GA_n, GP_n, PA_n, and PG_n polymers and are less likely to aggregate. Second, the GR_n and PR_n polymers might, by virtue of the abundance of arginine residues, be self-programmed to return to the nucleus after cytoplasmic translation (owing to the fact that nuclear localization signals tend to be enriched in basic amino acids). Third, these polymers are reminiscent of the $SRSF2_{G1}$, $SRSF2_{G2}$, and $SRSF2_{G1/G2}$ variants that bound to hnRNPA2 hydrogel droplets independent of the effects of the CLK1 enzyme (Fig. 1) and are associated tightly with nucleoli in living cells (Fig. 2).

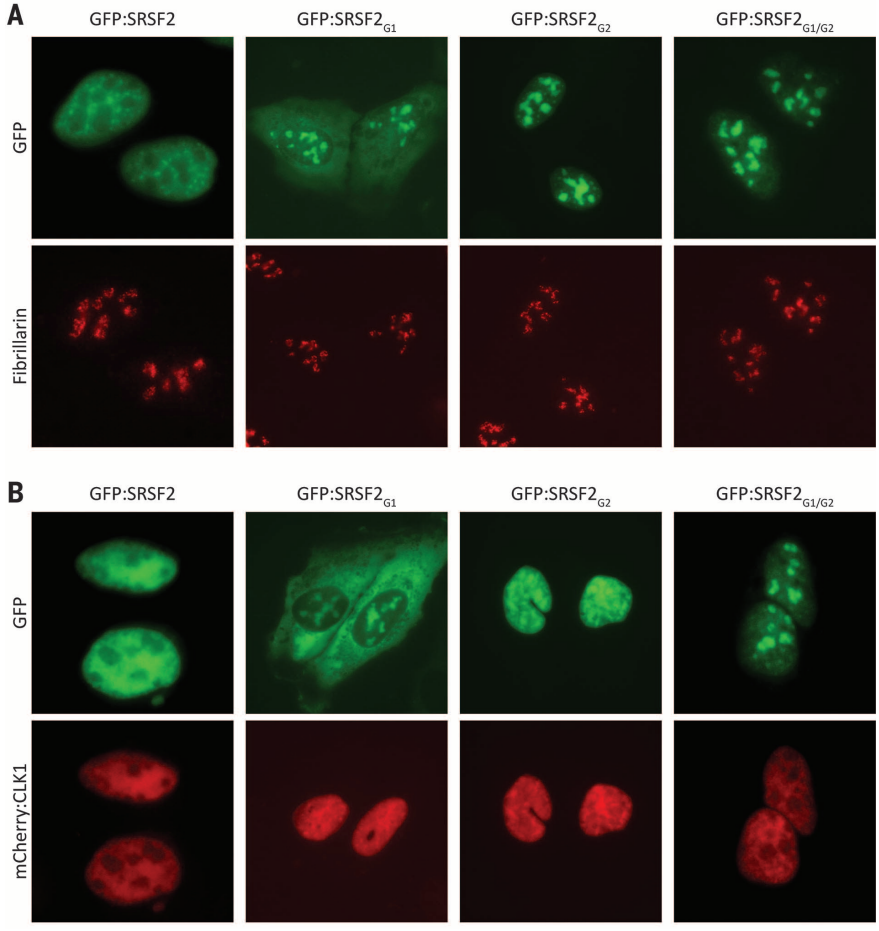

Fig. 2. Native or S-to-G mutated variants of SRSF2 localize to different nuclear puncta. GFP fusion proteins linked to either the native, full-length SRSF2, or the $SRSF2_{G1}$, $SRSF2_{G2}$ or $SRSF2_{G1/G2}$ mutants were transfected in U2OS cells in the absence (**A**) or presence (**B**) of a coexpressed mCherry:CLK1 fusion protein. The native SRSF2 protein localized to nuclear speckles and was dispersed into the nucleoplasm in the presence of cotransfected mCherry:CLK1. The $SRSF2_{G1}$ and $SRSF2_{G2}$ mutants localized to nucleoli as deduced by costaining with antibodies specific to the nucleolar marker, fibrillin. The $SRSF2_{G1}$ mutant was partially redistributed from nucleoli to the cytoplasm in the presence of mCherry:CLK1. The $SRSF_{G2}$ mutant was partially redistributed from nucleoli to the nucleoplasm in the presence of mCherry:CLK1. Coexpression of mCherry:CLK1 had no effect on the nucleolar localization of the $SRSF2_{G1/G2}$ mutant.

GFP derivatives were prepared that contained 20 repeats of the dipeptide sequence SR, GR, or PR (*22*). After expression in bacterial cells and purification, each fusion protein was incubated with hnRNPA2 hydrogels. Unlike GFP itself, which did not bind to any of the hydrogels used, the GFP:SR_{20}, GFP:GR_{20}, and GFP:PR_{20} fusion proteins bound avidly to hnRNPA2 hydrogel droplets. When protein-bound hydrogels were exposed to CLK1 or CLK2 in the presence of ATP, GFP:SR_{20} was liberated but not GFP:GR_{20} or GFP:PR_{20} (Fig. 3). We interpret these results in the same way as observations made with GFP:SRSF2 and its serine-to-glycine variants (Figs. 1 and 2). CLK1/2-mediated phosphorylation of the serine residues in the GFP:SR_{20} fusion protein is interpreted to facilitate its release from hnRNPA2 hydrogel droplets. Because the GR_n and PR_n polymers have no serine residues, they cannot be phosphorylated and released from hydrogels upon exposure to CLK1/2 and ATP.

The GR_n and PR_n RAN translation products of *C9orf72* penetrate cells, migrate to the nucleus, bind nucleoli, and kill cells

Polymeric versions of the GR_n and PR_n translation products of *C9orf72* were synthesized that contained 20 dipeptide repeats terminated by an epitope tag (*22*). The synthetic peptides were solubilized in aqueous buffer and applied to cultured U2OS cells (a human osteosarcoma cell line) for 30 min at 10 μM. The cells were then fixed and stained with antibodies capable of recognizing the hemagglutinin (HA) epitope tag. Both the GR_{20} and PR_{20} polymers entered cells, migrated to the nucleus, and bound to nucleoli (Fig. 4A). The morphology of U2OS cells was altered after prolonged exposure to the GR_{20} and PR_{20} translation products of *C9orf72* hexanucleotide repeats. Alteration in cell morphology was more pronounced for the PR_{20} peptide than for GR_{20}. Within 24 hours of exposure to 10 μM of PR_{20}, U2OS cells began to display a spindlelike phenotype. Upon exposure to 30 μM of the PR_{20} peptide for 24 hours, almost all cells were detached from the culture substrate and dead (fig. S3A). Similar effects on cell morphology and viability were observed for cultured human astrocytes (fig. S3B).

The stability of the GR_{20} and PR_{20} peptides was analyzed by immunoblotting. After the administration of a single dose of each peptide, U2OS cells were incubated for the indicated time periods. After retrieval of culture medium, cells were then washed with phosphate-buffered saline, lysed, and deposited onto nitrocellulose dot blots that were probed with antiserum specific to the HA epitope. These measurements gave evidence of a relatively short half-life for the GR_{20} peptide (20 to 30 min), but a much longer half-life for the PR_{20} peptide (72 hours) (fig. S4, A and B).

Cell viability was then measured for cultures exposed to varying levels of the PR_{20} (*22*). A median inhibitory concentration (IC_{50}) value of 5.9 μM was observed for the PR_{20} peptide (Fig. 4B). Similar cellular toxicity was observed for the

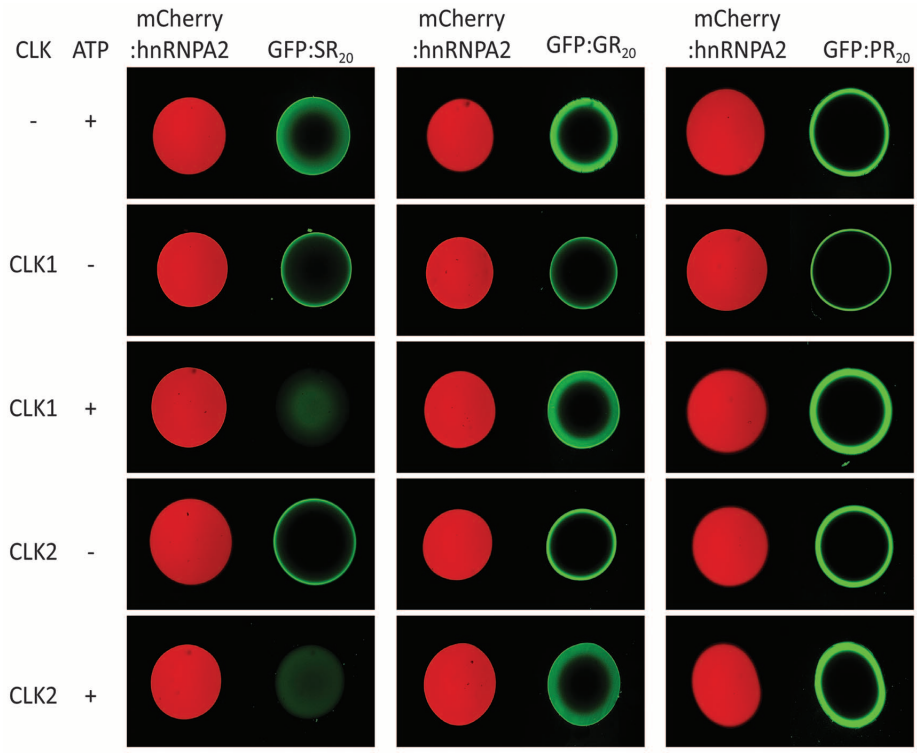

Fig. 3. Binding of translation products of *C9orf72* hexanucleotide repeat expansion to mCherry:hnRNPA2 hydrogel droplets. Recombinant fusion proteins linking GFP to 20 repeats of the SR, GR, or PR polymers (GFP:SR_{20}, GFP:GR_{20}, or GFP:PR_{20}) were applied to slide chambers containing mCherry:hnRNPA2 hydrogel droplets. After overnight incubation at 4°C; all three proteins were trapped to the periphery of the hydrogels droplets (top). When incubated with reaction mixtures containing either the CLK1 or CLK2 protein kinase enzymes, prebound GFP:SR_{20} was released from the hydrogels in an ATP-dependent manner. GFP:GR_{20} or GFP:PR_{20} prebound to mCherry:hnRNPA2 hydrogel droplets were immune to the release by CLK1 or CLK2, even in the presence of ATP.

GR_{20} peptide, but only when the GR_{20} peptide be added every 2 hours (Fig. 4C). Cell death in response to the PR_{20} peptide was also time-dependent. After administration of 10 μM of the PR_{20} peptide, half-maximal impact on cell viability was observed roughly 36 hours later (fig. S4E). When cells were exposed to a 30 μM dose of the peptide, 50% cell death was observed at 6 hours (fig. S4F).

Exposure of cultured cells to the GR_{20} and PR_{20} translation products of *C9orf72* impairs both pre-mRNA splicing and the biogenesis of ribosomal RNA

Having observed that GR_{20} and PR_{20} translation products of the *C9orf72* hexanucleotide repeats bound nucleoli and killed cultured cells, we wondered whether this might be the consequence of alterations in RNA biogenesis. To this end, cultured human astrocyte cells were exposed for 6 hours to the synthetic PR_{20} peptide and used to prepare RNA for deep sequencing. Computational analysis of the RNA-sequencing (RNA-seq) data predicted alteration in splicing in a variety of cellular mRNAs (*22*). Validation of predicted changes in pre-mRNA splicing was conducted by use of strategically designed polymerase chain reaction (PCR) primers (*22*). PCR products consistent with predicted alterations in splicing were subjected to DNA sequencing (fig. S5A). In all cases, predicted changes in pre-mRNA splicing were confirmed, with the degrees of effect on splicing ranging from modest, in the cases of the nascent polypeptide-associated complex subunit alpha (NACA) and RAN guanosine triphosphatase (GTPase) mRNAs, to severe, in the cases of the pentraxin-related protein PTX3 and the

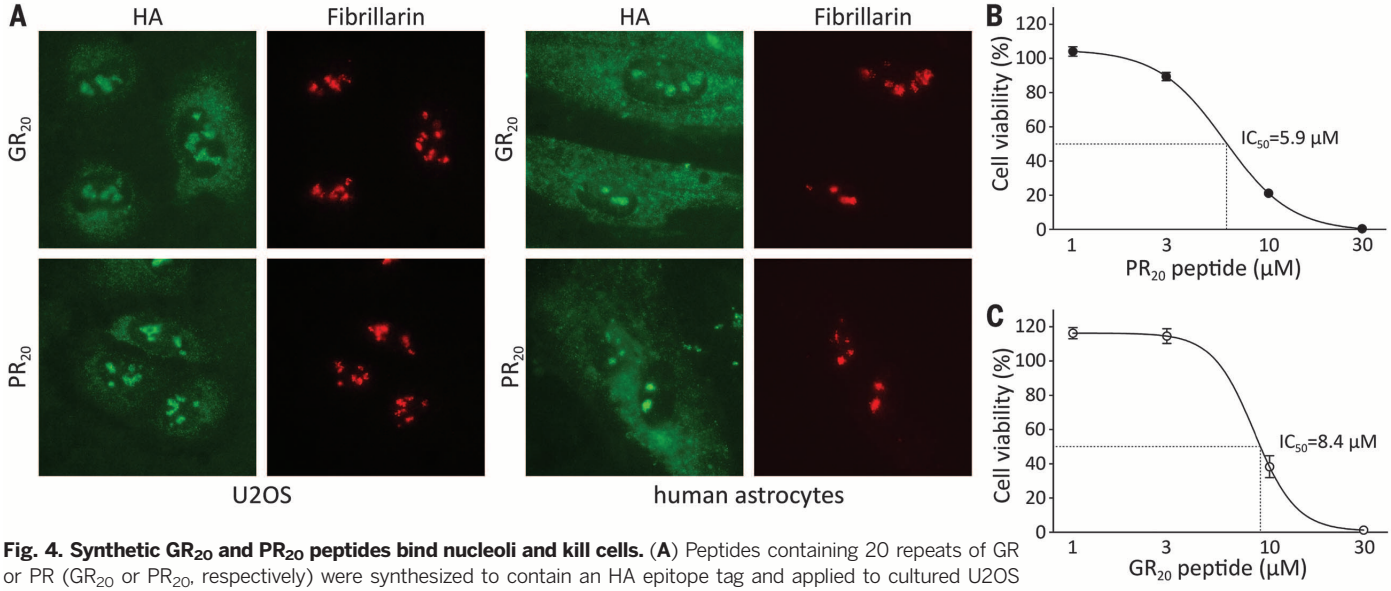

Fig. 4. Synthetic GR_{20} and PR_{20} peptides bind nucleoli and kill cells. (**A**) Peptides containing 20 repeats of GR or PR (GR_{20} or PR_{20}, respectively) were synthesized to contain an HA epitope tag and applied to cultured U2OS cancer cells (left) or human astrocytes (right). Cells were fixed and stained with either the HA-specific antibody (green signal) or an antibody to the nucleolar protein fibrillin (red signal). Both GR_{20} and PR_{20} synthetic peptides associated prominently with nucleoli. Measurements of U2OS cell viability revealed toxicity in response to both PR_{20} (**B**) and GR_{20} (**C**) synthetic peptides. Cell viability was measured at 72 or 12 hours after initial treatment of PR_{20} or GR_{20}, respectively. In the case of GR_{20} peptide, the medium was replaced every 2 hours to supplement fresh peptide. The PR_{20} and GR_{20} synthetic peptides killed U2OS cells with IC_{50} levels of 5.9 and 8.4 μM, respectively.

growth arrest and DNA damage-inducible GADD45A mRNAs. Administration of the PR_{20} peptide caused exon 2 skipping of the mRNA encoding the RAN GTPase, which resulted in removal of the first 88 residues of the protein (Fig. 5A and fig. S5B). Furthermore, PR_{20} administration caused exon 2 skipping of the mRNA encoding the PTX3, which predicted an in-frame deletion of 135 amino acids (Fig. 5B and fig. S5C). PR_{20} administration also caused the mRNA encoding NACA to contain a different 5′ untranslated region (5′ UTR) (Fig. 5C). Finally, PR_{20} administration caused the mRNA encoding GADD45A protein to include the full intronic sequences on both sides of exon 2 in the mature transcript, which altered the ORF in a manner expected to inactivate the GADD45A protein if translated from the aberrantly spliced mRNA (Fig. 5D).

Computational analysis of RNA-seq data further revealed changes in the abundance of a subset of cellular RNAs as a function of administration of the PR_{20} peptide (table S1). A large fraction of the altered RNAs encoded ribosomal proteins (Fig. 5E) or small nucleolar RNAs (snoRNAs). In both cases, PR_{20} administration enhanced RNA abundance. Having observed that both the GR_{20} and PR_{20} peptides bound to nucleoli and having observed changes in the abundance of snoRNAs and mRNAs encoding ribosomal proteins, we investigated the central task of nucleoli to synthesize mature ribosomal RNA (rRNA). Nine PCR primer pairs were designed to interrogate the synthesis and processing of rRNA (*22*). Three monitored the levels of the mature 18*S*, 5.8*S*, and 28*S* rRNAs. The other six primers were designed to monitor the 45*S* rRNA precursor, including pairs that probed: (i) the initial, 5′ end of the precursor that is eliminated along the pathway of rRNA maturation; (ii) the precursor junction at the 5′ end of 18*S* rRNA; (iii) the precursor junction at the 3′ end of 18*S* rRNA; (iv) the precursor junction at the 5′ end of 5.8*S* rRNA; (v) the precursor junction at the 3′ end of 5.8*S* rRNA; and (vi) the precursor junction at the 5′ end of 28*S* rRNA (see Fig. 5F). RNA was prepared from human astrocytes exposed for 12 hours to vehicle alone or to 10 μM or 30 μM of the PR_{20} peptide. Slight reductions in 28*S* rRNA were observed in the samples derived from cells treated with 30 μM of the PR_{20} peptide. To our surprise, the level of 5.8*S* rRNA was reduced by 70% under these conditions (Fig. 5F).

Evidence of impediments in the production of rRNA was confirmed upon evaluation of junctional PCR probes. The quantitative PCR (qPCR) primers specific for the 5′ transcribed spacer at the front end of the rRNA precursor revealed a 20% elevation of the precursor in cells exposed to the lower, 10 μM, concentration of the PR_{20} peptide. The first junctional probe also revealed an elevation in immature rRNA, the second junctional probe revealed normal levels of rRNA precursor, the third probe revealed roughly 20% attenuation of the precursor, the probe monitoring the 3′ junction of 5.8*S* rRNA revealed 40% attenuation, and the probe monitoring the 5′ junction of 28*S* rRNA revealed normal precursor levels. Cells exposed to 30 μM of the PR_{20} peptide revealed reductions in the 45*S* rRNA precursor consistent with a similar, 5′ to 3′ polarity of impediment. Indeed, the qPCR primer pair monitoring processing at the 3′ terminus of 5.8*S* rRNA revealed a 70% drop. Irrespective of whether these effects result from altered transcription of rRNA genes, altered processing of the 45*S* rRNA precursor, or both, these assays provide evidence of nucleolar dysfunction in cells treated with the

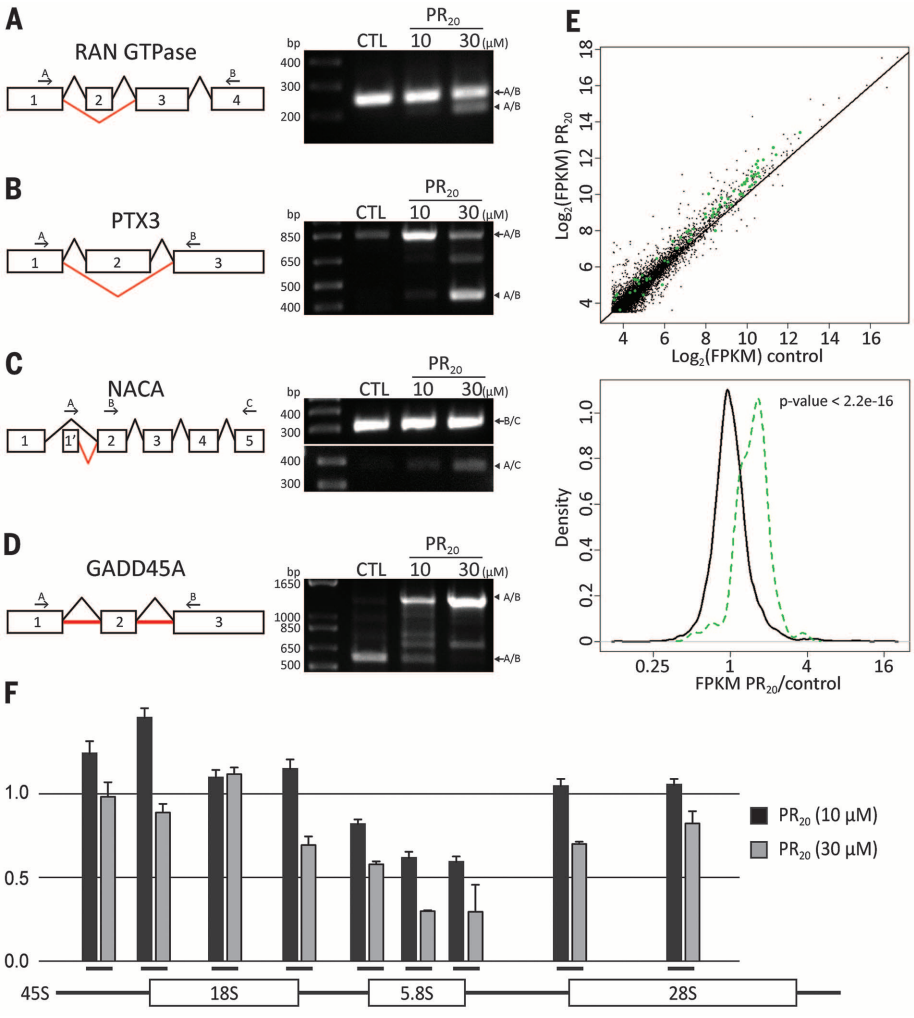

Fig. 5. Effect of PR_{20} peptide on RNA processing. Aberrant splicing of the RAN GTPase, PTX3, NACA, and GADD45A transcripts in PR_{20}-treated cells was validated by reverse transcription PCR (RT-PCR) (**A** to **D**). Schematic diagrams show either normal splicing (black lines) or missplicing (red lines). A bold red line in (D) indicates retention of intron. (A) RT-PCR analysis of RAN GTPase transcript: Arrow indicates normal transcript [252 base pairs (bp)], and arrowhead indicates exon 2-skipped transcript (212 bp). (B) RT-PCR analysis of PTX3 transcript: Arrow indicates normal transcript (844 bp), and arrowhead indicates exon 2–skipped transcript (442 bp). (C) RT-PCR analysis of NACA transcript: Arrow indicates normal transcript (386 bp), and arrowhead indicates transcript with aberrant 5′ UTR (314 bp). (D) RT-PCR analysis of GDD45A transcript: Arrow indicates normal transcript (573 bp), and arrowhead indicates intron-retention transcript (1283 bp). (**E**) Scatter plot of RNA abundance measured from RNA-seq data (top). RNA abundance [$\log_2$(fragments per kilobase of exon or FPKM)] for the control sample is shown on the *x* axis and RNA abundance for the PR_{20} treated sample on the *y* axis. Each dot represents a single mRNA species, with green dots representing transcripts of individual ribosomal protein genes. The distribution of RNA abundance (fold change) between the PR_{20}-treated sample and the control sample is shown in (E) (bottom). Black line represents the distribution of all genes, and green line represents the distribution of ribosomal protein genes. Expression of members of the ribosomal protein gene family was significantly up-regulated by PR_{20} treatment (P < 2.2e-16, Kolmogorov–Smirnov test). (**F**) Aberrant rRNA processing in PR_{20}-treated cells as analyzed by qPCR. Data are plotted as normalized fold-change against control and error is represented by standard deviation of triplicate experiments. The *y* axis indicates fold changes relative to untreated control. Black bars on the *x* axis below histograms indicate approximate locations of qPCR primers for 45*S*, 18*S*-5′ junction, 18*S*, 18*S*-3′ junction, 5.8*S*-5′ junction, 5.8*S*, 5.8*S*-3′ junction, 28*S*-5′ junction, and 28*S* rRNA (from left to right).

PR_{20} RAN translation product of the *C9orf72* hexanucleotide repeats.

The GR_n and PR_n synthetic peptides alter splicing of the EAAT2 transcript in a pattern identical to that observed in ALS patients

Having observed global alterations in pre-mRNA splicing in cells exposed to the PR_{20} synthetic peptide, we asked whether alterations in pre-mRNA splicing might have been observed in the study of patient-derived tissues. Splicing of the transcript encoding a glutamate transporter designated excitatory amino acid transporter 2 (EAAT2) is altered in ALS patients. Two hallmarks of the altered pattern were the skipping of exon 9 and the inclusion of 1008 nucleotides of intronic sequence downstream from the splice donor site of exon 7 (*23*).

In order to ask whether a similar pattern of derangement might result from exposure of cells to the PR_{20} synthetic peptide, we incubated cultured human astrocytes with 10 or 15 μM of the polymer for 36 hours, a time point corresponding to roughly 50% reduction in cell viability (fig. S4E). RNA was then extracted and subjected to PCR analysis as a means of resolving the architecture of the EAAT2 transcript (*22*). PCR products diagnostic of both the exon 9–skipped form of the EAAT2 mRNA, as well as the 1008-nucleotide extension of intron inclusion beyond the splice donor site of exon 7, appeared in a concentration-dependent manner in human astrocytes as a function of exposure to the PR_{20} polymer (Fig. 6). Both PCR products were sequenced and found to replicate the pattern of aberrant splicing first described in ALS patients precisely (fig. S6A).

It is possible that generalized cell toxicity commonly causes an idiosyncratic pattern of aberrant splicing of the EAAT2 mRNA, which could explain why cells poisoned by the PR_{20} peptide replicate the same pattern of improper splicing observed in patient samples. To test this hypothesis, human astrocytes were individually exposed to four other toxins, doxorubicin, taxol, staurosporin, and cytochalasin D. RNA was prepared from cells exhibiting clear evidence of toxicity and analyzed by PCR as a means of testing for the patterns of aberrant EAAT2 pre-mRNA splicing commonly observed in astrocytes treated with the PR_{20} peptide and from brain samples derived from patients suffering the GGGGCC repeat expansion in the *C9orf72* gene. None of the four toxins gave evidence of aberrant splicing of the EAAT2 mRNA (fig. S6B).

Discussion

Here we report several findings that may be relevant to both the basic science of gene expression and the pathophysiology of a specific type of neurodegenerative disease. First, alternative splicing factors containing SR domains interact with fibrous polymers of LC domains in a manner reversible by phosphorylation. When appended to a GFP reporter, these SR domains bind to hydrogel droplets formed from polymeric fibers derived from the LC domain of hnRNPA2. This binding is reversed upon phosphorylation of serine residues in the SR domains by either of two CDC2-like kinases, CLK1 and CLK2, that are known to phosphorylate SR domains in living cells (*16*, *17*). Mutational change of the serine residues of the SR domain in the SRSF2 alternative splicing factor to glycine resulted in repetitive GR_n sequences that retain binding to hnRNPA2 hydrogels, but are not affected by CLK1/CLK2-mediated phosphorylation.

Moving from test tubes to cells, cells expressing variants of SRSF2, wherein serine residues of its two SR domains were uniformly changed to glycine, revealed association of the altered splicing factor with nucleoli. Cotransfection of an expression vector encoding the CLK1 kinase failed to liberate the $SRSF2_{G1/G2}$ variant from its nucleolar localization. Together, these data give evidence of a pathway in which SR domain–containing splicing factors first enter a nucleolar compartment in a hypophosphorylated state (*21*) then migrate to nuclear speckles as a function of phosphorylation by the CLK1/2 family of protein kinase enzymes.

We do not know the identity of the nucleolar target of hypophosphorylated SR domains. Many aspects of the behavior of SR domains in cells can be mimicked by their attachment to hydrogel droplets composed of polymeric fibers of the LC domain of hnRNPA2, including that the interaction can be readily reversed by phosphorylation of serine residues by the CLK1/2 protein kinase enzymes. We speculate that the nucleolar target of hypophosphorylated SR domains will also represent a polymeric fiber not unlike the hnRNPA2 fibers described herein.

Two of the RAN translation products of the hexanucleotide repeats associated with disease variants of the *C9orf72* gene behaved as cytotoxins that impeded pre-mRNA splicing and the biogenesis of ribosomal RNA. The relevant peptides are polymers of one of two dipeptide sequences, GR_n or PR_n. The density of arginine residues favorable for solubility might also facilitate nuclear import and cell penetrability. Repetitive arginine residues might account for nuclear entry by mimicking the positive charge prototypical of nuclear localization signals (*24*, *25*). Likewise, arginine-rich peptides, such as the HIV TAT peptide, are readily able to penetrate cells (*26*). Here, both of the GR_{20} and PR_{20} peptides entered cells, migrated to the nucleus, and associated with the periphery of nucleoli. We hypothesize that the binding of GR_n and PR_n polymers to nuclear puncta suspected to represent an early stage in the complex process of pre-mRNA splicing (*21*) may clog the pathway. This concept of peptide-induced toxicity differs from earlier studies that gave evidence of cytoplasmic aggregates observed in HeLa cells expressing a fusion protein linking GFP to five repeats of the GR dipeptide (*7*), immunostaining assays of ALS disease tissue showing cytoplasmic aggregates of the GR RAN translation product (*9*), and immunostaining of ALS disease tissue showing cytoplasmic aggregates of the PR RAN translation product (*5*). Our concept of nucleolar binding of the PR_n and GR_n RAN translation products and consequential impediments to RNA biogenesis

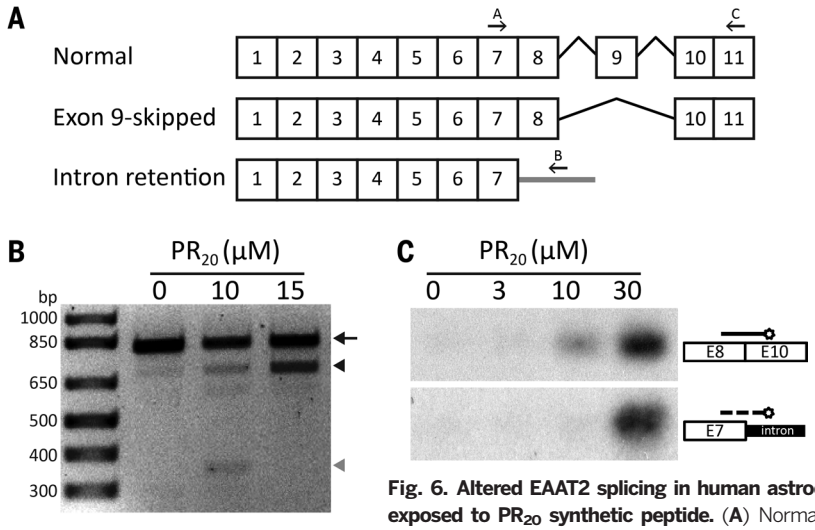

Fig. 6. Altered EAAT2 splicing in human astrocytes exposed to PR_{20} synthetic peptide. (**A**) Normal and aberrantly spliced EAAT2 transcripts reveal locations of exon 9 skipping and intron 7 retention. Arrows indicate the primers used for RT-PCR of EAAT2 transcripts (*22*). (**B**) RNA prepared from human astrocytes exposed to 0, 10 μM, or 15 μM synthetic PR_{20} peptide was interrogated with PCR primers diagnostic of the normal EAAT2 transcript (arrow), the exon 9–skipped variant (black arrowhead) or the intron 7–retention variant (gray arrowhead). No evidence of aberrant EAAT2 transcripts was observed in control cells. Cells exposed for 36 hours to 10 μM synthetic PR_{20} peptide showed equal amounts of the exon 9–skipped and intron 7–retention aberrant transcripts. Cells exposed for 36 hours to 15 μM synthetic PR_{20} peptide showed a significant increase in the amount of the exon 9–skipped EAAT2 transcript. (**C**) Southern blot probes specific to the exon 9–skipped and intron 7–retention aberrant EAAT2 transcripts revealed exclusive labeling of the PCR products specific to each mRNA isoform. Human astrocytes were exposed to zero, 3 μM, 10 μM, or 30 μM of the synthetic PR_{20} peptide for 6 hours. After PCR amplification and gel electrophoresis, PCR products were blotted onto nitrocellulose and hybridized with isoform-specific probes (*22*).

and earlier concepts of aggregate-mediated toxicity generated by any or all of the five RAN translation products of the sense or antisense transcripts of the *C9orf72* repeats are not necessarily mutually exclusive.

We offer three reasons to believe that the toxicities driven by the GR_n and PR_n RAN translation products may account for the pathophysiological deficits observed in nerve cell dysfunction in patients carrying repeat expansions in the *C9orf72* gene. First, very specific alterations in splicing of the EAAT2 mRNA have been described from brain tissue derived from *C9orf72* patients, including the skipping of exon 9 and the inclusion of 1008 nucleotides of intronic sequence distal to the splice donor site of exon 7. Administration of the PR_{20} peptide to human astrocytes derived from normal subjects led to the same changes in EAAT2 pre-mRNA splicing. Second, RNA-seq studies of cells exposed to the GR_{20} and PR_{20} peptides revealed changes in the expression of snoRNA known to be important for maturation of rRNA. These data properly predicted that peptide-treated cells would suffer deficits in rRNA maturation. Third, recent studies of brain tissue derived from patients carrying repeat expansions in the *C9orf72* gene have given evidence of nucleolar disorder, including impediments in the processing of the 45*S* ribosomal RNA precursor (*27*). Thus, we conclude that administration of the GR_{20} and PR_{20} peptides to normal human astrocytes leads to pathophysiological deficits that mimic those observed in disease tissue.

In the context of disease progression of both ALS and FTD patients carrying a repeat expansion in the *C9orf72* gene, nerve cell degeneration only begins after 40 or more years of age (*28*). How is it that RAN translation products appear with such delayed kinetics? Perhaps RAN translation of the hexanucleotide repeats may take place at very low levels in presymptomatic decades. Stochastically, the heavy burden of RNA biogenesis demanded of neurons may eventually lead to sufficient expression of the GR_n and/or PR_n peptides to begin to mildly impede nucleolar function and pre-mRNA splicing. This impediment might favor the generation of damaged ribosomes that could themselves favor RAN translation relative to normal protein synthesis. Alternatively, improperly spliced mRNAs might affect events such as the control of nuclear import and/or export as regulated by the RAN GTPase, perhaps favoring export of sense or antisense transcripts of the expanded hexanucleotide repeats in the *C9orf72* gene for cytoplasmic translation. If either or both of these alterations slightly favored production of the GR_n and/or PR_n peptides, the process could eventually snowball to the point of nucleolar catastrophy and nerve cell death.

We close with two final considerations. First, we do not know what pathway of cell death results from the toxic activities of the GR_n or PR_n polymers. If the death pathway were messy, spilling out cellular contents, it is possible that the GR_n and PR_n polymers of a dead neuron could be taken up by neighboring cells just as we have observed for cultured cells and so facilitate the pathological spread of toxicity. Second, we offer the idea that what has been witnessed in this work could reflect the failed birth of a gene. Whereas the repeat expansion in *C9orf72* can be considered to have generated a new protein-coding gene, it is ultimately toxic to the organism. Could it be that the scores of LC sequences associated with DNA and RNA regulatory proteins in eukaryotic cells evolved in this same manner?

REFERENCES AND NOTES

1. M. DeJesus-Hernandez *et al.*, *Neuron* **72**, 245–256 (2011).
2. A. E. Renton *et al.*, *Neuron* **72**, 257–268 (2011).
3. C. Lagier-Tourenne *et al.*, *Proc. Natl. Acad. Sci. U.S.A.* **110**, E4530–E4539 (2013).
4. S. Mizielinska *et al.*, *Acta Neuropathol.* **126**, 845–857 (2013).
5. T. Zu *et al.*, *Proc. Natl. Acad. Sci. U.S.A.* **110**, E4968–E4977 (2013).
6. T. Zu *et al.*, *Proc. Natl. Acad. Sci. U.S.A.* **108**, 260–265 (2011).
7. P. E. Ash *et al.*, *Neuron* **77**, 639–646 (2013).
8. C. J. Donnelly *et al.*, *Neuron* **80**, 415–428 (2013).
9. K. Mori *et al.*, *Science* **339**, 1335–1338 (2013).
10. M. Kato *et al.*, *Cell* **149**, 753–767 (2012).
11. I. Kwon *et al.*, *Cell* **155**, 1049–1060 (2013).
12. M. B. Roth, C. Murphy, J. G. Gall, *J. Cell Biol.* **111**, 2217–2223 (1990).
13. K. M. Neugebauer, J. A. Stolk, M. B. Roth, *J. Cell Biol.* **129**, 899–908 (1995).
14. A. M. Zahler, W. S. Lane, J. A. Stolk, M. B. Roth, *Genes Dev.* **6**, 837–847 (1992).
15. K. Colwill *et al.*, *EMBO J.* **15**, 265–275 (1996).
16. P. I. Duncan, D. F. Stojdl, R. M. Marius, K. H. Scheit, J. C. Bell, *Exp. Cell Res.* **241**, 300–308 (1998).
17. H. J. Menegay, M. P. Myers, F. M. Moeslein, G. E. Landreth, *J. Cell Sci.* **113**, 3241–3253 (2000).
18. B. E. Aubol *et al.*, *J. Mol. Biol.* **425**, 2894–2909 (2013).
19. A. I. Lamond, D. L. Spector, *Nat. Rev. Mol. Cell Biol.* **4**, 605–612 (2003).
20. M. Thiry, *Eur. J. Cell Biol.* **68**, 14–24 (1995).
21. P. A. Bubulya *et al.*, *J. Cell Biol.* **167**, 51–63 (2004).
22. Materials and methods are available as supplementary materials on *Science* Online.
23. C. L. Lin *et al.*, *Neuron* **20**, 589–602 (1998).
24. D. Kalderon, B. L. Roberts, W. D. Richardson, A. E. Smith, *Cell* **39**, 499–509 (1984).
25. C. Dingwall, J. Robbins, S. M. Dilworth, B. Roberts, W. D. Richardson, *J. Cell Biol.* **107**, 841–849 (1988).
26. A. D. Frankel, C. O. Pabo, *Cell* **55**, 1189–1193 (1988).
27. A. R. Haeusler *et al.*, *Nature* **507**, 195–200 (2014).
28. L. I. Bruijn, T. M. Miller, D. W. Cleveland, *Annu. Rev. Neurosci.* **27**, 723–749 (2004).

ACKNOWLEDGMENTS

We thank M. Brown for suggesting to S.L.M. that the RAN translation products of the hexanucleotide repeats expanded in the *C9orf72* gene might be involved in RNA biogenesis as understood in our solid-state conceptualization of information transfer from gene to message to protein. We also thank B. Tu, D. Nijhawan, T. Han, L. Avery, and M. Rosen for stimulating discussion, and J. Steitz, C. Emerson, B. Alberts, and A. Horwich for helpful comments on the composition of our manuscript. This work was supported by unrestricted endowment funds provided to S.L.M. by an anonymous donor.

SUPPLEMENTARY MATERIALS

www.sciencemag.org/content/345/6201/1139/suppl/DC1
Materials and Methods
Figs. S1 to S6
Table S1
References (*29*–*34*)

17 April 2014; accepted 23 July 2014
Published online 31 July 2014;
10.1126/science.1254917

REPORTS

SUPERCONDUCTIVITY

Light-induced collective pseudospin precession resonating with Higgs mode in a superconductor

Ryusuke Matsunaga,[1]* Naoto Tsuji,[1] Hiroyuki Fujita,[1] Arata Sugioka,[1] Kazumasa Makise,[2] Yoshinori Uzawa,[3]† Hirotaka Terai,[2] Zhen Wang,[2]‡ Hideo Aoki,[1,4] Ryo Shimano[1,5]*

Superconductors host collective modes that can be manipulated with light. We show that a strong terahertz light field can induce oscillations of the superconducting order parameter in NbN with twice the frequency of the terahertz field. The result can be captured as a collective precession of Anderson's pseudospins in ac driving fields. A resonance between the field and the Higgs amplitude mode of the superconductor then results in large terahertz third-harmonic generation. The method we present here paves a way toward nonlinear quantum optics in superconductors with driving the pseudospins collectively and can be potentially extended to exotic superconductors for shedding light on the character of order parameters and their coupling to other degrees of freedom.

Macroscopic quantum phenomena, such as superconductivity and superfluidity, emerge in a variety of physical systems, such as metals, liquid helium, ultracold atomic quantum gases, and neutron stars. One manifestation of the macroscopic quantum nature is the appearance of characteristic collective excitations. Indeed, phenomena associated with collective modes, such as second sound and spin waves in condensates, have been revealed in superfluid helium (*1*, *2*) and in ultracold atomic gases (*3*, *4*).

Generally, collective modes in ordered phases arising from spontaneous symmetry breaking are classified into (i) gapless phase modes [Nambu-Goldstone (NG) mode] and (ii) gapped amplitude modes (Higgs mode) (*5*–*7*). In charged-particle systems such as superconductors with long-range Coulomb interactions, the gapless NG mode becomes massive; that is, its energy is elevated to the plasma frequency as a result of the coupling to the gauge boson (photon field), which is referred to as the Anderson-Higgs mechanism (*8*, *9*). The Higgs amplitude mode in superconductors has been also studied theoretically (*6*, *10*–*15*); because it is not accompanied by charge fluctuations, it does not couple directly to electromagnetic fields in the linear response regime. This is why the Higgs mode in conventional *s*-wave superconductors was observed only recently after a nonadiabatic excitation with a monocycle THz pulse (*16*); previous observations were in a special case where the superconductivity coexists with charge density wave that makes the Higgs mode Raman-active (*17*, *18*). Hence, many questions regarding the Higgs mode in superconductors remain unresolved: How does the mode couple to strong electromagnetic fields in a nonlinear regime? Is it possible to dynamically control the Higgs mode and therefore the superconducting order parameter?

Recent advances in the intense THz generation technique (*19*, *20*) open a new avenue for studying matter phases in nonequilibrium conditions. Amplitude- and phase-resolved spectroscopy using multi-THz pulses has been realized (*21*), enabling the study of coherent transients in many-body systems in low-energy ranges. The purpose of the present work is to explore coherent nonlinear interplay between collective mode in a superconductor and THz light field by investigating the real-time evolution of the order parameter under the driving field of a multicycle (as opposed to monocycle) THz pulse.

In order to study evolutions on a picosecond time scale, we performed THz pump–THz probe spectroscopy (*16*, *22*) (Fig. 1A). To generate an intense multicycle THz pulse as a coherent driving source, we first created an intense monocycle THz pulse by the tilted-pulse front method with a $LiNbO_3$ crystal (*19*, *23*). The monocycle pulse then goes through a band-pass filter to produce a narrow-spectrum multicycle pulse. Three band-pass filters are used to generate the different center frequencies at 0.3, 0.6, or 0.8 THz, respectively, with their power spectra displayed in Fig. 1B. These photon energies are all below the superconducting gap of our NbN sample in the low-temperature limit, which is 1.3 THz (Fig. 1C); this implies that the pump pulse does not generate quasi-particles (QPs) in one-photon processes at low temperatures. The sample is an *s*-wave superconductor NbN thin film with 24-nm thickness grown on an MgO substrate (*24*) with superconducting critical temperature (T_c) = 15 K. The ultrafast dynamics of the superconducting order parameter driven by the multicycle pump pulse is then probed through the transmittance of a monocycle THz pulse that enters the sample collinearly with the pump pulse with a variable time delay. In general, we can detect the temporal waveform of the transmitted probe THz electric field, E_{probe}, by varying the time delay of another optical gate pulse and using the electrooptic (EO) sampling method. In this experiment, we fixed the timing of the optical gate pulse such that, in the absence of the pump, E_{probe} at this timing monotonically changes with temperature, reflecting the change of the order parameter. Temporal evolution of the order parameter induced by the THz pump is sensitively monitored through the change of E_{probe} relative to its value in the absence of the pump as a function of the pump-probe delay time, t_{pp} (*16*, *22*); we denote this change as δE_{probe}. For details, see (*25*). In the present case, we investigated the order parameter dynamics in the presence of coherently oscillating multicycle pump fields. The temporal waveform of the pump THz electric field E_{pump} is displayed in Fig. 1D for the center frequency of ω = 0.6 THz

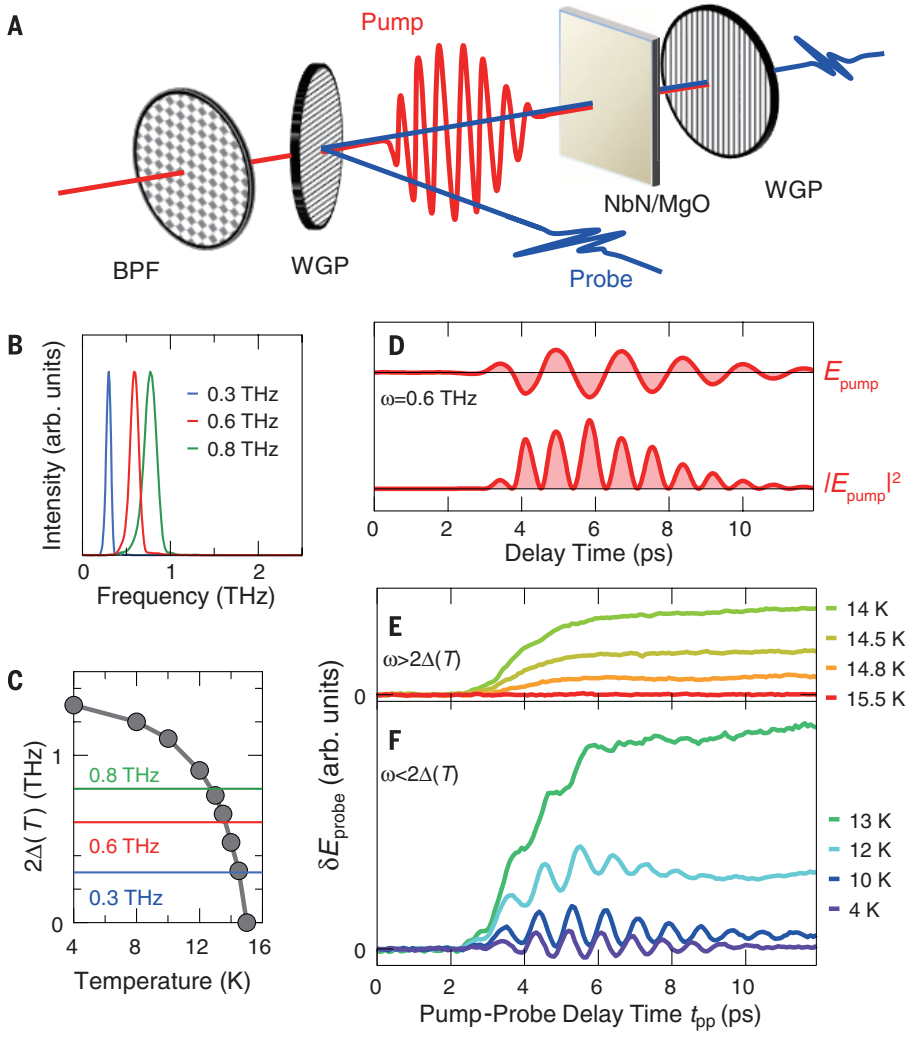

Fig. 1. THz pump–THz probe spectroscopy. (**A**) Schematic experimental setup for the THz pump–THz probe spectroscopy, where BPF is a metal-mesh band-pass filter and WGP a wire-grid polarizer. (**B**) Power spectra of the pump THz pulse with the center frequencies of ω = 0.3, 0.6, and 0.8 THz. (**C**) Temperature dependence of the superconducting gap energy 2Δ of the NbN sample evaluated from optical conductivity spectra based on the Mattis-Bardeen model (*36*). Horizontal lines indicate the center frequencies of the pump pulse. (**D**) Waveform of E_{pump} with the center frequency of ω = 0.6 THz, with the squared $|E_{pump}|^2$ also shown. (**E**) δE_{probe} as a function of t_{pp} in the temperature range $2\Delta(T) < \omega$. Increase of δE_{probe} corresponds to a reduction of the order parameter. (**F**) δE_{probe} against t_{pp} in the temperature range $2\Delta(T) > \omega$.

[1]Department of Physics, University of Tokyo, Hongo, Tokyo, 113-0033, Japan. [2]Kobe Advanced Research Center, National Institute of Information and Communications Technology, Hyogo 651-2492, Japan. [3]National Astronomical Observatory of Japan, Osawa, Mitaka, Tokyo 181-8588, Japan. [4]High Energy Accelerator Research Organization (KEK), Tsukuba, Ibaraki 305-0801, Japan. [5]Cryogenic Research Center, University of Tokyo, Yayoi, Tokyo 113-0032, Japan.
***Corresponding author. E-mail: matsunaga@thz.phys.s.u-tokyo.ac.jp (R.M.); shimano@phys.s.u-tokyo.ac.jp (R.S.)** †Present address: Terahertz Technology Research Center, National Institute of Information and Communications Technology, Tokyo 184-8795, Japan. ‡Present address: Shanghai Institute of Microsystem and Information Technology, Chinese Academy of Sciences, Shanghai 200050, China.

and the maximum electric field of 3.5 kV/cm. Figure 1E shows δE_{probe} with t_{pp} at T = 14 to 15.5 K, at which ω is greater than $2\Delta(T)$. In this temperature range, the probe electric field gradually increased as a function of t_{pp} to reach an asymptotic value, which indicates a reduction of the order parameter resulting from QP excitations (*22*). By contrast, at temperatures below 13 K where $2\Delta(T)$ exceeded ω (Fig. 1F), the long-term reduction of the order parameter became less prominent as temperature decreased, because the QP excitation is suppressed. We immediately noticed that an oscillatory signal emerges with a frequency of 1.2 THz (=2ω) during the pump pulse irradiation, which indicates that the order parameter oscillates with twice the frequency of the driving field.

We physically captured the 2ω oscillation of the order parameter in terms of the precession of Anderson's pseudospins (*26*, *27*). In the Bardeen-Cooper-Schrieffer (BCS) ground state, two electrons with wave numbers $\boldsymbol{k}$ and $-\boldsymbol{k}$ form a spin-singlet Cooper pair, with the BCS wave function given by

$$|\Psi_{BCS}\rangle = \prod_{\boldsymbol{k}}(u_{\boldsymbol{k}}|00\rangle_{\boldsymbol{k}} + v_{\boldsymbol{k}}|11\rangle_{\boldsymbol{k}}) \quad (1)$$

where $|00\rangle_{\boldsymbol{k}}$ and $|11\rangle_{\boldsymbol{k}}$ denote unoccupied and occupied, respectively, $\boldsymbol{k}$ and $-\boldsymbol{k}$. In Anderson's pseudospin formalism, the states $|11\rangle_{\boldsymbol{k}}$ and $|00\rangle_{\boldsymbol{k}}$ are represented by up and down pseudospins, respectively (*25*), where the BCS ground state is thought of as a quantum superposition of up and down pseudospins with amplitudes $v_{\boldsymbol{k}}$ and $u_{\boldsymbol{k}}$, respectively, for each $\boldsymbol{k}$ (Fig. 2A). The normal state has the pseudospins all up for $|\boldsymbol{k}| < k_F$ and all down for $|\boldsymbol{k}| > k_F$ at T = 0 (Fig. 2B), where k_F is the Fermi wave number. Within this representation, the BCS Hamiltonian simply reads $H_{BCS} = 2\sum_{\boldsymbol{k}} \boldsymbol{b}_{\boldsymbol{k}} \cdot \boldsymbol{\sigma}_{\boldsymbol{k}}$, where $\boldsymbol{\sigma}_{\boldsymbol{k}} = (\sigma^x_{\boldsymbol{k}}, \sigma^y_{\boldsymbol{k}}, \sigma^z_{\boldsymbol{k}})$ is the Anderson's pseudospin (*26*) mapped onto the Bloch sphere (Fig. 2C), whereas $\boldsymbol{b}_{\boldsymbol{k}} = (-\Delta', -\Delta'', \varepsilon_{\boldsymbol{k}})$ is a pseudomagnetic field acting on $\boldsymbol{\sigma}_{\boldsymbol{k}}$. Here, $\varepsilon_{\boldsymbol{k}}$ is the band dispersion measured from the Fermi energy, $\Delta = \Delta' + i\Delta'' = U\sum_{\boldsymbol{k}}(\sigma^x_{\boldsymbol{k}} + i\sigma^y_{\boldsymbol{k}})$ is the complex order parameter, and $U(>0)$ is the pairing interaction. In equilibrium, each pseudospin is aligned along the pseudomagnetic field. The time evolution of the BCS state is then described by the Bloch equation for the pseudospins,

$$\frac{\partial}{\partial t}\boldsymbol{\sigma}_{\boldsymbol{k}} = 2\boldsymbol{b}_{\boldsymbol{k}} \times s_{\boldsymbol{k}} \quad (2)$$

that is, the time evolution of the BCS state is represented as the motion of the pseudospins in the pseudomagnetic field. For a spatially homogeneous monochromatic electric field $\boldsymbol{E}\exp(i\omega t)$ irradiated onto a superconductor, the z component of $\boldsymbol{b}_{\boldsymbol{k}}$, in the nonlinear response regime, becomes (*25*)

$$\begin{aligned}\frac{\varepsilon_{\boldsymbol{k}-e\boldsymbol{A}(t)} + \varepsilon_{\boldsymbol{k}+e\boldsymbol{A}(t)}}{2} &= \varepsilon_{\boldsymbol{k}} + \frac{e^2}{2}\sum_{i,j}\frac{\partial^2\varepsilon_{\boldsymbol{k}}}{\partial k_i \partial k_j}A_i(t)A_j(t) + O(A^4) \\ &= \varepsilon_{\boldsymbol{k}} - \frac{e^2}{2}\sum_{i,j}\frac{\partial^2\varepsilon_{\boldsymbol{k}}}{\partial k_i \partial k_j}\frac{E_i E_j}{\omega^2}\exp(i2\omega t) + O(A^4)\end{aligned} \quad (3)$$

where $\boldsymbol{A}(t)$ is the vector potential representing the electric field. We can see that the leading term in the energy variation is $\sim\boldsymbol{A}(t)^2$, which is intuitively because electrons with charge $-e$ hybridize with holes with charge $+e$ in the condensed pair, leading to a nonlinear coupling between light and the condensate and to the pseudospin precession with the frequency 2ω. The coherent collective precession of the pseudospins (Fig. 2D) manifests itself macroscopically as the order parameter oscillation, and the change of the order parameter in turn affects the pseudomagnetic field. We calculated the time evolution of the order parameter self-consistently by numerically solving the Bloch equation for the multicycle pulse [see (*25*) for details]. The simulation indeed exhibits the order parameter oscillation with twice the frequency of the external electric field (Fig. 2E).

An analytic solution for the linearized Bloch equation can in fact be obtained (*28*), where the temporal variation of the order parameter amplitude $[\Delta(t) = \Delta + \delta\Delta(t)]$ turns out to behave around $2\omega = 2\Delta$ as

$$\delta\Delta(t) \propto \frac{1}{|2\omega - 2\Delta|^{1/2}}\cos(2\omega t - \phi) \quad (4)$$

with ϕ being a phase shift that depends on ω. The divergence of the amplitude at $2\omega = 2\Delta$ can be interpreted as a resonance between the induced pseudospin precession with frequency 2ω and the collective amplitude mode of the order parameter, namely the Higgs mode (*16*), with frequency 2Δ. We can then relate the nonlinear current density $\boldsymbol{j}_{NL}$ induced by the external ac field with the change in the order parameter $\delta\Delta(t)$ via (*25*) as

$$\boldsymbol{j}_{NL}(t) \propto \frac{e^2\Delta}{U}\boldsymbol{A}(t)\delta\Delta(t) \quad (5)$$

which takes a form of the London equation. This enables us to regard the nonlinear current, which reflects the dynamics of the order parameter, as a part of the supercurrent.

Because the coherent interaction between the superconductor and the THz electromagnetic radiation results in the nonlinear (2ω, 4ω, 6ω…) oscillations of the order parameter (Eq. 3), the nonlinear current in Eq. 5 should accommodate higher odd-order harmonics in the transmitted pump THz pulse. To confirm this, we performed a nonlinear transmission experiments for the pump THz pulse (without the probe pulse) (Fig. 3A). Figure 3B shows the waveforms of the transmitted pump THz pulse above (15.5 K) and below (10 K) T_c = 15 K; the waveform of the transmitted pulse below T_c is considerably distorted. The power spectra of the transmitted pump THz pulse are shown in Fig. 3C on a logarithmic scale and in Fig. 3D on an expanded linear scale at various temperatures. Below T = 13 K, a prominent peak appears around 1.8 THz, which indeed coincides with 3ω. The intensity at 3ω as a function of the pump electric field strength, depicted in Fig. 3E on a log-log scale, obeys $|E_{pump}|^6$ dependence, endorsing that the

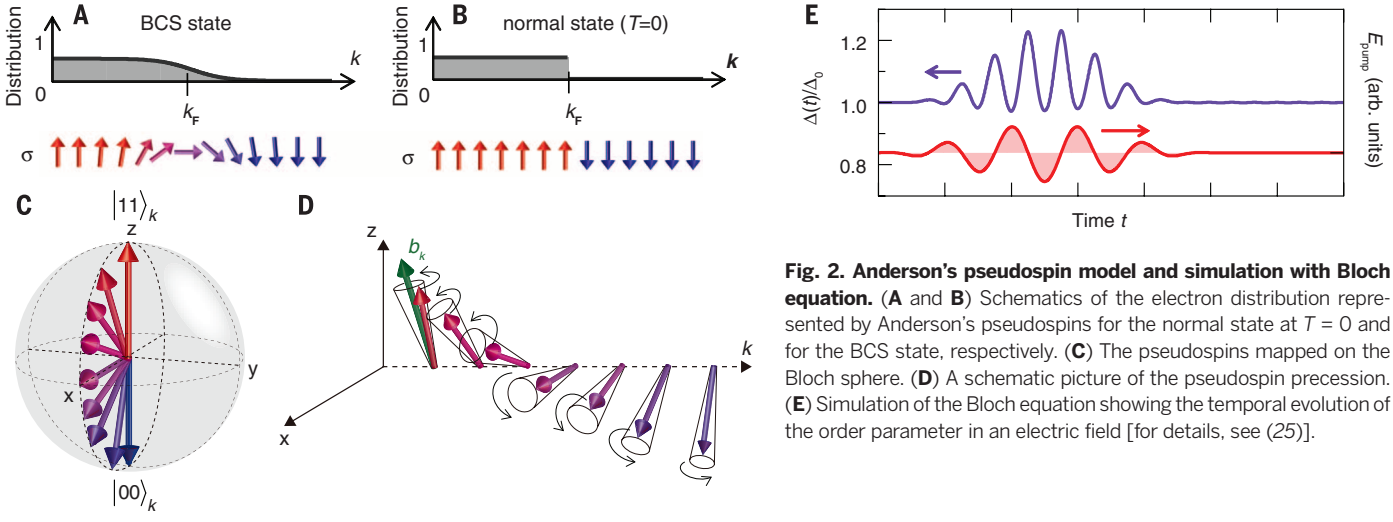

Fig. 2. Anderson's pseudospin model and simulation with Bloch equation. (**A** and **B**) Schematics of the electron distribution represented by Anderson's pseudospins for the normal state at T = 0 and for the BCS state, respectively. (**C**) The pseudospins mapped on the Bloch sphere. (**D**) A schematic picture of the pseudospin precession. (**E**) Simulation of the Bloch equation showing the temporal evolution of the order parameter in an electric field [for details, see (*25*)].

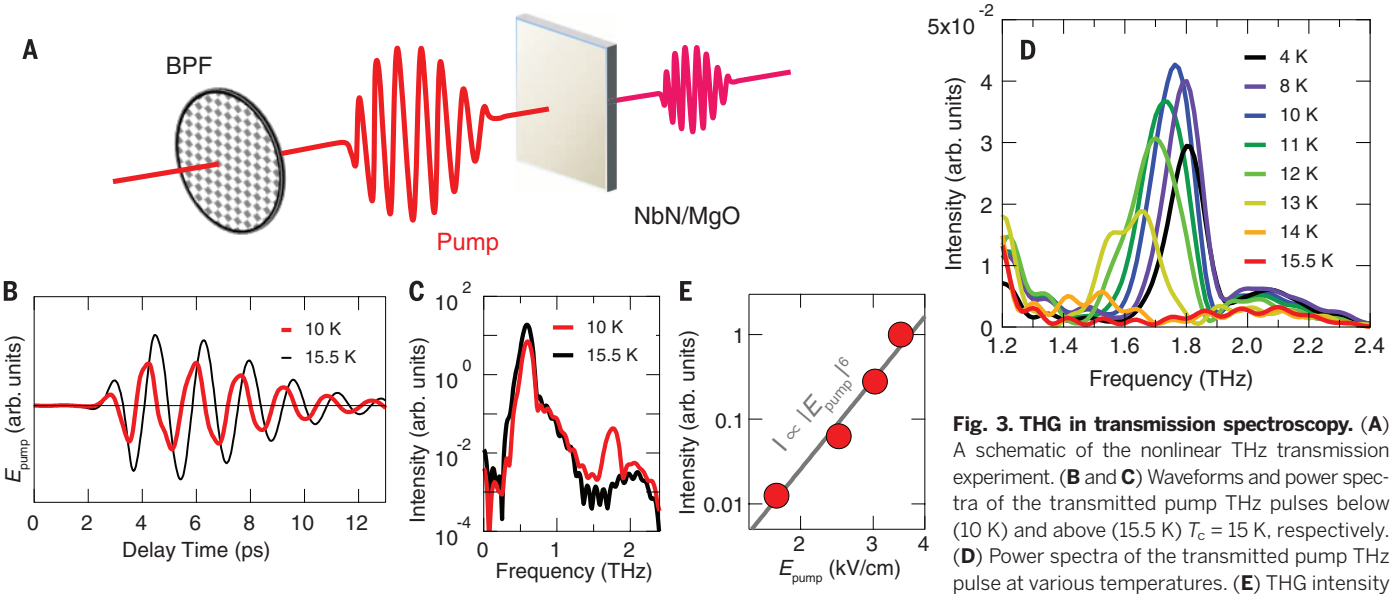

Fig. 3. THG in transmission spectroscopy. (**A**) A schematic of the nonlinear THz transmission experiment. (**B** and **C**) Waveforms and power spectra of the transmitted pump THz pulses below (10 K) and above (15.5 K) T_c = 15 K, respectively. (**D**) Power spectra of the transmitted pump THz pulse at various temperatures. (**E**) THG intensity as a function of the pump THz field strength.

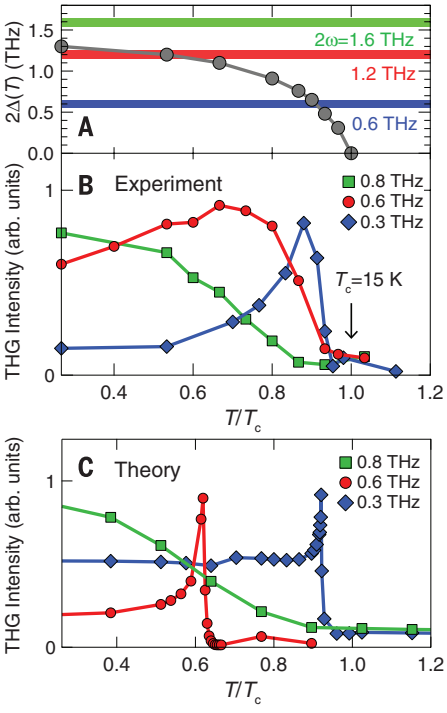

Fig. 4. Temperature dependence of the THG intensity. (**A**) Temperature dependence of the order parameter 2Δ(*T*) compared with twice the pump frequencies, 2ω (horizontal lines). (**B**) Measured temperature dependence of the THG intensities at ω = 0.3, 0.6, and 0.8 THz. (**C**) Calculated THG intensities as a function of temperature obtained by numerically solving the Bloch equation.

signal arises from the third harmonic generation (THG). The THG intensity at 10 K normalized by that of the incident pump pulse reaches 8×10^{-5}, which is high for a film with only 24-nm thickness and 3.5-kV/cm peak electric field (*29*). We could increase the interaction length up to about 0.2 μm, the penetration depth of the sample at 0.6 THz (*30*), which would result in even higher conversion efficiency. A shift of THG peak energy with temperature is discerned in Fig. 3D, which is attributed to the softening of the Higgs mode [2Δ(*T*)] toward T_c. The THG signal disappears before the softening completes because the resonant enhancement is rapidly suppressed when Δ(*T*) moves out of the narrow bandwidth of the incident pump field.

The 2ω oscillation of the order parameter and the THG were also observed for ω = 0.3 and 0.8 THz pumping. Figure 4B summarizes the temperature dependence of the THG intensities for ω = 0.3, 0.6, and 0.8 THz. For ω = 0.3 and 0.6 THz, the THG signal peaks at 13.5 and 10 K, respectively, whereas the THG signal for ω = 0.8 THz monotonically increases with decreasing temperature. Comparing the temperature dependence of the order parameter 2Δ(*T*) (Fig. 4A) with twice the pump frequency 2ω (=0.6, 1.2, and 1.6 THz), one can deduce that the peak in the THG does fall on 2ω = 2Δ(*T*). The THG intensity in Eq. 5 depends on the change of the order parameter amplitude, which is resonantly enhanced when 2ω approaches the inherent Higgs amplitude mode 2Δ(*T*). Indeed, the temperature dependence of the THG intensity calculated with Eq. 5 and shown in Fig. 4C agrees qualitatively with experiment in Fig. 4B. We conclude that the resonance of the Anderson's pseudospin precession in the superconductor is achieved by irradiation of THz pump, which results in large THG. The theoretical results in Fig. 4C exhibit sharp resonance peaks, which result from the lifetime of the Higgs mode assumed to be infinite (i.e., power-law decay) within the BCS approximation (*10*, *12*). In contrast, the observed resonance widths in Fig. 4B are finite, which may be caused by decaying channels for the Higgs mode and the finite spectral width of the pump pulse (Fig. 1B). There are in fact various possible decay processes—including scattering with single-particle excitations, impurities, phonons, or low-frequency NG mode that emerges near T_c (*31*)—for which systematic studies are desirable (*32*).

We last note that superconductors are known to exhibit highly nonlinear responses near the critical field or temperature, giving rise to nonlinear *I-V* characteristics and higher-order harmonics in transport measurements with a frequency range from a few hertz to microwave (*33*–*35*). By contrast, the large nonlinear optical effect revealed here originates from resonance of ac fields to the collective amplitude mode of the order parameter, which leads to the strong THG emission in THz frequency range.

The time-resolved observation of the THz higher-order harmonics will provide a unique avenue for probing ultrafast dynamics of the order parameter in out-of-equilibrium superconductors. It is highly intriguing to explore the quantum trajectories of the pseudospins on Bloch sphere in the nonperturbative light-matter interaction regime with much higher THz fields, which would result in a dynamics of superconducting order parameter not attained in conventional regimes. The present scheme using the nonlinear coupling between pseudospins and light can be also extended to unconventional superconductors, such as the cuprate or iron-pnictide, which would provide new insight about the high-T_c superconductivity and the interplay between the superconducting phase and other coexisting or competing orders.

REFERENCES AND NOTES

1. For a review, see, e.g.,A. J. Leggett, *Rev. Mod. Phys.* **47**, 331–414 (1975).
2. W. P. Halperin, L. P. Pitaevskii, Eds., *Helium III: Modern Problems in Condensed Matter Physics* (North-Holland, Amsterdam, 1990).
3. L. A. Sidorenkov *et al.*, *Nature* **498**, 78–81 (2013).
4. J. S. Krauser *et al.*, *Science* **343**, 157–160 (2014).

5. Y. Nambu, *Phys. Rev. Lett.* **4**, 380–382 (1960).
6. C. M. Varma, *J. Low Temp. Phys.* **126**, 901–909 (2002).
7. G. E. Volovik, M. A. Zubkov, *J. Low Temp. Phys.* **175**, 486–497 (2014).
8. P. W. Anderson, *Phys. Rev.* **130**, 439–442 (1963).
9. P. W. Higgs, *Phys. Lett.* **12**, 132–133 (1964).
10. A. F. Volkov, S. M. Kogan, *Zh. Eksp. Teor. Fiz.* **65**, 2038 (1973) [*Sov. Phys. JETP* **38**, 1018 (1974)].
11. R. A. Barankov, L. S. Levitov, B. Z. Spivak, *Phys. Rev. Lett.* **93**, 160401 (2004).
12. E. A. Yuzbashyan, M. Dzero, *Phys. Rev. Lett.* **96**, 230404 (2006).
13. T. Papenkort, V. M. Axt, T. Kuhn, *Phys. Rev. B* **76**, 224522 (2007).
14. N. Tsuji, M. Eckstein, P. Werner, *Phys. Rev. Lett.* **110**, 136404 (2013).
15. Y. Barlas, C. M. Varma, *Phys. Rev. B* **87**, 054503 (2013).
16. R. Matsunaga *et al.*, *Phys. Rev. Lett.* **111**, 057002 (2013).
17. R. Sooryakumar, M. V. Klein, *Phys. Rev. Lett.* **45**, 660–662 (1980).
18. P. B. Littlewood, C. M. Varma, *Phys. Rev. Lett.* **47**, 811–814 (1981).
19. J. Hebling, K.-L. Yeh, M. C. Hoffmann, B. Bartal, K. A. Nelson, *J. Opt. Soc. Am. B* **25**, B6 (2008).
20. For a review, see, e.g., T. Kampfrath, K. Tanaka, K. A. Nelson, *Nat. Photonics* **7**, 680–690 (2013).
21. F. Junginger *et al.*, *Phys. Rev. Lett.* **109**, 147403 (2012).
22. R. Matsunaga, R. Shimano, *Phys. Rev. Lett.* **109**, 187002 (2012).
23. R. Shimano, S. Watanabe, R. Matsunaga, *J. Infrared. Milli. Terahz. Waves* **33**, 861–869 (2012).
24. K. Makise, H. Terai, M. Takeda, Y. Uzawa, Z. Wang, *IEEE Trans. Appl. Supercond.* **21**, 139–142 (2011).
25. Supplementary materials are available on *Science* Online.
26. P. W. Anderson, *Phys. Rev.* **112**, 1900–1916 (1958).
27. Recently, a time-resolved Raman experiment in a high-T_c cuprate has been reported and accounted for by the dynamics of individual pseudospins corresponding to the charge fluctuations induced by an impulsive stimulated Raman process (*38*).
28. N. Tsuji, H. Aoki, http://arxiv.org/abs/1404.2711.
29. The conversion efficiency was estimated without compensating the frequency dependence of the EO-sampling detection coefficient for the 1-mm-thick ZnTe crystal. The correction would make the conversion efficiency even higher.
30. A. Kawakami, Y. Uzawa, Z. Wang, *Physica C* **412–414**, 1455–1458 (2004).
31. P. V. Carlson, A. M. Goldman, *Phys. Rev. Lett.* **34**, 11–15 (1975).
32. Such a study may reveal the underlying coupling strength of the superconducting order parameter with other excitations; for the case of charge-density-wave system; see, e.g., (*37*).
33. L. P. Gorkov, G. M. Eliashberg, *Zh. Eksp. Teor. Fiz.* **54**, 612 (1968) [*Sov. Phys. JETP* **27**, 328 (1968)].
34. J. C. Amato, W. L. McLean, *Phys. Rev. Lett.* **37**, 930–933 (1976).
35. O. Entin-Wohlman, *Phys. Rev. B* **18**, 4762–4767 (1978).
36. W. Zimmermann, E. H. Brandt, M. Bauer, E. Seider, L. Genzel, *Physica C* **183**, 99–104 (1991).
37. H. Schaefer, V. V. Kabanov, J. Demsar, *Phys. Rev. B* **89**, 045106 (2014).
38. B. Mansart *et al.*, *Proc. Natl. Acad. Sci. U.S.A.* **110**, 4539 (2013).

ACKNOWLEDGMENTS

This work was supported by a Grant-in-Aid for Scientific Research (grant nos. 25800175, 22244036, 20110005, 25104709, 25800192, and 26247057) and Advanced Photon Science Alliance by the Photon Frontier Network Program from Ministry of Education, Culture, Sports, Science, and Technology.

SUPPLEMENTARY MATERIALS

www.sciencemag.org/content/345/6201/1145/suppl/DC1
Materials and Methods
Supplementary Text
Figs. S1 to S3
References

11 April 2014; accepted 24 June 2014
Published online 10 July 2014;
10.1126/science.1254697

NANOMATERIALS

Self-assembly of magnetite nanocubes into helical superstructures

Gurvinder Singh,[1] Henry Chan,[2] Artem Baskin,[2] Elijah Gelman,[1] Nikita Repnin,[2] Petr Král,[2,3]* Rafal Klajn[1]*

Organizing inorganic nanocrystals into complex architectures is challenging and typically relies on preexisting templates, such as properly folded DNA or polypeptide chains. We found that under carefully controlled conditions, cubic nanocrystals of magnetite self-assemble into arrays of helical superstructures in a template-free manner with >99% yield. Computer simulations revealed that the formation of helices is determined by the interplay of van der Waals and magnetic dipole-dipole interactions, Zeeman coupling, and entropic forces and can be attributed to spontaneous formation of chiral nanocube clusters. Neighboring helices within their densely packed ensembles tended to adopt the same handedness in order to maximize packing, thus revealing a novel mechanism of symmetry breaking and chirality amplification.

Nanoscale particles often self-assemble into superstructures with distinctive spatial arrangements that are difficult to predict based on the nature of their building blocks (*1*–*9*). This is because the stabilization of such self-assembled materials results from a delicate competition among forces of comparable magnitudes, originating in van der Waals, Coulombic, magnetic, and other types of particle interactions (*10*). Although the structures of some systems are dominated by forces of a common origin [such as electrostatic interactions that govern the formation of open-lattice assemblies of peptide filaments (*7*) or colloidal crystals with a diamond-like lattice (*3*)], it is typically the interplay between various nanoscale forces that leads to the formation of highly complex materials, such as nanocrystal superlattices exhibiting polymorphism (*11*, *12*).

Self-assembly of nanoparticles driven by competing forces can result in truly unique structures, the diversity and complexity of which could be particularly striking if the building blocks were simultaneously coupled by short- and long-range forces of different symmetries. Such frustration could arise in ensembles of magnetic nanocrystals (NCs) whose axes of preferential magnetization (so-called "easy" axes) do not correspond to any of the directions favoring close packing. In the case of magnetite—the most abundant magnetic material on Earth, also present inside multiple living organisms in the form of NCs (*13*)—this condition is best fulfilled by cubic-shaped particles, whose easy axes (the [111] crystallographic direction; see Fig. 1B) connect two diagonally opposite corners of each cube. However, complex superstructures resulting from the competition between the shape anisotropy (favoring face-to-face interactions) and the magnetocrystalline anisotropy (favoring corner-to-corner interactions) have not been reported, perhaps because the former type of anisotropy typically dominates the latter (*14*, *15*). Here, we investigated the self-assembly of magnetite NCs at the liquid-air interface in the presence of external magnetic fields. Depending on the density of the NCs, we identified different types of self-assembled superstructures, including one-dimensional belts as well as single, double, and triple helices.

In our experimental setup (Fig. 1A), a drop of hexane solution of relatively monodisperse magnetite nanocubes (*16*–*18*) [average edge length = 13.4 nm, corner bluntness ρ = 23%; Fig. 1B and figs. S1, S2, S3, and S28A (*19*)] containing excess oleic acid (OA) was placed at the diethylene glycol (DEG)–air interface (*20*, *21*) in the presence of a magnetizing field (whose strength H was regulated in the range of 0 to 700 G). The solvent was allowed to evaporate within ~10 min. Our NCs are in the superparamagnetic (SPM) size regime; that is, the collective dipoles of individual NCs thermally fluctuate, and the directions of the dipole moments are random. When the NCs were exposed to an external magnetic field, the collective dipoles became partially aligned with the field direction, which allowed for the cooperative magnetic dipole-dipole coupling between the NCs. The resulting chains of single particles (fig. S9) further aggregated as the solvent evaporated, ultimately giving rise to higher-order superstructures at the solvent-air interface. These superstructures could be transferred onto a substrate of choice (e.g., a carbon-coated copper grid or a silicon wafer for inspection) (Fig. 1A). On the basis of electron microscopy images, we estimate that fewer than 1% of the NCs remained unassembled.

[1]Department of Organic Chemistry, Weizmann Institute of Science, Rehovot 76100, Israel. [2]Department of Chemistry, University of Illinois, Chicago, IL 60607, USA. [3]Department of Physics, University of Illinois, Chicago, IL 60607, USA.
*Corresponding author. E-mail: rafal.klajn@weizmann.ac.il (R.K.); pkral@uic.edu (P.K.)

The nature of these superstructures strongly depended on the surface concentration of the particles (*22*). For concentrations corresponding to less than ~20% of the monolayer coverage (or $\chi < 0.2$, where $\chi = 1$ corresponds to a densely packed monolayer of nanocubes coated with interpenetrating monolayers of OA), no long-range or well-defined structures were found (fig. S10). When $\chi \approx 0.2$, however, NCs assembled into parallel arrays of one-dimensional (1D) belts (*23*, *24*) with high aspect ratios (two to three NCs across and as long as 100 μm; Fig. 1C) and oriented parallel to the applied field (figs. S12 and S13). Individual cubes within these belts had their [100] crystallographic axes oriented parallel to the long axes of the belts (Fig. 1C, inset); thus, we refer to these assemblies as belts$_{100}$. This arrangement of the building blocks maximized the cube-cube contact within the assemblies (i.e., the assemblies were dominated by the shape anisotropy of the particles). The widths of these belts grew with increasing χ and decreasing H values.

To better understand these results, we modeled the arrangements of magnetic dipoles of individual SPM particles within belts by Monte Carlo simulations (*25*) [for additional details on the theoretical model, see (*19*) and figs. S20 to S28]. As Fig. 1D shows, dipole orientations in individual NCs are determined by the competition between dipole-dipole interactions [attractive when two parallel dipoles are within a cone with a polar angle $\theta < \cos^{-1}(1/\sqrt{3}) \approx 54^{\circ}$] and coupling to an external field (Zeeman coupling, which tends to orient the dipoles along the field lines). In the presence of a relatively weak (e.g., 167 G) field, the dipoles assume a "zigzag" configuration "unlocked" from the external field, favoring the magnetocrystalline anisotropy. As the field strength increases, the dipoles become more aligned; eventually, all of them are oriented along the field lines (e.g., at 668 G; Fig. 1D, bottom). However, this dipole arrangement is not favorable because of the magnetic repulsion between cubes lying side by side. To reduce these repulsive interactions, the belts become gradually thinner with increasing applied field [this also explains the equal spacings between individual belts—see, for example, fig. S8C].

In all experiments, the belts' long axes followed the lines of the applied magnetic field. Thus, we could induce the growth of belts tilted with respect to the liquid-air interface by modifying the direction of the applied magnetic field. In the presence of a field directed perpendicular to the liquid-air interface, the NCs assembled into arrays of pillars (fig. S11). Similar to the belts parallel to the interface, individual pillars repelled one another in the presence of a magnetic field, which resulted in their hexagonal close packing (fig. S11D).

Next, we simulated dipole orientations as a function of belt thickness in the presence of a constant applied magnetic field (Fig. 1E; here, H = 167 G). As belts became wider, magnetic dipoles were increasingly decoupled from the external field because of large induced fields

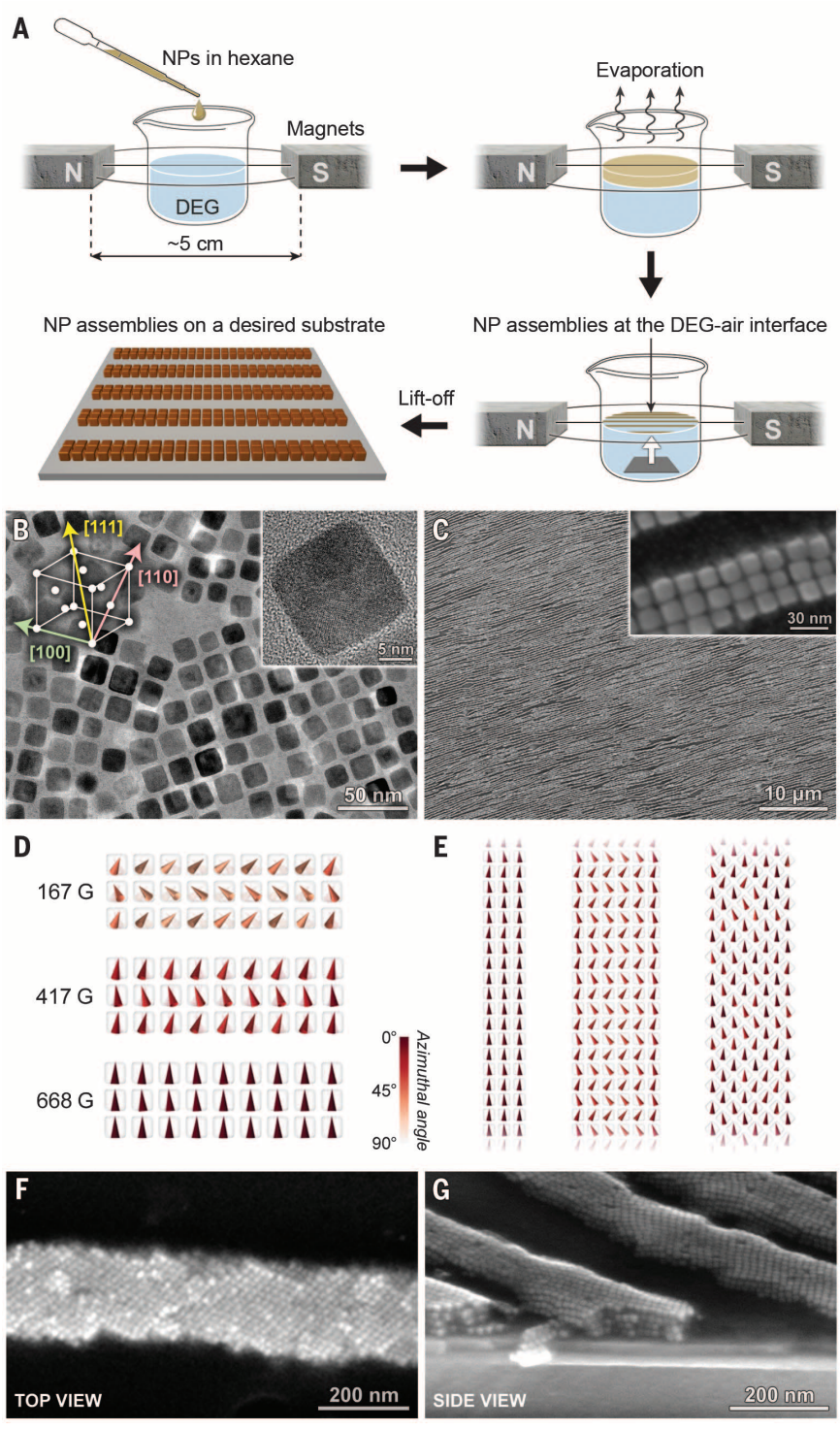

Fig. 1. Self-assembly of one-dimensional nanocube belts. (**A**) Schematic representation of the experimental setup. (**B**) Low- and high-magnification transmission electron microscopy (TEM) images of the building blocks, ~13-nm Fe_3O_4 nanocubes. The [111], [110], and [100] crystallographic directions correspond to the easy, intermediate, and hard axes of magnetization, respectively. (**C**) Low- and high-magnification scanning electron microscopy (SEM) images of belts$_{100}$. (**D**) Averaged orientations of dipoles in a nine-cube-wide belt$_{100}$ in the presence of increasing magnetic fields. (**E**) Orientations of dipoles in belts$_{100}$ of different widths and in a belt$_{110}$ under a relatively weak external field (H = 167 G). The energies of these structures are discussed in (*19*). (**F** and **G**) Top and side views of belts$_{110}$ by SEM.

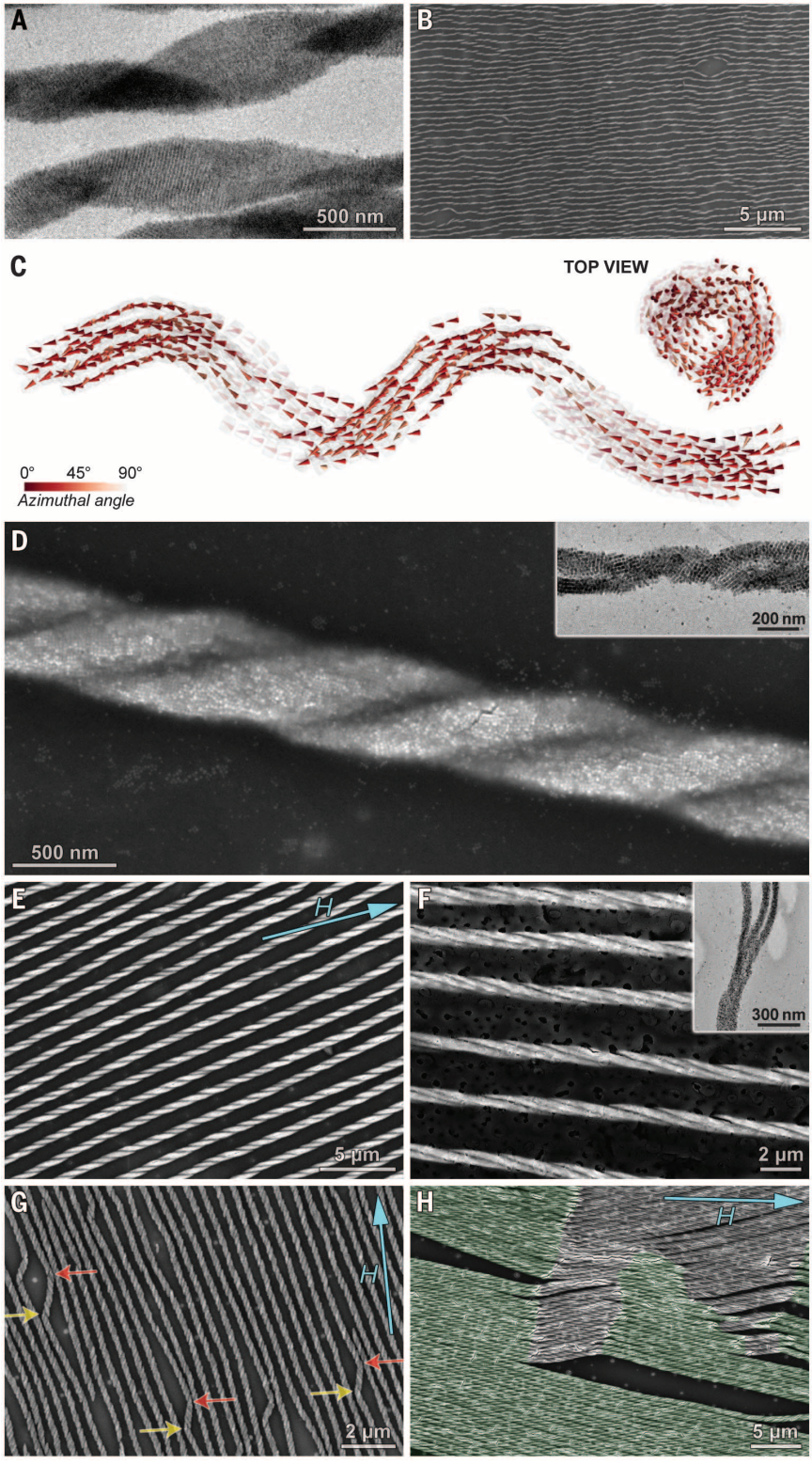

Fig. 2. Self-assembly of helical nanocrystal superstructures. (**A**) TEM image of individual single-stranded helices. (**B**) SEM image of a large array of single-stranded helices. (**C**) Snapshots from Monte Carlo simulations of a one-dimensional belt folding into a helix. (**D**) SEM image of a well-defined double helix. Inset shows a TEM image of two belts wrapping around each another. (**E**) SEM image of an array of double helices. (**F**) An array of triple helices and (inset) the end of a triple helix. (**G**) SEM image showing self-healing of double helices ("chirality self-correction"). Yellow and red arrows indicate sites of chirality inversion. (**H**) Collective switching of chirality. Gray and green colors indicate patches of right- and left-handed helices, respectively. In (E), (G), and (H), blue arrows show the direction of the applied magnetic field.

(Fig. 1E, center). To compensate for the ineffective Zeeman coupling, we rotated each cube by 45° such that their [110] axes were parallel to the field direction; we call the resulting assemblies belts$_{110}$. Although this new arrangement (Fig. 1E, right) was less favorable from the van der Waals interaction point of view (the belts' sides are ridged and not smooth), magnetization along the [110] direction (the "intermediate" axis) occurred more easily than along the [100] ("hard") axis (*26*, *27*) (for quantitative analysis of belts$_{100}$ versus belts$_{110}$, see fig. S22). The formation of belts$_{110}$ was experimentally observed in the narrow range of $1 < \chi < 1.5$ (e.g., Fig. 1, F and G, and fig. S8F).

The most striking manifestation of this trend was observed in experiments performed at $\chi > \sim 1.5$, where the nanocubes tended to orient their [111] axes—that is, the "easy" axes of magnetization—along the magnetic field lines. Because of this arrangement, the belts spontaneously folded (*28*–*30*), giving rise to single-stranded helices (*31*) (Fig. 2A and fig. S14). Monte Carlo simulations confirmed that the formation of helices is accompanied by a free energy minimization (Fig. 2C; see also fig. S23). A detailed analysis revealed that the helices originate from the packing of (transiently) chiral nanocube nuclei, which resulted from the competition of magnetic and spatial symmetries (fig. S21). Similar to the belts discussed above, the helices were evenly spaced and spanned long distances of up to several hundred micrometers (see, for example, Fig. 2B). The properties of these helices were mostly governed by the surface concentration of the NCs: High values of χ entailed large effective magnetic fields, thus promoting a rearrangement of the NCs from the original belt$_{100}$ ensemble (i.e., gradually decreasing the helical pitch). At the same time, high χ values contributed to the widening of the helices (i.e., decreasing interfilament distances). We also observed that individual single-stranded helices tended to wrap around each other to form double-stranded (Fig. 2, D and E, and figs. S15 and S16) or even triple-stranded (Fig. 2F) helices.

The relatively thin helices prepared at $1.5 < \chi < 2.0$ comprised equal populations of intermixed left- and right-handed structures, all oriented parallel to the applied field; Fig. 2A shows a right-handed helix (top) neighboring a left-handed one (bottom). At higher ($\chi > 2.0$) coverages, however, long axes of the helices were tilted with respect to the external field, with the tilt angles θ increasing with increasing χ values. At the same time, we observed that the helices were mostly of the same handedness (e.g., Fig. 2E). A clue to the origin of this selectivity is provided by experiments that yielded ill-defined mixtures of right- and left-handed helices (e.g., Fig. 2, G and H); these two types of helices were tilted at $+\theta$ and $-\theta$ angles with respect to the external magnetic field. To maximize packing within a given area, all of the NC assemblies should be oriented in the same direction and have the same handedness. There was no intrinsic preference for helices of either handedness; each experiment began with the nucleation of either right- or left-handed helices with equal probabilities. As the assembly

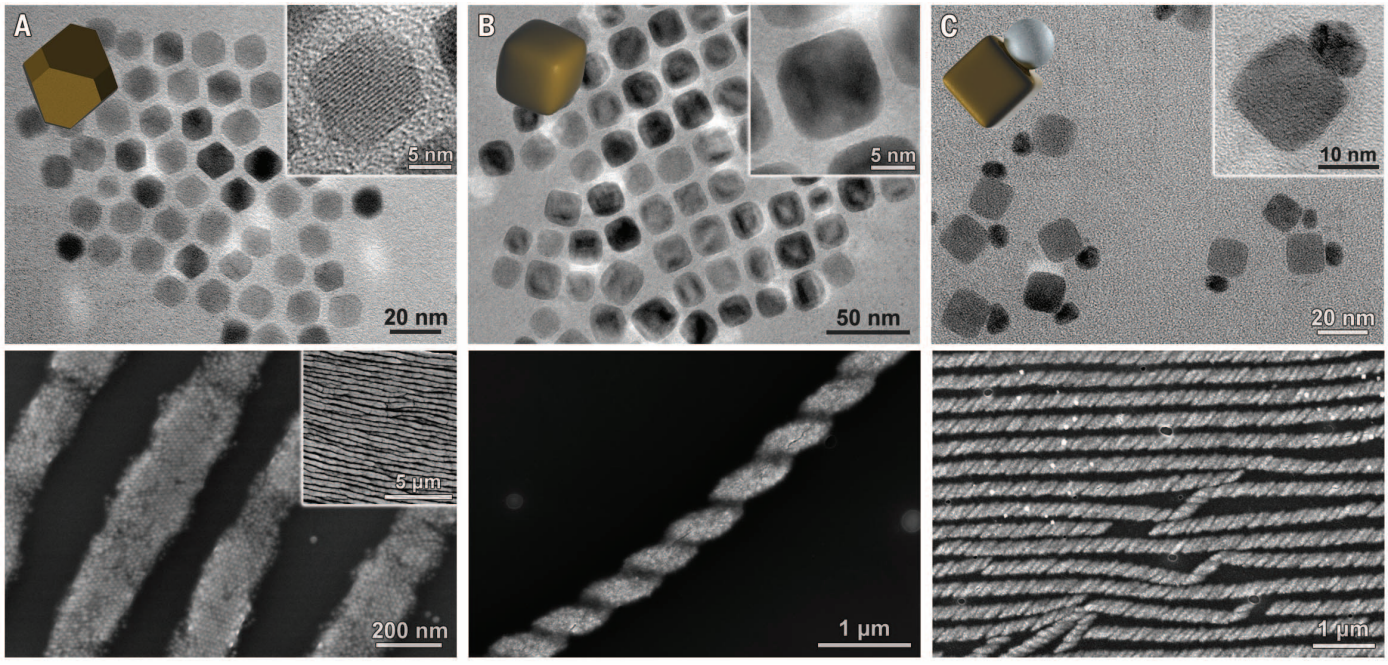

Fig. 3. Self-assembly of Fe_3O_4 nanocrystals of different shapes. (**A**) TEM images of truncated octahedra (top) and an SEM image of 1D belts that they assemble into (bottom; SEM image in the inset shows belts obtained at $\chi = 5$). (**B**) TEM images of rounded cubes (top) and an SEM image of the resulting helix (bottom). (**C**) TEM images of Fe_3O_4-Ag heterodimeric NCs (top) and an SEM image of an ensemble of helices (bottom). Insets in the top row are TEM images of individual nanocrystals obtained at high magnification.

progressed from one side of the dish to the other, however, the chirality of preformed helices determined those of their neighbors, and this process continued to yield large (up to 1 mm^2) domains of "enantiopure" helices.

However, defects were occasionally observed. The red arrows in the ensemble of right-handed helices in Fig. 2G point to sites where chirality inversion took place, giving rise to segments of left-handed structures. Segments of the "wrong" chirality were relatively short; the tendency to maximize packing provided the helices with the ability to "correct" their chirality, as denoted by the yellow arrows in Fig. 2G. We also observed "collective switching of chirality": When a critical number of helices changed their handedness, a domain of inverted helices was stably propagated (Fig. 2H).

To verify the key importance of magnetocrystalline anisotropy for forming helical assemblies, we performed additional assembly experiments using differently shaped magnetite NCs, including spheres, truncated octahedra, and rounded cubes, as well as Fe_3O_4-Ag heterodimeric particles (Fig. 3 and figs. S4 to S7), all of which were in the same size regime (10 to 15 nm). With spherical and octahedral building blocks, we did not observe assemblies other than the 1D belts—even at χ values as high as 5 (Fig. 3A, lower panel, inset). These observations can be rationalized by the lack of competition between the magnetic interactions and close packing: In the case of octahedral NCs, the magnetocrystalline and shape anisotropy act cooperatively to align the particles with their [111] axes oriented parallel to the applied field, whereas the spheres possess no shape anisotropy.

To further clarify these observations, we investigated how cube corner bluntness affected the structure of the assemblies by preparing rounded cubes (Fig. 3B; $\rho = 30\%$). We grew the NCs in the presence of a mixture of surfactants that stabilized the spherical and the cubic morphologies (OA and sodium oleate, respectively). The superstructures obtained at high χ values exhibited helicity, although the helicity was not as prominent as in superstructures obtained from the original cubes; such a result is consistent with the building blocks having shapes intermediate between those of the spheres and the cubes. Finally, we synthesized heterodimers, each comprising a cubic Fe_3O_4 domain and a spherical Ag domain (Fig. 3C, top). The presence of the Ag particles hindered efficient dipole-dipole interactions between the magnetite domain; nonetheless, well-defined helices were observed (Fig. 3C, bottom, and fig. S18B), although the belt-to-helix transition occurred at much higher (χ > ~5.0) particle densities—a threshold that is most likely governed by the size of the Ag domain.

We observed the emergence of helical nanoparticle superstructures during the self-assembly of superparamagnetic nanocrystals. We envision that the diversity of self-assembled superstructures could be further expanded by (i) decorating the surfaces of magnetite NCs with functional ligands (*32*), (ii) choosing SPM NCs of different shapes and compositions (e.g., Ni, Fe, and $CoFe_2O_4$) as starting materials, (iii) using mixtures of different NCs as building blocks (see fig. S19), and (iv) using complex or dynamic magnetic (*33*) fields during the self-assembly process.

REFERENCES AND NOTES

1. E. V. Shevchenko, D. V. Talapin, N. A. Kotov, S. O'Brien, C. B. Murray, *Nature* **439**, 55–59 (2006).
2. Z. Tang, Z. Zhang, Y. Wang, S. C. Glotzer, N. A. Kotov, *Science* **314**, 274–278 (2006).
3. A. M. Kalsin *et al.*, *Science* **312**, 420–424 (2006).
4. E. Auyeung *et al.*, *Nature* **505**, 73–77 (2014).
5. D. Nykypanchuk, M. M. Maye, D. van der Lelie, O. Gang, *Nature* **451**, 549–552 (2008).
6. T. Wang *et al.*, *Science* **338**, 358–363 (2012).
7. H. Cui *et al.*, *Science* **327**, 555–559 (2010).
8. M. A. Kostiainen *et al.*, *Nat. Nanotechnol.* **8**, 52–56 (2013).
9. K. Miszta *et al.*, *Nat. Mater.* **10**, 872–876 (2011).
10. K. J. M. Bishop, C. E. Wilmer, S. Soh, B. A. Grzybowski, *Small* **5**, 1600–1630 (2009).
11. E. V. Shevchenko, D. V. Talapin, S. O'Brien, C. B. Murray, *J. Am. Chem. Soc.* **127**, 8741–8747 (2005).
12. X. Ye, J. Chen, C. B. Murray, *J. Am. Chem. Soc.* **133**, 2613–2620 (2011).
13. D. Faivre, D. Schüler, *Chem. Rev.* **108**, 4875–4898 (2008).
14. R. E. Dunin-Borkowski *et al.*, *Science* **282**, 1868–1870 (1998).
15. M. W. Szyndler, R. M. Corn, *J. Phys. Chem. Lett.* **3**, 2320–2325 (2012).
16. M. V. Kovalenko *et al.*, *J. Am. Chem. Soc.* **129**, 6352–6353 (2007).
17. T. Wang *et al.*, *J. Am. Chem. Soc.* **134**, 18225–18228 (2012).
18. D. Kim *et al.*, *J. Am. Chem. Soc.* **131**, 454–455 (2009).
19. See supplementary materials on *Science* Online.
20. V. Aleksandrovic *et al.*, *ACS Nano* **2**, 1123–1130 (2008).
21. A. Dong, J. Chen, P. M. Vora, J. M. Kikkawa, C. B. Murray, *Nature* **466**, 474–477 (2010).
22. In that respect, our methodology is akin to assembling nanocrystals using the Langmuir-Blodgett technique. See also (*23*).
23. Large arrays of belts assembled from NCs of various compositions were previously prepared by evaporation-induced assembly (*24*); although this method bears some similarity to our results (e.g., NC assemblies were prepared at the liquid-air interface), the mechanism of assembly (based on contact-line instabilities) is conceptually different. In fact, we

did not observe the formation of any well-defined structures in the absence of an applied magnetic field (see, e.g., fig. S8J).
24. A. Dong *et al.*, *Nano Lett.* **11**, 841–846 (2011).
25. S. Brooks, A. Gelman, G. Jones, X.-L. Meng, *Handbook of Markov Chain Monte Carlo* (Chapman & Hall, London, 2011).
26. Z. Kakol, R. N. Pribble, J. M. Honig, *Solid State Commun.* **69**, 793–796 (1989).
27. Ü. Özgür, Y. Alivov, H. Morkoç, *J. Mater. Sci. Mater. Electron.* **20**, 789–834 (2009).
28. The formation of helices, and the self-assembly of NCs in our system in general, is likely facilitated by entropic forces; OA used in large excess during self-assembly may act as a depletion agent, inducing crystallization of NCs during hexane evaporation as reported previously (*29*).
29. D. Baranov *et al.*, *Nano Lett.* **10**, 743–749 (2010).
30. On the basis of measurements of electrophoretic mobility [see (*34*)] and the lack of literature reports on electric dipole moments of magnetite nanoparticles, we did not consider electrostatic and electric dipole-dipole interactions in our analysis of interparticle interactions. At the same time, we cannot exclude the possible presence of these interactions in our system.
31. S. Srivastava *et al.*, *Science* **327**, 1355–1359 (2010).
32. S. Das *et al.*, *Adv. Mater.* **25**, 422–426 (2013).
33. J. V. I. Timonen, M. Latikka, L. Leibler, R. H. A. Ras, O. Ikkala, *Science* **341**, 253–257 (2013).
34. Previous self-assembly experiments performed in nonpolar solvents excluded a significant role played by electrostatic interactions [e.g., (*35*, *36*)]. Although the degree of dissociation of OA in hexane (dielectric constant = 1.84) is negligible, the large excess of OA as well as the nature of our experimental setup (self-assembly at the liquid-air interface) might potentially promote dissociation of OA; to verify this possibility, we used a Malvern Zetasizer Nano ZS to perform electrophoretic mobility (μ_e) measurements of our nanocubes in hexane both in the absence and in the presence of additional OA (5% v/v). The results [0.00706 (±0.00104) × 10^{-4} cm^2 V^{-1} s^{-1} and 0.0218 (±0.00710) × 10^{-4} cm^2 V^{-1} s^{-1}, respectively] indicate that in both cases, the nanocubes are essentially neutral [compare with (*37*)].
35. Z. Chen, J. Moore, G. Radtke, H. Sirringhaus, S. O'Brien, *J. Am. Chem. Soc.* **129**, 15702–15709 (2007).
36. X. Ye *et al.*, *Nat. Chem.* **5**, 466–473 (2013).
37. S. A. Hasan, D. W. Kavich, J. H. Dickerson, *Chem. Commun.* **2009**, 3723–3725 (2009).

ACKNOWLEDGMENTS

Supported by Israel Science Foundation grant 1463/11, the G. M. J. Schmidt-Minerva Center for Supramolecular Architectures, and the Minerva Foundation with funding from the Federal German Ministry for Education and Research (R.K.) and by NSF Division of Materials Research grant 1309765 and American Chemical Society Petroleum Research Fund grant 53062-ND6 (P.K.).

SUPPLEMENTARY MATERIALS

www.sciencemag.org/content/345/6201/1149/suppl/DC1
Materials and Methods
Figs. S1 to S28
References (*38*–*92*)

31 March 2014; accepted 14 July 2014
Published online 24 July 2014;
10.1126/science.1254132

METAL ALLOYS

A fracture-resistant high-entropy alloy for cryogenic applications

Bernd Gludovatz,[1] Anton Hohenwarter,[2] Dhiraj Catoor,[3] Edwin H. Chang,[1] Easo P. George,[3,4]* Robert O. Ritchie[1,5]*

High-entropy alloys are equiatomic, multi-element systems that can crystallize as a single phase, despite containing multiple elements with different crystal structures. A rationale for this is that the configurational entropy contribution to the total free energy in alloys with five or more major elements may stabilize the solid-solution state relative to multiphase microstructures. We examined a five-element high-entropy alloy, CrMnFeCoNi, which forms a single-phase face-centered cubic solid solution, and found it to have exceptional damage tolerance with tensile strengths above 1 GPa and fracture toughness values exceeding 200 MPa·$m^{1/2}$. Furthermore, its mechanical properties actually improve at cryogenic temperatures; we attribute this to a transition from planar-slip dislocation activity at room temperature to deformation by mechanical nanotwinning with decreasing temperature, which results in continuous steady strain hardening.

Pure metals rarely display the mechanical properties required for structural applications. Consequently, alloying elements are added to achieve a desired microstructure or combination of mechanical properties, such as strength and toughness, although the resulting alloys invariably still involve a single dominant constituent, such as iron in steels or nickel in superalloys. Additionally, many such alloys, such as precipitation-hardened aluminum alloys, rely on the presence of a second phase for mechanical performance. High-entropy alloys (*1*–*3*) represent a radical departure from these notions. As equiatomic, multi-element metallic systems, they contain high concentrations (20 to 25 atomic percent) of multiple elements with different crystal structures but can crystallize as a single phase (*4*–*7*). In many respects, these alloys represent a new field of metallurgy that focuses attention away from the corners of alloy phase diagrams toward their centers; we believe that as this evolving field matures, a number of fascinating new materials may emerge.

The CrMnFeCoNi alloy under study here is a case in point. Although first identified a decade ago (*1*), the alloy had never been investigated mechanically until recently (*5*, *6*, *8*), yet is clearly scientifically interesting from several perspectives. It is not obvious why an equiatomic five-element alloy—where two of the elements (Cr and Fe) crystallize with the body-centered cubic (bcc) structure, one (Ni) as face-centered cubic (fcc), one (Co) as hexagonal close-packed (hcp), and one (Mn) with the complex *A*12 structure—should form a single-phase fcc structure. Furthermore, several of its properties are quite unlike those of pure fcc metals. Recent studies indicate that the alloy exhibits a strong temperature dependence of the yield strength between ambient and cryogenic temperatures, reminiscent of bcc metals and certain fcc solid-solution alloys (*6*). Strangely, any temperature-dependent effect of strain rate on strength appears to be marginal (*6*). Moreover, the marked temperature-dependent increase in strength is accompanied by a substantial increase in tensile ductility with decreasing temperature between 293 K and 77 K (*6*), which runs counter to most other materials where an inverse dependence of ductility and strength is invariably seen (*9*). Preliminary indications suggest that this may be principally a result of the alloy's high work-hardening capability, possibly associated with deformation-induced nanotwinning, which acts to delay the onset of any necking instability (i.e., localized plastic deformation that can lead to premature failure) to higher strains (*5*).

We prepared the CrMnFeCoNi alloy with high-purity elemental starting materials by arc melting and drop casting into rectangular-cross-section copper molds, followed by cold forging and cross rolling at room temperature into sheets roughly 10 mm thick. After recrystallization, the alloy had an equiaxed grain structure. Uniaxial tensile specimens and compact-tension fracture toughness specimens in general accordance with ASTM standard E1820 (*10*) were machined from these sheets by electrical discharge machining. [See (*11*) for details of the processing procedures, sample sizes, and testing methods.]

Figure 1A shows a backscattered electron (BSE) micrograph of the fully recrystallized microstructure with ~6-μm grains containing numerous recrystallization twins. Energy-dispersive x-ray (EDX) spectroscopy and x-ray diffraction (XRD) indicate the equiatomic elemental distribution and single-phase character of the alloy, respectively. Measured uniaxial stress-strain curves at room temperature (293 K), in a dry ice–alcohol mixture (200 K), and in liquid nitrogen (77 K) are plotted in Fig. 1B. With a decrease in temperature from 293 K to 77 K, the yield strength σ_y and ultimate tensile strength σ_{uts}

[1]Materials Sciences Division, Lawrence Berkeley National Laboratory, Berkeley, CA 94720, USA. [2]Department of Materials Physics, Montanuniversität Leoben and Erich Schmid Institute of Materials Science, Austrian Academy of Sciences, Leoben 8700, Austria. [3]Materials Sciences and Technology Division, Oak Ridge National Laboratory, Oak Ridge, TN 37831, USA. [4]Materials Sciences and Engineering Department, University of Tennessee, Knoxville, TN 37996, USA. [5]Department of Materials Science and Engineering, University of California, Berkeley, CA 94720, USA.
***Corresponding author. E-mail: georgeep@ornl.gov (E.P.G.); roritchie@lbl.gov (R.O.R.)**

increased by ~85% and ~70%, to 759 and 1280 MPa, respectively. Similarly, the tensile ductility (strain to failure, ε_f) increased by ~25% to >0.7; the strain-hardening exponent n remained high at ~0.4, such that there was an enhancement in the fracture energy (*12*) by more than a factor of 2. Table S1 provides a detailed summary of the stresses and strains at the three different temperatures, as well as the corresponding strain-hardening exponents.

In light of the extensive plasticity involved in the deformation of this alloy, we evaluated the fracture toughness of CrMnFeCoNi with nonlinear elastic fracture mechanics, specifically with crack-resistance curve (R curve) measurements in terms of the J integral. Analogous to the stress intensity K for linear elastic analysis, provided that specific validity criteria are met, J uniquely characterizes the stress and displacement fields in the vicinity of the crack tip for a nonlinear elastic solid; as such, it is able to capture both the elastic and plastic contributions to the fracture process. J is also equivalent to the strain energy release rate G under linear elastic conditions; consequently, K values can be back-calculated from J measurements assuming a mode I equivalence between K and J: specifically, $J = K^2/E'$, with $E' = E$ (Young's modulus) in plane stress and $E/(1 - \nu^2)$ (where ν is Poisson's ratio) in plane strain. E and ν values were determined by resonance ultrasound spectroscopy at each temperature (*13*).

Our toughness results for the CrMnFeCoNi alloy at 293 K, 200 K, and 77 K are plotted in Fig. 1C, in terms of $J_R(\Delta a)$–based resistance curves showing crack extension Δa in precracked and side-grooved compact-tension specimens as a function of the applied J. Using these R curves to evaluate the fracture toughness for both the initiation and growth of a crack, we measured a crack initiation fracture toughness J_{Ic}, determined essentially at $\Delta a \rightarrow 0$, of 250 kJ/m^2 at 293 K, which in terms of a stress intensity gives K_{JIc} = 217 MPa·m$^{1/2}$. Despite a markedly increased strength at lower temperature, K_{JIc} values at 200 K and 77 K remained relatively constant at K_{JIc} = 221 MPa·m$^{1/2}$ (J_{Ic} = 260 kJ/m^2) and K_{JIc} = 219 MPa·m$^{1/2}$ (J_{Ic} = 255 kJ/m^2), respectively. After

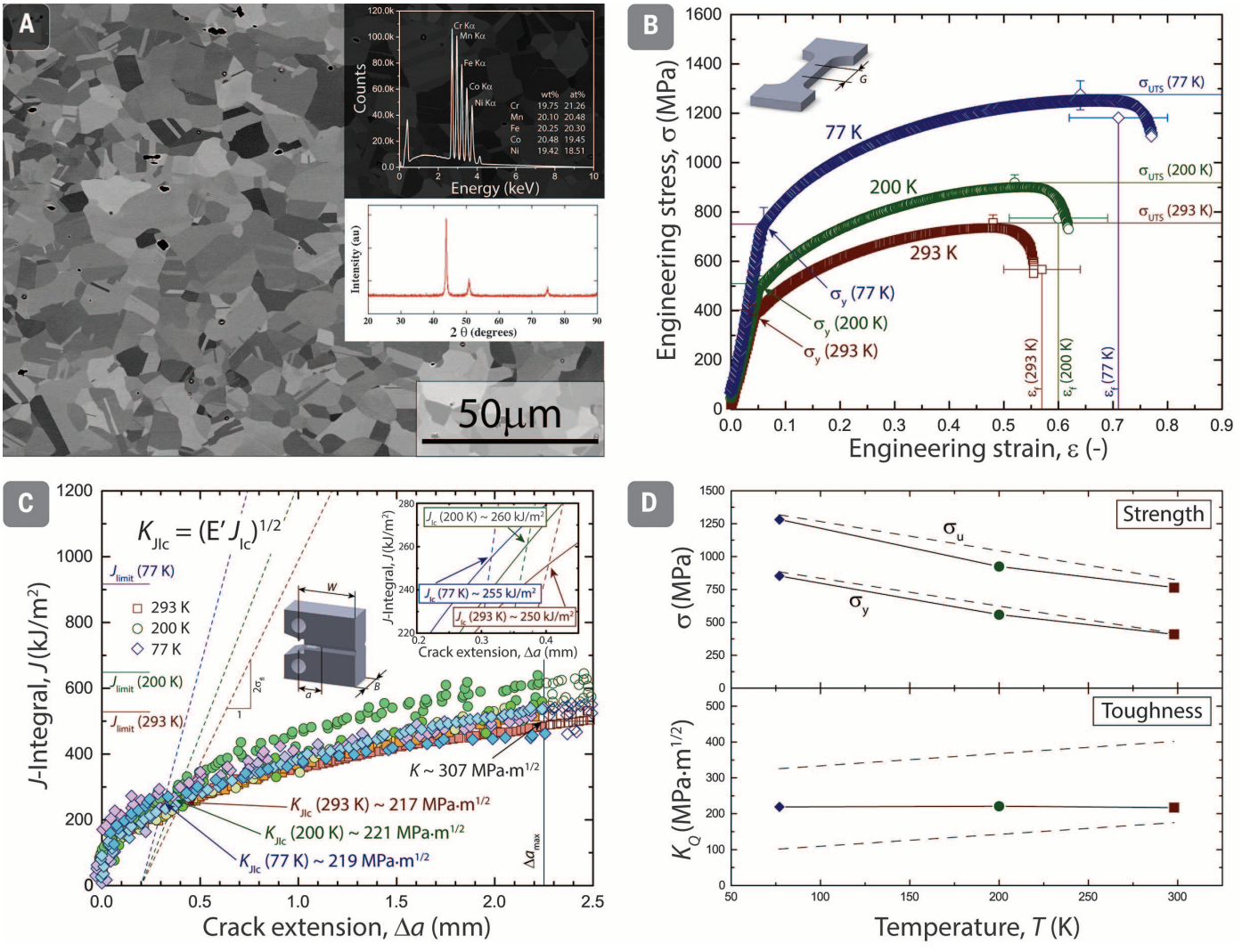

Fig. 1. Microstructure and mechanical properties of the CrMnFeCoNi high-entropy alloy. (**A**) Fully recrystallized microstructure with an equiaxed grain structure and grain size of ~6 μm; the composition is approximately equiatomic, and the alloy is single-phase, as shown from the EDX spectroscopy and XRD insets. (**B**) Yield strength σ_y, ultimate tensile strength σ_{uts}, and ductility (strain to failure, ε_f) all increase with decreasing temperature. The curves are typical tests at the individual temperatures, whereas the data points are means ± SD of multiple tests; see table S1 for exact values. (**C**) Fracture toughness measurements show K_{JIc} values of 217 MPa·m$^{1/2}$, 221 MPa·m$^{1/2}$, and 219 MPa·m$^{1/2}$ at 293 K, 200 K, and 77 K, respectively, and an increasing fracture resistance in terms of the J integral as a function of crack extension Δa [i.e., resistance curve (R curve) behavior]. (**D**) Similar to austenitic stainless steels (e.g., 304, 316, or cryogenic Ni steels), the strength of the high-entropy alloy (solid lines) increases with decreasing temperature; although the toughness of the other materials decreases with decreasing temperature, the toughness of the high-entropy alloy remains unchanged, and by some measures it actually increases at lower temperatures. (The dashed lines in the plots mark the upper and lower limits of data found in the literature.)

initiation, the fracture resistance further increased with extensive subcritical crack growth; after just over 2 mm of such crack extension, a crack growth toughness exceeding K = 300 MPa·m$^{1/2}$ (J = 500 kJ/m^2) was recorded [representing, in terms of ASTM standards, the maximum (valid) crack extension capacity of our samples]. Such toughness values compare favorably to those of highly alloyed, austenitic stainless steels such as 304L and 316L, which have reported toughnesses in the range of K_Q = 175 to 400 MPa·m$^{1/2}$ at room temperature (*14*–*16*), and the best cryogenic steels such as 5Ni or 9Ni steels, with K_Q = 100 to 325 MPa·m$^{1/2}$ at 77 K (*17*–*19*). Similar to the high-entropy alloy, these materials show an expected increase in strength with decreasing temperature to 77 K; however, unlike the high-entropy alloy, their reported fracture toughness values are invariably reduced with decreasing temperature (*20*) (Fig. 1D) and furthermore are rarely valid (i.e., they are size- and geometry-dependent and thus not strictly material parameters).

The high fracture toughness values of the CrMnFeCoNi alloy were associated with a 100% ductile fracture by microvoid coalescence, with the extent of deformation and necking behavior being progressively less apparent at the lower temperatures (Fig. 2, A and B). EDX analysis of the particles, which were found inside the voids of the fracture surface and acted as initiation sites for their formation, indicated either Cr-rich or Mn-rich compounds (Fig. 2B, inset). These particles are likely oxides associated with the Mn additions; preliminary indications are that they are absent in the Mn-free (CoCrFeNi) alloy (*6*). Both microvoid size and particle size varied markedly; the microvoids ranged in size from ~1 μm to tens of micrometers, with particle sizes ranging from <1 μm to ~5 μm (Fig. 2B, inset) with an average size of 1.6 μm and average spacing $d_p \approx 49.6$ μm, respectively.

To verify the high measured fracture toughness values, we used three-dimensional (3D) stereophotogrammetry of the morphology of these fracture surfaces to estimate local crack initiation toughness (K_i) values for comparison with the global, ASTM-based K_{JIc} measurements. This technique is an alternative means to characterize the onset of cracking, particularly under large-scale yielding conditions. Under mode I (tensile) loading, the crack surfaces completely separate from each other, with the regions of first separation moving the farthest apart and progressively less separation occurring in regions that crack later. Accordingly, the formation and coalescence of microvoids and their linkage with the crack tip allow for the precise reconstruction of the point of initial crack advance from the juxtaposition of the stereo images of each fracture surface. This enables an evaluation of the crack tip opening displacement at crack initiation, $CTOD_i$, which then can be used to estimate the local stress intensity K_i at the midsection of the sample at the onset of physical crack extension, where Δa = 0 (*21*). Specifically, we used an automatic fracture surface analysis system that creates 3D digital surface models from stereo-image pairs of the corresponding fracture surfaces taken in the scanning electron microscope (Fig. 2C); digitally reconstructing the crack profiles by superimposing the stereo-image pairs allows for a precise measurement of the $CTOD_i$s of arbitrarily chosen crack paths (which must be identical on both fracture surfaces). Figure 2D indicates two examples of the approximately 10 crack paths taken on both fracture surfaces of samples tested at 293 K and 77 K. The two corresponding profiles show the point at which the first void, formed ahead of the fatigue precrack, coalesced with this precrack to mark the initial crack extension, thereby locally defining the crack initiation event and

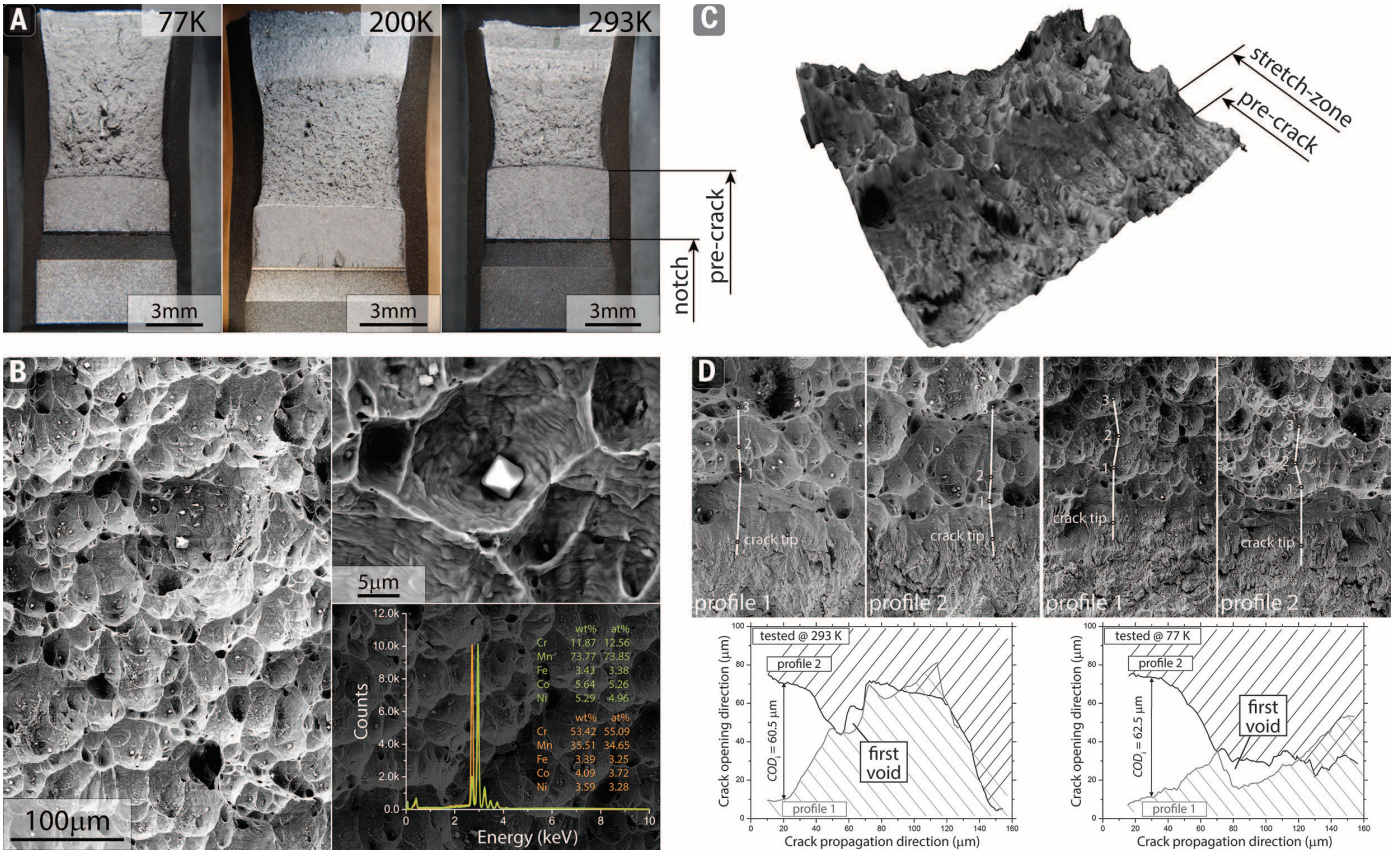

Fig. 2. Images of fractured CrMnFeCoNi samples. (**A**) Stereomicroscopic photographs of the fracture surfaces after testing indicate less lateral deformation and necking-like behavior with decreasing temperature. (**B**) SEM image of the fracture surface of a sample tested at room temperature shows ductile dimpled fracture where the void initiation sites are mainly Mn-rich or Cr-rich particles, as shown by the EDX data (insets). (**C**) Three-dimensional digital fracture surface models were derived from SEM stereo-image pairs, which indicate the transition from fatigue precrack to ductile dimpled fracture and the presence of the stretch zone. (**D**) Profiles of identical crack paths from both fracture halves of the fracture surface models were extracted to evaluate the crack tip opening displacement at the first physical crack extension, $CTOD_i$, which was then converted to J_i using the relationship of the equivalence of J and $CTOD$ (*50*).

the fracture toughness (*22*). Using these procedures, the initial crack tip opening displacements at crack initiation were found to be $CTOD_i = 57 \pm 19$ μm at 293 K and 49 ± 13 μm at 77 K. Using the standard *J-CTOD* equivalence relationship of $J_i \propto \sigma_o CTOD_i = K_i^2/E'$ gives estimates of the crack initiation fracture toughness: $K_i = 191$ MPa·m$^{1/2}$ and 203 MPa·m$^{1/2}$ at 293 K and 77 K, respectively. These values are slightly conservative with respect to the global *R* curve–based values in Fig. 1C; however, this is to be expected, as they are estimated at the initial point of physical contact of the first nucleated void with the precrack, whereas the ASTM-based measurements use an operational definition of crack initiation involving subcritical crack extension of $\Delta a = 200$ μm.

To discern the micromechanisms underlying the excellent fracture toughness behavior, we further analyzed the fracture surfaces of samples tested at 293 K and 77 K by means of stereomicroscopy and scanning electron microcopy (SEM). Some samples were additionally sliced in two halves, embedded, and metallographically polished for BSE microscopy and electron backscatter diffraction (EBSD) analysis of the region in the immediate vicinity of the crack tip and in the wake of the crack, close to the crack flanks, specifically "inside" the sample where fully plane-strain conditions prevail.

SEM images of the crack tip region of samples tested at ambient and liquid nitrogen temperatures show the formation of voids and their coalescence characteristic of the microvoid coalescence fracture process (Fig. 3A). A large population of the particles that act as the void

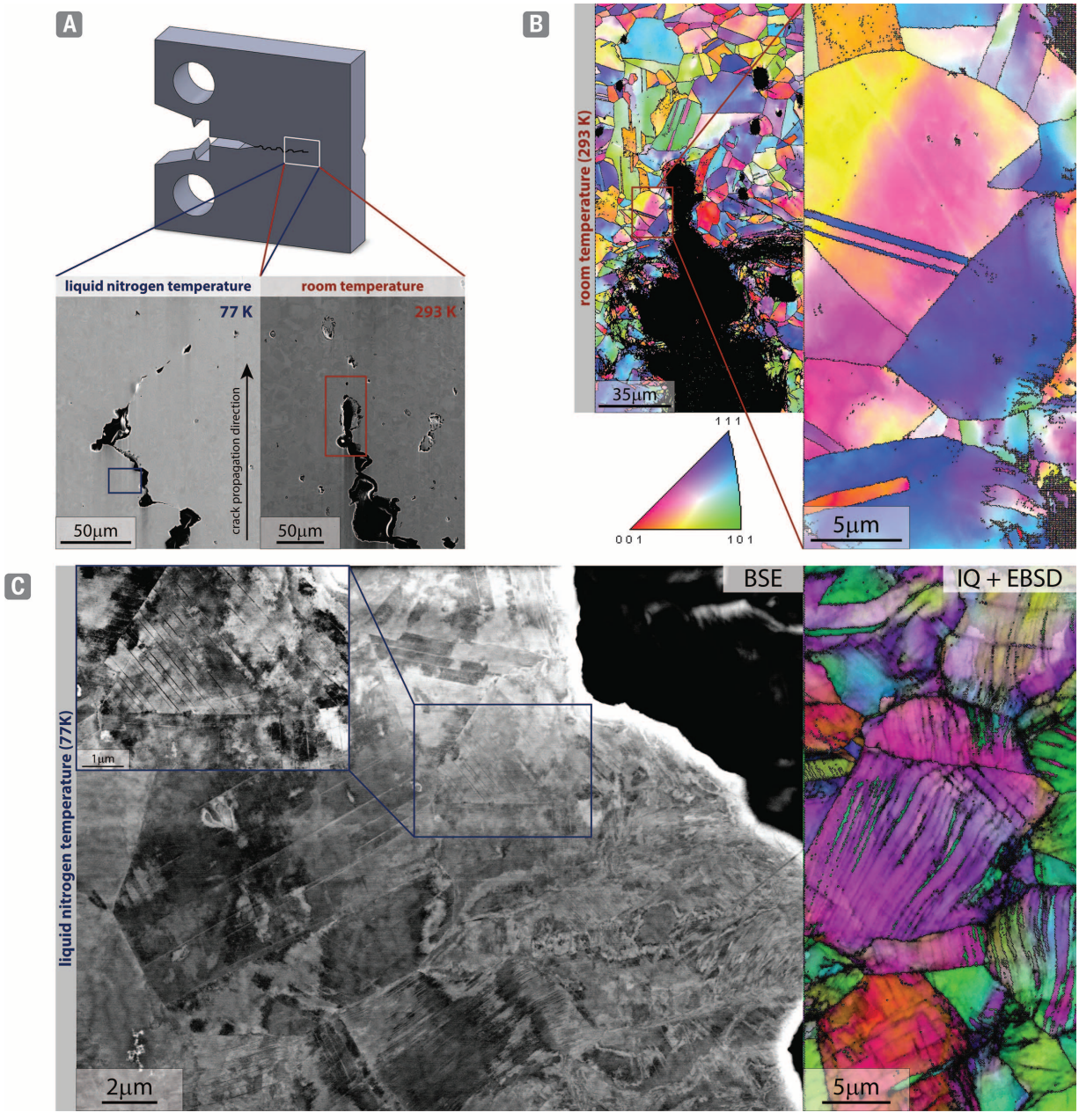

Fig. 3. Deformation mechanisms in the vicinity of the crack tip in the center (plane-strain) section of CrMnFeCoNi high-entropy alloy samples. (**A**) Low-magnification SEM images of samples tested at 293 K and 77 K show ductile fracture by microvoid coalescence, with a somewhat more distorted crack path at the lower temperature. (**B**) EBSD images show numerous annealing twins and pronounced grain misorientations due to dislocations—the primary deformation mechanism at 293 K. (**C**) At 77 K, BSE images taken in the wake of the propagated crack show the formation of pronounced cell structures resulting from dislocation activity. Both BSE and EBSD images show deformation-induced nanotwinning as an additional mechanism at 77 K. [The EBSD image is an overlay to an image quality (IQ) map, which is a measure of the quality of the collected EBSD pattern used to visualize certain microstructural features.]

initiation sites can be seen on the fracture surfaces (Fig. 2B); these particles have a substantial influence on material ductility and likely contribute to the measured scatter in the failure strains (Fig. 1B). Macroscopically, fracture surfaces at 77 K appear significantly more deviated from a mode I ($K_{II} = 0$) crack path than at 293 K (Fig. 3A). Although such deflected crack paths act to reduce the local crack-driving force at the crack tip (*23*) and hence contribute to the rising *R* curve behavior (i.e., crack growth toughness), this mechanism cannot be responsible for the exceptional crack initiation toughness of this alloy. Such high K_i values are conversely derived from the large *CTOD*s at crack initiation and are associated with the intrinsic process of microvoid coalescence; as such, they are highly dependent on the formation and size of voids, the prevailing deformation and flow conditions, and the presence of steady strain hardening to suppress local necking.

Using simple micromechanical models for fracture (*24*), we can take advantage of a stress state–modified critical strain criterion for ductile fracture to derive estimates for these high toughness values (*25*–*27*). This yields expressions for the fracture toughness in the form $J_{Ic} \approx \sigma_o \bar{\varepsilon}_f l_o^*$, where σ_o is the flow stress, $\bar{\varepsilon}_f$ is the fracture strain in the highly constrained stress state in the vicinity of the crack tip [which is roughly an order of magnitude smaller than the uniaxial tensile ductility (*28*)], and l_o^* is the characteristic distance ahead of the tip over which this critical strain must be met for fracture (which can be equated to the particle spacing d_p). Assuming Hutchinson-Rice-Rosengren (HRR) stress-strain distributions ahead of a crack tip in plane strain for a nonlinear elastic, power-law hardening solid (strain-hardening coefficient of *n*) (*29*, *30*), and the measured properties, specifically *E*, σ_o, ε_f, *n*, ν, and d_p, for this alloy (*11*), estimates of the fracture toughness of $K_{JIc} = (J_{Ic}E')^{1/2}$ of ~150 to 215 MPa·m$^{1/2}$ can be obtained for the measured particle spacing of $d_p \sim 50$ μm. Although approximate, these toughness predictions from the critical fracture strain model are completely consistent with a fracture toughness on the order of 200 MPa·m$^{1/2}$, as measured for the CrMnFeCoNi alloy in this study (Fig. 1C).

In addition to crack initiation toughnesses of 200 MPa·m$^{1/2}$ or more, this alloy develops even higher crack growth toughness with stable crack growth at "valid" stress intensities above 300 MPa·m$^{1/2}$. These are astonishing toughness levels by any standard, particularly because they are retained at cryogenic temperatures. A primary factor here is the mode of plastic deformation, which induces a steady degree of strain hardening to suppress plastic instabilities; expressly, the measured strain-hardening exponents of $n \sim 0.4$ are very high relative to the vast majority of metals, particularly at this strength level. Recent studies have shown that, similar to mechanisms known for binary fcc solid solutions (*31*, *32*), plastic deformation in the CrMnFeCoNi alloy at ambient temperatures is associated with planar glide of 1/2⟨110⟩ dislocations on {111} planes leading to the formation of pronounced cell structures at higher strains (*5*). However, at 77 K, in addition to planar slip, deformation-induced nanoscale twinning has been observed both previously (*5*) and in the present study (Fig. 3C) and contributes to the increased ductility and strain hardening at lower temperatures. Both the planar slip and nanotwinning mechanisms are highly active in the vicinity of the crack tip during fracture, as illustrated in Fig. 3. EBSD images taken ahead of the crack tip inside the sample of a fracture toughness test performed at room temperature show grain misorientations resulting from dislocation activity as the only deformation mechanism (Fig. 3B). Aside from numerous annealing twins resulting from the recrystallization step during processing, twinning does not play a role at ambient temperatures, with only a few single nanotwins in evidence. With decrease in temperature, cell structure formation is more apparent, as shown by the BSE image in Fig. 3C, taken in the wake of a crack propagating at 77 K. Here, however, excessive deformation-induced nanoscale twinning occurs simultaneously with planar dislocation slip, leading to a highly distorted grain structure, which can be seen in both the BSE and IQ + EBSD images in the vicinity of the growing crack. [The EBSD image is shown as an overlay of an image quality (IQ) map to enhance visualization of structural deformations of the grains.] Note that several other classes of materials show good combinations of strength and ductility when twinning is the dominant deformation mechanism. These include copper thin films (*33*–*36*) and the recently developed twinning-induced plasticity (TWIP) steels (*37*–*40*), which are of great interest to the car industry as high-Mn steels (*41*–*44*). We believe that the additional plasticity mechanism of nanotwinning in CrMnFeCoNi is critical to sustaining a high level of strain hardening at decreasing temperatures; this in turn acts to enhance the tensile ductility, which, together with the higher strength at low temperatures, preserves the exceptional fracture toughness of this alloy down to 77 K.

We conclude that the high-entropy CrMnFeCoNi alloy displays remarkable fracture toughness properties at tensile strengths of 730 to 1280 GPa, which exceed 200 MPa·m$^{1/2}$ at crack initiation and rise to >300 MPa·m$^{1/2}$ for stable crack growth at cryogenic temperatures down to 77 K. The alloy has toughness levels that are comparable to the very best cryogenic steels, specifically certain austenitic stainless steels (*15*, *16*) and high-Ni steels (*17*–*19*, *45*–*48*), which also have outstanding combinations of strength and ductility.

With respect to the alloy's damage tolerance, a comparison with the other major material classes is shown on the Ashby plot of fracture toughness versus yield strength (*49*) in Fig. 4. There are clearly stronger materials, which is understandable given that CrMnFeCoNi is a single-phase material, but the toughness of this high-entropy alloy exceeds that of virtually all pure metals and metallic alloys (*9*, *49*).

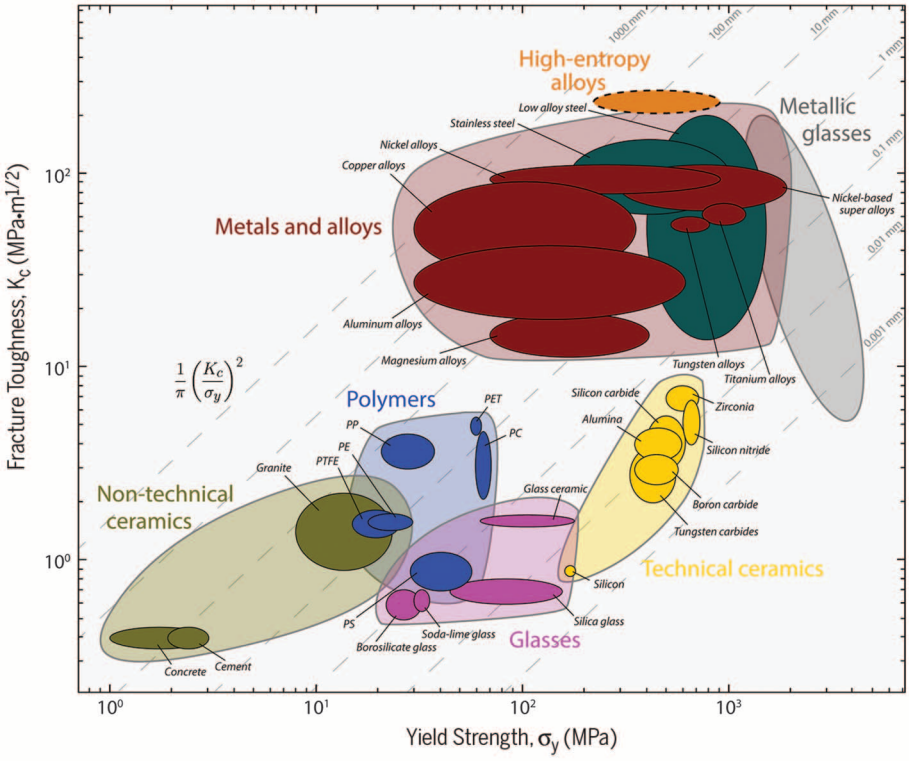

Fig. 4. Ashby map showing fracture toughness as a function of yield strength for high-entropy alloys in relation to a wide range of material systems. The excellent damage tolerance (toughness combined with strength) of the CrMnFeCoNi alloy is evident in that the high-entropy alloy exceeds the toughness of most pure metals and most metallic alloys (*9*, *49*) and has a strength comparable to that of structural ceramics (*49*) and close to that of some bulk-metallic glasses (*51*–*55*).

REFERENCES AND NOTES

1. B. Cantor, I. T. H. Chang, P. Knight, A. J. B. Vincent, *Mater. Sci. Eng. A* **375–377**, 213–218 (2004).
2. J.-W. Yeh *et al*., *Adv. Eng. Mater.* **6**, 299–303 (2004).
3. C.-Y. Hsu, J.-W. Yeh, S.-K. Chen, T.-T. Shun, *Metall. Mater. Trans. A* **35**, 1465–1469 (2004).
4. O. N. Senkov, G. B. Wilks, J. M. Scott, D. B. Miracle, *Intermetallics* **19**, 698–706 (2011).
5. F. Otto *et al*., *Acta Mater.* **61**, 5743–5755 (2013).
6. A. Gali, E. P. George, *Intermetallics* **39**, 74–78 (2013).
7. F. Otto, Y. Yang, H. Bei, E. P. George, *Acta Mater.* **61**, 2628–2638 (2013).
8. W. H. Liu, Y. Wu, J. Y. He, T. G. Nieh, Z. P. Lu, *Scr. Mater.* **68**, 526–529 (2013).
9. R. O. Ritchie, *Nat. Mater.* **10**, 817–822 (2011).
10. E08 Committee, *E1820-13 Standard Test Method for Measurement of Fracture Toughness* (ASTM International, 2013).
11. See supplementary materials on *Science* Online.
12. As a preliminary estimate of the fracture resistance, the area under the load displacement curve of a tensile test was used to compute the fracture energy (sometimes termed the work to fracture), which was calculated from this area divided by twice the area of the crack surface.
13. J. Maynard, *Phys. Today* **49**, 26–31 (1996).
14. K_Q values refer to fracture toughnesses that are not necessarily valid by ASTM standards (i.e., they do not meet the *J*-validity and/or plane strain conditions). Consequently, these toughnesses are likely to be inflated relative to truly valid numbers and are size- and geometry-dependent; they are not strictly material parameters. When comparing these values to the toughnesses measured in this study for CoCrFeMnNi, it is important to note that all values determined here for the high-entropy alloy were strictly valid, meeting ASTM standards for both *J* validity and plane strain.
15. W. J. Mills, *Int. Mater. Rev.* **42**, 45–82 (1997).
16. M. Sokolov *et al*., in *Effects of Radiation on Materials: 20th International Symposium*, S. Rosinski, M. Grossbeck, T. Allen, A. Kumar, Eds. (ASTM International, West Conshohocken, PA, 2001), pp. 125–147.
17. J. R. Strife, D. E. Passoja, *Metall. Trans. A* **11**, 1341–1350 (1980).
18. C. K. Syn, J. W. Morris, S. Jin, *Metall. Trans. A* **7**, 1827–1832 (1976).
19. A. W. Pense, R. D. Stout, *Weld. Res. Counc. Bull.* **205**, 1–43 (1975).
20. Note that despite the uncertainty in the (valid) toughness values for the stainless and high Ni steels, their upper toughness range could possibly be higher than the current measurements for the CrMnFeCoNi alloy. It must be remembered, however, that these materials are microalloyed and highly tuned with respect to grain size/orientation, tempering, precipitation hardening, etc., to achieve their mechanical properties, whereas the current CrMnFeCoNi alloy is a single-phase material that undoubtedly can be further improved through second-phase additions and grain control.
21. J. Stampfl, S. Scherer, M. Gruber, O. Kolednik, *Appl. Phys. A* **63**, 341–346 (1996).
22. J. Stampfl, S. Scherer, M. Berchthaler, M. Gruber, O. Kolednik, *Int. J. Fract.* **78**, 35–44 (1996).
23. B. Cotterell, J. Rice, *Int. J. Fract.* **16**, 155–169 (1980).
24. R. O. Ritchie, A. W. Thompson, *Metall. Trans. A* **16**, 233–248 (1985).
25. A. C. Mackenzie, J. W. Hancock, D. K. Brown, *Eng. Fract. Mech.* **9**, 167–188 (1977).
26. R. O. Ritchie, W. L. Server, R. A. Wullaert, *Metall. Trans. A* **10**, 1557–1570 (1979).
27. Details of the critical strain model for ductile fracture (*25*, *26*) and the method of estimating the fracture toughness are described in the supplementary materials.
28. J. R. Rice, D. M. Tracey, *J. Mech. Phys. Solids* **17**, 201–217 (1969).
29. J. W. Hutchinson, *J. Mech. Phys. Solids* **16**, 13–31 (1968).
30. J. R. Rice, G. F. Rosengren, *J. Mech. Phys. Solids* **16**, 1–12 (1968).
31. H. Neuhäuser, *Acta Metall.* **23**, 455–462 (1975).
32. V. Gerold, H. P. Karnthaler, *Acta Metall.* **37**, 2177–2183 (1989).
33. M. Dao, L. Lu, Y. F. Shen, S. Suresh, *Acta Mater.* **54**, 5421–5432 (2006).
34. L. Lu, X. Chen, X. Huang, K. Lu, *Science* **323**, 607–610 (2009).
35. K. Lu, L. Lu, S. Suresh, *Science* **324**, 349–352 (2009).
36. A. Singh, L. Tang, M. Dao, L. Lu, S. Suresh, *Acta Mater.* **59**, 2437–2446 (2011).
37. R. A. Hadfield, *Science* **12**, 284–286 (1888).
38. V. H. Schumann, *Neue Hütte* **17**, 605–609 (1972).
39. L. Remy, A. Pineau, *Mater. Sci. Eng.* **28**, 99–107 (1977).
40. T. W. Kim, Y. G. Kim, *Mater. Sci. Eng. A* **160**, 13–15 (1993).
41. O. Grässel, G. Frommeyer, C. Derder, H. Hofmann, *J. Phys. IV* **07**, C5-383–C5-388 (1997).
42. O. Grässel, L. Krüger, G. Frommeyer, L. W. Meyer, *Int. J. Plast.* **16**, 1391–1409 (2000).
43. G. Frommeyer, U. Brüx, P. Neumann, *ISIJ Int.* **43**, 438–446 (2003).
44. L. Chen, Y. Zhao, X. Qin, *Acta Metall. Sin. Engl. Lett.* **26**, 1–15 (2013).
45. D. T. Read, R. P. Reed, *Cryogenics* **21**, 415–417 (1981).
46. R. D. Stout, S. J. Wiersma, in *Advances in Cryogenic Engineering Materials*, R. P. Reed, A. F. Clark, Eds. (Springer, New York, 1986), pp. 389–395.
47. Y. Shindo, K. Horiguchi, *Sci. Technol. Adv. Mater.* **4**, 319–326 (2003).
48. J. W. Sa *et al*., in *Twenty-First IEEE/NPS Symposium on Fusion Engineering 2005* (IEEE, Piscataway, NJ, 2005), pp. 1–4.
49. M. F. Ashby, in *Materials Selection in Mechanical Design*, M. F. Ashby, Ed. (Butterworth-Heinemann, Oxford, ed. 4, 2011), pp. 31–56.
50. C. F. Shih, *J. Mech. Phys. Solids* **29**, 305–326 (1981).
51. C. J. Gilbert, R. O. Ritchie, W. L. Johnson, *Appl. Phys. Lett.* **71**, 476–478 (1997).
52. A. Kawashima, H. Kurishita, H. Kimura, T. Zhang, A. Inoue, *Mater. Trans.* **46**, 1725–1732 (2005).
53. A. Shamimi Nouri, X. J. Gu, S. J. Poon, G. J. Shiflet, J. J. Lewandowski, *Philos. Mag. Lett.* **88**, 853–861 (2008).
54. M. D. Demetriou *et al*., *Appl. Phys. Lett.* **95**, 041907, 041907–3 (2009).
55. M. D. Demetriou *et al*., *Nat. Mater.* **10**, 123–128 (2011).

ACKNOWLEDGMENTS

Sponsored by the U.S. Department of Energy, Office of Science, Office of Basic Energy Sciences, Materials Sciences and Engineering Division. All data presented in this article can additionally be found in the supplementary materials. Author contributions: E.P.G. and R.O.R. had full access to the experimental results in the study and take responsibility for the integrity of the data and the accuracy of the data analysis. The alloys were processed by D.C. and mechanically characterized by B.G., A.H., and D.C. Study design, interpretation and analysis of data, and preparation of the manuscript were performed jointly by B.G., A.H., D.C., E.H.C., E.P.G., and R.O.R. The authors declare no conflict of interest.

SUPPLEMENTARY MATERIALS

www.sciencemag.org/content/345/6201/1153/suppl/DC1
Materials and Methods
Supplementary Text
Fig. S1
Table S1

9 April 2014; accepted 18 July 2014
10.1126/science.1254581

CRYSTAL NUCLEATION

In situ TEM imaging of $CaCO_3$ nucleation reveals coexistence of direct and indirect pathways

Michael H. Nielsen,[1,2] Shaul Aloni,[2] James J. De Yoreo[3,4]

Mechanisms of nucleation from electrolyte solutions have been debated for more than a century. Recent discoveries of amorphous precursors and evidence for cluster aggregation and liquid-liquid separation contradict common assumptions of classical nucleation theory. Using in situ transmission electron microscopy (TEM) to explore calcium carbonate ($CaCO_3$) nucleation in a cell that enables reagent mixing, we demonstrate that multiple nucleation pathways are simultaneously operative, including formation both directly from solution and indirectly through transformation of amorphous and crystalline precursors. However, an amorphous-to-calcite transformation is not observed. The behavior of amorphous calcium carbonate upon dissolution suggests that it encompasses a spectrum of structures, including liquids and solids. These observations of competing direct and indirect pathways are consistent with classical predictions, whereas the behavior of amorphous particles hints at an underlying commonality among recently proposed precursor-based mechanisms.

Nucleation is a key step in the crystallization process, representing the initial transformation of a disordered phase into an ordered one. It is also the most difficult part of the process to observe because it happens on very short time and length scales. In the case of electrolyte solutions, there is an open debate as to whether classical nucleation theory (CNT), as initially developed by Gibbs (*1*), is a suitable framework within which to describe the process, or whether nonclassical elements such as dense liquid phases (*2*–*4*) or (meta)stable clusters (*5*) play important roles. Furthermore, uncertainty exists as to whether a final, stable phase can nucleate directly from solution or whether it forms through a multistep, multiphase evolution (*6*, *7*). In the case of multistep nucleation pathways, whether transformation from one phase to another occurs through nucleation of the more stable phase within the

[1]Department of Materials Science and Engineering, University of California, Berkeley, CA 94720, USA. [2]Molecular Foundry, Lawrence Berkeley National Laboratory, Berkeley, CA 94720, USA. [3]Physical Sciences Division, Pacific Northwest National Laboratory, Richland, WA 99352, USA. [4]Department of Materials Science and Engineering, University of Washington, Seattle, WA 98195, USA.
***Corresponding author. E-mail: james.deyoreo@pnnl.gov**

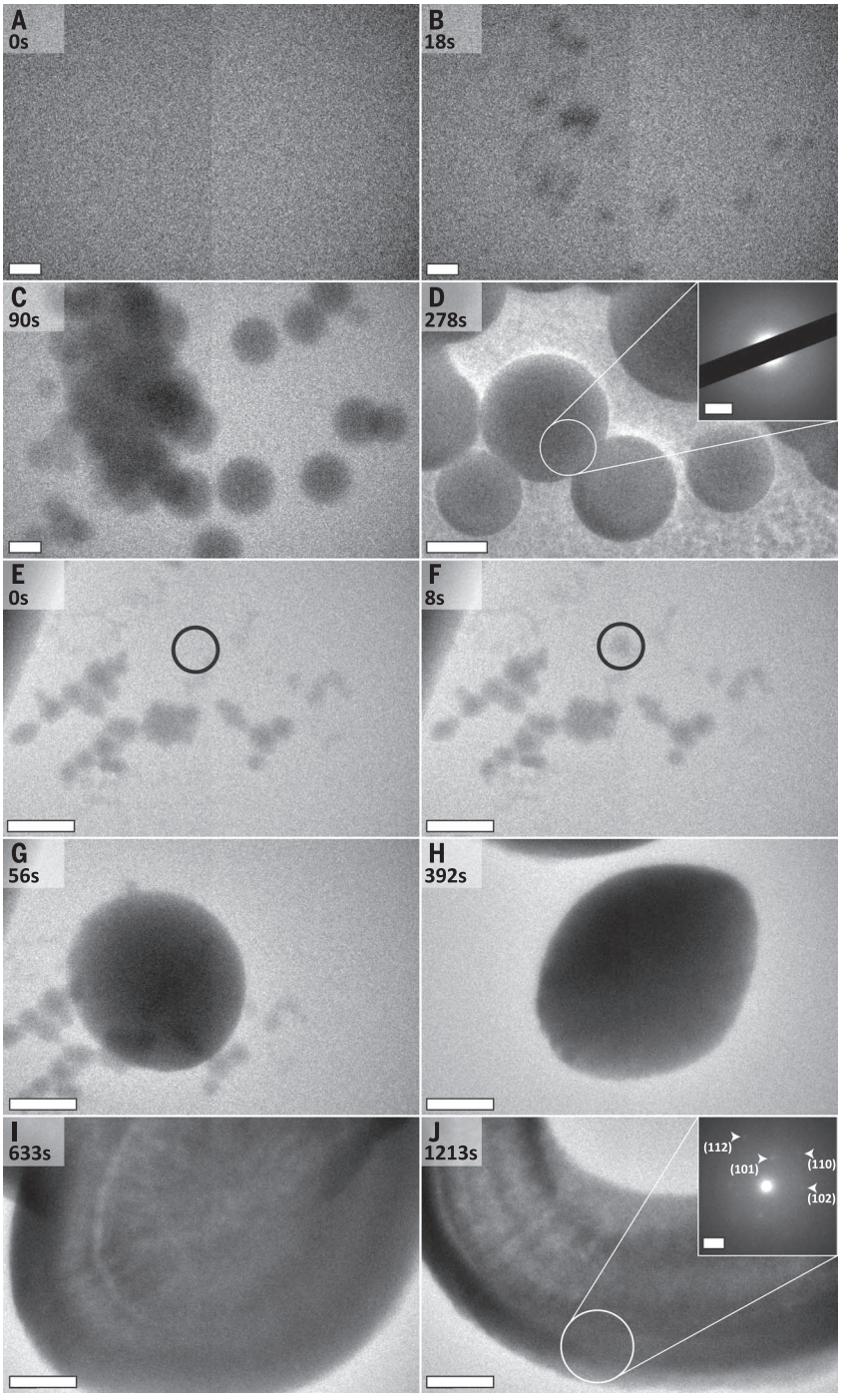

Fig. 1. Direct formation of ACC and vaterite. Frames from movie S1 show the fluid cell before nucleation (**A**) and during nucleation and growth of ACC (**B** to **D**). Diffraction analysis [inset to (D)], performed when the fluid layer thinned (see supplementary materials), confirms the amorphous nature of the particles. Frames from movie S2 follow vaterite formation and growth (**E** to **J**). Gray spots already present (E) are salt deposits that formed on the outer surface of the liquid cell window during cell assembly. In (E) and (F), the nucleation site of a vaterite particle is circled for clarity. The particle grows (G), merges with a second particle (H), and exhibits layering at the growth front and dissolution in the center (I and J). Diffraction analysis [inset to (J)] identifies the material as vaterite. Scale bars are 500 nm in (A) to (J) and 2 nm^{-1} in the insets to (D) and (J). Solution conditions—designated in all figure legends by [$CaCl_2$]:[$NaHCO_3$]/*R*($CaCl_2$):*R*($NaHCO_3$) with concentrations in millimolar and flow rates *R* in microliters per minute—are 50:50/10:0.2 for (A) to (D) and 40:40/9:1 for (E) to (J). Times listed in all figures are relative to the beginning of the associated movie.

existing precursor or through dissolution of the original phase and reprecipitation of the secondary phase is unclear (*8*, *9*). Although many studies have provided snapshots of the nucleation process (*8*) or followed the ensemble evolution of phases in solution (*9*), and simulations have produced predictions for certain solution conditions (*4*, *10*), in situ observations that follow the process from start to finish have been lacking.

The advent of liquid cell transmission electron microscopy (TEM) (*11*) permits imaging with nanometer-scale spatial resolution in time increments of fractions of a second. We used a dual-inlet flow stage (fig. S1) for in situ observations of $CaCO_3$ nucleation pathways over a range of solution conditions. The observations we report here elucidate the existence of a range of nucleation pathways occurring under identical or similar solution conditions, often simultaneously within a single experiment.

To introduce $CaCl_2$ and $NaHCO_3$ solutions of varying concentrations into the flow cell, we used a range of flow rates set independently for the two reagents (tables S1 and S2). In some experiments, supersaturations increased initially but eventually decreased until undersaturated so that dissolution was also observed. We recorded nucleation of both metastable and stable phases, including amorphous calcium carbonate (ACC), vaterite, aragonite, and calcite, typically exhibiting morphologies common for these phases (fig. S2). All nucleation events occurred on the top or bottom membrane of the fluid cell. The thickness of the fluid layer varied and sometimes thinned substantially during an experiment, facilitating collection of diffraction data for unambiguous phase identification. However, collection of diffraction data was not always possible, either because phase transformations took place while operating in imaging mode or because the solution layer thickness produced multiple scattering events that degraded the diffraction signal beyond use.

Amorphous calcium carbonate particles nucleated (Fig. 1, A and B, and movie S1) and grew to diameters of up to hundreds of nanometers (Fig. 1, C and D). Diffraction data confirmed the amorphous nature of the particles (Fig. 1D, inset). Similarly for vaterite, nucleation (Fig. 1, E and F, and movie S2) was followed by extensive growth (Fig. 1G); some crystals merged to form larger crystals (Fig. 1H) with visible texture (Fig. 1I). In some cases, at later stages of growth the growing outer edge exhibited a layered structure while the interior of the growing platelet dissolved away (Fig. 1J). The diffraction pattern (Fig. 1J, inset) identified the phase as vaterite.

We also observed multistep nucleation pathways starting with ACC (Fig. 2, and movies S3 to S5). ACC particles formed and grew to sizes ranging from hundreds of nanometers to micrometers (Fig. 2, A and E) before suddenly transforming to the aragonite "sheaf-of-wheat" morphology (Fig. 2, C and D) or vaterite (Fig. 2, F to H). Typically, the ACC particle began to shrink just before the appearance of a secondary phase (Fig. 2, B and F) on, or possibly just below, the

surface of the original particle. This shrinkage perhaps indicates either the expulsion of water from the amorphous particle or a sudden decrease in concentration leading to partial dissolution. This secondary phase grew rapidly, consuming the original amorphous particle (Fig. 2, C, D, G, and H). The two phases maintained constant physical contact throughout this transformation process. Because the surrounding medium is supersaturated with respect to the secondary phase, growth presumably also involves monomer addition from solution.

These two examples demonstrate the occurrence of multistep pathways of $CaCO_3$ crystal nucleation by which a metastable, amorphous precursor appears first and then transforms into a more energetically favorable crystalline phase through a direct, physical connection between the growing and shrinking phases. These multistep pathways contrast with direct pathways in which a crystalline phase nucleates from solution, either in the absence of ACC or independently of any amorphous particles that may have already formed. In this latter case, which is well documented (*9*, *12*–*14*), the nucleation of the crystalline phase is followed by dissolution of preexisting amorphous particles and reprecipitation onto the crystalline phase, as inferred from in situ optical (*12*, *13*) and x-ray studies (*9*). However, among the hundreds of experiments conducted, transformation

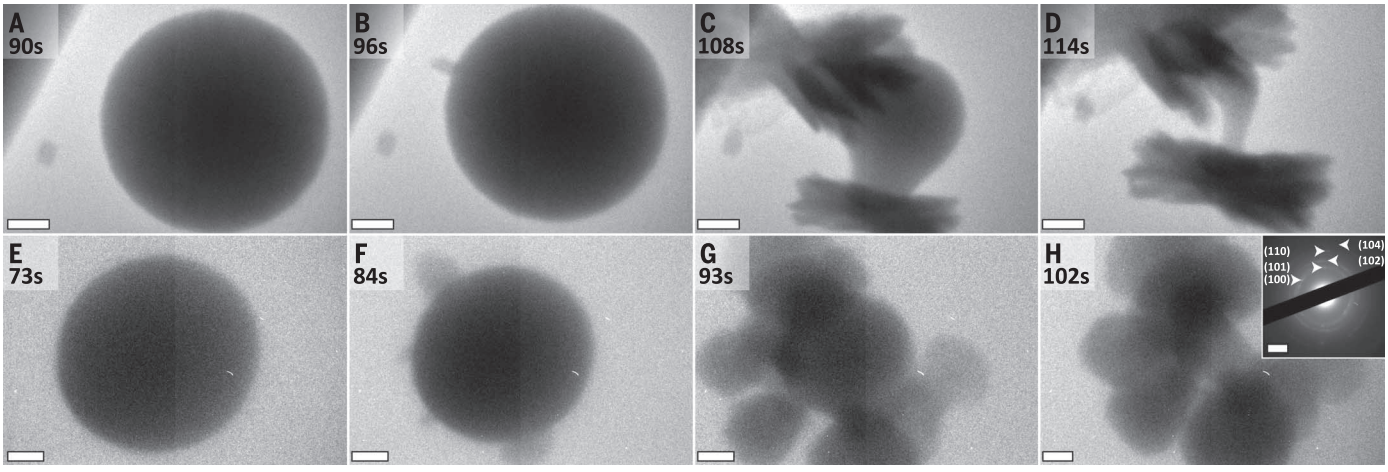

Fig. 2. Direct transformation of ACC to crystalline phases. Frames from movie S3 show a previously nucleated ACC particle (**A**), with the secondarily nucleated crystalline phase forming on or in the amorphous particle (**B**). The secondary phase, exhibiting typical aragonitic sheaf-of-wheat morphology, grows at the expense of the ACC, with the two phases maintaining physical contact during the entire transformation (**C** and **D**). Frames from movie S5 show a previously nucleated ACC particle (**E**), with secondarily nucleated vaterite plates forming on or in the amorphous particle (**F**). These plates grow at the expense of the ACC (**G** and **H**), in the same manner as above (C and D). Diffraction from the resulting plates identifies them as vaterite [inset to (H)]. Scale bars are 500 nm in (A) to (H) and 2 nm^{-1} in the inset to (H). Solution conditions are 30:100/10:0.2 for (A) to (H).

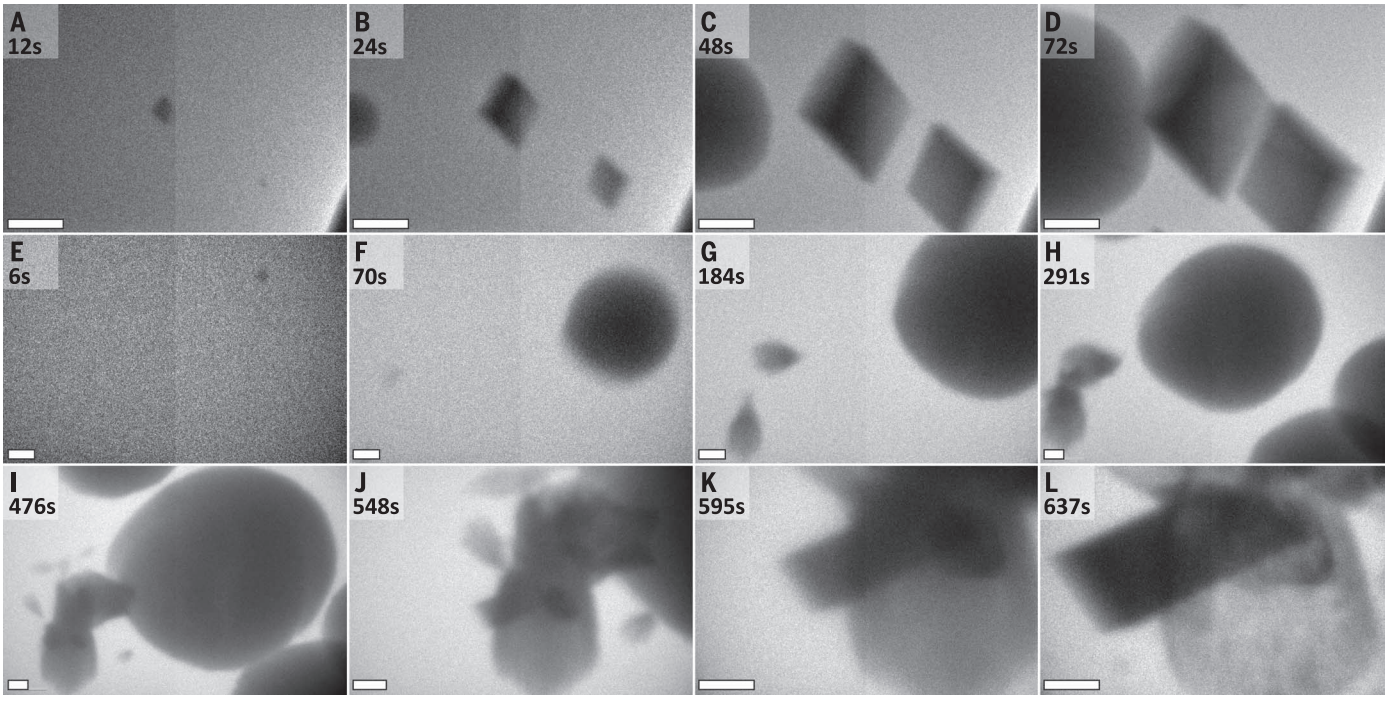

Fig. 3. Concurrent formation of multiple phases. Frames from movie S6 show simultaneous nucleation and growth of calcite crystals and either ACC or vaterite (**A** to **D**). The nitride window edge is visible at the bottom right corner of each panel. Frames from movie S7 show direct nucleation of vaterite (**E**) and aragonite (**F**) and subsequent growth (**G** and **H**). The formation of calcite occurs on aragonite (**I**), followed by calcite growth and concomitant dissolution of the aragonitic bundle (**J** to **L**). Scale bars are 500 nm in all panels. Solution conditions are 30:30/8:2 for (A) to (D) and 50:50/10:0.2 for (E) to (H).

of ACC into calcite (the most stable phase of $CaCO_3$) was never observed.

Additionally, we detected concurrent nucleation of multiple phases. For example, direct nucleation of calcite rhombohedra (Fig. 3, A to D, and movie S6) was observed alongside the formation of a (hemi-)spherical particle that, based on morphology, was either ACC or vaterite. Numerous optical studies have shown that ACC dissolves in the presence of calcite (*12*–*14*). Consequently, although the particle lacked any visible internal structure, as was typically seen in vaterite (Figs. 2, H to J, and 3, H and I), it is unlikely to be ACC.

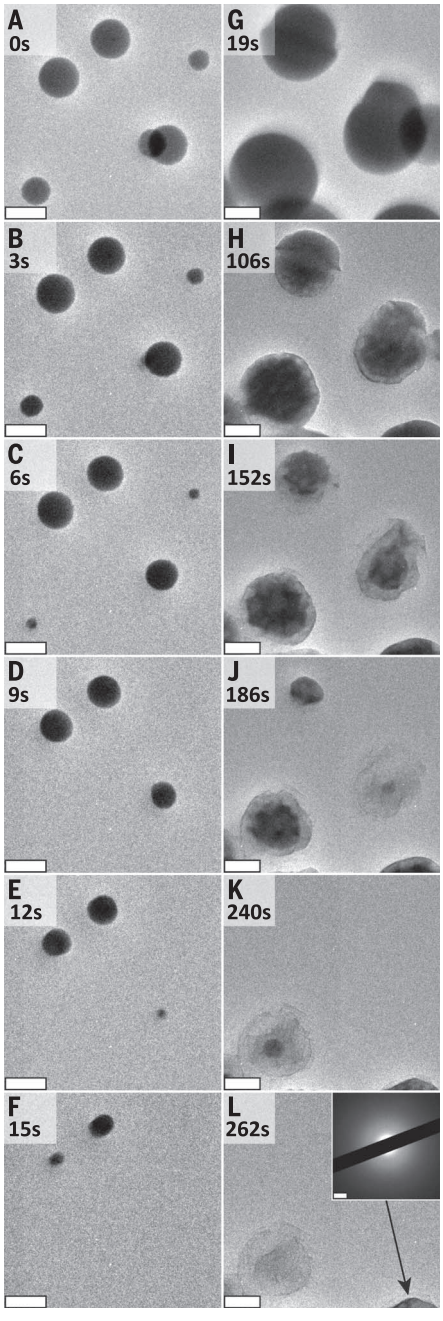

Fig. 4. Two dissolution behaviors of ACC. Frames from movie S11 show that some ACC particles undergo liquid-like shrinking and disappearance (**A** to **F**). At a later time in the same experiment, frames from movie S12 depict nearby ACC particles exhibiting solid-like behavior, becoming pitted and developing roughened edges (**G** to **L**) while still amorphous [inset to (L)]. Scale bars are 500 nm in (A) to (L) and 2 nm^{-1} for the inset to (L). Solution conditions are 100:100/10:0.2 for all panels.

Nucleation of multiple phases, followed by transformation to secondary phases, was also observed in a single experiment (Fig. 3, E to L, and movie S7). For example, a crystal with vateritic morphology first formed (Fig. 3, E to I) and continued to grow as bundles with aragonitic morphology formed in the vicinity and merged into larger aggregates (Fig. 3, F to J). A calcite rhombohedron then nucleated in apparent contact with the aragonitic bundle (Fig. 3I) and grew throughout the rest of the experiment (Fig. 3, J to L) as the aragonitic bundle dissolved (Fig. 3, K and L). We were unable to collect diffraction information to unequivocally assign phases in this experiment, leading to some ambiguity. Furthermore, because the image is a two-dimensional (2D) projection of a 3D volume, there is some uncertainty as to the precise location of the calcite nucleus relative to the surface of the bundle.

Contrary to our expectations, on the time scale of our experiments, ACC nucleation occurred only when the solution was exposed to the electron beam under sufficiently high solution concentrations (movie S8). Moreover, varying the electron dose accelerated, delayed, or prevented its formation (movies S9 and S10). By contrast, none of the crystalline phases showed such a relation to the electron beam; crystals were regularly found far from areas exposed to the beam.

We measured growth rates for ACC (fig. S6A), calcite (fig. S6B), and vaterite (fig. S6C) in 14 experiments, tracking observations of both single and multiple particles. All phases grew linearly, indicating that postnucleation growth occurred under steady-state solution conditions and was controlled by surface kinetics rather than diffusive transport (*15*). Although some growth curves exhibited single linear trends, others showed two distinct linear regions. This change in slope marked a drop in the growth rate and, therefore, supersaturation, suggesting a reduced rate of solute input to the cell, perhaps due to $CaCO_3$ nucleation near the cell inlet.

Finally, we observed multiple distinct dissolution behaviors for ACC particles under continued illumination by the electron beam, following thinning of the liquid layer. Some ACC particles underwent uniform shrinking to the point of complete disappearance, behaving as if they were liquid droplets evaporating into the surrounding medium (Fig. 4, A to F, and movie S11). By contrast, other ACC particles at a later time in the same experiment exhibited behavior indicative of a dissolving solid, becoming rough and pitted over time (Figs. 4, G to L, and movie S12) before finally disappearing. Others exhibited behavior combining or intermediate to these two end points.

The open questions about nucleation from electrolyte solutions are especially germane to the $CaCO_3$ system. Numerous studies have concluded that the final crystalline state often emerges long after the first appearance of ACC (*5*, *6*, *9*, *14*, *16*–*18*). Physical chemical analyses (*5*) and cryogenic TEM (*18*) have given rise to a model of nucleation in which stable multi-ion clusters aggregate to form this first amorphous phase, which then transforms directly to the crystalline phases. Based on x-ray diffraction and optical microscopy, other studies have concluded that nucleation is described well by CNT, and crystalline phases that appear after ACC do so through dissolution and reprecipitation (*9*, *12*). Ex situ TEM (*19*) and nuclear magnetic resonance data (*3*) indicate the existence of a dense liquid phase. Molecular dynamics simulations predict polymeric clusters (*10*), and dense liquid phases (*4*) form through spinodal decomposition with ACC then forming through partial dehydration. However, the existence of these phenomena remains unproven. Moreover, spectroscopic analyses have shown that many $CaCO_3$-based biominerals form through aggregation and crystallization of ACC exhibiting multiple hydrated states (*20*, *21*). The spatial resolution of the experiments described here does not allow us insight into the question of whether nucleation occurs via ion-by-ion attachment, as per CNT, or whether stable or metastable clusters serve as the primary species of addition. Our observations do, however, demonstrate that multiple nucleation pathways exist for the crystalline phases of $CaCO_3$, including both direct formation from solution and direct transformation from more disordered phases. Moreover, our findings show that these multiple pathways and phases are simultaneously available to the system at moderate to high supersaturations, as fully expected from classical considerations.

Our results also shed light on the process by which the disordered phases transform to the more ordered phase. In all cases for which we can definitively identify the starting point of the secondary nucleus, it lies approximately at the surface of the parent particle. This is consistent with previous in situ TEM observations of solidification in liquid $Au_{72}Ge_{28}$ droplets where the first ordered domain appeared at the surface (*22*). Presumably, the higher mobility of surface ions and, in the case of solutions, their ability to rapidly exchange with the solution lead to this phenomenon.

Because the experimental cells used in these experiments have fluid layer thicknesses ranging from hundreds of nanometers to micrometers, effects of confinement might be expected. However, over the range of sizes observed here, the lateral growth rates remain constant and thus do not appear to be affected by the cell dimensions. Effects of confinement on nucleation could be evident in two ways: The first is through a similarity in cell dimensions to critical nucleus size (*23*), and the second is by structuring of the liquid layer through proximity to the cell membranes (*24*, *25*). However, the cell dimensions are orders of magnitude above the ~1- to 10-nm critical sizes of the crystalline phases (*12*), as well as the ~10 Å thickness of the hydration layers (*24*, *25*).

The findings reported here also bear upon the controversy concerning the nature of ACC. Initially, a single amorphous phase was reported (*26*). Later experiments demonstrated the existence of both hydrous ACC and anhydrous ACC (*27*). Other research suggested the existence of two forms of hydrous ACC (*28*), as well as protovateritic ACC and proto-calcitic ACC (*29*), with each serving as a precursor to the respective crystalline phase. The dense liquid phase referred to above was recently proposed as yet another amorphous form. Our results call into question whether these are fundamentally distinct phases or whether they exist as points on a continuum. Though certainly not conclusive, the disparate modes of ACC dissolution observed in our study suggest that the term ACC refers to a spectrum of structures ranging from the dense liquid phase to the anhydrous form, rather than a single or even a few closely related structures. Finally, whereas our results clearly show that direct transformation of ACC to the crystalline phase of $CaCO_3$ readily occurs, we confirm previous suggestions from low-resolution optical measurements, macroscopic x-ray diffraction data (*12*–*14*), and x-ray microscopy (*30*) that direct transformation from ACC to calcite is unlikely. Indeed, this formation pathway has never been directly observed.

REFERENCES AND NOTES

1. http://web.mit.edu/jwk/www/docs/Gibbs1875-1878-Equilibrium_of_Heterogeneous_Substances.pdf
2. S. E. Wolf, J. Leiterer, M. Kappl, F. Emmerling, W. Tremel, *J. Am. Chem. Soc.* **130**, 12342–12347 (2008).
3. M. A. Bewernitz, D. Gebauer, J. Long, H. Cölfen, L. B. Gower, *Faraday Discuss.* **159**, 291–312 (2012).
4. A. F. Wallace *et al*., *Science* **341**, 885–889 (2013).
5. D. Gebauer, A. Völkel, H. Cölfen, *Science* **322**, 1819–1822 (2008).
6. H. Cölfen, M. Antonietti, *Mesocrystals and Non-Classical Crystallization* (Wiley, San Francisco, 2008).
7. A. E. S. Van Driessche *et al*., *Science* **336**, 69–72 (2012).
8. E. M. Pouget *et al*., *J. Am. Chem. Soc.* **132**, 11560–11565 (2010).
9. P. Bots, L. G. Benning, J. D. Rodriguez-Blanco, T. Roncal-Herrero, S. Shaw, *Cryst. Growth Des.* **12**, 3806–3814 (2012).
10. R. Demichelis, P. Raiteri, J. D. Gale, D. Quigley, D. Gebauer, *Nat. Commun.* **2**, 590 (2011).
11. M. J. Williamson, R. M. Tromp, P. M. Vereecken, R. Hull, F. M. Ross, *Nat. Mater.* **2**, 532–536 (2003).
12. Q. Hu *et al*., *Faraday Discuss.* **159**, 509–523 (2012).
13. J. Aizenberg, D. A. Muller, J. L. Grazul, D. R. Hamann, *Science* **299**, 1205–1208 (2003).
14. J. R. I. Lee *et al*., *J. Am. Chem. Soc.* **129**, 10370–10381 (2007).
15. A. A. Chernov, *Modern Crystallography III* (Springer, Berlin, 1984).
16. E. Beniash, J. Aizenberg, L. Addadi, S. Weiner, *Proc. R. Soc. London Ser. B* **264**, 461–465 (1997).
17. S. Weiner, I. Sagi, L. Addadi, *Science* **309**, 1027–1028 (2005).
18. E. M. Pouget *et al*., *Science* **323**, 1455–1458 (2009).
19. S. E. Wolf *et al*., *Nanoscale* **3**, 1158–1165 (2011).
20. L. Addadi, S. Raz, S. Weiner, *Adv. Mater.* **15**, 959–970 (2003).
21. Y. Politi *et al*., *Adv. Funct. Mater.* **16**, 1289–1298 (2006).
22. P. W. Sutter, E. A. Sutter, *Nat. Mater.* **6**, 363–366 (2007).
23. L. O. Hedges, S. Whitelam, *Soft Matter* **8**, 8624–8635 (2012).
24. L. Cheng, P. Fenter, K. L. Nagy, M. L. Schlegel, N. C. Sturchio, *Phys. Rev. Lett.* **87**, 156103 (2001).
25. J. I. Kilpatrick, S.-H. Loh, S. P. Jarvis, *J. Am. Chem. Soc.* **135**, 2628–2634 (2013).
26. L. Brečević, A. E. Nielsen, *J. Cryst. Growth* **98**, 504–510 (1989).
27. N. Koga, Y. Yamane, *J. Therm. Anal. Calorim.* **94**, 379–387 (2008).
28. A. V. Radha, T. Z. Forbes, C. E. Killian, P. U. Gilbert, A. Navrotsky, *Proc. Natl. Acad. Sci. U.S.A.* **107**, 16438–16443 (2010).
29. D. Gebauer *et al*., *Angew. Chem. Int. Ed.* **49**, 8889–8891 (2010).
30. J. Rieger, J. Thieme, C. Schmidt, *Langmuir* **16**, 8300–8305 (2000).

ACKNOWLEDGMENTS

We thank V. Altoe for the use of and assistance with the JEOL-2100F transmission electron microscope. This research was supported by the U.S. Department of Energy (DOE), Office of Basic Energy Sciences, Division of Chemical Sciences, Geosciences, and Biosciences at Pacific Northwest National Laboratory and Lawrence Berkeley National Laboratory. TEM was performed at the Molecular Foundry, Lawrence Berkeley National Laboratory, which is supported by the Office of Basic Energy Sciences, Scientific User Facilities Division. M.H.N. acknowledges support awarded by the U.S. Department of Defense, Air Force Office of Scientific Research, National Defense Science and Engineering Graduate Fellowship 32 CFR 168a, and the NSF under grant DMR-1312697. Pacific Northwest National Laboratory is operated by Battelle Memorial Institute for the DOE under contract DE-AC05-76RL01830.

SUPPLEMENTARY MATERIALS

www.sciencemag.org/content/345/6201/1158/suppl/DC1
Materials and Methods
Figs. S1 to S6
Tables S1 to S2
References (*31*–*33*)
Movies S1 to S12

28 March 2014; accepted 30 July 2014
10.1126/science.1254051

SUPERNOVAE

Early ^{56}Ni decay gamma rays from SN2014J suggest an unusual explosion

Roland Diehl,[1]* Thomas Siegert,[1] Wolfgang Hillebrandt,[2] Sergei A. Grebenev,[3] Jochen Greiner,[1] Martin Krause,[1] Markus Kromer,[4] Keiichi Maeda,[5] Friedrich Röpke,[6] Stefan Taubenberger[2]

Type Ia supernovae result from binary systems that include a carbon-oxygen white dwarf, and these thermonuclear explosions typically produce 0.5 solar mass of radioactive ^{56}Ni. The ^{56}Ni is commonly believed to be buried deeply in the expanding supernova cloud. In SN2014J, we detected the lines at 158 and 812 kiloelectron volts from ^{56}Ni decay (time ~8.8 days) earlier than the expected several-week time scale, only ~20 days after the explosion and with flux levels corresponding to roughly 10% of the total expected amount of ^{56}Ni. Some mechanism must break the spherical symmetry of the supernova and at the same time create a major amount of ^{56}Ni at the outskirts. A plausible explanation is that a belt of helium from the companion star is accreted by the white dwarf, where this material explodes and then triggers the supernova event.

SN2014J was discovered on 22 January 2014 (*1*) in the nearby starburst galaxy M82 and was classified as a supernova of type Ia (SN Ia) (*2*). This is the closest SN Ia since the advent of gamma-ray astronomy. It reached its optical brightness maximum on 3 February, 20 days after the explosion on 22 January at 14.75 UT (*3*). At a distance of 3.5 Mpc (*4*), a detailed comparison of models to observations across a wide range of wavelengths appears feasible, including gamma-ray observations from the ^{56}Ni decay chain.

Calibrated light curves of type Ia supernovae (SNe Ia) have become standard tools to determine cosmic distances and the expansion history of the universe (*5*), but we still do not understand the physics that drives their explosion (*6*, *7*). Their extrapolation as distance indicators at high redshifts, where their population has not been empirically studied, can only be trusted if a physical model is established (*5*). Unlike core-collapse SNe, which obtain their explosion energy from their gravitational energy, SNe Ia are powered by the release of nuclear binding energy through fusion reactions.

It is generally believed that carbon fusion reactions ignited in the degenerate matter inside a white dwarf star lead to a runaway. This sudden release of a large amount of nuclear energy is enough to overcome the binding energy of such a compact star and thus causes a SN Ia. A consensus had been for years that the instability of a white dwarf at the Chandrasekhar mass limit in a binary system with a main-sequence or (red) giant companion star was the most plausible model to achieve the apparent homogeneity (*6*). However, observations have revealed an unexpected diversity in SNe Ia in recent years (*8*), and increasing model sophistication along with reevaluations of more-exotic explosion scenarios have offered plausible alternatives. The consensus now

[1]Max-Planck-Institut für Extraterrestrische Physik, Giessenbachstrasse 1, D-85741 Garching, Germany [2]Max-Planck-Institut für Astrophysik, Karl-Schwarzschild-Strasse 1, 85741 Garching, Germany. [3]Space Research Institute, Russian Academy of Sciences, Profsoyuznaya 84/32, 117997 Moscow, Russia. [4]The Oskar Klein Centre and Department of Astronomy, Stockholm University, AlbaNova, SE-106 91 Stockholm, Sweden. [5]Department of Astronomy, Kyoto University, Kitashirakawa-Oiwake-cho, Sakyo-ku, Kyoto 606-8502, and Kavli Institute (WPI), University of Tokyo, 5-1-5 Kashiwanoha, Kashiwa, Chiba 277-8583, Japan. [6]Institut für Theoretische Physik und Astrophysik, Universität Würzburg, Emil-Fischer-Strasse 31, 97074 Würzburg, Germany.
*Corresponding author. E-mail: rod@mpe.mpg.de

leans toward a broader range of binary systems and more methods of igniting a white dwarf, independent of its mass. Destabilizing events such as accretion flow instabilities, He detonations, mergers, or collisions with a degenerate companion star are being considered (*9*–*12*).

Matter consisting of equal numbers of protons and neutrons (such as in C and O) binds these nucleons most tightly in the form of the ^{56}Ni nucleus. Therefore, ^{56}Ni is believed to be the main product of nuclear burning under sufficiently hot and dense conditions, such as in SNe Ia. The radioactive decay of ^{56}Ni then powers SN light through its gamma rays and positrons, with a decay chain from ^{56}Ni (time ~ 8.8 days) through radioactive ^{56}Co (time ~ 111.3 days) to stable ^{56}Fe. The outer gas absorbs this radioactive energy input and reradiates it at lower-energy wavebands [ulraviolet (UV) through infrared (IR)]. But neither the explosion dynamics nor the evolution toward explosions from white dwarf properties and from interactions with their companion stars can easily be assessed, because it remains difficult (*13*) to constrain different explosion models through observations. Some insights toward the nature of the binary companion star have been obtained from preexplosion data (*8*, *14*–*17*) and from its interactions with the SN (*18*–*20*).

Gamma rays can help in constraining inner physical processes. Although initially the SN Ia remains opaque even to penetrating gamma rays, within several weeks, more and more of the ^{56}Ni decay-chain gamma rays are expected to leak out of the expanding SN (*21*, *22*). The maximum of gamma-ray emission should be reached 70 to 100 days after the explosion, with its intensity declining afterward because of the radioactive decay of ^{56}Co (*23*). Simulations of the explosion and radioactive energy release have been coupled with radiative transport to show that the gamma-ray emission of the SN is characterized by nuclear transition lines between ~150 and 3000 keV and their secondary, Compton-scattered continuum from kilo–electron volt energies up to mega–electron volt energies (*22*, *24*–*26*).

Here we describe the analysis of data from the Spectrometer (SPI) on the International Gamma-Ray Astrophysics Laboratory (INTEGRAL) space mission with respect to gamma-ray line emission from the ^{56}Ni decay chain. INTEGRAL (*27*) started observing SN2014J on 31 January 2014 (*28*), about 16.6 days after the inferred explosion date. We analyzed sets of detector spectra from the Ge detectors of the SPI spectrometer (*29*, *30*), collected at the beginning of INTEGRAL's SN2014J campaign. SPI measures photon interaction events for each of its 15 Ge detectors that constitute the telescope camera. Imaging information is imprinted through a coded mask selectively shadowing parts of the camera for a celestial source (*29*). Changing the telescope pointing by ~2.1° after each ~3000 s, the mask shadow is varied for the counts contributed from the sky, whereas the instrumental background counts should not be affected by these small variations in telescope orientation.

In our analysis of SN2014J, we fitted the measured data to the combination of the expected coding pattern in the detector signals and our instrumental background model. In the fit, we adjusted intensities of the global background model and the point source located at a particular position in the sky. The fit was performed independently for each of the energy bins.

Instrumental background dominates the total count rate in SPI detectors, so its treatment is key to the data analysis. We performed fine spectroscopy of the measured spectra from each 3-day orbit, determining instrumental line features and the status of each detector in terms of intrinsic resolution and degradation. We then used this orbit-averaged spectral shape to fit the line intensity variations among individual pointings, adjusting the underlying continuum emission and the line feature amplitudes relative to the orbit averages. We attributed these line intensities to each of the Ge detectors as measured in orbit-integrated spectra (for details, see the supplementary materials). In this way, we avoid statistical limitations of invididual-detector spectra per telescope pointing and energy bin and still obtain a very good representation of background variations, in addition to a consistent description of the spectral evolution of instrumental background with time (*31*).

The Poissonian maximum likelihood determines the intensity of the celestial source and overall background. For the assumed source position, we derived an intensity spectrum, typically with ~1-keV spectral resolution (*32*). Our spectra for SN2014J were then analyzed for the presence of lines and their significances. Line parameters such as Doppler shifts or broadening can be derived from fitted line centroids and widths and their uncertainties in a next step. Varying the position of the source in the sky, we also mapped signals in spectral bands of interest across the observed sky area through an identical maximum-likelihood analysis. In this way, we can check whether a detected line consistently maps to the SN2014J location. From the same sky mapping of a spectral band where we did not identify a celestial line, we obtained a reference that checks for the appearance of possible artifacts from statistical fluctuations alone, also accounting for the trials of source positions inherent in such mapping. The data set analyzed here includes 60 pointings with an exposure of 150.24 ks for a 3-day period from 31 January to 2 February 2014; i.e., from 16.6 to 19.2 days after the supernova explosion.

We found the characteristic gamma-ray lines of ^{56}Ni decaying in a SN Ia: The spectra for SN2014J [at Galactic coordinates (l,b) = (141.427°, 40.558°)] show the two major lines at 158 and 812 keV (Fig. 1). The two line intensities are identical within uncertainties. Imaging analysis locates the signal at the position of SN2014J, within spatial-resolution uncertainties (Fig. 2). The measured gamma-ray line fluxes are (1.10 ± 0.42) 10^{-4} photons cm^{-2} s^{-1} (158 keV line) and (1.90 ± 0.66) 10^{-4} photons cm^{-2} s^{-1} (812 keV line). The observed lines are neither significantly velocity-broadened nor offset (from bulk-velocity Doppler shifts), although broad components could underlie our main signal. Line broadening from the observed ^{56}Ni corresponds to velocity spreads below ~1500 to 2000 km s^{-1}, and its bulk velocity

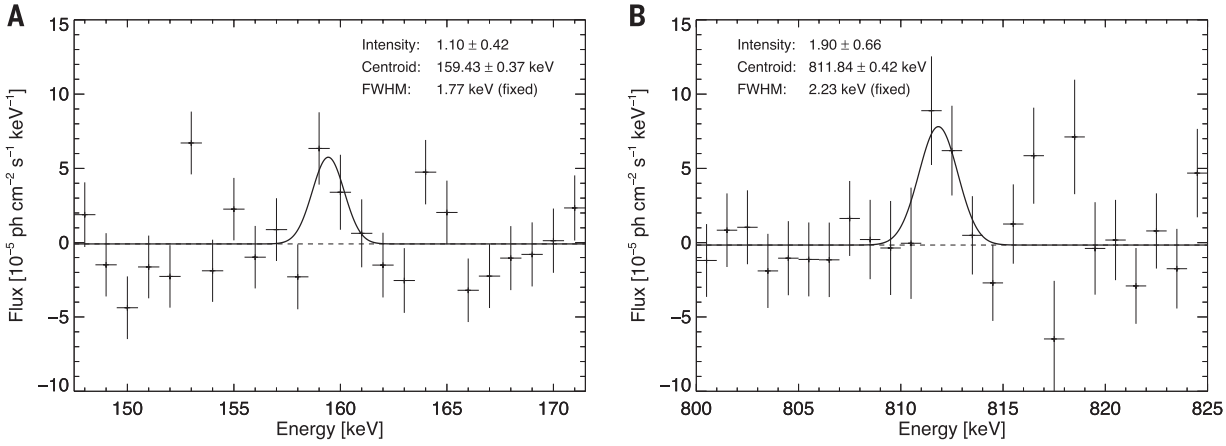

Fig. 1. Gamma-ray spectra measured with SPI/INTEGRAL from SN2014J. The observed 3-day interval around day 17.5 after the explosion shows the two main lines from ^{56}Ni decay, 158 keV (**A**) and 812 keV (**B**). In deriving these spectra, we adopted the known position of SN2014J and used the instrumental response and background model. Error bars are shown as 1σ. The measured intensity corresponds to an initially synthesized ^{56}Ni mass of 0.06 solar mass.

is below ~2000 km s^{-1} (see the supplementary materials and table S1.1 for details). The total measured flux can be converted to a ^{56}Ni mass seen to decay at ~18 days after the explosion that corresponds to 0.06 solar mass of ^{56}Ni at the time of the explosion.

Apparently, a substantial fraction of the total ^{56}Ni produced must have been close to the gamma-ray photosphere in the outer ejecta of the SN at this time, at a depth not exceeding a few grams per square centimeter in column density, and this is probably just the surface of a more massive concentration of ^{56}Ni outside the core. Having this much ^{56}Ni freely exposed is surprising in all explosion models, particularly considering the constraints on its kinematics from line widths and positions.

Observations of SN2014J at early epochs in optical/IR wavelengths also show signatures of an unusual explosion: The rise of supernova light shows that the expected behavior of increase with the square of time (*33*) occurred with some delay. An early steeper rise and possible shoulder may be suggested from observations during the hours after the supernova (*3, 20*), which smooth out after a few days. Also, spectra do not show the early C and O absorption lines that would be expected if a large envelope overlies the light source (*20*).

A single degenerate Chandrasekhar mass scenario appears unlikely from upper limits on x-ray emission that exclude a supersoft progenitor source (*34*) and from constraints from pre-explosion imaging (*20, 35*). A sub-Chandrasekhar mass model with a He donor, or a merger of two white dwarfs, may be better models for SN2014J and could also explain our observation of ^{56}Ni in the outer layer of the SN more readily. Moreover, we favor a He donor progenitor channel for this SN Ia, because population synthesis models (*36*) indicate a short delay time for such systems, as expected for a SN Ia occurring in a starburst galaxy such as M82. However, a classical double-detonation explosion scenario (*11, 37, 38*) is inconsistent with the observations. In this case, a ^{56}Ni shell engulfing the SN ejecta would be expected, resulting in broad, high-velocity gamma-ray emission lines, whereas narrow lines are detected in SN2014J. However, such an outer shell is expected to have an imprint on optical observables (*33, 39, 40*) that are not seen in SN2014J (*20*).

A modified but more speculative version of this model may work, however (Fig. 3). If He formed an equatorial accretion belt before it detonated, instead of accumulating in a shell, the kinematic constraints could be met, provided we observe the SN essentially pole-on. In fact, this idea is not new: Accretion belts have been discussed frequently in the context of classical novae (*41, 42*). Here we could have the situation of unstable mass transfer on the Kelvin-Helmholtz time scale from the He companion onto the white dwarf, before the explosion, which is possible if the He donor is more massive than the white dwarf and fills its Roche lobe. In case of a H-rich donor, this would be the standard scenario for supersoft x-ray sources (*43*), which has been

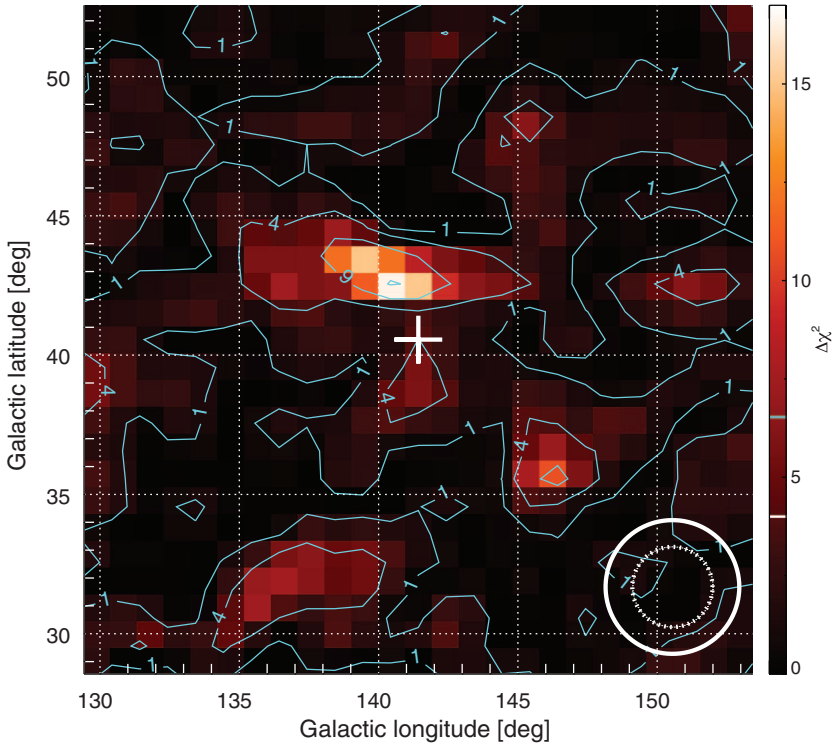

Fig. 2. Location of the ^{56}Ni line signal on the sky. The gamma-ray line emission at 158 and 812 keV is mapped onto the position of SN2014J (cross) within instrumental uncertainty (the circle at the bottom right shows the size of the instrument point spread function for strong sources, as 68% (1σ) (dotted lines) and 99% (2σ) (contour lines). The apparent offset is well within the 2σ contours of our point spread function and not significant.

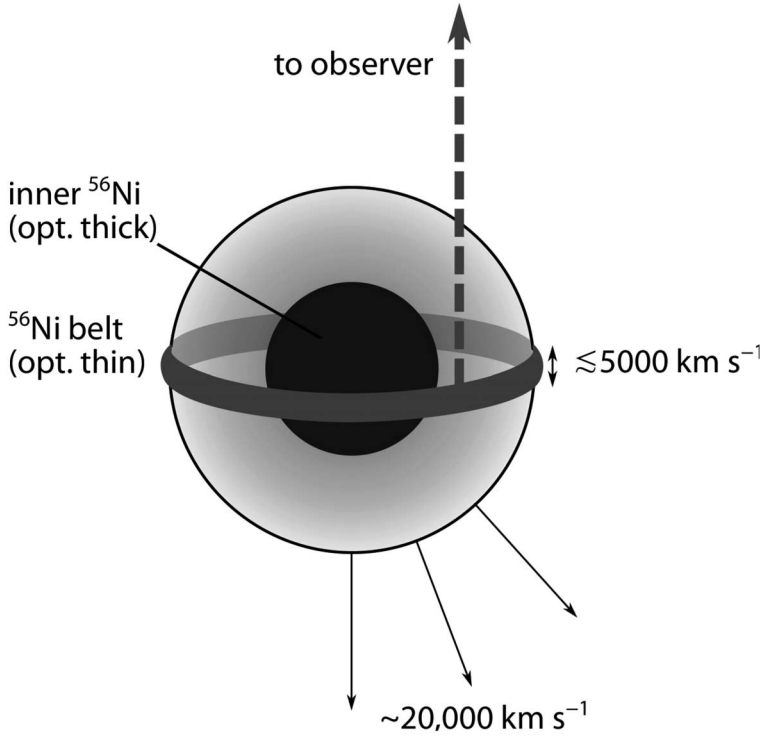

Fig. 3. Sketch of an ejecta configuration compatible with our observations. He accreted in a belt before the explosion produces the ^{56}Ni belt at the surface of the ejecta. The gamma rays can escape from the belt material, whereas the ^{56}Ni in the core (black) is still buried at high optical depths. opt., optically. A dashed arrow points to the observer.

excluded for SN2014J (*34*). But in this case, the accreted material is mostly He, and the accretion rate can be very high, up to 10^{-4} solar masses per year (*44*). If the white dwarf is rapidly rotating or if mass is accreted faster than it loses angular momentum and thus spreads over the white dwarf, a He belt will be accumulated.

An equatorial ring as inferred here might not be that uncommon. Recently, Hubble Space Telescope imaging of the light echo from the recurrent nova T Pyx revealed a clumpy ring (*45*). Once this belt becomes dense enough, explosive He burning may be ignited, leaving an ejecta configuration as shown in Fig. 3. This may be consistent with the observed gamma-ray and optical signals. Our radiation transfer simulations in UV/optical/near-IR (fig. S10) show that the Ni belt would not produce easily distinguishable features but would result in a normal SN Ia appearance, not only for a pole-on observer but also for an equatorial observer. In view of this, the interpretation of having this type of explosion as a common scenario is not rejected by statistical arguments (see the supplementary materials for more details).

The evolution of the ^{56}Co gamma-ray signal should reveal further aspects of the ^{56}Ni distribution in SN2014J. These lines with associated continua have been recognized to emerge in data from both INTEGRAL instruments (*46*), as more of the total ^{56}Ni produced in the SN becomes visible when the gamma-ray photosphere recedes into the SN interior.

REFERENCES AND NOTES

1. J. Fossey, B. Cooke, G. Pollack, M. Wilde, T. Wright, *Central Bureau Electronic Telegrams No.* **3792** (2014).
2. Y. Cao, M. M. Kasliwal, A. McKay, A. Bradley, *Astronomers Telegram*, no. 5786 (2014).
3. W. Zheng *et al.*, *Astrophys. J. Lett.* **783**, L23 (2014).
4. J. J. Dalcanton *et al.*, *Astrophys. J.* **183** (suppl.), 67–108 (2009).
5. A. Goobar, B. Leibundgut, *Annu. Rev. Nucl. Part. Sci.* **61**, 251–279 (2011).
6. W. Hillebrandt, J. Niemeyer, *Annu. Rev. Astron. Astrophys.* **38**, 191–230 (2000).
7. W. Hillebrandt, M. Kromer, F. K. Röpke, A. J. Ruiter, *Front. Phys.* **8**, 116–143 (2013).
8. W. Li *et al.*, *Nature* **480**, 348–350 (2011).
9. J. F. Guillochon, M. Dan, E. Ramirez-Ruiz, S. Rosswog, *Astrophys. J.* **709**, L64–L69 (2010).
10. S. Rosswog, D. Kasen, J. Guillochon, E. Ramirez-Ruiz, *Astrophys. J. Lett.* **705**, L128–L132 (2009).
11. M. Fink *et al.*, *Astron. Astrophys.* **514**, A53 (2010).
12. R. Pakmor *et al.*, *Astrophys. J.* **747**, L10 (2012).
13. F. K. Röpke *et al.*, *Astrophys. J. Lett.* **750**, L19 (2012).
14. M. C. P. Bours, S. Toonen, G. Nelemans, *Astron. Astrophys.* **552**, A24 (2013).
15. P. Ruiz-Lapuente *et al.*, *Nature* **431**, 1069–1072 (2004).
16. W. E. Kerzendorf *et al.*, *Astrophys. J.* **701**, 1665–1672 (2009).
17. B. E. Schaefer, A. Pagnotta, *Nature* **481**, 164–166 (2012).
18. J. S. Bloom *et al.*, *Astrophys. J. Lett.* **744**, L17 (2012).
19. B. J. Shappee, K. Z. Stanek, R. W. Pogge, P. M. Garnavich, *Astrophys. J.* **762**, L5 (2013).
20. A. Goobar *et al.*, *Astrophys. J.* **784**, L12 (2014).
21. P. Höflich, *Nucl. Phys. A.* **777**, 579–600 (2006).
22. S. A. Sim, P. A. Mazzali, *Mon. Not. R. Astron. Soc.* **385**, 1681 (2008).
23. J. Isern *et al.*, *Astron. Astrophys.* **552**, A97 (2013).
24. A. Summa *et al.*, *Astron. Astrophys.* **554**, A67 (2013).
25. K. Maeda *et al.*, *Astrophys. J.* **760**, 54 (2012).
26. L.-S. The, A. Burrows, *Astrophys. J.* **786**, 141 (2014).
27. C. Winkler *et al.*, *Astron. Astrophys.* **411**, L1–L6 (2003).
28. E. Kuulkers, INTEGRAL Target of Opportunity observations of the type Ia SN2014J in M82. *Astronomers Telegram*, no. 5835 (2014).
29. G. Vedrenne *et al.*, *Astron. Astrophys.* **411**, L63–L70 (2003).
30. J. P. Roques *et al.*, *Astron. Astrophys.* **411**, L91–L100 (2003).
31. T. Siegert, thesis, Technische Universität München, Munich, Germany (2013).
32. R. Diehl *et al.*, *Astron. Astrophys.* **441**, L117 (2003).
33. P. E. Nugent *et al.*, *Nature* **480**, 344–347 (2011).
34. M. T. B. Nielsen, M. Gilfanov, A. Bogdan, T. E. Woods, G. Nelemans, Upper limits on the luminosity of the progenitor of type Ia supernova SN2014J. http://arxiv.org/abs/1402.2896 (2014).
35. P. L. Kelly, *et al.*, http://arxiv.org/abs/1403.4250 (2014).
36. A. J. Ruiter, K. Belczynski, S. A. Sim, I. R. Seitenzahl, D. Kwiatkowski, *Mon. Not. R. Astron. Soc.* **440**, L101–L105 (2014).
37. M. Fink, W. Hillebrandt, F. K. Röpke, *Astron. Astrophys.* **476**, 1133–1143 (2007).
38. R. Moll, S. E. Woosley, *Am. Astron. Soc. Abstr.* **221**, no. 253.22 (2013).
39. M. Kromer *et al.*, *Astrophys. J.* **719**, 1067–1082 (2010).
40. P. Nugent, E. Baron, D. Branch, A. Fisher, P. H. Hauschildt, *Astrophys. J.* **485**, 812–819 (1997).
41. R. Kippenhahn, H. C. Thomas, *Astron. Astrophys.* **63**, 265 (1978).
42. A. L. Piro, L. Bildsten, *Astrophys. J.* **603**, 252–264 (2004).
43. J. Greiner, in *Lecture Notes in Physics* (Springer Verlag, Berlin, 1996), vol. 472, pp. 299–337.
44. W. Y. Law, H. Ritter, *Astron. Astrophys.* **123**, 33–38 (1983).
45. J. L. Sokoloski, A. P. S. Crotts, S. Lawrence, H. Uthas, *Astrophys. J.* **770**, L33 (2013).

ACKNOWLEDGMENTS

This research was supported by the Deutsche Forschungsgemeinschaft (DFG) cluster of excellence "Origin and Structure of the Universe" and from DFG Transregio Project No. 33 "Dark Universe." S.A.G. acknowledges support from the Russian Academy of Sciences, program RAS P-21. F.K.R. was supported by the DFG (Emmy Noether Programm RO3676/1-1) and the ARCHES prize of the German Ministry for Education and Research. The work by K.M. is partly supported by a Japan Society for the Promotion of Science Grant-in-Aid for Scientific Research (grant no. 23740141 and 26800100) and WPI, at the Ministry of Education, Culture, Sports. Science & Technology. We are grateful to E. Kuulkers for handling the observations and to X. Zhang for preparing our SPI data for the INTEGRAL SN2014J campaign. The INTEGRAL/SPI project has been completed under the responsibility and leadership of CNES Toulouse. We are grateful to the agencies and institutions of ASI, CEA, CNES, DLR, ESA, INTA, NASA, and OSTC for support of this ESA space science mission. INTEGRAL's data archive (http://www.isdc.unige.ch/integral/archive#DataRelease) is at the INTEGRAL Science Data Center in Versoix, Switzerland, and includes the SN2014J data used in this paper.

SUPPLEMENTARY MATERIALS

www.sciencemag.org/content/345/6201/1162/suppl/DC1
Materials and Methods
Supplementary Text
Figs. S1 to S10
Tables S1 and S2
References (*46*–*58*)

14 April 2014; accepted 21 July 2014
Published online 31 July 2014;
10.1126/science.1254738

EARTHQUAKE DYNAMICS

Intense foreshocks and a slow slip event preceded the 2014 Iquique M_w 8.1 earthquake

S. Ruiz,[1]* M. Metois,[2] A. Fuenzalida,[3] J. Ruiz,[1] F. Leyton,[4] R. Grandin,[5] C. Vigny,[6] R. Madariaga,[6] J. Campos[1]

The subduction zone in northern Chile is a well-identified seismic gap that last ruptured in 1877. The moment magnitude (M_w) 8.1 Iquique earthquake of 1 April 2014 broke a highly coupled portion of this gap. To understand the seismicity preceding this event, we studied the location and mechanisms of the foreshocks and computed Global Positioning System (GPS) time series at stations located on shore. Seismicity off the coast of Iquique started to increase in January 2014. After 16 March, several M_w > 6 events occurred near the low-coupled zone. These events migrated northward for ~50 kilometers until the 1 April earthquake occurred. On 16 March, on-shore continuous GPS stations detected a westward motion that we model as a slow slip event situated in the same area where the mainshock occurred.

Since the giant moment magnitude (M_w) 8.8 megathrust earthquake of 1877 (*1*–*4*), the ≥500-km-long region stretching from Arica (18°S) to the Mejillones Peninsula of Chile (24.5°S) (Fig. 1) has had relatively few major seismic events, with only moderate M_w < 8 events in 1933, 1967, and 2007 (*4*–*9*). On the basis of recent geodetic data (*5*, *10*, *11*), the degree of interseismic coupling (that is, the ratio between the interseismic slip rate and the plate-convergence velocity) in the area shows two distinct highly coupled segments (Loa and Camarones) separated by a low-coupling zone (LCZ) off the coast of Iquique (*5*). On 1 April 2014, a ~150-km-long portion of the gap broke in a M_w 8.1 earthquake after a strong precursory activity that started on 16 March (*12*, *13*). Understanding the complex nucleation phase

[1]Departamento de Geofísica, Facultad de Ciencias Físicas y Matemáticas, Universidad de Chile, Santiago, Chile. [2]Istituto Nazionale di Geofisica e Vulcanologia, Centro Nazionale Terremoti, Rome, Italy. [3]School of Environmental Sciences, University of Liverpool, Liverpool, UK. [4]Centro Sismológico Nacional, Facultad de Ciencias Físicas y Matemáticas, Universidad de Chile, Santiago, Chile. [5]Institut de Physique du Globe de Paris, Sorbonne Paris Cité, Université Paris Diderot, UMR 7154 CNRS, Paris, France. [6]Laboratoire de Geologie, UMR 8538 CNRS Ecole Normale Superieure, Paris, France.
*Corresponding author. E-mail: sruiz@dgf.uchile.cl

preceding the M_w 8.1 mainshock and its coseismic rupture should provide insights into the seismic gap history, present-day seismic hazard, and nucleation process of megathrust earthquakes.

Seismic activity preceding the Iquique earthquake initiated in a region between 19.5°S and 21°S, where coupling ranges from 0.2 to 0.5 (*5*); that is, the plates are slowly creeping past each other at a fraction of the plate rate (when the plates are fully locked, coupling is 1.0). This region was actively monitored because its seismic activity had steadily increased since 2008,

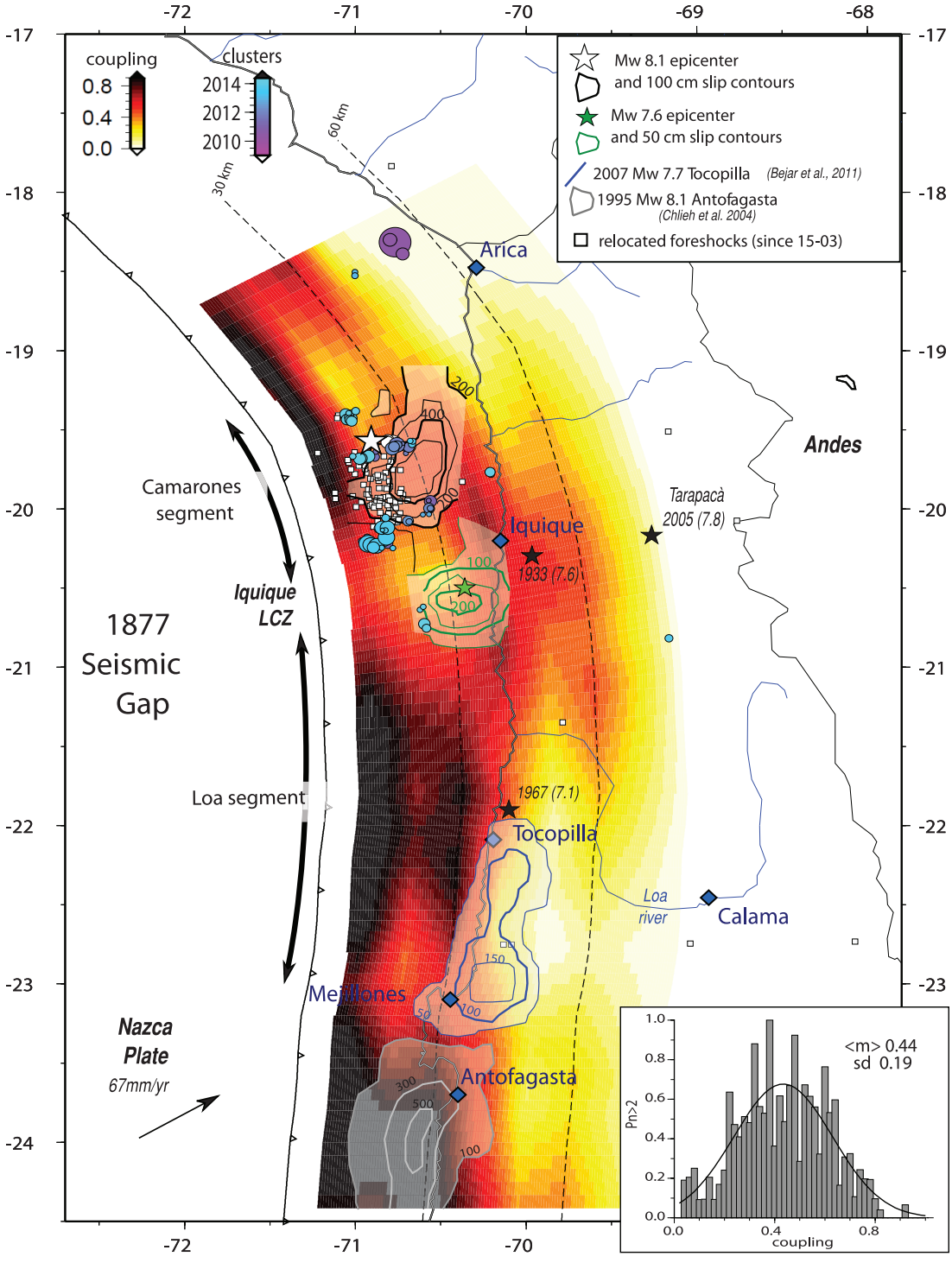

Fig. 1. Northern Chile seismic gap. Interseismic coupling was calculated from GPS measurements acquired in the zone since 2008. Slip contours are shown with continuous lines for the 2007 M_w 7.7 Tocopilla, 1995 M_w 8.0 Antofagasta, and 2014 M_w 8.1 and 7.6 Iquique earthquakes. Precursory seismicity from January to March 2014 is shown with light blue circles. Foreshocks from March 2014 are shown with open squares. The dashed lines denote the surface projection of the subduction interface isodepths. (**Inset**) Normalized probability that two or more $M_w < 7$ earthquakes occurred since 2008 (CSN catalog) as a function of the value of interseismic coupling. The upper right corner indicates the mean and standard deviation of the best-fit normal distribution.

with repeated interplate thrust events of magnitude <4.0. Several seismic clusters were located in this region by the National Seismological Center of Chile (CSN) (Fig. 1 and fig. S1); some of these clusters were associated with persistent microseismicity observed by the nearest seismological stations (fig. S2). Global catalogs reveal an increase in seismicity near Iquique since 2005, compared with the previous 10 years (fig. S3). To understand the seismicity that preceded the 1 April mainshock, we used the events listed in the CSN catalog to relocalize and estimate the focal mechanism of several foreshocks of this sequence. Simultaneously, we calculated the Global Positioning System (GPS) time series of the closest permanent stations up to the date of the mainshock and inverted for the slip rate on the plate interface (*14*).

The most recent seismic activity in northern Chile started on 4 January 2014, when a M_w 5.7 interplate thrust event took place at 20.69°S, 70.80°W on the southern edge of the Iquique LCZ (*5*). On 8 January, another M_w 5.7 event occurred in the same area. The automatic location system of CSN identified 30 events in a smaller region of 15 km by 15 km, in the period from 4 to 24 January 2014. Then on 12 January, a small cluster of six identified events occurred north of the previous ones at (19.7°S, 71.0°W). During February 2014, another small cluster occurred near 19.4°S, 71.0°W, where 16 events with local magnitude (ML) 2.4 to 4.0 were identified (Fig. 1, fig. S4, and table S1). On 15 March, the area was reactivated with 11 events of ML 2.6 to 4.6, followed on 16 March by the first big foreshock of M_w 6.7, ~50 km south and with a slightly deeper centroid (fig. S4). This event triggered a persistent precursory seismicity, including a M_w 6.3 earthquake on 22 March, which slowly moved northward and lasted until the occurrence of the 1 April 2014 M_w 8.1 event (Fig. 2 and fig. S4).

Overall, these foreshocks delineate a region that spans ~150 km along the strike of the subduction zone. We relocated this precursory seismicity and computed regional seismic moment tensor using a linear time-domain, broadband waveform inverse method (*15*) (Fig. 2). The centroid of the M_w 6.7 precursor of 16 March was only 10 km deep, in an area where the seismogenic interface is at a depth of ~20 km (*16*) (Fig. 2 and fig. S5). This event had a reverse focal mechanism with a strike of 277° that is at a sharp angle with respect to the trench (Fig. 2A). Over the course of 1 week, a persistent seismicity occurred in a zone of 10-km radius (Fig. 2C); most of these events were located inside the shallow South American plate and had very diverse focal mechanisms. On 22 March, a new M_w 6.3 foreshock occurred ~30 km north of the 16 March foreshock. After this event, precursory seismicity moved to the vicinity of the 22 March foreshock with depths and mechanisms indicating that it occurred at the plate interface (Fig. 2B).

From 16 March until the 1 April mainshock (i.e., for 17 days), all of the continuous GPS (cGPS) stations located along the coast between Iquique and Pisagua started to move trenchward (Fig. 3). This slowly increasing westward motion is in contrast to the usual inland-directed interseismic motion. The displacements measured during this period were quite large (>5 mm for the stations located between Iquique and Pisagua and ~1 cm at the PSGA station). Only a fraction of this cumulative displacement (up to 20%) can be attributed to the largest foreshock of 16 March (M_w 6.7), suggesting that slow aseismic slip was taking place offshore, concurrently with the development of the precursory seismicity. Whether this motion started slightly before or coincided with the 16 March foreshock is beyond the current GPS resolution. We inverted for the slip distributions on the subduction interface that best reproduce the observed displacements using Okada's formulas for an elastic half-space (*14*) (Fig. 4). We found a slip of ~0.8 m for the M_w 6.7 events of 16 March, located in a narrow area

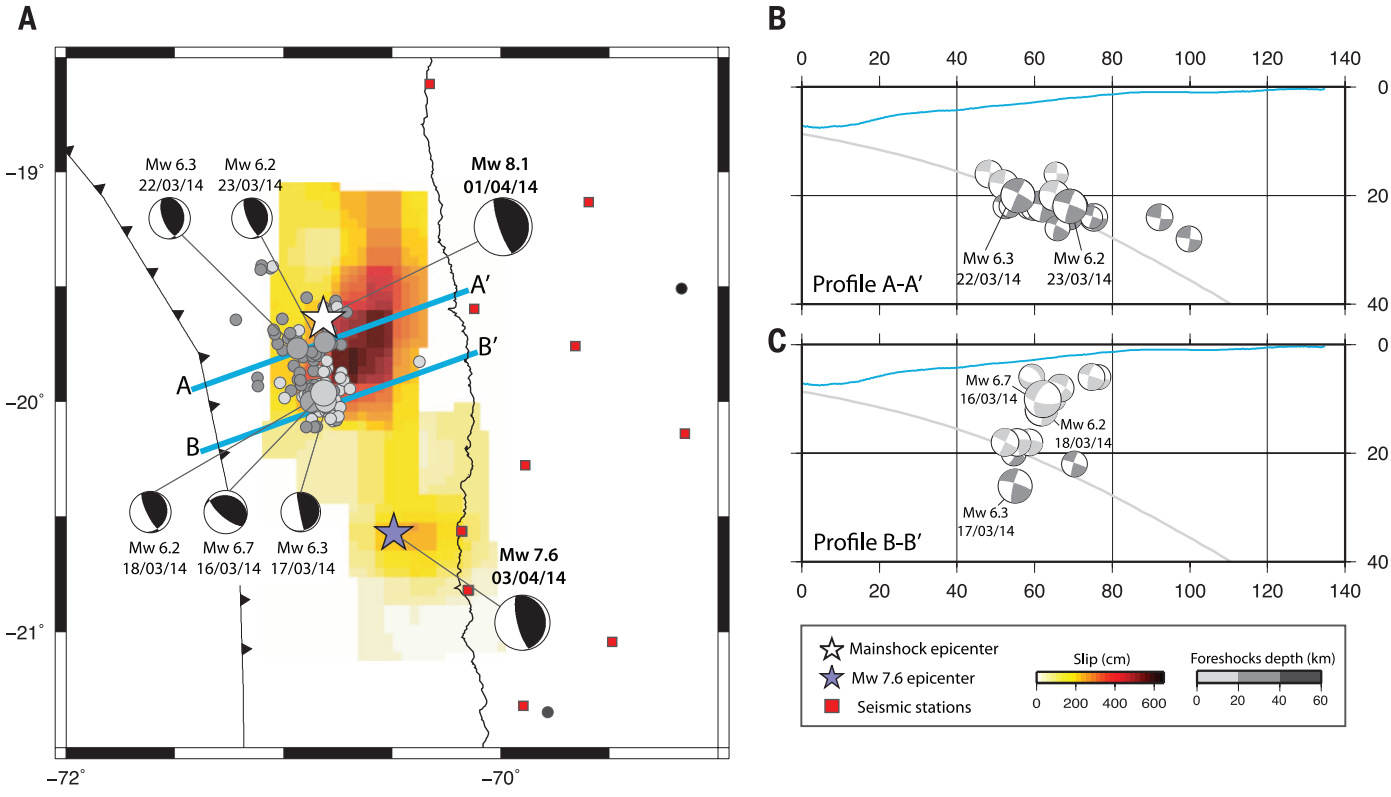

Fig. 2. Seismicity preceding the Iquique earthquake. (**A**) Gray dots show the foreshocks from 16 to 31 March; the intensity of the gray color indicates the depths of the events. The slip distribution of the M_w 8.1 and M_w 7.6 earthquakes inverted from far-field broadband records of the International Federation of Digital Seismograph Networks is shown with the color. (**B**) A 15-km-wide cross section along the A-A′ line shown in (A). (**C**) A 15-km-wide cross section along the B-B′ line shown in (A). In the vertical cross sections, we plot the focal mechanisms of events with M_w > 4.6. Mechanisms were computed by broadband moment tensor analysis. The gray curve shows the seismogenic contact according to (*16*).

in the vicinity of the CSN epicenter. We then computed the aseismic slip for the period from 10 March to the mainshock that extends over an area of 70 km by 20 km located between the foreshocks and the coast (Fig. 4).

The 1 April 2014 Iquique earthquake started with a small shock at the northern end of the region activated by the precursors that occurred in March (19.57°S, 70.91°W). The peak seismic moment release rate during the M_w 8.1 earthquake took place ~30 s after the initial nucleation (fig. S6). We used standard teleseismic methods (*17*) to invert for the coseismic slip of the main event and its large M_w 7.6 aftershock that occurred 2 days later (Fig. 2 and figs. S6 and S7). The maximum slip associated with these events was deeper than that of the March precursors and ~20 km inland, affecting areas of higher coupling (>0.6). Coseismic slip appears to overlap (at least partially) with the slow slip event (SSE) (Fig. 4), but no substantial coseismic slip occurred in the LCZ (Fig. 1). Whereas precursory seismicity migrated northward, the mainshock and its aftershock propagated toward the south, similar to what was observed for the 2007 M_w 7.8 Tocopilla earthquake (*7*, *8*).

The LCZ off the coast of Iquique can be assumed to play a key role in the events that occurred in northern Chile during, and in the 20 years preceding, this precursory sequence. The seismic swarms detected since 2008 occurred on the edges of the LCZ, and most moderate seismicity took place preferentially in zones of intermediate coupling (see inset in Fig. 1 and fig. S8), suggesting that aseismic creep occurring on the LCZ triggered seismic activity in its vicinity. Up to now, SSEs have remained undetected by the cGPS network operating in northern Chile for more than a decade. Nevertheless, the very inference of a LCZ off the coast of Iquique implies some degree of accommodation of plate convergence by aseismic slip, which might operate by repeated SSEs. We postulate that until now, either the magnitude of these SSEs was too small, or they occurred too far from the coast to be detected by GPS measurements. The only major change we detected in plate convergence in the area before 2014 was a long-term velocity change at the cGPS station operating in Iquique since 1995 (UAPE): its eastward velocity decreased after 2005 by ~20%, from 19.5 to 15.2 mm/year (fig. S9). This suggests that interseismic loading has been decreasing in the Iquique area during the past decade, probably reflecting a very SSE occurring on the decadal scale. This change could have been triggered by the deep intraslab 2005 M_w 7.7 Tarapacá earthquake that generated little postseismic relaxation (fig. S9).

Together with the fact that the M_w 8.1 mainshock and M_w 7.6 aftershock ruptures did not penetrate into the LCZ, the foreshock sequence and slow slip preceding the M_w 8.1 event argue for a creeping Iquique LCZ. Because SSEs are often associated with seismic swarms (*18*), we propose that the seismicity observed in northern Chile since 2008 was triggered by a SSE, developing for several years and accelerating during the final foreshock sequence as in the preslip model of nucleation (*19*). As suggested by many laboratory experiments (*20*), the SSE might have occurred in the nucleation zone of the impending megathrust rupture (Fig. 4). This precursory sequence included several shallow crustal events that took place near the 16 March foreshock; these events may be associated with the activation of a listric fault in the outermost fore-arc. This area is poorly known due to the lack of marine seismic profiles, but it may be similar to the eroded wedge enhanced by fracturing imaged at 22°S (*21*).

Several other subduction earthquakes were preceded by precursory seismic activity (*12*); in particular, the 1985 Valparaiso M_w 8.0 (*22*) and 2010 Maule M_w 8.8 (*23*) Chilean events and the

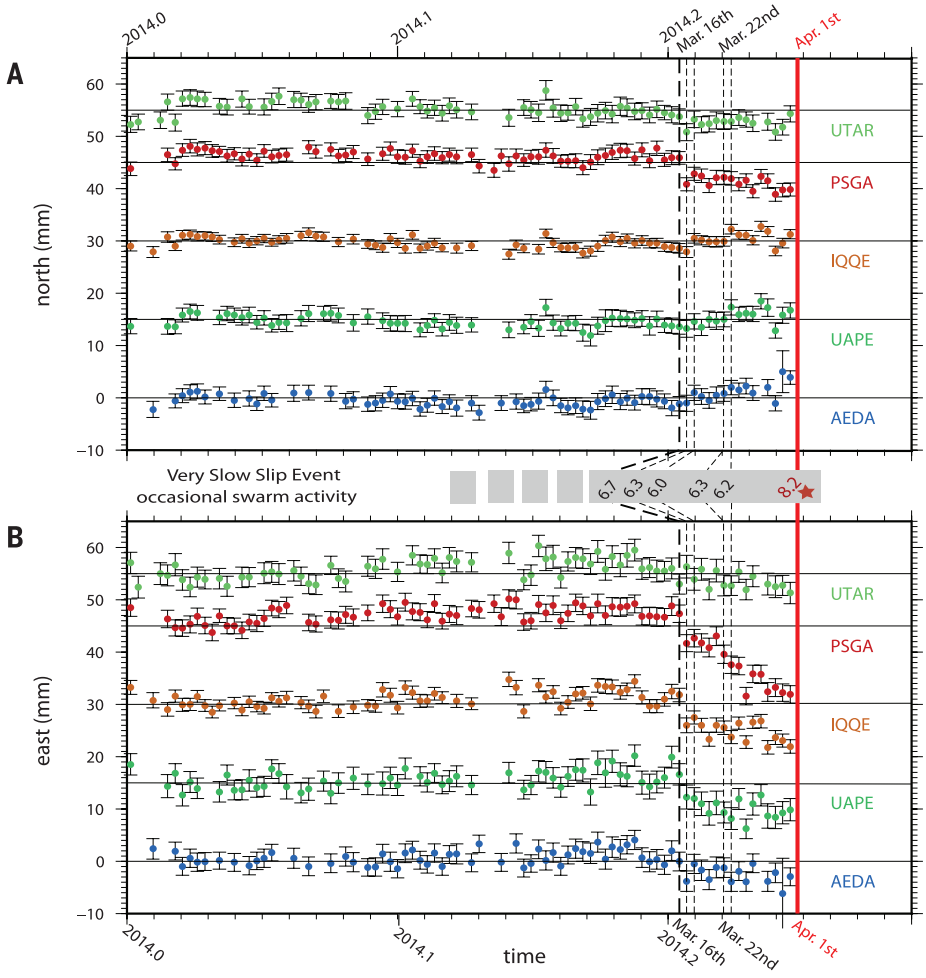

Fig. 3. Motion of coastal GPS stations preceding the Iquique earthquake. (**A**) North and (**B**) east components relative to a linear evolution model with seasonal variations estimated since 2012 (*14*). The thick red line denotes the origin time of the mainshock, whereas the black dotted lines show the occurrence times of the M_w > 6 foreshocks. Error bars indicate 1σ formal uncertainty.

2011 Tohoku-Oki earthquake (*24*). However, the size and duration of the precursory events of the 1 April mainshock are distinct. The occurrence of a SSE before the 2011 M_w 9.0 Tohoku-Oki earthquake and possibly the 2001 M_w 8.4 Arequipa earthquake (*24*, *25*) implies that SSE may be a common precursory feature and a potential triggering mechanism for large megathrust ruptures.

On the other hand, whether the shallowest part of the Camarones segment is still coupled and capable of producing a large earthquake or creeping aseismically is beyond the current resolution of the GPS network. The large aftershock of 3 April left the highly coupled Loa segment south of Iquique largely untouched. Several earthquakes of equivalent or larger magnitude may still rupture the deep intermediate-coupling areas of this segment.

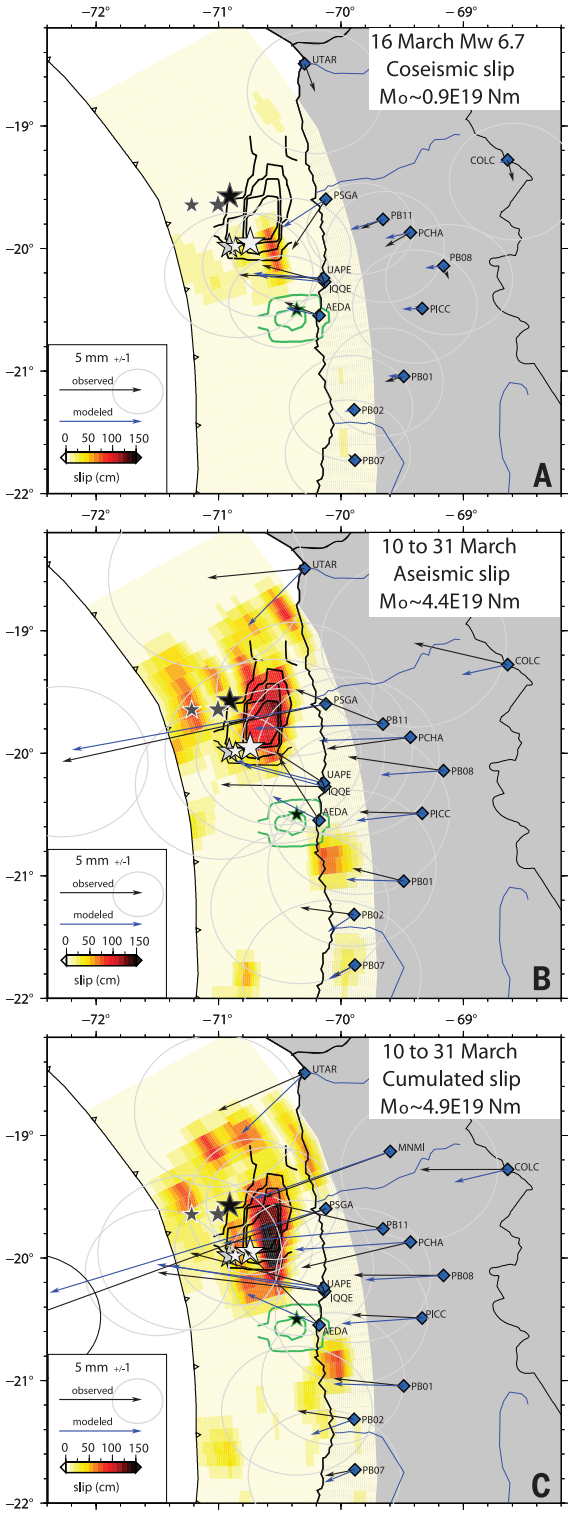

Fig. 4. Slip distribution preceding the Iquique earthquake. The slip distributions were inverted using Okada's equations for an elastic half-space from the surface displacements observed during the preseismic phase (*14*) (Fig. 3). (**A**) Coseismic slip due to the 16 March M_w 6.7 earthquake. (**B**) Aseismic slip for the period ranging from 10 to 31 March 2014. (**C**) Cumulative slip model for displacements observed from 10 to 31 March 2014. Black and green contours are the slip distributions for the mainshock and the main aftershock, respectively, already presented in Fig. 2. Mo, seismic moment.

REFERENCES AND NOTES

1. F. Montessus de Ballore, *Historia Sísmica de los Andes Meridionales* (Editorial Cervantes, Santiago, 1916).
2. E. Kausel, *Bol. Acad. Chil. Ciencias* **3**, 8–12 (1986).
3. C. Lomnitz, *Geofis. Panamericana* **1**, 151–178 (1971).
4. D. Comte, M. Pardo, *Nat. Hazards* **4**, 23–44 (1991).
5. M. Metois *et al*., *Geophys. J. Int.* **194**, 1283–1294 (2013).
6. M. Malgrange, R. Madariaga, *Geophys. J. R. Astron. Soc.* **73**, 489–505 (1983).
7. S. Peyrat *et al*., *Geophys. J. Int.* **182**, 1411–1430 (2010).
8. A. Fuenzalida, B. Schurr, M. Lancieri, M. Sobiesiak, R. Madariaga, *Geophys. J. Int.* **194**, 1216–1238 (2013).
9. E. R. Engdahl, A. Villaseñor, in *International Handbook of Earthquake and Engineering Seismology* (Academic Press, San Diego, 2002), part A, chap. 41.
10. M. Chlieh *et al*., *J. Geophys. Res.* **116**, B12405 (2011).
11. M. Béjar-Pizarro *et al*., *Nat. Geosci.* **6**, 462–467 (2013).
12. Th. Lay, H. Yue, E. Brodsky, C. An, *Geophys. Res. Lett.* **41**, 3818–3825 (2014).
13. Y. Yagi *et al*., *Geophys. Res. Lett.* **41**, 4201–4206 (2014).
14. Materials and methods are available as supplementary materials on *Science* Online.
15. M. E. Pasyanos, D. S. Dreger, B. Romanowicz, *Bull. Seismol. Soc. Am.* **86**, 1255–1269 (1996).
16. G. Hayes, D. J. Wald, R. L. Johnson, *J. Geophys. Res.* **117**, B01302 (2012).
17. M. Kikuchi, H. Kanamori, *Bull. Seismol. Soc. Am.* **81**, 2335–2350 (1991).
18. S. Ozawa, H. Suito, M. Tobita, *Earth Planets Space* **59**, 1241–1245 (2007).
19. W. L. Ellsworth, G. C. Beroza, *Science* **268**, 851–855 (1995).
20. S. Latour, A. Schubnel, S. Nielsen, R. Madariaga, S. Vinciguerra, *Geophys. Res. Lett.* **40**, 5064–5069 (2013).
21. E. Contreras-Reyes, J. Jara, I. Grevemayer, S. Ruiz, D. Carrizo, *Nat. Geosci.* **5**, 342–345 (2012).
22. D. Comte *et al*., *Science* **233**, 449–453 (1986).
23. R. Madariaga, M. Métois, C. Vigny, J. Campos, *Science* **328**, 181–182 (2010).
24. A. Kato *et al*., *Science* **335**, 705–708 (2012).
25. J. C. Ruegg, M. Olcay, D. Lazo, *Seismol. Res. Lett.* **72**, 673–678 (2001).

ACKNOWLEDGMENTS

We thank J. C. Ruegg for his initiative to study northern Chile with GPS, followed by J. B. De Chabalier, A. Socquet, D. Carrizo, and others after him. S.R., J.R., R.M., and J.C. acknowledge the support of the Chilean National Science Foundation project FONDECYT no.1130636 and S.R. of project FONDECYT no.11130230. This work received partial support from ANR-2011-BS56-017 and ANR-2012-BS06-004 of the French Agence Nationale de la Recherche. This is Institut de Physique du Globe de Paris contribution no. 3551. We thank Incorporated Research Institutions for Seismology Data Management Center (www.iris.edu/data/), International Plate Boundary Observatory Chile (http://geofon.gfz-potsdam.de/waveform/), Centro Sismológico Nacional (www.sismologia.cl), and International Associated Laboratory Montessus de Ballore for making raw data available to us.

SUPPLEMENTARY MATERIALS

www.sciencemag.org/content/345/6201/1165/suppl/DC1
Materials and Methods
Figs. S1 to S13
Tables S1 and S2
References (*26*–*32*)

14 May 2014; accepted 15 July 2014
Published online 24 July 2014;
10.1126/science.1256074

METALLOPROTEINS

A complex iron-calcium cofactor catalyzing phosphotransfer chemistry

Shee Chien Yong,[1]* Pietro Roversi,[2]*† James Lillington,[2]‡ Fernanda Rodriguez,[1] Martin Krehenbrink,[1]§ Oliver B. Zeldin,[1]|| Elspeth F. Garman,[1] Susan M. Lea,[2]¶ Ben C. Berks[1]¶

Alkaline phosphatases play a crucial role in phosphate acquisition by microorganisms. To expand our understanding of catalysis by this class of enzymes, we have determined the structure of the widely occurring microbial alkaline phosphatase PhoX. The enzyme contains a complex active-site cofactor comprising two antiferromagnetically coupled ferric iron ions (Fe^{3+}), three calcium ions (Ca^{2+}), and an oxo group bridging three of the metal ions. Notably, the main part of the cofactor resembles synthetic oxide-centered triangular metal complexes. Structures of PhoX-ligand complexes reveal how the active-site metal ions bind substrate and implicate the cofactor oxo group in the catalytic mechanism. The presence of iron in PhoX raises the possibility that iron bioavailability limits microbial phosphate acquisition.

Phosphate-containing macromolecules and metabolites are essential components of living cells. Under conditions of phosphate deficiency, microorganisms obtain phosphate from biologically derived organic compounds by producing extracytoplasmic alkaline phosphatases (*1*, *2*). Prominent among these enzymes are phosphate monoesterases of the PhoA and PhoX families, which are found in all three domains of life. The archetypal PhoA enzyme of *Escherichia coli* has been extensively studied (*2*), but PhoX alkaline phosphatases are minimally characterized and do not exhibit sequence similarity to other phosphotransfer enzymes. Genes encoding PhoX are abundant in ocean bacteria (*3*–*5*) and are also present in bloom-forming cyanobacteria (*6*), human pathogens (*7*, *8*), and eukaryotic green algae, including the model organism *Chlamydomonas reinhardtii* (*9*).

To establish the active-site architecture of PhoX, we have undertaken structural analysis of the enzyme from *Pseudomonas fluorescens* Pf0-1 (*10*). Recombinant *P. fluorescens* PhoX is a phosphomonoesterase with no phosphodiesterase activity and is able to cleave phosphorus-nitrogen bonds but not phosphorus-carbon bonds (fig. S1A). The purified PhoX protein is purple in color with several broad absorbance bands in the visible spectrum, indicating the presence of a prosthetic group (Fig. 1A). Addition of adenosine-5′-(β,γ-methylene)triphosphate (AMP-PCP), a nonhydrolyzable analog of the substrate ATP, causes changes in the visible spectrum (Fig. 1A), showing that the prosthetic group is associated with the substrate-binding site. We determined crystal structures for native PhoX and for PhoX in complex with AMP-PCP, phosphate, and the putative transition-state mimic vanadate. All four structures were determined to high resolution (1.1 to 1.5 Å) from crystals grown at the catalytic pH optimum of 8 (figs. S1B, S2A, and S3, and tables S1 and S2).

PhoX folds as a six-bladed β propeller (Fig. 2A). The active site of the enzyme lies at the bottom of the cavity at the center of the propeller and is accessible from only one face of the propeller through a channel (Fig. 2B). The active site in the native PhoX structure contains four metal ions, and a further metal ion is present in the structures of the three PhoX-ligand complexes. Proton-induced x-ray emission spectroscopy of a sample of the PhoX-phosphate complex detected 3.4 ± 0.3 atoms of calcium and 1.6 ± 0.1 atoms of iron per complex, with no other candidate elements (Co, Ni, Zn, Mg, and Mn) detectable. Individual metal ion sites in the PhoX structures were assigned as three Ca and two Fe ions on the basis of their coordination geometry and anomalous scattering at different wavelengths (fig. S2, B and C). All metal sites are fully occupied, and the B factors are similar for the Ca and Fe ions. The ions Fe_A, Fe_B, and Ca_A form a triangle at the bottom of the active-site cavity (Figs. 2 and 3). Ions Ca_B and (in the ligand complexes only) Ca_C lie above the plane of the first three ions and to one side of the cavity, with the plane containing the three Ca ions being almost perpendicular to that of the $Fe_AFe_BCa_A$ triangle. All five metal ions are coordinated by oxygen atoms provided either by the side chains of conserved residues, by water, or by the ligand molecules (Fig. 2C and figs. S3 and S4, A, D, and E, and table S3). Fe_A is additionally ligated by a thiolate side chain from invariant Cys^{179}. Substitution of individual amino acids coordinating Fe_A, Fe_B, Ca_B, or Ca_C resulted in PhoX variants with either no, or trace, catalytic activity (table S4).

Electron paramagnetic resonance (EPR) spectroscopy was used to determine the oxidation state of the PhoX iron atoms (Fig. 1B). The native PhoX protein was EPR-silent. However, partial reduction of the protein with dithionite led to the appearance of an EPR signal at an effective *g* value of 4.3 characteristic of monomeric

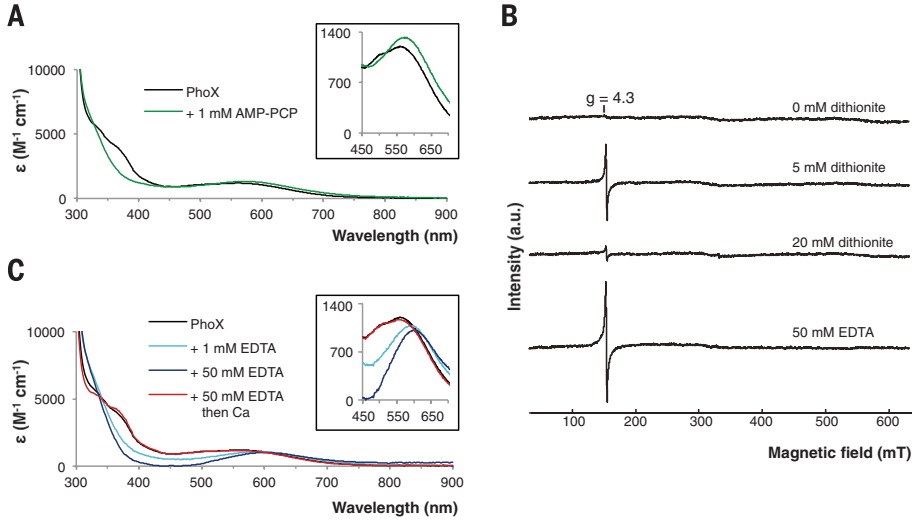

Fig. 1. Spectroscopic analysis of *P. fluorescens* PhoX. (**A**) Changes in the visible spectrum of PhoX (black line) upon addition of 1 mM AMP-PCP (green line). (**B**) EPR spectra of PhoX. The sample was progressively reduced with sodium dithionite as indicated. Alternatively, the sample was treated with Na_2EDTA. (**C**) Changes in the visible spectrum of PhoX (black line) upon addition of 1 mM (light blue line) or 50 mM (dark blue line) Na_2EDTA. The 50 mM Na_2EDTA sample was subsequently buffer-exchanged to remove the EDTA and then supplemented with 100 mM $CaCl_2$ (red line).

[1]Department of Biochemistry, University of Oxford, South Parks Road, Oxford OX1 3QU, UK. [2]Sir William Dunn School of Pathology, University of Oxford, South Parks Road, Oxford OX1 3RE, UK.
*These authors contributed equally to this work. †Present address: Department of Biochemistry, University of Oxford, South Parks Road, Oxford OX1 3QU, UK. ‡Present address: Department of Biological Sciences, Birkbeck College, Malet Street, London WC1E 7HX, UK. §Present address: Cysal GmbH, Mendelstrasse 11, 48149 Münster, Germany. §Present address: Cysal GmbH, Mendelstrasse 11, 48149 Münster, Germany. ||Present address: Stanford University, School of Medicine, James H. Clark Center, 318 Campus Drive, Stanford, CA 94305–5432, USA. ¶Corresponding author. E-mail: ben.berks@bioch.ox.ac.uk (B.C.B.); susan.lea@path.ox.ac.uk (S.M.L.)

high-spin Fe^{3+}. This behavior suggests that PhoX contains a pair of high-spin Fe^{3+} ions rendered EPR-silent by magnetic coupling, with reduction of one of the Fe^{3+} ions to the EPR-silent Fe^{2+} state revealing the EPR signal from the remaining Fe^{3+} ion. Because the two ions in the resulting mixed valence state no longer interact magnetically, it can be inferred that the Fe^{2+} ion has been released from the active-site cofactor. Thus, only the fully oxidized Fe^{3+}-Fe^{3+} state of the PhoX cofactor is catalytically viable. Further addition of sodium dithionite led to reduction of the remaining Fe^{3+} ion, rendering PhoX EPR silent again.

Within the $Fe_AFe_BCa_A$ triangle lies an atom that is within bonding distance of all three metal ions (Fig. 2C and table S3). The close to in-plane geometry suggests that this atom is an oxide ion (O^{2-}). This is confirmed by the structural identity between this part of the PhoX active site and $Fe_2CaO(CCl_3COO)_6(THF)_4$, an inorganic complex containing a μ_3-oxo-bridged $Fe^{3+}Fe^{3+}Ca^{2+}$ cluster with O-donor coordination (*11*)(fig. S5). The presence of a bridging oxo group explains the strong antiferromagnetic coupling of the two Fe^{3+} ions observed by EPR spectroscopy (Fig. 1B). The intense visible absorption bands of PhoX (Fig. 1A) are, likewise, characteristic of an oxo-bridged dinuclear Fe^{3+} unit (*12*), although Cys^{179} thiolate-to-Fe_A^{3+} ligand-to-metal charge transfer bands are also expected to contribute to the visible spectrum (*13*). The purple color of PhoX is, thus, distinct in origin from that of the well-known purple acid phosphatases in which the visible absorption is due to a tyrosinate-to-Fe^{3+} charge transfer (*14*).

PhoX had previously been considered to be an exclusively Ca-dependent enzyme based on the results of metal ion reconstitution experiments [e.g., (*7*, *8*, *15*)], although a biosynthetic requirement for Fe in *P. fluorescens* PhoX biosynthesis had been reported (*16*). In agreement with these earlier reconstitution studies, we found that the enzymatic activity of *P. fluorescens* PhoX was abolished by the metal ion chelator EDTA and that activity could be restored by the addition of Ca^{2+} ions alone (fig. S1C). However, EDTA treatment perturbed, rather than abolished, the visible transitions arising from the Fe_A-Fe_B pair, indicating that the Fe^{3+} ions remain bound to PhoX in the presence of EDTA (Fig. 1C). This conclusion was confirmed by EPR spectroscopy, which showed that only a small proportion (12% by spin quantitation) of the Fe bound to PhoX is extracted by 50-mM EDTA (Fig. 1B). Addition of Ca^{2+} ions to EDTA-treated enzyme restored the visible spectrum (Fig. 1C).

The PhoX-ligand complex structures show that the active-site metal ions form a scaffold that binds the terminal phosphoryl group of the substrate molecule. In the phosphate and vanadate complexes, all five metal ions have bonding interactions with the three terminal oxygen atoms of the ligand (Figs. 2C and 3C and fig. S4, B and C). In these structures, the ligand sits on the $Fe_AFe_BCa_A$ unit, with each terminal oxygen atom of the ligand placed above one of the three metal ions. In the AMP-PCP–bound structure, the phosphate group has a tilted orientation relative to the $Fe_AFe_BCa_A$ plane, and there is no interaction with Ca_A (Fig. 3B). This binding mode permits both the terminal and β-phosphate groups of AMP-PCP to make bonding interactions with Ca_A and Ca_B (Fig. 3B). Modeling studies (not shown) suggest that even for substrates without multiple phosphate groups, an initial tilted binding mode will usually be favored in order to avoid steric clashes with Ca_A and Ca_B. The sole conformational change in the protein that takes place on ligand binding to PhoX is movement of the guanidinium head group of conserved Arg^{385} to form a bonding interaction with one of the terminal oxygen atoms of the ligand (Fig. 2C). Replacing this arginine residue with alanine impairs PhoX activity, suggesting that Arg^{385} contributes to catalysis (table S4).

The primary mechanism of rate enhancement by phosphoryl transfer enzymes is thought to be provision of favorable geometric and electrostatic interactions with the transition state (*1*, *2*).

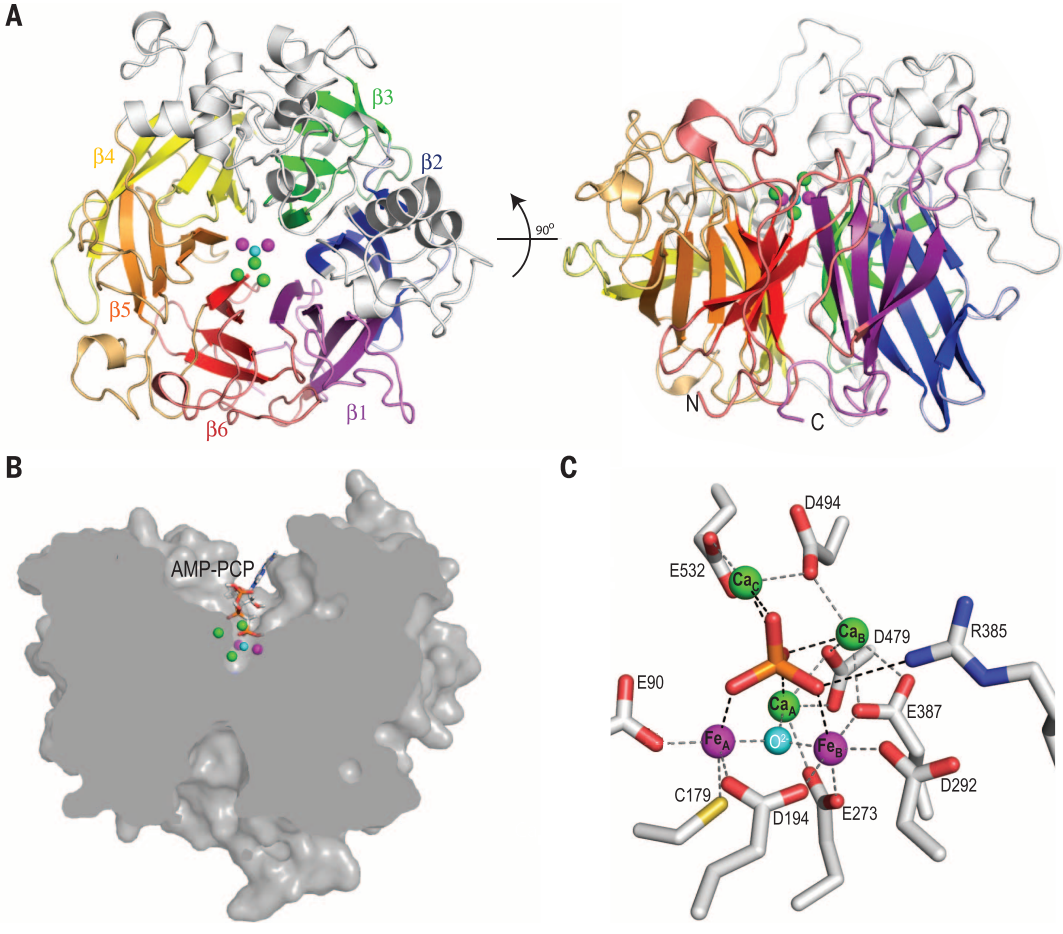

Fig. 2. Structure of *P. fluorescens* PhoX. (**A**) Cartoon representation of *P. fluorescens* PhoX viewed from above the active site (left) or from the side (right). The blades of the β propeller are shown in different colors and two α subdomains are colored gray. The active-site ions are represented by green (Ca^{2+}), magenta (Fe^{3+}), and cyan (O^{2-}) spheres. (**B**) Clipped surface representation of PhoX with AMP-PCP bound. (**C**) The PhoX active site containing bound phosphate. Interatomic separations that are within bonding distance are shown between the metal ions and protein side chains (gray dashed lines) and between the phosphate ion and coordinating groups (black dashed lines). These distances are tabulated in table S3.

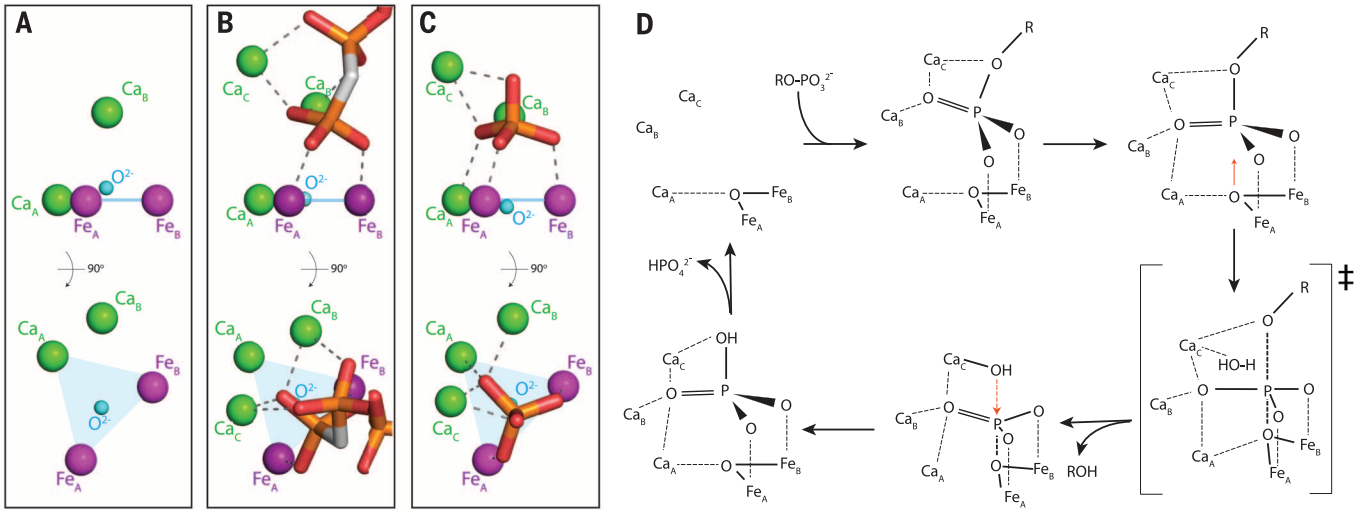

Fig. 3. Ligand binding to the PhoX active-site metals and proposed catalytic cycle. (**A** to **C**) The active-site metal ions and exogenous ligands are viewed from the side (top) and from the direction of substrate access (bottom). Atom representation is as in Fig. 2. Dashed lines indicate ion coordination bonds. The plane of the Fe_A-Fe_B-Ca_A ions is shown in blue. Water molecules are omitted for clarity but can be seen in fig. S4, A and D. (A) The native enzyme. Ca_C is not present in this structure. (B) The complex with the nonhydrolyzable substrate analog AMP-PCP. (C) The phosphate complex. (**D**) Possible model for the mechanism of PhoX. The substrate phosphoryl group initially binds in a tilted orientation (by analogy to the AMP-PCP binding mode), then packs down on to the active site by analogy to the binding mode of phosphate and vanadate. The observed phosphate complex would correspond to the final product complex in this model.

PhoX provides high-valency metal ions that are appropriately positioned to interact with all three terminal oxygen atoms of the phosphoryl group, and in the vanadate complex the ligand is appreciably distorted toward the presumed transition-state geometry (fig. S4C). Leaving group activation through coordination of the oxygen atom of the labile bond by Ca_C may also contribute to catalysis (Fig. 3, C and D, and fig. S4B) (*2*).

Enzymatic phosphoryl transfer reactions involve in-line displacement of the leaving group by a nucleophile (*2*). Examination of the PhoX-ligand structures shows that the metal-bridging oxide ion is the only plausible candidate nucleophile (Fig. 3, B and C, and fig. S4, B and C). In the phosphate and vanadate complexes, the oxide ion is positioned below the phosphorus atom and is directly in line with the scissile bond. The oxide ion also blocks access of other potential nucelophiles to the phosphorus atom (in all three PhoX-ligand complexes, the calculated water-accessible surface area of the phosphorus atom trans to the leaving group is 0.0 $Å^2$). There is small-molecule precedent for the hydrolysis of phosphate esters by an oxide ion bridging two Co^{3+} ions (*17*), and a metal-bridging oxide nucleophile has also been inferred to be present in one purple acid phosphatase (*18*). Oxide movement toward the phosphoryl P atom during catalysis would be facilitated by the weak Ca_A-oxide interaction and would be consistent with the observed movement of the oxide relative to the $Fe_AFe_BCa_A$ plane in response to ligand binding at the active site (+0.4/−0.2 Å) (Fig. 3, A to C, and fig. S4B). Due to the difficulty in abstracting a μ-bridging oxygen atom from between two Fe^{3+} ions, it is likely that the initial reaction product is resolved by a second in-line nucleophilic attack by a water molecule from the opposite side of the phosphorus atom (Fig. 3D). This water molecule would plausibly be activated by binding to Ca_C because this ion already interacts at the equivalent position with the oxygen atom of the substrate scissile bond (Fig. 3, C and D, and fig. S4B). Nevertheless, we cannot exclude the possibility that the active-site environment labilizes the μ-bridging oxygen atom to allow release of the initial product.

Our structural analysis suggests that PhoX has an almost exclusively inorganic mechanism in which the protein serves as a matrix for the catalytic metal ions. Distinctive features of the PhoX active site include a cofactor that combines Fe and Ca ions, Cys coordination to a Fe^{3+} ion that lacks a redox function, and the use of more than three metal ions to interact with a single phosphoryl group. It is also notable that the $Fe_AFe_BCa_AO$ fragment of the cofactor resembles extensively studied synthetic oxide–centered triangular metal complexes (*19*). Carboxylate-bridged Fe^{3+} pairs are used in other enzymes to catalyze redox reactions with oxygen (*12*) but in PhoX perform a nonredox role in which the high charge of the iron atoms is exploited to polarize the substrate. Like PhoX, some purple acid phosphatases use a di-iron center to carry out phosphoryl transfer reactions (*20*). However, in contrast to PhoX, the enzymatically active oxidation state of the iron pair is Fe^{3+}-Fe^{2+} (*21*), and the catalytic nucleophile is probably a metal-bridging hydroxide ion (*20*).

Genes coding for PhoX and PhoA are not normally found in the same bacterium (*4*), suggesting that these two types of alkaline phosphatase have equivalent physiological roles. PhoA activity depends on Zn^{2+} ions, which are present at low abundance in many environments (*22*), and this has led to the hypothesis that organisms expressing PhoX have an advantage in P and Zn colimited environments (*15*). However, our observation that PhoX requires Fe^{3+} ions as cofactors implies that PhoX activity will also be metal-limited by the low bioavailability of Fe in many environments (*23*). This hypothesis challenges the assumption that P and Fe have biochemically independent effects in colimiting conditions (*24*) and raises the possibility that combined Zn-Fe-P colimitation may occur in some environments through the requirement for either Zn or Fe for phosphate acquisition from organic phosphates. An environment where such considerations may apply is the western North Atlantic, where inorganic P and Zn concentrations are very low and Fe can also be in short supply (*22*, *25*, *26*).

REFERENCES AND NOTES

1. S. C. Kamerlin, P. K. Sharma, R. B. Prasad, A. Warshel, *Q. Rev. Biophys.* **46**, 1–132 (2013).
2. J. K. Lassila, J. G. Zalatan, D. Herschlag, *Annu. Rev. Biochem.* **80**, 669–702 (2011).
3. H. Luo, R. Benner, R. A. Long, J. Hu, *Proc. Natl. Acad. Sci. U.S.A.* **106**, 21219–21223 (2009).
4. M. Sebastian, J. W. Ammerman, *ISME J.* **3**, 563–572 (2009).
5. E. D. Orchard, E. A. Webb, S. T. Dyhrman, *Environ. Microbiol.* **11**, 2400–2411 (2009).
6. M. J. Harke, D. L. Berry, J. W. Ammerman, C. J. Gobler, *Microb. Ecol.* **63**, 188–198 (2012).
7. A. van Mourik, N. M. Bleumink-Pluym, L. van Dijk, J. P. van Putten, M. M. Wösten, *Microbiology* **154**, 584–592 (2008).
8. N. K. Roy, R. K. Ghosh, J. Das, *J. Bacteriol.* **150**, 1033–1039 (1982).
9. J. L. Moseley, C. W. Chang, A. R. Grossman, *Eukaryot. Cell* **5**, 26–44 (2006).
10. Materials and methods are available as supplementary materials on *Science* Online.
11. D. Prodius *et al.*, *Polyhedron* **25**, 2175–2182 (2006).

12. E. I. Solomon *et al*., *Chem. Rev.* **100**, 235–350 (2000).
13. V. S. Oganesyan, A. J. Thomson, *J. Chem. Phys.* **113**, 5003–5017 (2000).
14. B. P. Gaber, J. P. Sheridan, F. W. Bazer, R. M. Roberts, *J. Biol. Chem.* **254**, 8340–8342 (1979).
15. S. Kathuria, A. C. Martiny, *Environ. Microbiol.* **13**, 74–83 (2011).
16. R. D. Monds, P. D. Newell, J. A. Schwartzman, G. A. O'Toole, *Appl. Environ. Microbiol.* **72**, 1910–1924 (2006).
17. N. H. Williams, A. M. Lebuis, J. Chin, *J. Am. Chem. Soc.* **121**, 3341–3348 (1999).
18. G. Schenk *et al*., *Proc. Natl. Acad. Sci. U.S.A.* **102**, 273–278 (2005).
19. R. D. Cannon, R. P. White, *Prog. Inorg. Chem.* **36**, 195–298 (1988).
20. N. Mitić *et al*., *Chem. Rev.* **106**, 3338–3363 (2006).
21. D. L. Wang, R. C. Holz, S. S. David, L. Que Jr., M. T. Stankovich, *Biochemistry* **30**, 8187–8194 (1991).
22. R. W. Jakuba, J. W. Moffett, S. T. Dyhrman, *Global Biogeochem. Cycles* **22**, GB4012 (2008).
23. C. M. Moore *et al*., *Nat. Geosci.* **6**, 701–710 (2013).
24. M. A. Saito, T. J. Goepfert, J. T. Ritt, *Limnol. Oceanogr.* **53**, 276–290 (2008).
25. J. Wu, W. Sunda, E. A. Boyle, D. M. Karl, *Science* **289**, 759–762 (2000).
26. C. M. Moore *et al*., *Glob. Change Biol.* **12**, 626–634 (2006).

ACKNOWLEDGMENTS

We thank G. O'Toole for providing *P. fluorescens* Pf0-1 genomic DNA; J. Marcoux, B. Pilgrim, and A. Parkin for exploratory experiments; and F. Armstrong, T. Browning, J. McGrady, G. Henderson, D. Herschlag, C. Schofield, A. Thomson, C. Timmel, N. Williams, and R. Williams for valuable discussions. This work was funded by the University of Oxford, Pembroke College Oxford, Oxford Martin School Vaccine Design Institute, the Engineering and Physical Sciences Research Council, the Biotechnology and Biological Sciences Research Council (grant F02150X), and the European Molecular Biology Organization. Structure coordinates and x-ray data have been deposited in the Protein Data Bank with accession codes 4a9v, 4amf, 4alf, and 3zwu.

SUPPLEMENTARY MATERIALS

www.sciencemag.org/content/345/6201/1170/suppl/DC1
Materials and Methods
Figs. S1 to S5
Tables S1 to S4
References (*27*–*44*)

1 April 2014; accepted 7 July 2014
10.1126/science.1254237

MARINE MICROBES

Multiple nutrient stresses at intersecting Pacific Ocean biomes detected by protein biomarkers

Mak A. Saito,[1]* Matthew R. McIlvin,[1] Dawn M. Moran,[1] Tyler J. Goepfert,[1] Giacomo R. DiTullio,[2] Anton F. Post,[3] Carl H. Lamborg[1]

Marine primary productivity is strongly influenced by the scarcity of required nutrients, yet our understanding of these nutrient limitations is informed by experimental observations with sparse geographical coverage and methodological limitations. We developed a quantitative proteomic method to directly assess nutrient stress in high-light ecotypes of the abundant cyanobacterium *Prochlorococcus* across a meridional transect in the central Pacific Ocean. Multiple peptide biomarkers detected widespread and overlapping regions of nutritional stress for nitrogen and phosphorus in the North Pacific Subtropical Gyre and iron in the equatorial Pacific. Quantitative protein analyses demonstrated simultaneous stress for these nutrients at biome interfaces. This application of proteomic biomarkers to diagnose ocean metabolism demonstrated *Prochlorococcus* actively and simultaneously deploying multiple biochemical strategies for low-nutrient conditions in the oceans.

Marine photosynthetic activity in the oceans is largely controlled by nutrient and micronutrient availability. Although this process is critical to marine ecosystem structure, ocean-climate interactions, and nutrient cycling processes, the nutrient-addition incubation experiments typically used to assess which nutrients are limiting are time-intensive and subject to artifacts (*1*), making their deployment to broad geographic regions difficult. Nutrient limitation is commonly parameterized in marine ecosystem and biogeochemistry models so that growth is controlled by the single scarcest nutrient (relative to cellular requirements) (*2*); however, multiple scarce nutrients may also influence phytoplankton community structure (*3*, *4*). Molecular methodologies have shown potential for detecting in situ biomarkers for nutrient stress by measurement of up-regulated transcripts or proteins associated with nutrient scarcity (*5*, *6*), but they can have relatively broad biological specificity and can be difficult to deploy to a wide geographic region (*5*). With advances in mass spectrometry, microbial proteins have begun to be directly measured in complex natural environments; recent metaproteomic surveys of oceanic environments have identified and examined the relative abundance of biogeochemically relevant proteins (*7*, *8*).

In this study, we conducted calibrated quantitative mass spectrometry–based protein biomarker measurements using multiple reaction monitoring (MRM) to characterize nutrient limitation patterns for multiple nutrients on the abundant marine cyanobacterium *Prochlorococcus* (*9*). Samples were collected along a ~4500-km meridional transect through the central Pacific and equatorial Pacific Ocean initiating south of the Hawaiian Islands and ending near the Samoan Islands in October of 2011 (Fig. 1A). The equatorial Pacific is an ideal region to examine the range of nutrient stresses affecting phytoplankton because it crosses several biogeochemical biomes (*10*). Equatorial upwelling caused by Ekman divergence supplies cold, nitrogen-, and phosphorus-rich waters (Fig. 1B and fig. S1) (*11*), resulting in iron limitation of phytoplankton communities (*1*). In contrast, the subtropical gyres to the north and south are highly depleted in multiple nutrients (N, P, and micronutrients; Fig. 1B and fig. S1). The scarcity of multiple nutrients has made it difficult to experimentally determine a single primary limiting nutrient of primary productivity in oligotrophic regions (*3*), and as an alternative, marine ecosystem models have been used to predict iron and nitrogen limitation of the equatorial and subtropical gyre regions of the Pacific, respectively, with a sharp transition between them (*2*, *12*). *Prochlorococcus*, an oxygenic photoautotrophic cyanobacterium, is a major contributor to marine photosynthesis in tropical and subtropical oceanic regions (*1*, *13*) and was observed throughout the transect by its unique divinyl chlorophyll a pigment, particularly in the equatorial upwelling region when total chlorophyll a was also highest (Fig. 1C and fig. S1).

Peptide biomarkers were selected from proteins of interest identified within global metaproteome analyses of the microbial samples taken from this transect. These metaproteome analyses used numerous cyanobacterial genomes and Pacific metagenomes to enable protein identification specific to this region (table S2). Targeted methods were designed using peptide-specific parent to fragment ion transitions (table S3), and synthesized isotope-labeled peptides served as internal standards using MRM on a triple quadrupole mass spectrometer (*14*). Several proteins had been shown in laboratory culture studies of marine cyanobacteria to have potential use as biomarkers of iron and nitrogen stress, including iron deficiency protein IdiA (*5*); flavodoxin, which replaces iron-requiring ferredoxin under iron stress (*15*, *16*); and the global nitrogen response regulator NtcA that serves as a transcriptional activator for alternate forms of nitrogen (such as urea) and is under negative control by ammonium (*17*, *18*). We also targeted the urea transporter of *Prochlorococcus* as an additional nitrogen stress biomarker based on its presence in the metaproteome.

[1]Marine Chemistry and Geochemistry Department, Woods Hole Oceanographic Institution, Woods Hole, MA 02543, USA. [2]College of Charleston, Charleston, SC, USA. [3]Marine Biological Laboratory, Woods Hole, MA 02543, USA.
*Corresponding author. E-mail: msaito@whoi.edu

One challenge in deploying targeted proteomics to the oceans is the reliance of the MRM technique on exact sequence matches, which, in a complex environmental community, can result in the measurement of a subset of a protein's functional sequence diversity (fig. S2). Yet, genomic analysis of cyanobacterial genomes demonstrated that peptides targeted for *Prochlorococcus* nitrogen and iron stress were specific not only

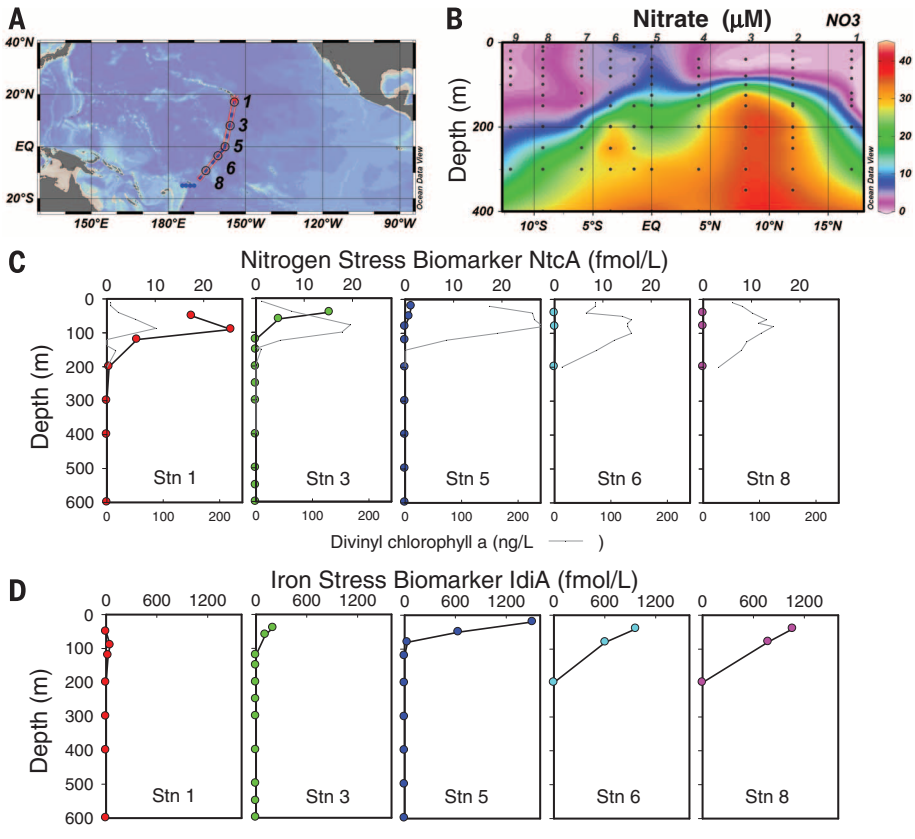

Fig. 1. Station locations, nitrate distributions, and vertical profiles of iron and nitrogen stress biomarkers. (**A**) Cruise track for the METZYME expedition in the central Pacific Ocean aboard the R/V *Kilo Moana* in October 2011 from Hawaii to Samoa (station coordinates in table S1). (**B**) Nitrate distributions along the transect (units of micromolar). Vertical profiles of (**C**) nitrogen and (**D**) iron stress biomarkers NtcA and IdiA, respectively, from the abundant marine cyanobacterium *Prochlorococcus marinus* as measured by targeted proteomics along the transect. With southward progression, a shift in nitrogen to iron stress was observed. Divinyl chlorophyll a distributions are also shown for comparison (in gray). Station 5 was located on the equator. Zero values below the photic zone, where *Prochlorococcus* is absent, demonstrate a lack of false positives.

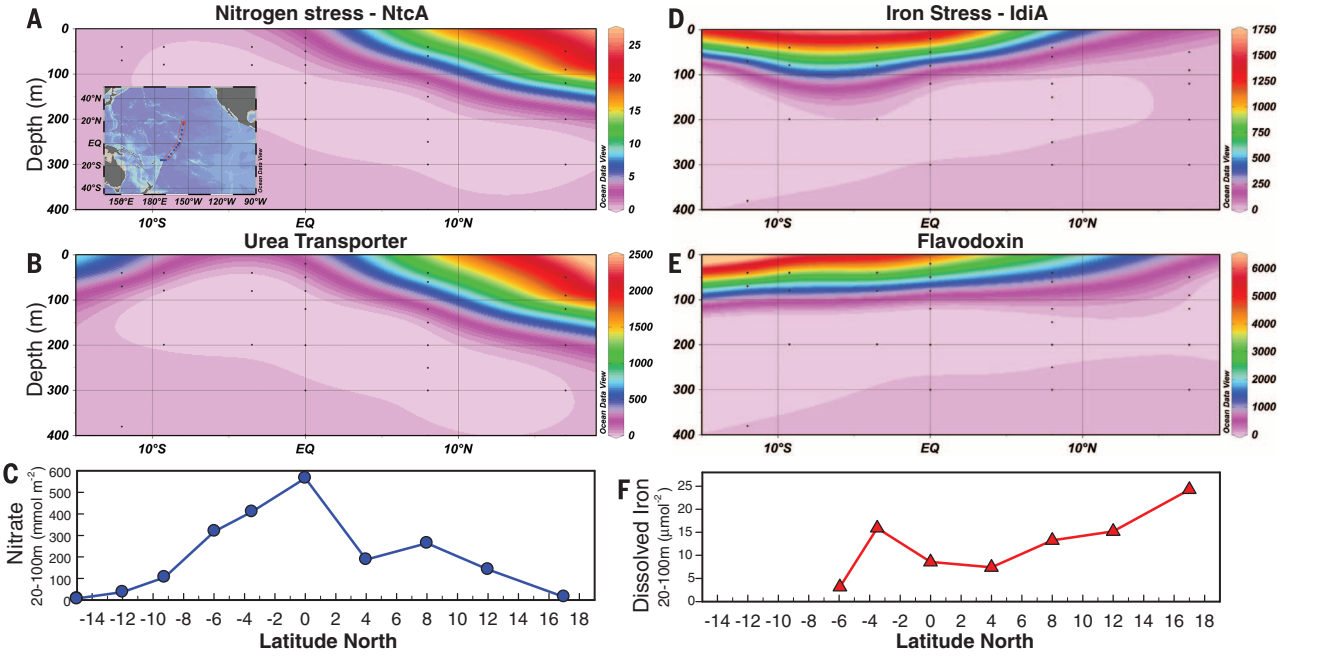

Fig. 2. Ocean sections of *Prochlorococcus* nitrogen and iron metabolic protein biomarkers. (**A** and **B**) NtcA and urea transporter for nitrogen stress in units of fmol/liter (inset: transect station map; peptide IDs 34 and 41 from tables S3 and S4), and (**D** and **E**) IdiA and flavodoxin for iron stress in units of fmol/liter (peptide IDs 27 and 31). (**C** and **F**) Depth-integrated nitrate and dissolved iron for the 20- to 100-m region. At stations 3 and 4, samples were not available at 20 m, so the 40-m values were used as a surface depleted estimate. When no 100-m sample was available, a value was extrapolated from adjacent depths (see table S3).

to the *Prochlorococcus* species, but also showed subspecies specificity to the two currently known high-light ecotypes of *Prochlorococcus* in the upper water column [table S4, the low-B/A I and low-B/A II clades (*19*)], with the exception of one of the two NtcA biomarkers that also targeted the related cyanobacterium *Synechococcus*. Hence, by selecting protein targets identified in metaproteomes that were generated with regional metagenomes and microbial genomes, we could target biomarkers that were representative and abundant for this region. Owing to this subspecies-level resolution, the data presented here are not normalized to *Prochlorococcus* population abundance, because defining and quantifying ecotypes can be challenging. Yet, the unnormalized protein concentration data are of biogeochemical value, as they can be directly related to ecological stoichiometry, nutrient uptake, and enzymatic activity.

The vertical profiles of these biomarker proteins identified a transition between regions of iron and nitrogen stress along the transect (Figs. 1 and 2). Biomarkers for IdiA and flavodoxin went from nondetectable to highly abundant upon entering the equatorial upwelling region as the integrated dissolved iron inventory (from 20 to 100 m) became depleted, from 24 μmol m^{-2} at station 1 to 3 μmol m^{-2} by station 7 (Fig. 2F). This decrease in integrated dissolved iron was observed despite a vertical structure that was more complex than that of nitrate owing to the regional hydrography and long-distance zonal transport of particulate iron (table S5) (*11*, *20*). In contrast, NtcA was abundant in the oligotrophic gyre region of the North Pacific, but became scarce in the equatorial Pacific as the integrated nitrate inventory (20 to 100 m) increased from 4 to 565 mmol m^{-2} (Fig. 2C). Nitrite and ammonia concentrations both increased at the equator and southward (fig. S6), consistent with NtcA distributions. Several criteria corroborate this method for diagnosing the nutritional status of environmental populations of *Prochlorococcus*. First, multiple independent protein biomarkers provided a consistent indication of nutritional stress (NtcA and urea transporter for nitrogen, and IdiA and flavodoxin for iron) and were oceanographically consistent with cyanobacterial proteins being nondetectable below the photic zone. Second, within two of these protein biomarkers, the urea transporter and flavodoxin, multiple peptides were targeted and yielded very similar geographical trends, with variations in abundance likely reflecting the diversity of protein sequence in the natural environment (table S2 and fig. S2). Third, inspection of individual fragmentation patterns (ms^2 spectra) from metaproteomic analyses showed consistent fragment patterns and a lack of interfering ions for the MRM analyses (figs. S3 and S4).

These protein biomarkers also provided insight into the forms of nitrogen used by *Prochlorococcus*. Although phytoplankton, including *Prochlorococcus*, are often considered to prefer ammonia as a source of nitrogen (*21*), nitrite (*21*), nitrate (*22*), urea (*8*, *22*, *23*), and cyanate (*24*) have also been observed to be available to *Prochlorococcus*. In this study, the *Prochlorococcus* urea transporter protein (UrtA) was among the most abundant proteins that we detected with concentrations of 1000 to 2500 fmol $liter^{-1}$ in the North Pacific Subtropical Gyre (NPSG), comparable to that of the iron transporter IdiA in the iron-limited regions to the south, implying that dissolved organic nitrogen was an important nutritional source for *Prochlorococcus*. Biomarkers for a subunit of the urease enzyme (UreC) and an ammonia transporter (Amt1) from high-light *Prochlorococcus* showed meridional distributions similar to that of NtcA and the urea transporter, but both were found at much lower abundances compared to the urea transporter (fig. S5 and tables S3 and S4). Low urease abundance is likely related to the enzyme's efficiency relative to the challenge of acquiring scarce urea. This urea utilization could be a useful chemical and ecological strategy for high-light *Prochlorococcus* in ammonia-limiting waters, allowing direct acquisition of this zooplankton waste product without the need for a heterotrophic microbial intermediary with urease capability. The low concentrations of ammonia and urea transporters on the equator (station 5, fig. S5) could reflect the use of the more abundant nitrate and nitrite (*25*) (nitrite was 1.8 to 7.5 times more abundant than ammonia, and nitrate was 17 times more abundant than nitrite in the upper 100 m; figs. S6 and S15). Alternatively, the abundant ammonia concentrations could have induced low ammonia transporter concentrations, or another ammonia transporter sequence was in use that was not being targeted in our study since the targeted peptide was only identified in one *Prochlorococcus* isolate genome (table S4).

Together these biomarker results reveal a gradation of adaptive responses between the NPSG and equatorial regions, with nitrogen and iron stress proteins co-occurring in the transition regions between biomes (Fig. 2). Comparing biomarker abundances with coherent and distinct ratios of NtcA:IdiA and UreA:IdiA peptide abundances at each station (Fig. 3, A and B, and table S6) showed the primary nutrient stress, consistent with previous incubation observations (*26*), yet also revealed co-stresses at biome transitions. Because the protein measurements were calibrated on an absolute scale, we calculated the cellular nitrogen being dedicated to both of these enhanced nitrogen and iron acquisition strategies for five *Prochlorococcus* proteins across this region

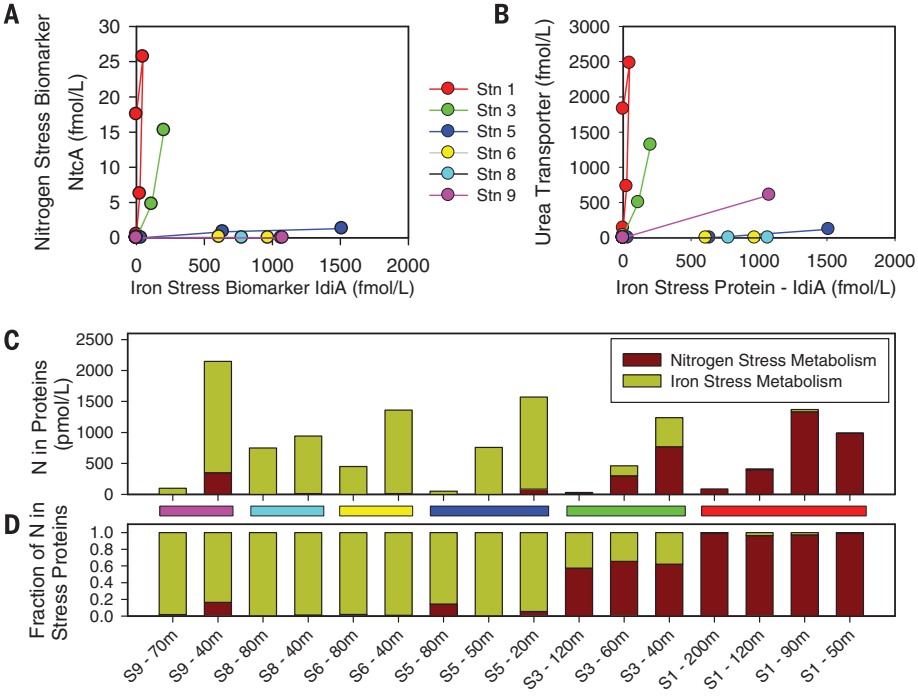

Fig. 3. Comparison of distributions of nitrogen and iron stress biomarkers across the transect. (**A**) Relationships between IdiA and NtcA biomarkers, with shallower depths tending to have increased protein abundances. (**B**) Comparison of distributions of urea transporter abundances and IdiA iron stress biomarker. The coherent ratios for these pairs of biomarkers was indicative of the unique combination of environmental stimuli tuning the protein expression of nutrient-scarcity responses (ratios of biomarkers presented in table S6). (**C**) The nitrogen content within each targeted protein was calculated and summed for selected nitrogen and iron metabolism proteins along the transect (NtcA, urea transporter, and glutamine synthetase for nitrogen metabolism and IdiA and flavodoxin for iron metabolism; peptide IDs 34, 41, 145, 27, 31) and (**D**) represented as a fraction of the total nitrogen for these five proteins. Color bars between (C) and (D) correspond to station symbols in (A) and (B).

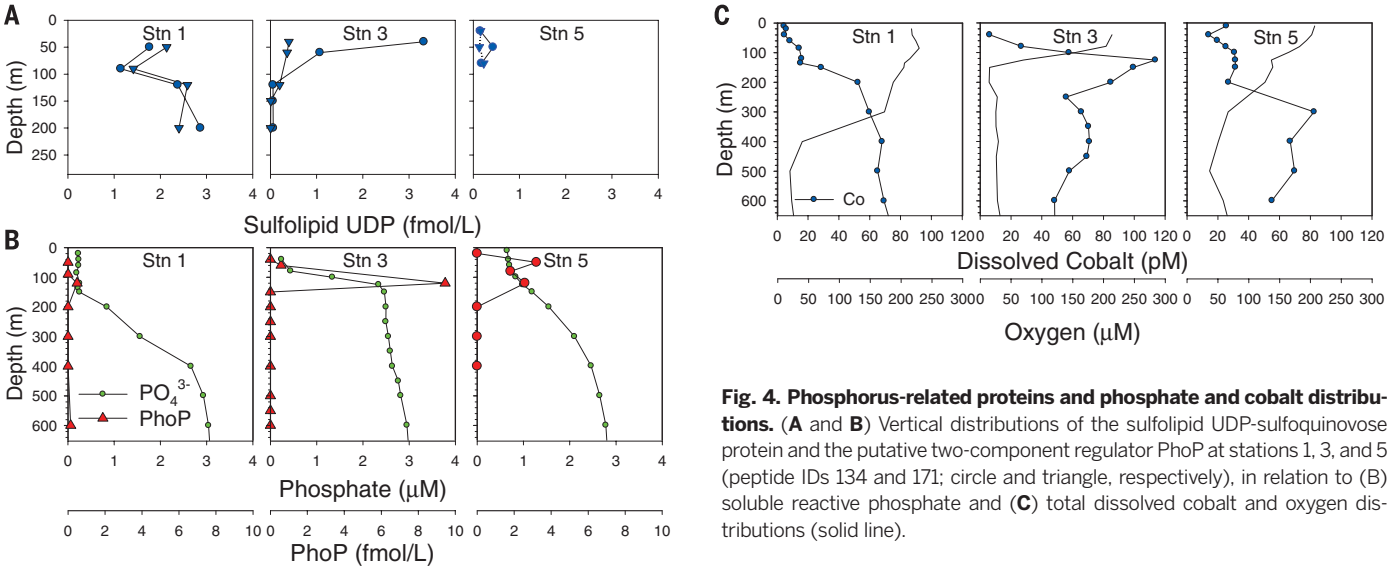

Fig. 4. Phosphorus-related proteins and phosphate and cobalt distributions. (**A** and **B**) Vertical distributions of the sulfolipid UDP-sulfoquinovose protein and the putative two-component regulator PhoP at stations 1, 3, and 5 (peptide IDs 134 and 171; circle and triangle, respectively), in relation to (B) soluble reactive phosphate and (**C**) total dissolved cobalt and oxygen distributions (solid line).

(Fig. 3C and fig. S7; IdiA, flavodoxin, NtcA, urea transporter, glutamine synthetase). Stations 3 and 9 had a considerable fraction of the nitrogen within this suite of five targeted proteins dedicated to the acquisition of both nutrients simultaneously (Fig. 3D and fig. S7, A and B). Although this estimate using selected proteins serves as a minimum nutritional estimate for the *Prochlorococcus* nitrogen and iron scarcity response, this analysis demonstrates that the community was deploying multiple nutrient acquisition strategies simultaneously, and hence was carrying the burden of an increased nutritional and energetic cost for maintaining both systems simultaneously as a potentially colimiting scenario. Moreover, although a previous study in a similar geographic region found that a novel low-iron ecotype dominated *Prochlorococcus* surface populations throughout (*27*), it is also possible that these biomarkers reflect an aggregated community signal of two or more coexisting high-light *Prochlorococcus* clades present in similar abundances. These results arguably present a challenge to current ecosystem parameterization influenced by Liebig's law of the minimum, where the required nutrient that is lowest in abundance relative to cellular requirements (e.g., cellular stoichiometry) solely controls growth rate by applying a minimum function to multiple Monod growth expression terms (*3*, *4*). Implicit in this minimum approach is an assumption that there is no metabolic or energetic penalty for the occurrence of more than one scarce nutrient simultaneously. Yet, these observations point to nutritional costs associated with maintaining the cellular machinery required to obtain a second scarce nutrient at the biomes' intersections.

Other nutrients, in addition to iron and nitrogen, were also scarce in this region and could influence primary productivity and community composition (*3*, *4*). Phosphorus and cobalt, in particular, are required for growth of *Prochlorococcus* (*28*, *29*) and were both highly depleted in the upper photic zone of the NPSG (Fig. 4, B and C). Two peptide biomarkers for the sulfolipid uridine 5-diphosphate (UDP) sulfoquinovose enzyme from high-light *Prochlorococcus* were found to be present at stations 1 and 3, but were diminished by station 5 as phosphate approached 1 μM in surface waters (Fig. 4A). *Prochlorococcus* uses this enzyme to replace phospholipids for sulfolipids as an adaptive response to phosphate scarcity (*30*). Deeper (low light) cyanobacterial communities responded to nutrient distributions along the transect. A protein homologous to the two-component phosphate response regulator PhoP in *Bacillus subtilis* (*31*) was identified during the metaproteome analyses (table S3) that corresponded to low-light *Prochlorococcus* ecotype and *Synechococcus* genomes (table S4). This two-component response regulator is one of seven identified in *Prochlorococcus* (*32*), yet was not previously observed to be responsive to phosphate scarcity (*29*). In this transect, this putative PhoP showed a similarity to the photic zone vertical distributions of phosphate and cobalt (Fig. 4), consistent with a role in regulation of phosphate metabolism near the nutricline. Notably, the expression of PhoP was opposite that of the two-component regulatory system PhoR identified in high-light *Prochlorococcus* ecotypes that is abundant under phosphate-scarcity rather than phosphate-replete conditions. PhoR is only present as a pseudogene in the low-light *Prochlorococcus* ecotype (*29*), implying that alternate response regulators such as PhoP are needed for regulation of low-light *Prochlorococcus* communities.

The distributions of the putative PhoP also resembled those of dissolved cobalt, whose distribution often correlates with that of phosphate (Fig. 4). Although cobalt is an essential micronutrient for *Prochlorococcus* and is the rarest of the metallic micronutrients in the sea (*28*), there are as yet no cyanobacterial biomarkers known to represent cobalt stress. The similarity to cobalt is also consistent with a metal requirement for the alkaline phosphatase enzyme, globally observed photic zone correlations of cobalt and phosphate (*33*), and several potential metal-related proteins within the gene neighborhood of *phoP* (including a transporter, protease, and carbonic anhydrase). Utilization of the micronutrient nickel also varied across the transect, yet in contrast to the low-abundance nickel-containing urease mentioned above, the nickel superoxide dismutase enzyme was highly abundant and increased in concentration toward the southern half of the transect, presumably in response to oxidative stress associated with iron-limiting physiology (fig. S6). Consistent with nickel superoxide dismutase being much more abundant than urease, the nickel measured in filtered particulate material was more abundant on the equatorial and southern regions of the transect (fig. S6).

These results show the utility of targeted metaproteomics in diagnosing nutrient stress of a major phytoplankton group, studying changes in ecological stoichiometry, and identifying novel regulatory components and their potential role in the systems biology of the oceans. Future climate is predicted to alter the oceanic biogeochemical provinces (*34*), with marine cyanobacterial populations expected to be affected, although it has been difficult to predict the nature of these impacts (*35*, *36*). Diagnostic measurements deployed over large geographic regions, such as the targeted metaproteomics methods shown here, could be valuable in characterizing the response to multiple influences.

REFERENCES AND NOTES

1. E. L. Mann, S. W. Chisholm, *Limnol. Oceanogr.* **45**, 1067–1076 (2000).
2. J. K. Moore, S. C. Doney, K. Lindsay, *Global Biogeochem. Cycles* **18**, GB4028 (2004).
3. C. M. Moore *et al.*, *Nat. Geosci.* **6**, 701–710 (2013).
4. M. A. Saito, T. J. Goepfert, J. T. Ritt, *Limnol. Oceanogr.* **53**, 276–290 (2008).
5. E. A. Webb, J. W. Moffett, J. B. Waterbury, *Appl. Environ. Microbiol.* **67**, 5444–5452 (2001).
6. D. Lindell, A. F. Post, *Appl. Environ. Microbiol.* **67**, 3340–3349 (2001).

7. S. M. Sowell *et al.*, *ISME J.* **3**, 93–105 (2009).
8. R. M. Morris *et al.*, *ISME J.* **4**, 673–685 (2010).
9. Materials and Methods are available on *Science* online.
10. G. Reygondeau *et al.*, *Global Biogeochem. Cycles* **27**, 1046–1058 (2013).
11. R. M. Gordon, K. H. Coale, K. S. Johnson, *Limnol. Oceanogr.* **42**, 419–431 (1997).
12. D. M. Karl, R. R. Bidigare, R. M. Letelier, *Deep Sea Res. Part II Top. Stud. Oceanogr.* **48**, 1449–1470 (2001).
13. F. Partensky, W. R. Hess, D. Vaulot, *Microbiol. Mol. Biol. Rev.* **63**, 106–127 (1999).
14. V. Lange *et al.*, *Mol. Cell. Proteomics* **7**, 1489–1500 7(2008).
15. J. LaRoche, P. W. Boyd, R. M. L. McKay, R. J. Geider, *Nature* **382**, 802–805 (1996).
16. A. W. Thompson, K. Huang, M. A. Saito, S. W. Chisholm, *ISME J.* **5**, 1580–1594 (2011).
17. D. Lindell, E. Padan, A. F. Post, *J. Bacteriol.* **180**, 1878–1886 (1998).
18. A. C. Tolonen *et al.*, *Mol. Syst. Biol.* **2**, 53 (2006).
19. G. Rocap, D. L. Distel, J. B. Waterbury, S. W. Chisholm, *Appl. Environ. Microbiol.* **68**, 1180–1191 (2002).
20. L. O. Slemons, J. W. Murray, J. Resing, B. Paul, P. Dutrieux, *Global Biogeochem. Cycles* **24**, GB3024 (2010).
21. L. R. Moore, A. F. Post, G. Rocap, S. W. Chisholm, *Limnol. Oceanogr.* **47**, 989–996 (2002).
22. J. R. Casey, M. W. Lomas, J. Mandecki, D. E. Walker, *Geophys. Res. Lett.* **34**, L10604 (2007).
23. B. Wawrik, A. V. Callaghan, D. A. Bronk, *Appl. Environ. Microbiol.* **75**, 6662–6670 (2009).
24. N. A. Kamennaya, A. F. Post, *Limnol. Oceanogr.* **58**, 1959–1971 (2013).
25. A. C. Martiny, S. Kathuria, P. M. Berube, *Proc. Natl. Acad. Sci. U.S.A.* **106**, 10787–10792 (2009).
26. G. R. DiTullio, D. A. Hutchins, K. W. Bruland, *Limnol. Oceanogr.* **38**, 495–508 (1993).
27. D. B. Rusch, A. C. Martiny, C. L. Dupont, A. L. Halpern, J. C. Venter, *Proc. Natl. Acad. Sci. U.S.A.* **107**, 16184–16189 (2010).
28. M. A. Saito, J. W. Moffett, S. W. Chisholm, J. B. Waterbury, *Limnol. Oceanogr.* **47**, 1629–1636 (2002).
29. A. C. Martiny, M. L. Coleman, S. W. Chisholm, *Proc. Natl. Acad. Sci. U.S.A.* **103**, 12552–12557 (2006).
30. B. A. S. Van Mooy, G. Rocap, H. F. Fredricks, C. T. Evans, A. H. Devol, *Proc. Natl. Acad. Sci. U.S.A.* **103**, 8607–8612 (2006).
31. S. M. Birkey, W. Liu, X. Zhang, M. F. Duggan, F. M. Hulett, *Mol. Microbiol.* **30**, 943–953 (1998).
32. I. Mary, D. Vaulot, *FEMS Microbiol. Lett.* **226**, 135–144 (2003).
33. A. E. Noble, M. A. Saito, K. Maiti, C. Benitez-Nelson, *Deep Sea Res. Part II Top. Stud. Oceanogr.* **55**, 1473–1490 (2008).
34. J. J. Polovina, J. P. Dunne, P. A. Woodworth, E. A. Howell, *ICES J. Mar. Sci.* **68**, 986–995 (2011).
35. P. W. Boyd, R. Strzepek, F. Fu, D. A. Hutchins, *Limnol. Oceanogr.* **55**, 1353–1376 (2010).
36. P. Flombaum *et al.*, *Proc. Natl. Acad. Sci. U.S.A.* **110**, 9824–9829 (2013).

ACKNOWLEDGMENTS

This work was made possible by NSF grants OCE-1031271, 1155566, and 1233261 Gordon Betty Moore Foundation grants 2724 and 3782, the Center for Microbial Research and Education, and the Woods Hole Oceanographic Institution Ocean Life Institute. We are grateful to the captain and crew of the R/V *Kilo Moana*, particularly V. Polidoro for his resourcefulness. We thank N. Hawco, D. Wang, and P. Balcom for sampling assistance and J. Dusenberry for programming assistance. We thank A. Santoro, J. Waterbury, and P. Chivers for helpful discussions and J. Blethrow and V. Zabrouskov (Thermo Scientific) for analyses on the prototype Fusion. Data for the Metyme Expedition are available at www.bco-dmo.org.

SUPPLEMENTARY MATERIALS

www.sciencemag.org/content/345/6201/1173/suppl/DC1
Materials and Methods
Supplementary Text
Figs. S1 to S18
Tables S1 to S6
References (*37*–*63*)

23 May 2014; accepted 25 July 2014
10.1126/science.1256450

PALEOCLIMATE

Greenland temperature response to climate forcing during the last deglaciation

Christo Buizert,[1]* Vasileios Gkinis,[2,3] Jeffrey P. Severinghaus,[4] Feng He,[5] Benoit S. Lecavalier,[6] Philippe Kindler,[7] Markus Leuenberger,[7] Anders E. Carlson,[1] Bo Vinther,[2] Valérie Masson-Delmotte,[8] James W. C. White,[3] Zhengyu Liu,[5,9] Bette Otto-Bliesner,[10] Edward J. Brook[1]

Greenland ice core water isotopic composition ($\delta^{18}O$) provides detailed evidence for abrupt climate changes but is by itself insufficient for quantitative reconstruction of past temperatures and their spatial patterns. We investigate Greenland temperature evolution during the last deglaciation using independent reconstructions from three ice cores and simulations with a coupled ocean-atmosphere climate model. Contrary to the traditional $\delta^{18}O$ interpretation, the Younger Dryas period was 4.5° ± 2°C warmer than the Oldest Dryas, due to increased carbon dioxide forcing and summer insolation. The magnitude of abrupt temperature changes is larger in central Greenland (9° to 14°C) than in the northwest (5° to 9°C), fingerprinting a North Atlantic origin. Simulated changes in temperature seasonality closely track changes in the Atlantic overturning strength and support the hypothesis that abrupt climate change is mostly a winter phenomenon.

The last deglaciation [~19 thousand to 11 thousand years before the present (ky B.P.)] is the most recent example of natural global warming and large-scale climate reorganization, providing an exceptional opportunity to study the interaction between different components of the climate system (*1*) and climate sensitivity to changes in radiative forcing (*2*). Much of the regional and global climate variability of this period can be explained as the superposition of two distinct modes (*3*, *4*): a global increase in surface temperature related to increased radiative forcing (Fig. 1C) and an interhemispheric redistribution of heat associated with variability in the Atlantic meridional overturning circulation (AMOC) strength (Fig. 1D).

High-resolution records of Northern Hemisphere (NH) high-latitude climate are provided by Greenland ice core water isotopic composition ($\delta^{18}O$ and δD), a proxy for local condensation temperature (Fig. 1A). Past water isotopic variations reflect site temperature (T_{site}) to first order (*5*) but are also influenced by changes to the atmospheric hydrological cycle, such as evaporation conditions (*6*, *7*), moisture origin and transport pathways (*8*, *9*), and precipitation intermittency or seasonality (*10*). Assuming a linear $\delta^{18}O$-T_{site} relationship suggests that Greenland climate did not begin to warm until the Bølling onset (14.7 ky B.P.), lagging much of the globe and implying a negligible Greenland temperature response to increasing atmospheric CO_2 (*11*–*14*). Such delayed Arctic warming is hard to reconcile with past sea levels and NH ice sheet extent that indicate substantial ice loss before the Bølling (*15*). This paradox is exemplified by lower Greenland summit $\delta^{18}O$ levels during the Younger Dryas period (YD, 12.8 to 11.7 ky B.P.) than during the Oldest Dryas period (OD, 18 to 14.7 ky B.P.), despite the rise in boreal summer insolation (Fig. 1B) and a ~50 parts per million increase in atmospheric CO_2 (*14*, *16*).

Accurate temperature reconstructions are required to improve our understanding of the mechanisms controlling Greenland climate during the last deglaciation and to benchmark transient climate simulations (*17*, *18*). Here, we circumvent the issues that confound water isotope interpretation by using four independent temperature reconstructions from three ice cores

[1]College of Earth, Ocean, and Atmospheric Sciences, Oregon State University, Corvallis, OR 97331, USA. [2]Centre for Ice and Climate, Niels Bohr Institute, University of Copenhagen, Denmark. [3]Institute of Arctic and Alpine Research, University of Colorado, Boulder, CO 80309, USA. [4]Scripps Institution of Oceanography, University of California–San Diego, La Jolla, CA 92093, USA. [5]Center for Climatic Research, Nelson Institute for Environmental Studies, University of Wisconsin, Madison, WI 53706, USA. [6]Department of Physics and Physical Oceanography, Memorial University, St. John's, Canada. [7]Division of Climate and Environmental Physics, Physics Institute and Oeschger Centre for Climate Change Research, University of Bern, Bern, Switzerland. [8]Laboratoire des Sciences du Climat et de l'Environnement, Institut Pierre Simon Laplace (UMR CEA-CNRS-UVSQ 8212), Gif-sur-Yvette, France. [9]Laboratory for Climate and Ocean-Atmosphere Studies, Peking University, Beijing 100871, China. [10]Climate and Global Dynamics Division, National Center for Atmospheric Research, Boulder, CO 80307, USA.
***Corresponding author. E-mail: buizertc@science.oregonstate.edu**

[North Greenland Eemian Ice Drilling (NEEM), North Greenland Ice Core Project (NGRIP), and Greenland Ice Sheet Project 2 (GISP2)] (Fig. 1, G to I), which we combine with transient general circulation model (GCM) simulations (*4*, *16*, *17*). Our work provides a consistent picture of the temporal, spatial, and seasonal trends in the Greenland surface temperature response to external (insolation) and internal (CO_2, AMOC, and ice topography) climate forcings during the last deglaciation.

Our primary T_{site} reconstruction method uses gas-phase $\delta^{15}N$-N_2 data (Fig. 1F) and the inversion of a dynamical firn densification model to find the T_{site} history that optimizes the fit to the $\delta^{15}N$ data through an automated algorithm. The method builds on earlier $\delta^{15}N$ work, in which mostly the abrupt transitions were investigated (*5*, *19*–*21*). Our approach also allows investigation of T_{site} evolution between abrupt transitions and robustly quantifies the uncertainty associated with the temperature reconstruction by exploring 216 combinations of densification physics and model parameters at each site. Details on the method are given in figs. S1 to S7 (*22*). For the NGRIP core, a second reconstruction method uses the temperature sensitivity of water isotope diffusion in the firn column (*23*). The isotope diffusion length is calculated along the core from high-resolution $\delta^{18}O$ data using spectral techniques. T_{site} is estimated from the diffusion length after accounting for firn densification, solid ice diffusion, and thinning due to ice flow. We perform a sensitivity study with 2000 reconstructions in which values of four key diffusion model parameters are altered. Both NGRIP reconstructions agree within uncertainty, and we therefore average the results. We further use transient climate simulations performed with the coupled ocean-atmosphere Community Climate System Model version 3 (CCSM3), which have been shown to capture correctly many aspects of deglacial climate history (*4*, *11*, *16*, *17*). The CCSM3 model has an equilibrium climate sensitivity of 2.3°C for a doubling of CO_2 (T31 grid), which is within the range of estimates from the Intergovernmental Panel on Climate Change (*24*).

First, we investigate the temperature difference between the YD and OD periods. Our reconstruction methods yield an ensemble of T_{site} reconstructions for each site, and we bin the results (Fig. 2A). For comparison, mean annual surface air temperature (SAT) changes from the GCM simulations are marked in black on the horizontal axes. All four reconstructions show that the YD period was warmer than the OD, on average by 4.5° ± 2°C (1 SD uncertainty). This contrasts with summit $\delta^{18}O$, which is more strongly depleted during the YD than the OD (*12*, *13*). Our reconstruction is consistent with increased CO_2 and boreal summer insolation during the YD relative to the OD (*16*), as well as NH non–ice core proxy synthesis results (Fig. 1E) that also exhibit a positive YD-OD difference (*11*). CCSM3 reproduces our reconstructed YD-OD warming well, simulating a 5.4°C YD-OD difference averaged over the sites. Transient simulations with an Earth system model of intermediate complexity also find a ~5°C YD-OD temperature difference (*18*). Our reconstructions are thus compatible with current understanding of the role of CO_2 forcing on climate. Additional CCSM3 simulations in which the different climatic forcings are isolated (*4*) suggest that the YD-OD warming due to greenhouse gas forcing is about three times as large as the warming caused by increased insolation (fig. S9). The T_{site} reconstructions show a poleward enhancement of the YD-OD signal, with warming being largest at the NEEM site. This spatial pattern is also captured in the CCSM3 model response (Fig. 2E). Whereas homogeneous Greenland warming is simulated in response to increased CO_2 or insolation, changes in the Laurentide ice sheet topography induce atmospheric circulation changes that affect North Atlantic climate and can explain the observed spatial gradient (fig. S9).

Second, we investigate the abrupt climatic events that are superimposed on the gradual warming of the background climate; the magnitudes of the abrupt warming/cooling (ΔT) at the Bølling (14.7 ky B.P.), YD (12.8 ky B.P.), and Holocene (11.6 ky B.P.) onset are shown in Fig. 2,

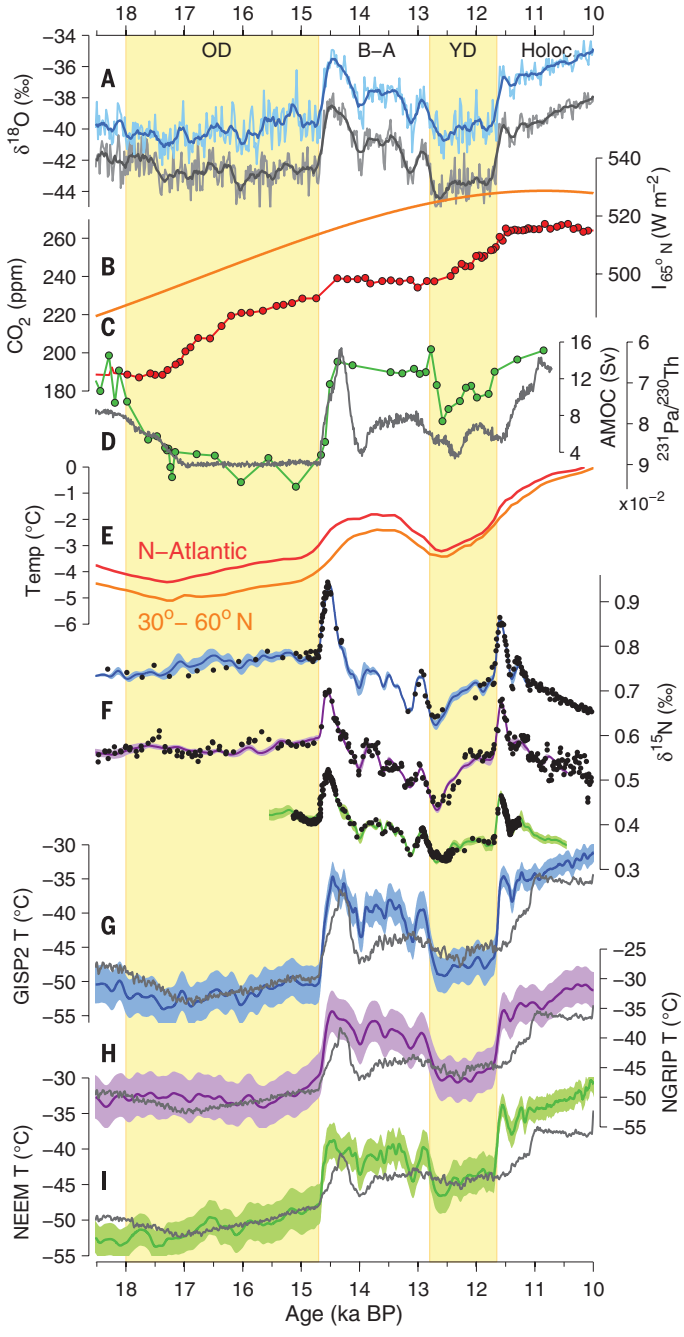

Fig. 1. Paleoclimate records and Greenland temperature reconstructions for the last deglaciation. (**A**) Greenland summit ice core $\delta^{18}O$ from GISP2 (blue) and GRIP [gray, offset by −3 per mil (‰) for clarity]. (**B**) The 21 June insolation at 65°N. (**C**) Atmospheric CO_2 mixing ratios (*14*). (**D**) Bermuda rise (core OCE326-GGC5) $^{231}Pa/^{230}Th$ as a proxy for AMOC strength (green) (*30*) and GCM AMOC strength (gray) in sverdrups (1 Sv = 10^6 m^3 s^{-1}). (**E**) Surface temperature stacks for 30°N to 60°N and North Atlantic region (*11*). (**F**) GISP2 (blue, offset by +0.3‰ for clarity), NGRIP (purple, +0.15‰ offset) and NEEM (green) model fit to $\delta^{15}N$ data (black dots). (**G** to **I**) Greenland temperature reconstructions with ±1 SD uncertainty envelope for GISP2 (blue), NGRIP (purple), NEEM (green), and CCSM3 GCM output (gray) (*16*, *17*).

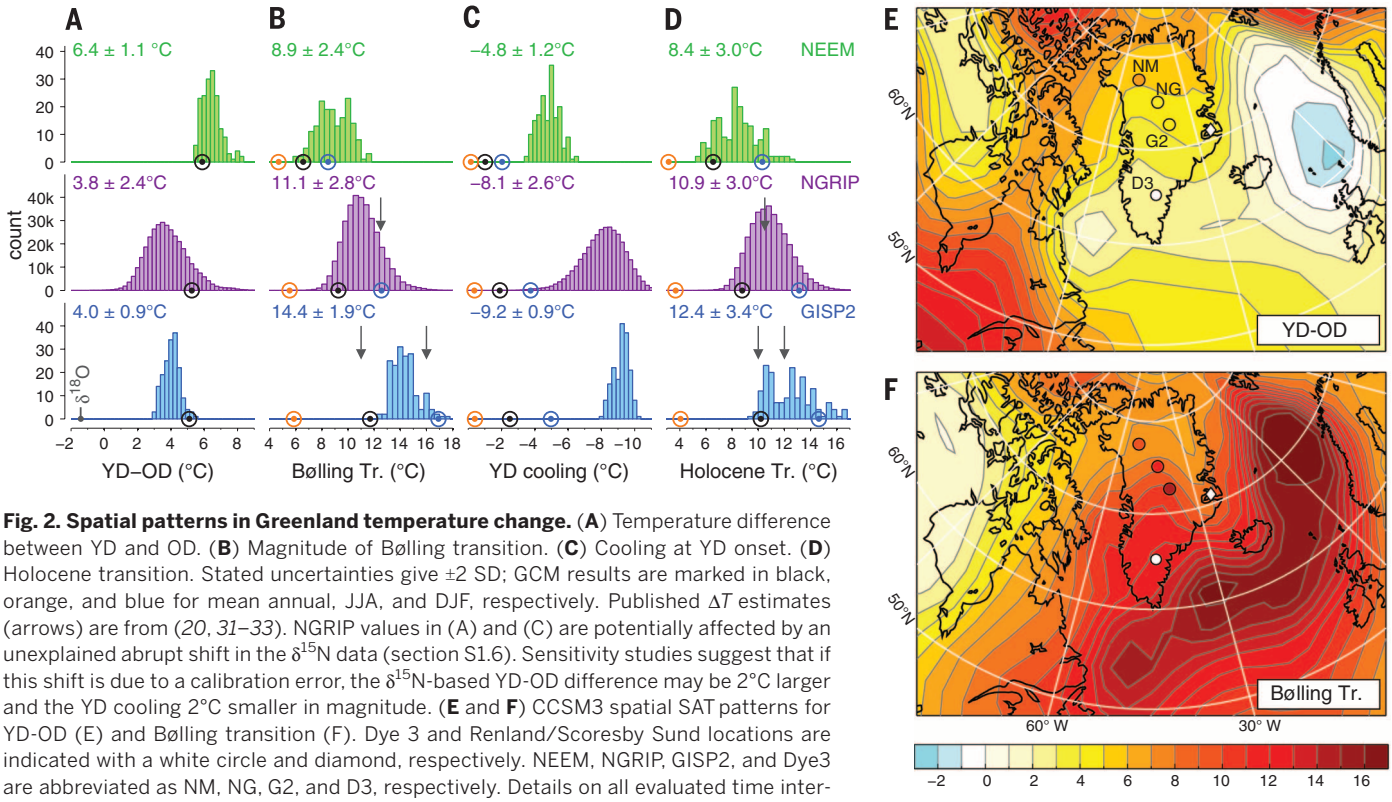

Fig. 2. Spatial patterns in Greenland temperature change. (**A**) Temperature difference between YD and OD. (**B**) Magnitude of Bølling transition. (**C**) Cooling at YD onset. (**D**) Holocene transition. Stated uncertainties give ±2 SD; GCM results are marked in black, orange, and blue for mean annual, JJA, and DJF, respectively. Published ΔT estimates (arrows) are from (*20*, *31*–*33*). NGRIP values in (A) and (C) are potentially affected by an unexplained abrupt shift in the $\delta^{15}N$ data (section S1.6). Sensitivity studies suggest that if this shift is due to a calibration error, the $\delta^{15}N$-based YD-OD difference may be 2°C larger and the YD cooling 2°C smaller in magnitude. (**E** and **F**) CCSM3 spatial SAT patterns for YD-OD (E) and Bølling transition (F). Dye 3 and Renland/Scoresby Sund locations are indicated with a white circle and diamond, respectively. NEEM, NGRIP, GISP2, and Dye3 are abbreviated as NM, NG, G2, and D3, respectively. Details on all evaluated time intervals are given in table S1 (*22*).

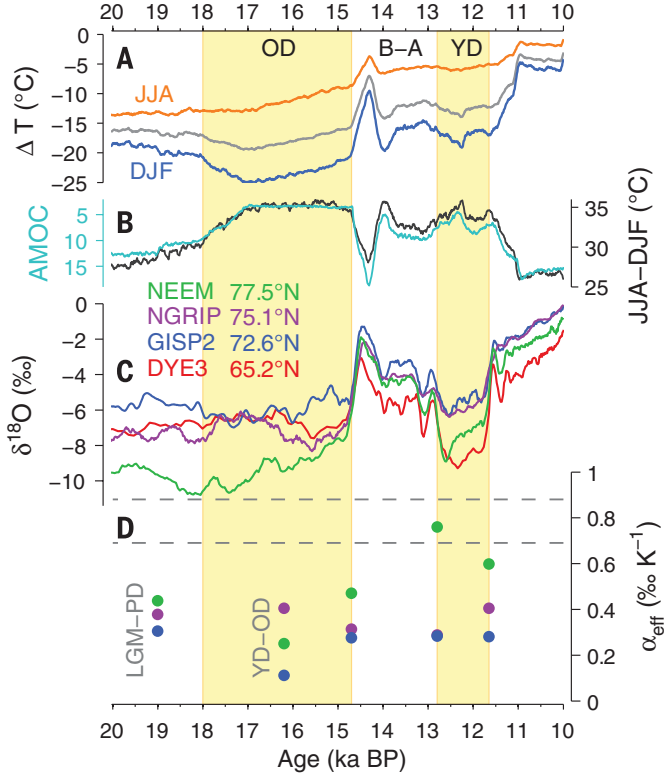

Fig. 3. Greenland isotopes and temperature seasonality. (**A**) Simulated summer (JJA), winter (DJF), and mean annual temperatures (gray) relative to the present day at Scoresby Sund (Fig. 2F), the site studied by Denton *et al*. (*26*). (**B**) CCSM3 temperature seasonality JJA-DJF (gray) and AMOC strength in sverdrups (turquoise). (**C**) $\delta^{18}O$ of four Greenland ice cores corrected for mean oceanic $\delta^{18}O$, relative to present-day $\delta^{18}O$. (**D**) Effective isotopic temperature sensitivity for GIPS2 (blue dots), NGRIP (purple), and NEEM (green), with present-day spatial isotope sensitivity (0.69 ‰ K^{-1}) and Rayleigh-type distillation model prediction (0.88 ‰ K^{-1}) (dashed lines).

B to D. At all sites, ΔT is larger at the Bølling transition than at the Holocene transition. For all three abrupt events, ΔT is smallest (5° to 9°C) in northwest Greenland (NEEM) and largest (9° to 14°C) in central Greenland (GISP2). This spatial gradient, which is not reflected in $\delta^{18}O$, is also observed for several Dansgaard-Oeschger events (*19*), suggesting that it is a robust feature of abrupt climate change over Greenland. CCSM3 fails to reproduce the timing of the Holocene transition and underestimates the ΔT magnitude of the Bølling and Holocene transitions by ~20% and the magnitude of the YD cooling by ~75%. Yet CCSM3 qualitatively captures the observed spatial ΔT gradient. In the simulations, AMOC invigoration at the Bølling onset is associated with maximum SAT change in the North Atlantic (Fig. 2F) due to increased northward oceanic heat transport and an associated reduction in sea-ice cover (fig. S10). As a result, the simulated SAT changes are largest for ice core sites closest to the North Atlantic (i.e., GISP2) and smallest in northwest Greenland.

In the simulations, AMOC variations are induced by a freshwater forcing to the North Atlantic, using a meltwater discharge scenario designed to be broadly consistent with available evidence of past sea level, ice sheet extent, and meltwater routing (*15*). We recognize that processes other than freshwater may have contributed to, and perhaps even caused, the AMOC and sea-ice variations of the deglaciation. Regardless of its cause, AMOC invigoration will

result in North Atlantic warming and a reduction in sea-ice cover, which in turn affects the atmospheric circulation and Greenland SAT. Atmosphere-only GCM experiments of North Atlantic sea-ice removal under Last Glacial Maximum (LGM) conditions show a ΔT pattern qualitatively similar to that simulated by CCSM3, suggesting that sea-ice variability by itself may be sufficient to explain this pattern (*25*). The northward reduction in ΔT magnitude that we reconstruct over Greenland is thus likely a fingerprint of the North Atlantic origin of abrupt climate change, irrespective of the precise roles played by freshwater forcing and AMOC variations.

Our T_{site} reconstructions provide annual mean temperatures, and to investigate seasonal temperature changes we turn to the CCSM3 simulations. Simulated Greenland temperature seasonality is strongly linked to AMOC strength and mean climate state, with large (small) seasonality during periods of weak (strong) overturning (Fig. 3B). Most of the seasonality signal is due to winter [December to February (DJF)] SAT, which changes more than summer [June to August (JJA)] SAT (Fig. 3A). The dominance of winter SAT is most clearly manifested during abrupt transitions, where simulated DJF ΔT (marked blue in Fig. 2, B to D) is much larger than JJA ΔT (orange). This contrasts with the (primarily CO_2-forced) YD-OD warming, for which DJF and JJA warming are nearly identical (within 10% of the mean annual change). Our simulations thus support the hypothesis that abrupt climate change is mostly a winter phenomenon (*25*–*28*). In the simulations, reduced AMOC strength and attendant heat transport (such as during the YD and OD) results in an extensive North Atlantic winter sea-ice cover (fig. S10). This extended sea ice, in turn, insulates the atmosphere from the moderating influence of the large oceanic heat capacity, resulting in extremely low winter SAT and increased temperature seasonality over Greenland. Because ablation of land-based ice occurs primarily during summer months, summer SAT is the main control on continental ice volume (*26*). If AMOC variability mainly affects winter SAT, as suggested by the CCSM3 simulations, it has only a limited effect on margin positions and ice volume, which may in part explain the paucity of YD moraines found across Greenland (*29*) and the continued sea-level rise across the OD and YD intervals (*15*). Our temperature reconstructions, as well as the strong AMOC-seasonality link we simulate, can inform efforts to understand and model Greenland ice sheet evolution during the deglaciation.

The independent reconstructions can be used to investigate nontemperature influences on $\delta^{18}O$. To this end, we calculate the effective isotope sensitivity $\alpha_{eff} = \Delta\delta^{18}O_{corr}/\Delta T$, with $\Delta\delta^{18}O_{corr}$ the change in $\delta^{18}O$ (corrected for mean ocean $\delta^{18}O$) associated with temperature change ΔT (Fig. 3D). As in other studies (*5*, *19*, *20*), we find that α_{eff} varies both between sites and in time, showing the limitations of the $\delta^{18}O$ paleothermometer. On average, α_{eff} at NEEM is closest to sensitivity values obtained from the present-day spatial $\delta^{18}O$-T_{site} relationship and Rayleigh-type distillation models (*7*). Going southward, α_{eff} decreases, reflecting an increasing net effect of nontemperature influences on $\delta^{18}O$. This meridional gradient in $\delta^{18}O$ bias is further demonstrated by the Dye3 core in south Greenland (Fig. 3C), where the YD-OD $\delta^{18}O$ anomaly is most pronounced. GCM simulations suggest that changes in precipitation seasonality most strongly affect South Greenland, in general agreement with the meridional α_{eff} gradient that we observe (fig. S11B). Moisture tracking in the CCM3 atmospheric GCM (*8*), furthermore, suggests an increased relative contribution of (strongly distilled) Pacific vapor during the LGM, which is most pronounced at NEEM (fig. S11A) and consistent with the observed stronger glacial $\delta^{18}O$ depletion at NEEM. The apparently stable and high α_{eff} values at NEEM may be caused by compensating $\delta^{18}O$ biases and do not necessarily imply a more faithful $\delta^{18}O$ paleothermometer. Our T_{site} reconstructions can be used in conjunction with GCM isotope modeling to unravel the ice core water isotopic signals ($\delta^{18}O$, deuterium excess, and ^{17}O excess), potentially providing constraints on atmospheric circulation changes during the last deglaciation.

In summary, our independent temperature reconstructions reveal the magnitude and spatial structure of deglacial Greenland temperature changes, for which $\delta^{18}O$ by itself does not provide reliable, quantitative information. Our work demonstrates the role of CO_2 in forcing Greenland climate during the last deglaciation, shows a spatial pattern of the abrupt deglacial transitions that fingerprints a North Atlantic origin, and identifies an important connection between AMOC strength and temperature seasonality. These results provide a valuable target to benchmark transient climate model simulations, can help refine estimates of past climate sensitivity, and can provide realistic climate forcing for Greenland ice sheet models during the last deglaciation.

REFERENCES AND NOTES

1. P. U. Clark *et al.*, *Proc. Natl. Acad. Sci. U.S.A.* **109**, E1134–E1142 (2012).
2. E. J. Rohling *et al.*, *Nature* **491**, 683–691 (2012).
3. J. D. Shakun, A. E. Carlson, *Quat. Sci. Rev.* **29**, 1801–1816 (2010).
4. F. He *et al.*, *Nature* **494**, 81–85 (2013).
5. C. Huber *et al.*, *Earth Planet. Sci. Lett.* **243**, 504–519 (2006).
6. E. A. Boyle, *Geophys. Res. Lett.* **24**, 273–276 (1997).
7. V. Masson-Delmotte *et al.*, *Science* **309**, 118–121 (2005).
8. P. L. Langen, B. M. Vinther, *Clim. Dyn.* **32**, 1035–1054 (2009).
9. C. D. Charles, D. Rind, J. Jouzel, R. D. Koster, R. G. Fairbanks, *Science* **263**, 508–511 (1994).
10. M. Werner, U. Mikolajewicz, M. Heimann, G. Hoffmann, *Geophys. Res. Lett.* **27**, 723–726 (2000).
11. J. D. Shakun *et al.*, *Nature* **484**, 49–54 (2012).
12. K. M. Cuffey, G. D. Clow, *J. Geophys. Res.* **102** (C12), 26383 (1997).
13. R. B. Alley, *Quat. Sci. Rev.* **19**, 213–226 (2000).
14. E. Monnin *et al.*, *Science* **291**, 112–114 (2001).
15. A. E. Carlson, P. U. Clark, *Rev. Geophys.* **50**, RG4007 (2012).
16. Z. Liu *et al.*, *Proc. Natl. Acad. Sci. U.S.A.* **109**, 11101–11104 (2012).
17. Z. Liu *et al.*, *Science* **325**, 310–314 (2009).
18. L. Menviel, A. Timmermann, O. E. Timm, A. Mouchet, *Quat. Sci. Rev.* **30**, 1155–1172 (2011).
19. M. Guillevic *et al.*, *Clim. Past* **9**, 1029–1051 (2013).
20. P. Kindler *et al.*, *Clim. Past* **10**, 887–902 (2014).
21. J. P. Severinghaus, E. J. Brook, *Science* **286**, 930–934 (1999).
22. Materials and methods are available as supplementary materials on *Science* Online.
23. V. Gkinis, S. B. Simonsen, S. L. Buchardt, J. W. C. White, B. M. Vinther, *Earth Planet. Sci. Lett.* (2014); http://arxiv.org/abs/1404.4201
24. J. T. Kiehl, C. A. Shields, J. J. Hack, W. D. Collins, *J. Clim.* **19**, 2584–2596 (2006).
25. C. Li, D. S. Battisti, D. P. Schrag, E. Tziperman, *Geophys. Res. Lett.* **32**, L19702 (2005).
26. G. H. Denton, R. B. Alley, G. C. Comer, W. S. Broecker, *Quat. Sci. Rev.* **24**, 1159–1182 (2005).
27. W. S. Broecker, *Global Planet. Change* **54**, 211–215 (2006).
28. J. Flückiger, R. Knutti, J. W. C. White, H. Renssen, *Clim. Dyn.* **31**, 633–645 (2008).
29. S. Funder, K. H. Kjaer, K. K. Kjeldsen, C. Ó. Cofaigh, in *Developments in Quaternary Science, Vol. 15,* In J. Ehlers, P. L. Gibbard, P. D. Hughes, Eds. (Elsevier B.V., Amsterdam, The Netherlands, 2011).
30. J. F. McManus, R. Francois, J. M. Gherardi, L. D. Keigwin, S. Brown-Leger, *Nature* **428**, 834–837 (2004).
31. C. Goujon, J. M. Barnola, C. Ritz, *J. Geophys. Res.* **108**, 4792 (2003).
32. J. P. Severinghaus, A. Grachev, B. Luz, N. Caillon, *Geochim. Cosmochim. Acta* **67**, 325–343 (2003).
33. A. M. Grachev, J. P. Severinghaus, *Quat. Sci. Rev.* **24**, 513–519 (2005).

ACKNOWLEDGMENTS

We are are indebted in countless ways to our mentor, friend, and colleague Sigfús J. Johnsen (1940–2013). We thank S. Marcott, D. Noone, J. Rosen, P. Langen, I. Seierstad, A. Landais, B. Minster, S. Falourd, and J. Shakun for fruitful discussions or assistance. Constructive comments by two anonymous reviewers helped improve the manuscript. We acknowledge funding through NSF grants 08-06377 (J.P.S.) and 0806414 (E.J.B.), the National Oceanic and Atmospheric Administration Climate and Global Change fellowship program, administered by the University Corporation for Atmospheric Research (C.B.), Agence Nationale de la Recherche through grants ANR VMC NEEM and ANR CEPS GREENLAND (V.M.-D.), and the U.S. NSF P2C2 program (A.E.C., Z.L., F.H., and B. O.-B.). This research used resources of the Oak Ridge Leadership Computing Facility, located in the National Center for Computational Sciences at Oak Ridge National Laboratory, which is supported by the Office of Science of the Department of Energy under contract DE-AC05-00OR22725. NEEM is directed and organized by the Center of Ice and Climate at the Niels Bohr Institute and U.S. NSF, Office of Polar Programs. It is supported by funding agencies and institutions in Belgium (FNRS-CFB and FWO), Canada (NRCan/GSC), China (CAS), Denmark (FIST), France (IPEV, CNRS/INSU, CEA, and ANR), Germany (AWI), Iceland (RannIs), Japan (NIPR), Korea (KOPRI), The Netherlands (NWO/ALW), Sweden (VR), Switzerland (SNF), United Kingdom (NERC) and the USA (U.S. NSF, Office of Polar Programs). NEEM data and temperature reconstructions are provided as supplementary data files.

SUPPLEMENTARY MATERIALS

www.sciencemag.org/content/345/6201/1177/suppl/DC1
Materials and Methods
Supplementary Text
Figs. S1 to S11
Tables S1 to S3
References (*34*–*102*)

17 April 2014; accepted 31 July 2014
10.1126/science.1254961

PLANT GENOMICS

The coffee genome provides insight into the convergent evolution of caffeine biosynthesis

France Denoeud,[1,2,3] Lorenzo Carretero-Paulet,[4] Alexis Dereeper,[5] Gaëtan Droc,[6] Romain Guyot,[7] Marco Pietrella,[8] Chunfang Zheng,[9] Adriana Alberti,[1] François Anthony,[5] Giuseppe Aprea,[8] Jean-Marc Aury,[1] Pascal Bento,[1] Maria Bernard,[1] Stéphanie Bocs,[6] Claudine Campa,[7] Alberto Cenci,[5,10] Marie-Christine Combes,[5] Dominique Crouzillat,[11] Corinne Da Silva,[1] Loretta Daddiego,[12] Fabien De Bellis,[6] Stéphane Dussert,[7] Olivier Garsmeur,[6] Thomas Gayraud,[7] Valentin Guignon,[10] Katharina Jahn,[9,13,14] Véronique Jamilloux,[15] Thierry Joët,[7] Karine Labadie,[1] Tianying Lan,[4,16] Julie Leclercq,[6] Maud Lepelley,[11] Thierry Leroy,[6] Lei-Ting Li,[17] Pablo Librado,[18] Loredana Lopez,[12] Adriana Muñoz,[19,20] Benjamin Noel,[1] Alberto Pallavicini,[21] Gaetano Perrotta,[12] Valérie Poncet,[7] David Pot,[6] Priyono,[22] Michel Rigoreau,[11] Mathieu Rouard,[10] Julio Rozas,[18] Christine Tranchant-Dubreuil,[7] Robert VanBuren,[17] Qiong Zhang,[17] Alan C. Andrade,[23] Xavier Argout,[6] Benoît Bertrand,[24] Alexandre de Kochko,[7] Giorgio Graziosi,[21,25] Robert J Henry,[26] Jayarama,[27] Ray Ming,[17] Chifumi Nagai,[28] Steve Rounsley,[29] David Sankoff,[9] Giovanni Giuliano,[8] Victor A. Albert,[4]* Patrick Wincker,[1,2,3]* Philippe Lashermes[5]*

Coffee is a valuable beverage crop due to its characteristic flavor, aroma, and the stimulating effects of caffeine. We generated a high-quality draft genome of the species *Coffea canephora*, which displays a conserved chromosomal gene order among asterid angiosperms. Although it shows no sign of the whole-genome triplication identified in Solanaceae species such as tomato, the genome includes several species-specific gene family expansions, among them *N*-methyltransferases (NMTs) involved in caffeine production, defense-related genes, and alkaloid and flavonoid enzymes involved in secondary compound synthesis. Comparative analyses of caffeine NMTs demonstrate that these genes expanded through sequential tandem duplications independently of genes from cacao and tea, suggesting that caffeine in eudicots is of polyphyletic origin.

With more than 2.25 billion cups consumed every day, coffee is one of the most important crops on Earth, cultivated across more than 11 million hectares. Coffee belongs to the Rubiaceae family, which is part of the Euasterid I clade and the fourth largest family of angiosperms, consisting of more than 11,000 species in 660 genera (*1*). We sequenced *Coffea canephora* ($2n = 2x = 22$ chromosomes), an outcrossing, highly heterozygous diploid, and one of the parents of *C. arabica* ($2n = 4x = 44$ chromosomes), which was derived from hybridization between *C. canephora* and *C. eugenioides* (*2*). A total of 54.4 million Roche 454 single and mate-pair reads and 143,605 Sanger bacterial artificial chromosome–end reads were generated from a doubled haploid accession, representing ~30× coverage of the 710-Mb genome (*3*). Additional Illumina sequencing data (60×) were used to improve the assembly (table S1) (*4*). The resulting assembly consists of 25,216 contigs and 13,345 scaffolds with a total length of 568.6 Mb (80% of 710 Mb), including 97 Mb (17%) of intercontig gaps. Eighty percent of the assembly is in 635 scaffolds, and the scaffold N50 (the scaffold size above which 50% of the total length of the sequence assembly can be found) is 1.26 Mb (table S2). A high-density genetic map covering 349 scaffolds and comprising ~64% of the assembly (364 Mb) and 86% of the annotated genes was anchored to the 11 *C. canephora* chromosomes (*4*). More than 96% of the scaffolds larger than 1 Mb were anchored (Fig. 1A).

We annotated 25,574 protein-coding genes (*4*) (table S6), 92 microRNA precursors, and 2573 organellar-to-nuclear genome transfers (*4*). Transposable elements account for ~50% of the genome (*4*), of which ~85% are long terminal repeat (LTR) retrotransposons. Large-scale comparison between *C. canephora* LTR retrotransposons and those of reference plant genomes shows outstanding conservation of several *Copia* groups across distantly related genomes, suggesting that horizontal mobile element transfers may be more frequent than generally recognized (*5*–*8*).

Structurally, the coffee genome shows no sign of a whole-genome polyploidization in its lineage since the γ triplication at the origin of the core eudicots (*9*) (Fig. 1B). Coffee contains exactly three paralogous regions for each of the seven pre-γ ancestral chromosomes (Fig. 1B). Coffee chromosomal regions show unique one-to-one correspondences with grapevine chromosomes (Fig. 1C and fig. S12) and a one-to-three correspondence with the tomato genome, which underwent a second lineage-specific triplication during its evolutionary history (*10*). Although grapevine, a rosid, is the most conservative core eudicot in terms of integrity of gross chromosomal structure, coffee displays less gene-order divergence to all other rosids, despite being an asterid itself (*9*). Coffee also shows little syntenic divergence relative to other sequenced asterids (Fig. 1D, table S17, and supplementary text).

To classify gene families in the *C. canephora* genome, we ran OrthoMCL on inferred protein sequences from coffee, grapevine, tomato, and *Arabidopsis* (*4*), generating 16,917 groups of orthologous genes (fig. S5). To examine coffee-specific gene family expansions with potential adaptive value, we fit different branch models implemented in BadiRate (*11*) to these orthogroups (*4*). In the coffee lineage, 202 orthogroups

[1]Commissariat à l'Energie Atomique, Genoscope, Institut de Génomique, BP5706, 91057 Evry, France. [2]CNRS, UMR 8030, CP5706, Evry, France. [3]Université d'Evry, UMR 8030, CP5706, Evry, France. [4]Department of Biological Sciences, 109 Cooke Hall, University at Buffalo (State University of New York), Buffalo, NY 14260, USA. [5]Institut de Recherche pour le Développement (IRD), UMR Résistance des Plantes aux Bioagresseurs (RPB) [Centre de Coopération Internationale en Recherche Agronomique pour le Développement (CIRAD), IRD, UM2)], BP 64501, 34394 Montpellier Cedex 5, France. [6]CIRAD, UMR Amélioration Génétique et Adaptation des Plantes Méditerranéennes et Tropicales (AGAP), F-34398 Montpellier, France. [7]IRD, UMR Diversité Adaptation et Développement des Plantes (CIRAD, IRD, UM2), BP 64501, 34394 Montpellier Cedex 5, France. [8]Italian National Agency for New Technologies, Energy and Sustainable Development (ENEA) Casaccia Research Center, Via Anguillarese 301, 00123 Roma, Italy. [9]Department of Mathematics and Statistics, University of Ottawa, 585 King Edward Avenue, Ottawa, Ontario K1N 6N5, Canada. [10]Bioversity International, Parc Scientifique Agropolis II, 34397 Montpellier Cedex 5, France. [11]Nestlé Research and Development Centre, 101 Avenue Gustave Eiffel, Notre-Dame-d'Oé, BP 49716, 37097 Tours Cedex 2, France. [12]ENEA Trisaia Research Center, 75026 Rotondella, Italy. [13]Center for Biotechnology, Universität Bielefeld, Universitätsstraße 27, D-33615 Bielefeld, Germany. [14]AG Genominformatik, Technische Fakultät, Universität Bielefeld, 33594 Bielefeld, Germany. [15]Institut National de la Recherche Agronomique (INRA), Unité de Recherches en Génomique-Info (UR INRA 1164), Centre de Recherche de Versailles, 78026 Versailles Cedex, France. [16]Department of Biology, Chongqing University of Science and Technology, 4000042 Chongqing, China. [17]Department of Plant Biology, 148 Edward R. Madigan Laboratory, MC-051, 1201 West Gregory Drive, University of Illinois at Urbana-Champaign, Urbana, IL 61801, USA. [18]Departament de Genètica and Institut de Recerca de la Biodiversitat (IRBio), Universitat de Barcelona, Diagonal 643, Barcelona 08028, Spain. [19]Department of Mathematics, University of Maryland, Mathematics Building 084, University of Maryland, College Park, MD 20742, USA. [20]School of Electrical Engineering and Computer Science, University of Ottawa, 800 King Edward Avenue, Ottawa, Ontario K1N 6N5, Canada. [21]Department of Life Sciences, University of Trieste, Via Licio Giorgieri 5, 34127 Trieste, Italy. [22]Indonesian Coffee and Cocoa Institute, Jember, East Java, Indonesia. [23]Laboratório de Genética Molecular, Núcleo de Biotecnologia (NTBio), Embrapa Recursos Genéticos e Biotecnologia, Final Av. W/5 Norte, Parque Estação Biológia, Brasília-DF 70770-917, Brazil. [24]CIRAD, UMR RPB (CIRAD, IRD, UM2), BP 64501, 34394 Montpellier Cedex 5, France. [25]DNA Analytica Srl, Via Licio Giorgieri 5, 34127 Trieste, Italy. [26]Queensland Alliance for Agriculture and Food Innovation, The University of Queensland, St. Lucia 4072, Australia. [27]Central Coffee Research Institute, Coffee Board, Coffee Research Station (Post) - 577 117 Chikmagalur District, Karnataka State, India. [28]Hawaii Agriculture Research Center, Post Office Box 100, Kunia, HI 96759-0100, USA. [29]BIO5 Institute, University of Arizona, 1657 Helen Street, Tucson, AZ 85721, USA.
***Corresponding author. E-mail: vaalbert@buffalo.edu (V.A.A.); pwincker@genoscope.cns.fr (P.W.); philippe.lashermes@ird.fr (P.L.)**

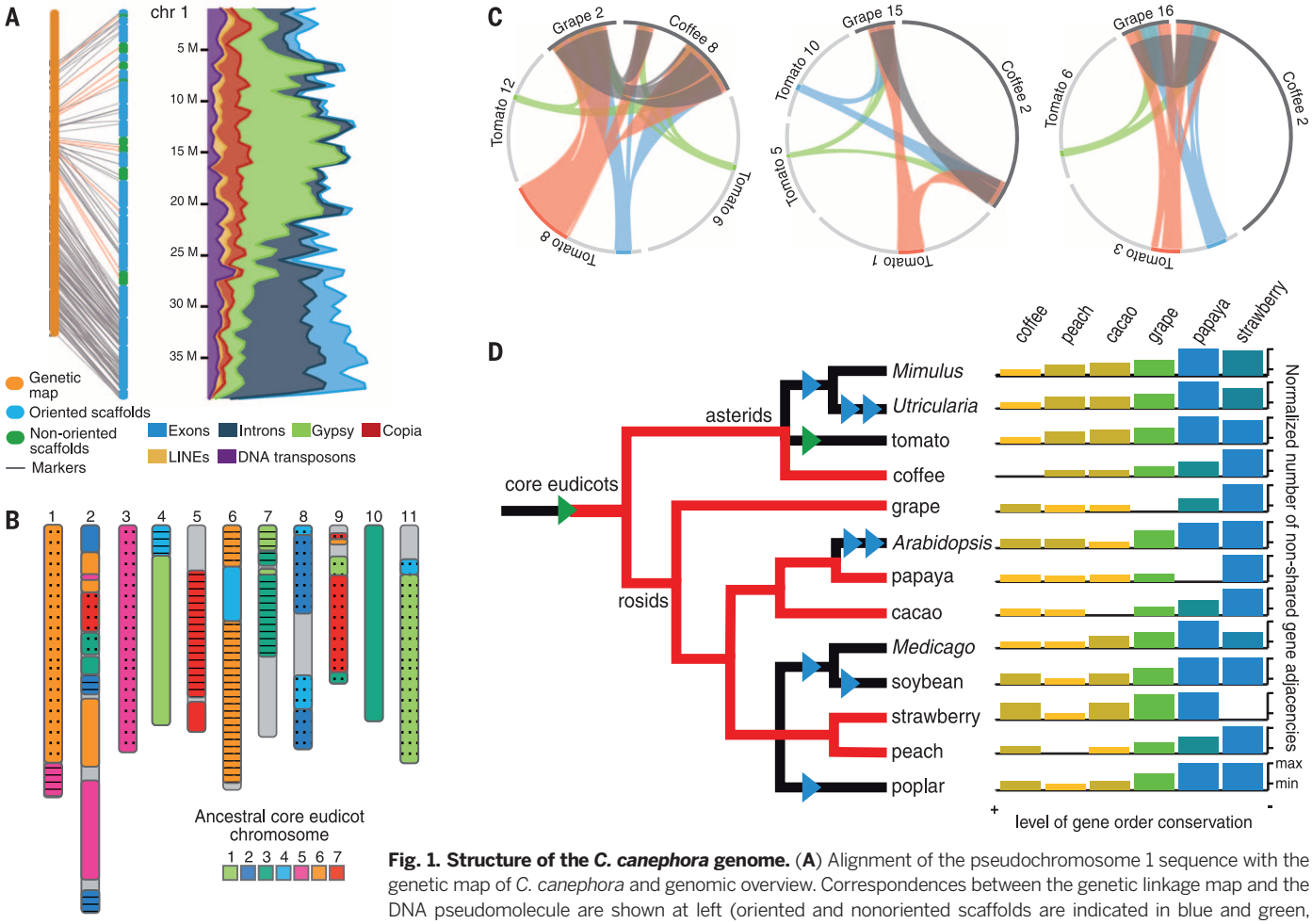

Fig. 1. Structure of the *C. canephora* genome. (**A**) Alignment of the pseudochromosome 1 sequence with the genetic map of *C. canephora* and genomic overview. Correspondences between the genetic linkage map and the DNA pseudomolecule are shown at left (oriented and nonoriented scaffolds are indicated in blue and green, respectively; gray lines denote consistent data; orange lines indicate markers with an approximate genetic location). The relative proportions (percentage of nucleotides) in sliding windows (1-Mb size, 500-kb step) of transposable elements (*Copia* in red, *Gypsy* in green) and genes (exons in blue, introns in dark blue) are shown at right. (**B**) Coffee chromosomal blocks descending from the seven ancestral core eudicot chromosomes. The three paralogous descendants of the seven ancestral chromosomes are shown in shared colors but different textures. (**C**) Comparison of three grapevine chromosomes (descendants of the prehexaploidization core eudicot chromosome) mapped to a single coffee chromosome and three regions in the tomato genome. (**D**) Phylogeny and genome duplication history of core eudicots. Arrowheads indicate tetraploidization (blue) or hexaploidization (green) events. Red lines trace lineages of six species that have not undergone further polyploidization. Bar graphs and colors reflect gene-order differences (table S17) between each of the six species (column labels) and the entire set, showing the gene order conservatism of coffee, especially among asterids, and of peach and cacao among rosids.

clustering 1270 genes were supported as expanded (Akaike information criterion > 2.7). Among gene ontology (GO) terms annotating these, 98 out of 4300 generic terms were significantly over- or underrepresented (table S14). Most GOs enriched in *C. canephora* ($P < 0.05$) belonged to two main functional categories: defense response and metabolic process, the later including different catalytic activities (table S15).

Among defense response functions, there is a clear expansion of nucleotide binding site disease-resistance genes (*12*, *13*) in the *C. canephora* genome (*4*). Most genes that grouped together within single orthogroups were tandemly arrayed, suggesting that *R* genes evolved by tandem duplication and divergence of linked gene families (supplementary text). Several gene functions involved in secondary metabolite biosynthesis are significantly expanded in the *C. canephora* genome, including enzymes associated with the production of phenylpropanoids such as flavonoids and isoflavones (naringenin 3-dioxygenase, isoflavone 2′-hydroxylase), alkaloids (strictosidine synthase, tropine dehydrogenase), monoterpenes (e.g., menthol dehydrogenase), and caffeine [*N*-methyltransferases (NMTs)] (Fig. 2). For example, indole alkaloids such as the monoamine oxidase inhibitor yohimbine and antimalaria drug quinine are prominent secondary compounds of the coffee family and its parent order, Gentianales (*14*), and the GO term indole biosynthetic process was highly enriched ($P < 0.001$) in coffee relative to tomato, grapevine, and *Arabidopsis*.

Caffeine is a purine alkaloid synthesized by several eudicot plants, including coffee, cacao (*Theobroma cacao*), and tea (*Camellia sinensis*) (Fig. 2). Caffeine is synthesized in both coffee leaves, where it has insecticidal properties (*15*), and fruits and seeds, where it inhibits seed germination of competing species (*16*). The late steps in caffeine biosynthesis are mediated by a series of NMTs (Fig. 2A) (*17*).

Among coffee-expanded genes, NMT activity is one of the more highly enriched GO terms (table S15). A single gene family (ORTHOMCL170) clusters 23 genes in coffee, but none in grapevine, tomato, or *Arabidopsis* (table S12), and this cluster contains genes encoding known enzymes of the caffeine biosynthetic pathway (*18*, *19*). Maximum likelihood (ML) phylogenetic analysis of ORTHOMCL170 with tea and cacao NMTs that have similar activities reveals species-specific gene clades (Fig. 2C). We analyzed these relationships in a broader evolutionary context by including genome-wide samples of NMTs from coffee, cacao, and other eudicot species. ML trees show that the genes encoding the closest *Arabidopsis* NMT relatives of coffee caffeine biosynthetic enzymes are involved in benzoic, salicylic, and nicotinic functions (*4*) (supplementary text). Caffeine biosynthetic NMTs from coffee nested within a gene clade distinct from those of cacao or tea, which group together as sister lineages. Thus, a

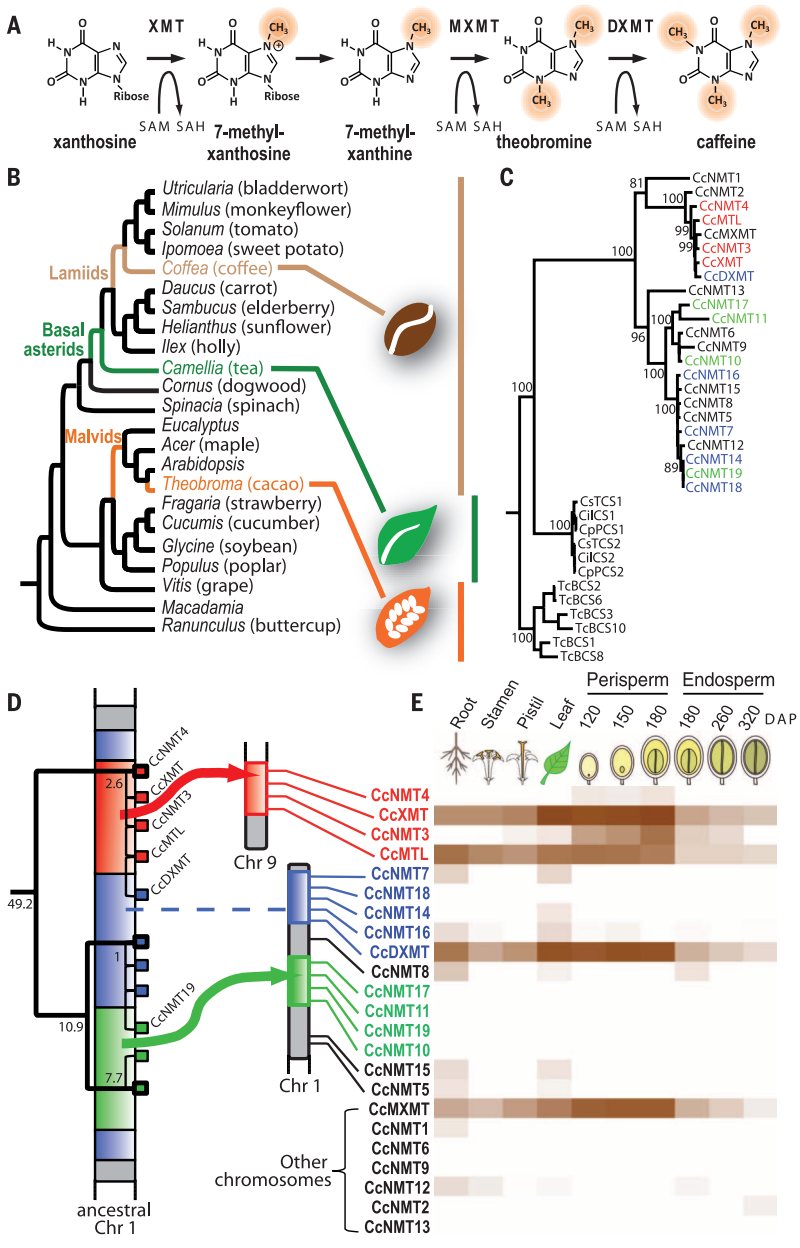

Fig. 2. Evolution of caffeine biosynthesis. (**A**) The principal caffeine biosynthetic pathway. Three methylation steps are necessary to produce caffeine from xanthosine, involving the successive action of three NMTs: xanthosine methyltransferase (XMT), theobromine synthase [7-methylxanthine methyltransferase (MXMT)], and caffeine synthase [3,7-dimethylxanthine methyltransferase (DXMT)]. SAM, *S*-adenosylmethionine; SAH, *S*-adenosylhomocysteine. (**B**) Evolutionary position of caffeine-producing plants with respect to other eudicots (phylogeny adapted from www.mobot.org/MOBOT/research/APweb/). (**C**) ML phylogeny of coffee, tea, and cacao NMTs. Bootstrap support values (percentages) from 1000 replicates are shown next to relevant clades. Branch lengths are proportional to expected numbers of nucleotide substitutions per site. Colors identify genes assignable to the genomic blocks denoted in (D). (**D**) (Left) A model summarizing the duplication history of coffee NMT genes, following the phylogeny in (C). Three distinct tandem gene arrays evolved in situ on chromosome 1 from nearby gene duplicates (bold squares). The red and green blocks, colored as in (C), translocated (to chromosome 9) or rearranged (to elsewhere on chromosome 1) from their ancestral locus (blue region), respectively. (Right) Gene orders on modern chromosomes. Translocation of the red block, containing the putative caffeine NMT metabolic cluster, left the phylogenetically derived *CcDXMT* gene behind. Similarly, *CcNMT19* is a derived gene within its own NMT clade that remained in place following movement of the green block. Numbers at branches indicate relative times since major duplication events or diversification times of the tandem arrays, calculated from approximately neutral synonymous substitution rates. (**E**) Expression profiles (reads per kilobase per million reads mapped) of known *Coffea canephora* NMTs. The genes in the putative metabolic cluster (along with *CcDXMT* and *CcMXMT*) exhibit similar expression patterns, higher in perisperm than endosperm. Data are plotted as log2 values. DAP, days after pollination.

minimum of two independent origins of caffeine biosynthetic NMT activity can be inferred, as proposed previously (*20*).

Microsynteny analyses of ORTHOMCL170, which includes three tandem arrays, show that some known and putative coffee caffeine synthase genes—*CcXMT* (encoding xanthosine *N*-methyltransferase), *CcMTL*, and *CcNMT3*—form a tight assemblage of coexpressed tandem duplicates (Fig. 2D) reminiscent of a metabolic gene cluster (*21*, *22*). Given that some plant metabolic gene clusters are of relatively recent origin (*23*), we sought to further unravel the role of gene duplication in the expansion of the coffee NMT gene family (Fig. 2D) (supplementary text). The three main coffee NMT clades in ORTHOMCL170 are distributed among a minimum of three genomic blocks; however, some phylogenetically recent tandem duplicates have moved away from their original positions via block rearrangements (Fig. 2D). One such movement involving the putative metabolic cluster appears to have left the *CcDXMT* gene (encoding 3,7-dimethylxanthine methyltransferase) behind, physically separated from its ancestral tandem array. In cacao, the functionally characterized *TcBCS1* gene has a tandem duplicate, but this pair of genes evolved independently from the NMT tandem arrays found in *C. canephora* (fig. S29). We also examined the role of positive selection (PS) in the evolution of caffeine biosynthesis among coffee, tea, and cacao (*4*) (supplementary text). We found significant evidence for PS [likelihood ratio test for PAML (Phylogenetic Analysis by Maximum Likelihood) branch-site test, $P = 5.78 \times 10^{-3}$ (*24*)] only for the coffee NMT lineage, indicating that the independent evolution of caffeine biosynthesis in coffee was adaptive and probably involved specific amino acid changes fixed by PS. These results highlight the distinct acquisition of caffeine biosynthesis in the coffee plant, providing an example of convergent evolution of secondary metabolic pathways encoded by tandemly duplicated genes.

Genomic functional diversification via tandem duplication may have helped shape other aspects of coffee bean chemical composition. Linoleic acid, which is produced by the oleate desaturase FAD2, is the major polyunsaturated fatty acid in the coffee bean (*25*, *26*), where it contributes to aroma composition and flavor retention after roasting (*4*). Coffee has six *FAD2* genes compared with one in *Arabidopsis*, and most of these have arisen from tandem duplications on chromosome 1 (fig. S33). RNA sequencing data suggest transcriptional specialization for two of the six *FAD2* copies, with *CcFAD2.3* being actively

transcribed in developing endosperm (supplementary text). Peak transcript abundance coincides with the dramatic increase in linoleic acid content that occurs during seed development at the perisperm-endosperm transition (*27*).

Our analysis of the adaptive genomic landscape of *C. canephora* identifies the convergent evolution of caffeine biosynthesis among plant lineages and establishes coffee as a reference species for understanding the evolution of genome structure in asterid angiosperms.

REFERENCES AND NOTES

1. E. Robbrecht, J. F. Manen, *Syst. Geogr. Plants* **76**, 85–146 (2006).
2. P. Lashermes *et al*., *Mol. Gen. Genet.* **261**, 259–266 (1999).
3. M. Noirot *et al*., *Ann. Bot. (London)* **92**, 709–714 (2003).
4. Materials and methods are available as supplementary materials on *Science* Online.
5. S. Schaack, C. Gilbert, C. Feschotte, *Trends Ecol. Evol.* **25**, 537–546 (2010).
6. A. Roulin *et al*., *BMC Evol. Biol.* **9**, 58 (2009).
7. M. El Baidouri *et al*., *Genome Res.* **24**, 831–838 (2014).
8. C. Moisy, A. H. Schulman, R. Kalendar, J. P. Buchmann, F. Pelsy, *Theor. Appl. Genet.* **127**, 1223–1235 (2014).
9. O. Jaillon *et al*., *Nature* **449**, 463–467 (2007).
10. S. Sato *et al*., *Nature* **485**, 635–641 (2012).
11. P. Librado, F. G. Vieira, J. Rozas, *Bioinformatics* **28**, 279–281 (2012).
12. S. H. Hulbert, C. A. Webb, S. M. Smith, Q. Sun, *Annu. Rev. Phytopathol.* **39**, 285–312 (2001).
13. L. McHale, X. Tan, P. Koehl, R. W. Michelmore, *Genome Biol.* **7**, 212 (2006).
14. F. Gleason, R. Chollet, *Plant Biochemistry* (Jones and Bartlett, Sudbury, MA, 2011).
15. J. A. Nathanson, *Science* **226**, 184–187 (1984).
16. A. Pacheco, J. Pohlan, M. Schulz, *Allelopathy J.* **21**, 39–56 (2008).
17. H. Ashihara, H. Sano, A. Crozier, *Phytochemistry* **69**, 841–856 (2008).
18. A. A. McCarthy, J. G. McCarthy, *Plant Physiol.* **144**, 879–889 (2007).
19. M. Ogawa, Y. Herai, N. Koizumi, T. Kusano, H. Sano, *J. Biol. Chem.* **276**, 8213–8218 (2001).
20. E. Pichersky, E. Lewinsohn, *Annu. Rev. Plant Biol.* **62**, 549–566 (2011).
21. B. Field, A. E. Osbourn, *Science* **320**, 543–547 (2008).
22. M. Matsuno *et al*., *Science* **325**, 1688–1692 (2009).
23. B. Field *et al*., *Proc. Natl. Acad. Sci. U.S.A.* **108**, 16116–16121 (2011).
24. J. Zhang, R. Nielsen, Z. Yang, *Mol. Biol. Evol.* **22**, 2472–2479 (2005).
25. D. Villarreal *et al*., *J. Agric. Food Chem.* **57**, 11321–11327 (2009).
26. S. Dussert, A. Laffargue, A. de Kochko, T. Joët, *Phytochemistry* **69**, 2950–2960 (2008).
27. T. Joët *et al*., *New Phytol.* **182**, 146–162 (2009).

ACKNOWLEDGMENTS

We acknowledge the following sources for funding: ANR-08-GENM-022-001 (to P.L.); ANR-09-GENM-014-002 (to P.W.); Australian Research Council (to R.J.H.); Natural Sciences and Engineering Research Council of Canada (to D.S.); CNR-ENEA Agrifood Project A2 C44 L191 (to G.Gi.); FINEP-Qualicafé, INCT-CAFÉ (to A.C.A.); NSF grants 0922742 (to V.A.A.) and 0922545 (to R.M.); and the College of Arts and Sciences, University at Buffalo (to V.A.A.). We thank P. Facella (ENEA) for Roche 454 sequencing and Instituto Agronômico do Paraná (Paraná, Brazil) for fruit RNA. This work was supported by the high-performance cluster of the SouthGreen Bioinformatics platform (UMR AGAP) CIRAD (www.southgreen.fr). The *C. canephora* genome assembly and gene models are available on the Coffee Genome Hub (http://coffee-genome.org) and the CoGe platform (www.genomevolution.org). Sequencing data are deposited in the European Nucleotide Archive under the accession numbers CBUE020000001 to CBUE020025216 (contigs), HG739085 to HG752429 (scaffolds), and HG974428 to HG974439 (chromosomes). Gene family alignments and phylogenetic trees for BAHD acyltransferases and NMTs are available in the GreenPhylDB (www.greenphyl.org/cgi-bin/index.cgi) under the gene family IDs CF158535 and CF158539 to CF158545, respectively. We declare no competing financial interests.

SUPPLEMENTARY MATERIALS

www.sciencemag.org/content/345/6201/1181/suppl/DC1
Materials and Methods
Supplementary Text
Figs. S1 to S33
Tables S1 to S27
References (*28*–*175*)

28 April 2014; accepted 29 July 2014
10.1126/science.1255274

GENOME EDITING

Prevention of muscular dystrophy in mice by CRISPR/Cas9–mediated editing of germline DNA

Chengzu Long,[1]* John R. McAnally,[1]* John M. Shelton,[2] Alex A. Mireault,[1] Rhonda Bassel-Duby,[1] Eric N. Olson[1]†

Duchenne muscular dystrophy (DMD) is an inherited X-linked disease caused by mutations in the gene encoding dystrophin, a protein required for muscle fiber integrity. DMD is characterized by progressive muscle weakness and a shortened life span, and there is no effective treatment. We used clustered regularly interspaced short palindromic repeat/Cas9 (CRISPR/Cas9)–mediated genome editing to correct the dystrophin gene (*Dmd*) mutation in the germ line of *mdx* mice, a model for DMD, and then monitored muscle structure and function. Genome editing produced genetically mosaic animals containing 2 to 100% correction of the *Dmd* gene. The degree of muscle phenotypic rescue in mosaic mice exceeded the efficiency of gene correction, likely reflecting an advantage of the corrected cells and their contribution to regenerating muscle. With the anticipated technological advances that will facilitate genome editing of postnatal somatic cells, this strategy may one day allow correction of disease-causing mutations in the muscle tissue of patients with DMD.

Duchenne muscular dystrophy (DMD) is caused by mutations in the gene for dystrophin on the X chromosome and affects approximately 1 in 3500 boys. Dystrophin is a large cytoskeletal structural protein essential for muscle cell membrane integrity. Without it, muscles degenerate, causing weakness and myopathy (*1*). Death of DMD patients usually occurs by age 25, typically from breathing complications and cardiomyopathy. Hence, therapy for DMD necessitates sustained rescue of skeletal, respiratory, and cardiac muscle structure and function. Although the genetic cause of DMD was identified nearly three decades ago (*2*), and several gene- and cell-based therapies have been developed to deliver functional *Dmd* alleles or dystrophin-like protein to diseased muscle tissue, numerous therapeutic challenges have been encountered, and no curative treatment exists (*3*).

RNA-guided, nuclease-mediated genome editing, based on type II CRISPR (clustered regularly interspaced short palindromic repeat)/Cas (CRISPR-associated) systems, offers a new approach to alter the genome (*4*–*6*). In brief, Cas9, a nuclease guided by single-guide RNA (sgRNA), binds to a targeted genomic locus next to the protospacer adjacent motif (PAM) and generates a double-strand break (DSB). The DSB is then repaired either by nonhomologous end-joining (NHEJ), which leads to insertion/deletion (indel) mutations, or by homology-directed repair (HDR), which requires an exogenous template and can generate a precise modification at a target locus (*7*). Unlike other gene therapy methods, which add a functional, or partially functional, copy of a gene to a patient's cells but retain the original dysfunctional copy of the gene, this system can remove the defect. Genetic correction using engineered nucleases (*8*–*12*) has been demonstrated in immortalized myoblasts derived from DMD patients in vitro (*9*), and rodent models of rare diseases (*13*), but not yet in animal models of relatively common and currently incurable diseases, such as DMD.

The objective of this study was to correct the genetic defect in the *Dmd* gene of *mdx* mice by CRISPR/Cas9–mediated genome editing in vivo. The *mdx* mouse (C57BL/10ScSn-*Dmd*^{mdx}/J) contains a nonsense mutation in exon 23 of the *Dmd* gene (*14*, *15*) (Fig. 1A). We injected Cas9, sgRNA, and HDR template into mouse zygotes to correct the disease-causing gene mutation in the germ line (*16*, *17*), a strategy that has the potential to correct the mutation in all cells of the body, including myogenic progenitors. Safety and efficacy of CRISPR/Cas9–based gene therapy was also evaluated.

[1]Department of Molecular Biology and Hamon Center for Regenerative Science and Medicine, University of Texas Southwestern Medical Center, Dallas, TX 75390, USA. [2]Department of Internal Medicine, University of Texas Southwestern Medical Center, Dallas, TX 75390, USA. *These authors contributed equally to this work. †To whom correspondence should be addressed. E-mail: eric.olson@utsouthwestern.edu

Initially, we tested the feasibility and optimized the conditions of CRISPR/Cas9–mediated *Dmd* gene editing in wild-type mice (C57BL6/C3H and C57BL/6) (see the supplementary materials). We designed a sgRNA to target *Dmd* exon 23 (fig. S1A) and a single-stranded oligodeoxynucleotide (ssODN) as a template for HDR-mediated gene repair (fig. S1B and table S1). The wild-type zygotes were co-injected with Cas9 mRNA, sgRNA-DMD, and ssODN and then implanted into pseudopregnant female mice. Polymerase chain reaction (PCR) products corresponding to *Dmd* exon 23 from progeny mice were sequenced (fig. S1, C to E). Efficiency of CRISPR/Cas9–mediated *Dmd* gene editing is shown in table S2.

We next applied the optimized CRISPR/Cas9–mediated genomic editing method to *mdx* mice (Fig. 1B). The CRISPR/Cas9–mediated genomic editing system will correct the point mutation in *mdx* mice during embryonic development via HDR or NHEJ (Fig. 1, C and D, and fig. S2A). "Corrected" *mdx* progeny (termed *mdx*-C) were identified by restriction fragment length polymorphism (RFLP) analysis and the mismatch-specific T7 endonuclease I (T7E1) assay (Fig. 1E, table S2, and supplementary materials). We analyzed a total of 11 different *mdx*-C mice. PCR products of *Dmd* exon 23 from seven *mdx*-C mice with HDR-mediated gene correction (termed *mdx*-C1 to C7) and four *mdx*-C mice containing NHEJ-mediated in-frame deletions of the stop codon (termed *mdx*-N1 to N4) were sequenced. Sequencing results revealed that CRISPR/Cas9–mediated germline editing produced genetically mosaic *mdx*-C mice displaying from 2 to 100% correction of the *Dmd* gene (Fig. 1E and fig. S2, B and C). A wide range of mosaicism occurs if CRISPR/Cas9–mediated repair occurs after the zygote stage, resulting in genomic editing in a subset of embryonic cells (*18*). All mouse progeny developed to adults without signs of tumor growth or other abnormal phenotypes.

We tested four different mouse groups for possible off-target effects of CRISPR/Cas9–mediated genome editing: (A) *mdx* mice without treatment (termed *mdx*), (B) CRISPR/Cas9–edited *mdx* mice (termed *mdx*+Cas9), (C) Wild-type control mice (C57BL6/C3H) without treatment (termed WT) and (D) CRISPR/Cas9–edited wild-type mice (termed WT+Cas9) (fig. S3A). Sequences of the target site (*Dmd* exon 23) and a total of 32 potential off-target (OT) sites in the mouse genome were predicted by the CRISPR design tool (http://crispr.mit.edu) and are listed in table S3. Ten of the 32 sites, termed OT-01 through OT-10, represent the genome-wide "top-10 hits." Twenty-two of the 32, termed OTE-01 through OTE-22 are located within exons.

Deep sequencing of PCR products corresponding to *Dmd* exon 23 revealed high ratios of HDR and NHEJ-mediated genetic modification in groups B and D but not in control groups A and C (fig. S3A and table S4). There was no difference in the frequency of indel mutations in the 32 potential off-target regions among the different groups (fig. S3, B and C, table S5, and supplementary materials). These results are also consistent with recent genome-wide studies showing that DNA cleavage by Cas9 is not promiscuous (*19*–*21*). Thus, off-target effects may be less of a concern in vivo than previously observed in vitro (*22*, *23*).

To analyze the effect of CRISPR/Cas9–mediated genomic editing on the development of muscular dystrophy, we performed histological analyses of four different muscle types [quadriceps, soleus (hindlimb muscle), diaphragm (respiratory muscle), and heart muscle] from wild-type mice, *mdx* mice, and three chosen *mdx-C* mice with different percentages of *Dmd* gene correction at 7 to 9 weeks of age. *mdx* muscle showed histopathologic hallmarks of muscular dystrophy, including variation in fiber diameter, centralized nuclei, degenerating fibers, necrotic fibers, and mineralized fibers, as well as interstitial fibrosis (Fig. 2 and figs. S4A and S5A). Immunohistochemistry showed no dystrophin expression in skeletal muscle or heart of *mdx* mice, whereas wild-type mice showed dystrophin expression in the subsarcolemmal region of the fibers and the heart (Fig. 2). Although *mdx* mice carry a stop mutation in the *Dmd* gene, we observed 0.2 to 0.6% revertant fibers, consistent with a previous report (*24*). *mdx*-C mice with 41% of the

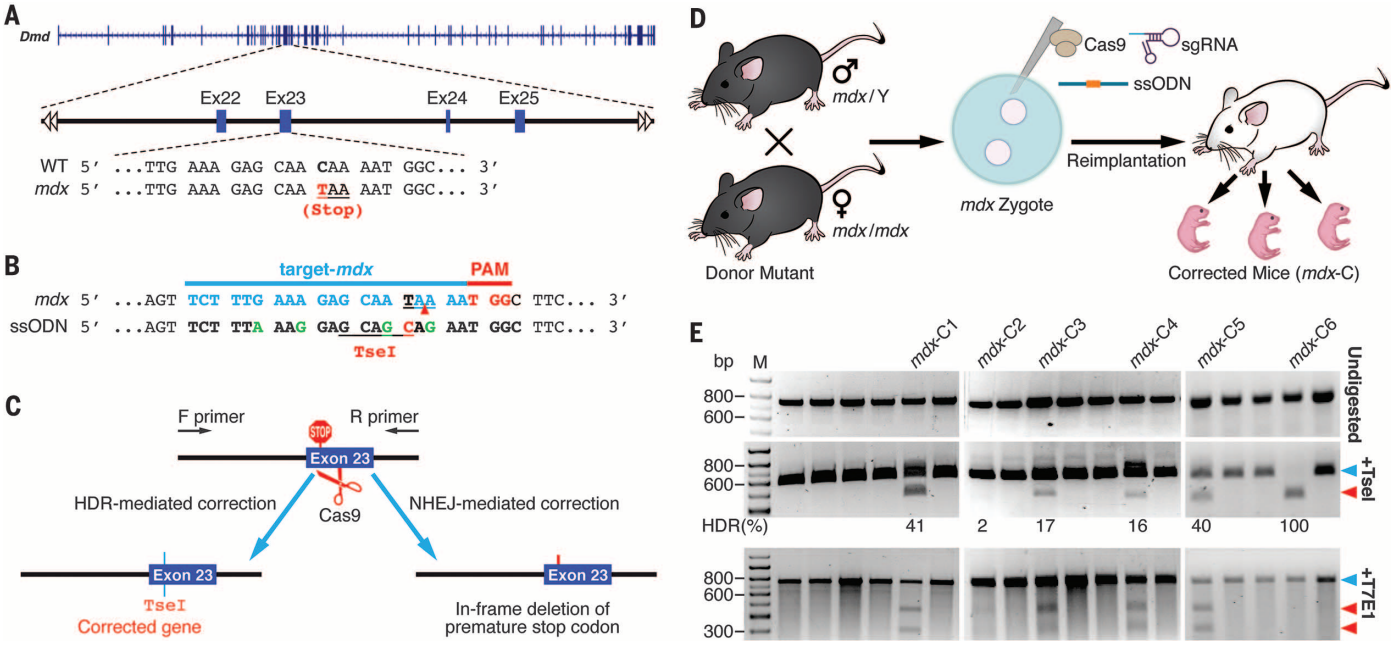

Fig. 1. CRISPR/Cas9–mediated *Dmd* correction in *mdx* mice. (**A**) Schematic of the targeted exon of mouse *Dmd* and sequence from wild-type (upper) and *mdx* mice (lower). The *mdx* point mutation (C to T) is marked in red, and the premature stop codon is underlined. (**B**) Schematic of the 20-nucleotide sgRNA target sequence of the *mdx* allele (blue) and the PAM (red). The red arrowhead indicates the Cas9 cleavage site. ssODN, which contains 90 base pairs (bp) of homology sequence flanking each side of the target site, was used as HDR template. ssODN incorporates four silent mutations (green) and adds a TseI restriction enzyme site (underlined) for genotyping and quantification of HDR-mediated gene editing (fig. S1B). (**C**) Schematic for the gene correction by HDR or NHEJ. The corresponding DNA and protein sequences are shown in fig. S2A. (**D**) Strategy of the gene correction in *mdx* mice via germline gene therapy. (**E**) Genotyping results of *mdx-C* mice with mosaicism of 2 to 100% corrected *Dmd* gene. Undigested PCR product (upper panel), TseI digestion (middle panel), and T7E1 digestion (lower panel) on a 2% agarose gel. The red arrowhead in the middle panel marks the DNA band indicating HDR-mediated correction generated by TseI digestion. The blue arrowhead marks the DNA band of the uncorrected *mdx* allele. The relative intensity of the DNA bands (indicated by blue and red arrowheads) reflects the percentage of HDR in the genomic DNA. The percentage of HDR is located under the middle panel. The band intensity was quantified by ImageJ (NIH). The blue and red arrowheads in the lower panel indicate uncut and cut bands by T7E1, respectively. M denotes size marker lane. bp indicates the length of the marker bands.

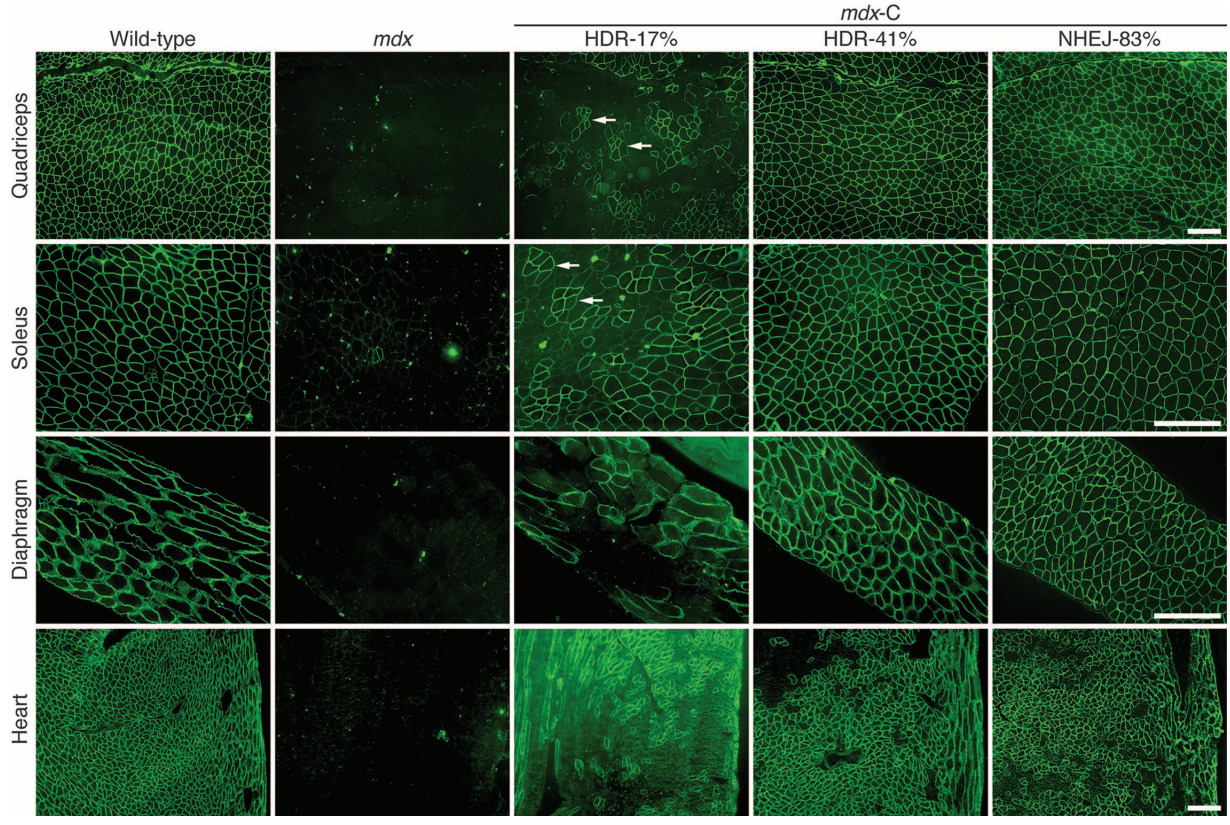

Fig. 2. Histological analysis of muscles from wild-type, *mdx*, and *mdx-C* mice. Immunostaining and histological analysis of muscles from 7- to 9-week-old wild-type, *mdx*, and *mdx*-C mice (HDR-17%, HDR-41%, or NHEJ-83%). Dystrophin immunofluorescence (green) in wild-type mice is present in all muscles, including quadriceps, soleus, diaphragm, and heart, and is absent in *mdx* mice, except for a single revertant fiber in skeletal muscle. Skeletal muscle from the HDR-17% mouse has a characteristic pattern of clusters of dystrophin-positive fibers adjacent to clusters of dystrophin-negative fibers, whereas HDR-41% or NHEJ-83% *mdx*-C skeletal muscle is composed of dystrophin-positive myofibers only. White arrows indicate the adjacent clusters of dystrophin-positive fibers. Scale bar, 100 μm.

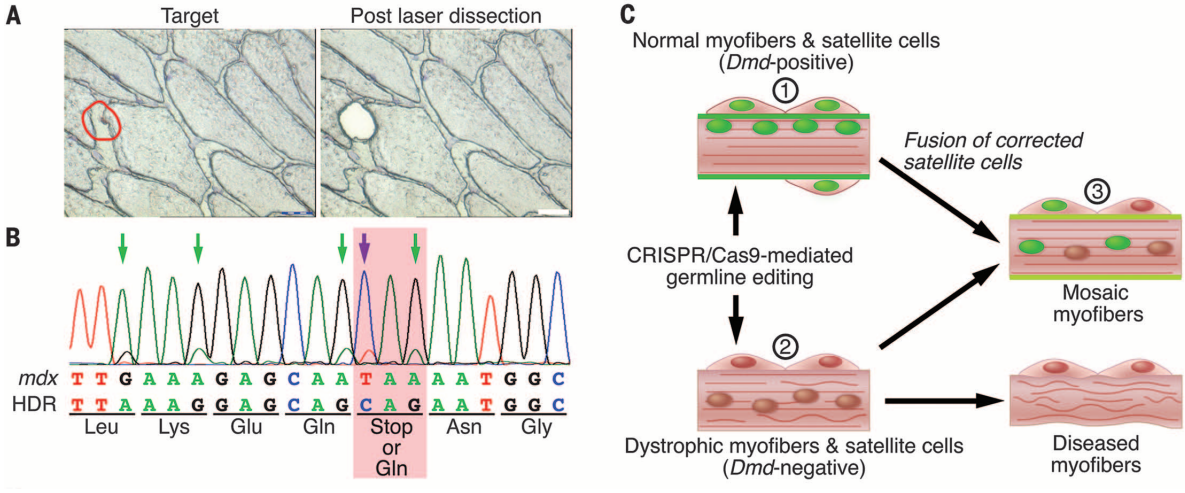

Fig. 3. Analysis of satellite cells from *mdx*-C mice and a model for rescue of muscular dystrophy by CRISPR/Cas9–mediated genomic correction. (**A**) Frozen sections of *mdx*-C gastrocnemius were mounted onto polyethylene membrane frame slides and immunohistochemically stained for Pax-7, a marker for satellite cells. Cross sections of muscle before (left) and after (right) laser dissection show the precise isolation of satellite cells (brown, in red circle). Scale bar, 25 μm. (**B**) PCR products corresponding to *Dmd* exon 23 were generated from genomic DNA isolated from satellite cells of *mdx*-C mice. PCR products were sequenced and show that CRISPR/Cas9–mediated genomic editing corrected a subset of satellite cells in vivo. Purple arrow indicates the corrected allele mediated by HDR. Green arrows indicate the silent mutation sites. The corresponding amino acid residues are shown under the DNA sequence. The red box indicates the corrected site. (**C**) A model for rescue of muscular dystrophy by CRISPR/Cas9–mediated genomic correction. There are three types of myofibers in *mdx*-C mice: (i) normal dystrophin-positive myofibers (green membrane) and satellite cells originating from corrected progenitors (green nuclei); (ii) dystrophic dystrophin-negative myofibers (brown membrane) and satellite cells originating from *mdx* progenitors (brown nuclei); and (iii) mosaic dystrophin-positive myofibers with centralized nuclei (green and brown nuclei) generated by fusion of corrected and *mdx* progenitors or by fusion of corrected satellite cells with preexisting dystrophic fibers. Immunostaining of the three types of myofibers in *mdx*-C mice is shown in fig. S8C.

Table 1. Serum creatine kinase (CK) levels and forelimb grip strength of wild-type, *mdx*, and *mdx*-C mice.

Litter	Mouse no.	Percent of correction	Sex	CK(U/L)	Forelimb grip strength (grams of force)					
					Trial 1	Trial 2	Trial 3	Trial 4	Trial 5	Avg. ± SD
No. 1	WT	–	M	318	170	163	140	132	169	154.8 ± 17.5
	mdx-04	0	M	6,366	64	56	52	59	57	57.6 ± 4.3
	mdx-06	0	M	7,118	102	123	109	79	97	102.0 ± 16.1
	***mdx*-C1**	**HDR-41%**	**M**	**350**	**141**	**150**	**154**	**143**	**133**	**144.2±8.1**
No. 2	WT	–	F	449	128	116	109	102	103	111.6 ± 10.7
	mdx-20	0	F	30,996	107	105	92	78	61	88.6 ± 19.3
	mdx-10	0	F	38,715	84	64	67	62	53	66.0 ± 11.3
	***mdx*-C3**	**HDR-17%**	**F**	**4,290**	**123**	**126**	**101**	**107**	**102**	**111.8±11.8**
No. 25	*mdx*-02	0	M	14,059	54	64	47	41	52	51.6 ± 12.1
	mdx-03	0	M	4,789	129	120	116	104	92	112.2 ± 35.6
	mdx-05	0	M	11,841	91	94	54	64	54	71.4 ± 24.0
	***mdx*-N1**	**NHEJ-83%**	**M**	**240**	**145**	**154**	**147**	**138**	**133**	**143.4±44.8**
	mdx-01	0	F	7,241	108	95	103	105	85	99.2 ± 30.5
	mdx-04	0	F	5,730	100	112	103	114	100	105.8 ± 32.3
	mdx-07	0	F	6,987	74	73	73	73	70	72.6 ± 19.6

mdx alleles corrected by HDR (termed HDR-41%) or with 83% correction by in-frame NHEJ (termed NHEJ-83%) showed complete absence of the dystrophic muscle phenotype and restoration of dystrophin expression in the subsarcolemmal region of all myofibers (Fig. 2). Strikingly, correction of only 17% of the mutant *Dmd* alleles (termed HDR-17%) was sufficient to allow dystrophin expression in a majority of myofibers at a level of intensity comparable to that of wild-type mice, and the muscle exhibited fewer histopathologic hallmarks of muscular dystrophy than *mdx* muscle (fig. S4A). The substantially higher percentage (47 to 60%) of dystrophin-positive fibers associated with only 17% gene correction (fig. S6, A and B) suggests a selective advantage of the corrected skeletal muscle cells. Western blot analysis showed restored dystrophin protein in skeletal muscle (quadriceps) and heart of *mdx*-C mice to levels consistent with percentages of dystrophin-positive fibers (figs. S4B and S6B).

To compare the efficiency of rescue over time, we chose *mdx-C* mice with comparable mosaicism of rescue of ~40%. As shown in fig. S7A, a 3-week-old *mdx*-C mouse with ~40% HDR-mediated gene correction (termed HDR-40%-3wks) showed occasional dystrophin-negative myofibers among a majority of dystrophin-positive fibers. In contrast, no dystrophin-negative fibers were seen in a mouse with comparable gene correction at 9 weeks of age, suggesting progressive rescue with age in skeletal muscle. In *mdx*-C mice with comparable mosaicism, we did not observe a significant difference in dystrophin expression in the heart between 3 and 9 weeks of age (fig. S7B), suggesting that age-dependent improvement may be restricted to skeletal muscle.

The widespread and progressive rescue of dystrophin expression in skeletal muscle might reflect the multinucleated structure of myofibers, such that a subset of nuclei with corrected *Dmd* genes can compensate for nuclei with *Dmd* mutations. Fusion of corrected satellite cells (the stem cell population of skeletal muscle) with dystrophic fibers might also progressively contribute to the regeneration of dystrophic muscle (*25*). To investigate this possibility, we identified satellite cells in muscle sections of *mdx*-C mice by immunostaining with Pax-7, a specific marker for satellite cells (fig. S8A). Using laser microdissection (see the supplementary materials), we dissected Pax-7 positive satellite cells and isolated genomic DNA for PCR analysis (Fig. 3A and fig. S8B). Sequencing results of PCR products corresponding to *Dmd* exon 23 from these isolated satellite cells showed the corrected *Dmd* gene (Fig. 3B). These results indicate that CRISPR/Cas9 genomic editing corrected the mutation in satellite cells allowing these muscle stem cells to rescue the dystrophic muscle (Fig. 3C and fig. S8C).

Serum creatine kinase (CK), a diagnostic marker for muscular dystrophy that reflects muscle leakage, was measured in wild-type, *mdx*, and *mdx*-C mice. Consistent with the histological results, serum CK levels of the *mdx*-C mice were substantially decreased compared with *mdx* mice and were inversely proportional to the percentage of genomic correction (Table 1). Wild-type, *mdx*, and *mdx*-C mice were also subjected to grip-strength testing to measure muscle performance, and the *mdx*-C mice showed enhanced muscle performance compared with *mdx* mice (Table 1).

Our results show that CRISPR/Cas9–mediated genomic editing is capable of correcting the primary genetic lesion responsible for muscular dystrophy (DMD) and preventing development of characteristic features of this disease in *mdx* mice. Because genome editing in the germ line produced genetically corrected animals with a wide range of mosaicism (2 to 100%), we were able to compare the percentage of genomic correction with the extent of rescue of normal muscle structure and function. We observed that only a subset of corrected cells in vivo is sufficient for complete phenotypic rescue. As schematized in Fig. 3C, histological analysis of partially corrected *mdx* mice revealed three types of myofibers: (i) normal dystrophin-positive myofibers; (ii) dystrophic dystrophin-negative myofibers; and (iii) mosaic dystrophin-positive myofibers containing centralized nuclei, indicative of muscle regeneration. We propose that the latter type of myofiber arises from the recruitment of corrected satellite cells into damaged myofibers, forming mosaic myofibers with centralized nuclei. Efforts to expand satellite cells ex vivo as a source of cells for in vivo engraftment have been hindered by the loss of proliferative potential and regenerative capacity of these cells in culture (*26*). Thus, direct editing of satellite cells in vivo by the CRISPR/Cas9 system represents a potentially promising alternative approach to promote muscle repair in DMD.

Genomic editing within the germ line is not currently feasible in humans. However, genomic editing could, in principle, be envisioned within postnatal cells in vivo if certain technical challenges could be overcome. For example, there is a need for appropriate somatic cell delivery systems capable of directing the components of the CRISPR/Cas9 system to dystrophic muscle or satellite cells in vivo. In this regard, the adeno-associated virus (AAV) delivery system has proven to be safe and effective and has already been advanced in clinical trials for gene therapy (*27*, *28*). Moreover, the AAV9 serotype has been shown to provide robust expression in skeletal muscle, heart, and brain, the major tissues affected in DMD patients. Other nonviral gene delivery methods, including injection of naked plasmid DNA (*29*), chemically modified mRNA (*30*, *31*), and nanoparticles containing nucleic acid (*32*), also warrant consideration. Another challenge with respect to the feasibility of clinical application of the CRISPR/Cas9 system is the increase in body size between rodents and humans, requiring substantial scale-up. More efficient genome editing in postnatal somatic tissues is also needed for the advancement of the CRISPR/Cas9 system into clinical use. Although CRISPR/Cas9 can effectively generate NHEJ-mediated indel mutations in somatic cells, HDR-mediated correction is relatively ineffective in postmitotic cells, such

as myofibers and cardiomyocytes, because these cells lack the proteins essential for homologous recombination (*33*). Coexpression of components of the HDR pathway with the CRISPR/Cas9 system might enhance HDR-mediated gene repair. Finally, safety issues of the CRISPR/Cas9 system, especially for long-term use, need to be evaluated in preclinical studies in large-animal models of disease. Despite the challenges listed above, with rapid technological advances of gene delivery systems and improvements to the CRISPR/Cas9 editing system (*33*), the approach we describe could ultimately offer therapeutic benefit to DMD and other human genetic diseases in the future.

REFERENCES AND NOTES

1. R. J. Fairclough, M. J. Wood, K. E. Davies, *Nat. Rev. Genet.* **14**, 373–378 (2013).
2. R. G. Worton, M. W. Thompson, *Annu. Rev. Genet.* **22**, 601–629 (1988).
3. J. C. van Deutekom, G. J. van Ommen, *Nat. Rev. Genet.* **4**, 774–783 (2003).
4. M. Jinek *et al.*, *Science* **337**, 816–821 (2012).
5. L. Cong *et al.*, *Science* **339**, 819–823 (2013).
6. P. Mali *et al.*, *Science* **339**, 823–826 (2013).
7. P. Mali, K. M. Esvelt, G. M. Church, *Nat. Methods* **10**, 957–963 (2013).
8. F. D. Urnov *et al.*, *Nature* **435**, 646–651 (2005).
9. D. G. Ousterout *et al.*, *Mol. Ther.* **21**, 1718–1726 (2013).
10. M. J. Osborn *et al.*, *Mol. Ther.* **21**, 1151–1159 (2013).
11. Y. Wu *et al.*, *Cell Stem Cell* **13**, 659–662 (2013).
12. G. Schwank *et al.*, *Cell Stem Cell* **13**, 653–658 (2013).
13. H. Yin *et al.*, *Nat. Biotechnol.* **32**, 551–553 (2014).
14. G. Bulfield, W. G. Siller, P. A. Wight, K. J. Moore, *Proc. Natl. Acad. Sci. U.S.A.* **81**, 1189–1192 (1984).
15. P. Sicinski *et al.*, *Science* **244**, 1578–1580 (1989).
16. H. Wang *et al.*, *Cell* **153**, 910–918 (2013).
17. H. Yang *et al.*, *Cell* **154**, 1370–1379 (2013).
18. S. T. Yen *et al.*, *Dev. Biol.* **393**, 3–9 (2014).
19. X. Wu *et al.*, *Nat. Biotechnol.* **32**, 670–676 (2014).
20. C. Kuscu, S. Arslan, R. Singh, J. Thorpe, M. Adli, *Nat. Biotechnol.* **32**, 677–683 (2014).
21. J. Duan *et al.*, *Cell Res.* **24**, 1009–1012 (2014).
22. V. Pattanayak *et al.*, *Nat. Biotechnol.* **31**, 839–843 (2013).
23. Y. Fu *et al.*, *Nat. Biotechnol.* **31**, 822–826 (2013).
24. S. R. Pigozzo *et al.*, *PLOS ONE* **8**, e72147 (2013).
25. H. Yin, F. Price, M. A. Rudnicki, *Physiol. Rev.* **93**, 23–67 (2013).
26. D. Montarras *et al.*, *Science* **309**, 2064–2067 (2005).
27. A. C. Nathwani *et al.*, *Mol. Ther.* **19**, 876–885 (2011).
28. M. A. Kotterman, D. V. Schaffer, *Nat. Rev. Genet.* **15**, 445–451 (2014).
29. B. Peng, Y. Zhao, H. Lu, W. Pang, Y. Xu, *Biochem. Biophys. Res. Commun.* **338**, 1490–1498 (2005).
30. M. S. Kormann *et al.*, *Nat. Biotechnol.* **29**, 154–157 (2011).
31. L. Zangi *et al.*, *Nat. Biotechnol.* **31**, 898–907 (2013).
32. T. J. Harris *et al.*, *Biomaterials* **31**, 998–1006 (2010).
33. P. D. Hsu, E. S. Lander, F. Zhang, *Cell* **157**, 1262–1278 (2014).

ACKNOWLEDGMENTS

We thank Z. Wang and B. Nelson for advice and constructive criticism; L. Sutherland, H. Zhou, and J. Ren for discussions and technical help; C. Xing and R. Kittler for analysis of off-target effects; S. Rovinsky and E. Plautz for grip-strength testing; and R. Hammer, J. Ritter, and J. Richardson for advice. We thank G. Church for hCas9 (human codon optimized Cas9) and the gRNA cloning vector plasmids. This work was supported by grants from NIH (HL-077439, HL-111665, HL-093039, DK-099653, and U01-HL-100401) and the Robert A. Welch Foundation (grant 1-0025 to E.N.O.).

SUPPLEMENTARY MATERIALS

www.sciencemag.org/content/345/6201/1184/suppl/DC1
Materials and Methods
Figs. S1 to S8
Tables S1 to S5
References (*34*–*37*)

7 April 2014; accepted 1 August 2014
Published online 14 August 2014;
10.1126/science.1254445

THE RIBOSOME

How the ribosome hands the A-site tRNA to the P site during EF-G–catalyzed translocation

Jie Zhou, Laura Lancaster, John Paul Donohue, Harry F. Noller*

Coupled translocation of messenger RNA and transfer RNA (tRNA) through the ribosome, a process catalyzed by elongation factor EF-G, is a crucial step in protein synthesis. The crystal structure of a bacterial translocation complex describes the binding states of two tRNAs trapped in mid-translocation. The deacylated P-site tRNA has moved into a partly translocated pe/E chimeric hybrid state. The anticodon stem-loop of the A-site tRNA is captured in transition toward the 30*S* P site, while its 3′ acceptor end contacts both the A and P loops of the 50*S* subunit, forming an ap/ap chimeric hybrid state. The structure shows how features of ribosomal RNA rearrange to hand off the A-site tRNA to the P site, revealing an active role for ribosomal RNA in the translocation process.

During the translocation step of the elongation phase of protein synthesis, the mRNA is advanced by one codon, coupled to movement of the tRNAs from the ribosomal A (aminoacyl) to P (peptidyl) and P to E (exit) sites, in a process catalyzed by elongation factor EF-G (*1*). First, the tRNAs move on the 50*S* subunit into P/E and A/P hybrid states, followed by movement of the tRNA anticodon stem-loops (ASLs) from the 30*S* subunit A and P sites to the P and E sites, respectively, coupled to movement of their associated mRNA codons (*2*). The first step is accompanied by intersubunit rotation (*3*–*7*), whereas the second step requires EF-G·guanosine triphosphate (GTP) and involves rotation of the 30*S* subunit head domain (*8*–*11*). Although much has recently been learned about the structural basis of P-tRNA movement to the E site (*9*, *10*, *12*, *13*), translocation intermediates containing A-tRNA are more difficult to trap. Thus, much of our thinking about the structural basis of A-tRNA and mRNA movement is based on crystal structures of EF-G bound to vacant (*14*) or P-tRNA–containing ribosome complexes trapped in classical (*15*) or hybrid states (*10*, *12*, *13*) and two cryogenic electron microscopy structures of 70*S* ribosome–EF-G complexes containing two tRNAs bound in P/E and A/P* hybrid states (*16*) or in ap/P and pe/E chimeric hybrid states (*11*). [We use lower-case letters to indicate that the tRNA is bound in a chimeric state within the small or large subunit, whereas upper-case letters indicate binding to the canonical A, P, or E sites of a subunit. For example, "pe/E" is meant to indicate that the ASL of the tRNA is bound between P-site elements of the small subunit head domain and E-site elements of the small subunit body, while its acceptor end is bound to the canonical E site of the large subunit.]

Center for Molecular Biology of RNA and Department of Molecular, Cell and Developmental Biology, University of California at Santa Cruz, Santa Cruz, CA 95064, USA.
***Corresponding author. E-mail: harry@nuvolari.ucsc.edu**

Here, we report the crystal structure of a 70*S* ribosome translocation intermediate containing EF-G, mRNA, and two tRNAs: a deacylated tRNA bound in the pe/E state and a peptidyl-tRNA trapped in an ap/ap chimeric hybrid state. The complex was formed with *Thermus thermophilus* 70*S* ribosomes, a 39-nucleotide mRNA, elongator $tRNA^{Met}$ in the P site, and *N*-acetyl-Val-$tRNA^{Val}$ in the A site. To trap the translocation intermediate, we added neomycin to block completion of translocation and fusidic acid to prevent release of EF-G (materials and methods and fig. S1). The structure was solved by using diffraction data to 3.8 Å obtained from a single crystal (table S1). Examples of electron density are shown in supplementary materials (figs. S2 to S13). Relative to the classical-state ribosome (*17*), the 30*S* subunit head undergoes a large 21° counterclockwise rotation, and the 30*S* body undergoes a 2.7° rotation relative to the 50*S* subunit (Figs. 1 and 2, A and B). The P-tRNA ASL moves with the 30*S* head into a position between the P site of the 30*S* head and the E site of the 30*S* body (pe chimeric state; Fig. 1, D and E), while its acceptor end moves fully into the 50*S* E site (Fig. 1C), forming a pe/E chimeric hybrid state (*9*–*11*). The A-tRNA ASL moves to within ~4 Å of the P-site elements of the 30*S* body (Fig. 1D); its elbow rotates toward the classical 50*S* P site, but its acceptor end is bound between the 50*S* subunit A and P sites (Fig. 1C), forming an ap/ap chimeric hybrid state. The large, EF-G–dependent rotation of the 30*S* head in our structure repositions helix H38 of 23*S* ribosomal RNA (rRNA), allowing the A-tRNA elbow to reach the position of the P-site tRNA elbow (fig. S14). Domain IV of EF-G is wedged into the site of convergence of the A-site mRNA codon, the anticodon loop of the ap/ap tRNA, and the 16*S* and 23*S* rRNAs at intersubunit bridge B2a, simultaneously contacting all four RNAs (fig. S15).

Although it is clear that 30*S* head rotation facilitates P-site ASL translocation (*9*–*11*), the A-site

ASL is translocated by a different mechanism. The P-site ASL moves precisely with 30*S* head rotation into the pe/E state, whereas the A-site ASL has moved further than the rotational movement of the head into the ap state on the 30*S* subunit (Fig. 1E). Movement of the A-site ASL precisely with head rotation would result in a severe clash with domain IV of EF-G as it is positioned in our complex, which, together with the contact formed between the tip of domain IV and the codon-anticodon helix of the ap/ap tRNA (fig. S16), suggests that movement of mRNA and ASL is coupled to that of domain IV. The additional displacement of the ap/ap ASL brings it close to the pe/E ASL (Fig. 2, C and D) (*11*). The position of the head may be stabilized by interaction between phosphate 1210 of 16*S* rRNA and domain IV of EF-G at Gly^{531} (G531).

Most notable is the rearrangement of the 16*S* rRNA 966 loop in the 30*S* head, which breaks away from the P site to reach toward the A site, where it initiates contact with the partly translocated ap/ap ASL (Fig. 2, E and F). This rearrangement involves disruption of the packing of $m^2{}_2$G966 against ribose 34 of the P-site ASL (*18*, *19*) and formation of a surface-fitting pocket around the ap/ap ASL by nucleotides A965, $m^2{}_2$G966, and C1400. In a crystal structure of the corresponding single-tRNA complex (*10*) (fig. S6), the pe/E tRNA ASL was found to maintain all canonical P-site contacts with the 30*S* head, including the 966 loop, as it rotates toward the E site. However, in the two-tRNA complex reported here, only a subset of the P-site 30*S* head interactions with the pe/E ASL are maintained, involving G1338, A1339, A1340, and the C-terminal tail of protein uS9. The formation of posttranslocation interactions simultaneously with disruption of pretranslocation interactions suggests a mechanism for how the ASLs are handed off between the A and the P sites. It may also represent an initial shift in contacts that must be disrupted to release the pe/E tRNA ASL before back-rotation of the 30*S* head in the final stages of translocation (*20*, *21*).

The network of interactions formed among the conserved loop 1 (residues 499 to 504) in domain IV of EF-G, the ap/ap ASL, and its mRNA codon (fig. S15) (*11*) are similar to those observed in the posttranslocation state (*15*), suggesting that they are maintained throughout the translocation cycle. Their resemblance to the minor-groove interactions made by A1492 and A1493 with the codon-anticodon helix in the decoding site (*22*) suggests that they may help to maintain correct codon-anticodon pairing during movement between the A and the P sites (*15*) and are consistent with the proposal that EF-G facilitates translocation by destabilizing interactions in the 30*S* decoding site (*23*).

Interactions between the mRNA and elements of the 30*S* head within the downstream mRNA entry tunnel have been proposed to carry the mRNA forward with the tRNA during head rotation (*17*). However, it is not clear that net

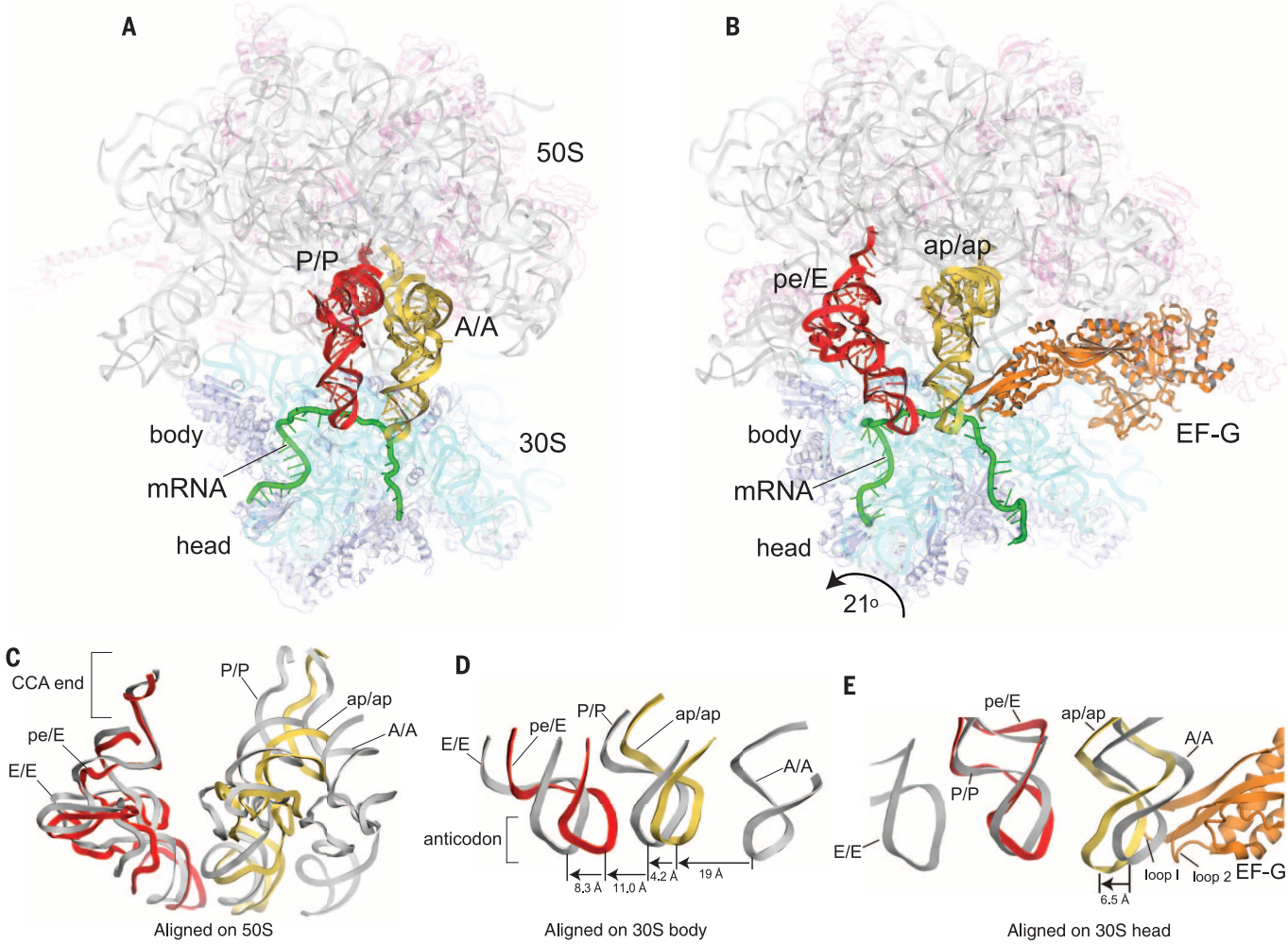

Fig. 1. Structure of trapped translocation intermediate containing EF-G, mRNA, and two partially translocated tRNAs. (**A**) A 70*S* ribosome with tRNAs bound in classical A/A and P/P states (*17*). (**B**) Translocation intermediate complex, showing tRNAs trapped in intermediate chimeric hybrid ap/ap and pe/E states. (**C**) Comparison of positions of tRNA in classical states and in the translocation intermediate, aligned on the 50*S* subunit; (**D**) relative positions of tRNA ASLs, aligned on the 30*S* subunit body or (**E**) head. Molecular components are colored throughout as follows: 16*S* rRNA, cyan; 30*S* proteins, blue; 23*S* rRNA, gray; 5*S* rRNA, light blue; 50*S* proteins, magenta; mRNA, green; A/A and ap/ap tRNAs, yellow; P/P and pe/E tRNAs, red; EF-G, orange.

movement of the mRNA could be sustained in this way, because these interactions are disrupted during head rotation. We find that the extended tail of the mRNA, as it emerges from the downstream tunnel, curves upward to bind to the surface of protein uS3 in the head of the subunit (Fig. 3 and fig. S17). Thus, forward head rotation would actively move the mRNA in the direction of translocation. Comparison of the position of a reference nucleotide on the mRNA in the rotated and nonrotated states further shows that forward head rotation would advance the mRNA by one codon (Fig. 3D), supporting the possibility that the mRNA is actively moved by the ribosome during translocation. Because the dimensions of the downstream tunnel exclude entry of an RNA helix, disruption of mRNA secondary structure by the ribosomal helicase (*24*) must occur at or near the entry to the tunnel, by interaction with the ribosome outside the tunnel. Binding of the mRNA tail immediately flanking the entrance to the tunnel exclusively to the 30*S* head provides such an interaction. The forces created by head rotation could thus destabilize base pairing in helical elements of mRNA as they enter the downstream tunnel.

In the classical state, C74 and C75 in the CCA tail of P-site tRNA form base pairs with G2252 and G2251, respectively, in the P loop (helix H80) of 23*S* rRNA, while C75 of the A-site tRNA pairs with G2553 in the A loop (H92) (*18*, *25*, *26*). These interactions position the peptidyl and aminoacyl moieties for the peptidyl transferase reaction (*27*), which leaves a deacylated tRNA in the P site and a peptidyl-tRNA in the A site. A critical step in translocation is therefore the subsequent movement of the peptidyl-CCA end from the A loop to the P loop. The structure of the translocation intermediate reveals a chimeric state, distinct from those previously described (fig. S18), in which the acceptor end of the peptidyl-tRNA interacts simultaneously with both the A and P loops (Fig. 4). In this state, base pairing of C75 with G2553 of the A loop is preserved, while movement of its acceptor stem into a position near that of classical P-site tRNA allows G2252 and G2253 in a rearranged P loop to contact the tRNA backbone at positions 72 and 70 (Fig. 4B). Thus, the end of the acceptor stem of the ap/ap tRNA is anchored on the P loop, facilitating transfer of its adjacent C74 and C75 residues from the A loop to the P loop. A76 of the ap/ap tRNA is oriented similarly to that observed for tRNA bound in the P/P classical state (*17*), with its *N*-acetyl-valine peptidyl moiety positioned at the entrance to the peptide exit tunnel, whereas C74 and C75 maintain their interactions with the A loop of 23*S* rRNA (Fig. 4 and fig. S19).

The ap/ap tRNA may correspond to intermediate states that have been characterized kinetically. Fluorescence-quenching kinetic studies identified an EF-G–dependent intermediate (INT) in which the peptidyl-tRNA elbow moves from the A site toward the P site but remains only partially reactive with the aminoacyl-tRNA mimic puromycin, suggesting that its CCA end is not fully accommodated into the P site (*28*). Kinetic studies in which a probe was attached directly to the peptidyl-tRNA CCA end identified EF-G–dependent translocation intermediates in which the acceptor end of peptidyl-tRNA moves toward the P site but remains puromycin-unreactive (*29*). The properties of these intermediates are compatible with the trapped ap/ap state observed in this study. The structure of this trapped translocation intermediate begins to describe how tRNA moves between the ribosomal A and P sites. The tRNA binding sites themselves are dynamic, forming simultaneous contacts between the A-tRNA and elements of both the A and P sites, resembling the passing of the baton in a relay race (*30*). This is seen for both 30*S* and 50*S* subunits. In the 30*S* subunit, rearrangement of the 966 loop of 16*S* rRNA releases G966 from the P-site ASL to contact the A-site ASL as it moves into the 30*S* P site (Fig. 2, E and F). In the 50*S* subunit, the A and P loops of 23*S* rRNA rearrange to allow both loops to contact the 3′-acceptor end of the A-site tRNA as it begins its transition into the 50*S* P site (Fig. 4). These findings show that the structural dynamics of ribosomal RNA play an active role in the mechanism of translocation.

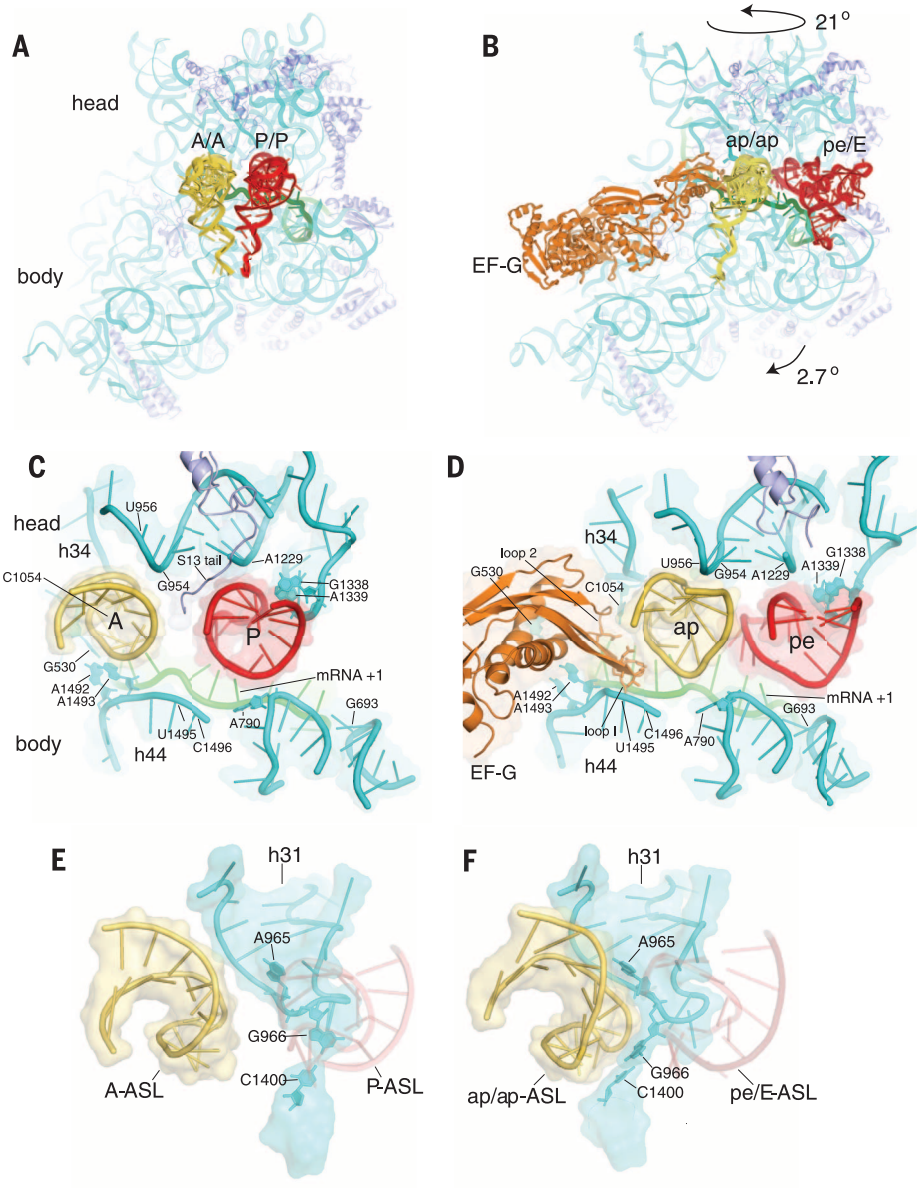

Fig. 2. Movement of tRNA ASLs on the 30S subunit and capture of translocating A-tRNA by P-site elements of the 30S subunit head. (**A** and **B**) Positions of tRNAs in the (A) classical-state ribosome and (B) translocation intermediate. (**C** and **D**) Interactions of the tRNA ASLs and mRNA as they move from the (C) A and P classical states to the (D) ap and pe chimeric hybrid states. (**E** and **F**) Rearrangement of the 966 loop (h31) of 16*S* rRNA in the 30*S* subunit head from its (E) classical P-tRNA–binding position to (F) forms a surface-fitting pocket around the ap/ap tRNA ASL.

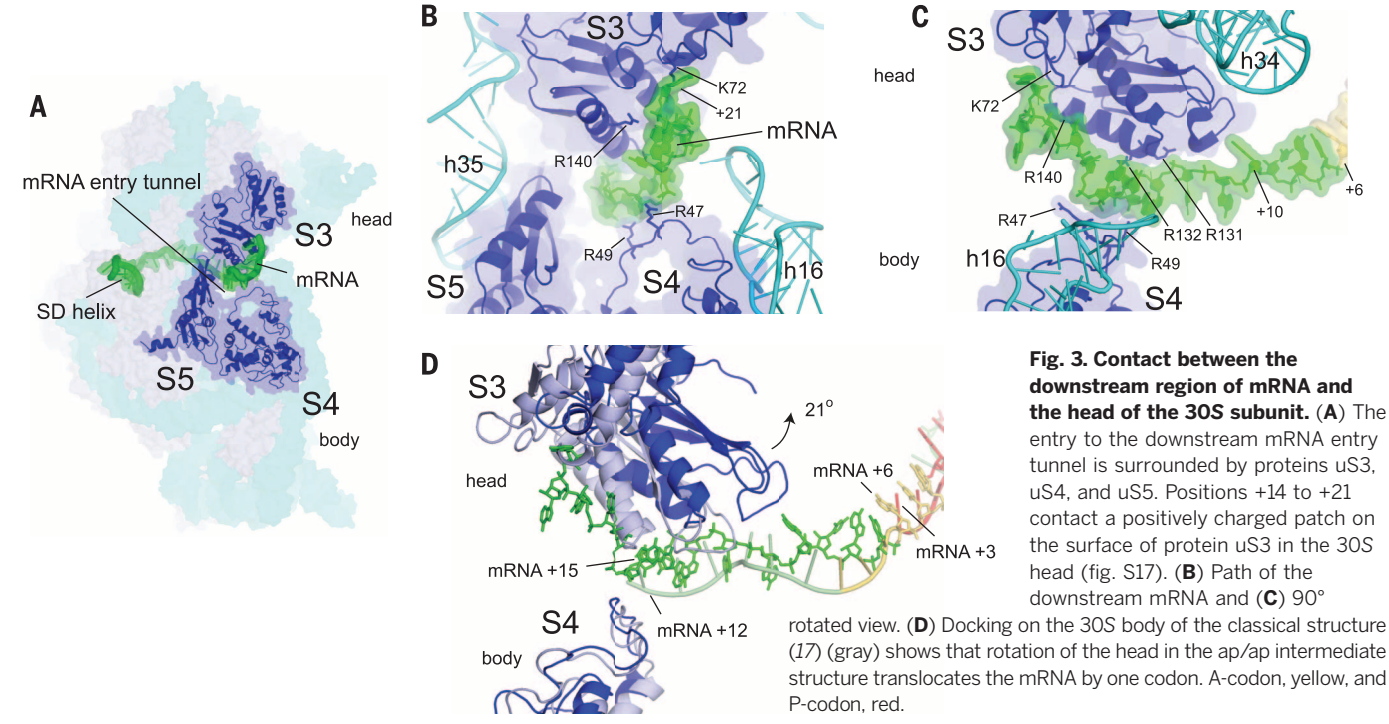

Fig. 3. Contact between the downstream region of mRNA and the head of the 30S subunit. (**A**) The entry to the downstream mRNA entry tunnel is surrounded by proteins uS3, uS4, and uS5. Positions +14 to +21 contact a positively charged patch on the surface of protein uS3 in the 30S head (fig. S17). (**B**) Path of the downstream mRNA and (**C**) 90° rotated view. (**D**) Docking on the 30S body of the classical structure (*17*) (gray) shows that rotation of the head in the ap/ap intermediate structure translocates the mRNA by one codon. A-codon, yellow, and P-codon, red.

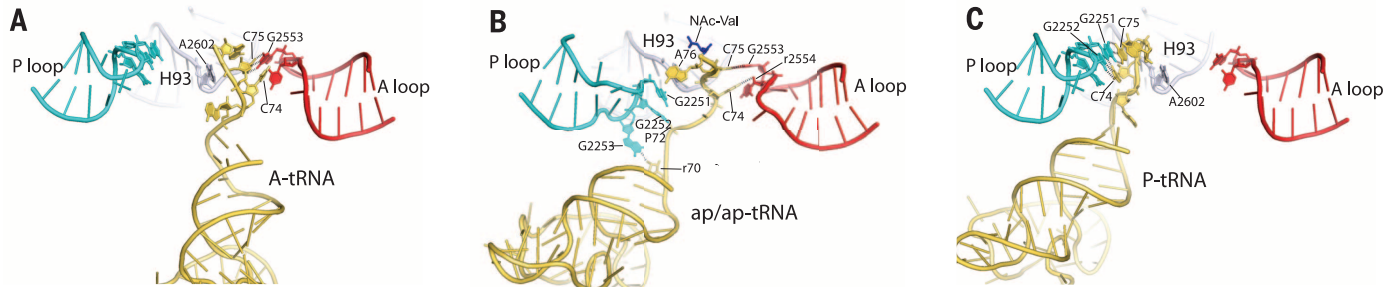

Fig. 4. The acceptor end of ap/ap tRNA simultaneously contacts the A and P loops of 23S rRNA. During translocation, the 3′ acceptor end of peptidyl-tRNA moves from the (**A**) classical A/A state to the (**B**) intermediate ap/ap state to the (**C**) classical P/P states, facilitated by conformational changes in the A and P loops.

REFERENCES AND NOTES

1. M. V. Rodnina, A. Savelsbergh, V. I. Katunin, W. Wintermeyer, *Nature* **385**, 37–41 (1997).
2. D. Moazed, H. F. Noller, *Nature* **342**, 142–148 (1989).
3. J. Frank, R. K. Agrawal, *Nature* **406**, 318–322 (2000).
4. M. Valle *et al.*, *Cell* **114**, 123–134 (2003).
5. X. Agirrezabala *et al.*, *Mol. Cell* **32**, 190–197 (2008).
6. P. Julián *et al.*, *Proc. Natl. Acad. Sci. U.S.A.* **105**, 16924–16927 (2008).
7. D. N. Ermolenko *et al.*, *J. Mol. Biol.* **370**, 530–540 (2007).
8. B. S. Schuwirth *et al.*, *Science* **310**, 827–834 (2005).
9. A. H. Ratje *et al.*, *Nature* **468**, 713–716 (2010).
10. J. Zhou, L. Lancaster, J. P. Donohue, H. F. Noller, *Science* **340**, 1236086 (2013).
11. D. J. Ramrath *et al.*, *Proc. Natl. Acad. Sci. U.S.A.* **110**, 20964–20969 (2013).
12. Y. Chen, S. Feng, V. Kumar, R. Ero, Y. G. Gao, *Nat. Struct. Mol. Biol.* **20**, 1077–1084 (2013).
13. D. S. Tourigny, I. S. Fernández, A. C. Kelley, V. Ramakrishnan, *Science* **340**, 1235490 (2013).
14. A. Pulk, J. H. Cate, *Science* **340**, 1235970 (2013).
15. Y. G. Gao *et al.*, *Science* **326**, 694–699 (2009).
16. A. F. Brilot, A. A. Korostelev, D. N. Ermolenko, N. Grigorieff, *Proc. Natl. Acad. Sci. U.S.A.* **110**, 20994–20999 (2013).
17. L. B. Jenner, N. Demeshkina, G. Yusupova, M. Yusupov, *Nat. Struct. Mol. Biol.* **17**, 555–560 (2010).
18. M. Selmer *et al.*, *Science* **313**, 1935–1942 (2006).
19. V. Berk, W. Zhang, R. D. Pai, J. H. Cate, *Proc. Natl. Acad. Sci. U.S.A.* **103**, 15830–15834 (2006).
20. B. R. Cunha, F. Peske, W. Holtkamp, W. Wintermeyer, M. V. Rodnina, *Translation* **1**, e24315 (2013).
21. Z. Guo, H. F. Noller, *Proc. Natl. Acad. Sci. U.S.A.* **109**, 20391–20394 (2012).
22. J. M. Ogle *et al.*, *Science* **292**, 897–902 (2001).
23. P. K. Khade, S. Joseph, *Nat. Struct. Mol. Biol.* **18**, 1300–1302 (2011).
24. S. Takyar, R. P. Hickerson, H. F. Noller, *Cell* **120**, 49–58 (2005).
25. R. R. Samaha, R. Green, H. F. Noller, *Nature* **377**, 309–314 (1995).
26. D. F. Kim, R. Green, *Mol. Cell* **4**, 859–864 (1999).
27. J. L. Hansen, T. M. Schmeing, P. B. Moore, T. A. Steitz, *Proc. Natl. Acad. Sci. U.S.A.* **99**, 11670–11675 (2002).
28. D. Pan, S. V. Kirillov, B. S. Cooperman, *Mol. Cell* **25**, 519–529 (2007).
29. W. Holtkamp *et al.*, *EMBO J.* **33**, 1073–1085 (2014).
30. L. V. Bock *et al.*, *Nat. Struct. Mol. Biol.* **20**, 1390–1396 (2013).

ACKNOWLEDGMENTS

This work was supported by NIH grants GM-17129 and GM59140. We thank the beamline staffs at the Advanced Light Source, Stanford Synchrotron Radiation Laboratory, and Advanced Photon Source for their expert support. Structures have been deposited with Protein Data Bank (PDB) accession numbers 4QS0, 4QS1, 4QS2, and 4QS3.

SUPPLEMENTARY MATERIALS

www.sciencemag.org/content/345/6201/1188/suppl/DC1
Materials and Methods
Figs. S1 to S20
Table S1
References (*31*–*49*)

21 April 2014; accepted 7 August 2014
10.1126/science.1255030

NEURODEGENERATION

C9orf72 repeat expansions cause neurodegeneration in *Drosophila* through arginine-rich proteins

Sarah Mizielinska,[1]* Sebastian Grönke,[2]* Teresa Niccoli,[2,3]* Charlotte E. Ridler,[1] Emma L. Clayton,[1] Anny Devoy,[1] Thomas Moens,[1,3] Frances E. Norona,[1] Ione O. C. Woollacott,[1] Julian Pietrzyk,[1] Karen Cleverley,[1] Andrew J. Nicoll,[1,4] Stuart Pickering-Brown,[5] Jacqueline Dols,[2] Melissa Cabecinha,[3] Oliver Hendrich,[2] Pietro Fratta,[1,6] Elizabeth M. C. Fisher,[1,6] Linda Partridge,[2,3]† Adrian M. Isaacs[1]†

An expanded GGGGCC repeat in *C9orf72* is the most common genetic cause of frontotemporal dementia and amyotrophic lateral sclerosis. A fundamental question is whether toxicity is driven by the repeat RNA itself and/or by dipeptide repeat proteins generated by repeat-associated, non-ATG translation. To address this question, we developed in vitro and in vivo models to dissect repeat RNA and dipeptide repeat protein toxicity. Expression of pure repeats, but not stop codon–interrupted "RNA-only" repeats in *Drosophila* caused adult-onset neurodegeneration. Thus, expanded repeats promoted neurodegeneration through dipeptide repeat proteins. Expression of individual dipeptide repeat proteins with a non-GGGGCC RNA sequence revealed that both poly-(glycine-arginine) and poly-(proline-arginine) proteins caused neurodegeneration. These findings are consistent with a dual toxicity mechanism, whereby both arginine-rich proteins and repeat RNA contribute to *C9orf72*-mediated neurodegeneration.

Frontotemporal dementia (FTD) and amyotrophic lateral sclerosis (ALS) are adult-onset, neurodegenerative diseases associated with personality change, language dysfunction, and progressive muscle weakness. These syndromes overlap genetically and pathologically, and can also co-occur in individuals and within families (*1*). An intronic GGGGCC hexanucleotide repeat expansion in *C9orf72* is the most common genetic cause of both FTD and ALS (C9FTD/ALS) (*2*–*4*) and can be found in patients diagnosed with all common neurodegenerative diseases (*5*). Healthy individuals carry fewer than 33 hexanucleotide repeats, with two repeats being the most common, whereas C9FTD/ALS cases carry between 400 and 4400 repeats (*2*, *5*, *6*).

The repeat expansion could cause disease by three possible mechanisms: (i) toxic sense and/or antisense repeat RNA species that sequester key RNA binding proteins, (ii) toxic dipeptide repeat (DPR) proteins generated by repeat-associated, non-ATG (RAN) translation, or (iii) reduced expression of *C9orf72*. The absence of a severe phenotype in a homozygous *C9orf72* mutation case (*7*) and the lack of *C9orf72* coding mutations (*8*) argue against loss of function as a primary mechanism. Neuronal aggregates of RNA, termed RNA foci, generated from both sense and antisense repeat transcripts are frequent in the brains of C9FTD/ALS patients (*9*–*13*). The GGGGCC repeat can be translated in all sense and antisense frames, two of which encode the same DPR; this results in five DPR proteins, all of which form inclusions in widespread brain regions (*10*, *12*, *14*–*18*). It is therefore of fundamental importance to understand the contributions of repeat RNA and DPR proteins to *C9orf72*-mediated neurodegeneration.

A major obstacle in the investigation of large expanded repeats is that they are inherently unstable. We used recombination-deficient *Escherichia coli* and a cloning strategy termed recursive directional ligation (*19*) to sequentially build seamless pure repeats from small GGGGCC-repeat units (fig. S1). This allowed generation of a stable range of pure repeats from 3 to a maximum of 103 (Fig. 1A). To dissect repeat RNA and DPR protein toxicity, we generated "RNA-only" repeats, using our cloning strategy to insert interruptions containing stop codons in all sense and antisense frames. In models of other non-coding repeat expansion disorders, interruptions comprising 4 to 11% of the total repeat sequence confer stability while maintaining pathogenicity in vitro and in vivo (*20*–*22*). One of three 6–base pair interruptions, each containing one stop codon in the sense and one in the antisense direction, were inserted every 12 GGGGCC repeats, resulting in a stop codon for all six (sense and antisense) frames, and interruptions that comprised 8% of the total sequence (fig. S2). We generated stop codon–interrupted RNA-only repeats equivalent in length to our pure repeats and longer RNA-only repeats up to ~288 (Fig. 1A). GGGGCC-repeat RNA forms a stable tertiary structure termed a G-quadruplex (*23*). Circular dichroism showed that the RNA-only repeats formed RNA G-quadruplexes similarly to pure repeat RNA (Fig. 1B), hence the interruptions did not affect the tertiary structure of the RNA. To investigate the formation of RNA foci, we expressed constructs in the human neuroblastoma cell line SH-SY5Y. RNA fluorescence in situ hybridization (FISH) showed that formation of RNA foci was length-dependent for both pure and RNA-only repeats, which, at equivalent length, had the same propensity to form foci (Fig. 1, C and D).

To differentiate between repeat RNA and DPR protein toxicity in vivo, we generated lines of the fruit fly *Drosophila melanogaster* carrying a range of our pure and RNA-only repeats under the UAS promoter, integrated into the same genomic location to ensure equivalent expression levels. When expressed specifically in the adult fly, the different repeats expressed sense transcripts at comparable levels and of the expected sizes, but no antisense transcripts (fig. S3A). RNA FISH showed that pure and RNA-only repeats were both able to generate RNA foci in *Drosophila* (fig. S4). Immunoblotting with an antibody to poly-(GR) (Fig. 2A) or to poly-(GP) (fig. S5B) showed that, as expected, the pure repeats generated DPR proteins and the RNA-only repeats did not. Constitutive expression of both 36 and 103 pure repeats in the eye, using the GMR-Gal4 driver, caused eye degeneration, whereas 36, 108, and ~288 RNA-only repeats had no effect under the same conditions (Fig. 2B). The toxicity of the pure repeats was thus attributable to the presence of DPR proteins. Increasing expression levels of the pure repeats by increasing the temperature (*24*) led to lethality from both 36 and 103 repeats (Fig. 2C and fig. S6) but for the RNA-only repeats had no effect, again demonstrating that the pure repeats caused lethality through the production of DPR proteins.

The GMR-Gal4 driver is expressed throughout *Drosophila* development. However, ALS and FTD are adult-onset diseases. To circumvent developmental effects, we confined expression of the repeat constructs to adult neurons, using the inducible elav-GeneSwitch driver. Expression of 36 and 103 repeats killed all flies by 30 days after eclosion. No effect was observed for 36, 108, and ~288 RNA-only repeats, which suggested that the neurotoxicity of the pure repeats was attributable to DPR protein production (Fig. 2D). To confirm this, we used a sublethal dose of cycloheximide to reduce protein synthesis in the flies expressing 36 and 103 pure repeats, which ameliorated the reduction in life span caused by the pure repeats (Fig. 2E). This result again showed that toxicity was attributable to DPR proteins.

To assess whether DPR protein expression alone was sufficient for toxicity, we generated "protein-only" constructs by using alternative codons to those found within the GGGGCC repeat. We compared the two arginine-containing DPR proteins, glycine-arginine (GR) and proline-

[1]Department of Neurodegenerative Disease, UCL Institute of Neurology, London WC1N 3BG, UK. [2]Max Planck Institute for Biology of Ageing, 50931 Cologne, Germany. [3]Department of Genetics, Evolution and Environment, Institute of Healthy Ageing, University College London, London WC1E 6BT, UK. [4]MRC Prion Unit, UCL Institute of Neurology, London WC1N 3BG, UK. [5]Institute of Brain, Behaviour and Mental Health, Faculty of Human and Medical Sciences, University of Manchester, Manchester M13 9PT, UK. [6]MRC Centre for Neuromuscular Disease, UCL Institute of Neurology, London WC1N 3BG, UK.
*These authors contributed equally to this work. **†Corresponding author. E-mail: a.isaacs@prion.ucl.ac.uk (A.M.I.); l.partridge@ucl.ac.uk (L.P.)**

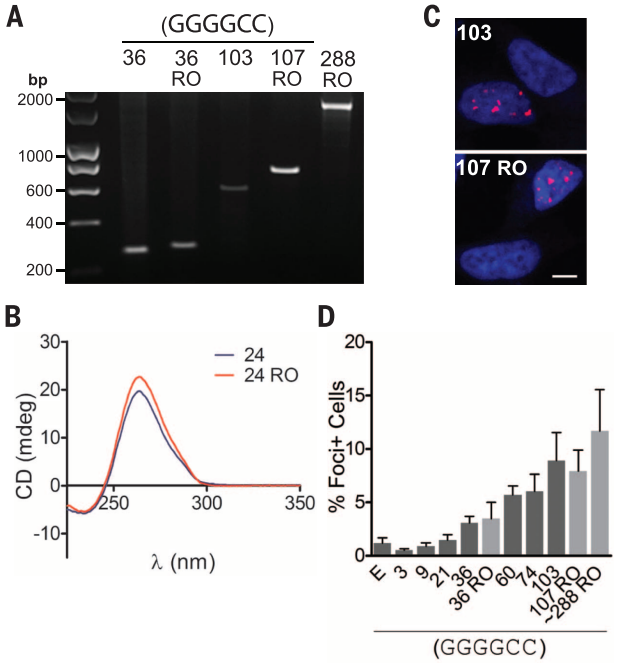

Fig. 1. Generation and characterization of expanded pure and RNA-only GGGGCC repeats. (**A**) Agarose gel showing pure GGGGCC repeats and stop codon–interrupted RNA-only (RO) repeats. (**B**) Circular dichroism (CD) spectra of 24 pure and 24 RO repeats showed characteristic RNA G-quadruplex structure with minima and maxima at 237 and 262 nm, respectively (*23*). (**C**) Confocal microscope images of nuclei (blue) in RNA FISH–labeled SH-SY5Y cells showed that 103 pure and 107 RO repeats both produced nuclear RNA foci (red). Scale bar, 5 μm. (**D**) Quantification of the number of SH-SY5Y cells containing RNA foci after transfection with pure and RO repeats of different lengths; E, empty vector. No difference was observed between equivalent-length pure and RO repeats [36 pure versus 36 RO, 103 pure versus 107 RO, one-way analysis of variance with Bonferroni test (selected pairs), $n > 3$; error bars represent SEM].

arginine (PR), with two neutral DPR proteins, proline-alanine (PA) and glycine-alanine (GA). When constructs containing 36 DPRs (equivalent to 36 pure GGGGCC repeats) were expressed in the fly eye, the arginine-containing DPR proteins GR and PR caused eye degeneration and lethality, whereas GA and PA DPR proteins had no effect (Fig. 3, A and C). Thus, the arginine-containing DPR proteins induced toxicity. We next generated longer protein-only sequences, of equivalent length to 103 pure repeats. Expression of $(PR)_{100}$ or $(GR)_{100}$ caused eye degeneration and increased lethality, whereas $(PA)_{100}$ and $(GA)_{100}$ had no effect (Fig. 3, B and C). Expression of $(PR)_{100}$ and $(GR)_{100}$ in adult neurons caused a substantial decrease in survival (Fig. 3D); a late-onset reduction in survival was also observed in $(GA)_{100}$-expressing flies, whereas $(PA)_{100}$ had no effect. Expression levels varied among the individual protein-only constructs but did not correlate with toxicity (fig. S3C), which was therefore attributable to the arginine-rich sequences. Thus, the highly basic arginine-containing DPR proteins drove *C9orf72* GGGGCC-repeat toxicity in *Drosophila* neurons.

Our data identified GR and PR DPR proteins as the predominant toxic protein species, although all five DPR proteins form inclusions in affected brain regions. Similarly, the distribution of poly-(GA) inclusions does not correlate well

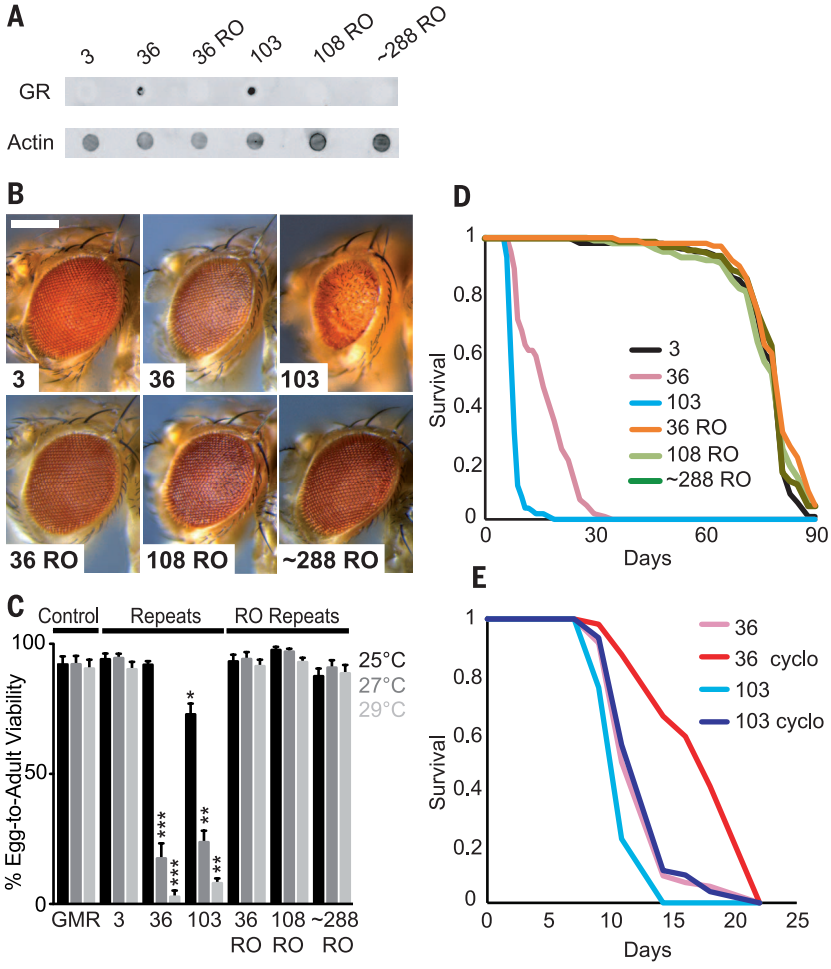

Fig. 2. Pure GGGGCC repeats caused toxicity via DPR proteins. (**A**) Dot blot showing that 36 and 103 pure repeats generated poly-(GR) proteins, whereas 3 pure repeats and 36, 108, and ~288 RNA-only (RO) repeats did not. Genotypes: *w;UAS-3/hsGal4*, *w;UAS-36/hsGal4*, *w;UAS-103/hsGal4*, *w;UAS-36 RO/hsGal4*, *w;UAS-108 RO/hsGal4*, *w;UAS-288 RO/hsGal4*. (**B**) Stereomicroscopy images of representative *Drosophila* eyes expressing pure or RO repeats using the GMR-GAL4 driver. We found that 36 pure repeats were mildly toxic, 103 pure repeats showed more overt toxicity, and 3 pure repeats and 36 and 108 RO repeats had no effect. Genotypes: *w;GMR-Gal4/+*, *w;GMR-Gal4/UAS-3*, *w;GMR-Gal4/UAS-36*, *w;GMR-Gal4/UAS-103*, *w;GMR-Gal4/UAS-36RO*, *w;GMR-Gal4/UAS-108RO*, *w;GMR-Gal4/UAS-288RO*. Scale bar, 200 μm. (**C**) Quantification of egg-to-adult viability showed that 36 and 103 pure repeats were lethal at higher temperatures, whereas RO repeats had no effect [Kruskal-Wallis test with Dunn's multiple comparison (selected pairs), $^{***}P < 0.001$, $^{**}P < 0.01$, $^{*}P < 0.05$; error bars represent SEM]. Genotypes were as in (B). (**D**) Survival of female flies expressing repeats in adult neurons using the elav-GeneSwitch (elavGS) driver; 36 and 103 pure repeats substantially decreased survival, whereas 36, 108, and 288 RO repeats had no effect ($P < 0.0001$, log-rank test). Genotypes: *w;UAS-3/+;elavGS/+*, *w;UAS-36/+;elavGS/+*, *w;UAS-103/+;elavGS/+*, *w;UAS-36 RO/+;elavGS/+*, *w;UAS-108 RO/+;elavGS/+*, *w;UAS-288 RO/+;elavGS/+*. (**E**) Flies expressing 36 and 103 pure repeats survived longer in the presence of cycloheximide than in its absence ($P < 0.001$, log-rank test). Genotypes: *w;UAS-36/+;elavGS/+*, *w;UAS-103/+;elavGS/+*.

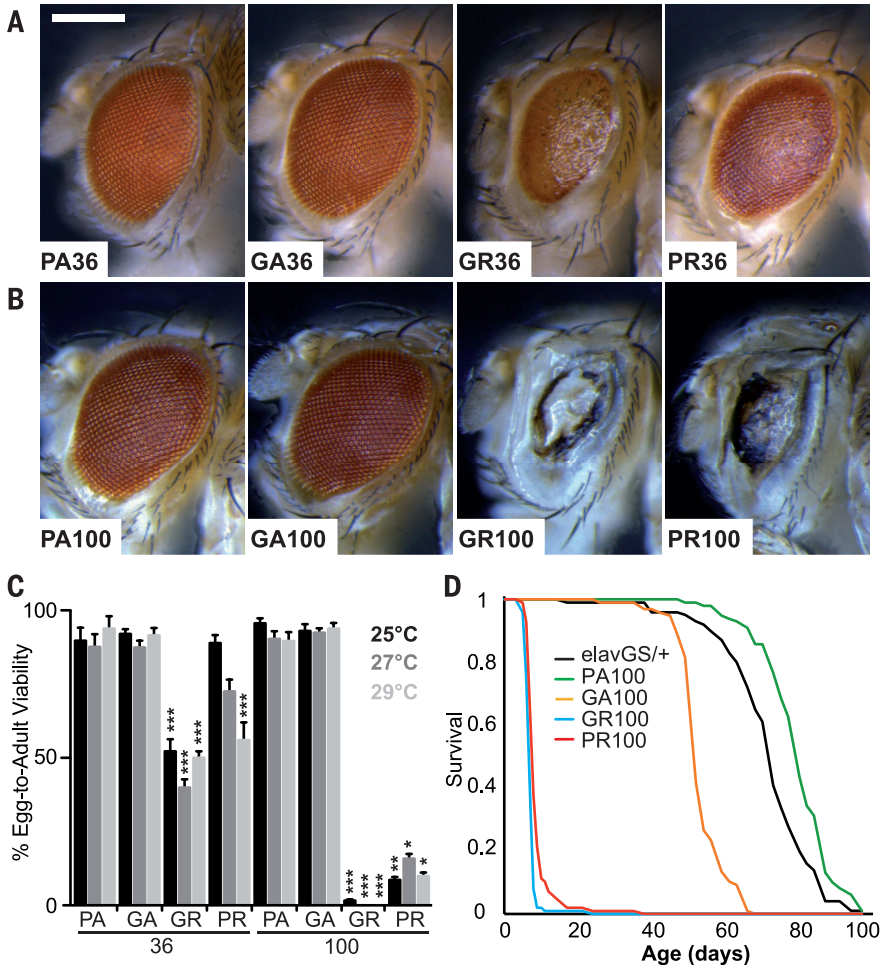

Fig. 3. DPR toxicity was caused by poly-GR and poly-PR proteins. "Protein-only" constructs for individual DPR proteins were expressed in the *Drosophila* eye [(A) to (C)] and the adult nervous system (D). (**A**) $(GR)_{36}$ and $(PR)_{36}$ caused eye degeneration, whereas $(GA)_{36}$ and $(PA)_{36}$ had no effect. Genotypes: *w;UAS-PA36/GMR-Gal4*, *w;UAS-GA36/GMR-Gal4*, *w;UAS-GR36/GMR-Gal4*, *w;UAS-PR36/GMR-Gal4*. Scale bar, 200 μm. (**B**) $(GR)_{100}$ and $(PR)_{100}$ caused extensive eye degeneration, whereas $(GA)_{100}$ and $(PA)_{100}$ had no effect. Genotypes: *w;UAS-PA100/GMR-Gal4*, *w;UAS-GA100/GMR-Gal4*, *w;UAS-GR100/GMR-Gal4*, *w;UAS-PR100/GMR-Gal4*. (**C**) Quantification of egg-to-adult viability showed that $(GR)_{100}$ and $(PR)_{100}$ caused a substantial reduction in survival, whereas $(GA)_{100}$ and $(PA)_{100}$ had no effect (Kruskal-Wallis test with Dunn's multiple comparison, selected pairs, $^{***}P < 0.001$, $^{**}P < 0.01$, $^{*}P < 0.05$; error bars represent SEM). Genotypes were as in (A) and (B). (**D**) Expression of $(GR)_{100}$ and $(PR)_{100}$ in adult neurons using the elav-GeneSwitch (elavGS) driver caused a substantial decrease in viability ($P < 0.001$, log-rank test); $(GA)_{100}$ caused a late-onset decrease in survival, and $(PA)_{100}$ or elavGS driver alone had no effect. Genotypes: *w;elavGS/+*, *w;UAS-PA100/+;elavGS/+*, *w;UAS-GA100/+;elavGS/+*, *w;UAS-GR100/+;elavGS/+*, *w;UAS-PR100/+;elavGS/+*.

with neurodegeneration (*25*). The presence of arginine in both of the highly toxic DPR species suggests a common pathological mechanism, perhaps attributable to their basic nature or a common structural motif. Restricted expression of *C9orf72* to specific neuronal populations (*26*), or a deficit in the affected neurons' ability to clear these particular proteins, may explain why these highly toxic proteins cause selective neurodegeneration. In patients, all five DPR proteins may be produced in a single neuron. Although our findings indicate that toxicity is driven by the arginine-rich DPR proteins, it remains possible that high focal levels of the other DPR proteins could contribute to cytotoxicity.

We have been able to separate RNA and DPR toxicity associated with *C9orf72* GGGGCC repeats and, surprisingly, our data suggest that the major toxic species are the DPR proteins. However, the DPR protein toxicity that we observed from overexpression of pure repeats does not rule out an additional contribution of RNA toxicity. Several lines of evidence suggest a toxic role of repeat RNA. In brains of C9FTD patients, RNA foci are most abundant in the frontal cortex, which has the greatest degree of neuronal loss, and frontal cortex RNA foci burden correlates with age at onset in C9FTD cases (*9*). GGGGCC repeats also sequester several RNA binding proteins, which could lead to toxicity (*13*, *27*–*31*). However, modeling RNA toxicity may require longer repeats that are closer to the pathological range seen in disease, possibly because a toxic threshold of repeat number must be crossed. A continuing conundrum is why the same expanded repeat can cause either pure FTD or pure ALS. Our data raise the possibility that the different patient phenotypes could be caused by differences in the relative contributions of RNA- or protein-mediated toxicity within distinct neuronal subtypes. A further prediction from this hypothesis is that genetic variants that affect RAN translation or DPR protein levels may also contribute to disease penetrance.

REFERENCES AND NOTES

1. P. Lillo, J. R. Hodges, *J. Clin. Neurosci.* **16**, 1131–1135 (2009).
2. M. DeJesus-Hernandez *et al.*, *Neuron* **72**, 245–256 (2011).
3. A. E. Renton *et al.*, *Neuron* **72**, 257–268 (2011).
4. E. Majounie *et al.*, *Lancet Neurol.* **11**, 323–330 (2012).
5. J. Beck *et al.*, *Am. J. Hum. Genet.* **92**, 345–353 (2013).
6. M. van Blitterswijk *et al.*, *Lancet Neurol.* **12**, 978–988 (2013).
7. P. Fratta *et al.*, *Acta Neuropathol.* **126**, 401–409 (2013).
8. M. B. Harms *et al.*, *Neurobiol. Aging* **34**, 2234.e13–2234.e19 (2013).
9. S. Mizielinska *et al.*, *Acta Neuropathol.* **126**, 845–857 (2013).
10. T. F. Gendron *et al.*, *Acta Neuropathol.* **126**, 829–844 (2013).
11. C. Lagier-Tourenne *et al.*, *Proc. Natl. Acad. Sci. U.S.A.* **110**, E4530–E4539 (2013).
12. T. Zu *et al.*, *Proc. Natl. Acad. Sci. U.S.A.* **110**, E4968–E4977 (2013).
13. Y. B. Lee *et al.*, *Cell Rep.* **5**, 1178–1186 (2013).
14. P. E. Ash *et al.*, *Neuron* **77**, 639–646 (2013).
15. T. Lashley, J. Hardy, A. M. Isaacs, *Neuron* **77**, 597–598 (2013).
16. K. Mori *et al.*, *Science* **339**, 1335–1338 (2013).
17. K. Mori *et al.*, *Acta Neuropathol.* **126**, 881–893 (2013).
18. T. Zu *et al.*, *Proc. Natl. Acad. Sci. U.S.A.* **108**, 260–265 (2011).
19. D. E. Meyer, A. Chilkoti, *Biomacromolecules* **3**, 357–367 (2002).
20. M. de Haro *et al.*, *Hum. Mol. Genet.* **15**, 2138–2145 (2006).
21. J. P. Orengo *et al.*, *Proc. Natl. Acad. Sci. U.S.A.* **105**, 2646–2651 (2008).
22. N. Sakamoto *et al.*, *J. Biol. Chem.* **276**, 27178–27187 (2001).
23. P. Fratta *et al.*, *Sci. Rep.* **2**, 1016 (2012).
24. J. B. Duffy, *Genesis* **34**, 1–15 (2002).
25. I. R. Mackenzie *et al.*, *Acta Neuropathol.* **126**, 859–879 (2013).
26. N. Suzuki *et al.*, *Nat. Neurosci.* **16**, 1725–1727 (2013).
27. S. Almeida *et al.*, *Acta Neuropathol.* **126**, 385–399 (2013).
28. C. J. Donnelly *et al.*, *Neuron* **80**, 415–428 (2013).
29. K. Mori *et al.*, *Acta Neuropathol.* **125**, 413–423 (2013).
30. D. Sareen *et al.*, *Sci. Transl. Med.* **5**, 208ra149 (2013).
31. Z. Xu *et al.*, *Proc. Natl. Acad. Sci. U.S.A.* **110**, 7778–7783 (2013).

ACKNOWLEDGMENTS

We thank J. Wadsworth and N. Alic for helpful discussion. Funding was provided by Alzheimer's Research UK (A.M.I.), the Motor Neurone Disease Association (A.M.I., E.M.C.F., P.F.), the Middlesex Hospital and Medical School General Charitable Trust (A.M.I.), National Institute for Health Research (NIHR)/University College London Hospitals Biomedical Research Centre (P.F.), BRT (T.M.), a NIHR Academic Clinical Fellowship (I.O.C.W.), the UK Medical Research Council (A.M.I., E.M.C.F., P.F.), the Wellcome Trust (L.P.), and the Max Planck Society (L.P.). Clones from the Isaacs lab will be distributed under material transfer agreements for academic use. L.P. dedicates this work to the memory of Noreen Murray.

SUPPLEMENTARY MATERIALS

www.sciencemag.org/content/345/6201/1192/suppl/DC1
Materials and Methods
Figs. S1 to S7
References (*32*–*35*)

2 June 2014; accepted 28 July 2014
Published online 7 August 2014;
10.1126/science.1256800

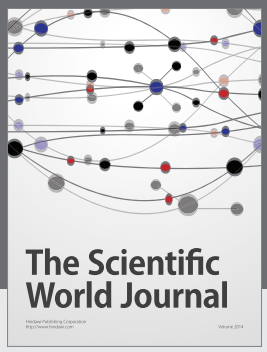

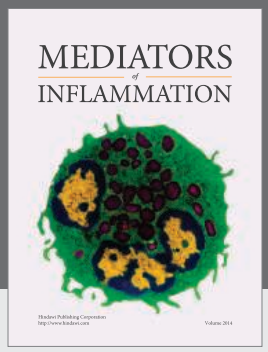

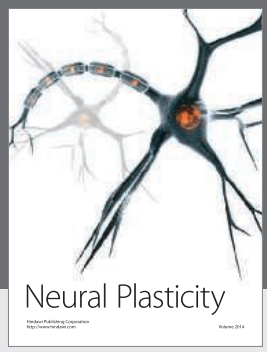

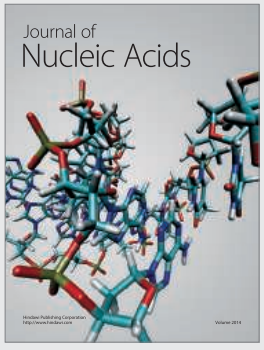

Hindawi

Submit your manuscripts at
http://www.hindawi.com

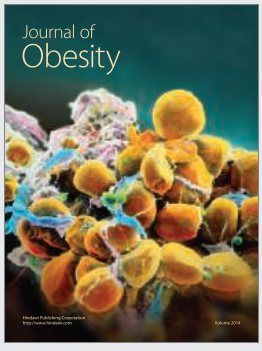

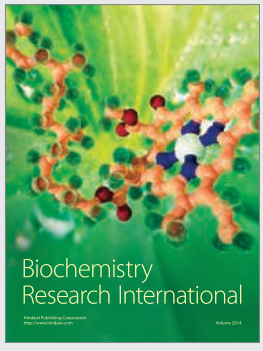

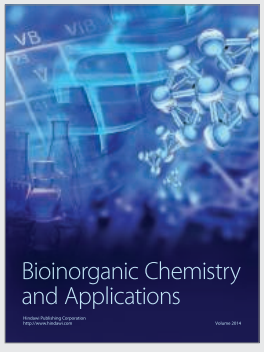

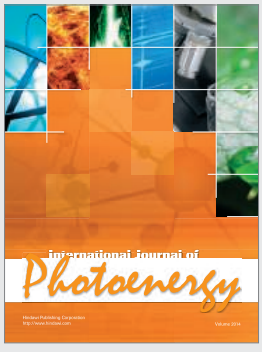

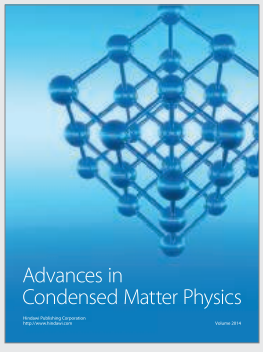

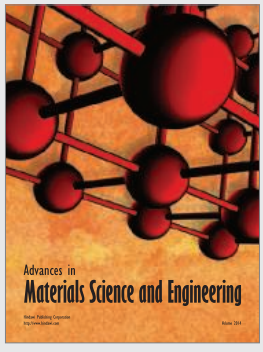

The BD Accuri™ personal flow cytometer

Flow cytometry within reach.™

The BD Accuri™ Cytometer is a personal flow cytometer that puts flow cytometry within reach. It gives you 4-color cell analysis in an affordable, transportable, and easy-to-use format.

Measuring just 11 x 14.75 x 16.5 inches (27.9 x 37.5 x 41.9 centimeters) and weighing just 30 pounds (13.6 kilograms), the BD Accuri Cytometer gives both novice and experienced researchers the power of multicolor analysis, when and where you need it. The software's intuitive interface guides you through workflows, making it easy to begin collecting and analyzing data—even if you have little flow cytometry knowledge or know-how.

Setup and maintenance are also simplified to increase availability and up-time. In the event service is required, just pack up the system and return it. A loaner system will be provided while your system is serviced.

For more information about how you can more easily access the power of flow cytometry in your lab, visit **bdbiosciences.com/go/accuri**.

Flow cytometry within reach.™

BD

Helping all people live healthy lives

BD Biosciences
2350 Qume Drive
San Jose, CA 95131
bdbiosciences.com

NEW ENGLAND BioLabs® Inc.

PASSION IN SCIENCE AWARDS™

What is your PASSION?

In celebration of our 40th anniversary, New England Biolabs® is pleased to announce our Passion In Science Awards™, recognizing those within the scientific community working to make a difference in the world through their science, humanitarianism, environmental stewardship or love of the arts.

Through September 30th, 2014, we invite you to nominate yourself or a colleague for one of these awards. Award winners will be our guests at a celebration at the NEB® campus in Ipswich MA, USA and will also receive a donation to help further their cause. Remember, no act is too big or too small.

Help us celebrate those individuals who demonstrate true passion in science.

Tell us your story.

Visit NEBPassionInScience.com

Science and art come together in the artwork displayed on the front of the NEB laboratory facility in Ipswich, MA, USA. *Artwork created by Nicole Gordon.*

Webinar

Culturing Human Cells:

Optimizing Growth Conditions for Immunotherapy

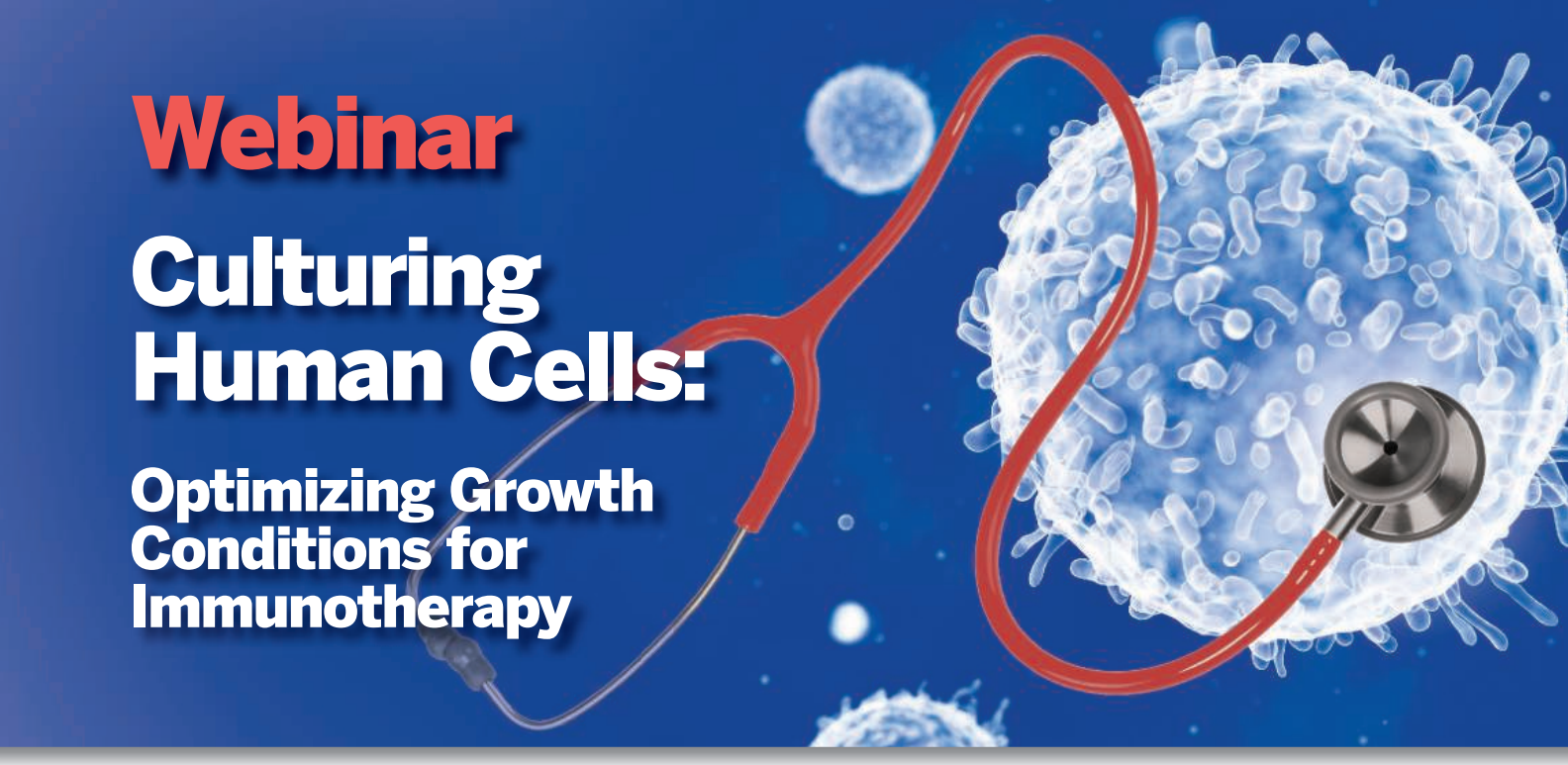

Wednesday, October 1, 2014

12 noon Eastern, 9 a.m. Pacific,
5 p.m. UK, 6 p.m. Central Europe

During the webinar, the panelists will:

- Highlight how immunotherapy is currently being applied in the clinic and those factors important to generating high-quality cells
- Discuss the importance of perfusion to achieving high cell yield and its effect on cell markers and characteristics
- Focus on optimization of culture conditions when generating cells for reperfusion into patients
- Answer your questions live during the webinar!

Register Now!

webinar.sciencemag.org

Growing human cells in culture for research is one thing, but the isolation and culture of high-quality cells that will be re-injected back into the donor is quite another. Manipulation and expansion of cells in a clinical setting carries its own unique requirements and complications. Growth and survival needs to be optimized and quality control is paramount. Often only a single opportunity for successful treatment is possible, so chances of success need to be maximized in all respects, including high-yield isolation of good quality cells from patients, cell culture conditions, cell characterization, and reperfusion back into patients. During this webinar, we will broadly discuss the process of immunotherapy as well as examine in more detail some of the most critical steps along the pathway to generating a therapeutic dose of modified cells.

Speakers

Laurence J. N. Cooper, M.D., Ph.D.
MD Anderson Cancer Center
Houston, TX

Michelle Janas, Ph.D.
GE Healthcare
Cardiff, Wales

Webinar sponsored by

Brought to you by the *Science*/AAAS Custom Publishing Office

Science AAAS

@SciMagWebinars

NGS Library Prep

MagSi-NGSPREP is a magnetic, bead-based tool that offers an efficient solution for DNA cleanup and size selection in next generation sequencing (NGS) applications. MagSi-NGSPREP supports all standard DNA clean-up protocols encountered during Next-Gen library preparation, including the classical one-sided and two-sided "solid phase reversible immobilization" size selection protocols. The simple and flexible protocols employed using MagSi-NGSPREP can be adjusted to your specific application and NGS platform. MagSi-NGSPREP can be used manually but is also easy to automate for high throughput processing. Using MagSi-NGSPREP, DNA fragments are bound directly onto the surface of the magnetic beads, leaving unincorporated nucleotides, primers, primer dimers, and other contaminants in solution. Following this the DNA fragments are eluted with low salt buffer or reagent grade water. The technology for binding of DNA fragments onto the applied magnetic nanoparticle surface does not require use of any hazardous chaotropic buffers.

AMS Biotechnology
For info: +44-(0)-1235-828200
www.amsbio.com

Water Purification System

ELGA LabWater's PURELAB flex 5 and 6 are all-in-one, fully automated, standalone water purification systems for ion chromatography built to eliminate the need for eluent monitoring and water refilling. Delivering volumes up to 10 L per day, the PURELAB flex 5 is perfect for general use labs, while the PURELAB flex 6 is optimized for usage above 10 L per day. A closed architecture avoids eluent contamination. The multi-usage systems deliver high-quality water throughout the workflow, including eluent generation, system rinsing, and general laboratory applications. They also reduce eluent preparation time compared to using bottled water. With these benefits, PURELAB flex 5 and 6 offer a unique "switch on and walk away" solution for ion chromatography, enhancing detection accuracy through improved water stability and purity.

Elga LabWater
For info: +44-(0)-2035-677300
www.elgalabwater.com

Automated Sample Storage

The BiOS M and L are two compact, high-density automated systems designed to fit into existing laboratories that require ultralow-temperature storage of sensitive biological samples. These flexible, energy-efficient, and scalable systems ensure the viability of 100,000 to over one million long-term samples. Laboratories depend on biobanks to supply well-annotated, high-quality samples that are collected within appropriate ethical parameters and under infallible conditions. The BiOS M and L are ideal for forensic applications, and medium-sized research and clinical repositories. Samples are held in labware that is both tracked and picked automatically without human intervention, thus avoiding the risk of inadvertent warming and degraded sample integrity. By adding smaller configurations of our high-capacity BiOS -80°C storage system more labs have access to state-of-the-art sample storage within steps of their sample preparation and analysis stations. This reduces the likelihood that results may be compromised.

Hamilton Storage Technologies
For info: 800-310-5866
www.hamilton-storage.com

Magnetic Bead Immunoprecipitation System

The SureBeads Magnetic Bead System provides researchers with a faster and easier alternative to agarose beads for immunoprecipitation (IP). Benefits include: reduced antibody consumption and sample loss, very low nonspecific binding, and optimized IgG binding capacity. Researchers have traditionally used agarose beads to precipitate and enrich proteins prior to Western blotting or mass spectrometry. Magnetic beads are an attractive alternative to agarose beads for several reasons, chiefly ease of use at the bench: magnetization is faster and more convenient than centrifugation for sample precipitation and washing steps. More researchers would likely switch to magnetic beads if they were not significantly more expensive than agarose beads. With the launch of the SureBeads System, scientists now have access to a high-performance, cost-effective magnetic bead system. SureBeads Protein A & G Conjugated Magnetic Beads are designed to work with the SureBeads 16-Tube Magnetic Rack.

Bio-Rad Laboratories
For info: 800-424-6723
www.bio-rad.com/newsurebeads

Spectrophotometer

SimpliNano is a simple-to-use microvolume spectrophotometer for straightforward concentration and purity measurements of nucleic acids and proteins. There are no moving parts in SimpliNano, making it reliable and easy to maintain, with excellent instrument reproducibility. The fixed path length means samples can be added and removed without the need for time-consuming calibration. Small volumes down to one microliter can be analyzed by pipetting directly into the built-in sample port, reducing sample loss, and eliminating the need for cuvettes or other sampling tools. Samples can be recovered or wiped away after measurement and the sample port is compatible with a variety of common laboratory chemicals. SimpliNano is programmed with a range of methods for conveniently measuring nucleic acid concentrations at 260 nm and proteins at 280 nm as well as purity. The spectrophotometer offers freedom of choice as it can be operated through its direct user interface, or through a PC with optional Datrys software.

GE Healthcare Life Sciences
For info: 800-526-3593
www.gelifesciences.com/spectros

Electronically submit your new product description or product literature information! Go to www.sciencemag.org/products/newproducts.dtl for more information.

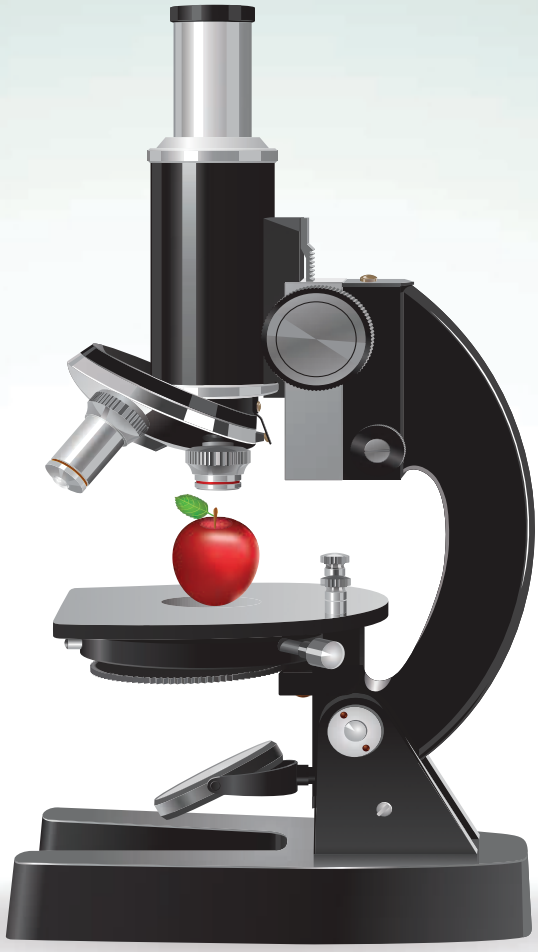

We're taking a closer look
at the evolving state of chemical education

How can we balance quality and excellence with access and affordability?

The laboratory as a venue for discovery science, peer-to-peer teaching, "flipped" classes, online courses leading to degrees or certifications, MOOCs and other innovations – what works, what doesn't? How will emerging national education policies affect classroom instruction? How can large research universities enhance student learning? How can small liberal arts institutions innovate for student success? How will classroom size, staffing and environment influence K-12 student performance?

Join us for an invigorating discussion of future directions for secondary, post-secondary and graduate chemical education.

2014 Conference on Chemical Research: Chemical Education

October 27-28 in Houston

THE Welch FOUNDATION

Advancing Chemistry. Improving Life.

Conference complimentary with registration.
Program and registration: www.welch1.org/chemical-conference

Does your antibody measure up?

Susan, Development Scientist,
has been with CST since 2003.

At CST, if it's not specific, it doesn't ship.

WB analysis of extracts from human prostate and testis using two development samples at 1:1000 dilution.

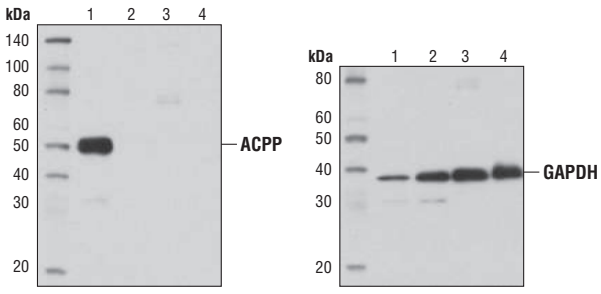

Prostatic Acid Phosphatase (D3Y5P) Rabbit mAb #12861: WB analysis of extracts from human prostate, testis, liver, and spinal cord using #12861 (left) and GAPDH (D16H11) XP® Rabbit mAb #5174 loading control (right) demonstrating prostate-specific expression of ACPP.

1 - Human Prostate Tissue
2 - Human Testis Tissue
3 - Human Liver
4 - Human Spinal Cord.

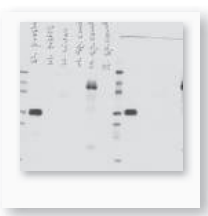

Skeptical? See the whole film at
www.cellsignal.com/wbskeptical

WB IP IHC IF F ChIP

For Research Use Only. Not For Use In Diagnostic Procedures.

14PADIHC_NONE0152ENG_02

Cell Signaling TECHNOLOGY®

Science Careers Advertising

For full advertising details, go to ScienceCareers.org and click For Employers, or call one of our representatives.

Tracy Holmes
Worldwide Associate Director
Science Careers
Phone: +44 (0) 1223 326525

THE AMERICAS

E-mail: advertise@sciencecareers.org
Fax: 202 289 6742

Tina Burks
Phone: 202 326 6577

Nancy Toema
Phone: 202 326 6578

Marci Gallun
Sales Administrator
Phone: 202 326 6582

Online Job Posting Questions
Phone: 202 312 6375

EUROPE / INDIA / AUSTRALIA / NEW ZEALAND / REST OF WORLD

E-mail: ads@science-int.co.uk
Fax: +44 (0) 1223 326532

Axel Gesatzki
Phone: +44 (0) 1223 326529

Sarah Lelarge
Phone: +44 (0) 1223 326527

Kelly Grace
Phone: +44 (0) 1223 326528

JAPAN

Katsuyoshi Fukamizu (Tokyo)
E-mail: kfukamizu@aaas.org
Phone: +81 3 3219 5777

Hiroyuki Mashiki (Kyoto)
E-mail: hmashiki@aaas.org
Phone: +81 75 823 1109

CHINA / KOREA / SINGAPORE / TAIWAN / THAILAND

Ruolei Wu
Phone: +86 186 0082 9345
E-mail: rwu@aaas.org

Science Careers
From the journal *Science* AAAS

ScienceCareers.org

Los Alamos NATIONAL LABORATORY EST. 1943

Los Alamos National Laboratory (LANL), a multidisciplinary research institution engaged in strategic science on behalf of national security, has a *single* open Center Leader position in the Center for Nonlinear Studies (CNLS). It will be filled either at the R&D Manager 4 or the R&D Scientist 5 level.

CENTER LEADER (R&D MANAGER 4) Job IRC34587

CENTER LEADER (SCIENTIST 5) Job IRC34586

The Center Leader provides scientific leadership and line management of the CNLS and plays an institutional and integrating role in collaboration with scientists throughout the Laboratory. The CNLS Center Leader is expected to develop and lead a program to target and create cooperative long-term research programs consistent with the Laboratory's strategic research objectives, to develop a strong working relationship with the CNLS External Advisory Committee, and to maintain effective working relationships throughout all levels of the Laboratory, government entities, academia and industry. The successful candidate will be expected to maintain an active research program while providing technical vision to nurture and support existing programs of others at the Center. The Center Leader should be energetic, results-oriented, a catalyst for change and an outstanding relationship builder. Line management responsibilities include accountability for quality research, management of financial and human resources, proactive support of Laboratory and Division safety, security, environment and diversity objectives, the communications/marketing strategy for the Center and collaboration with the Theoretical Division to help provide strategic direction for the organizations.

Position requires a Ph.D. degree in a scientific or engineering field relevant to the Center's activities and research or equivalent combination of education and experience. Demonstrated record of scientific accomplishment in one or more areas relevant to the Center as evidenced by an outstanding publication portfolio and/or a demonstrable national or international reputation is essential. Demonstrated experience in establishing and maintaining research collaborations, from the identification of new potential topics to forming teams, promoting proposals, and executing projects is also required.

Applicants may apply to both job postings at **careers.lanl.gov**

Applicants whose materials are received by October 31, 2014 will receive full consideration.

EOE

Science Careers

CER

"《科学》职业" 已经与赛尔互联(CER)开展合作。中国大陆的高校可以直接联系CER进行国际人才招聘。

请访问 Sciencecareers.org/CER 点得联系信息。

招募学术精英,《科学》是您的不二之选 Science

The NIH Intramural Research Program is Recruiting Tenure-Track "Earl Stadtman Investigators"

The National Institutes of Health, the U.S. government's premier biomedical and behavioral research enterprise, is pleased to announce its sixth annual call for "NIH Earl Stadtman Investigators," a broad recruitment of tenure-track investigators (assistant professor equivalent) for all NIH intramural programs. Scientific discoveries from our intramural laboratories, with their extensive infrastructure and critical mass of expertise, have a crucial role in both maintaining America's research excellence and advancing medical treatments and cures.

Come join the team whose hallmarks are stable funding, intellectual freedom, shared resources, and access to a wide range of scientific expertise. We seek creative, independent thinkers eager to take on high-risk, high-impact research. A fantastic array of scientists already has been hired through the "Stadtman" recruitment in the last five years.

A variety of basic and translational/clinical positions are available, with areas of active recruitment including (but not limited to): Behavioral Sciences, Biochemistry, Biomedical Engineering, Biophysics, Biostatistics, Cancer Biology, Cell Biology, Cell Metabolism, Chemical Biology, Chromosome Biology, Circadian Biology, Computational Biology/Bioinformatics (including natural language processing and text mining), Developmental Biology, Epidemiology, Genetics, Genomics, Health Disparities, Hearing & Balance, Immunology, Infectious Diseases, Microbiology, Molecular Pharmacology, Neurodevelopment, Neurosciences, Sensory Biology, Social Sciences, Structural Biology, Systems Biology, Toxicology, Translational and Clinical Research, and Virology.

Who we are: Among our approximately 1,100 principal investigators and 5,000 trainees are world-renowned experts in basic, translational, and clinical research. Our strength is our diversity in pursuit of a common goal, to alleviate human suffering from disease. Similar to academia, we offer our scientists the opportunity to mentor outstanding trainees at all levels (e.g., graduate students and postdoctoral fellows) in a research setting.

Whom we seek: For this broad, trans-NIH recruitment effort, we seek talented scientists with a clear and creative research vision who wish to contribute to the nation's health.

Qualifications/eligibility: Candidates must have an M.D., Ph.D., D.D.S./D.M.D., D.V.M., D.O., R.N./Ph.D., or equivalent doctoral degree and have an outstanding record of research accomplishments as evidenced by publications in major peer-reviewed journals. Applicants should be non-tenured scientists. Appointees may be U.S. citizens, resident aliens, or non-resident aliens with, or eligible to obtain, a valid employment-authorization visa.

How to apply: Applicants must submit four items: (1) a CV (which should include mentoring and leadership activities); (2) a three-page proposal titled Research Goals, i.e., the research you hope to perform at the NIH; (3) a one-page statement titled Long-term Research Vision and Impact, i.e., what you hope to achieve for yourself, your field, and society; and (4) contact information for three professional references. Submit these through our online application system at http://tenuretrack.nih.gov/apply between August 1 and **September 30, 2014 (11:59 p.m. EDT)**. You will be asked to designate a primary and secondary scientific area of expertise to aid in assigning your application to the appropriate review committee. Requests for letters of recommendation will be sent to your references when you submit your application. Reference letters will be accepted via upload to the website until October 7, 2014 (11:59 p.m. EDT). We cannot accept paper applications.

What to expect: Search committees of subject-matter experts will review and evaluate applicants based on publication record, scientific vision and potential scientific impact of current and proposed research, demonstrated independence, awards, and references. The committees will identify the most highly qualified candidates to invite to the NIH for a lecture in December 2014, open to the NIH scientific staff, and for subsequent interviews with the search committees. Search committee chairs and NIH Scientific Directors, who lead our intramural programs, will identify finalists for possible recruitment as Earl Stadtman Investigators. Candidates not selected as finalists can be considered for other open NIH research positions. The entire process from application review to job offer may take several months, depending on the volume of applications. Please find answers to frequently asked questions at http://tenuretrack.nih.gov/apply/faq/stadtman.html.

We call upon individuals who will open our eyes to possibilities we haven't yet envisioned, complement our scientific mission, and enhance our research efforts. More information about our program is at http://irp.nih.gov. The inspiring story of Earl and Thressa Stadtman's research at the NIH is at http://history.nih.gov/exhibits/stadtman. Specific questions regarding this recruitment effort may be directed to Dr. Roland Owens, Assistant Director, NIH Office of Intramural Research, at positions@mail.nih.gov. DHHS and NIH are Equal Opportunity Employers.

THE NIH IS DEDICATED TO BUILDING AN INCLUSIVE AND DIVERSE COMMUNITY IN ITS TRAINING AND EMPLOYMENT PROGRAMS

FRIEDRICH-ALEXANDER UNIVERSITÄT ERLANGEN-NÜRNBERG

NATURWISSENSCHAFTLICHE FAKULTÄT

The Faculty of Sciences invites applications for a

1. W3 Professorship (Chair) for Experimental Physics

at the Department of Physics (Institute of Condensed Matter Physics) to be filled by the earliest possible starting date.

The successful candidate is expected to represent the field adequately in teaching and research. We seek candidates with outstanding achievements in experimental physics whose research interests include the physics of new materials and/or light-matter interaction. The successful candidate's future research will ideally be broadly aligned with existing strengths and interests at the Department of Physics, the Collaborative Research Centre 'Synthetic Carbon Allotropes', the Cluster of Excellence 'Engineering of Advanced Materials', the Erlangen Graduate School in Advanced Optical Technologies or the Max Planck Institute for the Science of Light.

2. W2 Professorship for Theoretical Physics

(succession of Prof. Dr. H. Leschke)

at the Department of Physics to be filled by the earliest possible starting date.

The successful candidate is expected to represent the field adequately in teaching and research. Applicants should have a strong research record in statistical physics linked to geometric or algebraic methods which complements existing activities in mathematical physics at FAU.

Prerequisites for the positions are a university degree, university level teaching experience, a doctoral degree, and additional academic qualifications. These should be in the form of a Habilitation (post-doctoral thesis) or equivalent academic publications. The necessary qualifications may also have been acquired in a non-university context or through a junior faculty position (e.g. W1 Professor or Assistant Professor).

FAU expects applicants to become actively involved in the administration of academic affairs and welcomes experience in managing research projects and raising third-party funding.

The University of Erlangen-Nürnberg pursues a policy of intense student mentoring and therefore expects its teaching staff to be present during lecture periods.

FAU is an equal opportunities and family-friendly employer and is also responsive to the needs of dual career couples. In order to increase the number of women in leading positions, we specifically encourage women to apply.

Please submit your complete application documents (CV, list of publications excluding reprints, list of lectures and courses taught, for W3-Professorship for Experimental Physics research plan, certified copies of certificates and degrees, list of third-party funding) to the Dean of the Faculty of Sciences, Friedrich-Alexander-Universität Erlangen-Nürnberg, Universitätsstr. 40, 91054 Erlangen, by **October 10, 2014**. Please also send an electronic version to christine.karg@fau.de.

Grundzertifikat 2008 audit familiengerechte hochschule

www.fau.de

PRINCETON UNIVERSITY

ECOLOGY AND ENVIRONMENTAL BIOLOGY
Faculty Position

Princeton University's Department of Ecology and Evolutionary Biology seeks candidates for a tenured or tenure track faculty position in ecology and environmental biology. We are interested in broad thinkers who conduct integrative, conceptually oriented research on environment-related themes including biodiversity, climate change, physiology, biogeochemistry, conservation science, and agro-ecosystems.

Applicants should submit a vision statement, no longer than 2 pages, that outlines one or more major unsolved problems in their field and how they plan to address them. The vision statement should go beyond a précis of the applicant's prior and current research and should explain the connection to one or more important environmental issues.

Applications, including the vision statement, curriculum vitae, three reprints, and contact information for three references, should be submitted online via **http://jobs.princeton.edu**, requisition **#1400543**. Screening of applications will begin **October 31, 2014**.

Princeton University is an Equal Opportunity Employer. All qualified applicants will receive consideration for employment without regard to race, color, religion, sex, national origin, disability status, protected veteran status, or any other characteristic protected by law. This position is subject to the University's background check policy.

UIC University of Illinois at Chicago

The University of Illinois at Chicago, Department of Medicinal Chemistry and Pharmacognosy seeks candidates for two open rank (tenure-track Assistant, Associate, or Full Professor) positions. Our Department is rooted in drug discovery fostered by a highly collaborative atmosphere. Faculty members are expected to interact extensively with other laboratories in the department and affiliated research centers while developing/maintaining externally funded, independent research programs. Teaching in the professional and graduate programs of the College of Pharmacy is required. Candidates must possess a doctorate in chemistry, pharmacognosy, chemical or molecular biology, genomics, bioinformatics, or a related discipline. Postdoctoral experience is required. Applicants should complete an application package and submit a curriculum vitae, a research proposal (no more than 3 pages) describing plans for an independent research program, a list of possible intradepartmental collaborations, and the contact information for 3 references at: **https://jobs.uic.edu/job-board/job-details?jobID=44382&job=assistant-associate-or-full-professor**.

Position 1: Ideal candidates will possess expertise in the biosynthesis of natural products, including but not limited to the ability to mine genomes/genes and identify/manipulate biosynthetic pathways and secondary metabolite production.

Position 2: Successful applicants will focus on small molecule drug-lead development, including but not limited to biological target identification, imaging in biological systems, and/or semi-synthetic natural products chemistry with a heavy emphasis on its application toward biological systems.

Further information is available at **http://mcp.pharm.uic.edu**. Questions may be directed to **mcp@uic.edu**. For fullest consideration, submit full application materials by **October 03, 2014**.

The University of Illinois at Chicago is an Equal Opportunity, Affirmative Action employer. Minorities, women, veterans and individuals with disabilities are encouraged to apply.

UNSW AUSTRALIA

EMBL Australia

EMBL Australia Group Leaders

Accelerate your research career – fully funded research positions for 5 years

- Form and lead your own independent research group
- Modelled on the European Molecular Biology Laboratory (EMBL) to support independent, interdisciplinary, quality research
- Designed for high potential, early-career scientists who are dedicated to research excellence
- Form and lead your own independent research group
- Excellent salary package, including (where required) arrangements for relocation, travel, work permits and visas for the successful candidate and their family
- Position includes funding for a research team and generous annual research budget
- Based at new world-class life and medical research facilities at the Faculty of Medicine, the University of New South Wales (UNSW)
- Unique opportunity to join an innovative, growing organisation

EMBL Australia enables research groups to have access to the complementary facilities and expertise at EMBL and a growing network of groups at other national participating institutions.

Group Leaders in Single Molecule Science (2 positions): at the University of New South Wales, (UNSW), Sydney, Australia

At the UNSW Centre in Single Molecular Science we seek future research leaders to develop novel conceptual and experimental approaches for challenging problems in biology and medicine. The successful applicant will define and drive a new research field that seeks to understand complex biological processes and systems starting from the single molecule level, and to derive practical medical applications from that knowledge. It is now possible to map interactions of individual molecules in time and space within the cellular and tissue architecture and thus link molecular processes to functional outcomes. We seek researchers who help us turn this vision into reality.

Applicants with trans-disciplinary research experience are strongly encouraged. Research questions in cancer, immunology, neuroscience, cardiovascular biology and other fields are welcome. The successful applicants will lead a research team in a dynamic, highly collaborative, and internationally focused environment and have the opportunity to further expand their research program through external grants and fellowships.

UNSW has unique microscopy capabilities in super-resolution and single molecule imaging developed by the ARC Centre of Excellence in Advanced Molecular Imaging (www.imagingcoe.org) and supported by the Biomedical Imaging Facility. The Group Leaders also have access to UNSW facilities in nanofabrication, drug development, genomics, proteomics, animal models and the Mark Wainwright Analytical Centre.

More details are available at **www.sms.unsw.edu.au**.

EMBL Australia

The EMBL Australia Partner Laboratory is based on the EMBL model, with distributed, highly integrated research nodes focusing on complementary aspects of biological research. Currently there are three nodes: at Monash University's Australian Regenerative Medicine Institute, the University of Queensland's EMBL Australia Bioinformatics Resource and at SAHMRI in South Australia. Current research partners in EMBL Australia include the Group of Eight universities, CSIRO and SAHMRI in Adelaide. More details at **www.emblaustralia.org**

Interviews
Interviews will be held in Australia and are likely to be in the week commencing 24th November 2014 or the week commencing 23rd February 2015.

To apply
Please email (in English) a cover letter plus your CV, names and addresses of 3 referees and a summary of current and future research interests to: **embl.australia@unsw.edu.au**

Applications close: 19th October 2014

The anticipated commencement date is mid/late 2015

Faculty Career Feature

October 3, 2014

Reserve ads by September 16 to guarantee space

Ads accepted until September 26 if space is still available

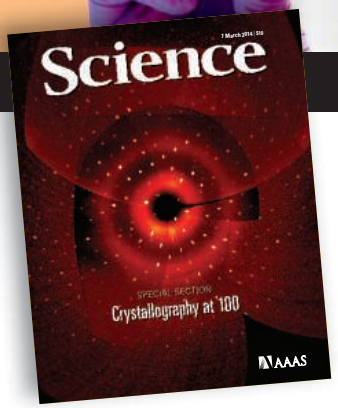

For recruitment in science, there's only one **Science**

Hiring Faculty? We've got a special feature for your **Faculty ads** this fall! The October 3 feature explores how faculty can best collaborate with professionals/other academics in different cultures and countries.

Why you should advertise in this issue of *Science*:

Reach: Your job ad is seen by 570,400 readers around the globe from varied backgrounds and it sits on special bannered pages promoting faculty positions. 60% of our weekly readers work in academia and 67% are Ph.D.s. *Science* connects you with more scientists in academia than any other publication.

- The October 3 issue includes a special bonus distribution to 25,000 scientists beyond our regular circulation

Results: If you are looking to hire faculty, *Science* offers a simple formula: relevant content that spotlights your ad + a large qualified audience = hiring success.

Find your next faculty member by advertising in this special feature.

To book your ad, contact:

advertise@sciencecareers.org
THE AMERICAS
202 326 6582
EUROPE/ROW
+44 (0) 1223 326500
JAPAN
+81 3 3219 5777
CHINA/KOREA/SINGAPORE/TAIWAN
+86 186 0082 9345

Science Careers
From the journal *Science* AAAS

ScienceCareers.org

Produced by the *Science*/AAAS Custom Publishing Office.

POSITIONS OPEN

ENDOWED CHAIR POSITION in The Department of Biology

The Department of Biology at Wheaton College (IL) seeks qualified applicants for the endowed Ruth Kraft Strohschein Chair in Biology. Requirements include a Ph.D., teaching experience, a solid research program in a biomedical-related field, and demonstration of integration of science and Christian faith. Scientists with neurobiology expertise are especially encouraged to apply. Send cover letter and curriculum vitae to **Dr. Jennifer Busch,** Biology Department Chair, at **e-mail: jennifer.busch@wheaton.edu.** Review of completed applications will begin in October 2014 and continue until the position is filled.

Wheaton College is an evangelical Protestant Christian liberal arts college whose faculty and staff affirm a Statement of Faith and adhere to lifestyle expectations of the Wheaton College Community Covenant. The College complies with federal and state guidelines for nondiscrimination in employment. Women and minority candidates are encouraged to apply. Read more about Wheaton College and its programs at **website: http://www.wheaton.edu/.**

Applications will be mailed to promising candidates.

DUKE UNIVERSITY Department of Chemistry

Duke University, Durham, North Carolina. The Department of Chemistry invites applications and nominations for a tenure-track position (at the **ASSISTANT** or recently promoted **ASSOCIATE PROFESSOR** level) to begin July 1, 2015. In addition to a commitment to teaching, candidates should have research interests in experimental physical/biophysical chemistry; we are particularly interested in enhancing interactions with our strong interdepartmental centers and institutes, such as the Fitzpatrick Institute for Photonics, the Duke Cancer Center, and the Center for Molecular and Biomolecular Imaging. Applications received by November 1 will be guaranteed consideration, although extraordinary applicants will be considered after this date. To guarantee consideration, all applicants should submit a curriculum vitae, list of publications, description of research interests and the names and e-mail addresses of three references (for requesting letters of recommendation) via the **website: https://academicjobsonline.org/ajo/jobs/4354.** *Duke University is an Affirmative Action/Equal Opportunity Employer committed to providing employment opportunity without regard to an individual's age, color, disability, genetic information, gender, gender identity, national origin, race, religion, or sexual orientation. Veterans are strongly encouraged to apply.*

ASSISTANT PROFESSOR Princeton University Department of Chemistry

The Department of Chemistry at Princeton University invites applications for two tenure-track Assistant Professor positions in chemistry with an emphasis on theory, inorganic materials, and organic chemistry. We seek faculty members who will create a climate that embraces excellence and diversity with a strong commitment to teaching and mentoring that will enhance the work of the department and attract and retain students of all races, nationalities, and genders. We strongly encourage applications from members of all underrepresented groups. Candidates are expected to have completed the Ph.D. in chemistry or a related field at the time of appointment. Applicants should submit a description of research interests, curriculum vitae, a list of publications, and contact information for three references online at **website: http://jobs.princeton.edu/applicants/Central?quickFind=65639.** The deadline for applications is October 15, 2014. *Princeton University is an Equal Opportunity Employer. All qualified applicants will receive consideration for employment without regard to race, color, religion, sex, national origin, disability status, protected veteran status, or any other characteristic protected by law. This position is subject to the University's background check policy.*

POSITIONS OPEN

BOSTON UNIVERSITY

The Department of Chemistry at Boston University invites applications from outstanding candidates for both a tenure-track and tenured position in the field of Organic Chemistry, broadly defined; one at the **ASSISTANT PROFESSOR** level and one at the **ASSOCIATE** or **FULL PROFESSOR** level starting July 1, 2015, pending Provost approval. Of particular interest for one of these positions is the general area of synthetic organic chemistry and catalysis including new reaction methodology development and/or asymmetric synthesis that may be combined with applications in natural product/bioactive molecule synthesis. The research focus of the second position will be in the area of organic materials including synthesis of novel biomaterials, polymers, optoelectronic, light-emitting, conductive, magnetic, or energy storage materials. The successful applicant will benefit from the department's supportive and collegial environment, which includes faculty possessing a wide range of complementary expertise including biochemistry and synthetic organic chemistry. The candidate will also interact closely with the Chemistry Department's Center for Chemical Methodology and Library Development (CMLD-BU, **website: http://cmld.bu.edu**) and the Materials Science & Engineering Division and related initiatives. Undergraduate teaching responsibilities will be in the areas of organic chemistry and materials, with the opportunity to develop graduate courses in the candidate's area of expertise. Applicants should apply by submitting a letter of interest, including teaching and research objectives, and current Curriculum Vitae, and arrange to have three letters of reference sent by October 1, 2014 through **website: https://academicjobsonline.org/ajo/jobs/4317.** *We are an Equal Opportunity Employer and all qualified applicants will receive consideration for employment without regard to race, color, religion, sex, national origin, disability status, protected veteran status, or any other characteristic protected by law. We are a VEVRAA Federal Contractor. Women and minorities are especially encouraged to apply.*

MATERIALS CHEMISTRY Dartmouth College Hanover, New Hampshire

The Department of Chemistry at Dartmouth College is seeking an outstanding applicant for an open rank (tenured or tenure-track) faculty position in Materials Chemistry starting July 2015. We seek candidates interested in making, measuring, and/or modeling materials, broadly defined including polymers, nanomaterials, surfaces/interfaces, and molecular sensors and machines. Candidates who will help lead, initiate, and participate in collaborative research projects within Chemistry as well as Dartmouth's Thayer School of Engineering and Geisel School of Medicine are particularly encouraged to apply. Teaching responsibilities will include participation in the undergraduate curriculum and advanced/graduate courses in their area of specialty. The department (**website: http://www.dartmouth.edu/~chem/**) is home to 17 tenured and tenure-track faculty with strong Ph.D. and M.S. programs and affiliated with Dartmouth's M.D.-Ph.D. program. Dartmouth College, a member of the Ivy League, is located in Hanover, New Hampshire (on the Vermont border). Dartmouth has a beautiful, historic campus, located in a scenic area on the Connecticut River. Recreational opportunities abound in all four seasons.

Applicants should submit curriculum vitae, a description of their research (funding and future plans), a statement of their teaching interests, and at least three reference letters (tenure-track) or names of three references (senior candidates). All inquiries and applications will be treated confidentially. Application materials should be submitted to **website: http://apply.interfolio.com/25556.** Applications received by October 1 will receive first consideration. *Dartmouth is an Equal Opportunity/Affirmative Action Employer with a strong commitment to diversity. In that spirit, we are particularly interested in receiving applications from a broad spectrum of people, including women, persons of color, persons with disabilities, veterans, or any other legally protected group.*

POSITIONS OPEN

FULL PROFESSOR Chemical Biology; Bioanalytical Chemistry TENURE-TRACK ASSISTANT PROFESSOR Chemical Biology; Structural Biology; Molecular Biophysics Indiana University, Bloomington

The Department of Chemistry at Indiana University invites applications for two positions: Full Professor and Tenure-track Assistant Professor, in chemical biology beginning August 2015. We are particularly interested in candidates with strong biomedical research interests including, but not limited to, cancer biology, who are interested in developing a strong partnership with the IU School of Medicine in Indianapolis. The search is open to all areas of chemical biology, from structural biology and molecular biophysics, to metabolic profiling and biomarker discovery, glycobiology, and bioanalytical chemistry. A Ph.D. in chemistry or a related field and postdoctoral experience are required. Successful candidates will be expected to have or develop a visible, externally funded research program. Primary teaching assignments will include graduate courses in chemical biology and undergraduate chemistry or biochemistry. Successful candidates will be named a trainer in our NIH-funded graduate training program in Quantitative and Chemical Biology at Indiana University (**website: http://www.chem.indiana.edu/qcb/**). Applications completed by October 15, 2014 will receive full consideration, but the review will continue until the position is filled. Interested candidates should review the application requirements and submit a complete curriculum vitae, a summary of future research plans, and arrange to have four letters of recommendation at **website: https://indiana.peopleadmin.com.** Questions regarding the position or application process can be directed to: **Professor Nicola L.B. Pohl, Chair, Faculty Search Committee, Department of Chemistry, Indiana University, 800 E. Kirkwood Avenue, Bloomington, IN 47405, e-mail: chemchair@indiana.edu.** *Indiana University is an Affirmative Action/Equal Opportunity Employer and especially encourages applications from women and members of minority groups.*

Tianjin University School of Pharmaceutical Science & Technology (SPST)
LOOKING TO BE THE FACE OF CHANGE ?

Have a look at the new international perspective of SPST. We are only wrapping up our first year of internationalization and just look at the faces of the people who have already joined our team for change.

Tianjin University (TJU) – School of Pharmaceutical Science and Technology (SPST) is building a world-class school of basic medical science comprising global talent, a cosmopolitan environment and state-of-the-art infrastructure. After a very successful 1st recruitment Symposium on Future Directions in Modern Pharmaceutical Science, SPST announces a call for faculty applications to participate in our 2nd recruitment Symposium.

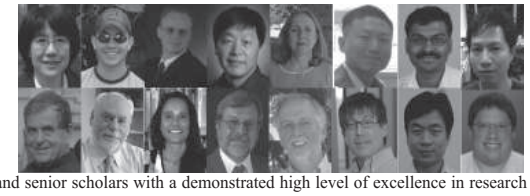

We seek junior and senior scholars with a demonstrated high level of excellence in research and dedication to teaching in English, to help build two major platforms: the **Institute of Drug Innovation and Development**; and, the **Institute for Molecular Design and Synthesis**.

Outstanding talent in all areas of pharmacy and basic medical science are sought (e.g., pharmaceutics, pharmacology and toxicology, structural biochemistry, chemical biology, biochemical engineering, pharmaceutical process, analytics, and formulation, pharma economics, bioinformatics, regulatory science, public health policy, computational chemistry and biology, and material science).

SPST is a signal program of the new Tianjin campus development plan, housed in building 24 of the main Tianjin campus and outfitted for the highest international standard of modern research.

The program will be run in English for research, teaching and internal administrative activities. Student recruitment at the graduate (MS and PhD) level will be internationally competitive; the undergraduate program will provide top class instruction in English and a broad-based liberal education experience accessible to an international and Chinese student body.

Does this progressive and forward looking development interest you? Can you see yourself as a productive member/partner of the team that will realize this vision? Do you know an investigator who meets the high standards TJU desires? Then contact us at infospst@tju.edu.cn

For full consideration, please submit before **October 15, 2014**, a current cv with personal references, a list of publications, a summary of research directions (2-3 pages), a statement of teaching interest (1 page) and up to 3 exemplary publications as a **single pdf file** [*LASTNAME_firstname_SPST_candidate.pdf*]

Competitive candidates will be invited by early November to participate in SPST's *Symposium on Directions in Modern Pharmaceutical Science December 3-6 2014.*

TJU-SPST is looking to find talent ready to change the landscape of higher education in China. Are you ready to be an element of change?

Job Vacancies in China's Universities

赛尔互联 CERNET

Science Careers
From the journal *Science* AAAS

赛尔互联：《科学》在中国大陆高校人才引进服务独家合作伙伴
CER is Science's exclusive agent for recruitment advertisement service in mainland China universities and colleges

China's Rapid Development
—— More Opportunities

- **South China University of Technology** (Shenzhen, China)
  DeanPositions offered: The School of Mathematics, The School of Physics and Optoelectronics, and The School of Electronic and Information Engineering.
- **Jiangsu University** (Jiangsu, China)
  SearchingTalents for following disciplines: Mechanical Engineering/ Environmental Science and Engineering/Computer Science and Technology/Chemistry/ Basic Medical/ Fine Arts...
- **Beijing Institute of Technology** (Beijing, China)
  Open Senior Faculty Positions offered: Equipment Science & Technology Engineering/ Mechanical Engineering/ Information and Communication Engineering/ Mathematics...
- **Xi' an Jiaotong University** (Xi' an, China)
  Faculty positions offered in the Joint School of Sustainable Development (JSSD) of Sustainable Energy, Sustainable Materials and Sustainable Systems.

For more details, visit http://www.eol.cn/

广告联系：赵佳 zhaojia@cernet.com +86 10 62603373

eol 中国教育在线 www.eol.cn 是赛尔互联旗下品牌

Faculty Positions Available at The Institute for Advanced Studies (IAS) and The Medical Research Institute (MRI), Wuhan University, Wuhan, China

武漢大学

Faculty Positions

Two newly founded institutes at Wuhan University in China, the Institute for Advanced Studies (IAS) and the Medical Research Institute (MRI), cordially invite applications for ~50 each, open-rank faculty positions in Biology, Chemistry, Physics, Material Sciences, and Medical Sciences.

All applicants must have a Ph. D or MD and a successful postdoctoral experience. Successful candidates will be expected to establish an active research program in relevant disciplines. We offer internationally competitive recruitment packages.

The applicants should submit, electronically, a full CV, a research statement and contact information of three referees in a single PDF file to wdgyy@whu.edu.cn (for IAS positions) or shuoffice@whu.edu.cn (for MRI positions).

Applications that apply for both institutes at the same time will not be accepted and further processed.

http://hr.whu.edu.cn/